The University Of Sheffield.

Department Of Mechanical Engineering

INVESTIGATION AND CHARACTERISATION OF THE WEAR MECHANISMS OF ABRADABLE COMPRESSOR LININGS

Nicola Fois

Thesis submitted for the Degree of Doctor of Philosophy

Abstract

During aero-engine operation, rotor misalignment, thermal and centrifugal dilatations, and unbalanced parts lead to contact between the rotating blade and the abradable lining of the surrounding casing. Observation of aero-engine service has highlighted undesirable issues and relative wear mechanisms that have created problems during operation, with significant reductions in aero-engine performance. Examples of issues observed were adhesive transfer of abradable material to the blade tip, along with blade wear. These observations have highlighted the final result of the contact between the blade and abradable; however, the complexity of introducing instruments to the aero-engine has led to a gap in knowledge with respect to the parameters that influence these wear mechanisms. This issue has provided the motivation for this research, where wear mechanism between a Ti-6Al-4V rotating blade and abradable material AlSi-hBN has been investigated on a scaled test platform. AlSi-hBN has been chosen as it represents the most common technology used in the compressor stage of the engine. Alternative approaches that characterised the wear mechanism in real time were introduced in order to try to explore the nature of the contact. The introduction of an innovative stroboscopic imaging technique allowed the progression of adhesive transfer / blade wear to be investigated in real time during a test, revealing that the standard practice of performing analysis of adhered material at the end of a test does not necessarily characterise the overall mechanics of adhesive transfer satisfactorily. In addition, the measurement of contact force and the calculation of the efficiency of cut and force ratio, highlighted different material behaviour in relation to the incursion rate and hardness. It was shown that it was difficult to dislocate the material at low incursion rate, with consolidation evident, whereas at higher incursion rates the material was well fractured. The measurement of the coating temperature highlighted the heat generated in the contact, along with the effect of changing coating hardness on the thermal properties of the abradable, leading to markedly different thermal behaviour at low hardness, and in particular at low incursion rate. The wear mechanisms observed, adhesive transfer, blade wear and cutting, were mainly incursion rate dependent, with a thermal wear mechanism at low incursion rate and a well cut mechanism at high incursion rate. At low incursion rate, different wear mechanisms

were observed in relation to the hardness, with adhesive transfer on the blade tip from the hard coating and blade wear in the test performed against the soft coating, with similar results observed at all blade speeds. A wear map was generated in relation to the input parameters, such as the incursion rate, speed and coating hardness, and also the reflected different thermal properties of the coating. This indicated that it is better to have a high thermally conductivity coating; therefore, the use of a hard AlSi-hBN is a better option, because less thermal damage was observed. The wear map with the highlighted wear regimes is a useful design tool with respect to planning running and handling manoeuvres for the engine, where the manufacturer has the option to control incursion parameters. As these represent the most significant incursion performed, this finding is of particular benefit.

Acknowledgements

A Lisha, mamma, papá and Stefano.

I wish to express my gratitude to my supervisor Dr. Matthew Marshall for his guidance, advice and support throughout my studies. I am also grateful to Dr. Jonathan Stringer for his guidance, time and continue support at the start of my studies.

Also, I wish to express my gratitude to my industrial sponsor, Rolls Royce Plc, and all group of Surface Engineering, in particular a sincere thank you to John T. Gent for his guidance and his industrial support. Additionally, my sincere thanks also go to Glen Pattinson for his industrial support, and also to Lloyd Pallet. Furthermore my sincere thanks to Michael Taylor who thermally sprayed the samples for my studies.

I also place on record, my sense of gratitude to one and all, who directly or indirectly, have supported me in these studies.

Table of Contents

Nomenclature and Symbols

AlSi-polyester		Aluminium Silicon Polyester
AlSi-hBN		Aluminium Silicon hexagonal Boron Nitride
AlSi		Aluminium Silicon
hBN		Hexagonal Boron Nitride
Ti-6Al-4V		Titanium 6 wt% Aluminium 4 wt% Vanadium
NiCrAl		Nickel Chrome Aluminium
PLC		Programmable Logic Controller
SANS		Small angle neutron scattering
SEM		Scanning electron microscope
$t_{1/2}$	[s]	Time to reach half of the maximum temperature
s	[m]	Sample thickness
α	[m^2 s^{-1}]	Thermal diffusivity
M 320		Metco 320 (AlSi-hBN)
IP		Intermediate pressure
HP		High pressure
R15Y		Rockwell 15Y Hardness
Al_2O_3		Aluminium oxide
V	[m s^{-1}]	Blade impact speed

I_p	[µm pass^{-1}]	Incursion per pass
I_s	[µm s^{-1}]	Incursion speed
R	[m]	Rotor radius at blade tip
$L(t)$	[m]	Theoretical Rub Length
t	[s]	Time
EDXRF		Energy dispersive X-ray fluorescence
FRF		Frequency response function
FRF(jω)		Fourier transform of the frequency response function
FFT		Fast Fourier Transform
F(jω)		Fourier transform of the dynamometer signal
H(jω)		Fourier transform of input impulse
$[FRF]^H$		Hermiatian matrix of the FRF
$\{F_{dyno}\}$		Fourier transform of dynamometer signal (matrix)
$\{F_{compensated}\}$		Fourier transform of signal compensated (matrix)
{B}		Matrix for support calculation
{A}		Matrix for support calculation
$\overline{FRF}$		Conjugate of FRF
$F_{dyno}(j\omega)$		Fourier transform of the dynamometer signal
M_i	[kg]	Inertia mass matrix

a	[m s^{-2}]	Acceleration of the system
$F_{compensated\ accelerometric}$		Accelerometric force compensation
$F_{compensated}$		Force compensated with FRF
M	[kg]	Plate mass
C	[N s m^{-1}]	Damping coefficient
K	[N m^{-1}]	Stiffness
x_1	[m]	Displacement of plate
$\dot{x}_1$	[m s^{-1}]	Velocity of plate
$\ddot{x}_1$	[m s^{-2}]	Acceleration of the plate
x_2	[m]	Displacement of base plate
$\dot{x}_2$	[m s^{-1}]	Velocity of base plate
$\ddot{x}_2$	[m s^{-2}]	Acceleration of the plate
$X_{free\text{-}vibration}$	[m]	Displacement of the free-vibration
X_0	[m]	Static displacement
ζ		Damping factor
ω_n	[rad s^{-1}]	Natural frequency of vibration
φ	[rad]	Phase of the displacement
X_{forced}	[m]	Displacement of the forced phase
X_{20}	[m]	Static displacement
Ω	[rad s^{-1}]	Frequency of force
φ_1	[rad]	Phase of displacement 1

$A_{0\text{-}1,2,3,4,5}$	[m^2]	Area underlying the initial blade length
$A_{1,2,3,4,}$	[m^2]	Area underlying the blade profile after the test
S	[m]	Variable value of rub length
E	[m]	Variable value of rub length
p_1	[mm m^{-1}]	Fitting coefficient
p_2	[mm m^{-1}]	Fitting coefficient
R^2		Coefficient of determination
n		The number of points analysed
f_i		Interpolation data
SS_{tot}		Total sum of squares
SS_{res}		Total sum of squares of residual
F_i	[N]	Force at defined incursion rate
F_{normal}	[N]	Average normal force
$F_{tangential}$	[N]	Average tangential force
F_i/I_{pass}	[N pass μm^{-1}]	Force per unit of incursion rate
Pe		Peclet number
$V_{in\ feed}$	[m s^{-1}]	Velocity of in feed
$Pe_{modified}$		Modified Peclet number
$(C_p)_{blade}$	[J kg^{-1} K^{-1}]	Specific heat capacity of the blade
$(\rho)_{blade}$	[kg m^{-3}]	Density blade

$(\lambda)_{blade}$	[W m^{-1} K^{-1}]	Thermal conductivity blade
$(C_p)_{coating}$	[J kg^{-1} K^{-1}]	Specific heat capacity of the coating
$(\rho)_{coating}$	[kg m^{-3}]	Density coating
$(\lambda)_{coating}$	[W m^{-1} K^{-1}]	Thermal conductivity coating

List of Figures

List of Tables

1. Introduction

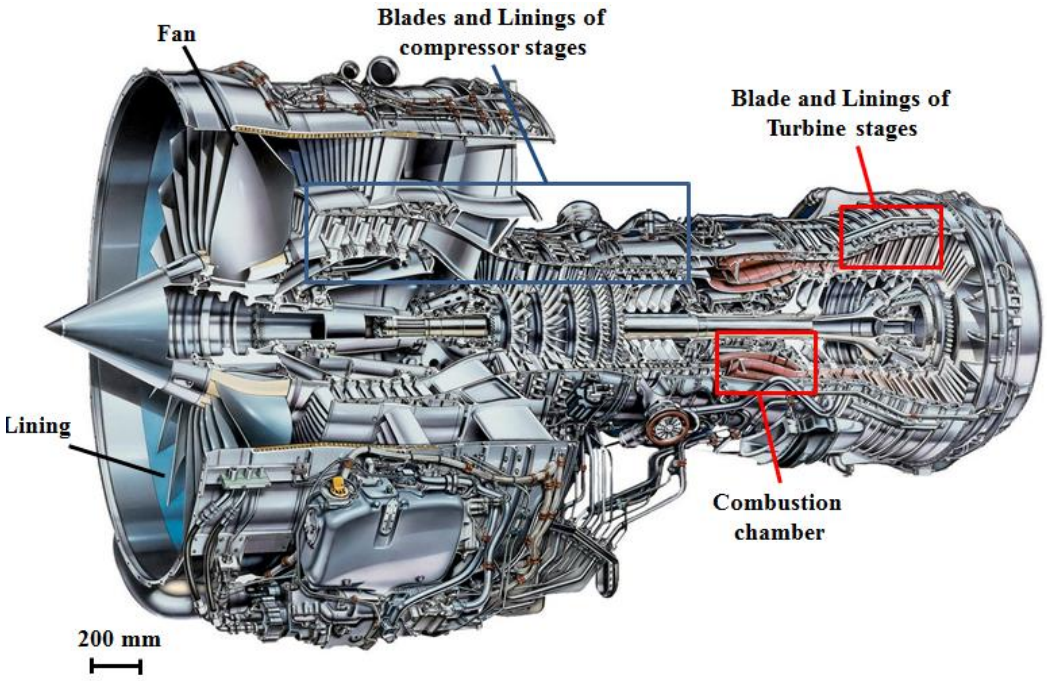

Figure 1.1. Aero-engine with highlighted compressor and turbine blades and corresponding linings (Image provided by Rolls Royce Surface Engineering Group).

The aero-engine, as shown in Figure 1.1, is composed of a fan, compressor stages, combustion chamber and turbine stages. Abradable materials have been used as linings for the casing wall for about the last 50 years. Abradable linings allow tip clearances between the rotating blades and the casing wall to be minimised. This helps to obtain improvements in efficiency and stall margin, and also reduces fuel consumption.

During engine operation, rotor misalignment, thermal and centrifugal dilatations, and unbalanced parts can cause the rotating blades to strike the wall of the surrounding casing. Introducing an abradable material that is characterised by good abradability and erosion resistance improves the efficiency of an aero-engine, as the coating will wear in preference to the blade, which will result in only a local clearance increase. Otherwise, without an abradable material present on the casing wall, the blade tip will wear, resulting in an overall increase in clearance and an overall decrease in performance. Previous investigations analysed the abradable material's wear mechanisms with different approaches. Typically these involved experimental analyses, where the wear mechanics were reproduced with an experimental platform or test, although in some cases analytical models were developed. In this study, the wear mechanisms of abradable linings were analysed and investigated using a scaled experimental test platform capable of reproducing the wear mechanism observed in aero-engines. Additionally, a series of techniques were developed, capable of recording the dynamic response during the contact, in order to understand the nature of the mechanism. Finally, a wear map was generated in relation to the key parameters, in order to understand and analyse the different wear mechanisms; and this wear map could be used to influence the design of the abradable material. This chapter presents an overview of abradable linings, with their basic function, property, composition and wear mechanics detailed.

1.1. Abradable material

Abradable materials are composite materials [1-6], used in, for example, rotor path linings, low, intermediate and high pressure compressor seals and high pressure turbine seals. These materials minimise the blade tip clearances, which improves the efficiency of the aero-engine and increases the stall margins of the compressor. Compressor stall is a particularly bad occurrence, which should be avoided as it generates a periodic stress on the blade that can lead to fatigue failure. The use of abradable materials increases the efficiency and minimises the fuel consumption of the aero-engine, resulting in a fuel cost saving. Figure 1.2 shows a schematic of the system, with a section of a compressor stage showing the location of the abradable seal. A typical sealing system, with an un-shrouded blade, is where the blade tip cuts directly into an abradable material counterpart that is attached to a fan, compressor or

turbine casing. The un-shrouded blade has significant savings in terms of efficiency and maintenance, because it weighs less and is subjected to low centrifugal stresses on the blade [7].

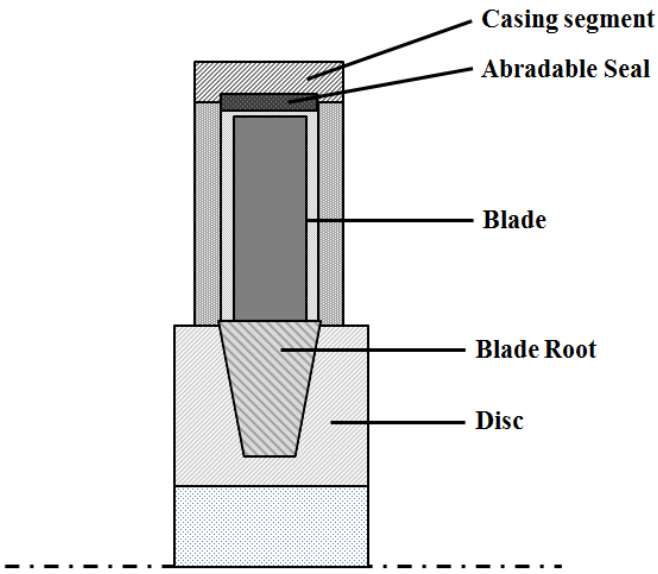

Figure 1.2. Cross-section of a compressor stage showing the rotating blade and the location of the abradable seal.

During aero-engine operation, contact between the rotating blade and the coating of the casing is a consequence of misalignment, thermal and centrifugal dilations and unbalanced parts, common in flight phase, with low incursion of the blade on the coating at every pass [8]. A high incursion interaction of the blade every pass represents the running and handling phase of the jet engine [9, 10]. This phase [9] is made using an abradable material removal tool, consisting of a blade with a curved profile that can be positioned between adjacent leading and trailing blades, to remove the abradable material in order to follow the contour / curvature of the blade housing and improve the sealing. Before the use of abradable materials, when the rotating blades impinged the inner wall of the casing linings, wear occurred on the blade tips, generating an overall clearance increase between the blade tips and the inner wall, with a decrease of efficiency due to fluid leakage around the aerofoil. With the introduction of the abradable material, the wear location was changed and it occurred locally on the abradable lining, thus avoiding a significant leakage increase or reduction in performance [3]. Figure 1.3 shows a schematic rotor with blades shrouded by a casing. The figure highlights the evolution of rotor clearance during

the rub interaction: in the first case where an abradable material was used, and in the second case without an abradable material. The figure highlights three phases: pre-rubbing (Figure 1.3a), interaction (Figure 1.3b), and clearance after rub interaction (Figure 1.3c).

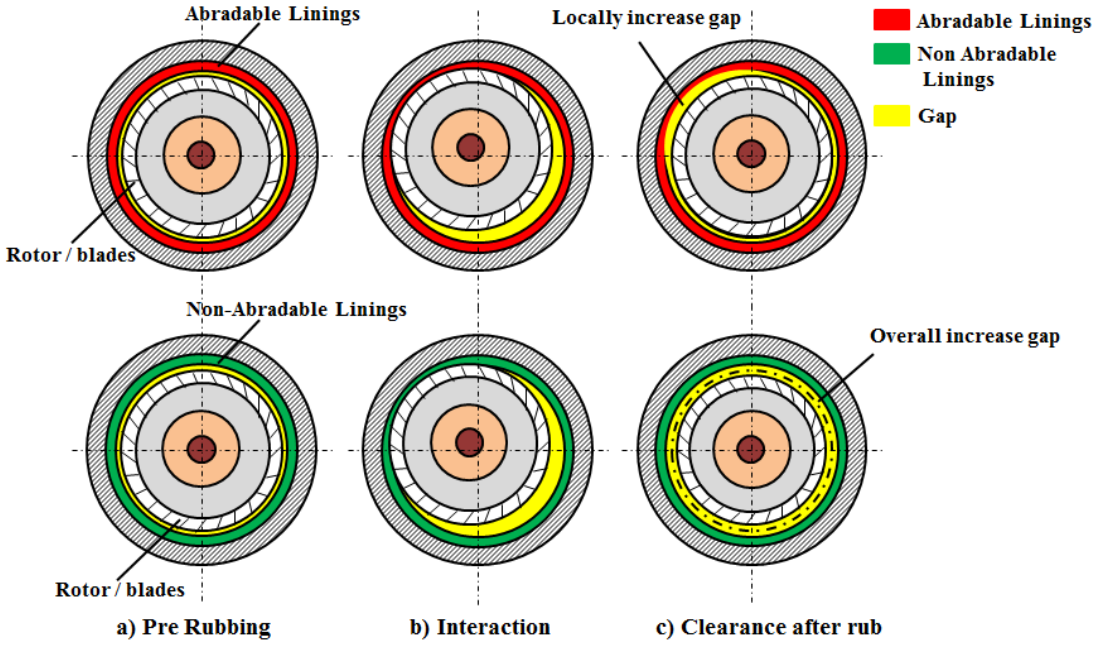

Figure 1.3. Evolution of rotor clearance during the rub interaction in three phases: a) Pre-rubbing; b) Rub interaction; c) Clearance after rub interaction. Top: Ideal abradable interaction; Bottom: Non-abradable interaction.

In the case without an abradable material, a reduction of rotor diameter increased the clearance between the blade tip and the rotor, resulting in a decrease in performance and an increase in fuel consumption of the aero-engine.

1.2. Composition and working range

The abradable material is a composite material that needs to be 'soft' enough to have a good abradability, but also 'hard' enough to withstand the erosion force of the air flow at high speed, and be resistant to oxidation, corrosion and thermal failure. Typically, abradable materials are composed of three structural components [4-5]: a metal matrix, a solid lubricant and porosity. The metal matrix gives strength as well as oxidation and hot-corrosion resistance, while the pores or voids enable the energy from the blade incursion to be transferred to the metal matrix, fracturing the inter-particle bonds. The solid lubricant, also called the dislocator phase, is designed to

shear easily, and minimises the coating's transfer to the blade; it also reduces the size of the debris, ensuring that abradable debris is sufficiently small so as not to block cooling holes, cause erosion downstream or create problems in the combustion chamber. The ideal behaviour of the abradable material during the interaction between the rotating blade and the coating should be such as not to damage the blade, with wear localised on the abradable material and with the surface remaining smooth after the wear in order to reduce aerodynamic losses. The common roughness of the abradable material after service is around 600μm [6]. Figure 1.4 highlights the technology used for the abradable material and blade in relation to the temperature of operation of the compressor of the aero-engine.

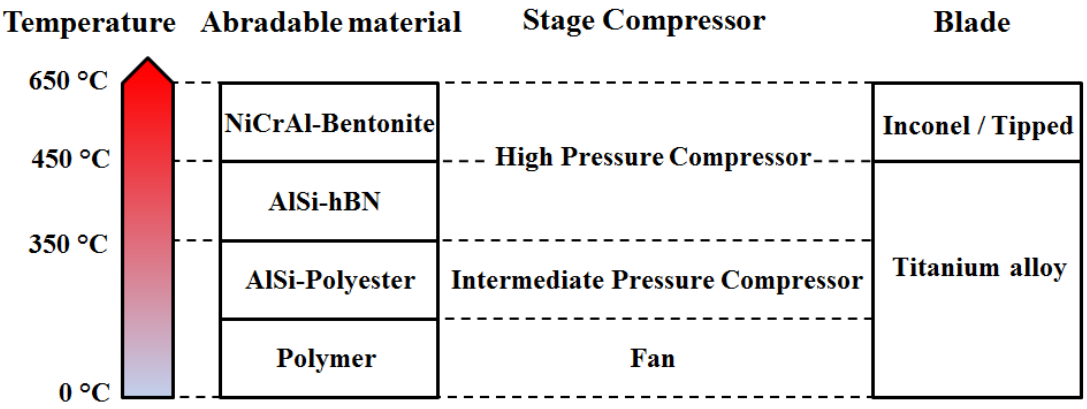

Figure 1.4. Technology of abradable material and respective blade in relation to the gas path temperature in an aero-engine compressor.

In the fan and intermediate pressure compressor, where the peak temperatures are around 350 °C, the most common abradable material is AlSi-polyester, in which the metal matrix is an aluminium alloy with a polyester dislocator phase which improves the abradability and helps to reduce the adhesive transfer to the blade tip [8]. For the intermediate and high pressure compressor, operating at higher temperatures up to 450 °C, the most common abradable coating used is AlSi-hBN [4], in which an aluminium alloy, Aluminium Silicon (AlSi), is the metal matrix and hexagonal boron nitride (hBN) is the solid lubricant phase. Figure 1.5 shows the microstructure of an abradable coating.

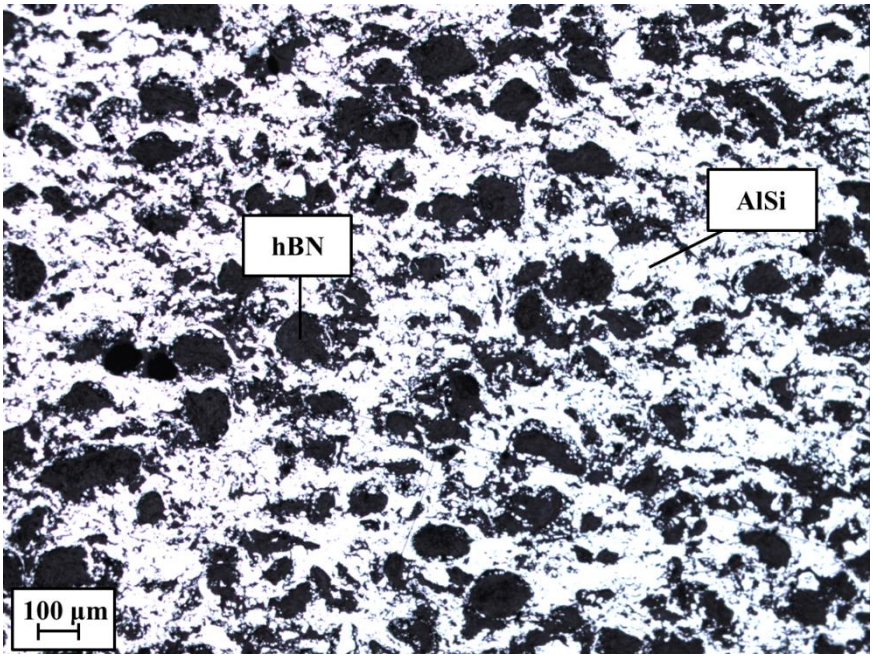

Figure 1.5. Microstructure of the AlSi-hBN coating.

The AlSi-hBN abradable coating is a suitable material for rubbing against titanium alloy blades; a typical alloy is Ti-6Al-4V [7, 11]. For higher temperature service above 900 °C, NiCrAl is the metallic phase and bentonite acts as the dislocator phase; it is used to disjoint the metallic phase and makes the coating sufficiently friable so that it can wear during rubbing against mainly nickel alloy blades. In the next section, the wear mechanics observed on aero-engines will be described.

1.3. Contact mechanics and wear mechanisms

Abradable materials such as AlSi-hBN [12, 13], which was analysed in this research and is the most common abradable coating in compressor stages [1-4], are thermally sprayed using a plasma gun [14]. Various parameters influence the thermal spray process and therefore the properties of the coating, which in turn influence the performance of the aero-engine, and will be explained in detail in Chapter 2. As highlighted in Section 1.1, during operation of an aero-engine the rotating blades make contact with the casing lining, and the introduction of an abradable material used on the inner wall of the surrounding casing improves the overall compressor efficiency. The abradable material should have a good abradability, but also a good erosion, oxidation, corrosion and thermal resistance. Therefore, depending on the contact conditions, different wear mechanisms are triggered. Observation of the

service data from the aero-engine highlights undesirable issues and relative wear mechanics that have created problems during operation, with an associated significant reduction of the aero-engine performance. An example of issues observed in aero-engines is the adhesive transfer of abradable material on the blade tip [6-7, 11, 15-17], occurring when heat generated during the contact is sufficient to melt the abradable material, transferring it to the blade and solidifying on it. Figure 1.6 shows the blade tip and the relative abradable surface when adhesive transfer was observed.

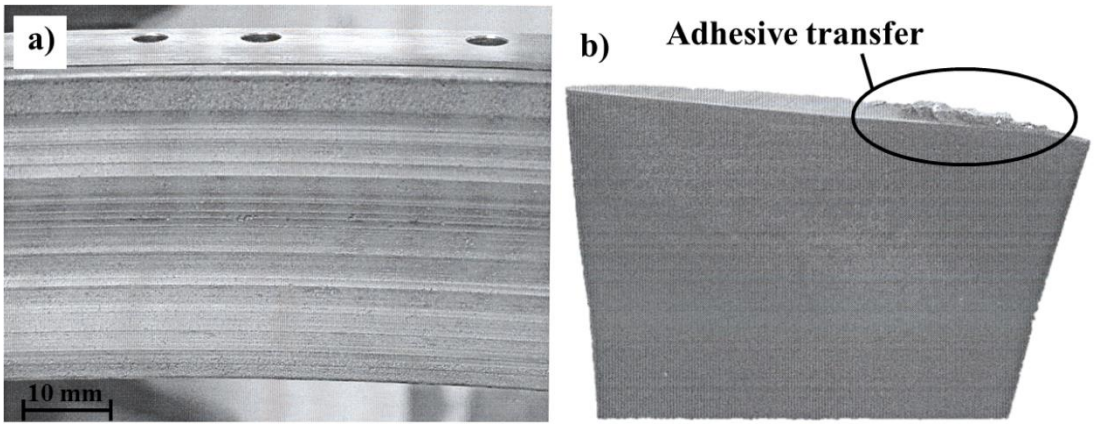

Figure 1.6. Adhesive transfer on an aero-engine: a) Grooving on the abradable surface; b) Adhesive pick up on the blade tip [17].

An adhesive transfer on the blade tip leads to a grooved surface on the coating, as shown in Figure 1.6a, with a reduction in aerodynamic performance and sealing efficiency. Also, the hard deposits of the material on the blade subsequently fracture off, generating small amounts of debris that could block the cooling holes of the combustion chamber or cause erosion. This wear mechanism is common in a light rub condition, during the climb stage of the flight cycle, where the rub contact is insufficient to cut or abrade the coating, but is enough to cause high friction in the contact and adhesive transfer. Additionally, a more problematic issue is when the overall clearance increases with blade wear due to overheating [6], with consequent air leakage and a drastic reduction in performance. Additionally, delamination of the coating or coating loss [16, 17] caused by poor bond strength of the coating, which is correlated to inadequate surface preparation in the spray process, increases the clearance gap considerably and the delaminated material could damage different parts of the engine with a catastrophic result. Figure 1.7 shows an example of a coating that had suffered from a delamination failure.

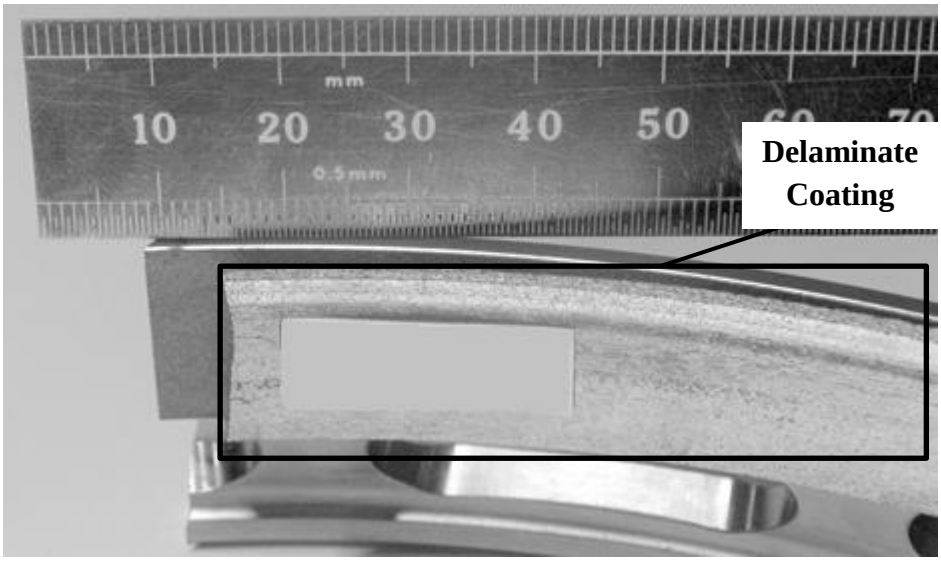

Figure 1.7. Abradable coating having suffered a delamination failure [17].

Furthermore, during the contact, plastic deformation of the coating [6] could form a striated surface as shown in Figure 1.8.

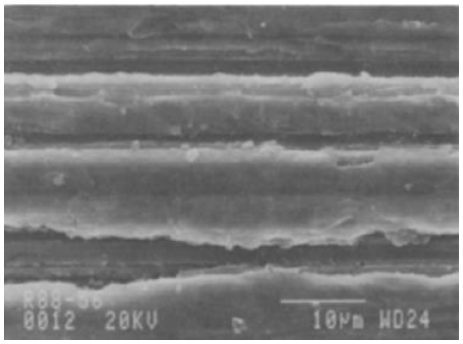

Figure 1.8. Microscope image of the striated surface of an AlSi-plastic coating subjected to deformation [6].

The plastic deformation is due to the blade rubbing on the surface instead of cutting, and plastically deforming the coating. As the incursion proceeds, the deformation can increase, leading to progressive hardening of the coating and this makes future interactions more violent.

Other failures of the abradable coating could occur without contact between blade and coating, for example: erosion, corrosion and thermal shock cracking [17]. Erosion, corrosion and oxidation are mechanisms detected without rub interaction. Erosion is caused by the gas stream and particles, often of sand and salt, which flow over the abradable surface. This mechanism is a less common failure mechanism and

is a consequence of the coating being sprayed too soft. Figure 1.9 shows an abradable coating which has suffered from erosion damage, with a dramatic effect on engine performance.

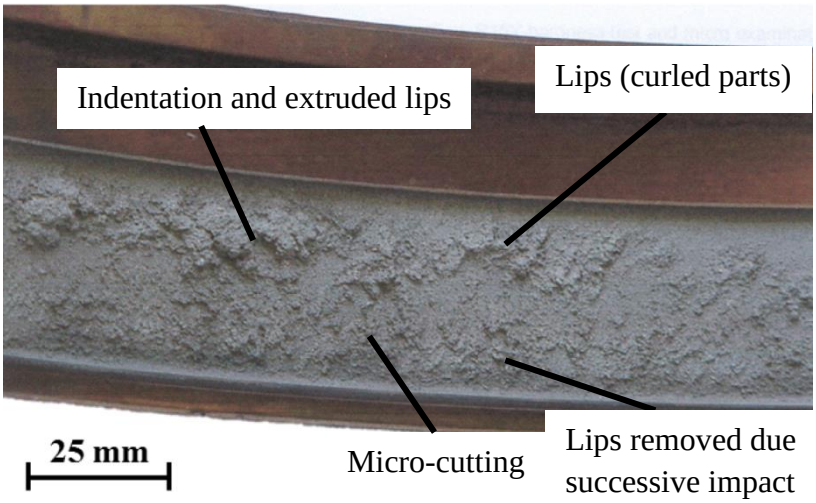

Figure 1.9. Erosion damage on abradable coating AlSi-graphite [17].

As shown in the figure, the coating has suffered from erosion due to the impact of abrasive particles. A normal impact of the abrasive particles produces indentations and extruded lips, where some lips fall off due to successive impacts. Additionally, abrasive particles that impact at a low angle generated micro-cutting and plowing traces and curled parts, and then successive impacts can easily break these deformed regions [17]. Corrosion of the abradable material happens when exposure to moisture generates a galvanic cell between the coating and the substrate. Advanced corrosion may result in delamination of the coating, with an increase of the blade gap. Thermal shock cracking can also be observed on the abradable surface [16, 17]: this is due to the difference of thermal expansion coefficients between the coating and the substrate. The engine cycle can generate a state of stress in the coating that leads to a crack on the surface which alters the clearance gap, and also to material loss with a dramatic effect on the engine. Observation of the abradable linings and blades from service [16, 17] highlighted different issues and problematic wear mechanisms where the abradable material did not work properly. Therefore, an abradable material should wear with a smooth surface, without blade tip damage and with no material transfer. This would provide desirable wear mechanism, where the blade tip acts as a cutting tool when it interacts with the abradable coating, with a smooth surface (below 200μm roughness R_a) and a shiny appearance of the rub surface.

The problems observed highlighted the need to understand the behaviour of the abradable material and to analyse and identify the reasons that lead to the undesirable mechanisms in order to improve the performance of the aero-engine. Observation of blade and abradable linings from service highlighted the final result of the contact, but the complexity and difficulties of applying instruments to the aero-engine led to a gap in knowledge between the influencing parameters and the wear mechanics output. Therefore, the need to understand the reasons and the influencing parameters that can lead to issues like adhesive transfer drove this research to reproduce the wear mechanics using an experimental test platform and to develop a series of experimental techniques in order to monitor the wear mechanics during the contact. Hence, this research presents an investigation of the wear mechanics of the abradable linings on a scaled test platform, and successive developments, including instrumentation capable of recording the dynamic response during the contact, were made in order to investigate the influencing factors behind each wear mechanism observed.

1.4. Project scope

The aim of this research is investigate the wear mechanism in an aero-engine between the rotating blade and the abradable coating at a macro-level, to develop a range of techniques capable of investigating transfer conditions during the contact and to understand the fundamental principles and influencing factors behind each macro-level wear mechanism observed. The wear mechanisms were therefore investigated on a scaled test platform, capable of recreating the wear mechanisms observed between rotating blade tips and abradable coating that occur in an aero-engine compressor. The research focuses on the wear mechanism of an Aluminium Silicon hexagonal Boron Nitride (AlSi-hBN) abradable coating and a titanium alloy (Ti-6Al-4V) blade, which is the most common technology, developed for the compressor stage, and is a point of interest of Rolls Royce Surface Engineering Group.

The objectives of the work were as follows:

- Identify the large scale wear mechanisms and key measurements and techniques required to investigate the abradable contact.

- Update an existing experimental test platform to include instrumentation capable of recording dynamic response during the contact.

- Characterise wear mechanics for a range of abradable conditions and material hardness and investigate the relative material response.

- Consider how the test inputs are linked to the wear mechanisms and how they could be connected to abrasion behaviour, and how the input parameters can be used to influence the material response, and therefore the wear mechanics.

1.5. Thesis layout

Chapter 1 gives an introduction to the research, with the focus on why aero-engines use abradable materials, their functionality, and the relative improvement obtained when these materials are used. Then the abradable material composition and the common technology used in the aero-engine compressor are discussed. Finally, the wear mechanism observed in the compressor after engine operation is highlighted. Additionally, the aim and the objectives of this research are presented.

Chapter 2 presents experimental analyses made previously on abradable materials. It is divided mainly into: experimental tests, to try to analyse and replicate the wear mechanisms and evaluate the abradability and erosion of the coating; material based tests, based on mechanical property, microstructure analysis, thermal analysis and material process to manufacture the abradable materials; and numerical modelling of the contact by numerical simulation of the contact mechanics.

Chapter 3 presents an observation of the sample material tested during the research, and also the experimental test platform and the instrumentation introduced in this study.

Chapter 4 presents the methodology of this research. Firstly the input parameters of the experimental test are presented. Then the test protocol of the experimental platform is introduced. Finally, the post-test analysis of the samples and the analysis during the contact are presented.

Chapter 5 presents the analysis of the test sample post-test, based on the visual analysis of the blade and coating, with identification of the different wear

mechanisms in relation to the input parameters, and a quantitative analysis based on blade length and weight change recorded before and after the test. Finally, a spectrometric analysis of the material transfer was made, in order to characterise the composition of the transferred material.

Chapter 6 introduces a novel approach for monitoring the wear mechanics during the test. A stroboscopic technique is used that is capable of investigating the nature of the blade tip strike, and the change of the blade tip length is monitored during a number of constant strikes.

Chapter 7 presents the measurement of the contact force, and also a relative analysis of the contact force.

Chapter 8 introduces an analysis of the material response based on a section of the material sample post-test. The coating temperature measurements during the contact and the thermal property analysis of the sample are also presented.

Chapter 9 presents a discussion where all results and techniques developed during this research are analysed in order to understand the influence of the input parameters on the abrasion behaviour.

Finally, conclusions and references are presented through Chapter 10 and 11 respectively.

2. Literature Review

In this chapter, the previous investigations on abradable coatings are presented. Previous investigations on abradable materials can be grouped into three main categories: experimental studies that try to replicate the wear mechanism and evaluate the abradability and erosion of the coating, material-based tests, and numerical modelling of the contact. The chapter will present the current studies as regards abradability results that have been obtained using a range of experimental platforms and the approaches taken in order to characterise the wear mechanisms, highlighting the positive and aspects and the relative limitations. The material

characterisations from material-based tests and studies using numerical models that simulated the contact between the blade and the abradable material will also be presented.

2.1. Testing of abradable materials

2.1.1. Abradability tests

One approach frequently followed is to investigate the different wear mechanisms experimentally in order to gather more information to support modelling activity.

Borel [6] analysed the wear mechanism observed in aero-engines from the interaction between the rotating blade and the abradable coating, with a focus on Aluminium Silicon polyester abradables. Using a full test rig to reproduce the wear mechanism, the aim was to understand the correlation between the structural parameters and the coating behaviour. This research generated a correlation between the coating roughness, blade weight variation and the relative wear mechanism, as shown in Figure 2.1.

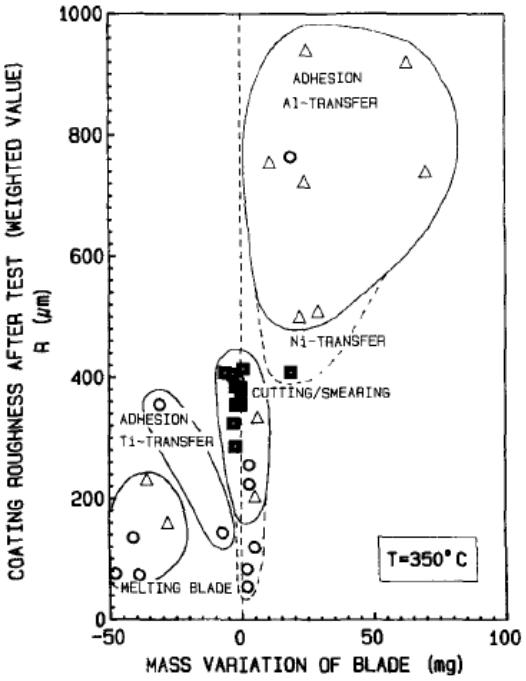

Figure 2.1. Coating roughness vs the weight blade variation for AlSi-plastic and Nickel-graphite [6].

Adhesive transfer was observed from the coating to the blade (aluminium transfer) with a very rough surface, and also transfer from the blade to the coating (titanium transfer). A cutting mechanism and melting blade were also highlighted. In this research the wear mechanisms were presented in relation to the blade impact speed and the incursion conditions, where major changes to the wear mechanism were highlighted at different incursion rates. At a low incursion rate, adhesive transfer was observed, and at a high incursion rate a cutting wear mechanism was observed, and when the speed increased the region of the cutting phase increased. Also the analysis of abradable samples with different plastic melting points highlighted different adhesive transfers. On the sample with lower plastic melting point with respect to the testing temperature of 350°C, an adhesive transfer was observed at almost all incursion rates. This indicated a correlation between the organic phase and the adhesive transfer from the coating to the blade. Additionally, the analysis generated a wear map that focused on the output of the different wear mechanisms observed, but with limited data points.

As highlighted in work by Borel [6], and Chapter 1, where aero-engine in-service issues were discussed, the main wear mechanisms were observed are known to be incursion rate dependent. At low incursion rats adhesive transfer from the coating to the blade tip was observed, with a grooved surface present on the abradable. With an increase of the incursion rate, a cutting mechanism was observed where the blade acted like a cutting tool, fracturing and removing the material. Experimental analysis of machining processes has provided a large body of research with respect to the interaction between tool and the workpiece, and the chip formation mechanics of this process. Of particular relevance are studies undertaken by Grzesik, Zorev, Shaw, Hofy and Iska [18 – 22] where the energy required to remove a unit volume of material are analysed. A low energy requirement was shown to represent a high efficiency of cut, with the material shearing effectively, while a high energy required represented poor chip formation.

Additionally, Sun, Astakhov and Grzesik [23 – 25] used the force ratio, namely the ratio between the tangential and normal contact forces, in order to evaluate the material behaviour. They highlighted that a low force ratio implied a deformation of the material, where the incursion of the tool is smaller than the minimum un-deformed chip, as illustrated in Figure 2.2a. With an increase of the incursion, the

tool starts to shear the material and generates a chip with some deformation of the material still occurring (Figure 2.2b). Once the incursion is higher than the un-deformed chip, a high force ratio prevails, and the entire depth of cut is removed as a chip (Figure 2.2c).

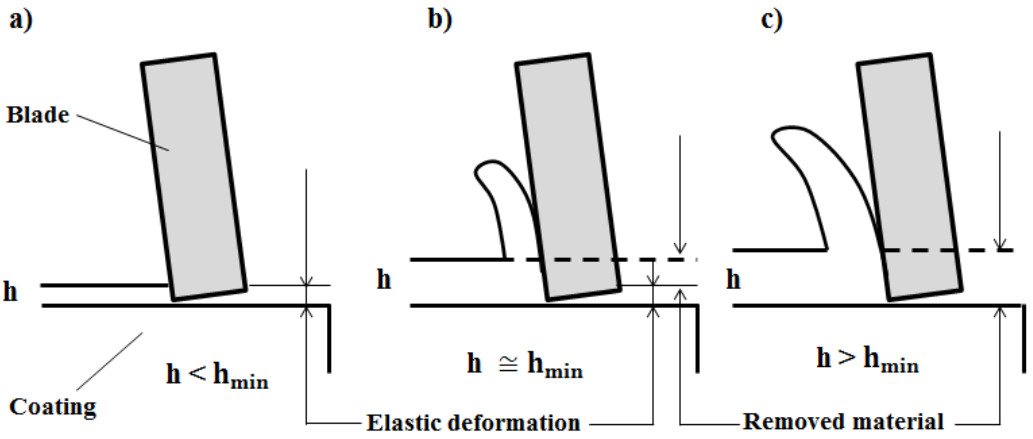

Figure 2.2. Schematic of chip formation: a) Elastic deformation; b) Elastic deformation and chip formation; c) Material removed.

These studies provide a useful approach to analyse cutting process, and therefore will be further investigated in the analysis of the blade/abradable contact made during this research.

In terms of experimental investigation of abradable materials, the investigations of Sporer and Wilson [3, 7] analysed different technologies of abradable material applied to the compressor stage and in the turbine stage, and the abradability of the coating was studied with a full scale test rig. From the test performed with an AlSi-hBN abradable sample, adhesive transfer that decreased with speed was observed at low incursion rate, and with an incursion rate higher than 50µm s^{-1}, a cutting mechanism was observed. Also, at an intermediate condition, blade wear was observed. In general, this research was based on the observation of samples and the blade wear was evaluated in percentage terms in relation to the total percentage of incursion depth as a function of different incursion speeds and blade impact speeds. Additionally, it highlighted a different erosion resistance in relation to the superficial hardness, but did not emphasise whether different hardnesses generated different wear mechanisms.

Also, the research conducted by Bounazef [15] used the same full-scale test rig as the previously mentioned research. Figure 2.3 shows the Sulzer Metco abradability test rig [3, 7, 11, 15] that reproduces the conditions observed in an aero-engine.

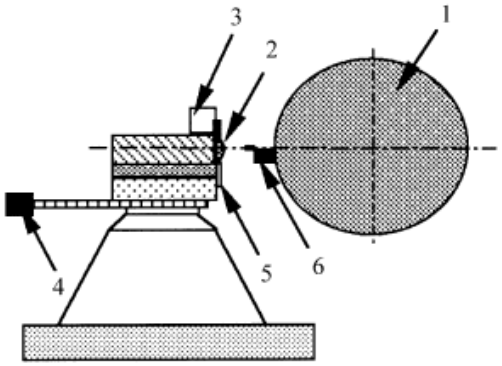

1 : Rotor

2 : Abradable material coating

3 : Thermocouple

4 : Electrical stepper motor

5 : Cutting force sensor

6 : Blade

Figure 2.3. Schematic picture of full test rig [15].

The study produced a wear map, which showed the change in length of the blade as a result of the incursion, and the percentage of material transfer. Figure 2.4 shows the transfer in relation to the incursion speed and the blade velocity, while Figure 2.5 shows a wear map where the different mechanisms are highlighted in relation to the same input parameter.

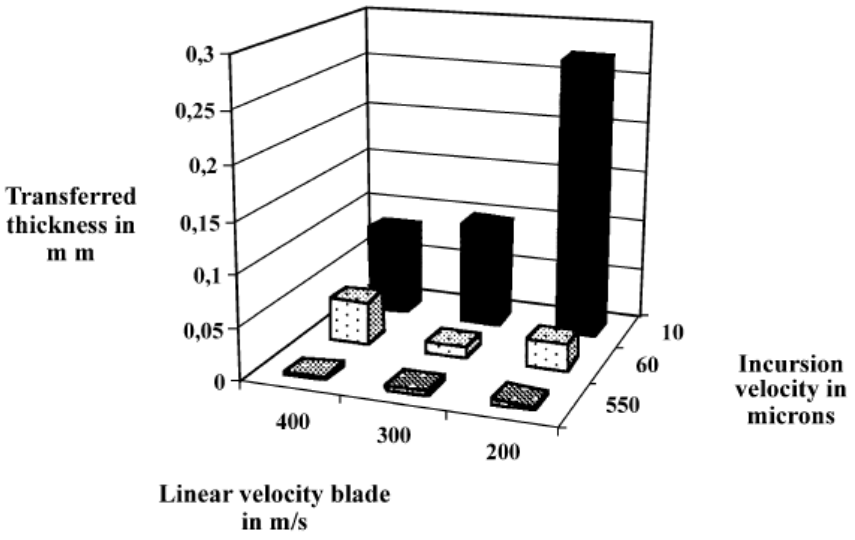

Figure 2.4. Wear map – transfer thickness in relation to the incursion and blade velocity [15].

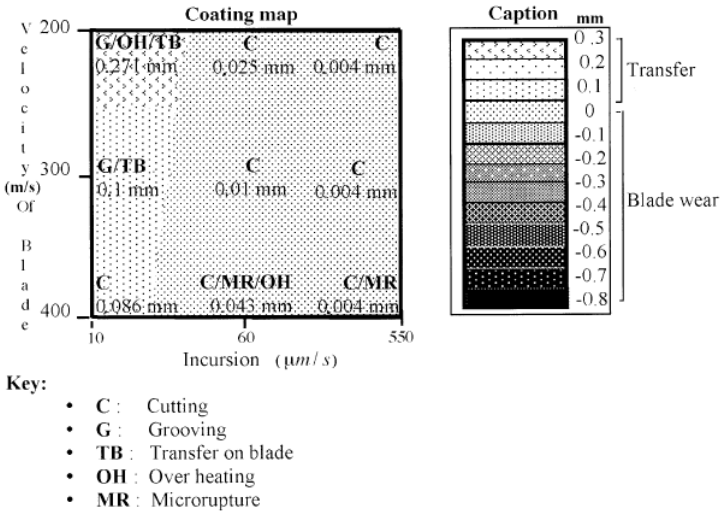

Figure 2.5. Wear map – different wear mechanism in relation of the incursion and blade velocity [15].

It was concluded that the material transfer was minimised by high blade speed and incursion velocities for AlSi-hBN abradable coatings, but the study failed to consider the nature of the adhesion and the manner in which it propagates, and therefore the wear map highlighted only a change of the blade from the condition recorded before and after the test. Also, a limited data set was analysed and with no insight into the transition of the wear mechanism, while other investigations with a similar test rig were focused on measuring the force of a blade strike as well as the temperature.

Therefore, Padova [26, 27, 28] in his research developed a full test rig, and focused on the analysis of the contact force presented for a range of incursion conditions between an Inconel blade and a steel casing and also with an abradable material. In this test rig, the interaction between the blade and the concave lining was initiated by a misalignment of the stator, while in the previous research a simplified contact between a rotating blade and a flat coating was used in order to analyse the contact. Figure 2.6 shows the experimental test rig with the stator, the rotor and an overview of the platform.

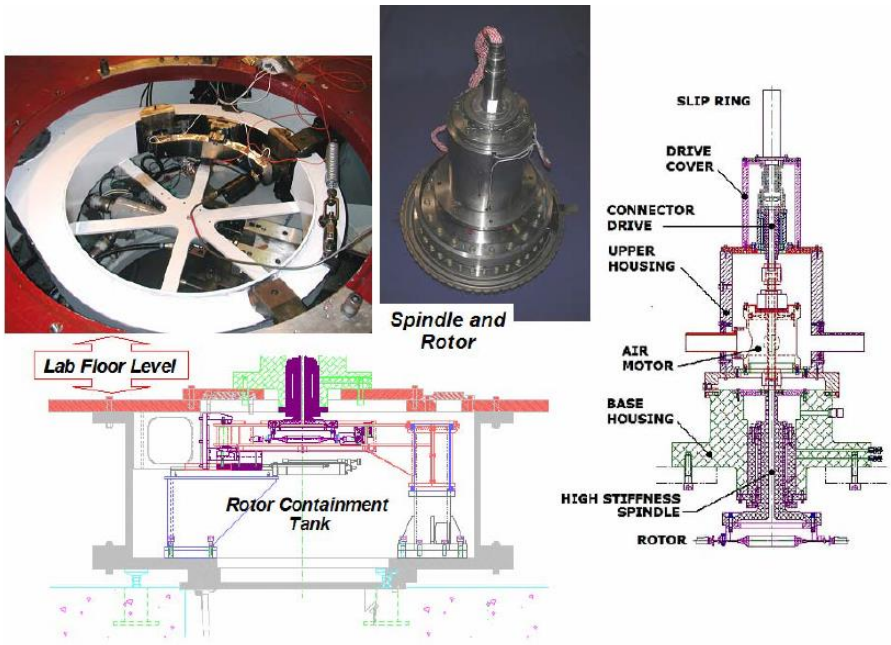

Figure 2.6. Experimental test platform [26].

During these studies the contact force, the temperature and the stress on the blade were measured. The study did not consider the resulting wear mechanisms and analysed the interaction between blade and coating or steel without specifying the abradable sample tested. The research was more focused on large incursion rates and analysis of the contact force. Therefore, a relation between the cutting force and the incursion rate was determined. The research highlighted a linear relationship between the load and the incursion rate for low interference between blade and coating, a non-linear transition region as the incursion rate increased, followed by an asymptotic region where load showed minimal increase with incursion rate. The influence of blade tip speed was also considered, and the study highlighted a decrease in the amount of material removed radially with a decrease of the blade speed, with a corresponding increase in the region where a linear relationship between incursion

rate and load was present. Also the introduction of a coating on the casing surface reduced the contact force and the blade stresses compared with the contact with an untreated steel casing; additionally, a dynamic analysis of the system was performed in order to calculate the contact force, and to remove the vibration component implied due to the large dimension of the stator where the dynamometer was located. However, overall the data set was relatively small, and the force measurements were not linked to wear, meaning that little insight was attained into the behaviour of abradable materials.

The study by Baiz [29] analysed the dynamic contact and the wear between a flexible blade and abradable coating. Figure 2.7 shows the experimental test rig used in the research.

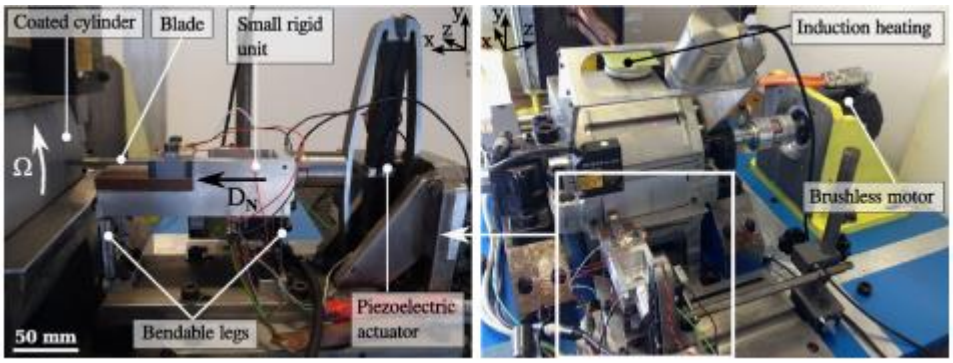

Figure 2.7. Experimental test rig with different views and the instrumentations [29, 30].

The piezoelectric actuator incurred the flexible blade on a coated cylinder, and different parameters, such as incursion speed, number of blade contacts, seal geometry and material removal, normal force and blade displacement, were monitored using high speed videography and force transducers, with the aim of monitoring the interaction between the blade and the abradable seal. This study highlighted the influence of the incursion depth and incursion speed on the amplitude of blade deflection. The study also showed that surface roughness influenced the degree of the blade deflection. Whilst providing a useful insight, the results were limited by the very low blade tip speed (19m s^{-1}) at which tests were performed. Therefore, Mandard's study [30] was performed at a blade speed of 92m s^{-1} where the contact forces were measured and also estimated from indirect measurement. The force was correlated with the wear profile of the abradable seal, where wear lobes were in phase with the estimated force. But overall the data set was relatively small

and the convex design of the abradable linings was the opposite of aero-engine representative concave contact geometries.

The research conducted by Ahrens [31] evaluated the contact force during the rubbing phase, and also the relation with friction and the dependence on rotating speed. This research highlighted that the friction coefficient depends not only on sliding speed but also on the load; the amount of data was relatively small, but otherwise a useful insight to the dynamic analysis of the force signal was performed.

A different application of the analysis of cutting force was made in Sutter's research [32]. Sutter used an experimental pneumatic gun in order to achieve high speed orthogonal cutting, which simulated the contact between the blade and the coating in an impact test. The study analysed the cutting force against test parameters such as the velocity of impact. A proportional increase of the force was measured with the increase of interaction depth, and also an increase of the edge of the blade increased the force, highlighting the influence of the blade tip geometry on the applied interaction. Unfortunately, this meant that the study was unable to consider the cyclic nature of an abrasion and the heat generated.

In the study conducted by Laverty [33], the rub mechanism and rub energy was studied between rotating blade and a fibermetal lining, in relation to incursion rate, blade speeds, incursion depth, blade thickness, blade material (nickel and titanium alloys) and number of blades. A regression analysis of the data was performed between rub energy and independent wear variables, and analysed and compared in terms of regression coefficient. In this analysis, the incursion rate was found to be the most important parameter influencing the rub energy and the wear mechanism, while blade speed and blade thickness showed moderate influence and the incursion depth had a low effect. Otherwise, change in blade material did not produce significant change in wear mechanism in the contact with the fibermetal; additionally the testing with multiple blades produced higher total rub energy than the test performed with a single blade, with reduction of the heat load per blade, but the wear results were not significantly different.

Overall, in this research, the complexity of the test rig led to small data sets and issues with the level of instrumentation that could be successfully applied; also the wear mechanism was characterised only from assessment of the change of blade

length and weight before and after the test without highlighting the nature of the mechanism.

2.1.2. Wear rate – scratch testing

Alternative analyses concerning abradability have focused on wear rate [34, 35], defined as the volume lost from the wearing surface per unit sliding distance. The wear rate depends on different parameters such as normal load, the sliding speed, the initial temperature, as well as the thermal, mechanical, and chemical properties of the materials in contact. Due to the influence of all of these parameters on the wear mechanics, it is often difficult to predict the wear rate. In the research done by Maozhong Yi [36], in order to analyse the relationship between sliding wear volume and the load and hardness of the coating, a pin on disc testing method was used. This showed that the abradability decreases when the hardness of the coating is increased. Also, scratch testing was used [37], where a sharp tip was drawn across the coated surface under constant, incremental or progressive load. Indeed the test showed that abradability and progressive abradability hardness (PAH), namely energy per unit of volume of material abraded, had dependence on the test conditions. Specifically, it was found that abradability and PAH changed with groove length due to densification ahead of the slider. Therefore, when the groove length and indentation depth increased, this implied that more material needed to be abraded requiring a greater energy input, and therefore an increased scratching resistance was recorded due to the densification through compression of the soft abradable. But overall, the work did not reproduce the condition of the contact between the blade tip and the coating and it is still inconclusive as to how well the results correlate to actual abradable performance.

2.1.3. Erosion resistance

Another area of focus for testing is the erosion resistance of the abradable material. Abradable materials need to be ‘soft’ enough to have a good abradability, but also ‘hard’ enough to withstand the erosion force of the air flow at high speed and also from solid particles present in the flow. Therefore, erosion resistance represents an essential property that abradable coatings need to have in order to avoid erosion damage during engine operation. The erosion resistance is obtained in accordance with the specification GE E50TF121CL-A [38], and expressed by an erosion number

as a function of the test time and the depth of erosion [39]. The erosion number is expressed in s mil^{-1} and represents the time in seconds necessary to erode 25.4μm of the coating thickness. A higher erosion number means better erosion resistance, and research has established that the erosion limit of 2s mil^{-1} represents the lower acceptable limit for abradable coatings [13, 40]. Figure 2.8 shows the erosion number for different abradable materials in relation to the hardness of the coating.

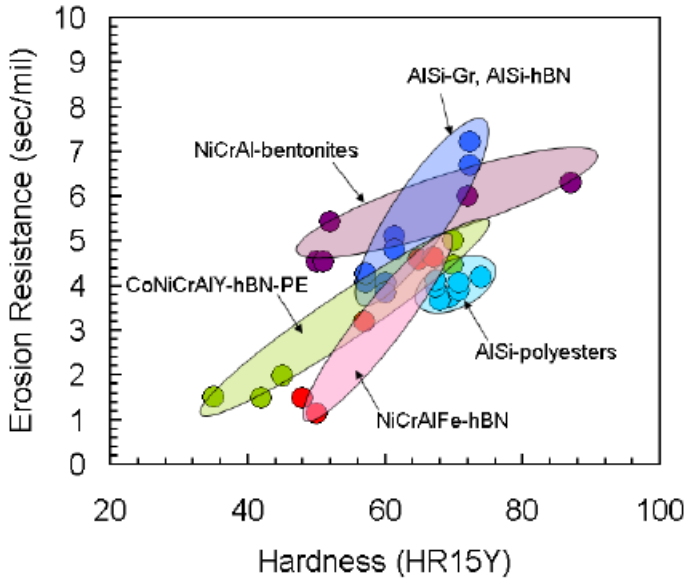

Figure 2.8. Erosion resistance of abradable material against the hardness [7].

As shown in the figure, an increase of the hardness highlighted an increase of the erosion resistance. However, going back to the abradability test, no one has explored the role of hardness on the abradability of the coating and therefore choosing the abradable coating based on maximising the erosion performance sacrifices the abradability of the coating. Also, Yi's research [41] presented a study of erosion of abradable coatings using an experimental vacuum sand erosion machine. Figure 2.9 shows a diagram of the erosion tester.

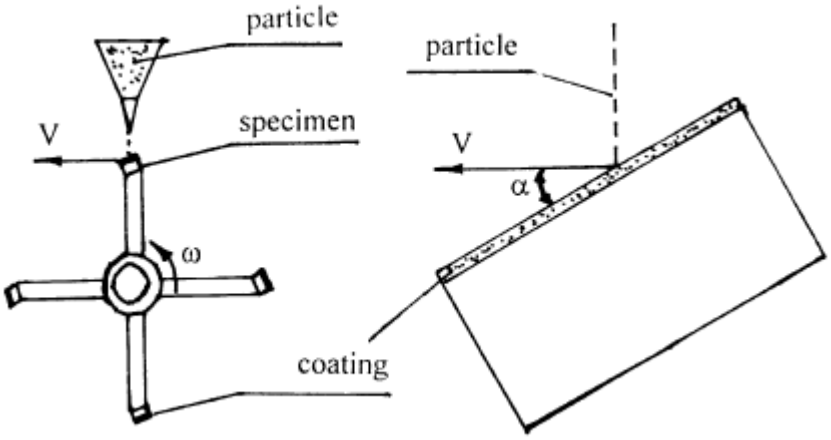

Figure 2.9. Schematic diagram of erosion machine [41].

The test was made with 100 mesh abrasive particles at different impact angles, 30°, 60° and 90°. This research highlighted a linear relationship between erosion time and mass loss, and observed higher erosion with impact angle of 60°, and also explained a mechanism of erosion in relation to the impact angle.

2.2. Material processing and material properties

In this section the basic knowledge of the abradable material processing and the influencing parameters in the process will be analysed. Rhys Jones [42, 43] analysed the thermal spray coating process used in aero-engines and its application. Abradable coatings, like aluminium silicon hexagonal boron nitride (AlSi-hBN) analysed in this research, are thermally sprayed using a plasma gun [14, 42, 43]. As highlighted in the work of Rhys Jones [42, 43], the thermal spray process is a technique where the material in the form of powder is introduced into a plasma stream and sprayed onto a surface with a gun. The plasma gun consists of a cathode, usually made of tungsten, and a hollow anode or a nozzle made from copper. Two electrodes from the power supply connected to the cathode and nozzle generate an electric arc between them. This produces the dissociation and ionisation of the gas introduced into the gun chamber, with the formation of a high temperature thermal plasma [14]. The arc generates a rapid increase of gas temperature, while the nozzle generates an expansion, and this generates a plasma with high thermal and kinetic energies. The gun is always water cooled to protect the components from the high energy plasma. The material to be sprayed is injected into the plasma stream in the form of powder by a feeder unit, where the powder is carried in an inert gas stream. The particles of

the powder, after being semi-melted and accelerated in the plasma, impact the substrate and generate the coating. Figure 2.10 shows a thermal spray process, with a section of a plasma gun, with the water inlet for cooling down the component, the gas inlet, the anode and cathode.

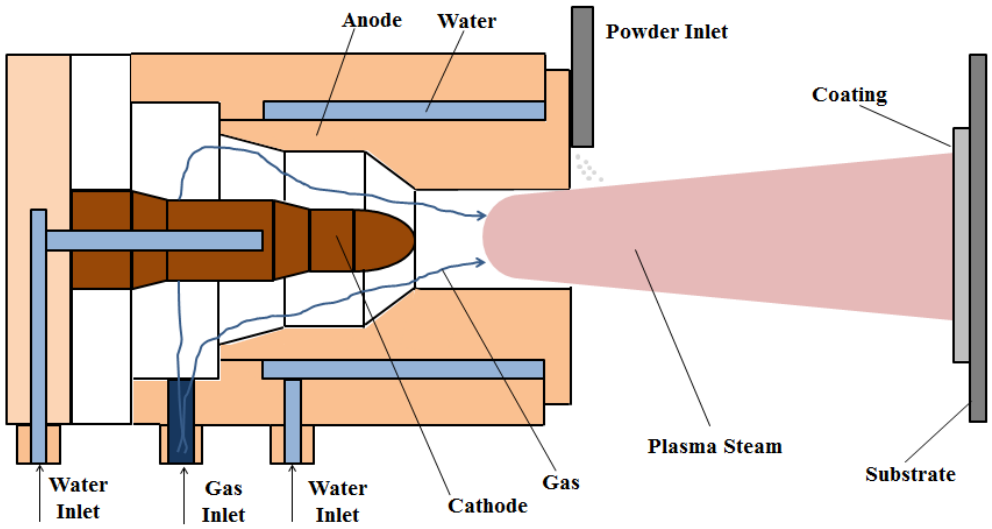

Figure 2.10. Section of plasma gun.

2.2.1. Thermal spray parameters

Different parameters, such as arc current, velocity of particle and primary gas flow, influence the thermal spray process and therefore the properties of the coating [14].

The research done by Vardelle and Fauchais [44] examined different influencing parameters in the thermal spray process in order to diagnose and control the process. Especially, an increase of the arc current increased the particle temperature and velocity. Additionally, it was found that a small percentage of a secondary gas like hydrogen helps to increase the arc current and increases the plasma enthalpy and reduces oxidation.

Furthermore, Dorfman's work [45] analysed the influence of thermal spray process parameters like particle velocity and temperature of the coating, in order to increase the documentation concerning parameters influencing the final coating property. The focus was especially on nickel-based abradable coating, where an increase of deposition efficiency was observed with an increase of particle velocity and temperature. Additionally the highest erosion resistance was observed at the highest

temperature and particle speed, as well as a tensile strength and hardness change in relation to particle speed and temperature.

Additionally, as highlighted by Pawlowski [14], an important parameter is the arc voltage of the gun that generated the gas ionization and then generated the plasma. This depends on the geometry of the anode and cathode, and a greater distance between them increases the arc voltage. Furthermore, this work showed that the position and the orientation where the powder is injected into the plasma [14] determined a thermal gradient and gas velocity variations. Therefore, most of the systems introduced the powder and injected it in a radial direction in order to acquire the highest temperature and forward momentum of the plasma. Additionally, another influencing aspect is the spray distance [14], which influences the particle speed and temperature, a decrease of particle speed and temperature occurring with an increase in the spray distance.

Another important parameter in the thermal spray process is the primary gas flow rate, which is a critical parameter to modify the hardness of the coating [13, 45, 46], and will be analysed in the next section.

However, a defined value of each parameter analysed permits the thermal spray technique to spray different coatings from different powder particles.

2.2.2. Hardness of AlSi-hBN in relation to the primary gas flow

The research conducted by Oerlikon Metco and Lugscheider [13, 46] highlighted that the coating hardness of thermally sprayed AlSi-hBN is primarily dependent on the deposition rate, which is a function of the powder flow rate, the current input and associated ionisation temperature of the gas, spray distance and the primary gas flow. Lugscheider's research [46] was focused on the analysis of the input parameters that influence the coating hardness. Therefore, it was highlighted that an increase of the primary gas flow led to a decrease of the particle temperature and a cooling of the flow. Conversely, an increase of the flow rate determined a higher particle velocity and therefore an increased deposition rate. Cold particles were less densely distributed and therefore a softer coating was made, and the superficial hardness of the coating decreased. Also, Lugscheider [46] highlighted the input current as being an important parameter that influences the coating hardness; in fact an increase

determines an increase of plasma temperature, so the hot particles lead to a harder coating. The same consideration could be made for the voltage and the power applied to the spray gun.

In particular, the research conducted by Oerlikon Metco [13] as illustrated in Figure 2.11, shows with summarising graphs the relation between hardness and primary gas flow (Figure 2.11a), plasma plume intensity against hardness (Figure 2.11 b), and the hardness changes with particle velocity (Figure 2.11 c).

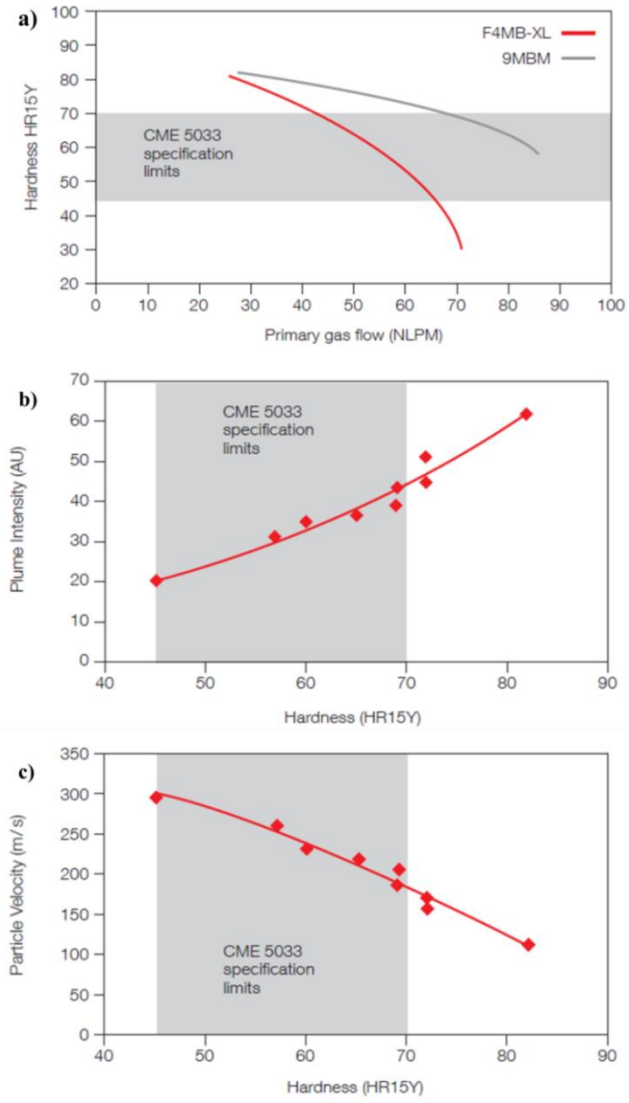

Figure 2.11. Parameters influencing coating hardness: a) Primary flow; b) Plasma intensity; c) Particle velocity [13].

CME 5033 is the Rolls Royce specification for the preparation techniques of AlSi-hBN abradable coatings [47]. Additionally, with regard to the abradable AlSi-hBN,

Table 2.1 summarises the nominal weight percentage of the chemical composition of the powder commonly used in the thermal spray process [12].

	Weight [%]			
	Al	**Si**	**Boron Nitride**	**Organic Binder**
AlSi-hBN	Balance	8	20	8

Table 2.1. Weight percentage of the powder of AlSi-hBN.

Furthermore, Oerlikon Metco [13] highlighted different percentages of the constituents in the microstructure of AlSi-hBN with different hardnesses. Also, the different hardnesses implied different concentrations of residual binder. The binder is used in the manufacturing process to agglomerate AlSi and hBN and help to minimize the hBN loss during the plasma spray process, where the concentration increased with the hardness.

2.3. Material analysis

Another way to analyse abradable materials is from the determination of material properties, for example the mechanical and thermal properties.

Johnston [5] presented a mechanical assessment of AlSi-hBN, NiCrAl-Bentonite, and NiCrAl-Bentonite, typical abradable samples used in the compressor stage as mentioned in the Introduction chapter. Using a novel method of manufacture, a self-supporting freestanding sample of abradable material [48] was sprayed in a mould material made from a dissolvable polymer that was able to withstand the temperatures of thermal spray operation. This method produced a freestanding coating for a tensile test; this compared favourably to the standard test method for thermal spray coating [49], in which a coated sample is sprayed in a cylindrical sample and then glued to another cylindrical sample, where the adhesive could penetrate the porosity of the material and reinforce the coating. Johnston's research [5, 48] produced a repeatable method to evaluate the mechanical property of the freestanding abradable material. During this research the ultimate tensile stress,

Young's modulus and the mean strain to failure were calculated for a series of abradable materials. Figure 2.12 shows the tensile stress vs strain curve for AlSi-hBN.

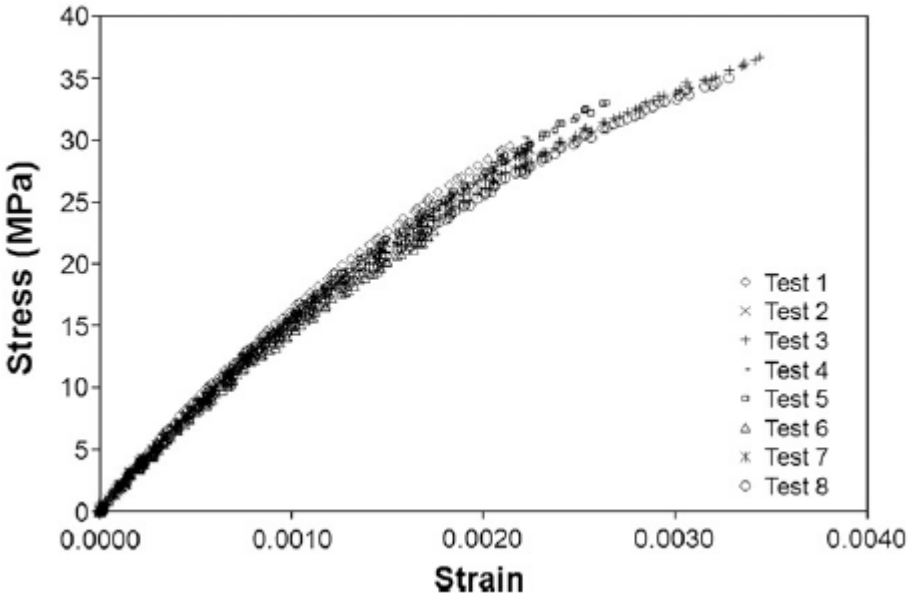

Figure 2.12. Tensile stress vs strain for AlSi-hBN [5].

During this research it was found that the ultimate tensile stress and the Young's modulus of the AlSi-hBN was superior to the Ni-based coating; conversely, the strain to failure of AlSi-hBN was significantly lower, and the different levels of porosity between the systems was highlighted as responsible for the difference. Therefore, this research fully characterised the mechanical response of freestanding abradable materials, avoiding the influence of substrate or adhesive that could alter the microstructure of a coating with high porosity.

Additionally, differences in the coating hardness were reflected in different tensile strengths and bond strengths of the components of AlSi-hBN [12, 13], as shown in Figure 2.13.

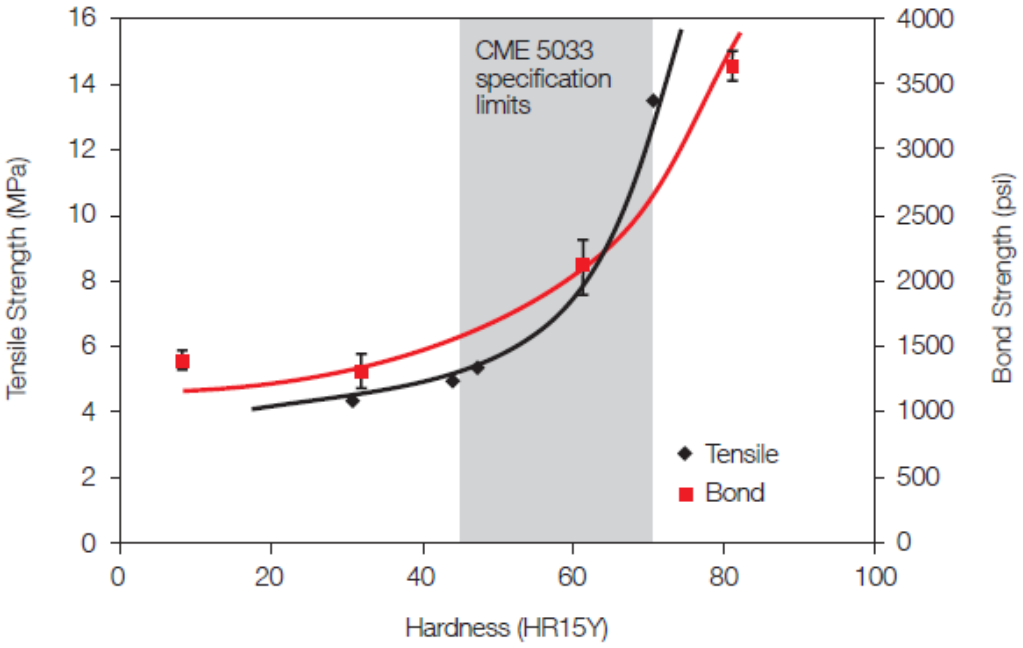

Figure 2.13. Tensile and bond strength vs hardness of abradable AlSi-hBN [13].

2.4. Material preparation

In this section the previous research on material preparation will be analysed and a series of techniques used to characterise the constituent compositions will be investigated.

A series of contributions from Blann and Vander Voort [50-53] highlighted the recommended preparation in order to observe the material with a microscope, with the aim of maintaining the original features of the material without introducing cracks. The first step represented the sectioning of the thermal spray coating, and therefore the sample needed to be cut with a diamond blade as highlighted by the material guide [54] where in general the selection of the blade is in relation to the substrate material [55], where the blade needed to cut into the coating towards the substrate to avoid delamination. The second step as highlighted by Blann and Vander Voort's work [50-53], represented the mounting of the sample, protecting the sample during the process of grinding and polishing of the surface of interest. As highlighted during these studies, for a dense coating a suitable process is thermosetting consisting of a compression moulding. Conversely, for coatings with a porous type of abradable material or friable specimen, in order to preserve the integrity, a vacuum impregnation of the pores by epoxy is suggested [50], where the high pressure of the

thermosetting process could change the structure of a friable coating. Vacuum impregnation [51] permits the epoxy to enter inside the pores of the coating with a correct filling to allow retention of the porosity in the structure and clearly distinguish between the different features of the coating. Additionally, the third step is represented by the grinding phase that is used to remove damage introduced by sectioning, and produced a flat surface, followed by a polishing phase carried out in order to have a clean scratch-free surface. Additionally, a series of technical material guides [50, 54, 55] provided instructions for each step in order to prepare the material to be observed with the microscope.

The preparation step as highlighted above was used by different researchers in order to analyse the microstructure in order to determine the composition of the sample.

The analysis of the image of the sample is a useful technique for analysing the composition of the sample. Faraoun [4, 56] developed an image analysis procedure to quantify the different components of the abradable coating in relation to shape, size and orientation. In this study [4, 56], a construction of equivalent images was made by replacing each particle in the microstructure by a corresponding ellipse that fitted the particle geometrically, and enable the volume fractions of metal matrix, porosity and solid lubricant phase to be obtained. Figure 2.13 shows the equivalent image of an AlSi-hBN sample and a NiCrAl-bentonite sample, generated with the complete procedure [4, 56].

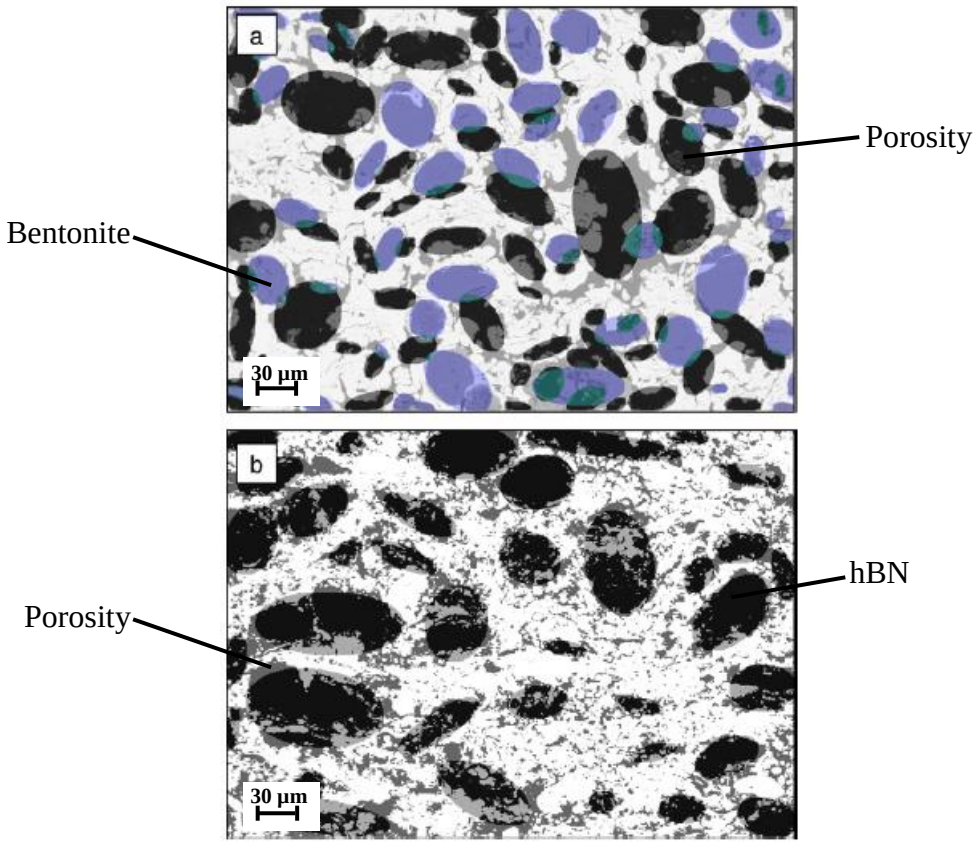

Figure 2.14. Equivalent image generation for: a) NiCrAl-bentonite, blue particle bentonite, black particle porosity; b) AlSi-hBN, black particle hBN [4].

The image analysis of AlSi-hBN showed that it was characterised by 40% of hBN particles and 5% of porosity constituted of elongated pores at intersplat boundaries; the image analysis of NiCrAl-bentonite highlighted a volume with 30% of porosity and 25% of bentonite. Additionally the equivalent image was used in a finite element analysis in order to determine the mechanical properties [56].

Matejicek's research [57] highlighted the use of different techniques like image analysis, electron probe microanalysis and X-ray diffraction in order to determine the composition and different techniques to determine the porosity. The research indicated that it was difficult to discriminate hBN and porosity in abradable materials like AlSi-hBN using image analysis; however an epoxy impregnation of the pores permitted a clear distinction of the pores under UV light. Overall, the image analysis provided the phase composition in relation to the optical reflectivity, the electron probe microanalysis provided the elemental composition, and the X-ray diffraction the phase composition. However, whilst the latter is not sensitive to minor chemical variation, the electron probe microanalysis is more sensitive and provided location

information of the element, but with less ability to provide composition for a heterogeneous sample. Overall, the results from the three techniques were complementary if converted to the same units. Additionally, the different techniques used to evaluate the porosity, like mercury intrusion porosimetry, water immersion and helium pycnometry, provided a higher value of porosity than the image analysis due to the ultrafine pores inside the hBN not being individuated on the image, and also the influence of surface roughness, where surface depressions are counted as pores.

As highlighted above, it is difficult to identify the hexagonal boron nitride (hBN) from the porosity in the abradable coating. However, the analysis by Sulzer Metco [58] indicated that by using polarised light, the hBN appeared light in colour and shiny, and permitted the hBN to be identified from porosity.

Furthermore, the study by Deshpande [59] based on image analysis, small angle neutron scattering (SANS) and micro-tomography, evaluated the porosity of thermal spray coatings in order to highlight that image analysis represented a reliable method for characterisation of porosity of coatings. The fraction of porosity measured by image analysis differed by a factor of 2 compared with techniques such as SANS; but using an SEM, with better depth resolution compared to that of an optical microscope, reduced the difference to approximately 1.25. The difference between image analysis and SANS on the globular porosity of around 1-2% was due to the different sensitivity to different ranges of pore size, where SANS had a higher resolution of 1nm while image analysis with a zoom of 200X could detect pores with diameters 2–5μm, but SANS did not detect pores larger than 4–5μm. Nevertheless, the analysis based on the calculation of the porosity in relation to the particle size and powder type indicated the same trend measured with different techniques, and authenticated the validity of the image analysis.

2.5. Thermal analysis

Another important analysis represented the measurement of thermal conductivity of the abradable material, presented in the research of Sporer [11], where the thermal conductivity and diffusivity were calculated for different abradable coatings. The thermal diffusivity was measured using a laser flash method [60, 61], and a specific heat capacity was calculated using a differential scanning calorimeter; the thermal

conductivity was determined by multiplying the density by the specific heat and the thermal diffusivity.

The laser flash method [60] consisted of generating an energy pulse on the sample surface at a predetermined temperature. The pulse raises the sample temperature. A high speed infrared detector above the surface detects the time dependent temperature on the sample surface, and in relation to the time ($t_{1/2}$) to reach half of the maximum temperature and in relation to the sample thickness (s), the thermal diffusivity (α) could be determined, as shown in Equation (2.1).

$$\boldsymbol{\alpha = 0.1388 \cdot \frac{s^2}{t_{1/2}}} \tag{2.1}$$

Unlike the previous research, the temperature and thermal analysis was performed mainly with numerical analysis for abradable samples.

Therefore, in the work of Bolot and Tan [62, 63], in order to understand the material behaviour of abradable materials, the thermal property of the coating was predicted through a numerical model and compared with experimental measurements. Through a microscopy image of the coating microstructure a finite element mesh was generated in order to quantify the heat flux in the coating and determine the numerical value of thermal conductivity of the thermal spray coating. Bolot's model [62] was focused on the abradable coating AlSi-polyester, and two finite element packaged were compared. The different numerical values obtained were attributed to the different discretisation methods; however, it was difficult to establish which was the better method. Also, the model generated a value that differed from the experimental value by a factor of 1.1-1.2, and therefore the techniques need further development.

Tan's model [63] was focused on different thermal spray coatings like yttria-stabilized zirconia. Through an image analysis, a finite element model was made and, as observed in Bolot's study [62], a large variation between numerical and experimental values was observed. The reason for the difference could be correlated from the image magnification and resolution, but also because of the simplification of a two dimensional model, and therefore further development was required.

Wang [64, 65] developed a thermal model that analysed the influence of temperature in the contact. The model was also validated with a limited set of experimental data. The model showed maximum temperatures for a titanium blade striking a NiCrAl coating, with respect to when the titanium blade strikes an AlSi coating. It examined how the elastic modulus would be expected to change due to the temperature, and introduced criteria where, at any time that the modulus of the coating is higher than that of the blade, the atomic bonds are broken at the tip of the blade, and it is worn, and this happens in the contact between titanium blade and NiCrAl coating. When the titanium blade contacted an AlSi coating, the modulus of the blade was always higher than that of the coating, implying that the blade could rub the coating without excessive wear occurring. However, the modelling approach was limited, due to the lack of detailed experimental data to validate it.

2.6. Modelling of the contact

Another analysis of the contact between the rotating blade and abradable material was made through a numerical model that simulated the contact. This work by Legrand and Pierre [66] generated a numerical model of a contact between a blade and the casing. The contact was simulated by assuming a temperature gradient equivalent to a multi-harmonic load that distorted the casing. The simulated contact assumed a uniaxial cutting, in a quasi-static compression, as shown in Figure 2.15.

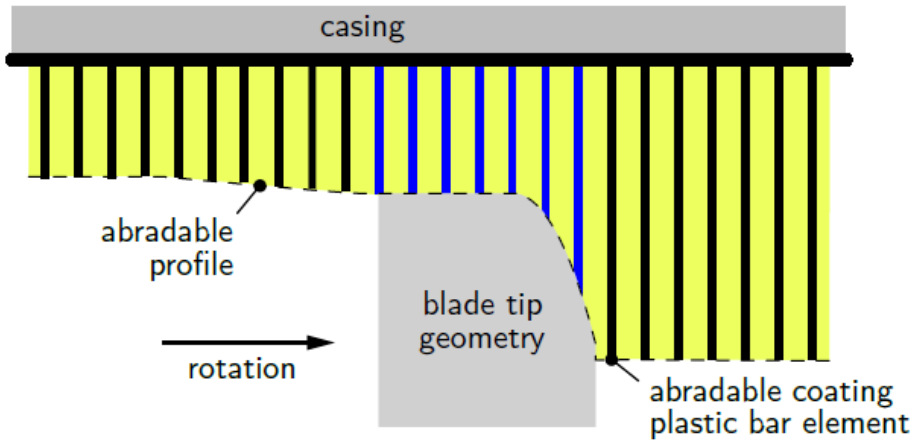

Figure 2.15. Model of the contact [66].

Additionally, the wear of the coating was evaluated from the abradable profile. Therefore, this analysis showed limited results, and also did not consider the

heterogeneous nature of abradable material, and finally there was no comparison with any experimental data.

Peyraut's research [67] presented a model of the contact between blade and the abradable coating, with a simplification of sliding contact, and analysed the contact stress and temperature. Figure 2.16 shows the finite element model.

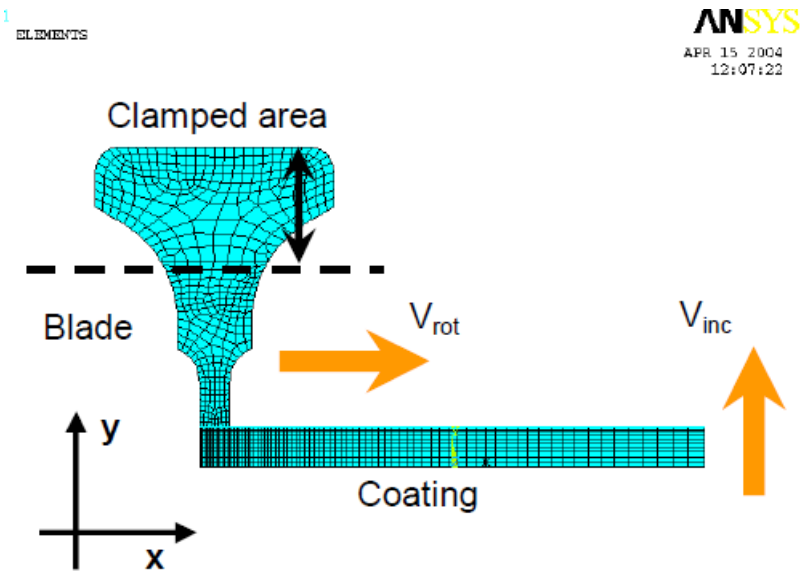

Figure 2.16. Model of the contact [67].

The numerical result was compared with the experimental result and the stress and temperature were plotted against the percentage of wear. This represented a step forward with respect to previous work, but lacked in comparing the stress result, obtained from the contact model, with an experimental force measurement. Additionally, Peyraut [68] developed a finite element model of the hardness measurement of an abradable material in order to identify the plastic parameters of the material, and a correlation between hardness and coating thickness was determined, with a decrease of the hardness with a decrease of the thickness. Finally, the comparison between experimental and numerical method confirmed the validity of the model.

However, in general the numerical analysis had limitations due to the simplification applied and also because of the small number of data points presented.

2.7. Conclusions

The overall work performed on abradable materials was divided into tests with an experimental test platform, material analysis and modelling. The experimental tests were focused only on the analysis of the wear mechanism based on the observation of the sample after the test without focusing on the nature of the mechanism. Overall, the mechanism was quantified for adhesive transfer and blade wear in terms of percentage variation before and after the test, producing a small amount of data points with a lot of scatter that made it hard to draw a firm conclusion. Additionally, the material analysis of the coating provided material characterisation in terms of mechanical and thermal properties, giving useful information on the basic material knowledge. The numerical approach had limitations due to the simplification applied and also a small number of data points were presented and were not compared with experimental results. Finally, research on the machining process gives approaches to analyse the material behaviour. However, overall, all previous work lacks a complete analysis of the wear mechanisms with an explanation of what drives the behaviour observed.

Therefore, the aim of this research was to go further and deeper into the analysis of the wear mechanism in order to understand the nature of the wear mechanism, with a real time monitor of different parameters, using a scaled test rig. This research aimed to identify the wear mechanism observed on the compressor stage, between a rotating titanium alloy blade and abradable material of aluminium silicon hexagonal boron nitride. This research was the first to try to explore the nature of the wear mechanism through a series of alternative approaches, which characterised the wear mechanism in real time during the test. Therefore, an evolution of blade length change, contact force and temperature were measured, and additionally a material response was analysed in order to identify the main parameter influencing the wear mechanism, and to generate a wear map that would highlight the different wear mechanisms in relation to the parameter. Then finally a wear map could be used in the design phase of a new material in order to obtain a desirable wear mechanism.

3. Apparatus and Samples

In this chapter the samples used during this research and the experimental platform are presented. The first part of the chapter analyses the samples that were used and characterises their properties. The later part of the chapter presents the basic experimental platform as it existed at the start of the project and then explains the successive developments and instrumentation that were introduced in the course of this study.

As highlighted in the introduction chapter, during an aero-engine's operation, the rotating blades may strike the wall of the surrounding casing of abradable material.

The wear mechanisms observed between the blade tip and the abradable material were reproduced and investigated on a scaled test platform [1]. The experimental test rig was designed at The University of Sheffield (Figure 3.1). In this study, successive design developments were made in order to improve the analysis of the wear mechanism. The test rig is capable of generating the wear conditions observed for abradable linings in an aero-engine compressor [1], with the aim being to increase information regarding the behaviour of abradable linings and to develop a wear map. The abradable material tested was AlSi-hBN (see Metco 320), where AlSi is the metal matrix and hBN (hexagonal boron nitride) is the solid lubricant phase. This abradable material is operated in an aero-engine at temperatures up to 450 °C, in intermediate pressure compressor (IP) and high pressure compressor (HP) casings. In these stages of the compressor the rotating blade is manufactured from titanium. Figure 3.1 shows the experimental platform used during this research to investigate the wear mechanics between the rotating blade and the abradable material.

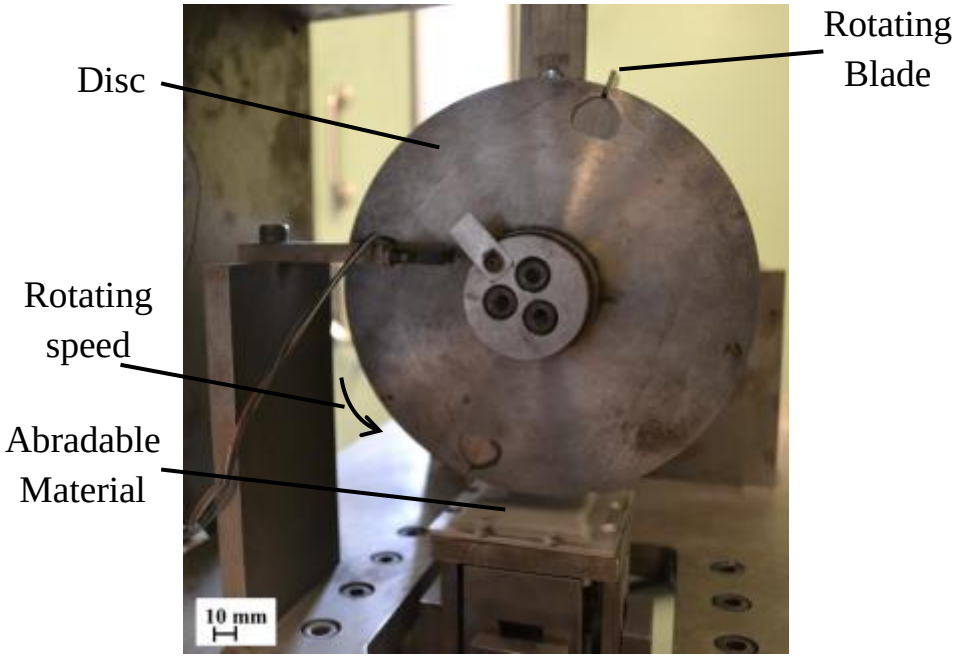

Figure 3.1. Experimental platform [1].

3.1. Test Samples

3.1.1. Abradable material

The abradable material tested was AlSi-hBN (Aluminium Silicon hexagonal Boron Nitride), Metco 320 [12]. The coating consists of a metal matrix of AlSi (aluminium silicon), solid lubricant phase of hBN (hexagonal boron nitride) and porosity. The material is used in aero-engines and has good abradability and erosion resistance, and operates at temperatures up to 450 °C. Typically, AlSi-hBN abradable materials used in aero-engine compressors are manufactured with hardness in the range 45 to 75 [13, 47] when measured using a Rockwell R15Y hardness indenter. In this study, coatings with different hardnesses were tested in order to characterise the wear mechanics in the typical range used in aero-engines: high hardness R15Y 72.3, intermediate hardness R15Y 63 and R15Y 59.6, and for the low hardness R15Y 54.6 was chosen because a softer coating implied a low erosion resistance, along with poor resistance to oxidation, corrosion and thermal failure [13]. The coatings were thermally sprayed.

3.1.2 Thermal spray equipment and process

The coating was produced using thermal spray equipment. The equipment comprised a spray gun, a controller and a material feeder. The spray gun was a plasma gun Sulzer Metco F4 (Sulzer Metco, Switzerland), which is operated with a maximum rated power of 55kW and is typically used in the aero-engine industry [69]. Figure 3.2 shows the Sulzer Metco F4 MB90 –XL which was used to thermally spray the coating.

Figure 3.2. Sulzer Metco gun F4 MB90-XL [69].

The model used was right-angled, thus the angle of spray was 90°; it operated with combinations of argon and hydrogen, which were used for the primary and secondary gas flows respectively. Table 3.1 summarises the main spray gun specifications.

Spray gun specifications		
Power [kW]	55	
Nozzle [mm]	6	
Injector	*Diameter [mm]*	2
	Distance [mm]	6
Amperage [A]	500	
Deposit Efficiency [%]	50 – 80 %	
Spray rate [g/min]	40 - 80	

Table 3.1. Spray gun Sulzer Metco F4 MB90-XL specifications.

The material, sprayed from the spray gun in powdered form, was injected into the plasma stream via a feeder unit which carried the powder in an inert gas stream. The feeder unit is a volumetric thermal spray feeder for atmospheric plasma (Twin 120 A, Sulzer Metco) [70]. Figure 3.3 shows a picture of the feeder unit and a schematic picture of the functional principle.

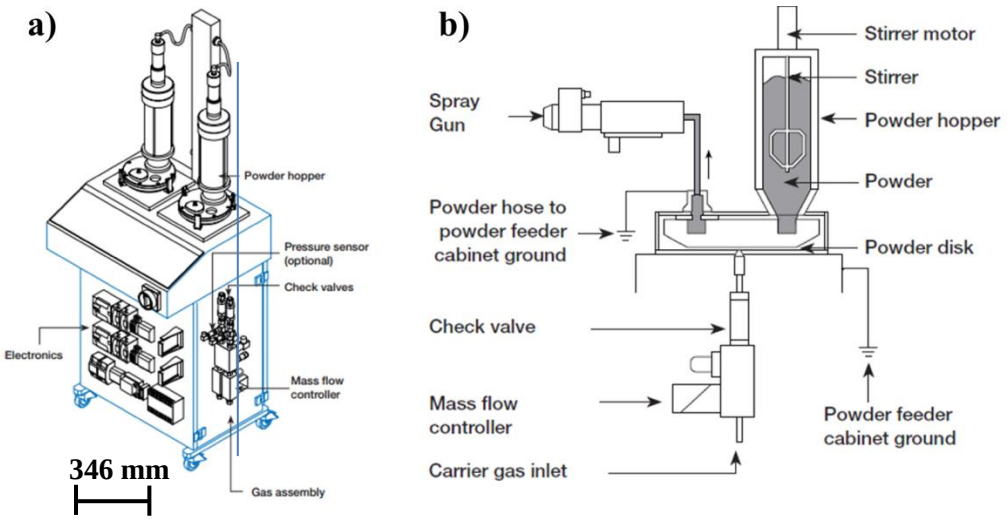

Figure 3.3. Feeder unit: a) Unit; b) Functional principle [70].

The material in powder form was located inside a powder hopper. The powder feed rate was controlled volumetrically by the rotation of the powder disc. The carrier gas conveyed the spray powder to the spray gun. The carrier gas and all parameters needed to set the thermal spray system in order to make the coating are controlled by a PLC system (Sulzer Metco 9MC) [71]. The coating property is primarily dependent on the deposition rate [14], which is a function of the powder flow rate, the current input and associated ionisation temperature of the gas, the spray distance and the primary gas flow, as highlighted in Chapter 2. The same powder type (Sulzer Metco 320) [12] was used to spray the coating. Table 3.2 summarises the thermal spray specifications, given by Rolls Royce Surface Engineering group, used to make the samples tested.

	Hardness R15Y 54.6	Hardness R15Y 59.6	Hardness* R15Y 63.0	Hardness R15Y 72.3
Plasma gun	F4	F4	7 mb	F4
Nozzle [mm]	6	6	GH	6
Powder injector	2mm (105°)	2mm (105°)		2mm (105°)
Carrier gas (Argon) [SLPM]	8	6	8	8
Primary gas (Argon) [SLPM]	80	50	93	50
Secondary gas (Hydrogen) [SLPM]	10	8	6	10
Current [A/s]	600	500	400	600
Volt	77	70	83	73
Power [kW]	46.2	35.5	32.6	42.8
Powder flow [g/min]	55	30	65	55
Spray distance [mm]	140	120	150	140
Powder batch	W84062	W82877	W79605	W82877
D/E rate [mm]	0.06 per Cycle	0.061 per Cycle	0.05 per Cycle	0.04 per Cycle

***N.B. This set of samples was made with a different thermal spray gun by Rolls Royce Plc; therefore different parameters needed to be set in order to obtain a specific hardness value [13].**

Table 3.2. Spray gun parameters.

As highlighted in the table, two samples tested had similar values of hardness R15Y 59.6 and 63. This was because the sample with hardness R15Y 63.0 was tested at an early phase of this research, and the instrumentation of the test platform was developed through the project and was therefore not identical for all samples tested. The samples with hardness R15Y 63.0 was initially tested using only the stroboscopic technique, without dynamometer and pyrometer. Therefore, another sample of similar hardness was sprayed, and hardness of R15Y 59.6 was obtained

due to the variability of the thermal spray process, and the second sample was investigated with all the instrumentation.

3.1.3. Hardness measurements of abradable samples

The abradable coating was sprayed onto a stainless steel plate (80 x 80 x 3mm) in order to fit the coating onto the Z-microscope stage with the attachment hole, as shown in Figure 3.4.

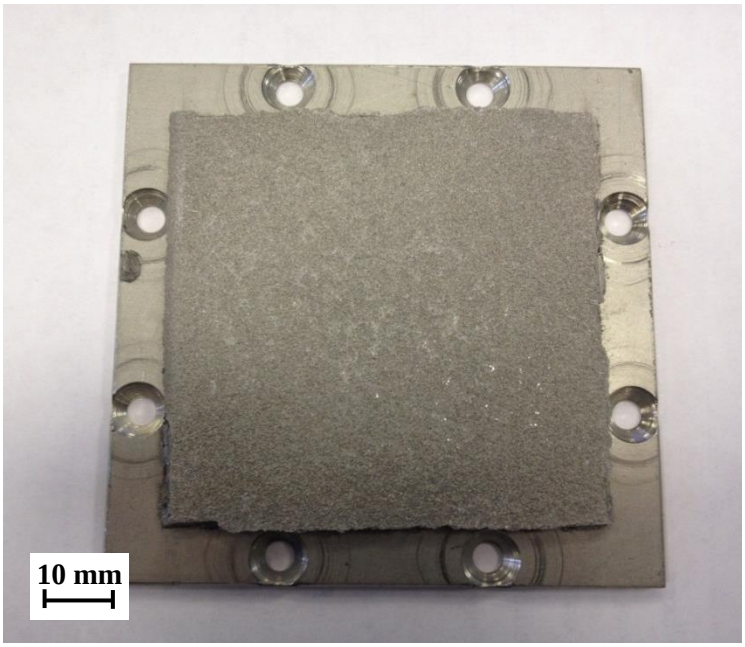

Figure 3.4. AlSi-hBN abradable coating spray on stainless steel plate.

Each sample with thickness 3mm was lightly ground with 320 grit Al_2O_3 grinding paper to remove any surface imperfections and generated a surface profile of less than 400µm [72]; this is a typical surface roughness of abradable linings. The abradable coating hardness was measured with a superficial Rockwell hardness scale R15Y used for soft and thin material [73]. The hardness test consisted of indenting the abradable coating with a steel ball indenter. An average of ten indentations was calculated. A 1/2" diameter steel ball indenter, connected with the hardness machine, was forced into the material under a preliminary minor load (Figure 3.5, Phase A) of 3kgf. The machine then applied an additional major load of 12kgf (Figure 3.5, Phase B) and increased the penetration of the indenter. When equilibrium was reached the major load was removed (Figure 3.5, Phase C), and this reduced the depth of penetration. The permanent increase in depth of penetration (e) was used to calculate

the hardness value. The difference between a constant of 100 units (E) and the permanent increase in depth represented the value of hardness. Figure 3.5 summarises the superficial Rockwell principle.

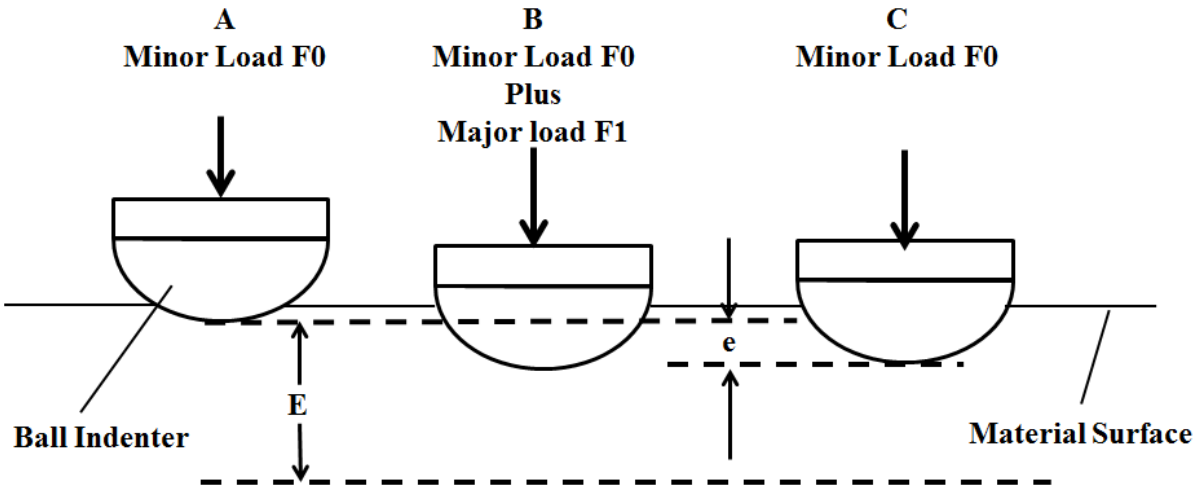

Figure 3.5. Superficial Rockwell R15Y principle.

This research will analyse four different samples, each with a different hardness value: A) Hard, B) Intermediate 1, C) Intermediate 2, and D) Soft. Table 3.3 summarises the average hardness and the relative standard deviation over 10 measurements taken on the experimental samples.

	Hardness [R15Y]
A) Hard	72.3 ± 2.2
B) Intermediate 1	63.0 ± 2.1
C) Intermediate 2	59.6 ± 3.1
D) Soft	54.6 ± 2.5

Table 3.3. Rockwell R15Y hardness of tested abradable sample.

3.1.4. Abradable sample characterisation

In order to characterise the abradable material microstructure, the samples were sectioned and mounted, and inserted into a vacuum bell jar for impregnation with epoxy resin. Post-impregnation, the samples were placed inside an oven for two hours at 50 °C in order to solidify the resin, then the surface to be analysed was ground and polished in order to obtain a clear smooth surface to analyse on the optical microscope. The phase of grinding and polishing is highlighted in the methodology chapter. The microstructures of the coatings were analysed using a Nikon Eclipse LV150 microscope with magnification ratios of x5 and x10. Figure 3.6a shows the microstructure of the abradable coating. The metal phase aluminium-silicon is white, the solid lubricant phase hexagonal boron nitride is dark grey, and the porosity present in the coating is black. A higher magnification of the microstructure (Figure 3.6b) highlights the hexagonal boron nitride as dark grey with a lamellar structure.

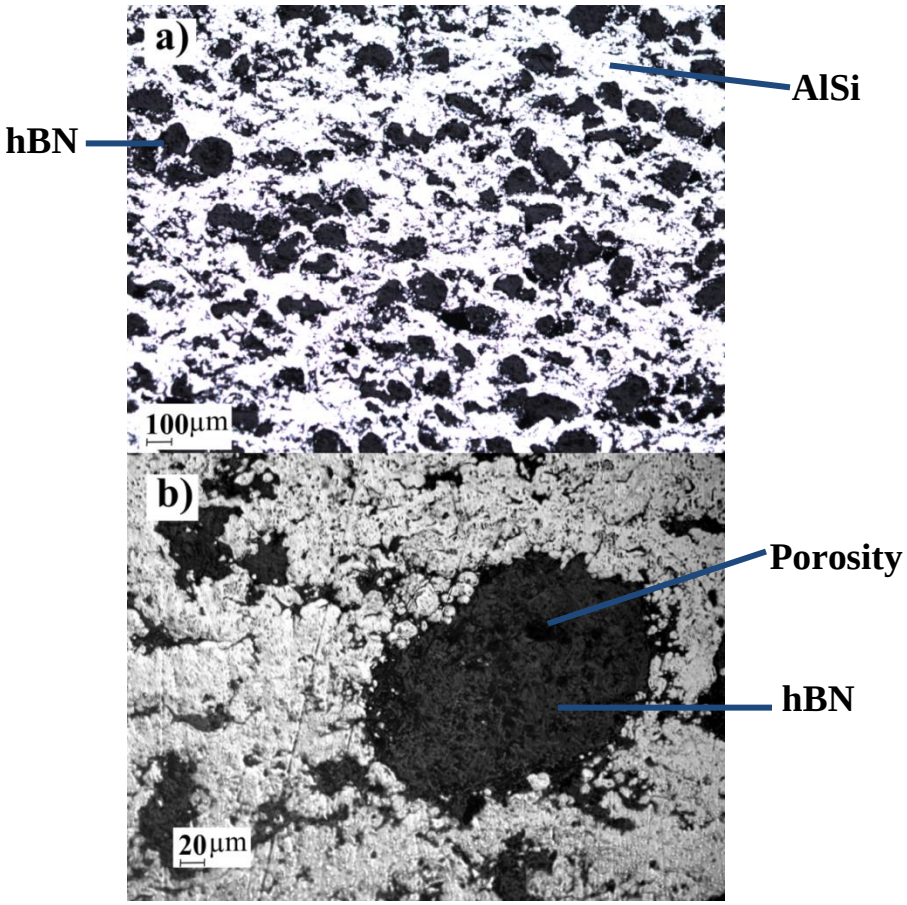

Figure 3.6. a) Microstructure of AlSi-hBN; b) Magnification highlighting the lamellar hexagonal boron nitride and the presence of the dark black porosity.

Figure 3.7 shows the microstructure of the coating with hardness R15Y 54.6 (Figure 3.7a) and the harder R15Y 72.3 (Figure 3.7b) AlSi-hBN coatings.

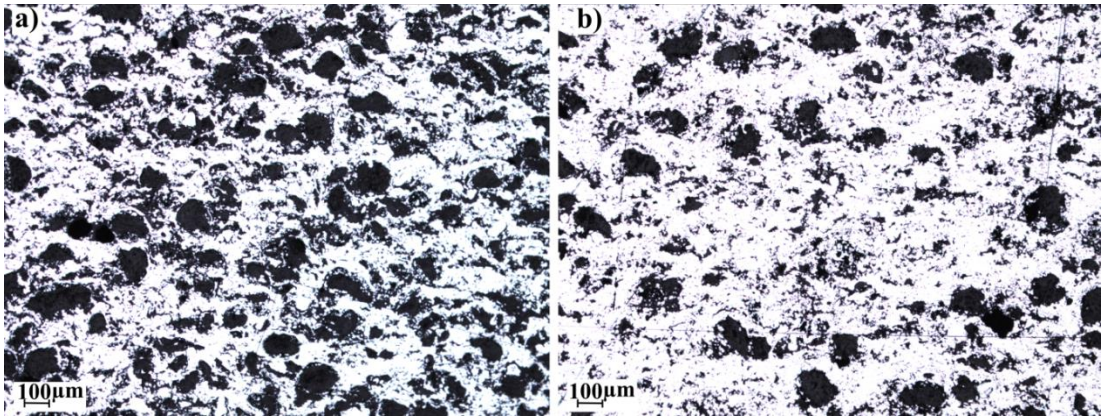

Figure 3.7 Microstructure of AlSi-hBN for different hardness: a) Soft coating hardness R15Y 54.6 ± 2.5; b) Hard coating hardness R15Y 72.3 ± 2.2.

Figure 3.7 shows clear differences in the microstructure between the softer coating (Figure 3.7a) and the harder coating (Figure 3.7b). The image shows different phase contents, especially for the concentration of hexagonal boron nitride and porosity, where low hardness shows higher levels of hexagonal boron nitride and less metal (AlSi) phase [13]. However, as highlighted in the figures, the distinction between porosity and hexagonal boron nitride is not clear, and it is therefore difficult to make clear judgments with respect to how the microstructure has changed. In order to give a quantitative distinction of the material composition with different hardnesses, the microscope images of the coating structure were investigated using a segmentation of the image acquired [4, 54]. The first step consisted of applying a binary threshold to the images in order to highlight the Aluminium-Silicon phase. The second step consisted of applying polarised light [58] with the microscope on the sample; this allowed the hBN to be separated from the porosity on the microstructure of the coating. Under the polarised light the hBN appeared light in colour and shiny, while the porosity was black, as shown in Figure 3.8.

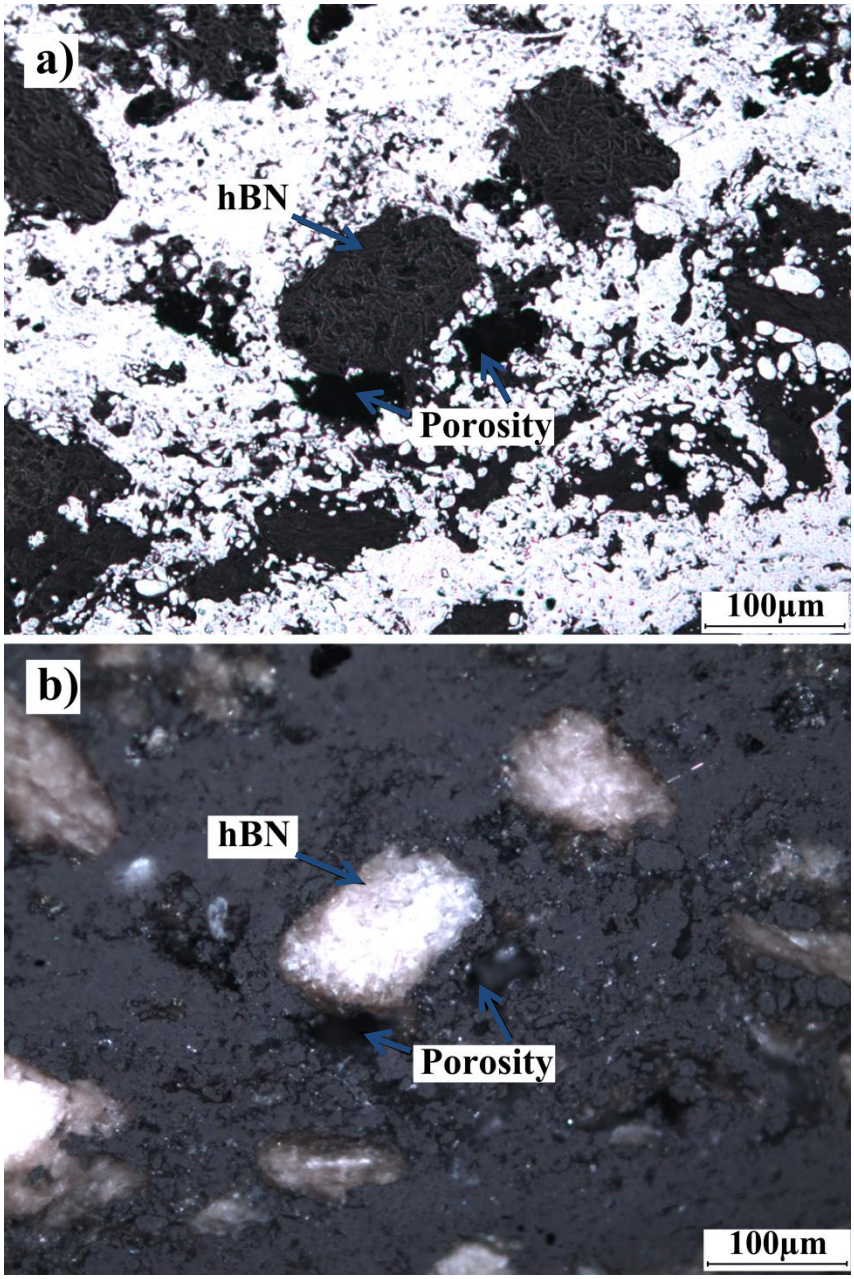

Figure 3.8. Microstructure of harder AlSi-hBN under: a) Normal light; b) Polarized light.

The segmentation of the microstructure images of the R15Y 54.6 ± 2.5 coating are shown in Figure 3.9.

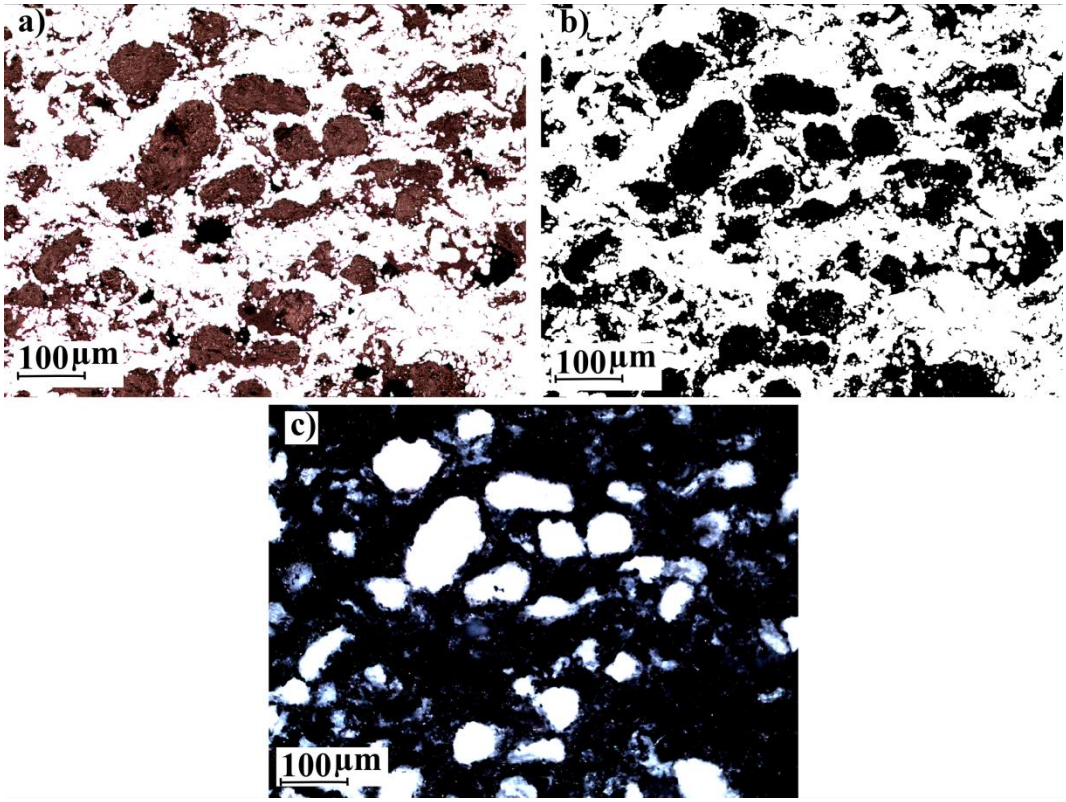

Figure 3.9. Segmentation of microstructure image of R15Y 54.6 ± 2.5 hardness sample: a) Original microscope image; b) Binary image; c) Image with polarised light.

Using the software IMAGE J [74], the volume fractions of the different constituent phases were analysed using these images. Using the binary-segment image (Figure 3.9b) the volume fraction of Al-Si was determined, while the volume fraction of hBN was determined using the polarised light image (Figure 3.9c), and finally the residual volume fraction was considered as porosity. Table 3.4 shows the analysis of the volume fractions of the constituent phases for the abradable sample tested.

	R15Y 54.6 ± 2.5	**R15Y 59.6 ± 3.0**	**R15Y 63.0 ± 2.1**	**R15Y 72.3 ± 2.2**
Metal matrix [%]	41.7 ± 2.66	50.23 ± 7.73	51.39 ± 1.22	54.44 ± 2.42
Porosity [%]	4.25 ± 0.68	2.11 ± 0.84	2.26 ± 0.24	2.67 ± 0.41
hBN particles [%]	54.05 ± 2.51	48.12 ± 7.38	46.35 ± 1.32	42.89 ± 2.66

Table 3.4. Volume fraction of the constituent phases of AlSi-hBN coating.

As shown in the table, a low hardness shows a higher level of hBN and a reduced metal phase. Conversely, an increase of the hardness coating corresponds to an increase of the metal phase, and a decrease of the solid lubricant phase. This study will analyse the influence of the coating hardness on the wear mechanics.

3.2. Blade sample

The blade was manufactured a from titanium alloy, a material used in the compressor stage of the aero-engine [6]. The flat titanium blades were manufactured by a wire erosion process from a 2mm thick flat plate of Ti-6Al-4V at Promach-3D Ltd. (Derby). The blade was manufactured flat in order to simplify the contact. This approach generated two force components during the contact, rather than three like a twisted contour blade. However, as previously discussed, the wear mechanics obtained between the blade and abradable coating were the same as those evaluated on the aero-engine during operation and on other full-scale test platforms [6, 15, 16]. Figure 3.10 shows the drawing with the dimensions of the blade used, as designed by the Rolls-Royce Surface Engineering group.

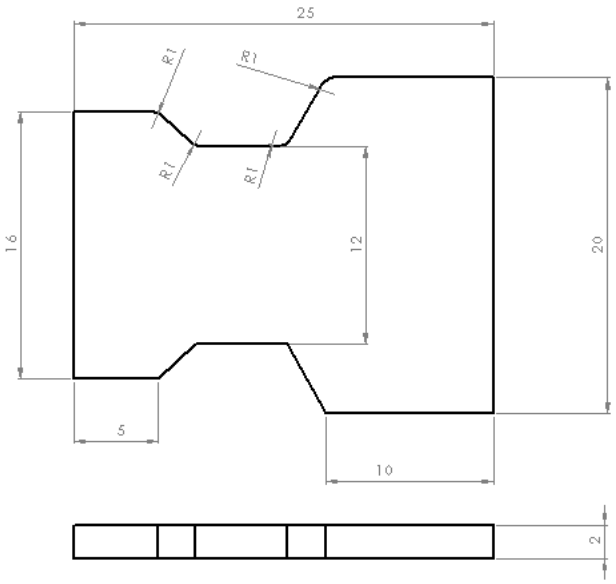

Figure 3.10. Design of the Ti-6Al-4V blade.

The nominal length is 25mm, with a square edge. The material used was Grade 5, and Table 3.5 summarises the composition by weight of titanium, aluminium and vanadium.

	(Ti)	**(Al)**	**(V)**
Weight [%]	90.06 ± 0.04	5.96 ± 0.16	4.04 ± 0.04

Table 3.5. Composition of the Ti-6Al-4V blade.

The hardness was measured using a Vickers micro-hardness tester (Mitutoyo, HM101 Series 810) with a load of 1kg applied over a dwell time of 10s. The hardness value was 373.6 ± 2.6HV. The Young's modulus of the blade was 108.5 ± 3.3GPa, calculated using a nanoindentation machine [75]. Figure 3.11 shows a titanium blade used during the research.

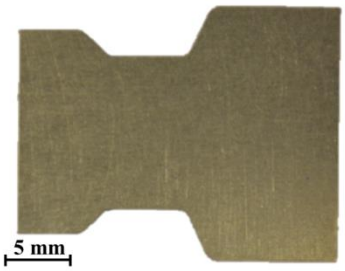

Figure 3.11. Flat titanium blade.

3.3. Test rig

In this section test rig is presented. The rig had been previously developed at The University of Sheffield [1], and in this study a series of developments were made along with the addition of further instrumentation, in order to study the contact between rotating blade and coating. The test rig was able to raise an abradable sample into the rotating blade, and reproduced the contact observed in an aero-engine. The rotating portion of the rig comprised two blades coupled to a disc. The disc was in turn coupled to a spindle, which was under the control of an inverter controller, allowing setting of the rotation speed. A stage, on which an abradable sample could be placed, was present under the disc. This was an electrical Z-axis microscope stage connected with a programmable stage controller. The whole rig was mounted on a bench, which was fixed to the floor in order to reduce the vibration of the test rig during the test. Figure 3.12 shows the front view (Figure 3.12a) and side view (Figure 3.12b) of the experimental test rig.

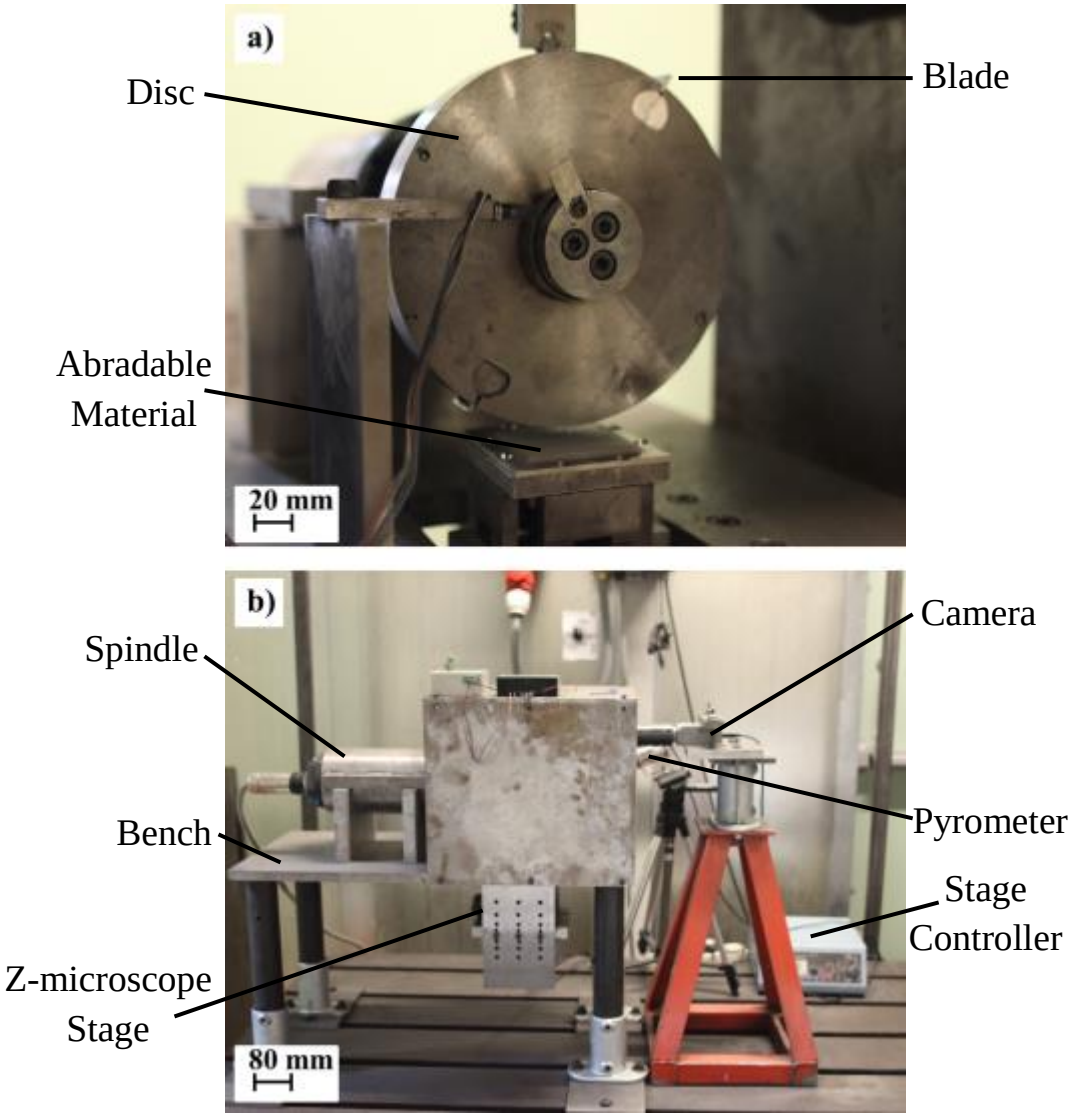

Figure 3.12. Test Rig: a) Front image of the test rig; b) Lateral image of the test rig.

The horizontally orientated spindle was a GM HSP 120g high frequency grinding spindle (GMN Paul Müller Industrie GmbH & Co., K.G, Germany) with permanent grease lubrication. Table 3.6 summarises the spindle specifications.

Rotation speed [rpm]	**Tool interface**	**Power specification**		
		Torque [Nm]	**Power [kW]**	**At speed [rpm]**
21000	HSK-C40	6.9	13	18000

Table 3.6. Spindle specifications.

An inverter controller allowed the setting of the rotating speed of the spindle. The metal disc was designed to be fitted onto an HSK-C40 tool (Coventry Engineering Group Ltd, Coventry UK), coupled with the tool interface of the spindle. The disc was made with two holes 180° opposed for balance, where each contained two clamps. Each set of clamps were capable of holding one blade. For each test a single active blade was loaded into the clamps with a shorter dummy blade also loaded for balance, as shown in Figure 3.13. The disc was fixed using a screwdriver, after being coupled with the tool interface of the spindle.

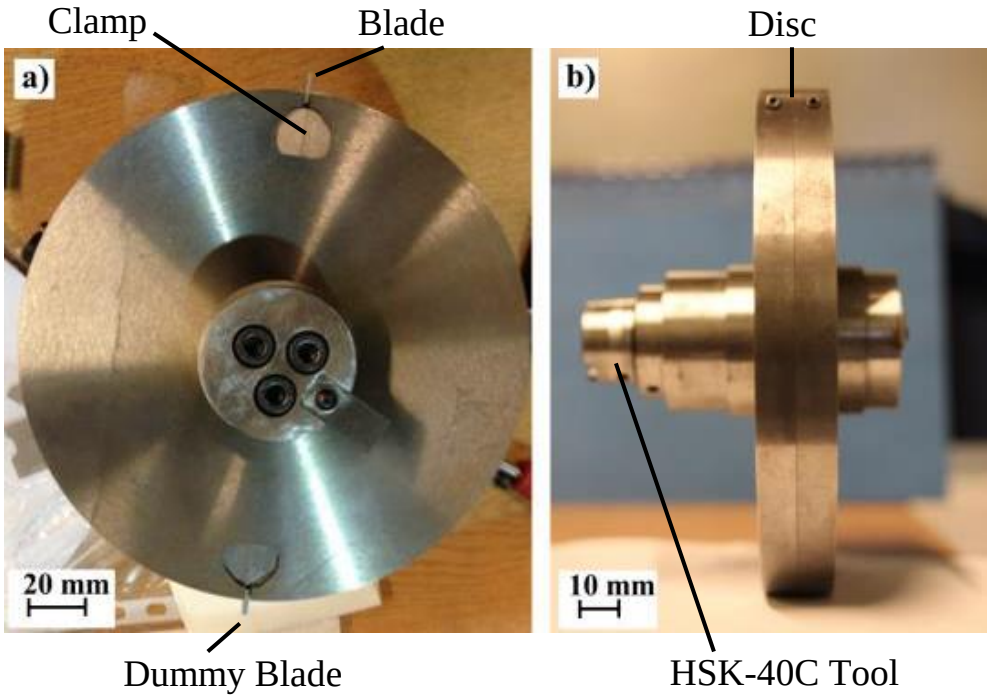

Figure 3.13. Disc of test rig: a) Frontal Image of the disc; b) Lateral image of the disc.

The previous design of the clamp system had the same silhouette as the blade, in order to hold the blade specimen, and was inserted inside the hole on the disc with an interference fit between the clamp and the hole [1]. In this study, the clamp system was re-designed with a different locking system, in order to avoid clamp disassembly, making it possible to use different blade shapes, by changing the clamps. The new blade clamps had two 'recess holes', oriented at 45° with respect to the blade, as shown in Figure 3.14a. Additionally, two threaded holes were made on the outer circumferential edge of the disc in order to insert two grub screws through the disc (Figure 3.14b) and to apply pressure on the surface of one clamp in order to lock it. The orientation of the screw was at 45° with respect to the blade position, in the opposite direction to the disc rotation in order to apply an opposing force to the

normal and tangential force applied on the blade tip during the contact, thus avoiding the disassembly of the screw during the contact between the blade and the coating.

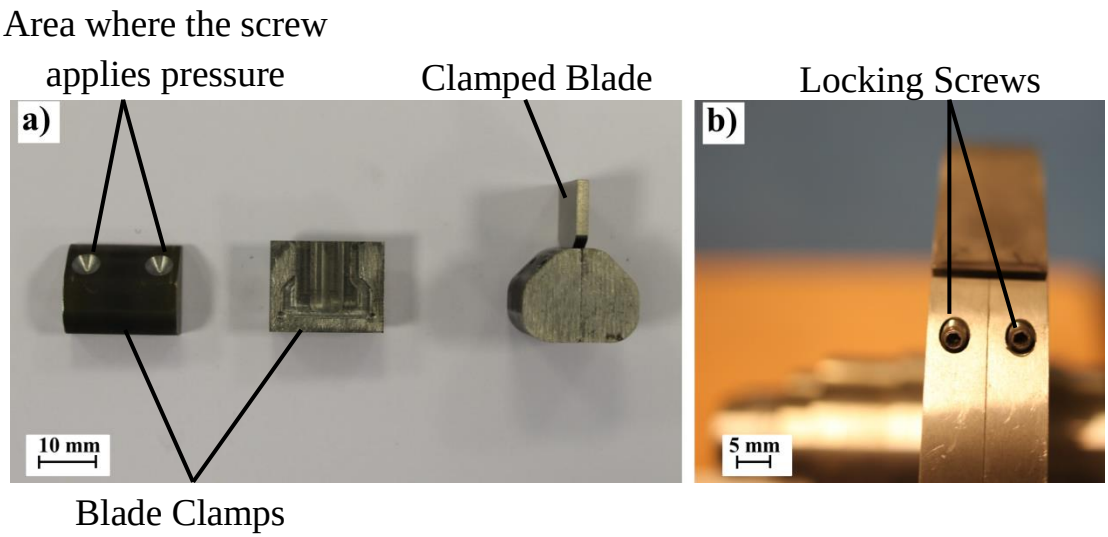

Figure 3.14. Blade Lock System: a) Blade clamps; b) Lock system.

Only one removable blade specimen contacted the abradable coating; the other blade was a dummy blade 180° opposed to it for balancing. The metal disc with a rotor radius at blade tip of 0.0925m was coupled with the spindle, which was capable of rotating the blade with an impact velocity of up to 200ms^{-1}.

In order to reproduce the wear contact between the rotating blade and the abradable lining on an aero-engine, a Z-axis microscope stage allowed movement of the abradable material fitted on it and reproduced the blade incursion on the abradable material. The Z-microscope stage, located below the blade, was fixed on a steel plate parallel to the bench plate and connected with it through two vertical plates. A hole was made on the bench plate in order to allow the microscope stage to be beneath the blade. Figure 3.15 shows the Z-microscope stage position on the test rig, and the plate where it was connected.

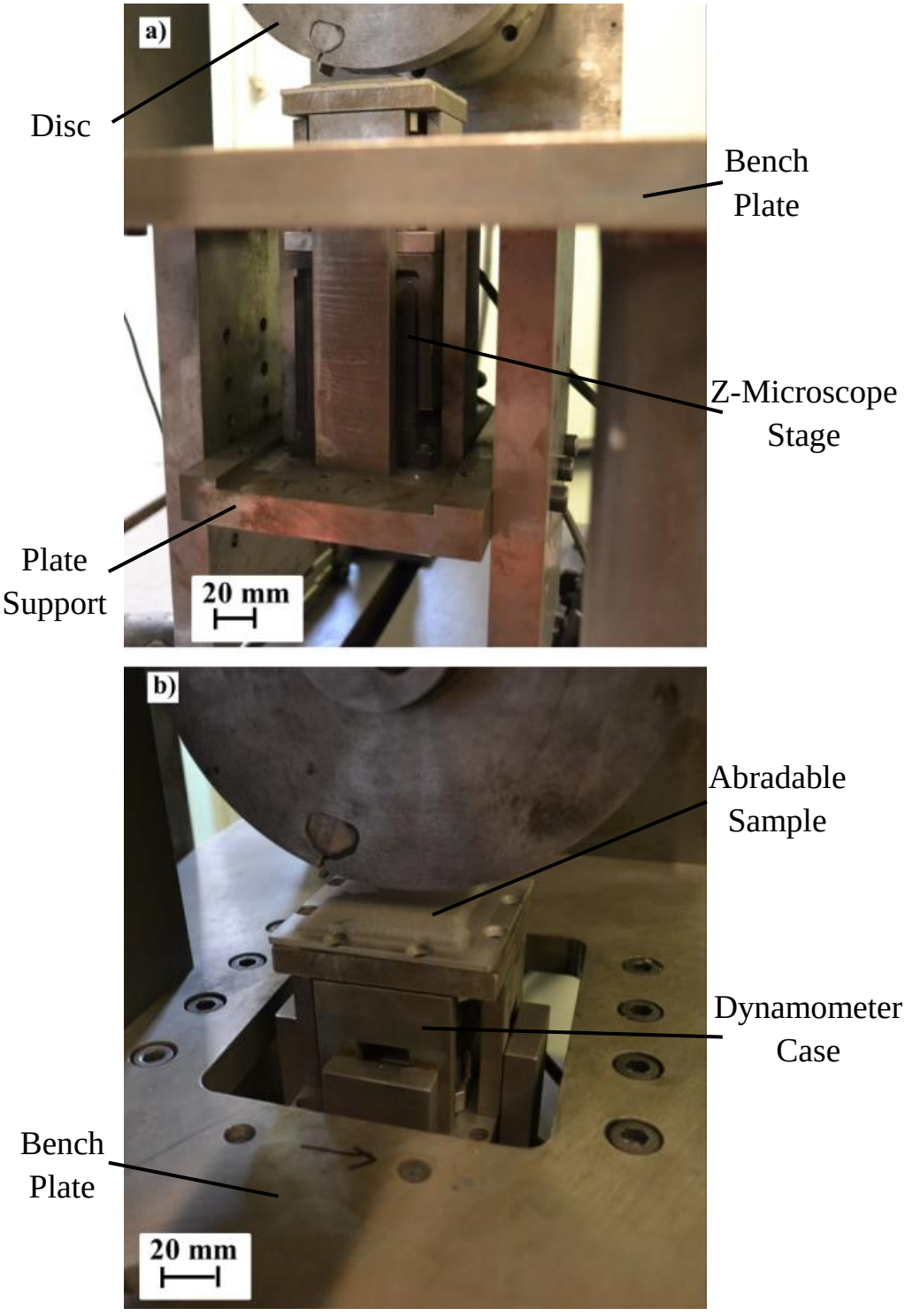

Figure 3.15. Z-axis microscope position, a) Frontal view; b) Top view.

The Z-axis stage was an OptoSigma SGSP80-20ZF motorized stage (Laser 2000 (UK) Ltd., Northants, UK) connected to a programmable stage controller, which allowed incursions between 0.1-2000µms^{-1} at intervals of 0.1µms^{-1} to occur between the blade and coating; Table 3.7 summarises the stage specifications.

Model	Travel distance [mm]	Load capacity [Kg]	Positional repeatability [mm]	Sensibility travel speed [µm/s]	Maximum travel speed [µm/s]
SGSP80-20ZF	20	15	< 0.01	0.1	2000

Table 3.7. Z-axis microscope stage specifications.

During the test, the load applied on the microscope stage was bigger than the load capacity, but as it was periodic and non-continuous, this allowed the stage to work correctly during the tests. The programmable stage controller SHOT-202 (OptoSigma, Laser 2000 (UK) Ltd., Northants, UK), connected with a Z-microscope stage with DMINIS cable (OptoSigma, Laser 2000 (UK) Ltd., Northants, UK), enabled the user to control the movement of the Z axis. The controller was connected to a Personal Computer with an RS232C interface, and allowed a series of movements to be programmed. Figure 3.16 shows the Z-microscope stage connected to the stage controller.

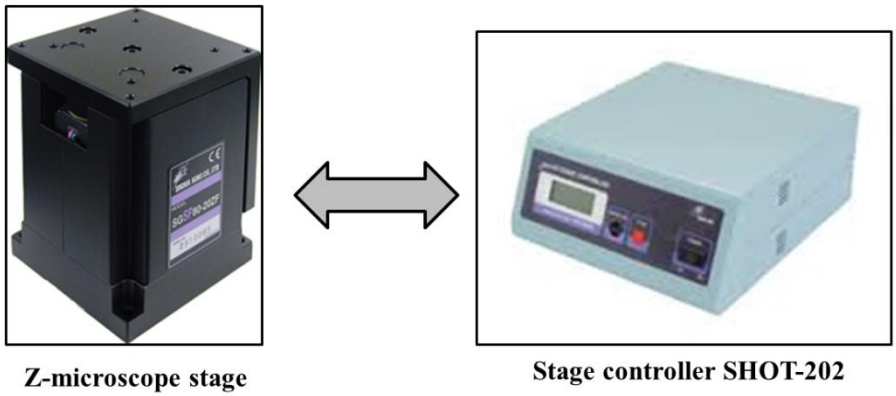

Figure 3.16. Z-microscope stage and stage controller.

The abradable sample was mounted onto a case fixed on the Z-microscope stage, which was designed during this research to hold a dynamometer, which was not present in the previous design, as shown in Figure 3.17.

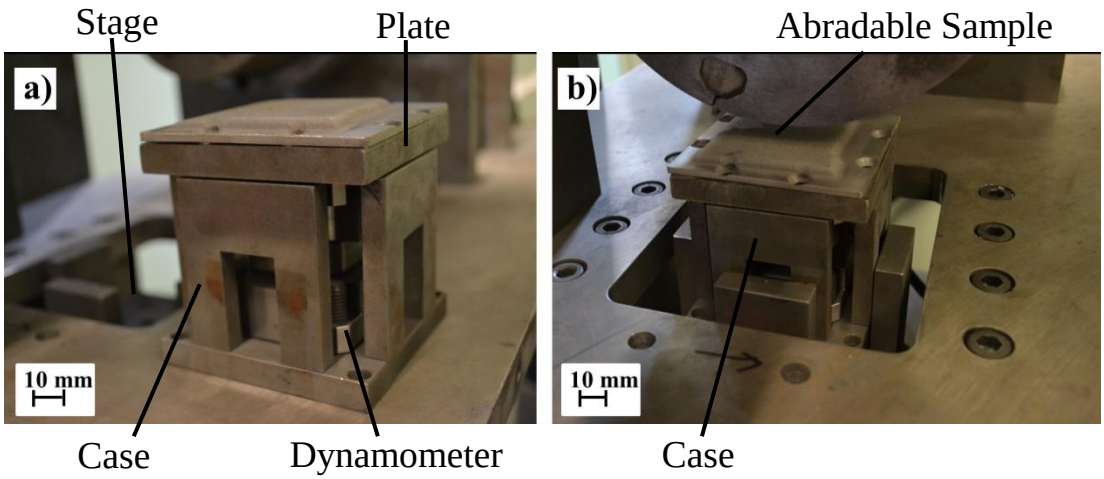

Figure 3.17. Sample support: a) Sample support and dynamometer case; b) Zoom of the sample case mounted onto the stage.

In the tests made in the first application of the experimental test rig [1], the Z-microscope stage was controlled using software developed by SIGMA-KOKI Co., Ltd, (Tokyo, JP), but in this project it was controlled with LabVIEW [76] (National Instruments, LabVIEW 2009) in order to synchronise the stage movement with the measurements recorded. LabVIEW is an interface software that enables communication with different machines. The decision to use it was made in order to synchronise the movement of the Z-microscope stage with the output data from all instruments, with the aim of characterising the wear mechanics in real time. The software developed will be analysed in Section 3.5. Therefore, the test platform reproduced the contact observed in an aero-engine, through the Z-microscope that was able to raise the abradable coating into the rotating blade. The platform was then instrumented in order to investigate the mechanics of the abrasion process.

3.4. Test platform instrumentation

Previous research, highlighted in the literature review chapter, focused on the analysis of the wear mechanics between the blade tip and the coating, based mainly on the analysis of the blade tip and the coating before and after the test, generating a wear map in relation to blade length change or weight change. During this research a stroboscopic imaging technique was used, capable of investigating the nature of the blade tip during the test. The camera was located on the top head of the disc, instead of in the contact area where it was located on the basic test platform [1]. Also, a

dynamometer plate was added to measure the contact force associated with a blade strike, and a laser pyrometer was introduced to measure the temperature of the coating during the test. During each test, the new position of the camera allowed the stroboscopic technique to continuously capture a side profile of the blade tip after a constant number of strikes, and successive image processing allowed the blade length change during the test to be determined. Figure 3.18 shows a schematic diagram of the test rig.

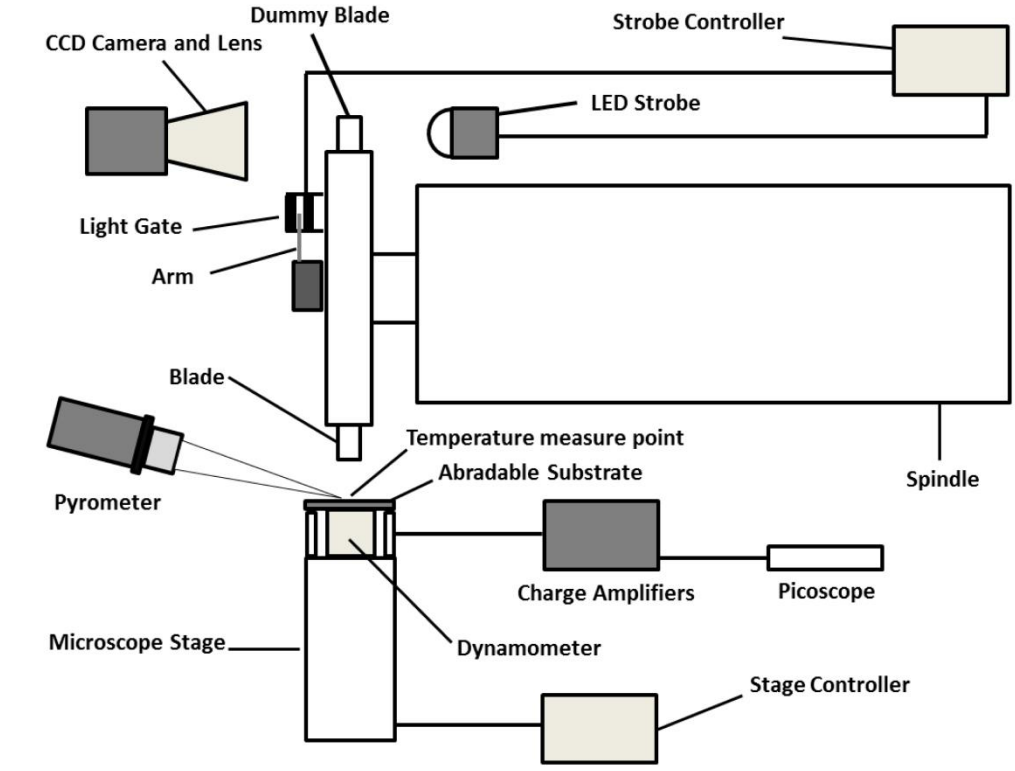

Figure 3.18. Block diagram of the test rig.

3.4.1 Stroboscopic imaging technique

The stroboscopic imaging technique enabled the state of the blade tip to be monitored after a number of strikes, and both the adhesive transfer of material to the blade tip and the blade wear during the test to be investigated. The stroboscopic set-up was composed of an LED, LED strobe controller, light gate and CMOS camera with a macro-zoom lens. The LED (LUMEX SSL-LX100TI23UPGC, Premier Farnell UK Ltd., Leeds, UK) was located at the top dead centre position, with a plastic support, as shown in Figure 3.19. Table 3.8 summarises the LED specification and Figure 3.20 shows the main dimensions of the LED.

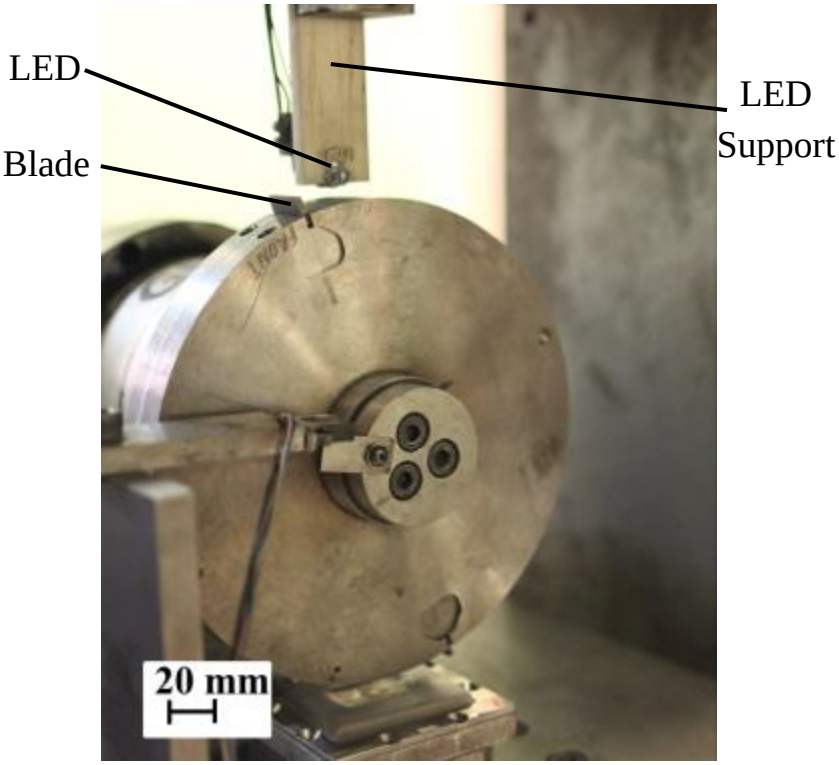

Figure 3.19. LED position.

	Min	**Typical**	**Max**
Forward voltage [V]		3.5	4.0
Reverse voltage [V]	5		
Steady current (safe limit) [mA]			350
Power dissipation (safe limit) [W]			1.4

Table 3.8. LED specification.

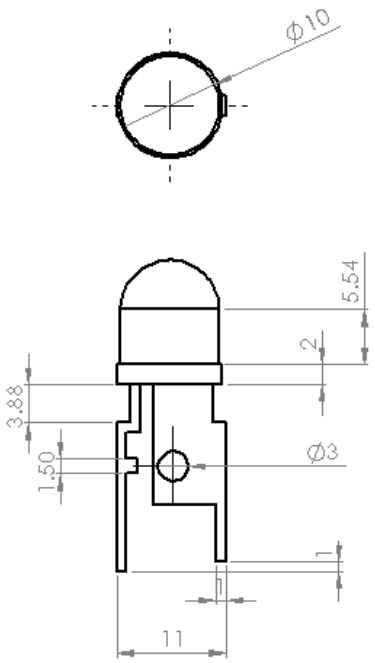

Figure 3.20. LED dimensions.

The LED was powered by an LED strobe controller (Gardasoft RT200F-20, Stemmer Imaging Ltd., Surrey, UK), which produced a pulse with an appropriate delay triggered by a light gate, providing the energy to produce a burst of light from the LED and allowing the camera to capture a side of the blade profile after a constant number of strikes. The controller was configured to output pulses based on an external trigger signal received at the controller's input and generated a pulse output in relation to the set parameters. Table 3.9 summarises the controller specification.

Controller Specification	
Output current	From 0 mA to 20A in steps of 5 mA. Up to 3A per channel continuous or 20 A pulsed.
Output power	Max 30 W per channel
Timing	From 1 µs to 999 ms in step of 1 µs/100 µs
Delay from trigger to pulse	From 3 µs to 999 ms in steps of 1 µs/100 µs
Timing repeatability	Delay + Pulse up to 10 ms: 0.1 µs for pulse width and 2 µs for delay. Otherwise 100 µs
Output voltage	0 V to 47 V

Table 3.9. LED Strobe controller specifications.

The trigger pulse was supplied by means of a light gate (Optek OPB916B, RS Components Ltd., Northants., UK). A rigid metal arm was mounted onto the disc and positioned in a way such that the light gate was interrupted during the rotation of the disc and the trigger pulse was generated. Figure 3.21 shows the rigid metal arm and the light gate.

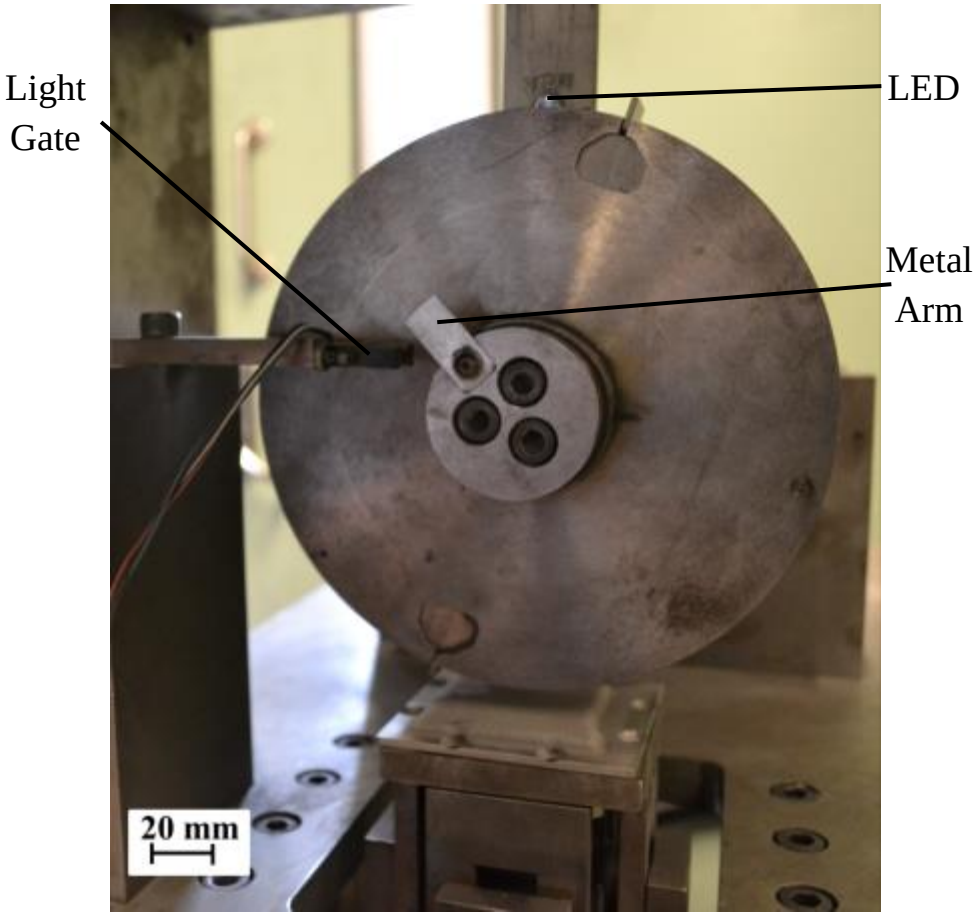

Figure 3.21. Rigid metal arm and light gate.

The trigger pulse was then used, after an appropriate set delay, to send a high energy (40V, 20A) short duration (1μs width) electrical pulse to the LED. This pulse was beyond the maximum rating of the LED (Table 3.8), but because of the very low duty cycle (between 0.02 – 0.05%) in relation to the low pulse width, no damage was caused to the LED. The energy burst of light from the pulse illuminated the blade and allows the image to be captured on camera. The short duration of the LED flash enabled side-on images of the moving blade to be captured with minimal motion blur. Figure 3.22 shows a schematic block of the LED lighting system.

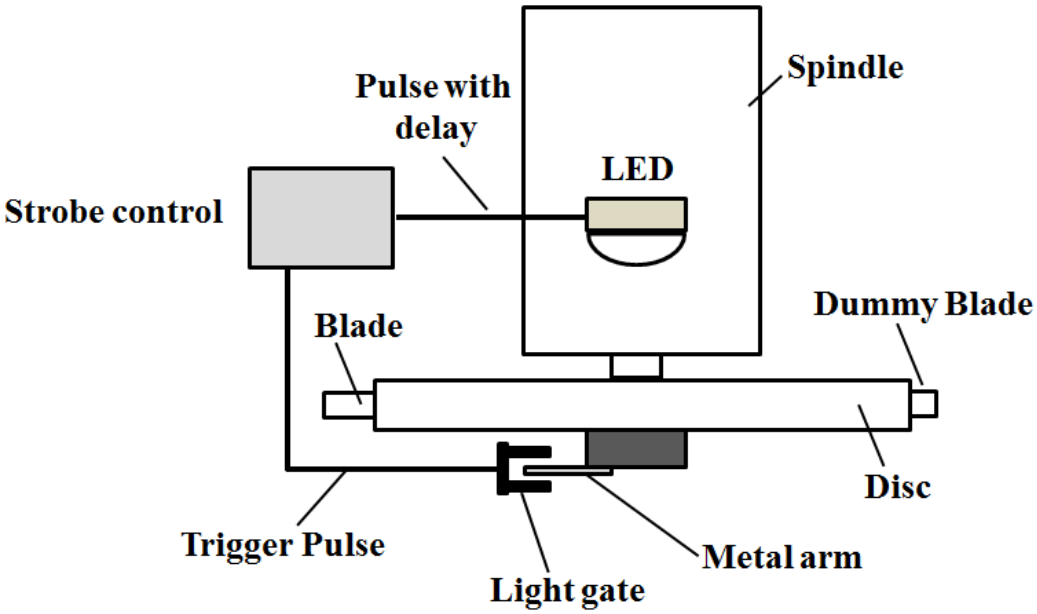

Figure 3.22. Schematic block of LED, LED strobe and light gate.

In order to capture a side of the blade profile after a strike, it was necessary to set an appropriate delay on the strobe controller. The value of the delay was in relation to the linear speed of the blade tip. The determination of the correct value was made in relation to the relative angular distance between the light gate and the position where the blade profile was acquired. Table 3.10 summarises the values of the delay for the different blade speeds investigated.

Blade tip speed [m/s]	**Delay [μs]**
100	96
150	61
200	45

Table 3.10. Values of delay in relation to the blade tip speed.

A CMOS camera (Pixelink PL-B741U, Scorpion Vision Ltd., Hants., UK) with a macro zoom lens (Computar MLH-10x, Scorpion Vision Ltd., Hants, UK) was positioned orthogonal to the spindle. In the previous design, the camera was

connected to the test platform. During this study, this was re-designed with a support connected to the floor and without physical connection to the test rig in order to avoid any motion of the camera from the spindle vibration during the test. A green filter (HMC filter multi-coated) was added in order to filter the green colour of the LED from the image acquisition. Figure 3.23 shows the camera position.

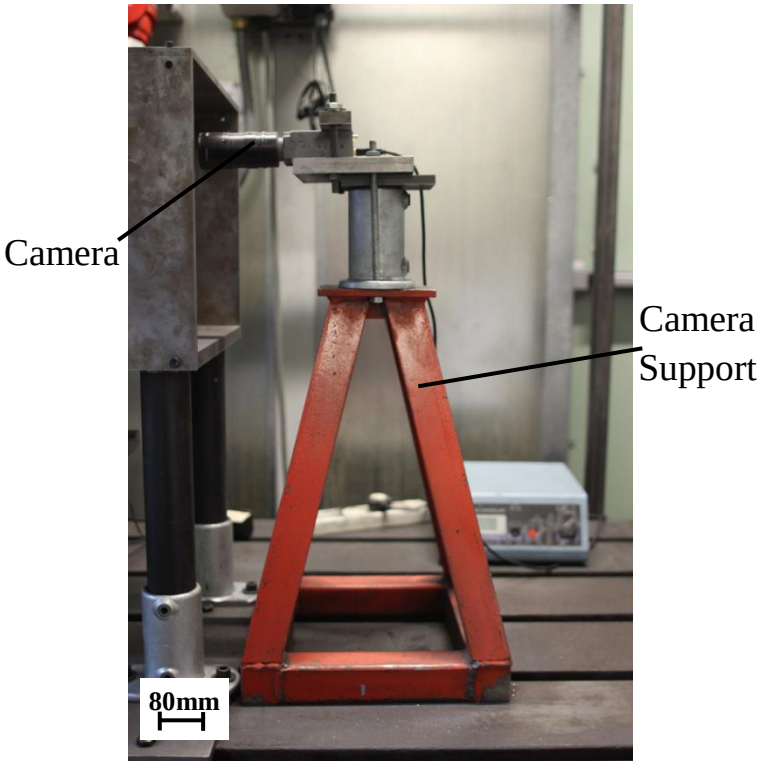

Figure 3.23. Camera position.

The CMOS camera had a 1.3 megapixel sensor with image resolution of 1280 x 1024 pixels and a frame rate of 27 frames per second. This allowed the blade shape after a number of constant strikes to be acquired, and the nature of the wear mechanics of the blade tip to be determined, together with the blade length change during the test. The acquired image from the camera was analysed during this research via LabVIEW [76]. The software was capable of recording approximately 13 pictures every second, and saved these images with a naming convention based on the time when a given image was taken. Using this approach, it was possible to understand how the blade length changed during a test. Figure 3.24 shows a blade tip image recorded from the stroboscopic imaging technique.

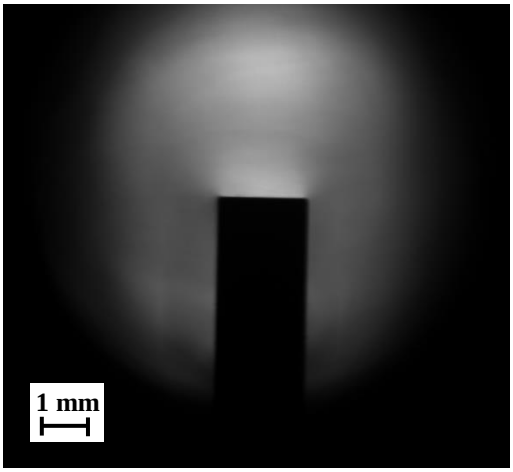

Figure 3.24. Acquired image of the blade.

The camera was focused on the near side of the blade, with the depth of focus ending prior to the far edge. The camera with macro-lens had a focal length of 23.33mm. The far edge of the blade was at a distance of 210 mm from the camera; therefore the distance between the nearest and furthest objects in a scene that appeared acceptably sharp in an image (depth of field [77]) was 5.88mm from the far edge, compared with the 20mm of blade depth observed. Notwithstanding this, the technique quantified the image and helped to understand the trend of the blade length change. The post-processing of the pictures allowed the length change of the blade after a number of constant strikes to be determined. Analysis of the images will be examined in Chapter 4.

The stroboscopic imaging technique allowed blade length change over 11.44µm to be acquired. The sensitivity was obtained from the comparison of the minimum variation of the blade length reached between a series of images acquired during the test, where 11.44µm corresponded to 1 pixel of an image of 1280 x 1024 pixels resolution. Further details will be presented in Section 4.2.3.

3.4.2 Force measurement

In this research a dynamometer was added in order to measure the contact force between the strike blade and the abradable material. It used a piezoelectric dynamometer (Kistler Instruments Ltd., Hook, UK, Type 9347 C), connected to a charge amplifier (Kistler Instruments Ltd., Hook, UK, Type 5070A), and a digital oscilloscope (Pico Technology, Cambridge, UK, 3000 series, PicoScope 3404 B).

The dynamometer measured the contact force using a quartz piezoelectric force link. The three component force sensor was manufactured under preload between two plates. The dynamometer was able to measure along all three cartesian directions, two components along the plane of the coating and one component normal to it. During the contact between the rotating blade and the coating, only the components along the direction of the rotating blade (Tangential Force) and normal to the coating (Normal Force) were different from zero. Figure 3.25 shows the force direction in the experimental platform.

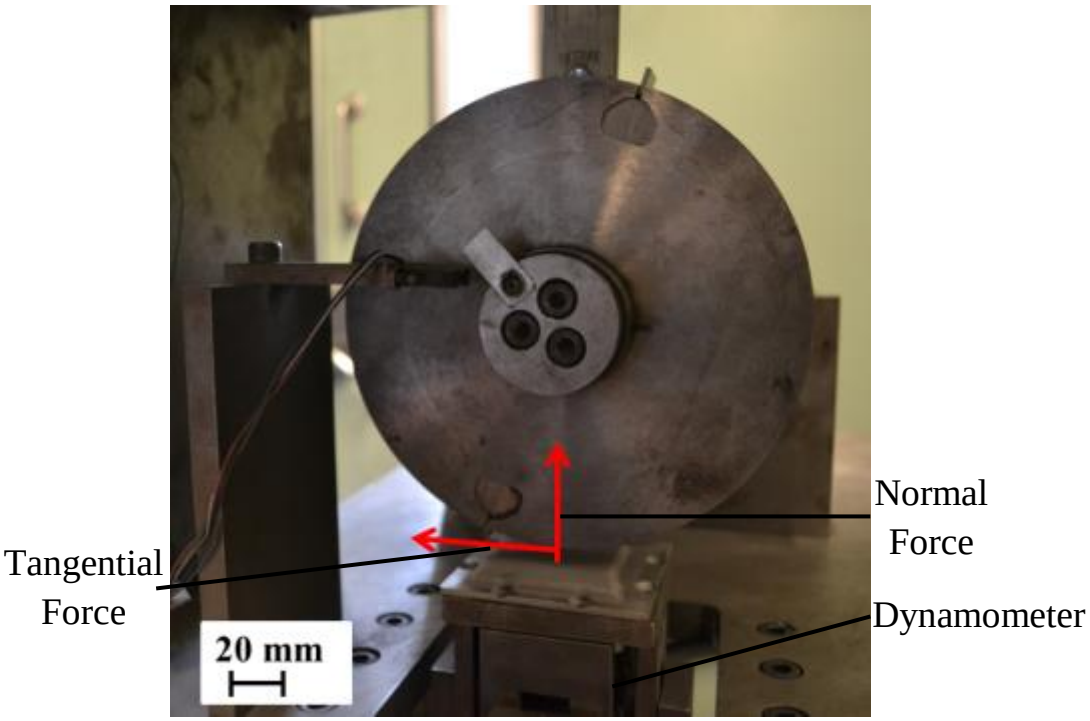

Figure 3.25. Direction of the force.

The dynamometer was mounted over the microscope stage and below the coating, inside a case designed not to compress it. The 80mm x 80mm plate where the coating was fixed was connected with the dynamometer, and the support was 1mm smaller than the dynamometer to avoid compression of the dynamometer when the screws were fastened. Figure 3.26 shows the design system where the dynamometer was inserted.

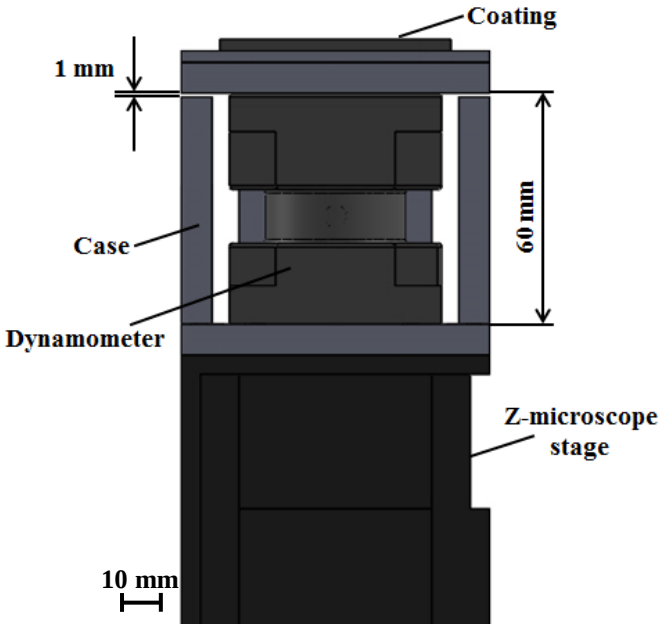

Figure 3.26. Dynamometer case.

The piezoelectric dynamometer had a normal contact force range of −30kN to +30kN and a longitudinal force range of −5kN to +5kN, and allowed an overload of 10%. The dynamometer was a piezoelectric sensor with a sensitivity of $-3.7 pCN^{-1}$ and $-7.8 pCN^{-1}$ respectively for the normal and longitudinal axes. Additionally, the dynamometer had a high rigidity of the sensor for both directions (Table 3.11), and natural frequencies of 3.6kHz and 10kHz respectively for the longitudinal and normal axes, characterising its dynamic response. The dynamic response of the dynamometer will be further investigated in Chapter 4. Table 3.11 summarises the main dynamometer specifications.

Dynamometer specification	
Normal range [N]	-30 … 30
Longitudinal range [N]	-5 … 5
Overload [%]	10
Sensitivity [pC/N]	≈-3.7 (Normal axis) ≈-7.8 (Longitudinal axis)
Rigidity [N/µm]	1300 (Normal axis) 500 (Longitudinal axis)
Natural frequency [kHz]	10 (Normal axis) 3.6 (Longitudinal axis)

Table 3.11. Dynamometer technical data.

The dynamometer works in accordance to a piezoelectric principle; it produces an electrical signal proportional to the applied force. The signal was conducted via an electrode to the 3-pole connector connected to a charge amplifier that amplified the signal, which was recorded using the digital oscilloscope.

The charge amplifier (Type 5070A 4 channel) converted the electric charge produced by the dynamometer into a scaled voltage (voltage output ±10V). Prior to the test, the relation between the voltage (V) and the force (N) was set at 800N/V for the normal axis and at 500N/V for the longitudinal axis. Table 3.12 summarises the technical data of the charge amplifier.

Charge amplifier specification	
Number of channels	4
Connector type	BNC neg.
Measuring range FS [pC]	± 200 … 200000
Error (0 …50 °C) typ./max [%]	< ± 0.3 / < ± 1
Frequency range (20Vpp) [kHz]	≈0 … > 45
Output voltage [V]	± 10
Output current [mA]	< ± 2

Table 3.12. Charge amplifier technical data.

The digital oscilloscope, which captured the voltage signal from the charge amplifier, was able to sample at a rate of 1GHz per channel. The sample rate would be halved with two channels and would be a quarter with three or four channels, with time bases ranging from $2nsdiv^{-1}$ to $200sdiv^{-1}$. The data acquisition could have been controlled with the software PicoScope 6, but instead LabVIEW was again used to synchronise data sets. Table 3.13 summarises the technical data of the digital oscilloscope; Figure 3.27 summarises the contact force acquisition signal.

Digital oscilloscope technical data	
Bandwidth (-3dB) [MHz]	60
Resolution (vertical) [bit]	8
Channel	4
Max sampling rate	1GHz (1 channel), 500Hz (2 channels), 250Hz (3 or 4 channels)
Buffer memory [Mega sample]	8
DC accuracy	± 3 % of full scale
Time base ranges [s/div]	2 to 200

Table 3.13. Digital oscilloscope technical data.

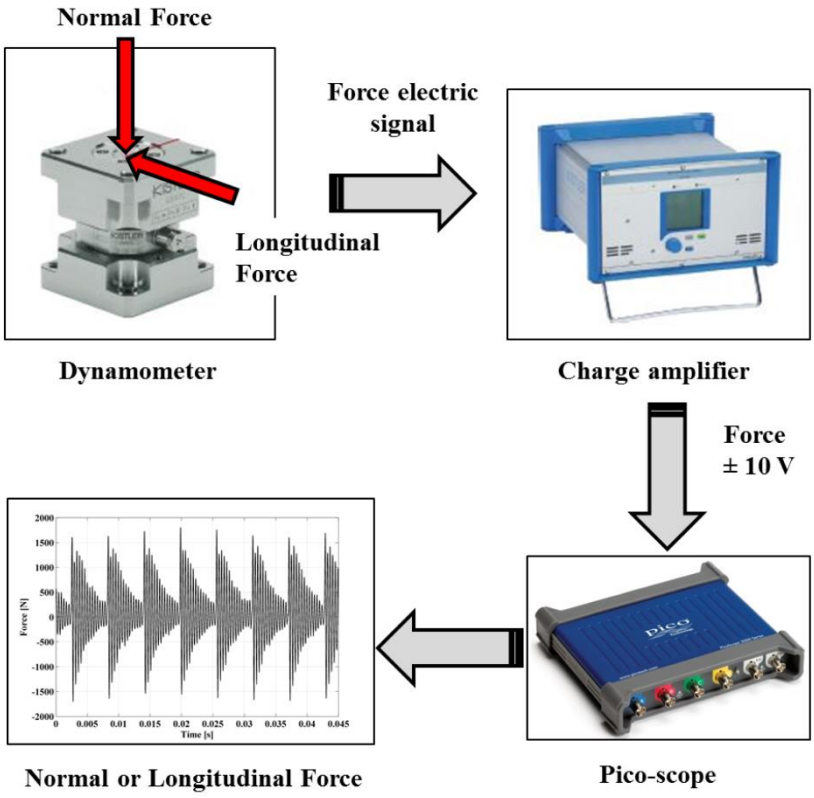

Figure 3.27. Force measurement system.

As shown in Figure 3.27, when a force was applied on the dynamometer, it produced an electric signal proportional to the force applied; the charge amplifier converted then electric signal to a scaled voltage, with calibrated correlation 800N/V for the normal force and 500N/V for the longitudinal force. A digital oscilloscope controlled by a program developed in LabVIEW allowed the acquisition of the signal at known times during the test. More details of the synchronisation of data acquisition will be given in Section 3.5 and Appendix 1.

3.4.3 Temperature measurement

The test rig was instrumented with a pyrometer (CTLM-3H1CF3-C3, Micro-Epsilon, Koenigbacher, Germany [78]) in order to measure the temperature of the coating. The pyrometer was a non-contact infrared sensor, with a spectral range of 2.3µm, and was capable of measuring temperatures from 150 °C to 1000 °C. The sensor had two laser beams that converged to a focal point before broadening at longer distances, and the two laser spots that were produced, indicated the diameter of the outer circumference where the temperature was measured. The optical resolution of the sensor was 300:1, and therefore the spot size changed in relation to the position of the sensor (Figure 3.28).

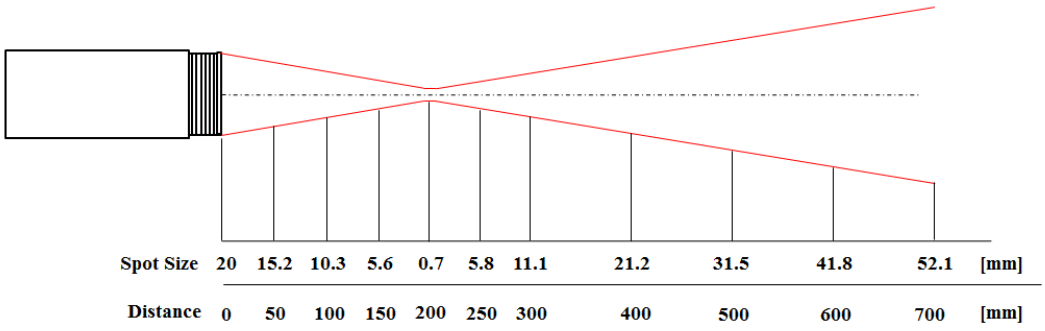

Figure 3.28. Optical resolution of the sensor.

In relation to the optical resolution, the temperature sensor was mounted separately from the test rig on a tripod with a measuring spot size of 4.23mm on the coating where the blade would strike. Figure 3.29 shows the sensor, the position on the experimental platform and the point on the surface where the temperature was measured. Table 3.14 summarises the pyrometer's technical specification.

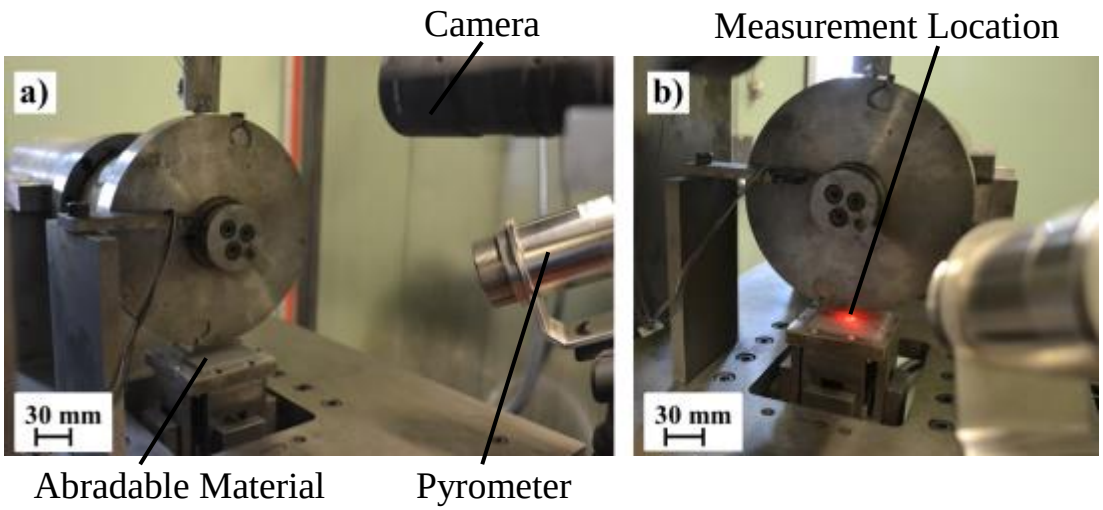

Figure 3.29. Temperature sensor: a) Pyrometer position; b) Measurement location.

Pyrometer specification	
Optical resolution	300:1
Temperature range [°C]	150 to 1000
Spectral range [µm]	2.3
System accuracy	± (0.3 % of reading + 2 °C)
Temperature resolution (digital) [°C]	± 0.1
Emissivity/gain	0.1 to 1.1
Response time [ms]	1 (90%)
Outputs	0/4 to 20 mA, 0 to 5/10 V, thermocouple J,K

Table 3.14. Pyrometer technical specification.

Emissivity [52] was an important parameter. The pyrometer had a single spectral length, that measured the temperature in relation to the radiation emitted, and the emissivity was a parameter correlated to this [52, 78]; therefore, it was necessary to

set the emissivity on the instrument before starting the test. The value of the emissivity was determined by experiment [79, 80, 81], and is analysed in the following paragraph.

The determination of the emissivity of the abradable material was made using a calibrated contact thermocouple type K [79] connected to a digital thermometer (Tenma, 72-7712, Farnell, Leeds, UK), the pyrometer and an oven. The abradable sample was heated inside the oven and the surface temperature was measured using a thermocouple that showed the temperature of the coating, and with the pyrometer sensor that measured the temperature in relation to the value of the emissivity [80, 81]. The emissivity of the pyrometer sensor was changed until the pyrometer sensor showed the same temperature as measured by the contact sensor. Figure 3.30 shows a schematic diagram of the system.

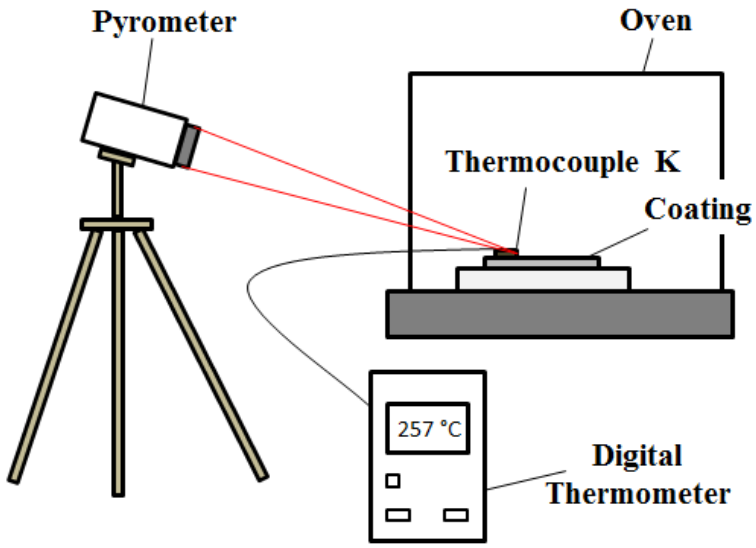

Figure 3.30. Schematic diagram of the system for determining the emissivity.

The type K thermocouple was able to measure the temperature from −200 °C to +1372 °C with an accuracy of ± 0.8 °C, and was connected to a digital thermometer with display resolution of 0.1 °C. The value of emissivity that allows the pyrometer to measure the same temperature as the thermocouple was 0.96. This was determined in a test between 150 °C and 400 °C (typical temperature range measured during the experimental test) in the heating phase, and also in the cooling phase, when the oven was switched off. During this process the temperature was read every 2 minutes with

both sensors. Figure 3.31 shows the temperature measured on the coating by the two sensors.

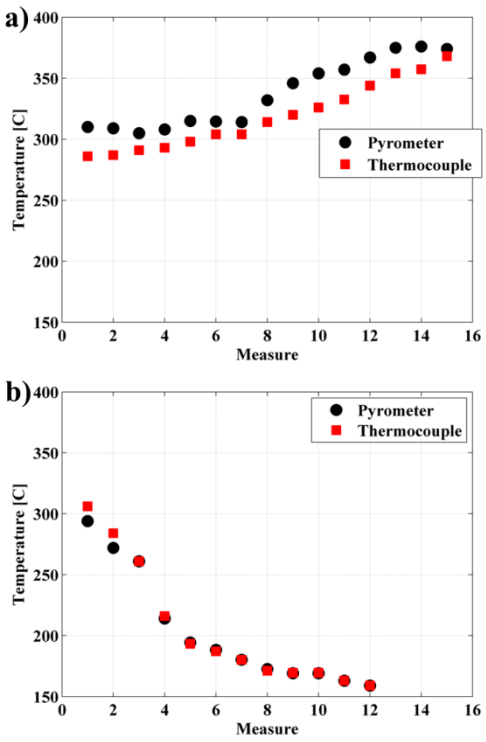

Figure 3.31. Temperature measured with pyrometer and thermocouple: a) Heating phase; b) Cooling phase.

Figure 3.31 shows slightly different temperatures measured by the pyrometer and the thermocouple. This is because the pyrometer had a faster time response than the thermocouple: the time response for the pyrometer was 1ms, while the thermal inertia of the thermocouple was around 2.25s [78, 82]. In the cooling phase, where the oven temperature dropped down slowly, the different time response between the two sensors was negligible. Overall, the similar trend of the temperatures measured by the pyrometer and the thermocouple highlighted that the value of the emissivity set on the pyrometer was correct, and did not change in the temperature range measured.

In order to record the temperature measured during the test, the emissivity was set at 0.96 and the temperature was recorded using software developed in LabVIEW.

3.5. Data acquisition and synchronisation

In this work, a LabVIEW program was developed to control the experimental test platform and to acquire all data from the devices used; hence, it was able to control the Z-axis microscope stage, and acquire the images using the camera, as well as the contact force and the coating temperature. The program was developed instead of using the software of each device, in order to synchronise the data acquisition and save all data at known times during the test. It was developed step by step in order to control each device, and each single program was integrated with the aim of synchronising the control and data acquisition. It was therefore divided into four parts: Z-microscope stage control, the acquisition of data from the camera, and the acquisition of data from the dynamometer and pyrometer. Each of these programs is analysed in detail in Appendix 1. Each acquisition and control program communicated independently with its respective instrument, and in order to synchronise the acquisition, each program was inserted into a case structure. This initialised the acquisition of the data and the movement of the Z microscope stage after a 'Start' button was pushed. All data were saved by name with known times in order to synchronise the data acquired. Figure 3.32 shows the block diagram of the experimental test platform control program, with the single programs highlighted.

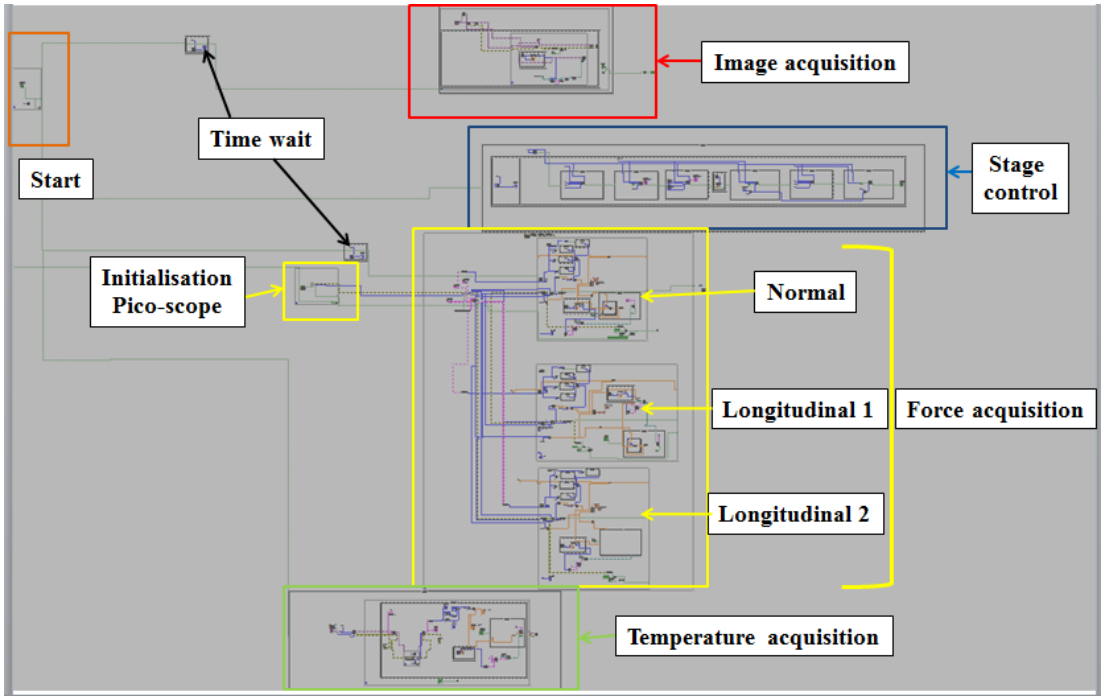

Figure 3.32. Block diagram of the LabVIEW program.

In Figure 3.32, the different programs that allowed control and synchronisation of the equipment introduced in this research were highlighted in different coloured boxes. The orange box highlights the initialisation of the program where the 'Start' button was located: this allowed the initialisation of all single programs connected with it through a case structure 'True' and 'False'. The red box highlights the part of the program that acquired and saved the images from the camera. The blue box represents the program to control the Z-microscope, and the yellow and green boxes respectively represent the program for force and temperature acquisition.

Before each test, the first step was to run the program, initialise the Pico-scope, and then to click the 'Start' button to start the test. At the same time the image, force and temperature acquisitions started, and the microscope stage moved in relation to the previously set parameters. In order to synchronise the acquisition times of the different programs, the activation was connected with a case structure controlled by the 'Start' button. A time delay was introduced in order to synchronise all structures. In addition, in order to have more accuracy in the time synchronisation, all data were saved with a name convention based on the time when they were acquired. Figures 3.33 and 3.34 show a front panel of the LabVIEW program.

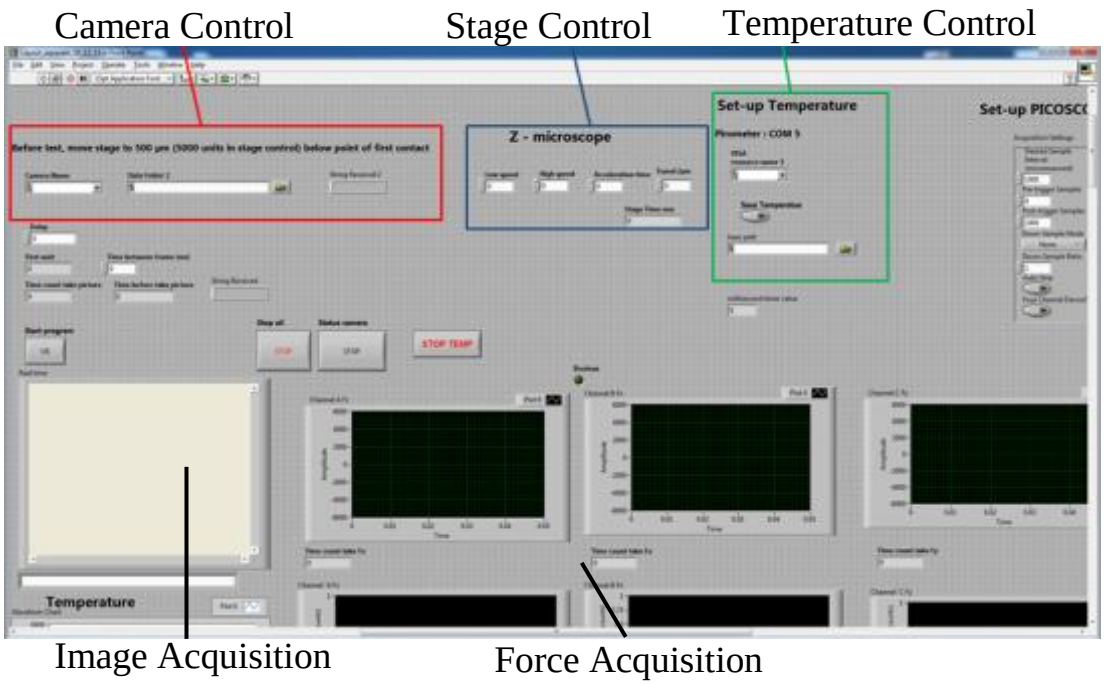

Figure 3.33. Front panel of LabVIEW program.

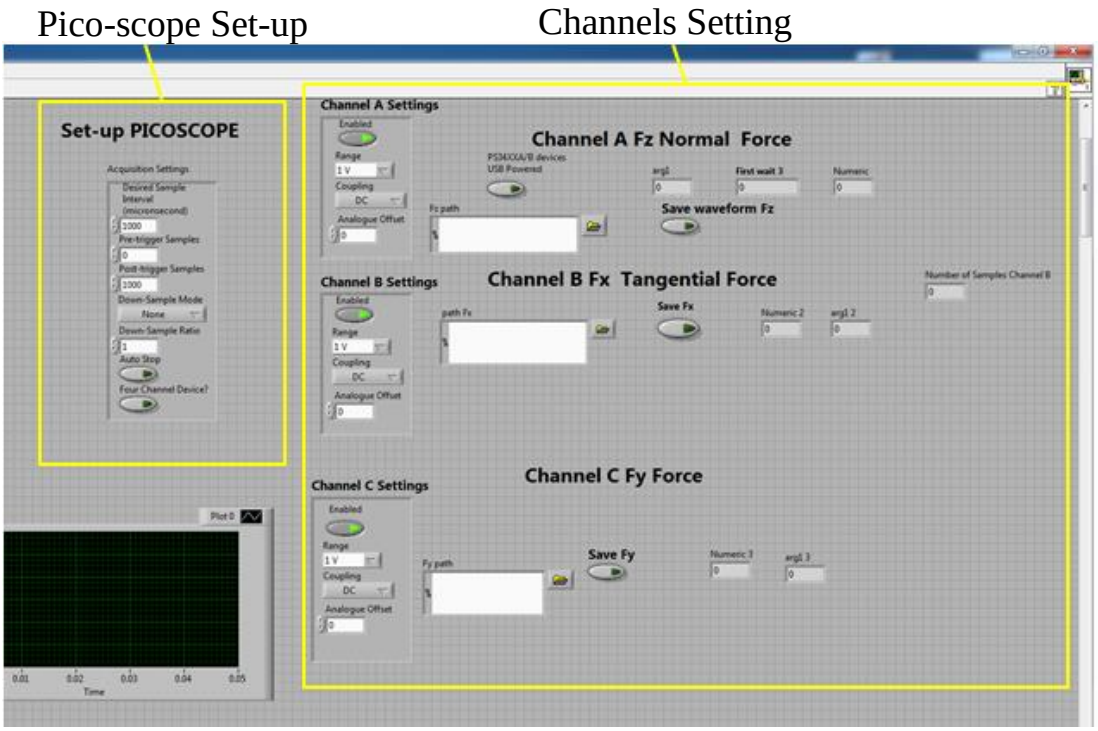

Figure 3.34. Front panel of LabVIEW program.

Before the test started, in 'Camera control' highlighted in Figure 3.33 with a red box, the port device of the camera needed to be found in order to communicate with the program; then the path where the image would be saved needed to be set. In 'Stage control', highlighted in Figure 3.33 with a blue box, the incursion speed and incursion depth were set in relation to the test conditions, which would establish the movement of the Z-microscope stage. The green box in Figure 3.33 indicates the 'Temperature control', where the communicating port device had to be found and the saving path set. Regarding to the 'Force acquisition' setting, Figure 3.34 shows the 'Pico-scope Set-up', where the sample acquisition of the signal was set at 10µs, with the range for each channel set at 10V; finally the saving path also needed to be set. The sample acquisition represented the resolution of the signal acquired. For example, during the test the frequency of strike was 172Hz or 344Hz if the blade speed was $100ms^{-1}$ or $200ms^{-1}$ respectively, so with a sample interval of 10µs, around 580 points of the signal between contact strikes at low blade speed could be obtained. This represented a good value in order to analyse the force contact strike, obtained by the minimum possible sample interval set on the software. Additionally, the correlation between voltage and force on the charge amplifier was 800N/V, so

the program could easily acquire a force up to 8000N. If the force was higher, the calibration correlation between force and voltage could be changed on the charge amplifier.

3.6. Chapter summary

- AlSi-hBN abradable materials with hardnesses R15Y 54.6, 59.6, 63.0 and 72.3 and a titanium blade were characterised for material properties. The microstructure analysis of the coating highlighted clear differences between the softer coating when compared with the harder coating, where a softer coating showed a higher level of hBN and a reduced metal phase, and a harder coating showed a lower level of hBN and an increased metal phase.

- An experimental test rig that reproduced the contact between the rotating blade and the casing of the compressor was analysed and improved in order to monitor, in real time, the wear mechanics of the blade and the abradable coating.

- A stroboscopic imaging technique was introduced on the test platform in order to monitor the nature of the wear mechanics and capture the blade profile during the test.

- A dynamometer was introduced on the test platform in order to measure the contact force during the test.

- A laser pyrometer was introduced in order to measure the coating temperature.

- The test protocol and data acquisition were made with a program developed in LabVIEW. The program enabled the acquisition, at known times, of image, force and temperature data, and allowed the input of test conditions (incursion speed and incursion depth) to be set.

4. Methodology

This chapter presents the methodology of the experimental test between the rotating blade and the abradable material. The first section introduces the parameters of the experimental test followed by analysis of the test protocol of the experimental test rig that reproduced the wear mechanisms observed between the blade tip and the abradable material. In the later section of the chapter, the post-test analysis is introduced in order to characterise the wear mechanics. The first part of this section consists of the analysis of the sample before and after the test was performed. The blade length and weight change were recorded, the blade tip profile was captured,

and the abradable wear surface was observed. The abradable surface and blade tip were analysed using an energy dispersive X-ray fluorescence spectrometer, with the aim of analysing the chemical composition of the wear mechanics. The second part consists of the analysis of data obtained from the instrumentation of the test rig, the analysis of the stroboscopic imaging in order to obtain the blade length change after a constant number of strikes, the contact force and the temperature of the coating. Finally, a methodology is introduced for mounting the abradable sample in order to analyse the microstructure of the coating. It was used to control samples pre-test and also a selected sample of interest post-test.

4.1. Test parameters

4.1.1. Test input parameters

In the tests performed, the input parameters were:

1. *Blade impact speed;*
2. *Incursion per pass / incursion speed;*
3. *Incursion depth;*
4. *Hardness of the abradable sample.*

The *blade impact speed* (*V*) is the linear velocity of the rotating blade tip; it is set using the inverter controller of the spindle. During the test the arc of the contact continuously changes in relation to the incursion depth; therefore, the speed vector angle of the first contact changes. Further consideration will be made when the other incursion parameters are introduced. Figure 4.1 shows the vector of the blade impact speed along the rotating trajectory of the blade tip.

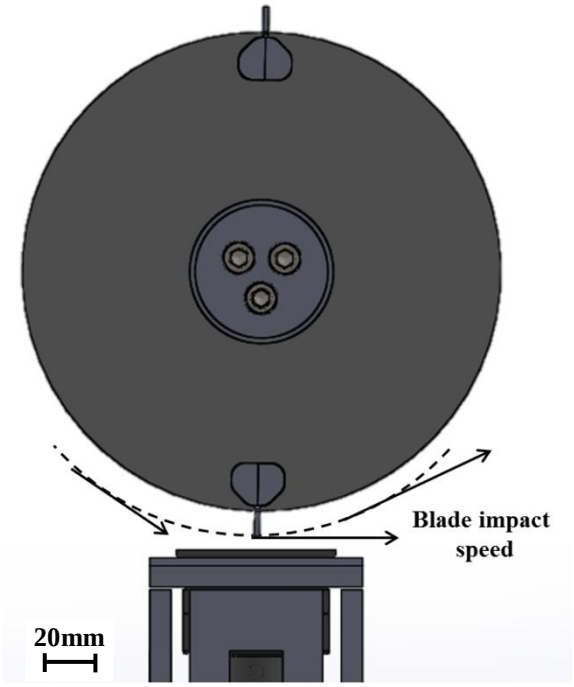

Figure 4.1. Blade impact speed.

The experimental setup was capable of rotating the blade with an impact of a velocity of up to 200m s^{-1}. In this series of tests the blade impact speed was varied between 100 and 200m s^{-1} to allow the wear mechanics of the aero-engine to be reproduced [1, 6, 7, 15, 16, 17]. Previous researches had highlighted that different impact velocities produced similar wear mechanisms and the minimum speed tested produced a similar wear mechanism to those observed in the aero-engine [1, 6, 15].

The *incursion per pass* (I_p) is defined as the axial depth of the material removed by the rotating blade during a single strike of the coating. The *incursion speed* (I_s µm s^{-1}) is the rate that the microscope stage advances the abradable surface in the Z-axis direction. It is a combination of *incursion per pass* I_p (µm $pass^{-1}$), rotor *radius at blade tip R* (0.0925m) and *blade impact speed V* (m s^{-1}), and is calculated as shown in Equation (4.1).

$$I_S = \frac{I_p \cdot V}{2 \cdot \pi \cdot R} \tag{4.1}$$

The microscope stage is able to incur at speeds between 0.1 and 2000µm s^{-1} at intervals of 0.1µm s^{-1}. In the tests performed the incursion speed varied between

3.4µm s^{-1} and 344µm s^{-1}. These test parameters were selected as they had been previously identified as generating similar wear mechanisms to those observed in aero-engines [1, 6, 1, 11], and were the same incursion conditions as obtained on the Sulzer test rig [3, 7, 11, 15]. The main aim of using this parameter was to test the abradable coating and reproduce the wear mechanics observed in aero-engines and to study extreme conditions of contact, one with a low incursion speed and one with a high incursion speed, in order to investigate the key factors and the properties that influenced the wear mechanics. The low incursion rate represented the interaction of the flight phase [8] generated from thermal and centrifugal dilatations and unbalanced parts, while the high incursion rate represented the handling phase of the jet engine [9, 10]. In addition, it showed how the material responded between low and high incursion rates in relation to the size of the particles of the abradable material [14].

The *incursion depth* is the final cutting depth of the test. It was kept constant at 2mm in relation to the limitation of the coating thickness of around 3mm; also, the incursion depth was chosen based on previous results and observations of maximum wear depths of the abradable lining in aero-engines between 1 and 2.4mm [6, 11, 15, 16]. Figure 4.2 shows the incursion depth on the coating.

Figure 4.2. Schematic diagram of the abraded test sample highlighting the incursion depth.

A combination of the blade impact speed, incursion speed and blade tip radius allows calculation of another parameter, the theoretical rub length (*L(t)* (m)). The theoretical rub length *L(t)* is the sum of the lengths of the rub during the test. This parameter is limited by the thickness of the coating and is a combination of the input parameters analysed before, namely incursion speed I_s (m s^{-1}), time *t* (s), radius at blade tip *R* (0.0925m) and the theoretical number of strikes *n*, and is calculated as shown in Equation (4.2).

$$L(t) = \sum_{i=1}^{n} 2 \cdot R \cdot acos\left(\frac{R - I_i \cdot t_i}{R}\right) \tag{4.2}$$

Figure 4.3 shows the rub length at 'i' passes in Figure 4.3a, and Figure 4.3b shows the rub length at the end of the test.

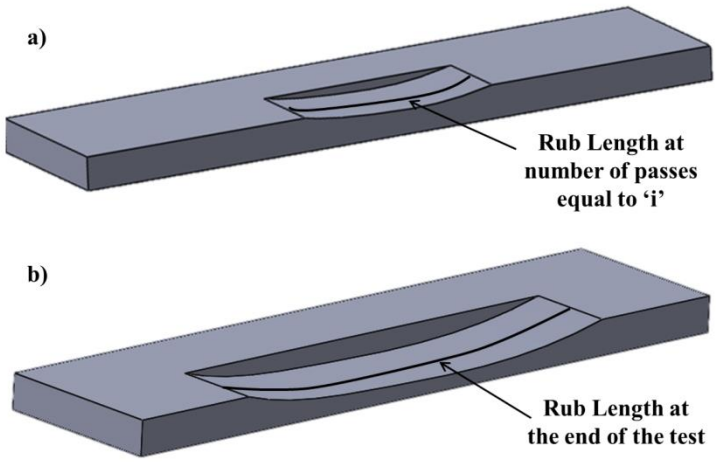

Figure 4.3. Theoretical rub length: a) At 'i' pass; b) At the end of the test.

The theoretical rub length is a parameter that shows the total length of rub and it will be analysed later. The increase of the incursion depth determined an increase of the arc of contact, as shown in Figure 4.3, and therefore this determined a continuous increase of the speed vector angle when the blade first contacted the abradable as the number of passes increased.

The *hardness of the coating* is the superficial Rockwell hardness of the abradable sample and its measurement was described in the previous chapter. Microstructure analysis of the sample highlighted clear differences between the softer coating and the harder coating, with different compositions of hBN and porosity.

The wear mechanics between the rotating blade tip and abradable sample were investigated in relation to input parameters of impact blade speed, incursion speed, incursion depth and coating hardness.

4.1.2. Test parameters of the experimental platform

The wear mechanics were investigated in relation to the input parameters, as highlighted in the previous section. The samples were tested with different incursions per pass, hardness and blade speed, and constant incursion depth. Previous work highlighted that the incursion per pass / incursion speed is a dominant parameter with respect to the wear mechanics [1, 3, 6, 15, 26, 33]. The incursion rates were chosen in relation to previous studies that reproduced the wear mechanics observed in the aero-engine, e.g. adhesive transfer, melting, blade wear and cutting [1, 6]. During engine operation, rotor misalignment, thermal and centrifugal dilatations and unbalanced parts determine a contact between the rotating blade and abradable coating, and a low incursion speed represented these interactions in the flight phase. An example of blade and coating interaction is on warm restart: this occurs when the engine is running at steady state and is shut down, it then cools down and is restarted. The disc remains hot and expands radially, while the abradable shroud ring cools and retracts; therefore, the clearance is reduced and contact occurs [17]. While, high incursion rate condition represents the handling phase of the jet engine.

Previous research [1, 3, 6, 15, 26, 33] highlighted a common low incursion rate of 0.02μm $pass^{-1}$, and high incursion rate of 2μm $pass^{-1}$, where different wear mechanics were observed [6]. Additionally on the remaining samples intermediate incursion rate values were tested in order to explore the transition of the mechanics. The incursion depth was kept constant at 2mm in relation to the limitation of the coating thickness of around 3mm. Also the incursion depth was chosen based on previous results and observations of maximum wear depths of the abradable linings between 1mm and 2.4mm [6, 11, 15, 16]. Coating thicknesses greater than 3mm were not considered, as these are known to increase the susceptibility of the coating to crack and spall formation during the contact between the blade and the coating, due to the thermal expansion coefficient mismatch between coating and casing during a flight cycle and also due to residual stresses [16, 17].

Previous research [1, 3, 6, 33] highlighted that an increase of the blade speed produced similar wear mechanics, highlighting less influence on wear mechanics with different speeds. Therefore the primary focus of the research was on the influence of the incursion rate. However, the influence of the blade speed was still

analysed, especially at low and high incursion rates, and in relation to the sample availability also at intermediate incursion rates.

The analysis of the microstructure of samples with different hardnesses showed different compositions of hBN and porosity, as highlighted in Section 3.1.4., and implied different abradabilities, tensile strength and erosion resistance [13]. Therefore the hardnesses of the samples were chosen based on Rolls Royce specification in the window of hardness between R15Y 45 and 75 [14]. In this range, the abradable material should be 'soft' enough to have a good abradability, but also 'hard' enough to withstand erosion. As highlighted in Section 3.1.1, this research analysed coatings with hardness R15Y 72.3, R15Y 63.0, R15Y 59.6 and R15Y 54.6. The softer coating was chosen, with hardness R15Y 54.6, because a softer coating implied a low erosion resistance, along with poor resistance to oxidation, corrosion and thermal failure [13]. Table 4.1 highlights the tests performed in relation to the incursion rate per pass for different hardness samples and in relation to the blade speed.

Blade speed				
100 m s^{-1} 150 m s^{-1} 200 m s^{-1}				
Incursion rate per pass [µm]	**R15Y 54.6**	**R15Y 59.6**	**R15Y 63.0**	**R15Y 72. 3**
0.02	● ● ●	● ● ●	● ● ●	● ● ●
0.04		● ●		●
0.06		● ● ●		● ● ●
0.08				●
0.1	● ● ●	● ●	● ● ●	● ●
0.14				●
0.2	● ● ●	● ● ●		● ● ●
0.3	●		● ● ●	
0.4				●
0.6	●		● ● ●	
1	●	● ● ●	● ● ●	● ●
2	● ● ●	● ● ●	● ● ●	● ● ●

Table 4.1. Test parameters.

4.1.3. Test protocol

In the experimental platform the contact between the rotating blade and the abradable linings was recreated by controlling the movement of the Z-microscope stage with a defined speed of incursion on the blade. Before the start of the test, the Z-microscope stage with abradable material fixed on top was moved 5mm below the blade tip. The distance of 5mm was chosen as a reasonable distance to avoid any contact between the rotating blade and the coating before the test started. The spindle control set the desired rotating speed, and therefore the blade impact speed. When the spindle reached the desired rotating speed, the Z-microscope stage with the abradable coating was raised and the blade tip engaged with the substrate material. At this point, the coating incurred on the rotating blade tip at a constant speed rate. When a depth of 2mm was reached (distance travelled of the Z microscope stage) the coating was withdrawn from the blade tip to the initial position 5mm below the blade tip. Figure 4.4 shows a schematic frontal view of the relative position between the blade tip and microscope stage (Figure 4.4a) and during the test when the microscope stage with the coating incurring on the blade tip at a constant speed (Figure 4.4b).

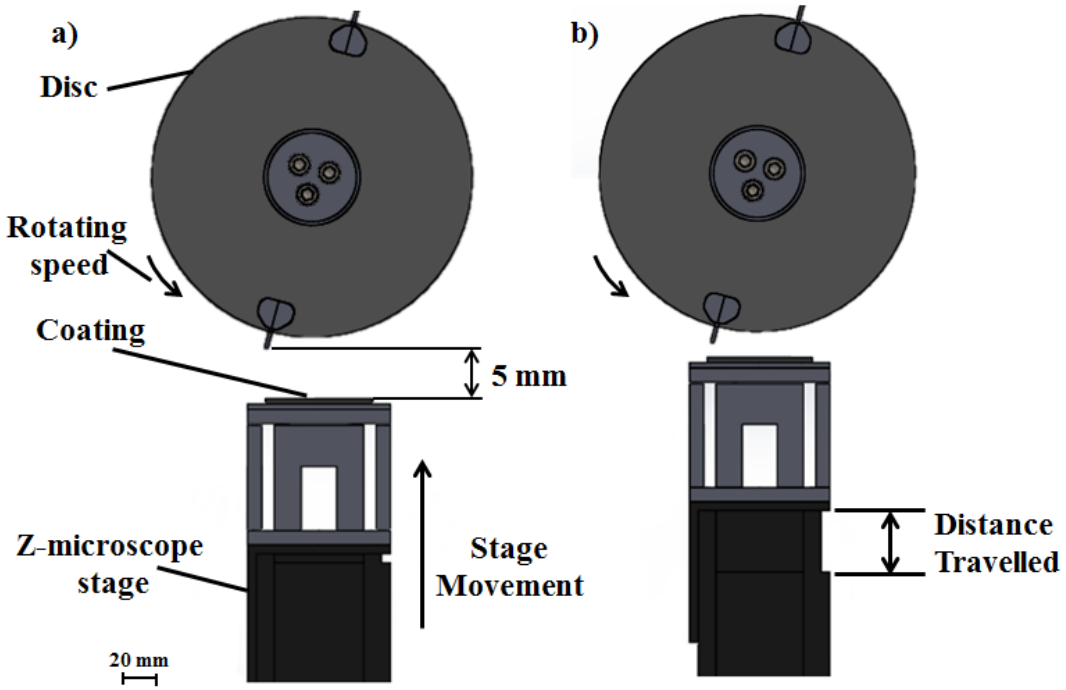

Figure 4.4. Test rig incurring phase: a) Microscope stage raising; b) Contact between blade tip and coating at constant incursion speed.

After the test, the blade length, weight change, and blade profile were recorded. Because instrumentations of the test platform were developed during this research, not all of the instrumentation was available for all the samples tested. During the test, the blade tip profile was measured with a stroboscopic imaging technique, the force measurement and temperature were acquired respectively with a dynamometer and pyrometer, and also the blade tip and the substrate was analysed post-test. However, for example, the samples with hardness R15Y 63 were tested in the initial phase of the research and only the stroboscopic technique was applied; therefore a sample with similar hardness, R15Y 59.6, was tested in order to investigate that hardness with all instrumentation.

4.2. Analysis of the experimental test

The analysis of the wear mechanics between the blade and the coating was divided into two main parts: analysis of the sample post-test and analysis during the test. In the first part, the samples were analysed and observed post-test in order to identify the different wear mechanics. Blade length and weight were recorded before and after every test in order to monitor the mechanics of the contact. An image of the blade captured with a light box allowed the blade profile to be determined. The chemical composition of the material transfer was analysed with an EDXRF machine. In the second part, the data analysis obtained from the instrumentation of the test platform was evaluated. Finally, the material response was analysed by sectioning the sample and observing it with an optical microscope.

4.2.1 Analysis post-test

The length and weight of the blade sample were recorded before and after the test in order to quantify the change in the contact mechanics on successive analyses. The first step in the analysis post-test was the visual analysis of the abradable sample and the blade in order to observe the difference compared with the sample before the test and identify the wear mechanics, such as adhesive transfer on the blade tip, thermal damage, blade wear, melt transfer, cutting or grooving. Figure 4.5 shows the abradable and blade samples before and after the test, where the visual analysis highlighted the wear mechanism.

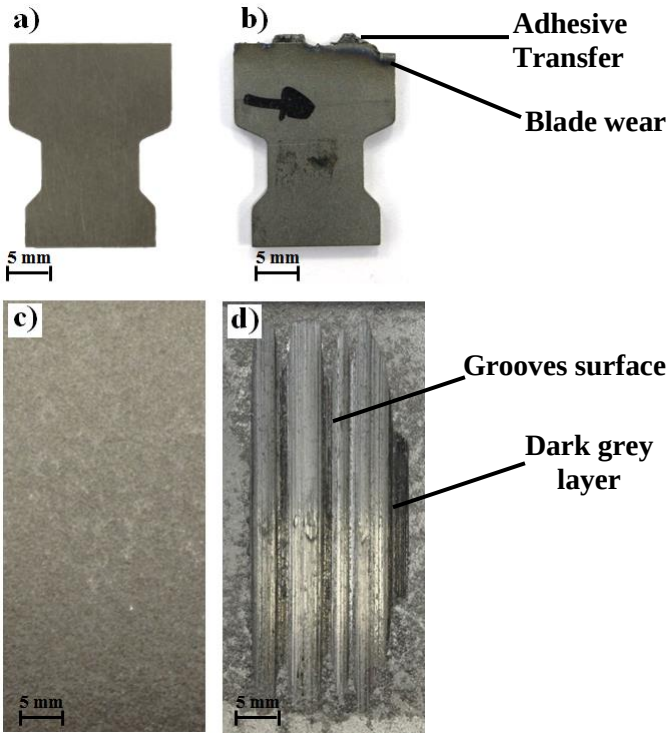

Figure 4.5. Blade (a, b) and abradable (c, d) samples before and after the test, for the test performed at incursion rate of 0.02μm pass^{-1}, blade speed 100m s^{-1} and coating hardness R15Y 72.3.

As shown in the figure, the sample observation shows the change on the blade tip and abradable coating, highlighting the wear mechanics, in this case adhesive transfer, grooving, a dark layer on the coating and blade wear. The next step was a quantitative analysis of the blade, using the blade length and weight change previously recorded. In this way, the blade length and the weight were recorded before and after every test. The blade length was measured using a micrometre (resolution ±0.001mm) and the blade weight by using an electronic balance (Sartorius electronic analytical balance basic^{plus} BP210D, resolution ±0.0001g). The images of the blade and the coating were recorded using a DSLR camera (Nikon D3100, zoom lens 18-55mm Nikon, Japan) connected on a tripod and positioned above a light box (Quasar A4 Lightbox, Scientific Laboratory Supplies Ltd., Yorkshire, UK). The image of the blade acquired on the light box allows the blade profile to be determined. Figure 4.6a shows the experimental set-up, with Figure 4.6b showing an example of a captured blade image.

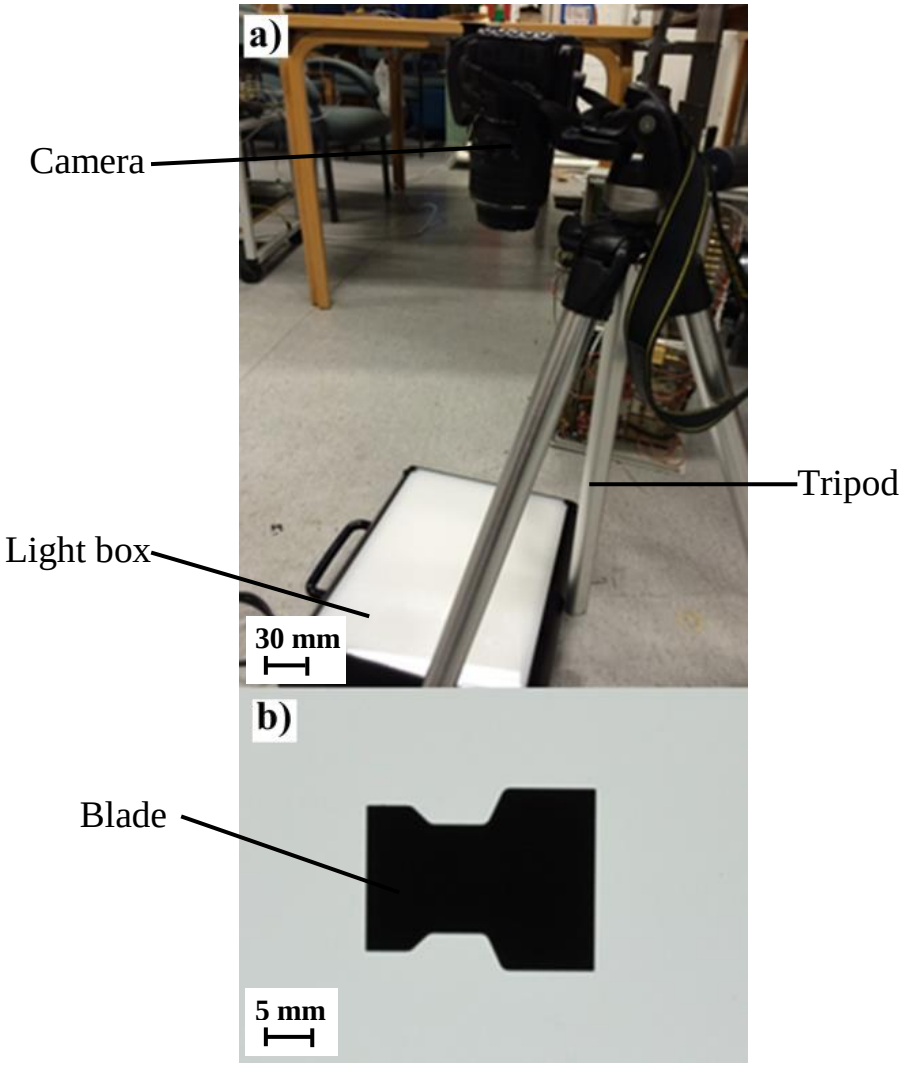

Figure 4.6. Image system acquisition: a) Experimental set-up; b) Image acquired.

The image of the blade, Figure 4.6b, was analysed using IMAGE J in order to obtain the blade profile. The image was segmented from the rest of picture, and was then de-speckled, converted to binary, and the profile of the blade determined. A program developed in MATLAB analysed the blade profile and calculated the average blade length and the maximum blade length. Figure 4.7 shows the profile of the blade obtained with IMAGE J (Figure 4.7a), and the blade tip profile with a dashed line that represents the initial length, the average blade length and the maximum length.

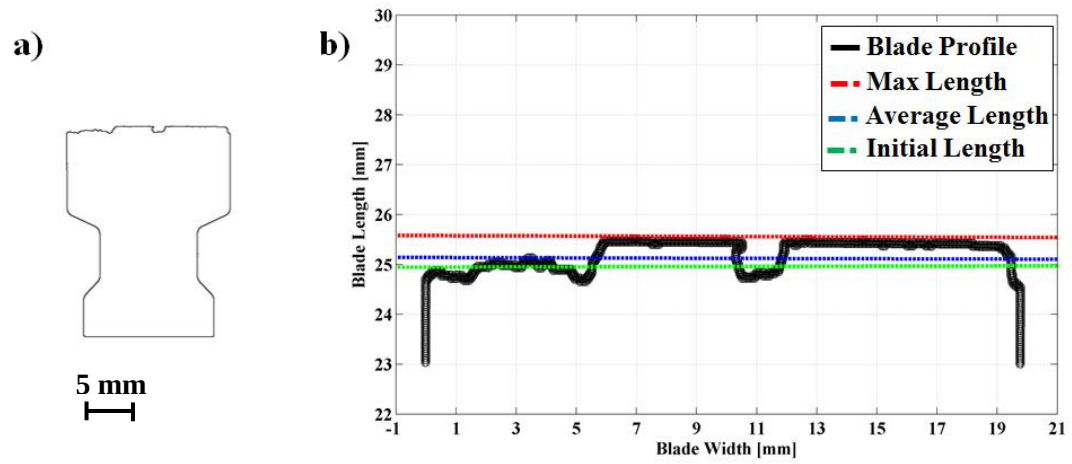

Figure 4.7. Blade profile analysis of test 2µm pass^{-1}, 200m s^{-1}, R15Y 72.3: a) Blade edge; b) Blade tip profile.

This analysis provided information on the wear mechanics between the blade tip and the abradable coating, by obtaining the average length of the blade tip and evaluating the blade length change between the final length and the previously recorded initial length. However, this approach did not analyse the nature of the blade tip strike on the abradable material, but only the condition before and after the test, so it provided no insight into the process of adhesive transfer. The adhesion / melt transfer were then analysed by X-ray analysis in order to obtain their chemical composition.

4.2.2. Analysis of chemical composition of sample

The abradable sample surfaces and blade tip were analysed using an energy dispersive X-ray fluorescence spectrometer (EDXRF, Fischerscope X-RAY XAN 250, Lymington, UK) in order to examine the chemical composition of the material transfer from the blade tip to the coating and vice-versa. Figure 4.8a shows the EDXRF machine and Figure 4.8b the detector collimator where the sample was located, while Figure 4.8c presents an example of an area of analysis of the material transfer on the blade tip.

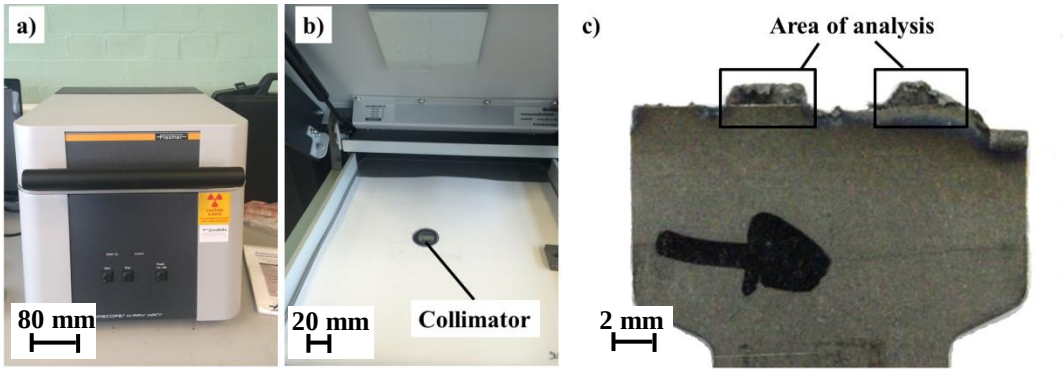

Figure 4.8. X-ray fluorescence spectrometer: a) Machine; b) X-ray fluorescence spectrometer, c) Example of area of analysis of the blade (0.02µm pass^{-1}, 100m s^{-1}, R15Y 72.3).

4.2.3. Analysis of stroboscopic imaging technique data

The stroboscopic imaging technique was capable of investigating the nature of the blade tip strike on the abradable material, and in particular the adhesive transfer during the test. The image of the blade tip acquired with the stroboscopic technique was processed in order to obtain the length change of the blade after a number of constant strikes. In order to do this, it was necessary to determine the profile of the blade edge in a Cartesian coordinate system. This image analysis was done using IMAGE J, a scientific image processing software package. As a first step, the blade image was segmented from the rest of the picture. This involved drawing a circle or rectangle on the image captured by the camera (Figure 4.9), in the correct position so as to isolate the image of the blade.

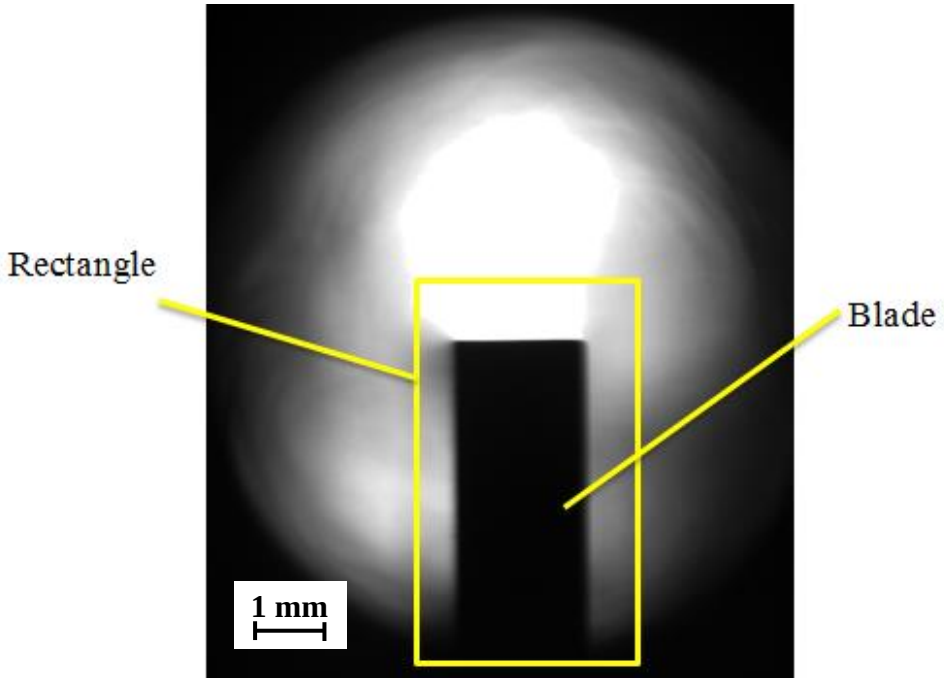

Figure 4.9. Image of the blade acquired test 2µm pass^{-1}, 100m s^{-1}, R15Y 72.3.

Figure 4.9 shows the blade tip imaged at top dead centre after striking the abradable coating. In the picture a rectangle highlighting the region of interest for image processing was included. The blade image was then segmented using the rectangle, as shown in Figure 4.10.

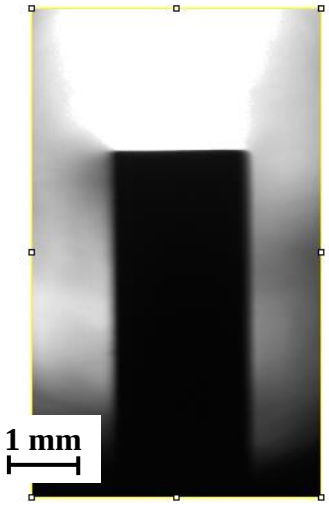

Figure 4.10. Image of the blade segmented.

After the image was segmented, it was de-speckled. A filter was used to remove small defects due to dust, since small dots can influence the image analysis, and then the image was converted in binary form in order to obtain a blade profile, as shown in Figure 4.11.

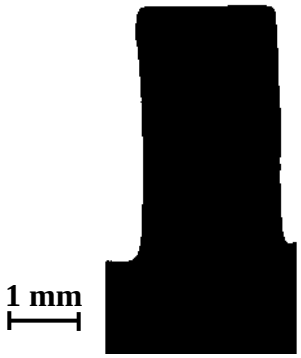

Figure 4.11. Image of the blade after clear outside / de-speckle / convert in binary form.

From the image obtained in Figure 4.10, a function was used to find the edges of the blade, and finally save the x, y coordinates of the blade edge (Figure 4.11). The coordinates were recorded in a Cartesian system with the origin at the bottom left hand corner of the segmented image.

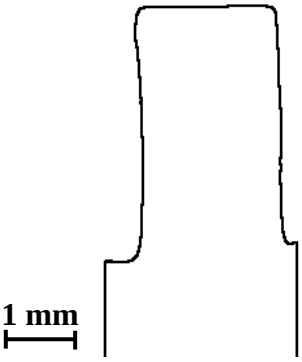

Figure 4.12. Edge of the blade.

The maximum length of the blade and the tip profile were measured by comparing the profile of the blade to a control image that represented the blade profile captured before the contact between the blade and coating. In relation to the incursion parameters, the number of images recorded in a test can vary from 100 to 9000; therefore, a macro program was developed for IMAGE-J to automatically process all the images. This program processed all of the images from a test, and wrote the coordinates of the edge of the blade to a text file in each case (see Appendix 2). The text file containing the coordinates of the blade profile was analysed in MATLAB. The MATLAB program that was developed extracted the maximum length of the

blade, and returned a vector *'lengMAX'* containing this information; it then calculated its change with respect to the initial measurement recorded pre-test and returned a vector *'dl'* containing the change in length of the blade at each time step that an image was acquired. Figure 4.13 shows a series of blade profile images where the current blade length and the relative maximum adhesion observed are highlighted.

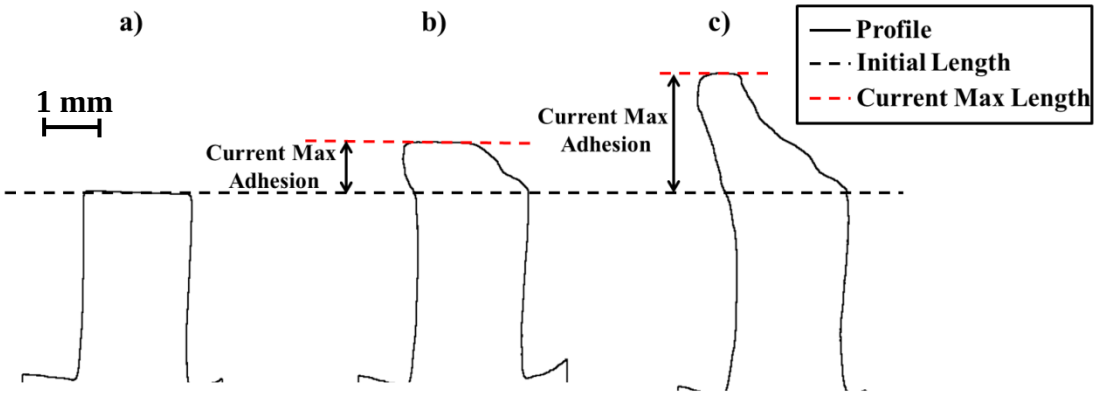

Figure 4.13. Blade profile for the test at incursion rate of 0.02µm pass^{-1}, blade speed of 100m s^{-1}, coating hardness R15Y 72.3, captured at time: a) 0s; b) 66.4s; c) 294.55s.

As shown in the figure, the analysis of the blade profile with respect to the initial blade length allowed this research to measure the blade length change during the evolution of the test. The technique allowed the blade tip profile to be quantified as a rough surface, with a sensitivity of 11.44µm. In order to obtain the sensitivity of the technique, a series of blade tip images was analysed with IMAGE J. The process was the same as for the previously mentioned blade analysis, with the image being segmented, de-speckled and converted into binary form and then the edge was found. However, in this case a series of two consecutive images was analysed before the test started and the blade length variation was calculated in order to obtain the minimum variation of blade length that the stroboscopic imaging system was able to measure. The minimum variation of blade length was measured from how many pixels difference was observed between two consecutive images. The value obtained was 1 pixel of an image of 1280 x 1024 pixels, which corresponds to a sensitivity of 11.44 ± 0.46µm.

The blade length change could be plotted against the incursion depth and the time of the test or theoretical rub length calculated in relation to the time that the image was acquired.

4.2.4. Analysis of force measurement

A piezo-electric dynamometer was mounted below the abradable coating in order to measure the contact force, as discussed in Section 3.4.2. During the test, the dynamometer produced an electric signal proportional to the force produced from the contact between the rotating blade tip and the coating. The electric signal was amplified and converted into a scaled voltage by the charge amplifier, and it was recorded using the digital oscilloscope. Everything was controlled by LabVIEW software. Figure 4.14 shows a typical force signal recorded during the test (2µm pass^{-1} and 100m s^{-1} with coating hardness R15Y 54.6) for a series of blade strikes on the abradable material at known times.

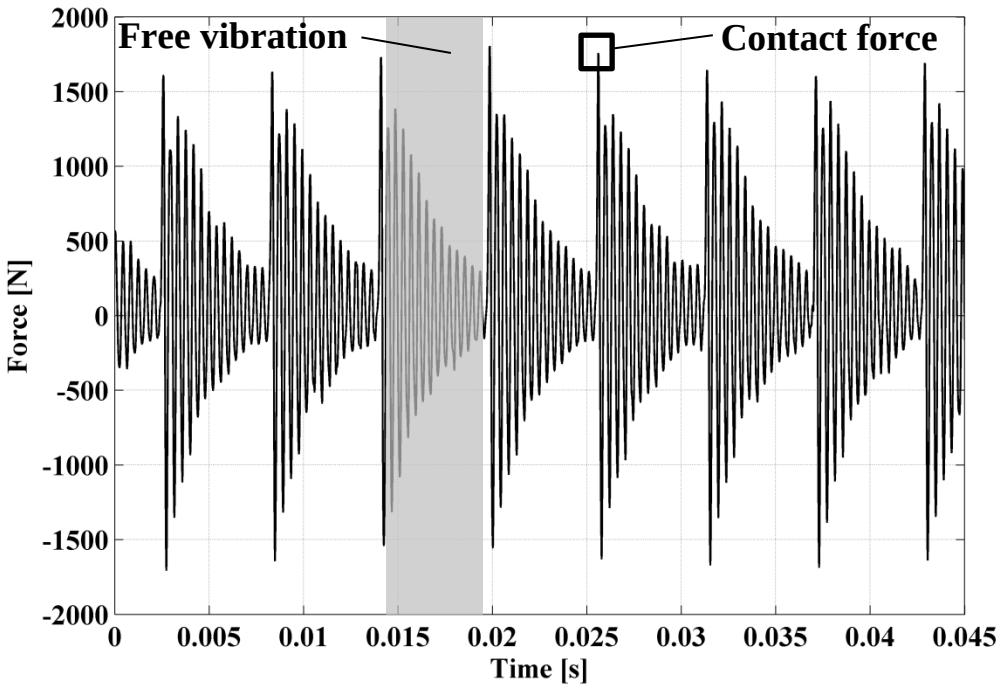

Figure 4.14. Force measurement (normal component) recorded for multiple blade strikes (Test 2µm pass^{-1} and 100 m s^{-1} with coating R15Y 54.6).

As shown in the figure, the force signal had a major peak representing the blade strike and thus the contact force, followed by a period of free vibration (grey area)

prior to the blade re-striking the abradable coating. Figure 4.15 shows a single force strike of the blade tip on the coating.

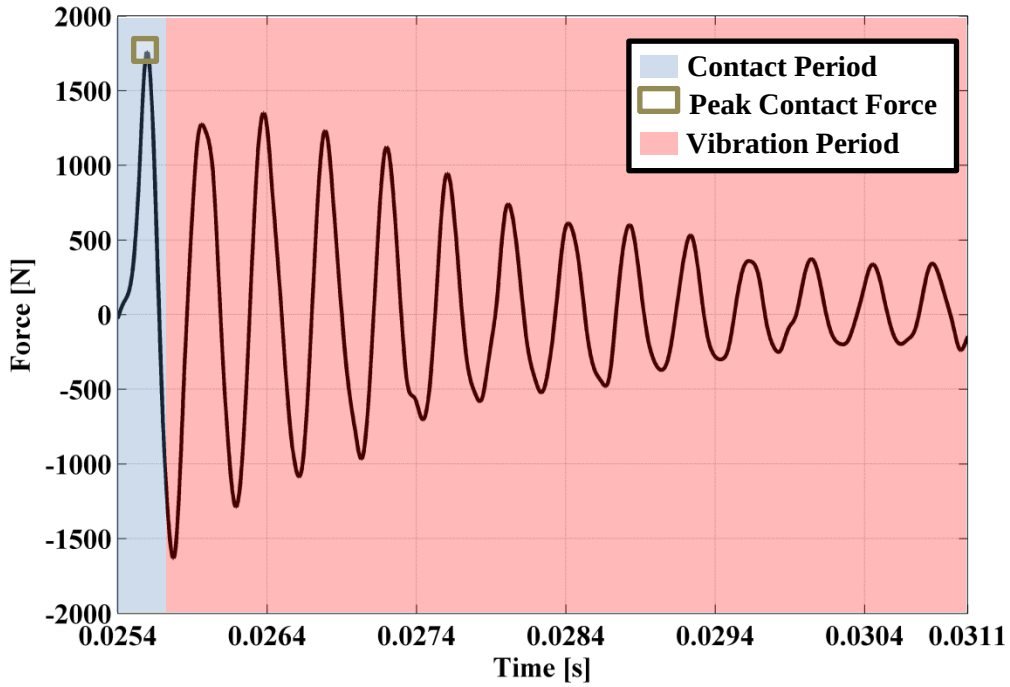

Figure 4.15. Force measurement for a single strike recorded at time of 0.0254s (Test 2µm pass^{-1} and 100m s^{-1} with coating R15Y 54.6).

As shown in the figure, the azure area represents the expected contact time based on the blade speed and length of the contact arc at this point in the incursion, while the light red area represents the vibration period. The cutting process is a dynamic process where a periodic contact of the blade onto the coating in relation to the blade speed generates a periodic force, as highlighted in Figure 4.14. Therefore, the dynamometer along with the entire test platform exhibited a dynamic response [83], as illustrated in Figures 4.14 and 4.15. Therefore, if the periodic force is in the proximity of the natural frequency of the system, this generally leads to signal distortion, with amplification of the force signal and vibration [84], and the value of the force measured does not represent the real value of the contact force. It is important to know the natural frequencies of the system in order to be able to determine the frequency working range of the dynamometer and understand if the dynamometer is measuring the real contact force; if not, it will be necessary to apply a relative correction to the signal.

Therefore the first step was to demonstrate that the maximum peak of the force in the contact period represented the contact force between the rotating blade and the coating, and to understand if the free vibration interacted with the contact force peak, or not. In order to analyse the contact force, a comparison was made between the contact duration measured at different points in the incursion and the theoretical value previously calculated. The theoretical value was the ratio between the length of the contact arc and the blade tip speed. The length of the contact arc was a combination of incursion speed, radius at blade tip and blade tip speed. Equation (4.3) shows the theoretical value of the contact time.

$$\boldsymbol{Calculated\ contact\ time} = \frac{\boldsymbol{Length\ contact\ arc}}{\boldsymbol{V}} = \frac{\boldsymbol{2 \cdot R \cdot acos\left(\frac{R - I \cdot t}{R}\right)}}{\boldsymbol{V}} \qquad (4.3)$$

where the length of contact arc is a combination of radius at blade tip (R), incursion per pass (I), time (t), and blade speed (V).

Figure 4.16 shows the correlation between the measured and the calculated contact time values for the test at an incursion rate of 2µm pass^{-1} and a blade tip speed of 100m s^{-1} and coating hardness R15Y 54.6.

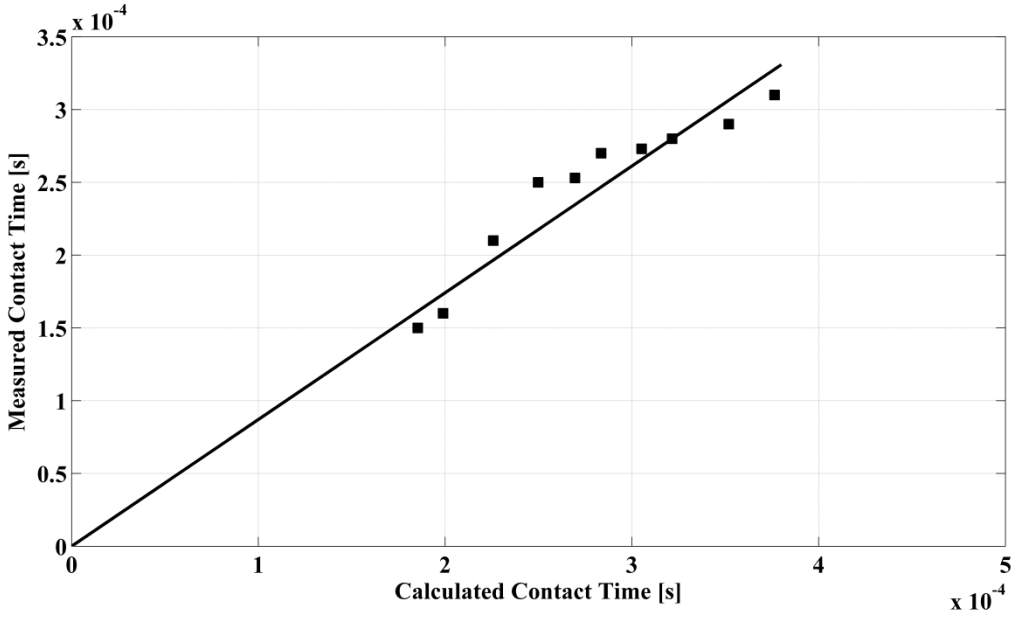

Figure 4.16. Measured contact time vs calculated contact time (Test 2µm pass^{-1}, 100 m s^{-1}, R15Y 54.6).

As shown in Figure 4.16, a linear correlation was observed between the measured contact time and the theoretical calculated contact time, which indicated that the blade strike was correctly identified during the test, and highlighted that the free vibration period did not interact with the contact period. This approach has been used previously and analysed by Ahrens [31] in order to confirm whatever vibration of the dynamometer influences the measured contact force.

As mentioned above, the natural frequency of the system and the relative frequency working range needed to be determined in order to know if the signal measured from the dynamometer was amplified and distorted or not. Therefore, a modal analysis of the system was performed to determine the frequency response function (FRF) of the system, which enabled the natural frequency to be determined [85, 86]. If the analysis of the frequency response highlighted a modal frequency close to the working range, the signal would be amplified and the phase distorted: in this case, in order to obtain the real value of the contact force, it would be necessary to apply a compensation to the signal. The FRF represented the relation between the real value of the cutting force and the value measured by the dynamometer; therefore a correction to the signal could be applied using an FRF [86].

Section 4.2.4.1 describes how a modal analysis was performed and the FRF function determined, and the need for compensation was investigated. Section 4.2.4.2 explains how an accelerometric compensation [87] was made in order to analyse the inertia effect of the system and the free vibration of the force components.

4.2.4.1. Dynamic analysis of the system and dynamic compensation

A modal analysis was performed in order to determine the natural frequencies of the dynamometer, and the FRF function was then determined. Next, the FRF was used in order to correct the force signal and to understand if compensation of the signal was required. The modal analysis was performed using an impulse hammer (PCB 086C01, sensitivity 11.65mV^{-1}, PCB Piezotronic, Inc. USA), an accelerometer (PCB 352B10, sensitivity 1.02$mV/m/s^2$, PCB Piezotronic, Inc. USA) and a National Instruments data acquisition system (NI USB-4431, 24 bit resolution). The test consisted of locating the accelerometer on the dynamometer plate in one direction of the system, for example the normal direction, with the impulse hammer hitting the plate. Then the hammer input pulse force, the accelerometer output signal and the

dynamometer output force response were acquired for each direction of the dynamometer (normal and two tangential directions on the plane). Figure 4.17 shows a schematic diagram of the modal analysis test of the system.

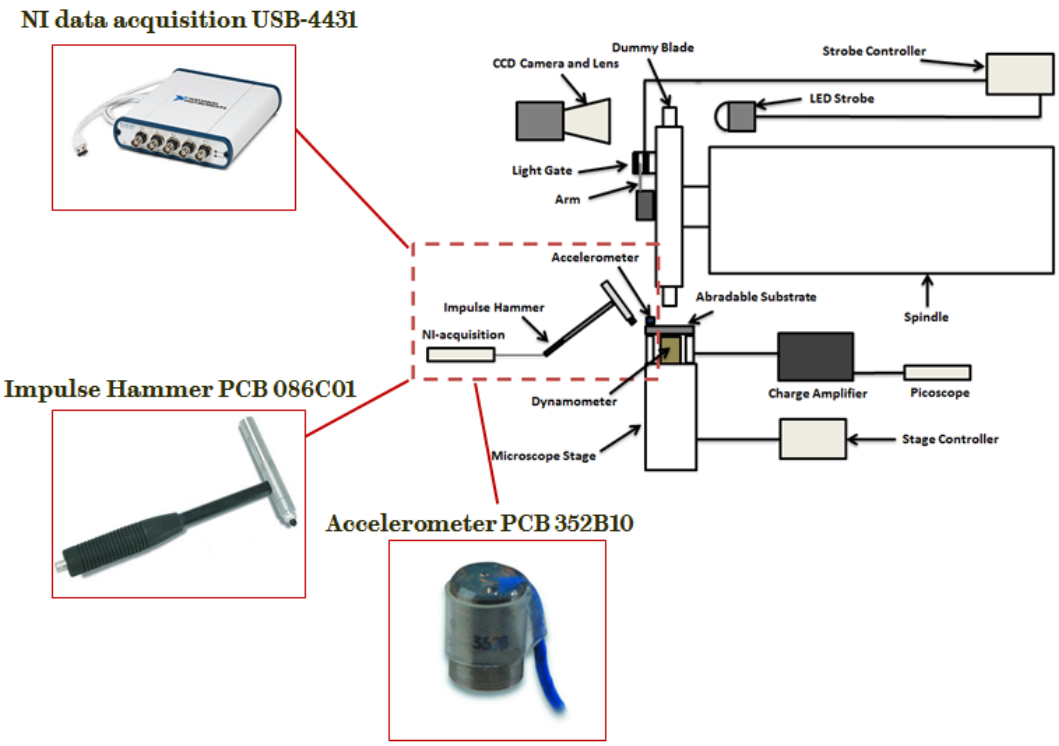

Figure 4.17. Schematic diagram of the modal analysis test of the system.

Figure 4.18 shows the input force in the time domain applied with the hammer and the relative output recorded with the dynamometer.

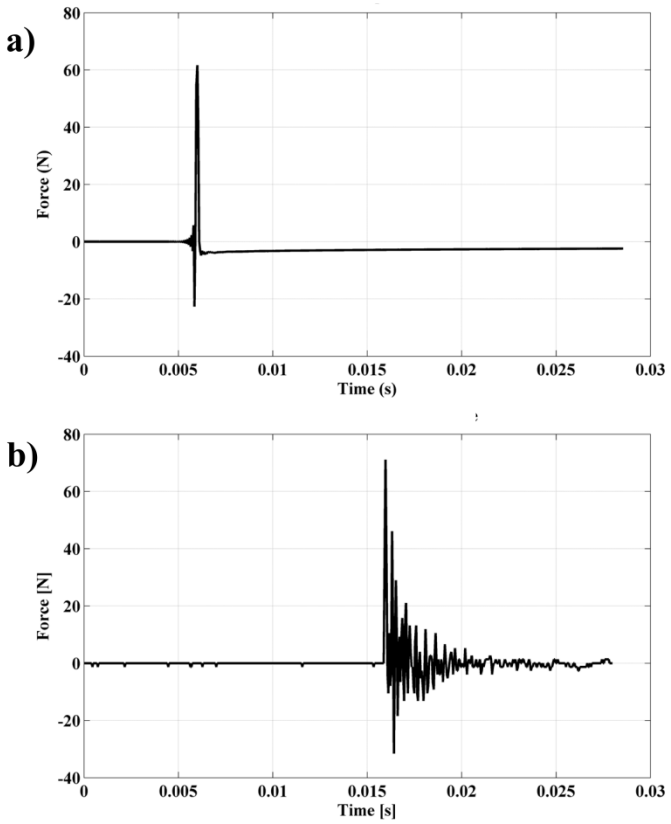

Figure 4.18. Force in time domain: a) Hammer input; b) Dynamometer output.

The FRF [85] of the system was calculated using the hammer force input and both the dynamometer and accelerometer outputs, in order to compare the two approaches. The FRF was given by the ratio between the output force from the dynamometer or acceleration from the accelerometer and the input force from the hammer, with both signals in the frequency domain [86]. As a first step, a Fast Fourier Transform (FFT) of the signals was applied [86, 88]. Equation (4.4) shows the FRF expression.

$$\boldsymbol{FRF(j\omega)} = \frac{\boldsymbol{F(j\omega)}}{\boldsymbol{H(j\omega)}} \tag{4.4}$$

where the output variable *F(jω)* is the Fourier transform of the response signal produced by the dynamometer, and the input variable *H(jω)* is the Fourier transform of the excitation impulse generated by the hammer.

The FRF calculation was made with a program developed in MATLAB, using the function 'tfestimate' [89, 90] that calculated the FRF from the input and output signals. The natural frequency of the system was 8.3kHz in the normal direction and 2.7kHz in the tangential direction; these were below the freestanding frequency of the dynamometer [91]. This was because of the mounting configuration of the dynamometer when it was inserted on the test platform. The high natural frequency of the system meant a wide range of working frequencies where the force signal was not amplified or distorted.

However, in order to verify if the signal measured was amplified and if correction of the signal was necessary, a compensation to the signal was made using the FRF to apply the dynamic compensation to the measured signal. During the test, the rotating blade contacted the abradable coating and generated a contact force measured by the dynamometer. Using this measured force and the FRF previously calculated in the modal analysis, the force applied on the dynamometer was determined, as shown in the schematic diagram in Figure 4.19.

$$FRF = \frac{Force\ measured}{Force\ Applied}$$

Figure 4.19. Schematic diagram of the force analysis.

In order to apply the dynamic compensation to the measured force signal [26, 86], the applied signal force was calculated, which represented the dynamically compensated force. In order to calculate the dynamically compensated force, the FRF function needed to be inversed, but as the matrix was rectangular it could not be inversed directly [86]. Therefore, as it was complex, the FRF was multiplied by the Hermitian transpose of the FRF ($[FRF]^H$), as shown in Equation (4.5).

$$[\boldsymbol{FRF}]^{\boldsymbol{H}} \cdot \{\boldsymbol{F_{dyno}}\} = [\boldsymbol{FRF}]^{\boldsymbol{H}} \cdot [\boldsymbol{FRF}] \cdot \{\boldsymbol{F_{compensated}}\} \quad (4.5)$$

The Hermitian matrix is the transpose of the conjugate of the matrix. The two following matrices were then introduced:

$$\{\boldsymbol{B}\} = [\boldsymbol{FRF}]^{\boldsymbol{H}} \cdot \{\boldsymbol{F_{dyno}}\} \quad (4.6)$$

$$[\boldsymbol{A}] = [\boldsymbol{FRF}]^{\boldsymbol{H}} \cdot [\boldsymbol{FRF}] \quad (4.7)$$

In the next step the matrix [A] was inverted and the compensated force ($F_{compensated}$) was calculated using the Equation (4.8).

$$\{\boldsymbol{F_{compensated}}\} = [\boldsymbol{A}]^{-\mathbf{1}} \cdot \{\boldsymbol{B}\} \quad (4.8)$$

Additionally [86] direct inverse of Equation (4.4) was also performed in order to calculate the compensated force.

$$\mathbf{F_{compensated}(j\omega)} = \frac{\overline{\mathbf{FRF}} \cdot \mathbf{F_{dyno}(j\omega)}}{\overline{\mathbf{FRF}} \cdot \mathbf{FRF}} \quad (4.9)$$

where $\overline{FRF}$ is the conjugate of the *FRF*, and $F_{dyno}(j\omega)$ is the fast Fourier transform of the dynamometer force measurement.

The first step in this latter approach was to calculate the conjugate of the FRF and then the FFT of the measured force signal; subsequently using Equation (4.9) the compensated force was calculated in the frequency domain. In order to obtain the dynamically compensated force in the time domain, an inverse fast Fourier transform was applied. Figure 4.20 shows the components of measurements representing the blade contact, the dynamically compensated force and the force measured by the dynamometer (un-compensated force).

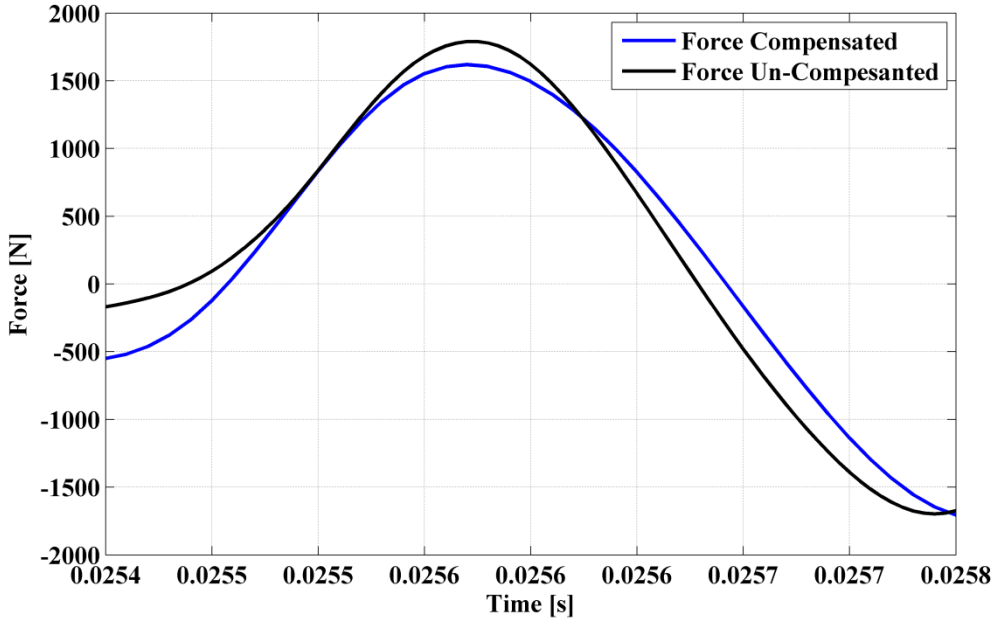

Figure 4.20. Dynamically compensated and un-compensated force measurements for a single strike recorded at time of 0.0254s (Test 2µm pass^{-1} and 100m s^{-1} with coating R15Y 54.61).

The force components representing the contact between the blade and the coating did not change within the accuracy of the FRF with the compensation applied. Additionally, the frequency of blade strike during the test was between 172Hz and 344Hz in relation to the blade speeds respectively of 100m s^{-1} and 200m s^{-1}. However, these frequencies were below the modal frequency of the dynamic system, more than three times of the frequency bandwidth of the FRF of the system [86]; therefore the measured cutting force represented the cutting force.

The analysis of the time of contact, the modal analysis and the compensation of the force signal highlighted that the maximum peak of the force represented the actual force, and the free vibration observed was due to the mass inertia of the system and did not interact with the contact phase. However, in order to perform a complete analysis and highlight the individual strikes, an accelerometric compensation was made and this is presented in the next section.

4.2.4.2. Accelerometric compensation

An accelerometric compensation [87, 92, 93, 94] was applied to the system, with the specific aim of analysing the inertial effects on the blade contact and the free vibration components of the force measurements. In order to avoid the effect of the free vibration, the acceleration force of the system was subtracted from the compensated force, as shown in Equation (4.10).

$$\boldsymbol{F_{compensated\ accelerometric} = F_{compensated} - (M_i \cdot a)} \quad (4.10)$$

where 'M_i' is the inertia mass, which represents the mass of the plate located on the top of the dynamometer [87], and *'a'* is the acceleration of the system.

During the contact, the system was excited by an impulse force with the correct frequency in relation to the rotating blade speed. Figure 4.21 shows the free body diagram of the system.

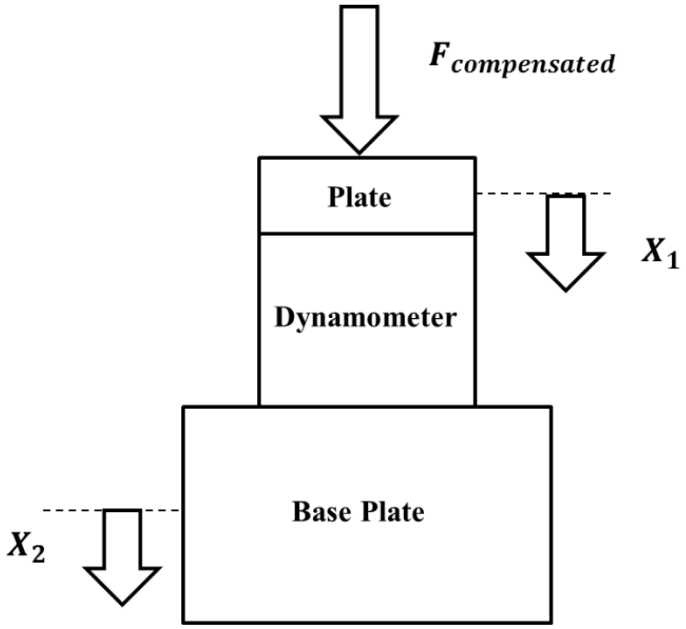

Figure 4.21. Free diagram of the dynamometer.

The plate responded with a displacement, calculated from the differential equation of motion of the system, as shown in Equation (4.11) [87].

$$\boldsymbol{M \cdot \ddot{x}_1 + C \cdot (\dot{x}_1 - \dot{x}_2) + K \cdot (x_1 - x_2) = F_{compensated}} \quad (4.11)$$

where *'M'* is the plate mass, *'C'* is the damping coefficient, *'K'* is the stiffness, *'x_1'*, *'$\ddot{x}_1$'*, '$\dot{x}_1$' are the displacement, velocity and acceleration of the plate, respectively, and *'x_2'*, '$\dot{x}_2$' are the displacement and velocity of the base plate.

Assuming the term '$C \cdot \dot{x}_2$' is negligible in comparison with the term from the plate, and where the term *'$K \cdot (X_1 - X_2)$'* is equal to the force measured from the dynamometer ($F_{measured}$), the equation becomes:

$$\boldsymbol{M \cdot \ddot{x}_1 + C \cdot (\dot{x}_1) + F_{measured} = F_{compensated}} \quad (4.12)$$

The solution of Equation (4.12) allowed the dynamically compensated force to be determined after determining the acceleration components of the system.

The acceleration was not calculated using an instrument during the test, but was calculated in an analytical way from the hypothesis that the system had a single degree of freedom and that the force applied on the dynamometer plate was a harmonic force with a frequency in relation to the blade tip speed [92, 93]. The differential equation of the free body was:

$$\boldsymbol{M \cdot \ddot{x} + C \cdot \dot{x} + K \cdot x = F_{compensated}(\Omega \cdot t)} \quad (4.13)$$

where 'Ω' is the frequency of the compensated force applied on the dynamometer plate.

The force signal, as shown in Figure 4.14, is characterised by a contact period and free-vibration period, but, as can be seen in Figure 4.15, the dynamometer measured the contact force, then in the time between one strike and the next the system vibrated, and the vibration reduced before the blade again strikes on the coating. Therefore, in order to apply the accelerometric compensation of the signal, the acceleration component obtained in the free vibration condition was applied to compensate the free-vibration phase, and the acceleration component from the external force was applied to compensate the forced contact phase [92]. The

acceleration of the free-vibration was the solution of the homogeneous equation of Equation (4.13), while the acceleration force was the particular integral of Equation (4.13). The displacement solutions are shown in Equations (4.14, 4.15).

$$\mathbf{X_{fre-vibration} = X_0 \cdot e^{-\zeta\omega_n t} \cdot \sin\left((\omega_n \cdot \sqrt{1-\zeta^2}) \cdot t - \varphi\right)} \quad (4.14)$$

In Equation (4.14) '$X_{free\text{-}vibration}$' is the displacement of the free-vibration phase, 'X_0' is the static displacement (X_0=2.9 10^{-4} m), 'ζ' is a damping factor (ζ=0.022091), 'ω_n' is the natural frequency of vibration (ω_n= 15217rad s^{-1}) and 'φ' is the phase of the displacement (ϕ = 0.04548rad).

$$\boldsymbol{X_{forced} = X_{20} \cdot cos(\Omega \cdot t - \varphi_1)} \quad (4.15)$$

In Equation (4.15) 'X_{forced}' is the displacement of the forced phase, 'X_{20}' is the static displacement (X_{20}= 1.32 10^{-5}m), 'Ω' is the frequency of force (Ω= 1080 rad s^{-1} at 100m s^{-1} blade tip speed) and 'φ_1' is the phase of the displacement (ϕ_1 = 0.00315455rad).

The acceleration components were calculated from the second order differential of Equations (4.14, 4.15). Then the inertial force was obtained by multiplying the inertial mass (M = 0.67kg) by the acceleration components. Using Equation (4.10) the dynamometer force was dynamically compensated. Figure 4.23 shows the compensated force after the dynamic compensation of the FRF and the acceleration measurements, and the un-compensated force measurements.

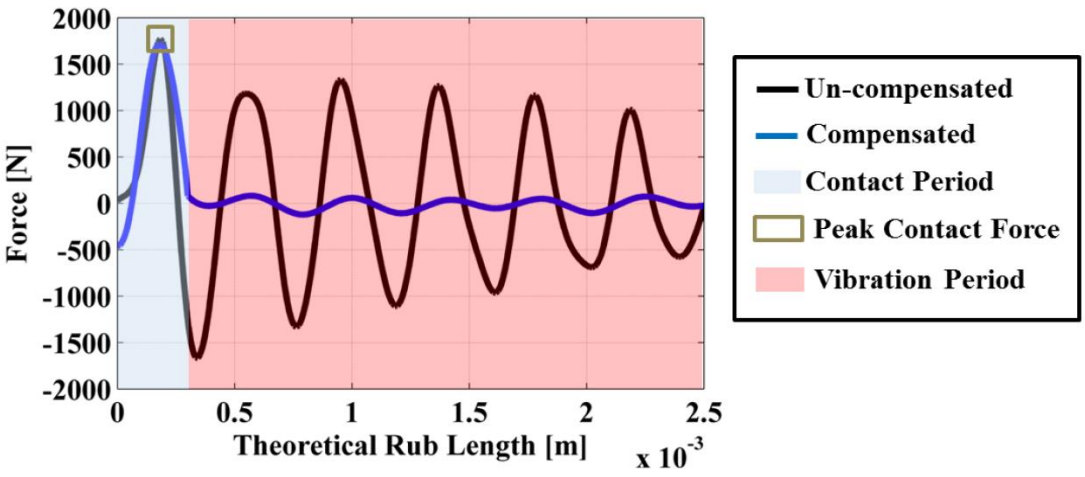

Figure 4.23. Dynamically compensated and un-compensated force measurements.

The peak contact force after the compensation was reduced by less than 9%; however, this signal reduction did not prejudice the force measurement analysis. Therefore, a linear trend between the measured time of contact and the theoretical contact (Figure 4.16) indicates that the blade strike was correctly identified and the free vibration period did not influence the contact period. In general, the components of the measurement representing the blade contact did not change (within the accuracy of the FRF and acceleration compensations of 0.19dB [86]) with compensation applied, indicating that it was not required in this case. Overall, the signal force was analysed in order to validate the force measurement and verify if the dynamometer measured the contact force without amplification or distortion. Summarising the analysis, it showed that the contact time did not interact with the free vibration phase, and the modal analysis showed a high frequency response of the system. However, a compensation was made to the signal in order to observe if the signal changed and by how much. Additionally, an accelerometric compensation was performed in order to remove the free vibration phase, and a single strike was observed without the free vibration signal. Overall, the component of the force did not change even after compensation of the force signal, and therefore the compensation was not necessary.

The measurements recorded for the tangential force were similar in nature, and the blade contact was clearly evident. In the tests performed, both normal and tangential components of the contact force were measured directly for each strike, and uncompensated values were recorded in the investigation.

4.2.5 Analysis of temperature data

The temperature of the coating was measured during the test using the pyrometer. The measurement was made at a single point on the surface of the abradable material where the blade strikes, as shown in Figure 4.24. Using the software developed in LabVIEW, the coating temperature was acquired at a known time. This was used to synchronise the temperature measured with the blade length change and force measurement, in order to know the trend of the parameter measurement during the incursion phase.

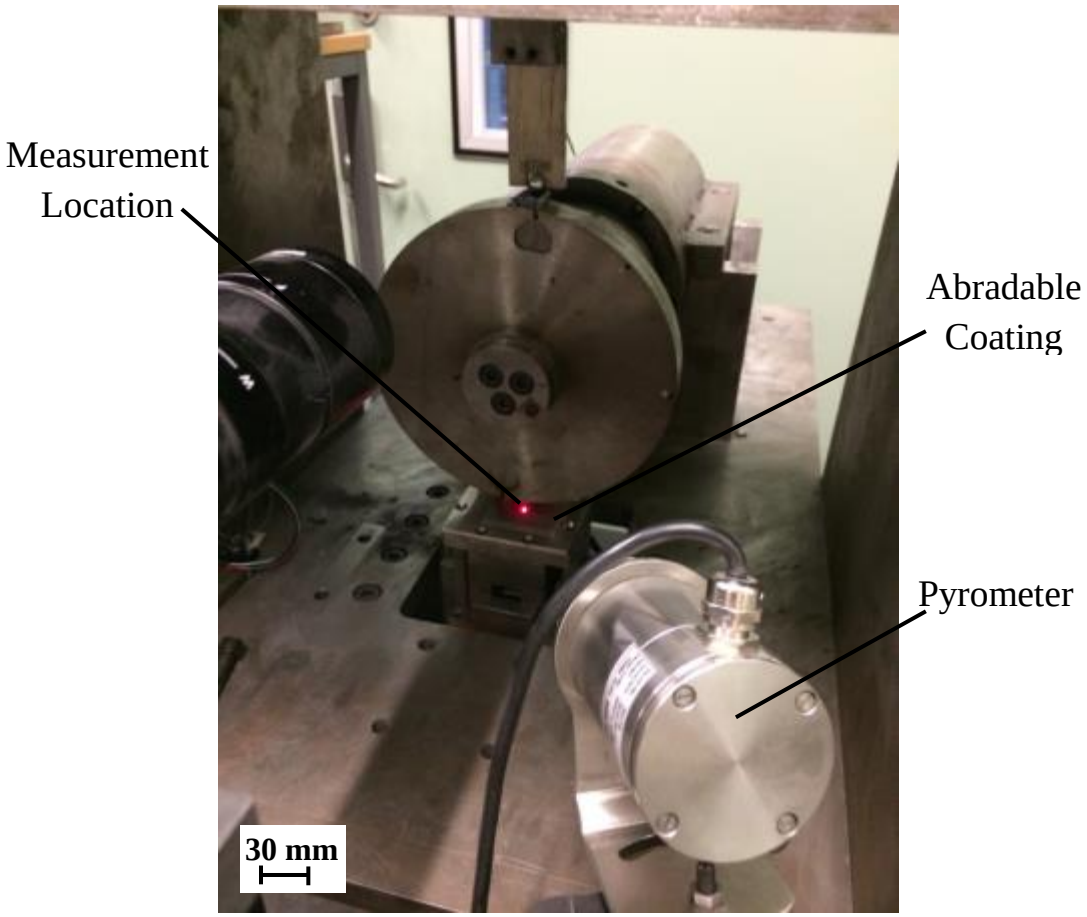

Figure 4.24. Location of temperature measurement.

4.2.6. Analysis of material response

The material response represented the response of the sub-surface of the abradable material as observed through the microstructure of the sample. In order to achieve it, a section of the abradable sample was taken. The section was taken before performing the test in order to highlight the material structure and then after the test

for different incursion conditions, with the aim of characterising the material response. The samples were sectioned in areas where differences were observed, for example, grooving or material transfer. The section was made in longitudinal and transverse directions with respect to the direction of the blade strike on the coating. The longitudinal section highlighted the material structure along the blade direction for all rub surfaces, while a transversal section could highlight different material responses, for example on a grooved surface. Figure 4.25 shows the longitudinal and transverse sections with respect to the direction of the blade strike.

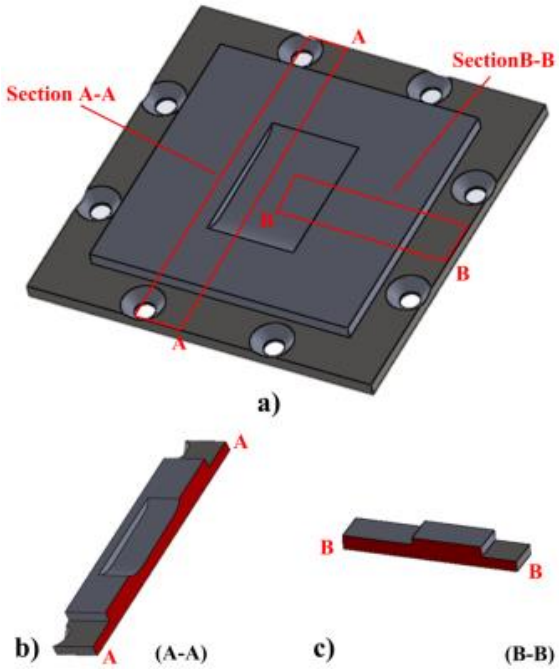

Figure 4.25. Section of abradable material: a) Coating; b) Longitudinal section; c) Transverse section.

The sectioning was made using abrasive cut-off wheels 0.03" (0.8mm) thick with Al_2O_3 for the abrasive material (Buehler Ltd., USA, 11-4207-010), using a precision cutting machine (IsoMet^{TM} 5000, Buehler Ltd., USA). The samples were inserted in a mould and placed in a vacuum chamber (Vacuum Impregnation equipment I, No. 20-1382-160 Buehler Ltd., USA) for resin impregnation. As shown in the literature review, the vacuum impregnation using epoxy resins (Epothin^{TM}, Epoxy resin 20-3440-032, Buehler Ltd., USA) and epoxy hardener (Epothin^{TM}, Epoxy hardener 20-3442-016, Buehler Ltd., USA) is the procedure recommended for the preparation of porous and friable coatings, such as thermally sprayed coatings [50-55]. The vacuum impregnation removes air from pores, crevices and cracks, thus permitting the epoxy

to enter them, and a perfect filling of the porous areas allows a correct retention of the pore structure in order to clearly distinguish between the different features of the coating [51, 57]. Figure 4.26 shows the vacuum impregnation equipment.

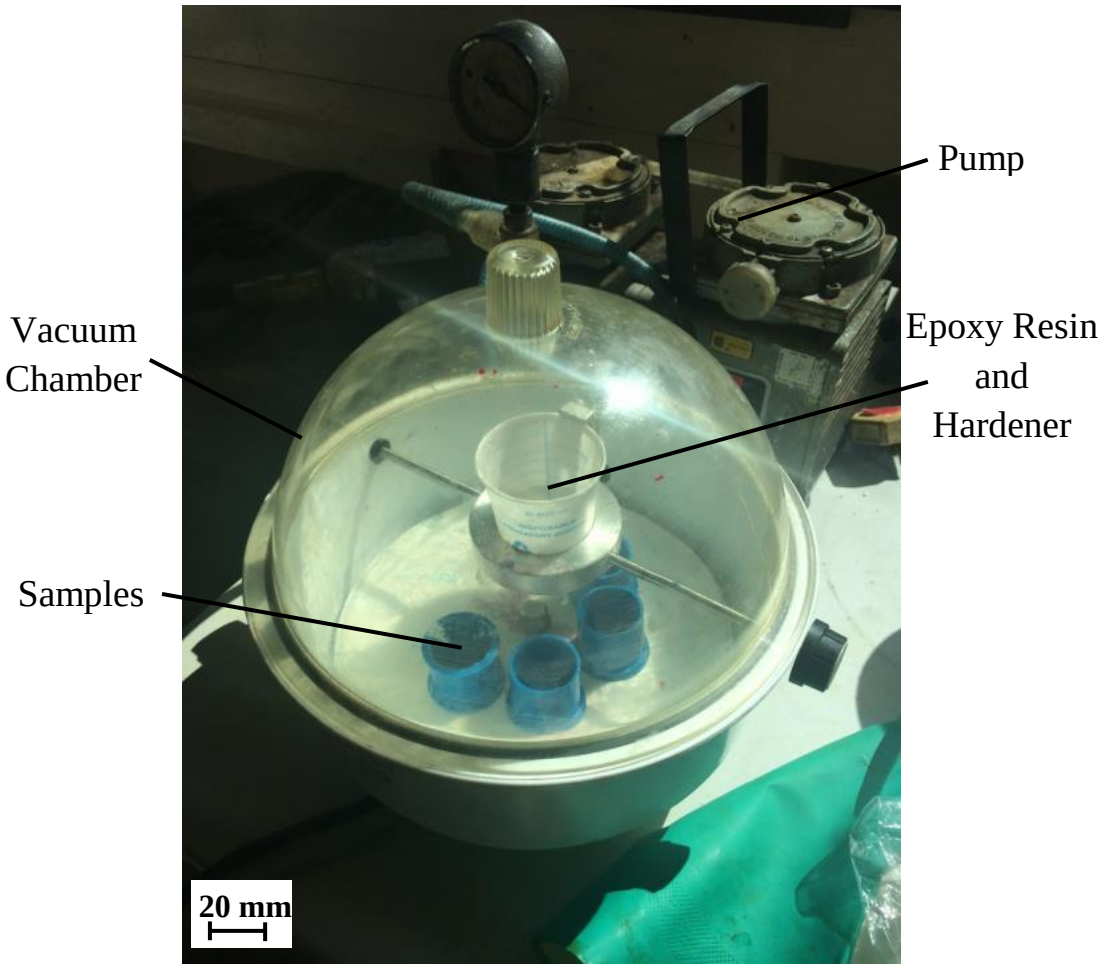

Figure 4.26. Vacuum impregnation equipment.

After the vacuum impregnation, the samples were placed inside an oven for two hours at 50 °C in order to solidify the resin.

The next phase was the grinding phase, which is a very important phase [50–55] of the sample preparation sequence because it removes damage introduced by sectioning, and also removes the initial depth of deformation from the cutting phase, producing a flat surface. The surface of the sample to be prepared was abraded using a graded sequence of abrasive papers, starting with a coarse abrasive followed by progressively graded finer ones. The damage on the sample produced by each preparation step must be removed by the subsequent step. To minimise heat-generated damage and to maximise grinding paper life, water was used to lubricate the process. The grinding phase was carried out using a grinding / polishing machine

(Automet 250, Buehler Ltd., USA). The grinding steps and the grades of silicon carbide abrasive paper used are shown in Table 4.2.

Grinding Phase Steps						
Step	**SiC Paper Grit**	**Lubricant**	**Single Force [N]**	**Head Speed [rpm]**	**Base Speed [rpm]**	**Time [s]**
1	120	Water	20	60	150	120
2	180	Water	20	60	150	120
3	240	Water	20	60	150	120
4	360	Water	20	60	150	120
5	600	Water	20	60	150	120
6	1200	Water	20	60	150	120

Table 4.2. Grinding phase steps.

The first step needed to be repeated until the sample surface was flat. Then, in the next step, the grade of the abrasive paper was increased, as shown in Table 4.2, for 2 minutes, until the last grinding step where a finer abrasive paper was used. The next phase was the polishing phase, which was required in order to have a scratch-free surface with high reflectivity, so that the structure of the sample could be observed using the microscope. Table 4.3 summarises the polishing steps.

Polishing Phase Steps						
Step	**Abrasive**	**Cloth**	**Single Force [N]**	**Head Speed [rpm]**	**Base Speed [rpm]**	**Time [s]**
1	6µm diamond	MD DAC	20	60	150	360
2	1µm diamond	MD DAC	20	60	150	260
3	OPS	MD Chem	20	60	150	60

Table 4.3. Polishing steps.

In the first step of the polishing phase, an abrasive cloth (MD DAC, Struers) made with satin woven acetate was used, in conjunction with a diamond suspension of 6µm (Struers Ltd.), for 6 minutes. After cleaning the sample surface, the second step was made using a 1µm diamond suspension. Then the final step used a colloidal silica suspension (OPS, Struers Ltd.) in order to have a clean scratch-free surface. The samples were analysed using an optical microscope (Nikon Eclipse LV150) with magnification ratios of x5 and x10.

4.3. Chapter summary

- The input parameters of the test, which reproduced the contact between the rotating blade and the abradable material, were: blade tip speed, incursion speed, and incursion depth. Additionally, a combination of these parameters determined the theoretical rub length that represented the total length of the rub surface. Furthermore the superficial hardness of the coating represented another input parameter.

- The contact between the blade and the coating was recreated by controlling the movement of the Z-microscope stage with a defined speed of incursion on the blade.

- The methodology of the wear mechanics analysis was divided into two parts: analysis of the sample before and after the test, and analysis during the test using a stroboscopic imaging technique, force measurement, temperature measurement and material sectioning.

- For analysis of the sample post-test, the blade length and weight were recorded before and after the test in order to quantify the change in the contact mechanics. Additionally, the chemical composition of the material transfer was analysed with an EDXRF machine.

- The wear mechanics were analysed using a stroboscopic imaging technique capable of investigating the nature of the blade tip, and in particular the adhesive transfer and blade wear. Analysis of the image analysis provided the blade length change during the test.

- The analysis of the force signal obtained from the dynamometer and the relative compensation applied to the signal highlighted the high frequency response of the system, and even with application of compensation to the signal no significant change was observed, therefore, the force measured represented the contact force.

- Finally, the pyrometer measured the temperature of the coating during the test, and then the material response was analysed using a section of the sample post-test.

5. Wear Mechanisms

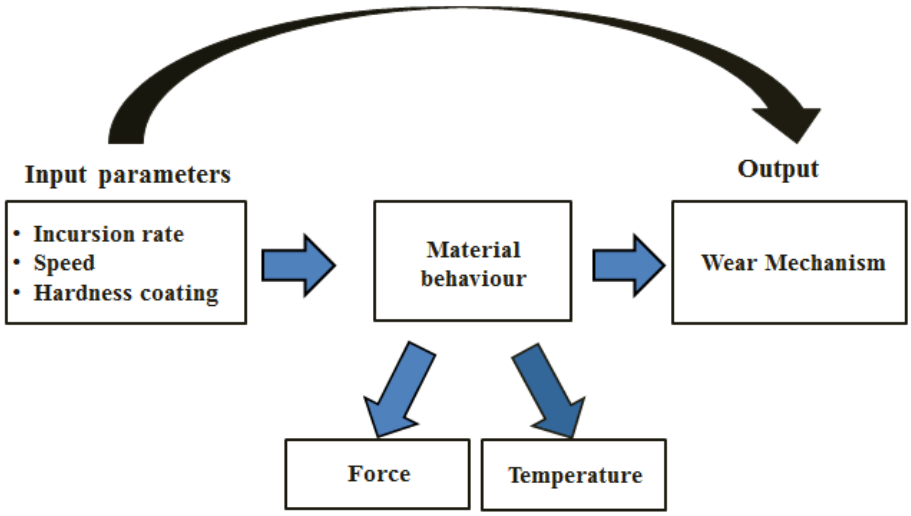

Figure 5.1. Overview of wear mechanism.

As highlighted in the figure, the wear tests broadly indicated the input conditions that influence the wear mechanism, and presumably result in differing forces and temperatures. In this chapter the wear mechanisms will be analysed, then in the following chapters the wear mechanism will be analysed in relation to the force, temperature and material response. This chapter presents the results obtained during the tests performed with a titanium (Ti-6Al-4V) rotating blade and AlSi-hBN abradable material in relation to the input parameters. The analysis of the contact

between blade and coating, as mentioned previously in Chapter 3 (Section 3.4.3) was performed with four different hardnesses (soft, intermediate with two hardnesses, and hard) of the coating in relation to the aero-engine specification, with different incursion conditions (Chapter 4, Section 4.1.2). The wear mechanisms observed were detailed with images of the blade tip and coating surface. Additionally, the blades were analysed and the blade length and the weight change were measured before and after the test in order to highlight the main changes and correlate them with the wear mechanics. The main mechanisms observed were adhesive transfer from the coating to the blade, characterised by grooving on the abradable material, blade wear and relative blade transfer to the abradable surface, and cutting wear indicated by good dislocation of the abradable sample. The experimental tests showed different wear mechanics between softer and harder coatings, especially at low incursion rates, where the wear mechanism was found to be hardness dependent.

5.1. Wear mechanics

The wear mechanisms were detailed from the images of the blade and the coating captured after the test, in relation to the incursion parameters and sample hardnesses listed in Table 4.1 in Section 4.1.2.

5.1.1. Wear mechanics of sample with hardness R15Y 72.3

Figure 5.2 shows the blade and the abradable sample at the end of the test performed at a blade speed of 100m s^{-1}, an incursion rate of 0.02µm $pass^{-1}$, and abradable coating hardness R15Y 72.3.

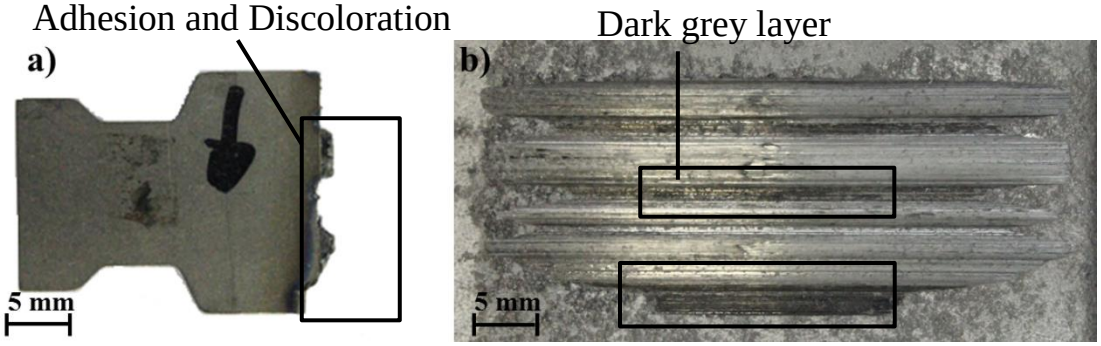

Figure 5.2. Sample post-test for an incursion rate of 0.02µm $pass^{-1}$ at 100m s^{-1} blade speed and abradable sample hardness R15Y 72.3: a) Blade; b) Coating.

Figure 5.2 shows adhesive transfer to the blade tip, with non-uniform transfer and different degrees of adhesion across the blade profile. The coating was characterised by a grooved surface, with the hollow surface corresponding to the location of the adhesive transfer on the blade tip, and the major peak of the grooved surface corresponding to the location of thermal damage on the blade tip, highlighted by a discoloration of the titanium (Figure 5.2a). Also, a dark grey layer was observed on the top of the groove. Overall, the main wear mechanism observed was adhesive transfer on the blade tip, but also blade wear corresponding to the location of the thermal damage. Further investigation of the composition of the adhesive transfer and dark grey layer will be made in Section 5.3. Figure 5.3 shows the blade and abradable material post-test at an incursion rate of 2µm pass^{-1}, with abradable sample hardness R15Y 72.3 and a blade speed of 100m s^{-1}.

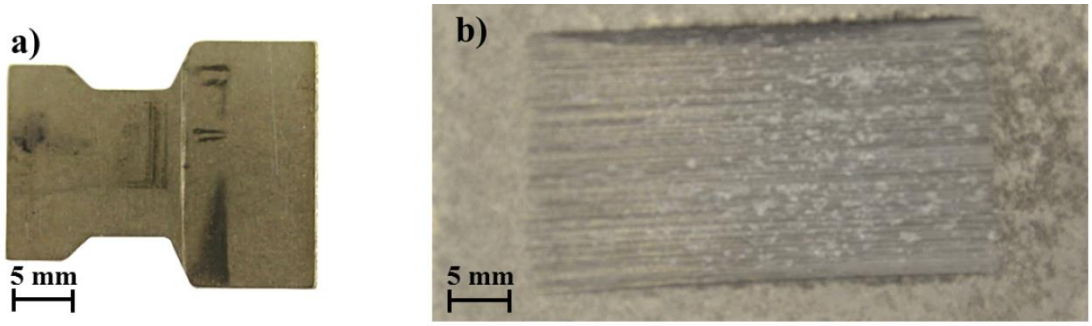

Figure 5.3. Sample post-test for an incursion rate of 2µm pass^{-1} at 100m s^{-1} blade speed and abradable sample hardness R15Y 72.3: a) Blade; b) Coating.

The blade was observed to cut the abradable material well, with a smooth surface (lightly grooved) that had a dull appearance in comparison to the surface observed at the low incursion rate. There was no thermal damage on the blade, with minimal blade wear. These results highlighted a different wear mechanism between low and high incursion rates, where the mechanism started from adhesive transfer and ended in cutting wear. The different mechanisms with respect to incursion rate were also highlighted from the analysis of the blade and coating after the test, with a gradual increase of the incursion rate from low to high, for a blade speed 100m s^{-1} and coating hardness R15Y 72.3, as shown in Figure 5.4.

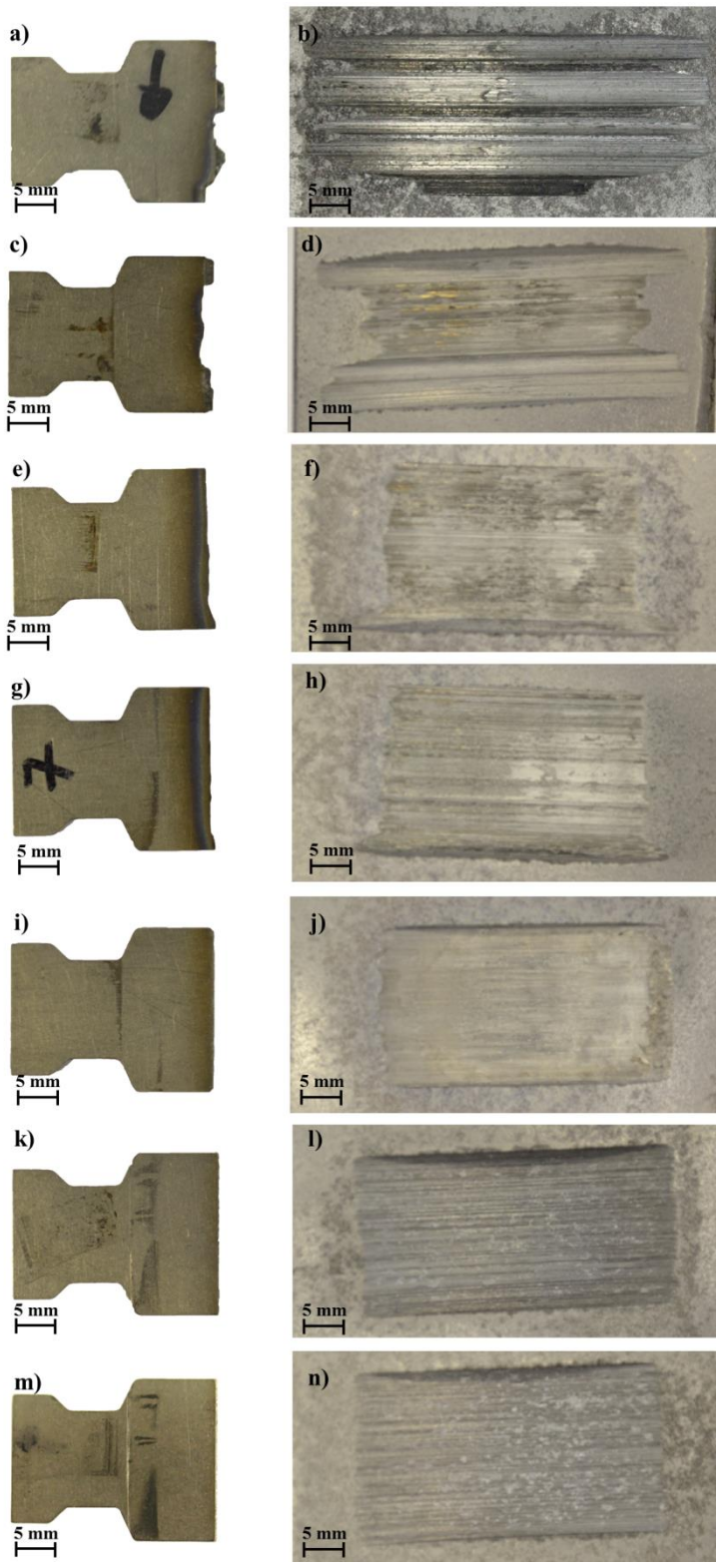

Figure 5.4. Image of the blade and coating post-test at 100m s^{-1} blade speed with abradable sample hardness R15Y 72.3 and incursion rate: 0.02µm $pass^{-1}$: a) Blade, b) Coating; 0.04µm $pass^{-1}$: c) Blade, d) Coating; 0.06µm $pass^{-1}$: e) Blade, f) Coating; 0.08µm $pass^{-1}$: g) Blade, h) Coating; 0.2µm $pass^{-1}$: i) Blade, j) Coating; 1µm $pass^{-1}$: k) Blade, l) Coating; 2µm $pass^{-1}$: m) Blade, n) Coating.

As shown in the figure, a gradual change of the wear mechanism was observed with increasing incursion rate. At a low incursion rate there was an adhesive transfer on the blade tip and a grooved surface (Figure 5.4 a, b and b, c), and with a gradual increase of the incursion rate, a clean cutting occurred. As shown in Figure 5.4 i, j, k, l, m, n, a negligible adhesive transfer / blade wear or thermal damage was observed. From observing the substrates post-test, the transition of the mechanism was observed to occur at an incursion rate of 0.06µm·pass^{-1} when a well-cut surface began to be seen, with the corresponding test samples shown in Figure 5.4 e, f. The observation of the sample post-test highlighted a significant influence of the incursion rate on the wear mechanism, with a gradual transition of the wear mechanism with an increasing incursion rate. In the next section, the influence of the blade speed on the wear mechanism will be analysed.

5.1.2. Wear mechanics of sample with hardness R15Y 72.3 at different blade speeds

The samples post-test with hardness R15Y 72.3 were observed at the same incursion rate but different blade speeds, in order to understand the influence of the speed on the wear mechanism. Figure 5.5 shows the blade and abradable samples post-test at a low incursion rate (0.02µm pass^{-1}) for different blade speeds (100, 150, 200m s^{-1}).

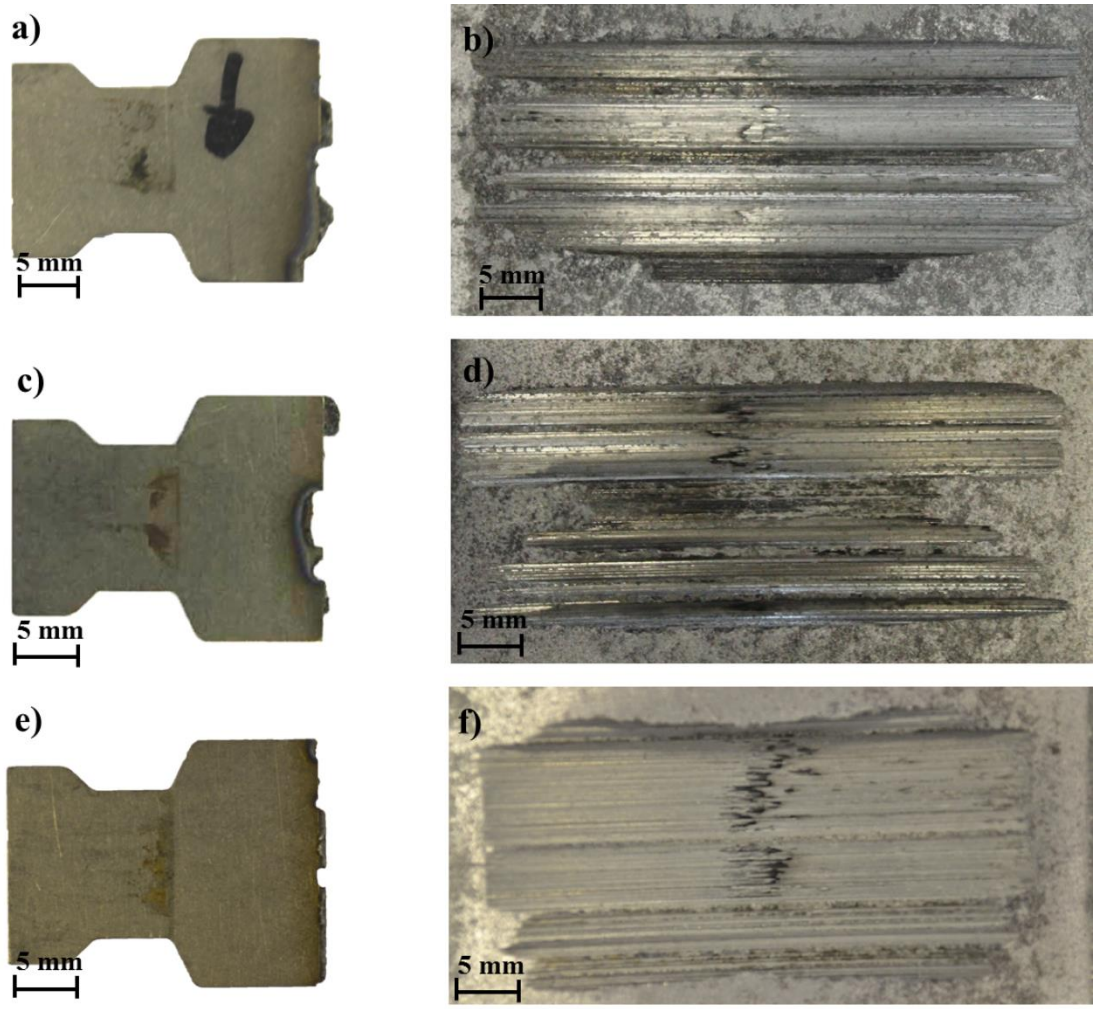

Figure 5.5. Image of the blade and coating post-test for abradable hardness R15Y 72.3 at an incursion rate of 0.02µm pass^{-1} and blade speed of: a - b) 100m s^{-1}; c - d) 150m s^{-1}; e - f) 200m s^{-1}.

As shown in the figure, the dominant wear mechanism was adhesive transfer to the blade tip, with different levels of adhesion across the blade profile, and thermal damage on the blade tip and grooving on the surface. Observation of the blade tip revealed a reduction of adhesive transfer and thermal damage with increasing blade speed. Additionally, an increase in speed led to a surface with less grooving on the abradable (Figure 5.5 b, d, f). Figure 5.6 shows the blade and the abradable sample (R15Y 72.3) at a high incursion rate (2µm pass^{-1}) and different blade speeds (100, 150, 200m s^{-1}).

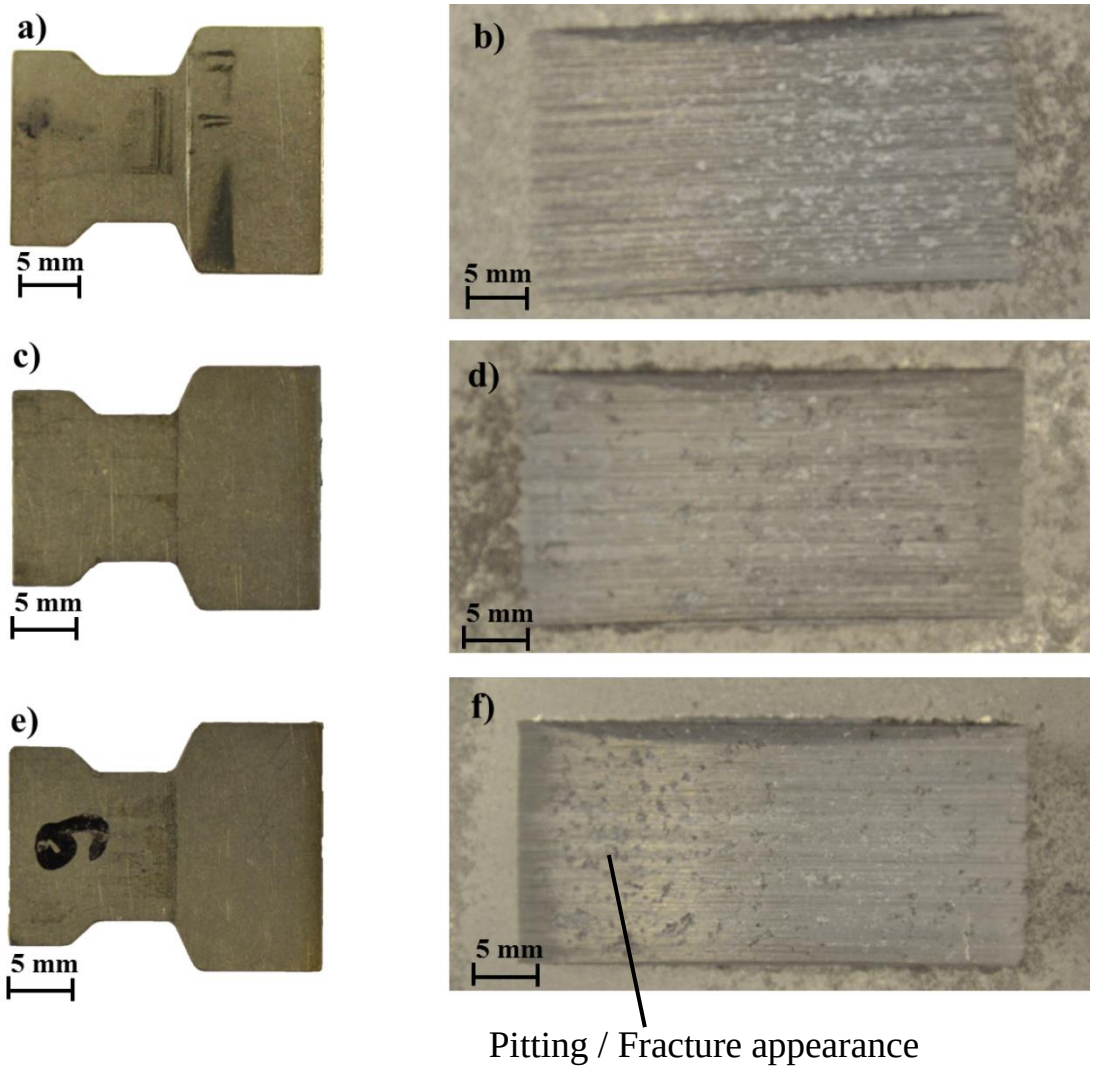

Figure 5.6. Image of the blade and coating post-test for abradable hardness R15Y 72.3: and incursion rate of 2µm pass^{-1}, at blade speed: 100m s^{-1}: a) Blade, b) Coating; 150m s^{-1}: c) Blade, d) Coating; 200m s^{-1}: e) Blade, f) Coating.

As shown in Figure 5.6, at a high incursion rate the dominant wear mechanism was cutting of the abradable surface for all the different speeds. The blade was characterised by minimal blade wear or negligible adhesive transfer, with no thermal damage on the blade tip and a dull appearance of the rubbed abradable surface. At increasing speeds, fracture of the coating was evident from the dull appearance of the surface and pull-out of the abradable was observed from the pitting / cracking on the surface, especially at the middle and high speeds (Figure 5.6 d, f). The increase in the speed did not highlight a significant change in the wear mechanics, but in general a reduction of adhesion was observed at a low incursion rate with the increase of speed, suggesting an increase of the efficiency of cut. Observation of the samples

post-test revealed that the transition of the mechanism still remained at an incursion rate of 0.06µm pass^{-1}, as shown in Figure 5.7 for different speeds.

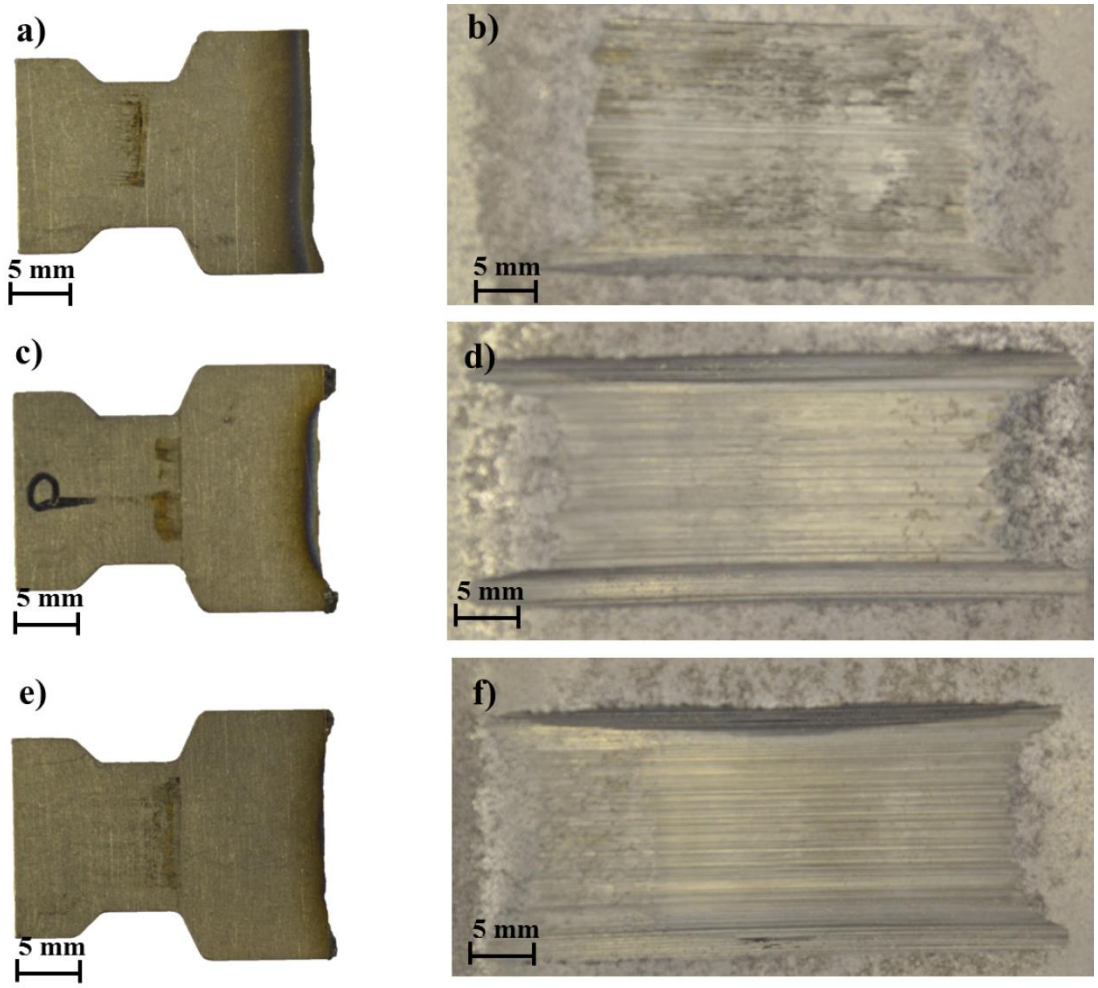

Figure 5.7. Image of the blade and coating post-test for abradable hardness R15Y 72.3 and incursion rate of 0.06µm pass^{-1} at blade speed: 100m s^{-1}: a) Blade, b) Coating; 150m s^{-1}: c) Blade, d) Coating; 200m s^{-1}: e) Blade, f) Coating.

As shown in the figure, a well cut surface with dull appearance and minimal grooving was observed for all speeds, with the thermal damage on the blade tip reducing at higher speeds. The samples highlighted similar wear mechanisms, suggesting that the wear mechanics transition was still at 0.06µm pass^{-1} at higher speeds. The remaining images of blade and coating for the test performed in relation to Table 4.1 at intermediate incursion parameters are included in Appendix 3.

5.1.3. Wear mechanics at different abradable hardnesses

The blade and the abradable sample post-test were observed for the tests performed for different hardnesses and a blade speed of 100m s^{-1}. The influence of the blade speed for the rest of the abradable sample hardnesses will be analysed in the next section. Figure 5.8 shows the blade and the abradable sample post-test at an incursion rate of 0.02µm $pass^{-1}$ for coating hardness R15Y 54.6.

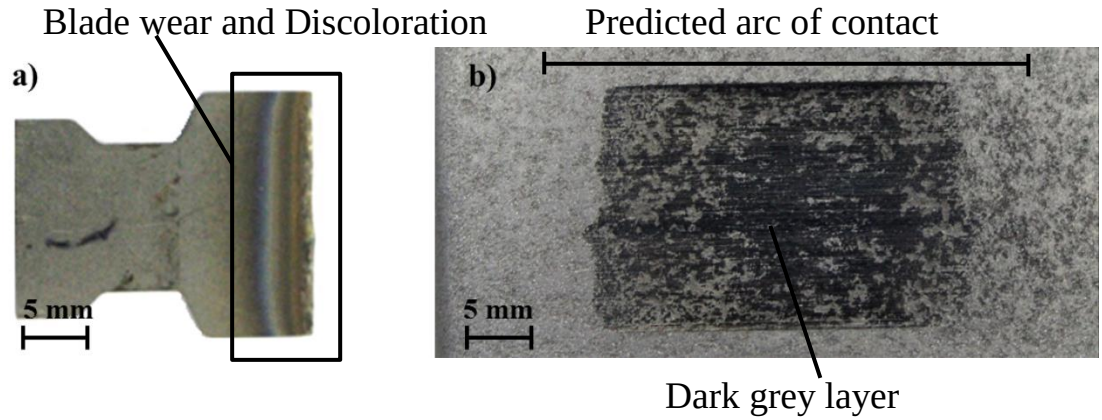

Figure 5.8. Sample post-test for an incursion rate of 0.02µm $pass^{-1}$, at 100m s^{-1} blade speed and abradable sample hardness R15Y 54.6: a) Blade; b) Coating.

As shown in the figure, the main wear mechanism observed at a low incursion rate on the coating with hardness R15Y 54.6 was blade wear. On the blade tip, significant thermal damage occurred, highlighted by discoloration of the titanium due to tempering during the test, and melt wear of the blade was also observed, with dark grey material transferred to the surface of the abradable material. Further analysis of the composition of the transfer will be made in Section 5.3. It should also be noted that, due to the reduced length of the blade, the arc of contact on the abradable coating was reduced, and the rub length would be lower than the predicted value (Section 4.1.1, calculation of the theoretical rub length), as highlighted in Figure 5.8. The different wear mechanisms observed highlighted a change of the mechanism in relation to the hardness at a low incursion rate.

In the test performed with intermediate hardnesses (R15Y 63 and R15Y 59.6) at a low incursion rate, a mix of wear mechanics, adhesive transfer and blade wear, was observed, as shown in Figure 5.9.

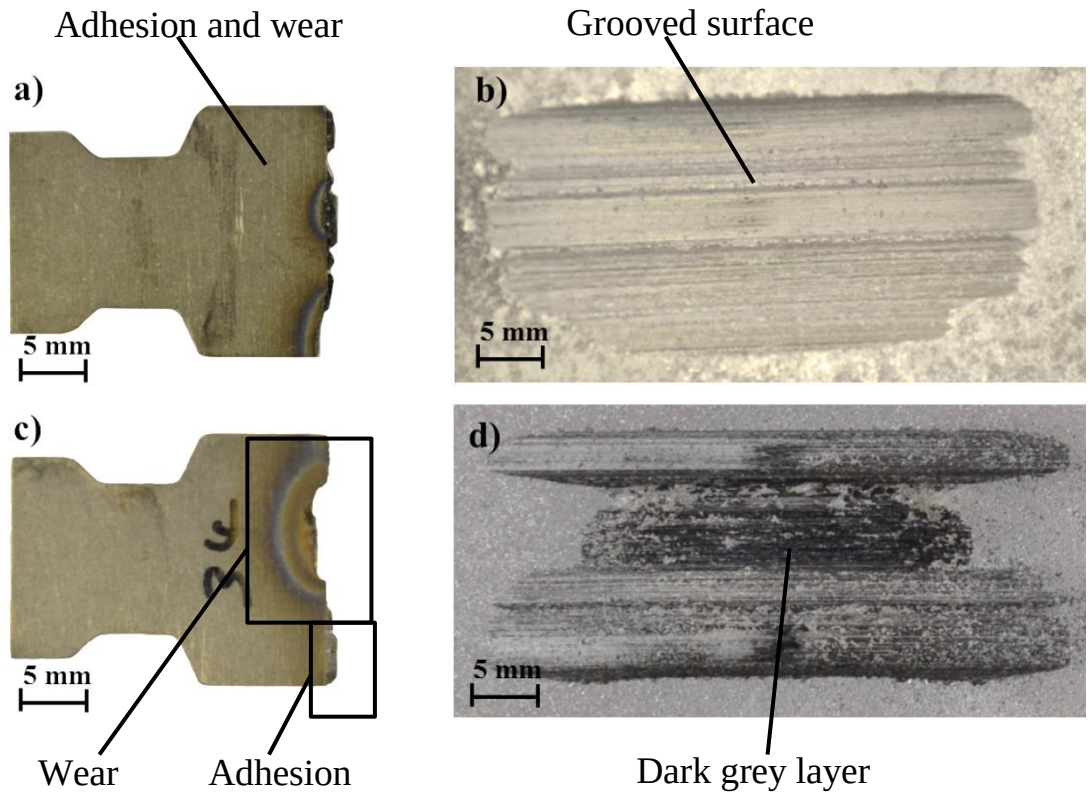

Figure 5.9. Image of the blade and coating post-test for an incursion rate of 0.02µm pass^{-1}, at 100m s^{-1} blade speed: Hardness R15Y 63: a) Blade, b) Coating; Hardness R15Y 59.6: c) Blade, d) Coating.

As shown in the figure, on the coating performed with intermediate hardnesses there was a mix of wear mechanics, adhesive transfer and blade wear, and a dark layer of transfer on the rub surface, with significant thermal damage on the blade tip highlighted by titanium discoloration.

Especially on the sample with hardness R15Y 59.6, the surface of the coating was characterised by grooving due to adhesive transfer on the blade tip, but also on the central part of the rub surface there was blade wear with thermal damage and a corresponding dark grey transfer on the coating, similar to that observed on the coating with hardness R15Y 54.6, as shown in Figure 5.8b. The observation of the wear mechanics at a low incursion rate on a coating with hardness R15Y 59.6, as shown in Figure 5.9, suggests that this hardness value represented a transition of the wear mechanism at a low incursion rate due to the mix of wear mechanics that were observed between the hard and soft coatings.

It should be noted that at an incursion rate of 2µm pass^{-1} for hardnesses R15Y 63, 59.6 and 54.6, and at blade speed 100m s^{-1} (different blade speeds will be analysed in the next section), the same wear mechanism was observed, as shown in Figure 5.10.

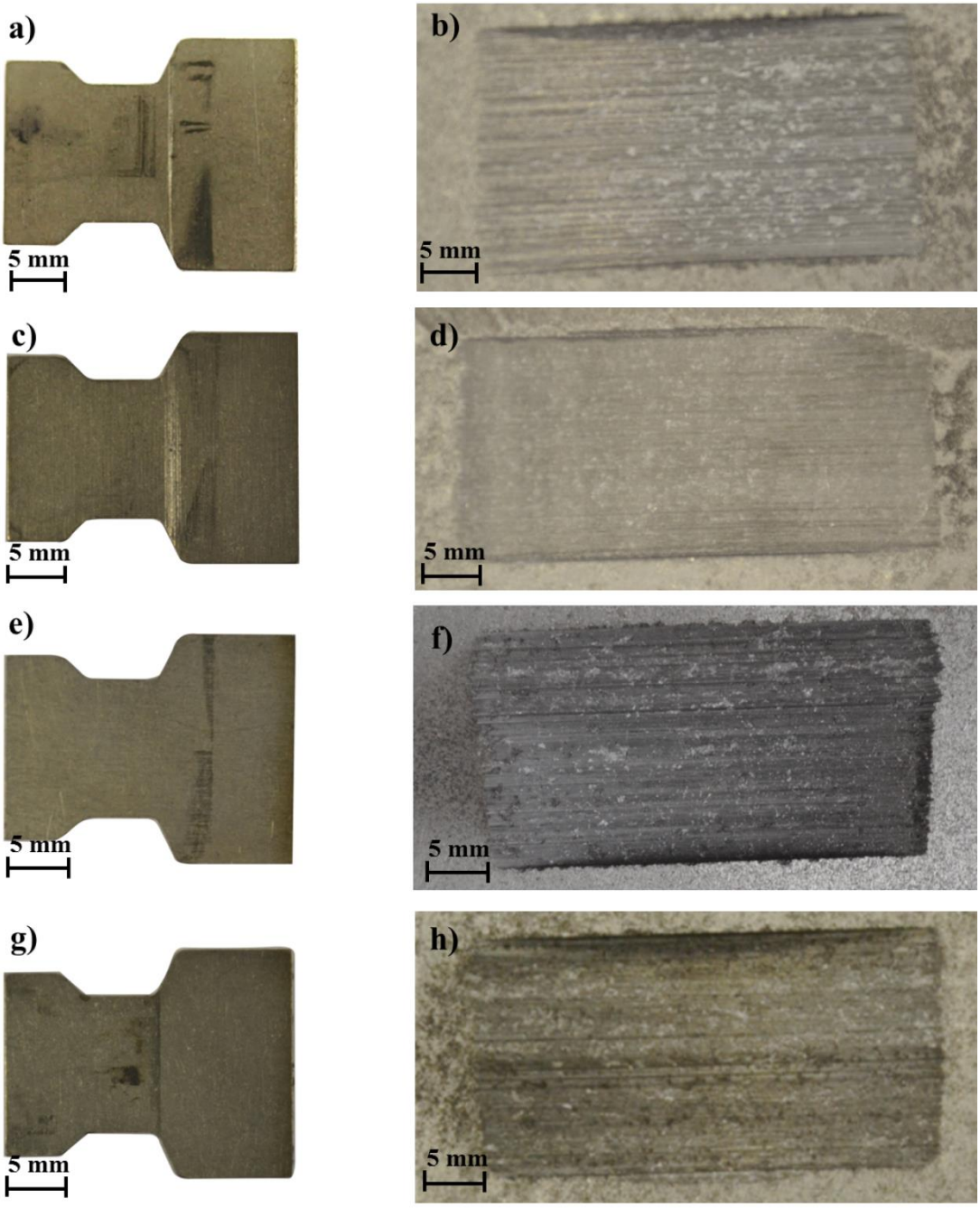

Figure 5.10. Image of the blade and coating post-test for an incursion rate of 2µm pass^{-1}, at 100m s^{-1} blade speed with abradable sample hardness: R15Y 72.3: a) Blade, b) Coating; R15Y 63: c) Blade, d) Coating; R15Y 59.6: e) Blade, f) Coating; R15Y 54.6: g) Blade, h) Coating.

As shown in the figure, the blade cut the abradable material well, with a smooth surface in all test performed at different hardnessess. A slight discolouration of the blade tip was observed on the test performed against the coating with hardness R15Y 59.6 (Figure 5.10e). The same wear mechanism at a high incursion rate indicated that the wear mechanism was only hardness dependent at a low incursion rate.

The effect on the transition was not analysed on the test performed on the sample with hardness R15Y 63 because it was tested at an early stage of this research; instead, samples with similar hardness R15Y 59.6 were tested. The observation of the samples at an intermediate incursion rate suggested that the transition mechanism on the coating with hardness R15Y 59.6 was still at 0.06µm pass^{-1}, as shown in Figure 5.11. Otherwise, the observation of the sample tested on the coating with hardness R15Y 54.6 highlighted a transition from blade wear at an incursion rate of 0.2µm pass^{-1}, as shown in Figure 5.11.

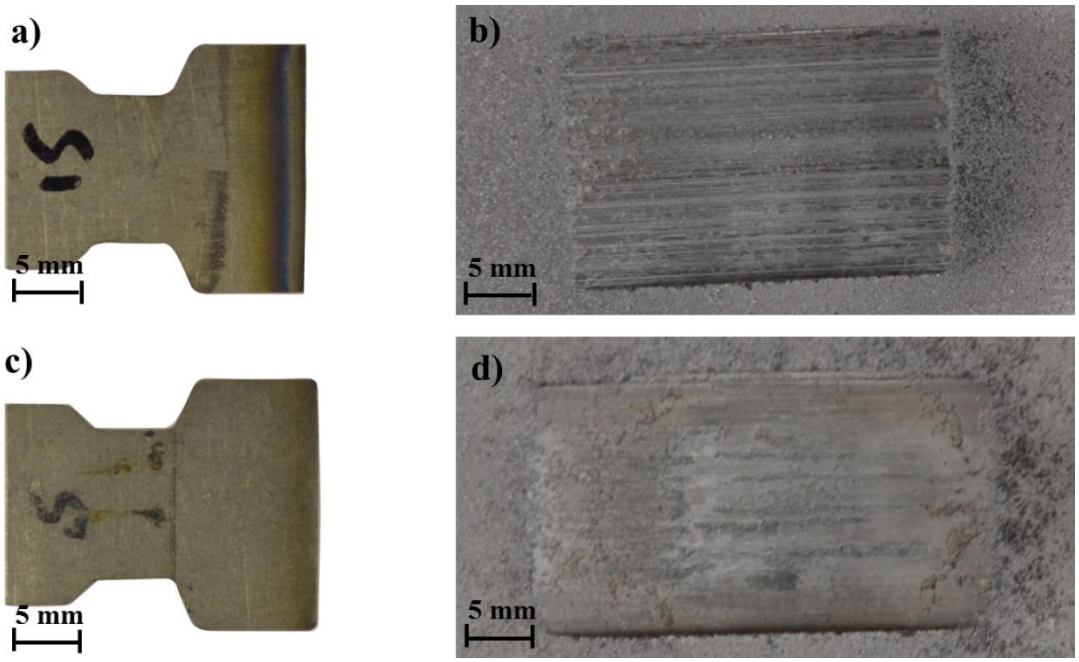

Figure 5.11. Image of the blade and coating post-test at 100m s^{-1} blade speed with abradable sample hardness: R15Y 59.6 at incursion rate 0.06µm pass^{-1}: a) Blade, b) Coating; R15Y 54.6 at incursion rate 0.2µm pass^{-1}: c) Blade, d) Coating.

The images of sample and coating for all tests performed are presented in Appendix 3.

5.1.4. Influence of the blade speed for the remaining abradable sample hardnesses

On the hard coating (R15Y 72.3), it was observed that increasing the speed did not lead to significant changes in the wear mechanism. However, this section considers the influence of the blade speed, which was analysed for the rest of the sample hardnesses. On the abradable sample with hardness R15Y 63, a mix of adhesion transfer and blade wear was observed at a low incursion rate for different speeds, as shown in Figure 5.12.

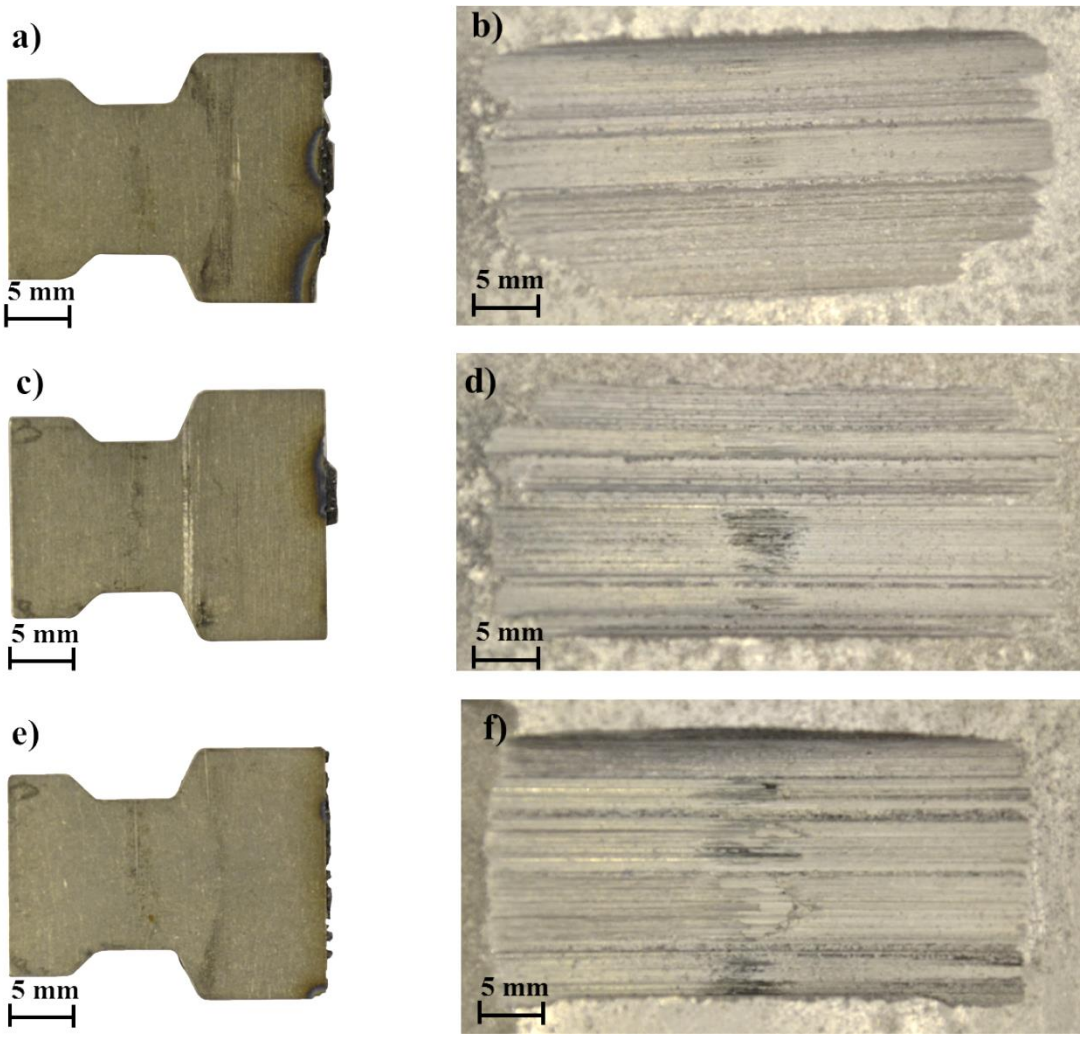

Figure 5.12. Image of the blade and coating post-test for an incursion rate of 0.02µm pass^{-1}, abradable sample hardness R15Y 63 and blade speed: 100m s^{-1}: a) Blade, b) Coating; 150m s^{-1}: c) Blade, d) Coating; 200m s^{-1}: e) Blade, f) Coating.

The mix of adhesion and blade wear was observed especially at low and intermediate speeds (Figure 5.12 a, c), with thermal damage on the blade tip. An increase in the blade speed reduced the adhesive transfer on the blade tip and the surface appearance was less grooved (Figure 5.12 e, f).

At a high incursion rate, an increase of the blade speed led to good cutting, with a similar result being obtained as that at 100m s^{-1} in Figure 5.10 c, d. Figure 5.13 shows the blade and abradable sample post-test with coating hardness R15Y 63 and an incursion rate of 2µm $pass^{-1}$.

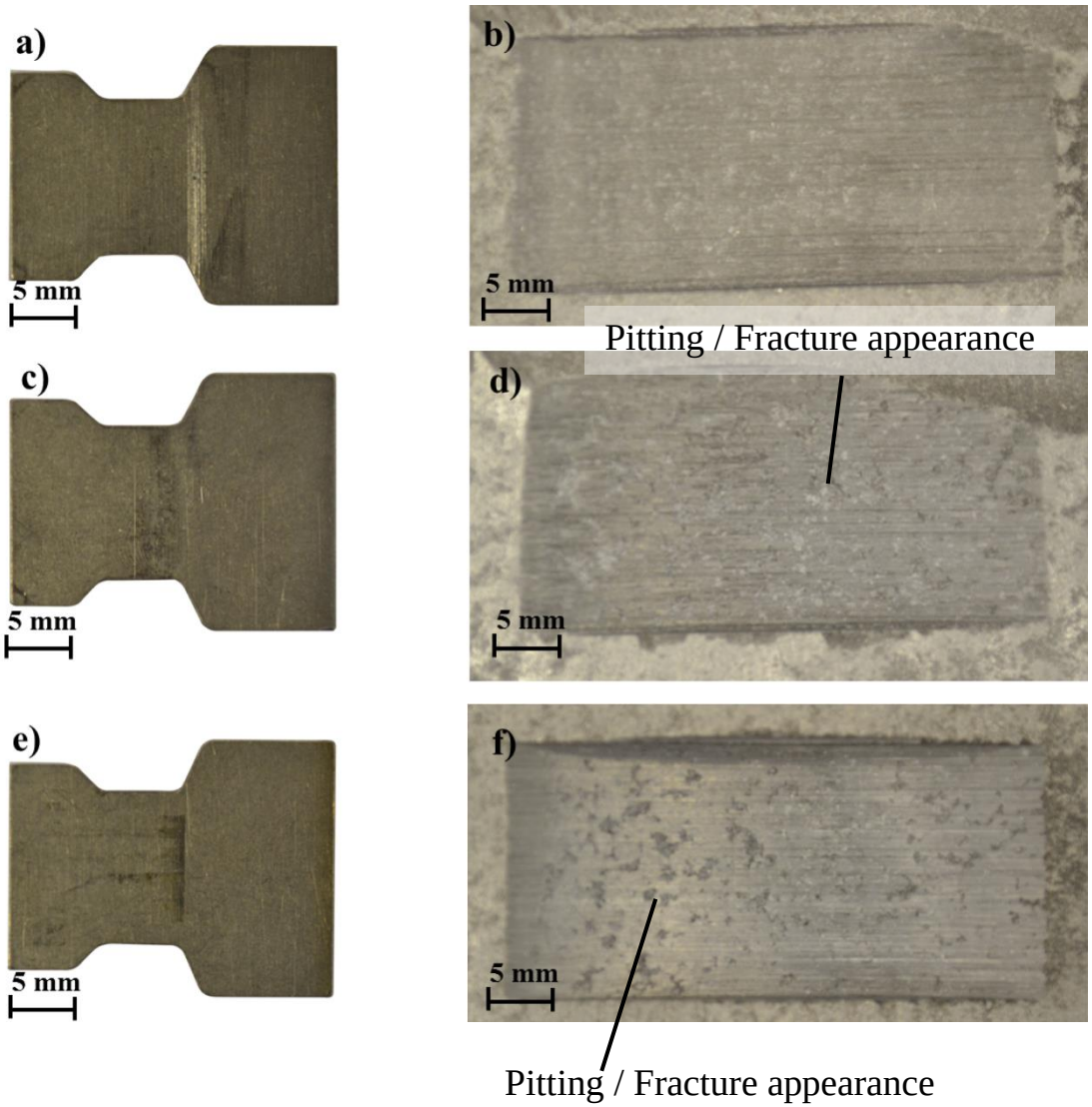

Figure 5.13. Image of the blade and coating post-test for an incursion rate of 2µm $pass^{-1}$, abradable sample hardness R15Y 63 and blade speed: 100m s^{-1}: a) Blade, b) Coating; 150m s^{-1}: c) Blade, d) Coating; 200m s^{-1}: e) Blade, f) Coating.

As shown in the figure, the blade cuts the abradable material well, with the surface having a smooth appearance at all blade tip speeds, as observed for hardness R15Y 72.3. Also, at intermediate and higher speeds, fracture of the coating (Figure 5.13 d, f) was highlighted from the material pull out from the surface, with a pitted appearance to the surface, with slight blade tip discoloration at higher speed (Figure 5.13e). On the test performed with coating hardness R15Y 59.6, a mix of adhesive transfer and blade wear at low incursion rate was observed, as shown in Figure 5.14.

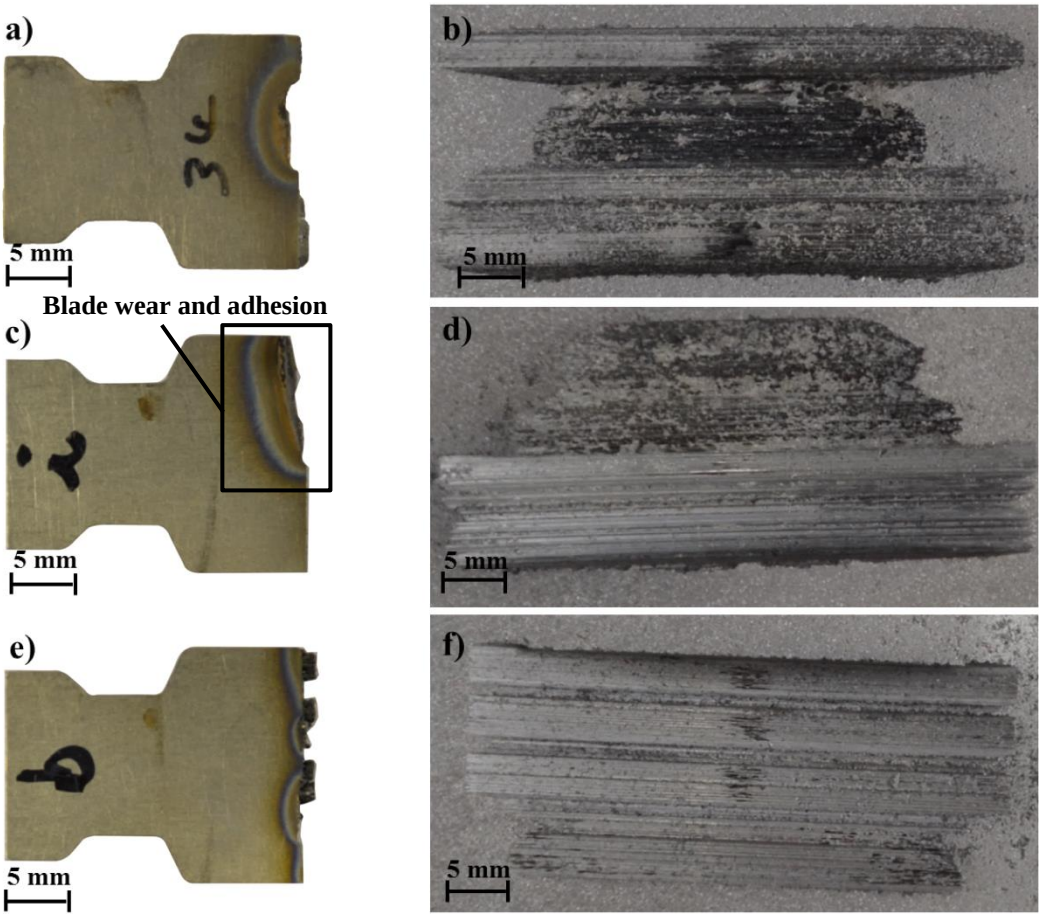

Figure 5.14. Images of the blade and coating post-test for abradable hardness R15Y 59.6 at incursion rate 0.02µm pass^{-1}, and blade speed: 100m s^{-1}: a) Blade, b) Coating; 150m s^{-1}: c) Blade, d) Coating; 200m s^{-1} e) Blade, f) Coating.

These samples represented a good example of where a mix of wear mechanics was observed. An adhesive transfer and blade wear along the blade tip were observed at a low incursion rate, especially at 100 and 150m s^{-1} blade speeds (Figure 5.14 a, b-c, d). Also, at 150m s^{-1} an adhesive transfer was observed on part of the worn blade (Figure 5.14 c). This suggests that an initial blade wear occurred with transfer on the

coating generating a dark layer on the rub surface, and then adhesive transfer from the coating to the blade started (Figure 5.14 c, d); this was another clear example of the mix of wear mechanisms observed. At higher speeds, blade wear and adhesion transfer on the blade tip and thermal damage were observed, but generally with increased speed the grooves on the rubbing surface were reduced, as shown in Figure 5.14f.

The blade and the coating post-test with coating hardness R15Y 59.6 with an incursion rate of 2µm pass^{-1} are shown in Figure 5.15 for the different blade speeds.

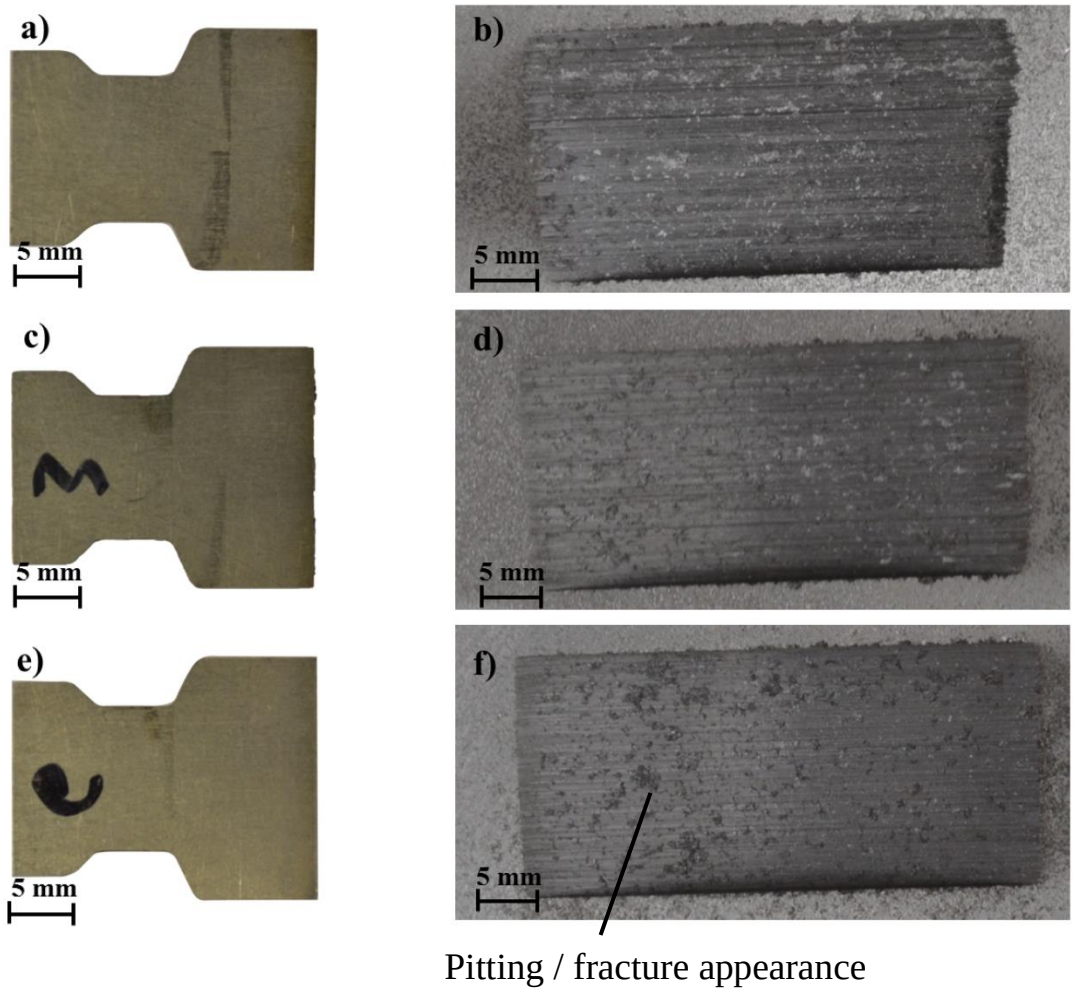

Figure 5.15. Image of the blade and coating post-test for abradable hardness R15Y 59.6 at incursion rate 2µm pass^{-1} and blade speed of: 100m s^{-1}: a) Blade, b) Coating; 150m s^{-1}: c) Blade, d) Coating; 200m s^{-1}: e) Blade, f) Coating.

At a high incursion rate, clean cutting was observed at all blade speeds (Figure 5.15). The transition of the wear mechanics observed at 0.06µm pass^{-1} for different speeds

can be seen in Appendix 3, where all sample images for the tests performed are presented.

Figure 5.16 shows the blade and the abradable sample post-test at a low incursion rate for the coating with hardness R15Y 54.6 at different blade tip speeds.

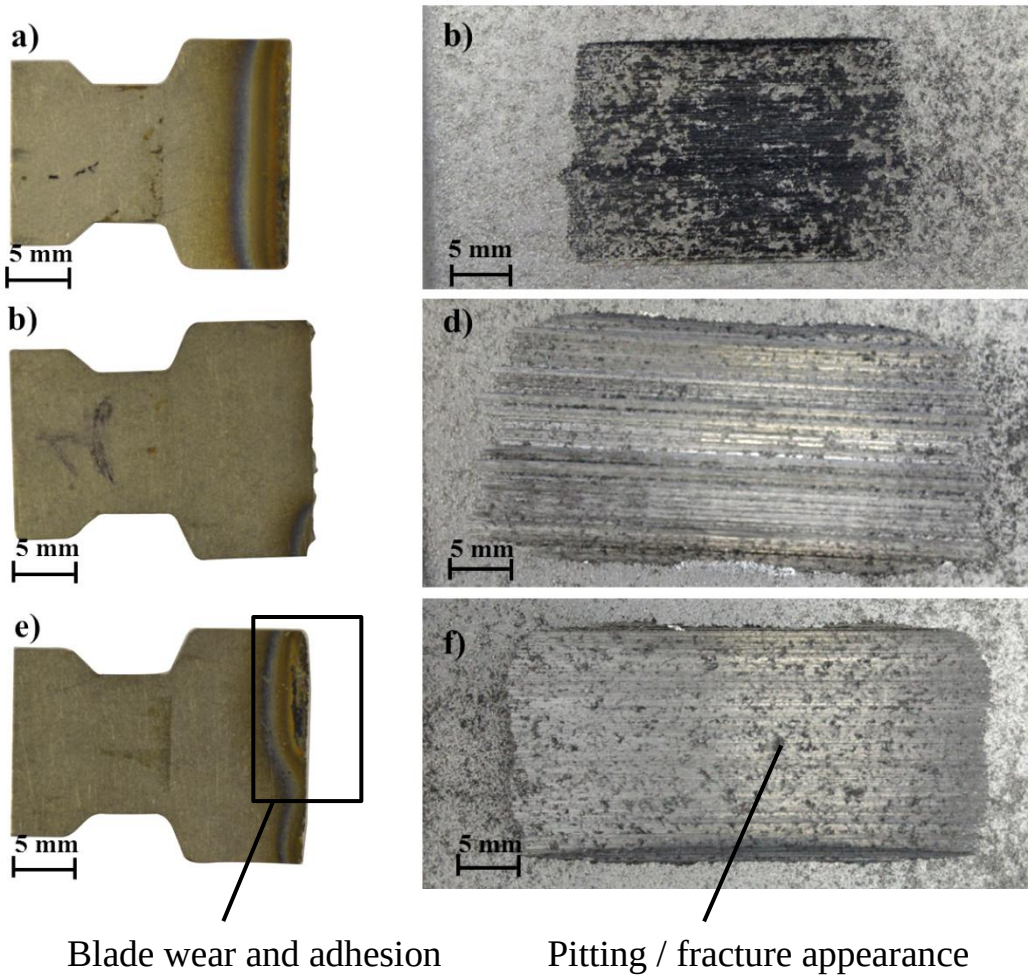

Figure 5.16. Image of the blade and coating post-test for abradable hardness R15Y 54.6 at incursion rate 0.02µm pass^{-1} and blade speed: 100m s^{-1}: a) Blade, b) Coating; 150m s^{-1}: c) Blade, d) Coating; 200m s^{-1}: e) Blade, f) Coating.

At a low incursion rate, blade wear was observed, with a dark grey transfer observed on the surface of the coating at low speed. An increase of the blade speed reduced the blade wear as well the dark grey transfer, as shown in Figure 5.16 c, d-e, f. Thermal damage was observed on all blade tips, especially at low and high blade speeds. At high speed, an adhesive transfer was observed on the blade tip on the part of the blade wear, as shown in Figure 5.16e. This suggests that after initial blade

wear, an adhesive transfer occurred, and the corresponding coating surface was characterised by clean cutting, with the surface showing pitting / cracking on the rub area (Figure 5.16f); therefore further investigations will be made.

Figure 5.17 shows the blade and coating post-test at a high incursion rate for the test with coating hardness R15Y 54.6 for all blade speeds.

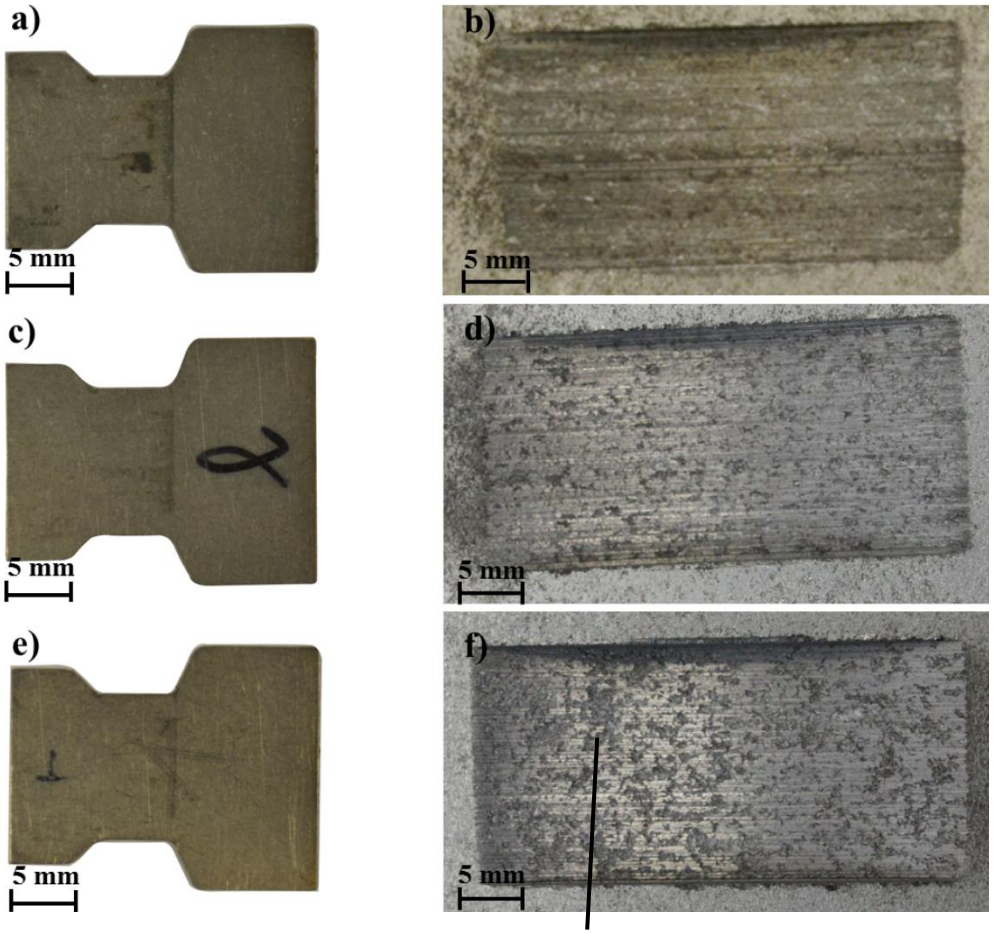

Figure 5.17. Image of the blade and coating post-test for abradable hardness R15Y 54.6 at incursion rate 2µm pass^{-1} and blade speed: 100m s^{-1} a) Blade, b) Coating; 150m s^{-1}: c) Blade, d) Coating, 200m s^{-1}: e) Blade, f) Coating.

As shown in Figure 5.17, at a high incursion rate, a similar cutting wear mechanism was observed for different speeds. At the higher incursion rate, the well-cut surface along with a pitted / fractured appearance, especially at intermediate and high speeds (Figure 5.17 d, f), suggests that the coating was fractured during the contact; this was also observed for other tests performed at a high incursion rate and high speed.

Observation of the sample suggests that a transition still remains at 0.2µm pass^{-1}, even with the increase in speed, as shown in Figure 5.18.

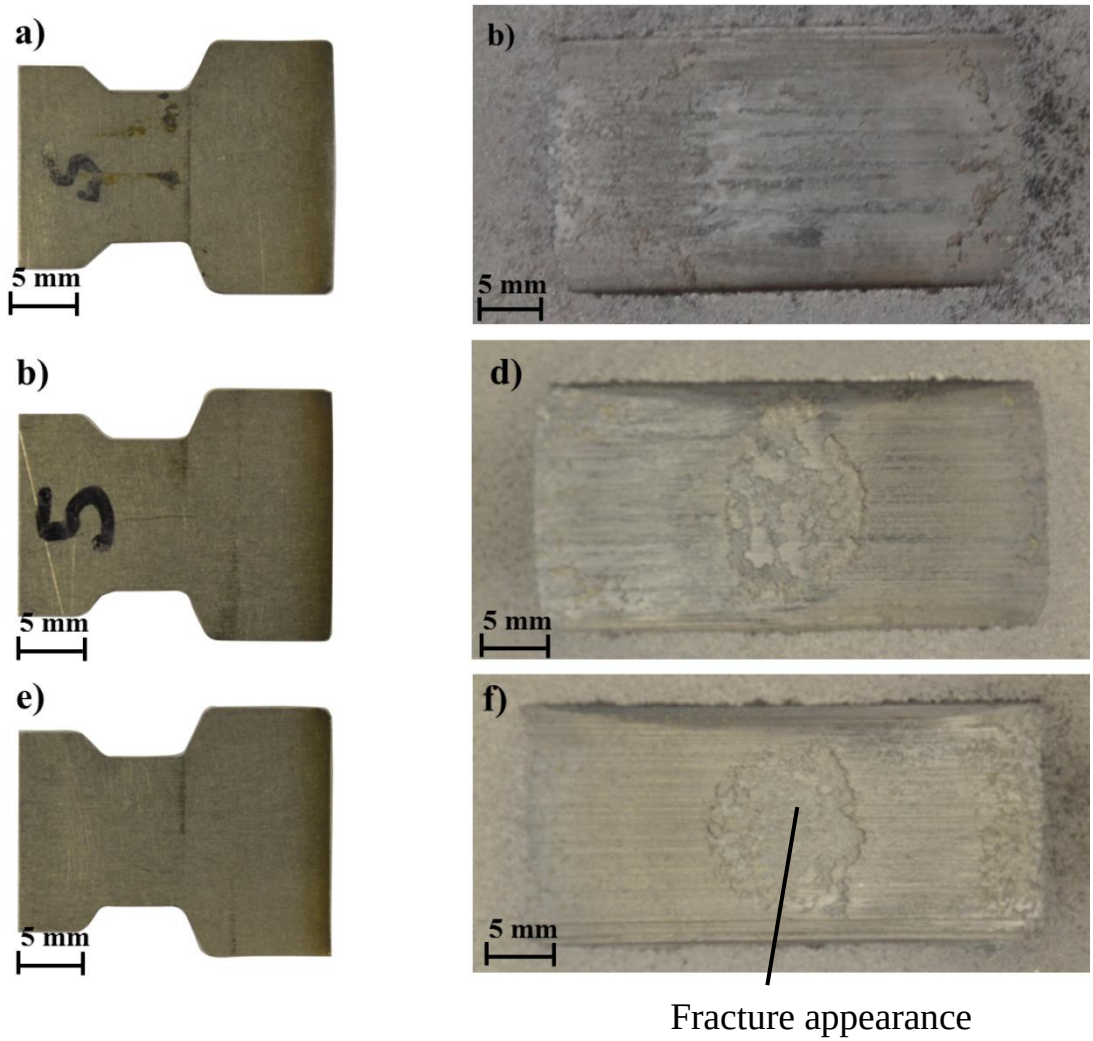

Figure 5.18. Image of the blade and coating post-test for abradable hardness R15Y 54.6: and incursion rate of 0.2µm pass^{-1}, at blade speed: 100m s^{-1}: a) Blade, b) Coating; 150m s^{-1}: c) Blade, d) Coating; 200m s^{-1}: e) Blade, f) Coating.

As shown in the figure, there was no significant blade variation or thermal damage, and a well-cut rub surface with a fractured appearance, especially at intermediate and high speeds (Figure 5.18 d, f).

5.2. Wear mechanisms observed

Figure 5.19 summarises the wear mechanisms that were observed in the sample post-test for all tests performed. The rest of the sample post-test images relating to the test conditions are attached in Appendix 3.

Based on the observations of the samples post-test, it appears that the incursion rate and the hardness of the sample have a significant influence on the wear mechanisms occurring during the incursion. At low incursion rate, the main wear mechanisms observed were adhesive transfer, blade wear and a mix of adhesive transfer and blade wear. At a high incursion rate, minimal blade wear and well-cut surfaces were mainly observed, independently of the hardness of the coating. The observations of the sample highlighted the significant influence of the hardness on the wear mechanism, especially at a low incursion rate.

With a hard coating, the main mechanism was adhesive transfer from the coating to the blade tip, with grooved abradable surface. A decrease in the hardness produced a mix of adhesive transfer and blade wear, also with grooving and a dark grey layer on the coating surface, as shown with abradable material with hardness R15Y 59.6. In the test performed with the coating with hardness R15Y 54.6, the main mechanism was a worn blade and melt wear on the coating surface.

Overall the blade speed did not highlight a significant change of the wear mechanics, but in general a reduction of adhesion and blade wear was observed with the increase of speed. Therefore, on the soft coating some difference was observed, especially at a low incursion rate, with a reduction of the dark grey layer, and some adhesive transfer was observed. Additionally there was a well-cut surface at high speed; therefore further investigation needs to be conducted during the research.

Additionally, an increase of speed at high incursion rate revealed fracture of the coating from a cracked and pitted appearance on the rub surface. As the dislocator phase present in the abradable material is designed to shear easily, an increase of the incursion rate suggests fracturing of the coating and ability to dislocate. Also, a higher speed suggests more impact energy and more efficiency of cutting; however further investigation into this will be carried out during this research.

In conclusion, the wear mechanism was observed to be dependent on the incursion rate, and was related to the hardness of the coating at a low incursion rate. Therefore, the next section discusses the amount of wear and adhesion as analysed through the maximum change of the blade length and weight, measured before and after the test. This was performed in order to quantify the different wear mechanisms and obtain a trend of adhesion and wear in relation to the test parameters.

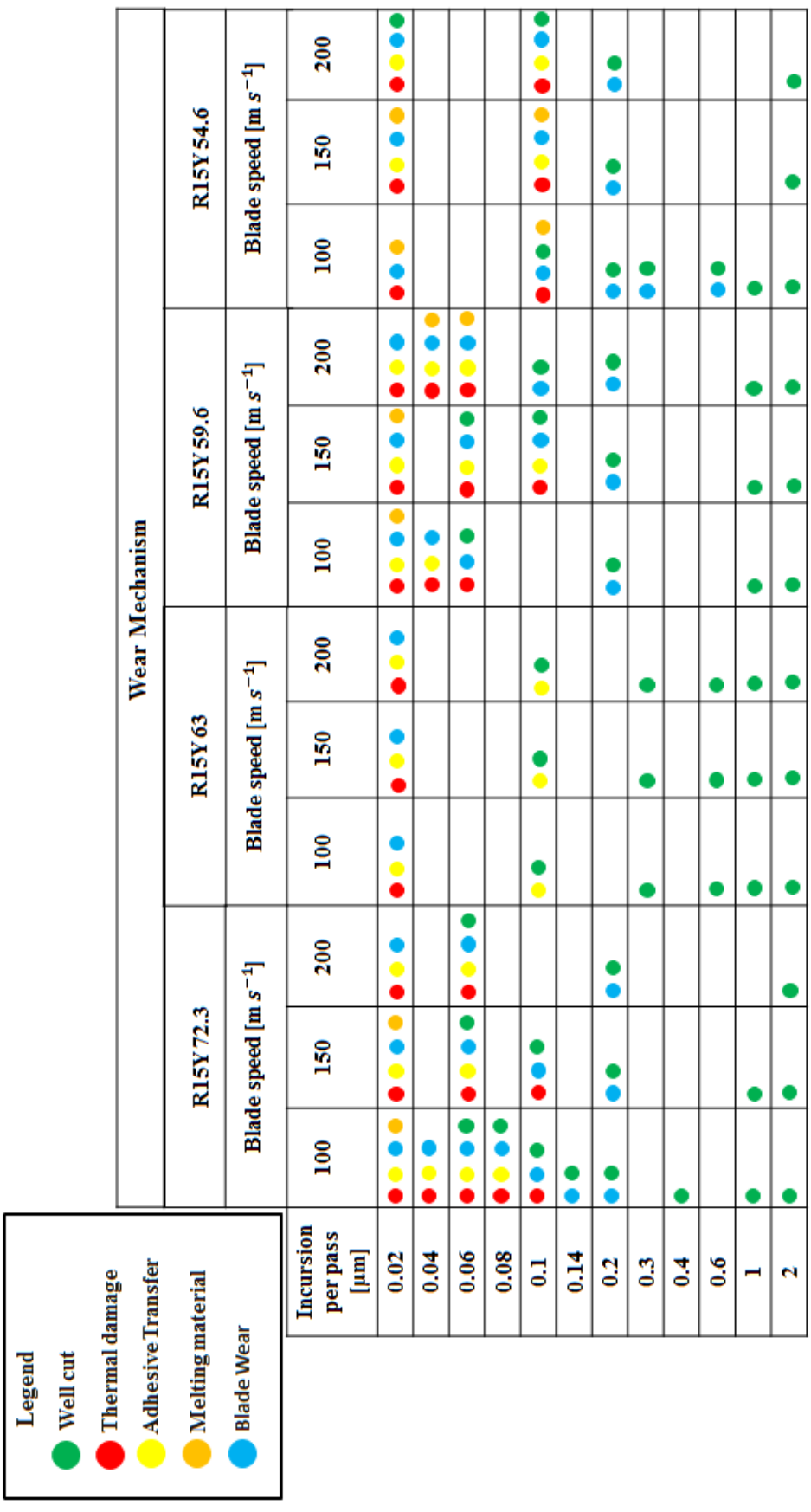

Figure 5.19. Wear mechanisms observed on the test performed.

5.3. Maximum blade length and weight change

The blade length and weight were measured before and after the test, as mentioned in Section 4.2.1, and the maximum blade length and weight change were analysed for all tests performed in relation to the incursion rate, speed and coating hardness.

5.3.1. Blade length and weight change with hardness R15Y 72.3

The blade length and weight change were calculated for the sample tested against the coating with hardness R15Y 72.3. The post-test maximum blade length was measured and compared with the initial blade length. Figures 5.20 and 5.21 show the maximum blade length and weight change for the coating with hardness R15Y 72.3.

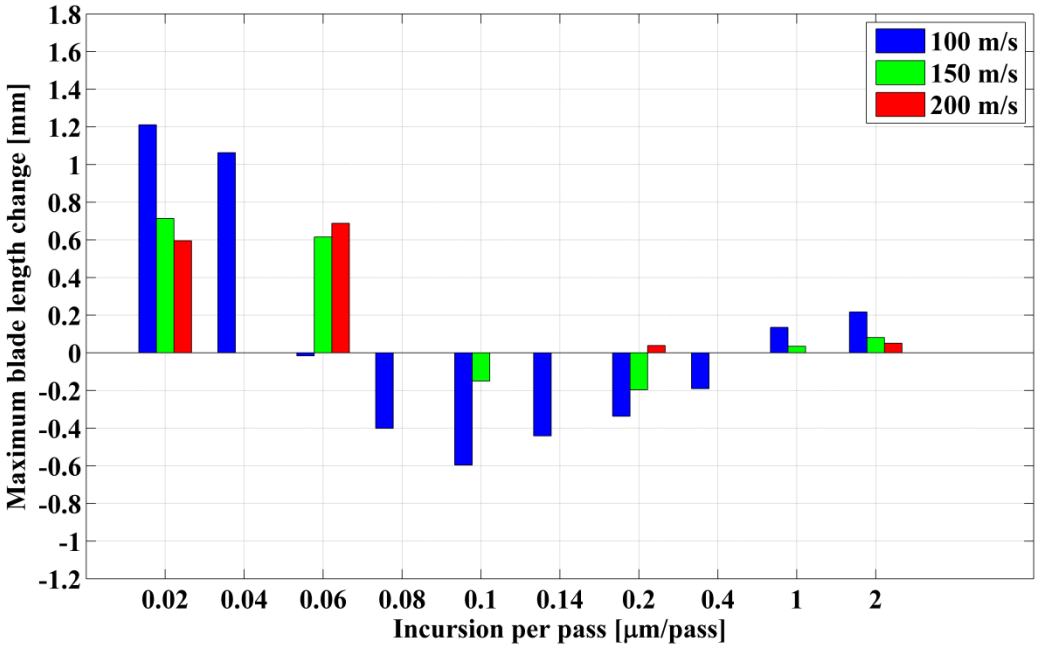

Figure 5.20. Maximum blade length change vs the incursion rate for the tests with coating R15Y 72.3.

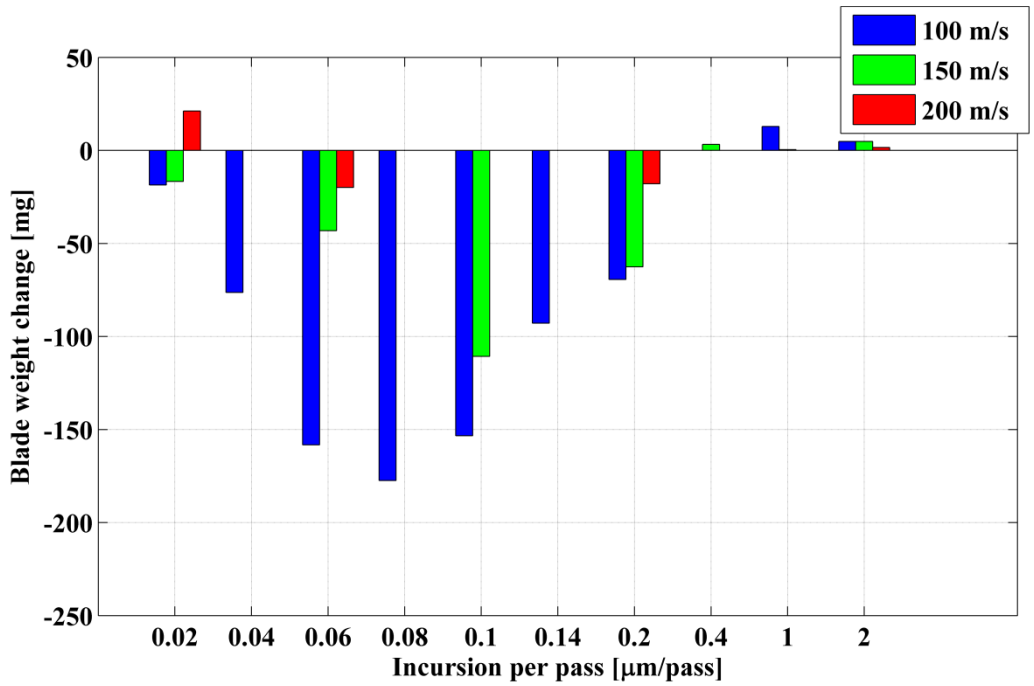

Figure 5.21. Blade weight change vs incursion rate for the tests with coating R15Y 72.3.

As shown in Figure 5.20, a positive value of the blade length change was measured at low incursion rate. This highlighted an increase of the blade length after the test. The increase in the blade length quantified the adhesive transfer observed on the blade tip after the tests. For the tests performed at incursion rate of 0.08, 0.1, 0.14 and 0.2µm pass^{-1}, a negative blade length change was recorded, representing a reduction from the initial blade length during the test, and therefore wear of the blade tip was observed. This could be associated with the mechanical friction between the blade and the coating during the contact and the difficulty of fracturing the coating. At higher incursion rates, a slightly positive blade length change was measured, representing a small degree of adhesion, and a well-cut surface was observed.

As shown in Figure 5.21, the measured blade weight change had a negative value for almost all of the test conditions, representing a decrease of the blade weight after interaction with the abradable coating. This result at first seems anomalous, as an increase in length would be expected to show a proportional increase in weight. But this did not happen, which suggests a non-uniform wear mechanism on the blade, where adhesive transfer and blade wear occur at different points along the blade profile. This was observed previously at a low incursion rate for example, for the test

at an incursion rate 0.02µm pass^{-1} and blade speed 100m s^{-1} and hardness R15Y 72.3 (Figure 5.2).

The analysis based on the maximum blade length value is not influenced if blade wear occurred when adhesive transfer was observed. Therefore, in order to take into consideration a mix of wear mechanics along the blade tip, the average length was measured using the blade profile captured as explained in Section 4.2.1. Figure 5.22 shows the image of the blade tip and the blade tip profile for the test at an incursion rate of 0.02µm pass^{-1} and blade speed 100m s^{-1} and coating hardness R15Y 72.3, and highlights the initial, and the maximum and minimum blade lengths.

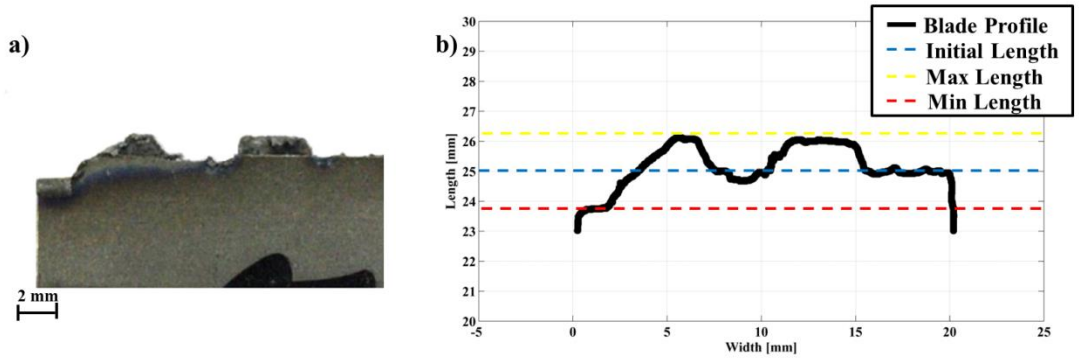

Figure 5.22. Test performed at incursion rate of 0.02µm pass^{-1} and blade speed 100m s^{-1}, coating hardness R15Y 72.3: a) Blade tip, b) Blade profile.

The profile in Figure 5.22 highlights that the minimum length of the blade was below the initial length: this suggests blade wear. Also a different density between the blade and adhesive transfer material would be a possible explanation for the increase in length and decrease in weight; however, further investigation will be carried out in Section 5.4.2. Therefore, the non-uniform adhesion along the blade tip suggests that it could be useful to calculate the average blade length change instead of the maximum blade length change, in order to consider the effect of the minimum blade length on the calculation. Figure 5.23 shows the average blade length change calculated from the average final blade length and the initial blade length for the test performed with the coating with hardness R15Y 72.3.

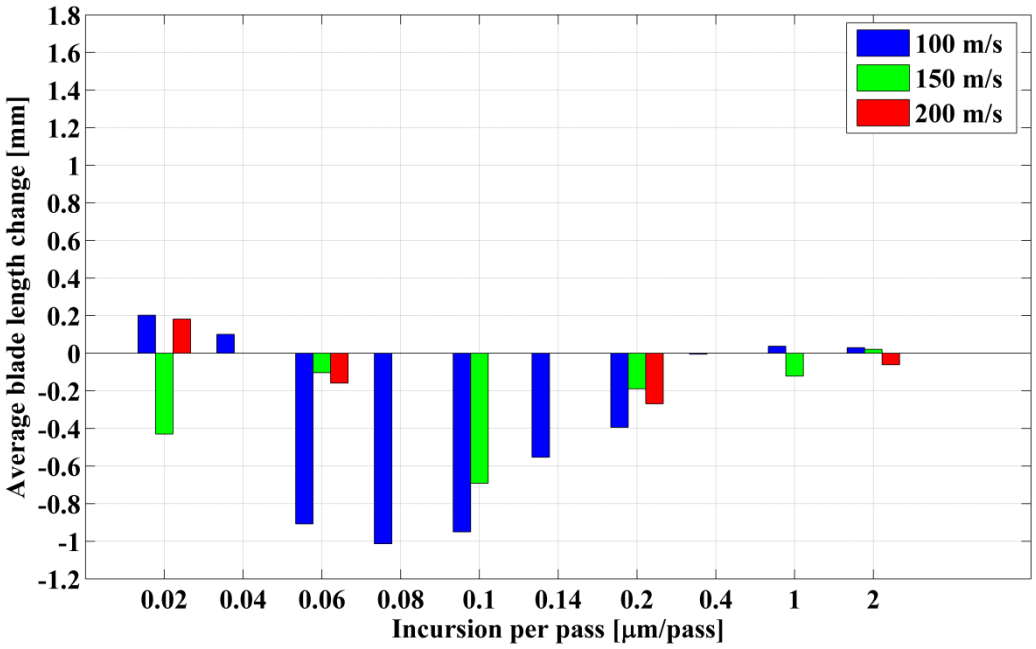

Figure 5.23. Average blade length change vs the incursion rate for the tests with coating R15Y 72.3.

The blade length change using the average length shows an overall reduction of the blade, as shown in the figure, and therefore a decrease in the blade length change. The presence of blade wear, where the blade length was below the initial blade length, reduced the average length of the blade compared with the analysis based on the maximum length. At some incursion rates, such as 0.06μm pass^{-1}, the negative average blade length change followed the negative blade weight change, but at high incursion rates, where the blade cut the abradable sample, a decrease in the average blade length was measured where an increase in weight was also measured. However, overall, from observation of the graph, it is still difficult to find a trend in the wear mechanics.

The average blade length change included the influence of an observed mix of wear mechanics, but underestimated the level of adhesion measured on the blade, and it did not really give much more insight when combined with weight change data, and it did not represent an improvement in classifying the different wear mechanisms. However, high adhesion could be correlated to a high level of potential debris in the engine [1, 3, 6, 11, 15], and therefore it was important to know the maximum length observed and evaluate the potential mix of adhesion from the observation of the

blade weight change. Consequently, the rest of the test was analysed using the maximum length of the blade in order to calculate the blade length change.

5.3.2. Blade length and weight change with hardnesses R15Y 63 and 59.6

The maximum blade length and weight change were calculated for the sample tested against coatings with hardness R15Y 63 and 59.6. These samples are discussed in the same section because they were characterised by a similar value of hardness. Figure 5.24 and Figure 5.25 show the blade length and weight change results obtained from the coating with hardness R15Y 63.

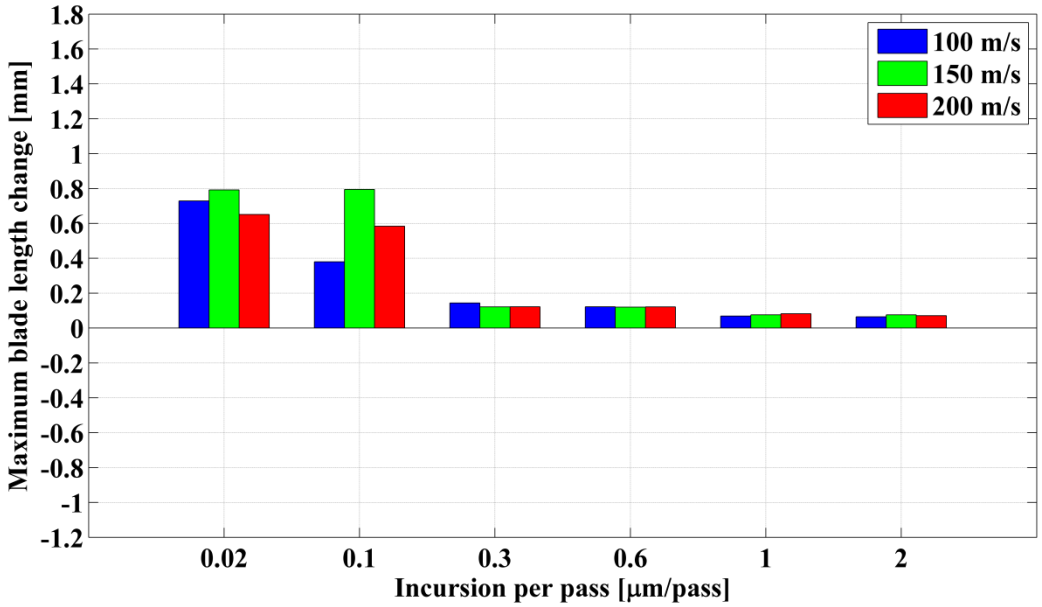

Figure 5.24. Maximum blade length change vs the incursion rate for the tests with coating R15Y 63.

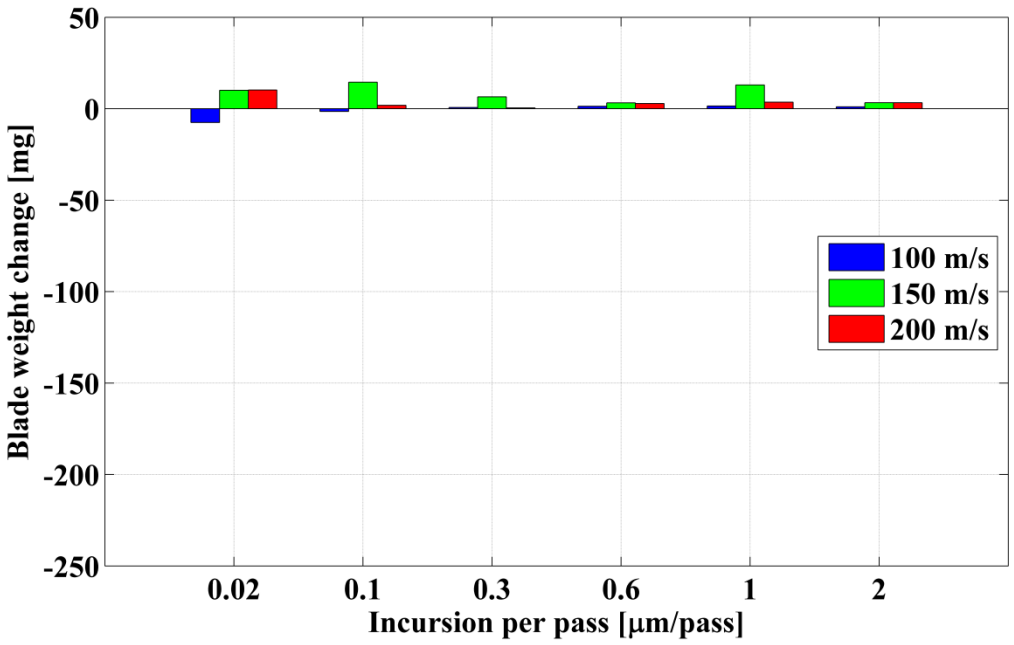

Figure 5.25. Blade weight change vs the incursion rate for the tests with coating R15Y 63.

The trend observed highlighted a reduction of the blade length with the speed, except at intermediate speed where there was a lower variation of blade weight compared with the tests performed against the coating with hardness R15Y 72.3. A positive blade weight change suggested that the blade wear observed in Figure 5.9a did not reduce the weight compared to the increase from the adhesive material. Also the level of adhesion was lower compared with the hard coating R15Y 72.3, and a progressive blade reduction was observed from low to high incursion rates, when the wear mechanism changed progressively from adhesion to clean cutting.

Figure 5.26 and Figure 5.27 show the blade length and weight change for the coating R15Y 59.6.

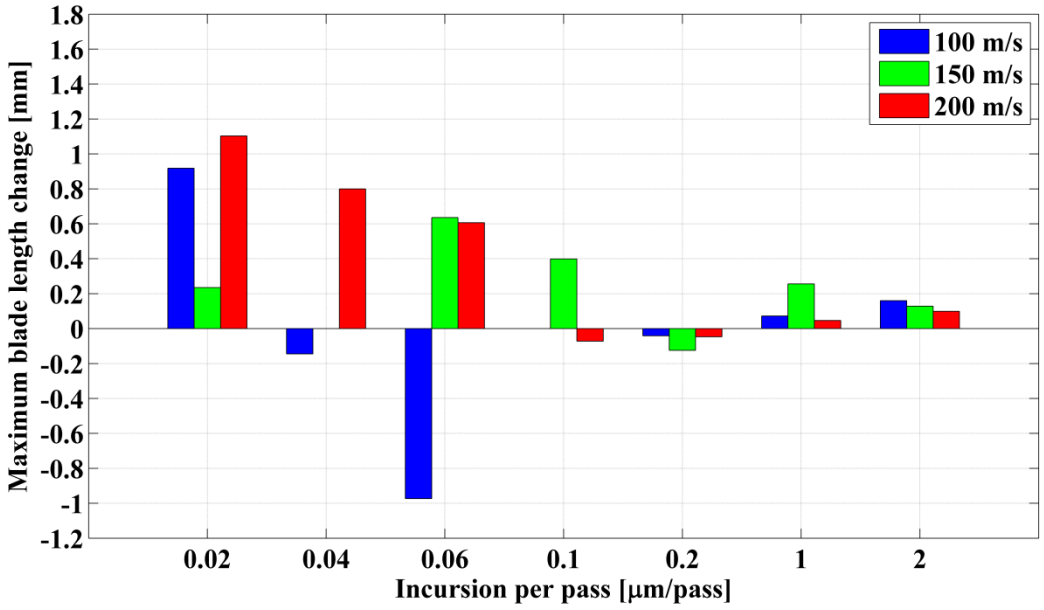

Figure 5.26. Maximum blade length change vs the incursion rate for the tests with coating R15Y 59.6.

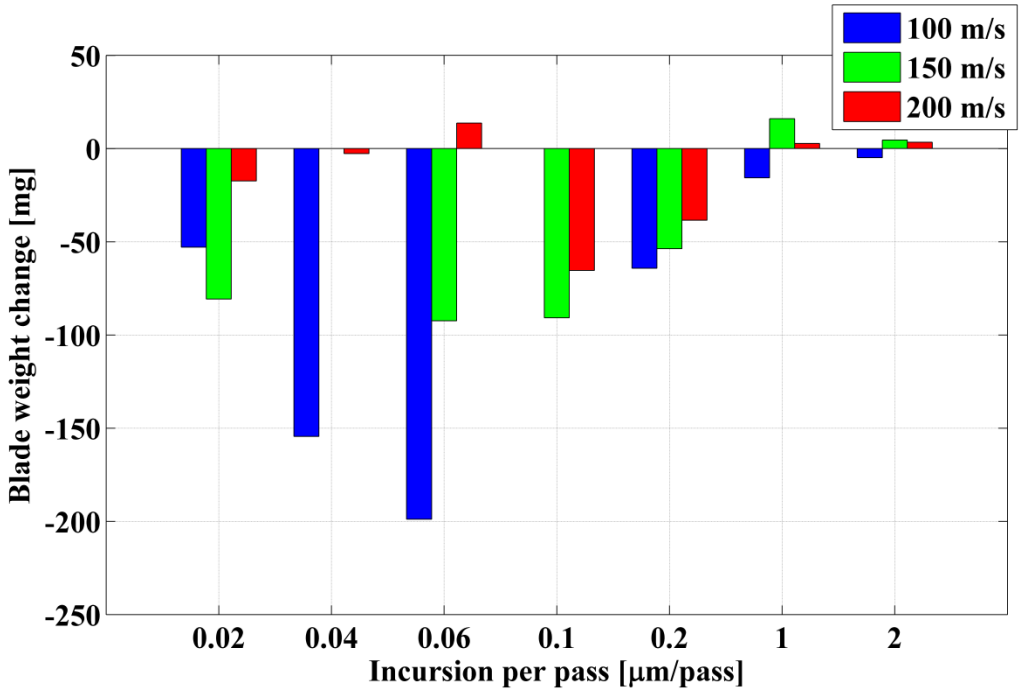

Figure 5.27. Blade weight change vs the incursion rate for the tests with coating R15Y 59.6.

Observation of the maximum blade length revealed a maximum length comparable with the hard coating, but also a blade reduction, especially at 0.06µm pass^{-1}. The results at this hardness were more variable, especially in the maximum blade length change, and a non-uniform trend was observed with incursion rate or even with

speed. As highlighted previously, a negative blade weight change and positive blade length change suggest a combination of adhesion and blade wear, as seen in the analysis of the sample post-test, where adhesion transfer but also blade wear and dark grey transfer on the coating surface were observed, as shown in Figure 5.14.

Also with the coating R15Y 59.6, different results were measured compared with the coating with similar hardness, R15Y 63, where positive values of blade length and weight were recorded. Observation of the material post-test (Figures 5.12 and 5.14) showed adhesion transfer and blade wear at low incursion rates for both hardnesses, but more evident on the coating R15Y 59.6. The variability from the graphs (Figures 5.26, 5.27) suggests that the coating R15Y 59.6 could have a hardness that represented a threshold on the mechanism, from adhesive transfer observed mainly on the hard coating to blade wear observed mainly on the soft coating.

5.3.3. Blade length and weight change with hardness R15Y 54.6

The maximum blade length and weight change were calculated for the sample tested against coating with hardness R15Y 54.6. Figures 5.28 and 5.29 show the maximum blade length and weight change measured for the coating R15Y 54.6.

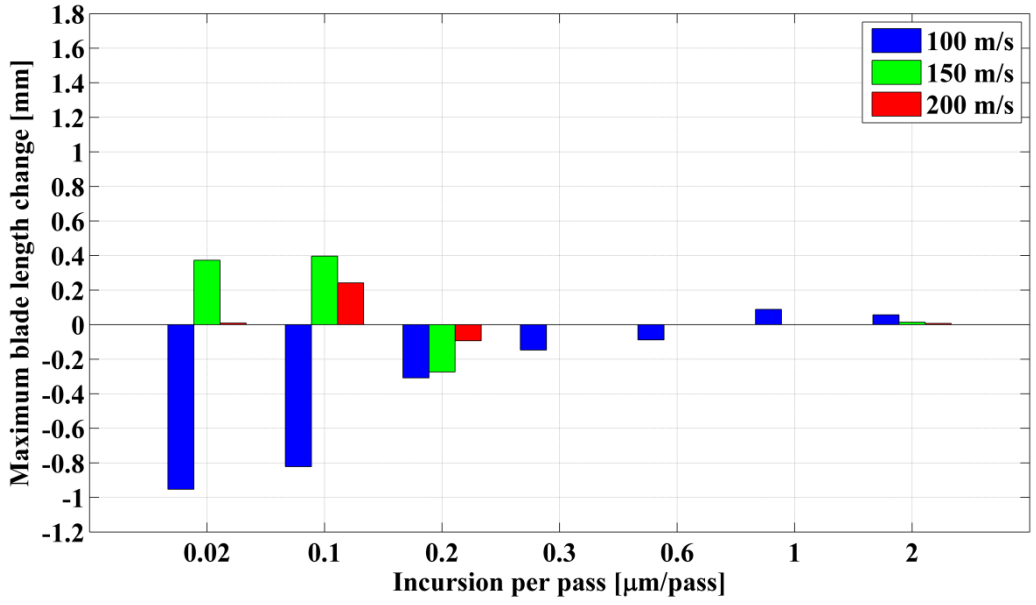

Figure 5.28. Maximum blade length change vs the incursion rate for the tests with coating R15Y 54.6.

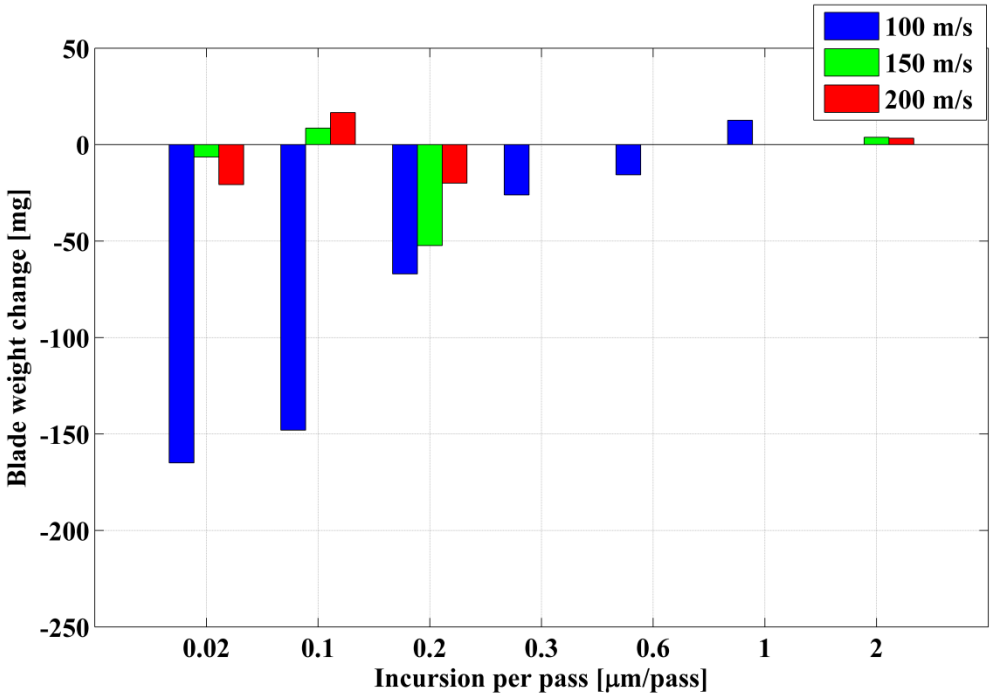

Figure 5.29. Blade weight change vs the incursion rate for the tests with coating R15Y 54.6.

At low incursion rates at 100m s^{-1} a significant reduction of the blade length and weight were measured, while at higher incursion rates the blade length variation was less than 7µm. In this case, a significant reduction of the blade length and weight corresponded to blade wear observed in Figure 5.16, especially at low speed.

However, with an increase of the speed some differences were observed. At intermediate speeds blade wear was observed (Figure 5.16b), but also some material adhered to the blade tip at low incursion rates; therefore, an increase in the blade length was measured and less dark grey material was observed on the rub surface (Figure 5.16c). Also a decrease of the weight suggested a mix of wear mechanisms.

At high speed, blade wear was observed on the blade tip (Figure 5.16c), but also material adhering to the wear part was observed (Figure 5.16c), and this could suggest a mix of wear mechanisms, blade wear followed by adhesive transfer; this could explain the positive blade length change and negative weight change. Also at an incursion rate of 0.1µm $pass^{-1}$ at intermediate and high speeds, increases in the blade length and weight were measured, where observation of the sample (Appendix 3) showed a mix of adhesion and wear. In comparison, at 0.2µm $pass^{-1}$ a decrease in the blade length was measured with a clean cut surface, with a similar result for all

speeds (Figure 5.18). Further investigation into the influence of the speed will be made in the next chapters.

5.3.4. Summary of blade and weight change results

This analysis of the blade gave an evaluation of blade length and weight change. A positive value of the blade length change represented an adhesive transfer on the blade tip, while a negative blade length change represented blade wear.

In general this analysis gives an overall idea of whether there was adhesive transfer or blade wear, and in general a reduction of adhesion and blade wear was observed with an increase of the incursion rate, but this did not allow identification of an overall trend because of the scatter and the variability of the blade and weight changes in relation to incursion rate, hardness and speed. In many ways these results offer no further insight when compared to the images of the blade and abradable samples presented in Section 5.1.

Also, when a mixed wear mechanism was observed on the material post-test, especially on the test performed with coating hardness R15Y 72.3 and R15Y 59.6 at low incursion rate, a decrease of the blade weight and a corresponding increase in blade length were measured, which suggests that a different density between the blade and adhesive transfer material would be a possible explanation. Further analysis will be made in Section 5.4.2.

Additionally, on the test performed on the coating hardness R15Y 54.6, a decrease in the blade length and weight were measured, with blade wear at low incursion rates, while with an increase of speed a mix of blade wear and adhesion was observed; therefore further analysis will be required.

Furthermore, at high incursion rates for all tests, a slight increase of the blade length was measured that represented an initial adhesion on the blade tip, where the blade cut a clean surface.

The analysis of the maximum blade length change represented the method used in the past to analyse the wear mechanism on an abradable material [3, 6, 7, 11, 15, 36] and did not represent the nature of adhesive transfer or wear mechanism, but only the final condition. Therefore, in this research a stroboscopic imaging technique will be introduced in order to monitor the blade tip length and observe the progression of the

wear mechanics during the test after a number of constant strikes; the results will be presented in Chapter 6.

Further investigation of the wear mechanisms observed will be discussed in the next section; where the composition of the adhesive transfer and dark layer on the rub surface were observed and also a blade analysis was made in order to justify the increase in maximum blade length and relative decrease of blade weight measured when a mix of the wear mechanisms was observed.

5.4. Analysis of the material transfer

The material transfer observed on the blade tip and also on the coating surface was analysed in order to identify its nature. Adhesive transfer on the blade tip was observed in the tests with intermediate and harder samples (R15Y 59.6, R15Y 63 and R15Y 72.3), and a series of samples at a low incursion rate were analysed as shown in Table 5.1. The dark grey layer of material transfer on the coating surface was observed on the soft coating (R15Y 54.6), on the intermediate abradable samples (R15Y 59.6) and on the top of the grooving of the harder coating (R15Y 72.3). Table 5.1 summarises the samples analysed where adhesive transfer and dark layer material transfer were observed on the sample post-test in Section 5.1.

Test	Analysis
0.02µm pass^{-1} / 100m s^{-1} / R15Y 72.3	Adhesive on blade tip
0.02µm pass^{-1} / 100m s^{-1} / R15Y 59.6	Adhesive on blade tip
0.02µm pass^{-1} / 200m s^{-1} / R15Y 54.6	Adhesive on blade tip
0.02µm pass^{-1} / 100m s^{-1} / R15Y 54.6	Coating surface
0.02µm pass^{-1} / 100m s^{-1} / R15Y 59.6	Coating surface
0.02µm pass^{-1} / 100m s^{-1} / R15Y 72.3	Top of the grooving

Table 5.1. Sample analysed.

The nature of the material transfer was analysed with an energy dispersive X-ray fluorescence (EDXRF) spectrometer (Fischerscope X-RAY XAN 250, Fischer

Instrumentation, Lymington, UK). The machine recorded the spectrum of the blade and the abradable samples in terms of the photon count per second [cps] at a given energy level, and highlighted the constituent elements of the area analysed. The analysis and nature of the material transfer on the blade tip is described in Section 5.4.1, and the analysis of the material transfer on the coating surface is similarly described in the following section.

5.4.1. Material transfer on the blade tip

The material transfer observed on the blade tip was analysed using a 10kV filter with a 1000A anode current of the spectrometer used to acquire the spectrum, because it guaranteed greater ability to highlight low atomic number elements. The adhesive transfer to the blade observed in the test with 0.02µm pass^{-1} incursion rate and 100m s^{-1} blade speed and R15Y 72.3 hardness was investigated. Figure 5.30 shows the area of acquisition and the acquired spectrum.

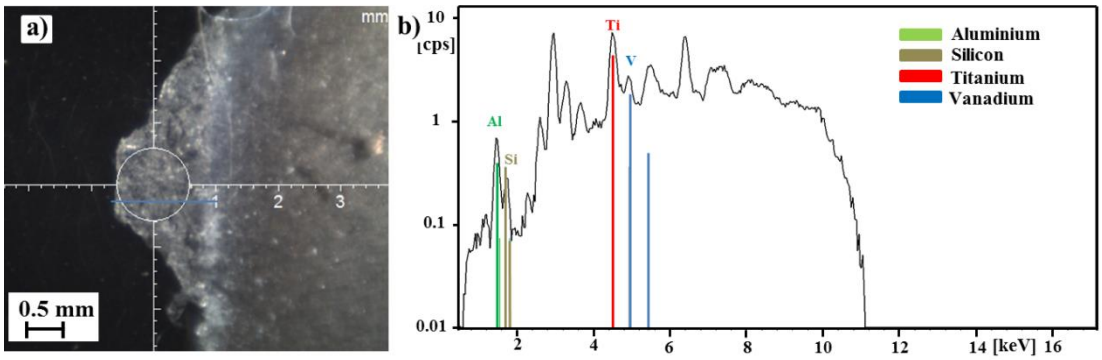

Figure 5.30. EDXRF analysis of blade tip adhesive transfer for the test with hardness R15Y 72.3, 0.02µm pass^{-1}, 100m s^{-1}: a) Analysis area; b) Spectrum.

As shown on the spectrum, the presence of aluminium and especially of silicon, an element only present in the abradable coating, confirmed that the adhesive transfer had occurred from the coating to the blade tip. Also, in the spectrum the presence of titanium and vanadium, constituents of the blade, suggested that the adhered material was a mixture of both the blade and coating. The presence of these elements could be from blade wear observed along the blade tip; however the titanium and vanadium were of a negligible percentage compared with the aluminium and silicon phases. It should also be noted that the peak in the spectrum at around 3keV was due to argon present in the atmosphere during measurement.

A series of twenty measurements was recorded using a 30µm diameter sample area, and an average was obtained. As shown in Table 5.2, the aluminium and silicon phases were significant, indicating that the adhered material was primarily due to pick-up from the coating, and the quantities of titanium and vanadium were negligible.

	(Al)	**(Si)**	**(Ti)**	**(V)**
[% weight]	82.83 ± 0.79	15.27 ± 0.48	1.84 ± 0.36	0.06 ± 0.04

Table 5.2. Composition of adhered material observed on the blade in test R15Y 72.37, 100m s^{-1}, 0.02µm $pass^{-1}$.

The adhesive transfer from the coating on the blade tip assumed a density equal to the coating; this suggests that the adhesive transfer had a lower density compared with the blade, and therefore the increase in weight of the blade could not be compared with the decrease of weight correlated with the blade wear. Therefore, an investigation of the mixed wear mechanism will be described in the Section 5.4.2.

Additionally, the adhesive transfer observed on the blade from the test performed at an incursion rate 0.02µm $pass^{-1}$, blade speed 100m s^{-1} at coating hardness R15Y 59.6, was observed with EDXRF analysis. The EDXRF analysis was performed on the adhesive transfer observed on the edge on the blade (Figure 5.31a), and also in the central part, where a dark layer transfer was observed on the coating (Figure 5.31b), where this looked like a re-initiation of adhesion after blade wear.

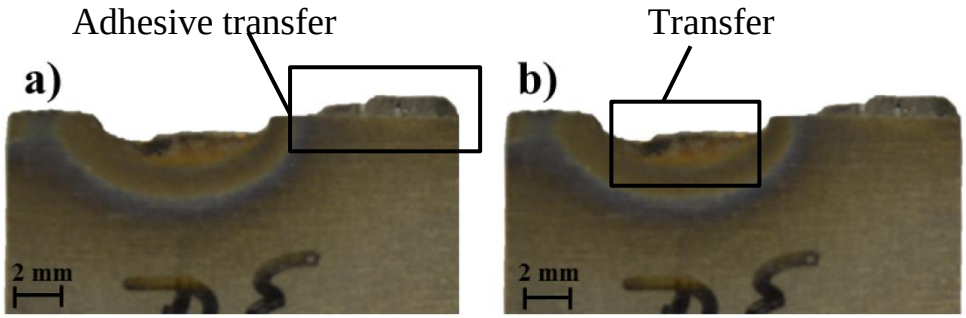

Figure 5.31. Analysis of blade tip from test with coating hardness R15Y 59.6 coating, 0.02µm $pass^{-1}$, 100m s^{-1}: a) Area analysis adhesive transfer; b) Area analysis transfer.

The analysis of the adhesive transfer highlighted in Figure 5.31a confirmed the adhesive transfer from the coating to the blade tip, with aluminium and silicon phases having a significant presence, as shown in Table 5.3. As shown in Figure 5.31b, material transfer was observed on the worn area of the blade. The analysis of the composition of the material revealed the presence of silicon, which suggests blade wear and successive adhesive transfer, as shown in Table 5.3.

	(Al)	**(Si)**	**(Ti)**	**(V)**
Adhesive transfer Blade tip (Figure 5.30a)	64.34 ± 2.54	31.78 ± 1.24	3.72 ± 3.54	0.16 ± 0.23
Material Transfer (Figure 5.30b)	35.36 ± 0.24	12.1 ± 1.06	50.5 ± 0.90	2.04 ± 0.08

Table 5.3. Weight constituent phase of material transfer on the blade on the test at blade speed 100m s^{-1}, incursion rate 0.02μm $pass^{-1}$, and coating hardness R15Y 59.6.

The composition of the material transfer was similar for all the tests analysed, except on the area of blade wear shown in Figure 5.31b, where a high concentration of titanium was measured. This occurred because the smallest collimator of the spectrometer was not small enough and when analysed the adhesive transfer also included part of the blade material. However, the presence of aluminium and silicon confirmed an adhesive transfer from the coating to the blade on the blade wear surface.

In the test performed at an incursion rate of 0.02μm $pass^{-1}$, blade speed 200m s^{-1} with coating hardness R15Y 54.6, a material transfer was observed on the blade tip on a blade wear surface, as shown in Figure 5.32, and the material transfer compositions are summarised in Table 5.4.

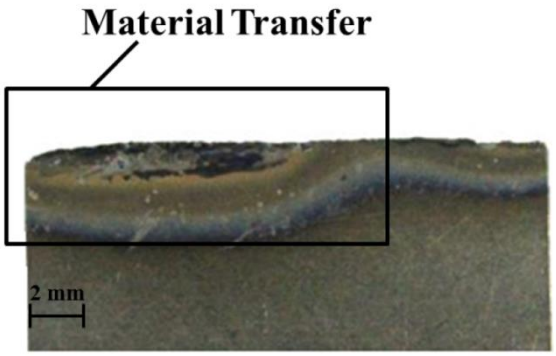

Figure 5.32. Analysis of blade tip from test with coating hardness R15Y 54.6, 0.02μm pass^{-1}, 200m s^{-1}: Area of analysis.

	(Al)	(Si)	(Ti)	(V)
Adhesive transfer Blade tip (Figure 5.31)	44.6 ± 3.66	14.62 ± 0.48	38.86 ± 3.97	0.16 ± 0.23

Table 5.4. Weight constituent phase of material transfer on the blade on the test at blade speed 200m s^{-1}, incursion rate 0.02μm pass^{-1}, and coating hardness R15Y 54.6.

The concentration of aluminium and silicon indicated adhesive transfer from the coating to the blade. This suggests that an adhesive transfer occurred after the blade wear, and the nature of the composition of the transfer also suggests this. The high concentration of titanium was correlated to the small dimension of the adhesion compared with the collimator.

The constituent phase analysis of the blade tip highlighted adhesive transfer from the coating to the blade tip, mainly in the test performed on the harder coating. Also with the intermediate coating a similar adhesive composition was found, which indicated that the adhesive transfer observed was of the same nature as from the coating surface. The analysis of the blade sample that rubbed against the soft coating at low incursion rate and high speed, as shown in Figure 5.32, showed an adhesive transfer after blade wear. Therefore, an analysis of the progression of the wear mechanics will useful in understanding the nature of the contact; and will be carried out using the stroboscopic imaging technique in Chapter 6.

5.4.2. Investigation of the mix of wear mechanisms

Especially at low incursion rates for the hard coating and intermediate hardness coating, the analysis of the blade length and weight change showed an increase of the blade length and a corresponding decrease of blade weight. This suggests a mix of wear mechanics, an adhesive transfer and wear along the blade tip, and therefore the blade tip observation highlighted a non-uniform adhesion on the blade (Figure 5.2). In order to investigate if a mix of wear mechanisms occurred, an SEM image was acquired of the test performed at 0.02μm pass^{-1}, 100m s^{-1} and hardness R15Y 72.3, as shown in Figure 5.33.

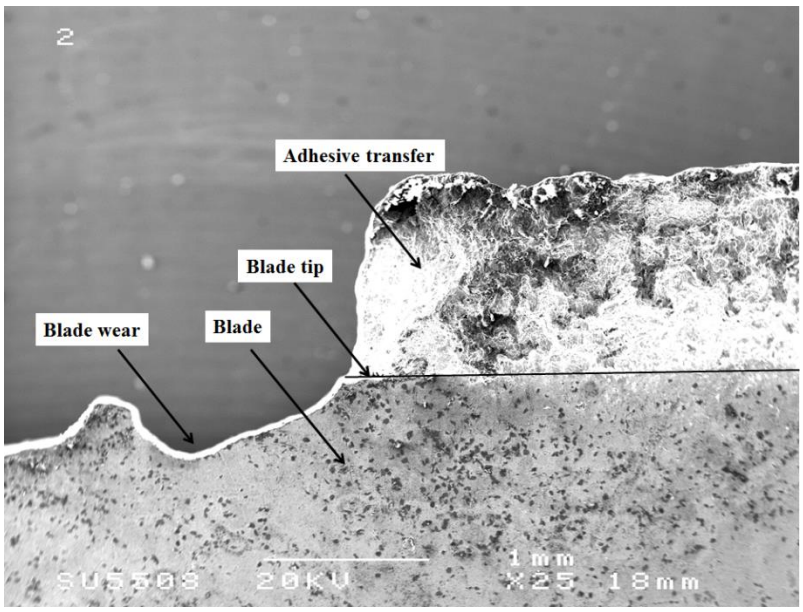

Figure 5.33. Blade tip of the test performed at incursion rate of 0.02μm pass^{-1}, blade speed 100m s^{-1} and coating hardness R15Y 72.3.

As shown in the figure, an adhesive transfer was observed on the blade tip, but also wear on the blade was observed, highlighted by the material removed below the line of the blade tip.

As discussed in Section 5.3, even with an increase of the blade length, a decrease of blade weight was measured; this suggests that the reason was correlated to the different densities of the blade and adhesive transfer material. Therefore, an analytical calculation of the blade weight post-test was made in order to try and justify the decrease in the blade weight change occurring even with an increase in the blade length change.

The analysis was performed for the blade from the test with coating hardness R15Y 72.3, blade speed 100m s^{-1} and incursion rates of 0.02 and 0.04µm $pass^{-1}$, where non-uniform adhesion was observed. The analysis consisted of determining the weight increase and decrease of the blade in relation to the blade length change, through calculation of the increase or decrease of the blade volume and the relative variation of the area underlying from the blade profile analysed with respect to the initial blade length, as shown in Figure 5.34.

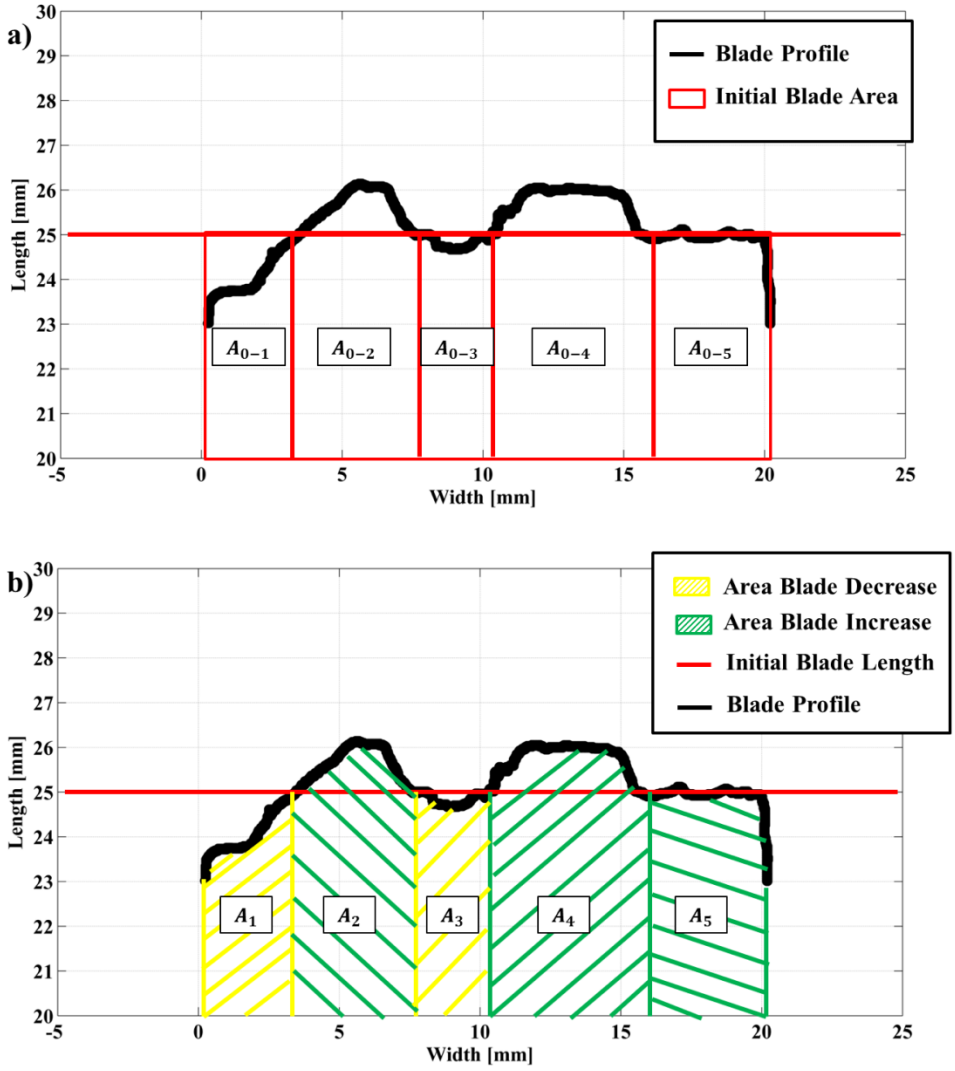

Figure 5.34. Analysis of the blade profile: a) Areas in relation to the initial blade length; b) Areas in relation to the increase and decrease of the initial blade length (test 0.02µm $pass^{-1}$, 100m s^{-1}, R15Y 72.3).

As shown in the figure, the profile of the blade was divided into five different areas; the underlying area from the profile was calculated with a numerical integration [95].

The first step was to calculate the area ($A_{0\text{-}1,2,3,4,5}$) underlying from the initial blade length (Figure 5.34a), then the area ($A_{1,2,3,4,5}$) underlying from the blade profile after the test was performed, with increase and decrease of the blade length (Figure 5.34b). The difference between the two areas represented the increase or decrease of area on the blade tip with respect to the initial length.

In order to calculate the volume, the area was multiplied by the blade thickness and then the density of the material. The blade observation highlighted that the adhesive transfer had an average thickness around 1.4mm (test 0.02µm pass^{-1}), thinner with respect to the thickness of the 2mm blade. The density at the blade wear was assumed to be the density of Ti-6Al-4V (4.43g cm^{-3}) [96], while for the increase in volume the composition analysis of the material transfer highlighted that this was from the coating. Therefore, it was assumed that the density was equal to the density of the abradable sample (1.57g cm^{-3}). Then the analytical value of the blade weight change was compared with the measured one, as summarised in Table 5.5.

Incursion rate	**Analytical Weight increase [g]**	**Analytical Weight decrease [g]**	**Analytical Blade Weight change [g]**	**Blade weight change measured [g]**
0.02	0.0154	0.0266	-0.0112	-0.0186
0.04	0.0237	0.1221	-0.0984	-0.076

Table 5.5. Analytical calculation of the blade weight change for the test performed with coating hardness R15Y 72.3 and blade speed 100m s^{-1}.

As shown in the table, a difference was observed between the analytical weight change and the measured change, but the analytical method justified the blade weight reduction even with an increase of the blade length, and therefore a lighter adhesive material on the blade tip did not determine an increase of the blade weight compared with the blade wear observed. The analytical calculation indicated that even when the main wear mechanism was adhesive transfer, when also blade wear was observed, a higher density of the titanium blade compared with the density of

the material adhered implied a decrease of the blade weight. This result highlights that length and weight change results cannot be considered in isolation.

5.4.3. Material transfer on the coating surface

Observation of the coating after the test revealed a dark grey material transfer on the surface of the coating. Therefore, in this section an analysis of the composition of the transfer was made using the X-ray fluorescence (EDXRF) spectrometer. The material transfer was observed on the abradable sample with hardness R15Y 54.6, at an incursion rate 0.02µm pass^{-1} and a blade speed of 100m s^{-1}, and also on the top of the grooving of the test performed on the coating with hardness R15Y 72.3 and incursion rate 0.02µm pass^{-1} and blade speed of 100m s^{-1}, and also on the coating at low incursion rate and hardness R15Y 59.6. The nature of the transfer composition was measured with a spectrometer using a nickel 50kV primary filter and an anode current of 1000A. Figure 5.34 shows the area of analysis (Figure 5.35a) and the relative spectrum measured (Figure 5.35b).

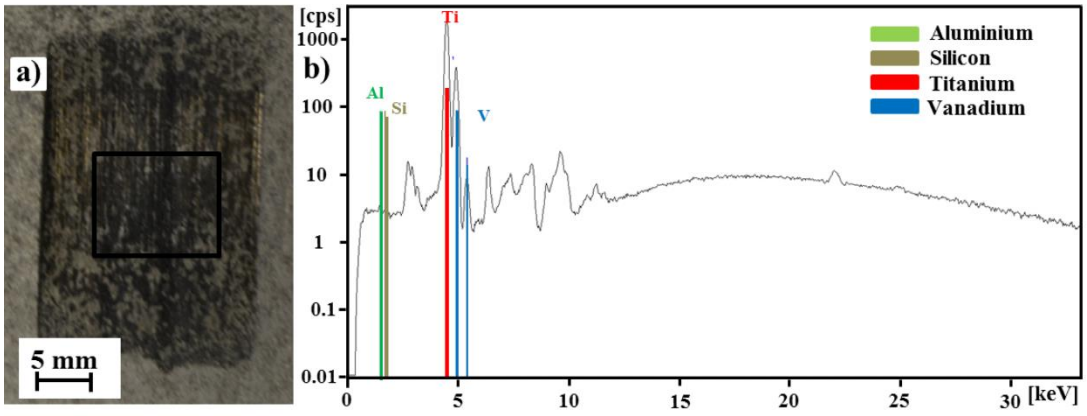

Figure 5.35. EDXRF analysis of the abradable sample R15Y 54.6: a) Analysis area coating R15Y 54.6, 0.02µm pass^{-1}, 100m s^{-1}; b) Spectrum.

Figure 5.35b shows the spectrum, where titanium and vanadium (comprising two peaks as a result of both alpha and beta emissions) were identified as present on the surface of the abradable sample, and were transferred from the blade. The constituent weight element percentages of the material transfer were then calculated over a series of twenty points, and summarized in Table 5.6.

	(Al)	(Si)	(Ti)	(V)
[% weight]	51.48 ± 3.09	28.89 ± 2.76	18.98 ± 1.4	0.69 ± 0.06

Table 5.6. Composition of adhered material observed on the abradable sample R15Y 54.6, 100m s^{-1}, 0.02µm $pass^{-1}$.

The titanium phase was significant, indicating that the adhered material on the coating surface was from the blade. The thickness of the transfer layer was also measured and was found to have an average value of 4.01 ± 0.89µm, recorded over a series of twenty points.

The same analysis was performed on the hard sample on the top of the grooves (R15Y 72.3, 0.02µm $pass^{-1}$, 100m s^{-1}), where adhesive transfer from the blade to the coating was identified, corresponding to the area of the thermal damage on the blade tip, and also on the intermediate hardness coating (R15Y 59.6, 0.02µm $pass^{-1}$, 100m s^{-1}). Figure 5.36 shows the analysis area and the relative spectrum.

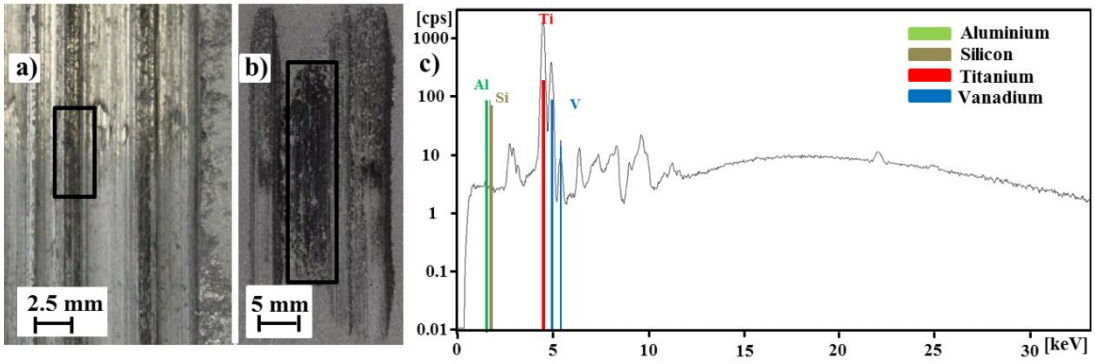

Figure 5.36. EDXRF analysis of the abradable sample: a) Analysis area on the groove; b) Analysis area of coating with hardness R15Y 59.6 at low incursion rate; c) Spectrum.

On the test with 0.02µm $pass^{-1}$, 100m s^{-1} and hardness R15Y 72.3, on the groove the spectrum highlighted an adhesive transfer of titanium from the blade tip. Similarly in Figure 5.35b, for the test on the sample with hardness R15Y 59.6 (0.02µm $pass^{-1}$, 100m s^{-1}), titanium transfer from the blade tip was identified. Table 5.7 shows the phase constitution of the adhesive transfer.

Test	(Al)	(Si)	(Ti)	(V)
0.02µm pass^{-1} 100m s^{-1} R15Y 72.3	17.43 ± 22.89	42.43 ± 9.22	38.63 ± 14.47	1.48 ± 0.64
0.02µm pass^{-1} 100m s^{-1} R15Y 59.6	49.36 ± 2.10	27.02 ± 3.09	22.73 ± 2.23	0.89 ± 0.13

Table 5.7. Weight composition of adhered material observed on the abradable sample.

Also in both cases the thickness of the transfer layer was measured and was found to have an average value of 0.67 ± 0.20µm and 3.74 ± 0.077µm for the tests on abradable sample coatings R15Y 72.3 (0.02µm pass^{-1}, 100m s^{-1}) and R15Y 59.6 (0.02µm pass^{-1}, 100m s^{-1}), respectively.

The analysis of the material transfer composition indicated that the dark grey layer observed on the soft coating, also on the coating with intermediate hardness and on the top of groove on the hard coating, and at low incursion rate, was titanium transfer from the blade to the coating surface. A variable thickness layer of titanium was also measured in relation to the level of the blade wear. Therefore, on the soft coating where a significant blade reduction was observed, a thicker layer was measured, and with an increase of the hardness the blade wear was reduced, as was the thickness of the titanium layer.

5.5. Analysis of the blade

Observation of the blade revealed thermal damage on the blade tip; therefore, further analysis was made in order to monitor the blade tip and understand if this caused a mechanical change to the blade. In order to do this, a hardness measurement was performed on the blades. The blade samples post-test were analysed, with a focus on the blade that incurred the hardness coating at low blade speed, where different wear mechanics were observed at low, intermediate and high incursion rates. The hardness measure was made with a Vickers micro-hardness tester (Mitutoyo, HM101 Series 810) with a load of 1kg applied with a dwell time of 10 seconds. The tests were performed on the longitudinal section of the blade specimens (Figure 5.37a) mounted in Bakelite (Figure 5.37b). In order to have a flat surface to analyse, the samples

were ground and polished. The measurements were recorded at 0.5mm intervals from the blade tip up to a maximum distance of 3mm, as shown on the image of the blade in Figure 5.37c.

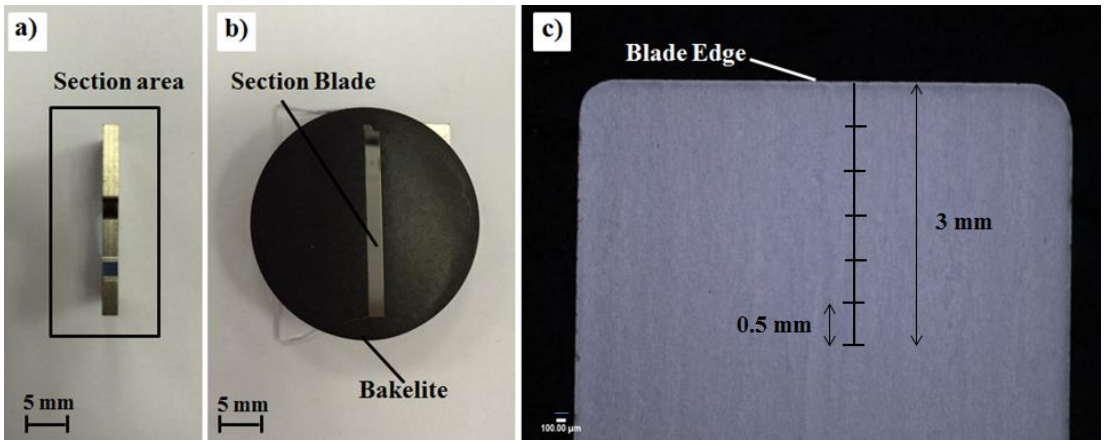

Figure 5.37. Measure of the hardness on the sectioned blade sample: a) Section area; b) Section of blade mounted on the Bakelite, test R15Y 72.3 0.02µm pass^{-1}, 100m s^{-1}; c) Microstructure of the blade sample before the test.

The measurement was also performed on an unused blade and a value of 397.4 ± 4.1HV was recorded. Figure 5.38 shows the average hardness measurements on three repeats performed along the distance from the blade edge, for three incursion rates respectively where adhesion, transition mechanism and cutting were observed when the blade incurred against the coating hardness R15Y 72.3.

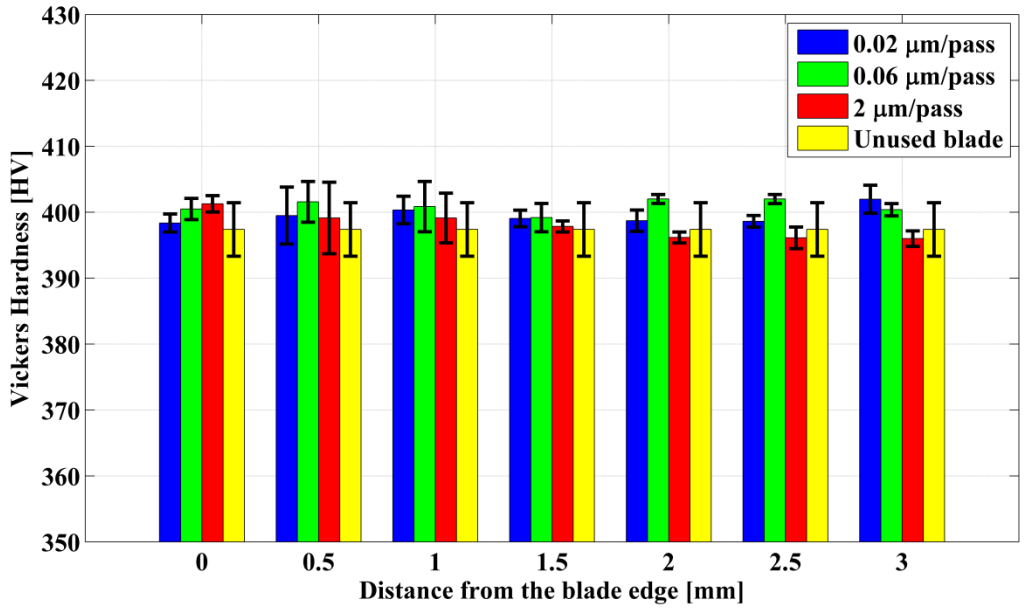

Figure 5.38. Hardness measurement of the blades incurred against the abradable material R15Y 72.3 vs the distance from the blade edge, at blade speed of 100m s^{-1} and incursion rates of 0.02, 0.06 and 2µm $pass^{-1}$, and unused blade.

No significant variation of the hardness for each blade was observed with respect to the distance from the blade edge tip. Similar values were reported at all incursion rates, and similarly compared with the unused blade.

The hardness on the blade tip was also measured for the test performed against the coating with hardness R15Y 54.6 at incursion rates of 0.02, 0.2 and 2µm $pass^{-1}$, where blade wear, transition mechanism and cutting were observed respectively. Figure 5.39 shows the average hardness measured along the blade tip against the distance from the blade edge incurred against coating R15Y 54.6.

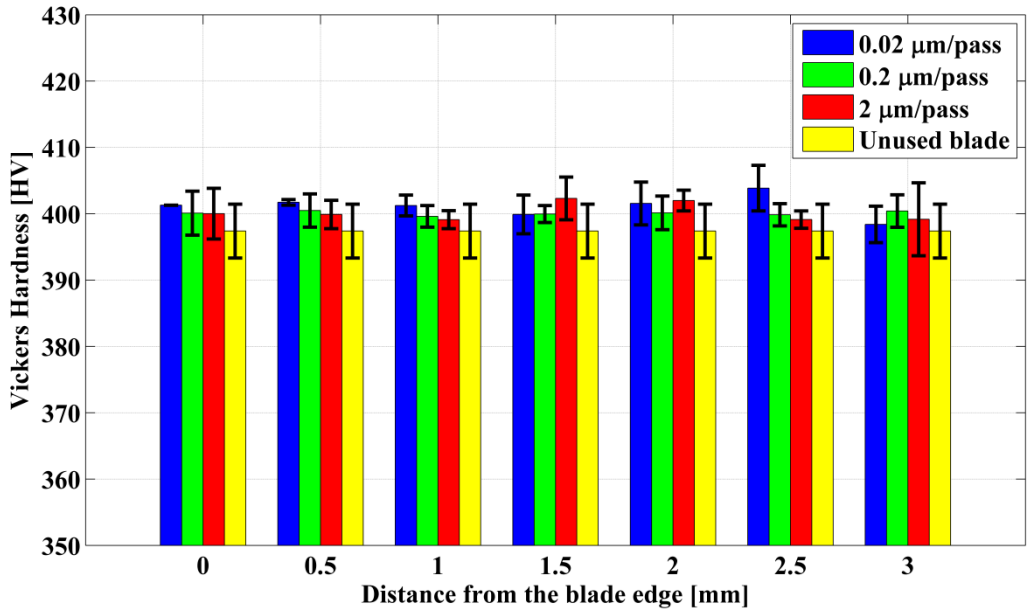

Figure 5.39. Hardness measurement of the blades incurred against the abradable material R15Y 54.6 vs the distance from the blade edge, at blade speed of 100m s^{-1} and incursion rates of 0.02, 0.2 and 2µm $pass^{-1}$, and unused blade.

As shown in the figure, there was no significant difference in hardness of the blade when incurring on the coating at different incursion rates, and also, even with evident thermal damage on the blade tip, the hardness did not change compared with the unused blade. The value of hardness measured after the test was still in the range of common hardness of a titanium blade [96].

A further investigation of the blade tested against the hard coating was made using nanoindentation [75] using a Berkovich Tip [75] on the blade sample that incurred the hard coating at 0.02µm $pass^{-1}$. The hardness was measured with a matrix with a step of 500µm between indentations from the edge of the blade tip. An average hardness of 397.4 ± 34.1 HV was measured. The hardness value was similar to the one obtained with macro-hardness. The increased scatter was correlated to the large matrix of the data acquired and different hardness measurements in relation to the area of the indent, corresponding to the phases of Ti-6Al-4V [96].

Also, Young`s modulus of the blade post-test was measured using the load-displacement curve from the experimental readings of indenter load and depth penetration [75]. In relation to the contact area and the elastic contact stiffness [97,

98], the reduced modulus (E_r) was calculated and then the modulus of the sample was calculated from contact mechanics [75], as shown in Equation (5.1):

$$E_{mat} = (1 - \upsilon_{mat}^2) \cdot \left(\frac{1}{E_r} - \frac{1-\upsilon_i^2}{E_i}\right)^{-1} \quad (5.1)$$

where E_{mat} represents the material Young's modulus, v_{mat} represents the material's Poisson's ratio (0.342 for Ti-6Al-4V [96]), and E_i and v_i are the Young's modulus and the Poisson's ratio of the indenter (Diamond Berkovich indenter, Elastic modulus 1141GPa, Poisson's ratio of 0.07 [75]).

The Young's modulus of the blade after the test performed was equal to 106.38 ± 1.89GPa, which was a similar value with respect to that of the manufactured blade of 108.53 ± 2.35GPa.

No significant change in macro-hardness, nanoindentation and Young's modulus suggested that there was no relevant change in ductility of the blade sample after the test.

5.6. Discussion

In this chapter the test samples were assessed post incursion, through observation of the sample morphology. This approach clearly highlighted different wear mechanisms, and adhesive transfer on the blade tip, blade wear and a dark grey transfer layer on the rub surface, and cutting wear were identified. This approach also allowed the changes in the wear mechanics with incursion rate, speed and hardness, to be assessed qualitatively.

For example, in the case of the sample tested at low incursion rate, adhesive transfer from the coating to the blade tip, and a grooved surface in the hard coating were observed. A decrease in the hardness produced a mix of adhesive transfer and blade wear, as observed on the test performed with the medium hardness sample. Finally, in the test performed with the soft coating, a blade wear and a melt wear transfer on the coating were observed. In order to try and quantitatively explore these changes in wear mechanics, both the blade length and weight change were investigated. This approach was in line with other studies on abradable materials [3, 6, 7, 15]. However, this approach failed to identify clear relationships, and significant general

trend caused by the variability of the blade and weight changes in relation to incursion rate, hardness and speed were observed.

Furthermore, when a mix of adhesion and wear were observed, an increase in blade length change and a decrease of blade weight were measured, these results seem anomalous. Analytical calculation of the blade weight change revealed that the higher density of the titanium blade, compared with the density of the material adhered, implied a decrease of the blade weight overall. This result also suggests that analysis of the change in blade length and weight before and after the test cannot be used independently, as has been done by many authors in previous research studies [3, 6, 7, 15], where only post-test blade length change has been analysed. Furthermore, the above discussion also highlights the weakness of this type of data set in general.

Expanding on this point, as highlighted the analysis of the blade change does not give any information about the progression of wear mechanism during the contact, and the final condition may not be entirely representative of the wear mechanics present. This represents a clear limitation on this technique's capacity to classify a wear mechanism.

Therefore, during this research a stroboscopic imaging technique was introduced in order to monitor the blade tip during the contact. The aim of this was to study the progression of the adhesion and wear during the contact and to gain a better understanding of the influence of hardness, incursion rate and speed on the wear mechanics.

Furthermore, contact force and coating temperature and analysis of material response from material sectioning were examined in order to investigate the nature of the wear mechanism, and to try to understand the reasons that drive the wear mechanisms observed. These investigations will be described in later chapters.

5.7. Chapter summary

- In relation to the incursion rate and hardness, especially at low incursion rate, different wear mechanisms were observed, with no significant overall change with an increase of the speed.

- On a hard coating, at low incursion rate, an adhesive transfer from the coating to the blade tip with a corresponding grooved surface were observed, with titanium transfer on the major peak on the groove with respect to thermal damage on the blade.

- On the soft coating, at low incursion rate, blade wear and titanium transfer from the blade to the coating was observed, with a melt layer on the rub surface.

- At intermediate coating hardness, at low incursion rate, a mix of blade wear and adhesive transfer was observed, suggesting that it represents a transition hardness value for mechanisms.

- At high incursion rate, a similarly well-cut surface was observed independently from hardness, and good cutting wear with negligible adhesive transfer / wear suggested that the blade acted like a cutting tool fracturing the material.

- Increasing the speed reduced the adhesive transfer and wear, and overall there was no significant change in wear mechanics, only some change on the soft coating, where a mix of adhesion and wear was observed.

- There was no clearly identified general trend, and a great deal of scatter, with the analysis of the blade length and weight change, and no evaluation of the evolution of the nature of the wear mechanism was obtained.

- The hardness measurement of the blade sample showed no significant change after the test, suggesting no change in ductility.

6. Stroboscopic Imaging Technique Results

As described in Chapter 5, the wear mechanics were investigated by observing and measuring the specimens at the end of the test. The analysis was based on the final result obtained on the blade tip and coating, but with no analysis relating to the wear progression or to the nature of the contact. The analysis of the sample post-test did not highlight a general trend in order to classify the wear mechanism.

Therefore, this chapter describes the results obtained with a stroboscopic imaging technique that was introduced in order to monitor the blade profile during the test, especially adhesive transfer and blade wear. This represents a significant advance, as

to date researchers have only considered blade condition at the end of the test and have therefore gained only limited insight into the process of adhesive transfer. To understand the nature of the adhesive transfer is also very important, because some hard deposits of material on the blade could subsequently fracture off, generating small amounts of debris and creating a problem for the engine. It may also be the case that the final condition of the sample does not represent the maximum adhesion.

The first part of the chapter will describe how, as highlighted in Section 3.4.1, the stroboscopic technique allows a side view of the blade tip to be acquired during the test. A series of images acquired during the test will be investigated in order to observe the evolution of the wear mechanics. Initially the focus was on the coating with hardness R15Y 72.3 at different incursion rates and constant speed, where high levels of adhesion were observed. Afterwards the tests that were performed with the rest of the samples and different blade speeds will also be analysed.

Then, the blade length change during the test was determined from the image analysis, as shown in Section 4.2.3, and was plotted against the theoretical rub length, which represented the total length of rub on the coating (Section 4.1.1). Previous research [34, 36] showed that the abradability of the material depends upon the length of the groove generated, and therefore the length of material removed, as highlighted in Archard's [34] equation where the wear is a function of the sliding distance. Hence, the blade length change was represented against the total rub length, which is a combination of the input parameters of the test, which are blade speed, incursion speed and blade radius and time, and gives a representation of the material removed during the test.

The second part of the chapter describe further investigations that were made into adhesion and blade wear, focusing on the rate of adhesion / wear with the aim of characterising the mechanics and understanding their nature.

6.1. Blade images captured for R15Y 72.3

A series of side blade tip images acquired during the test using the stroboscopic imaging technique are presented in order to monitor the wear mechanism after a given number of strikes. The images captured during the test represent a side view of the rotating blade, as shown in Figure 6.1a, and therefore the corresponding blade profile captured from the camera represented to the current maximum blade length along the blade width, as shown in Figure 6.1 b, c.

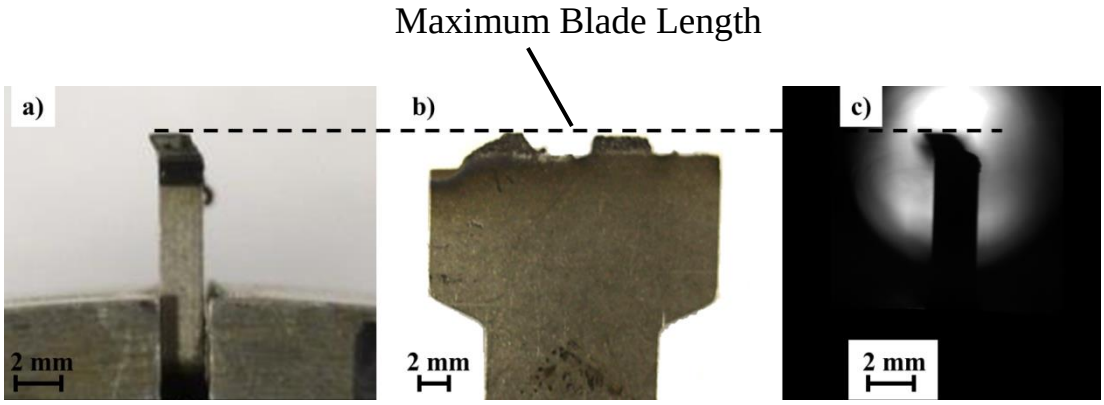

Figure 6.1. Blade view at test R15Y 72.3, 100m s^{-1}, 0.02µm $pass^{-1}$: a) Side view; b) Front view; c) Side view image acquired with the stroboscopic technique.

In this section the focus was on the test performed on coating hardness R15Y 72.37, because the observation of the sample had revealed a high level of adhesion. Figure 6.2 shows a series of blade tip images recorded from the test with an incursion rate of 0.02µm $pass^{-1}$ and blade speed of 100m s^{-1}.

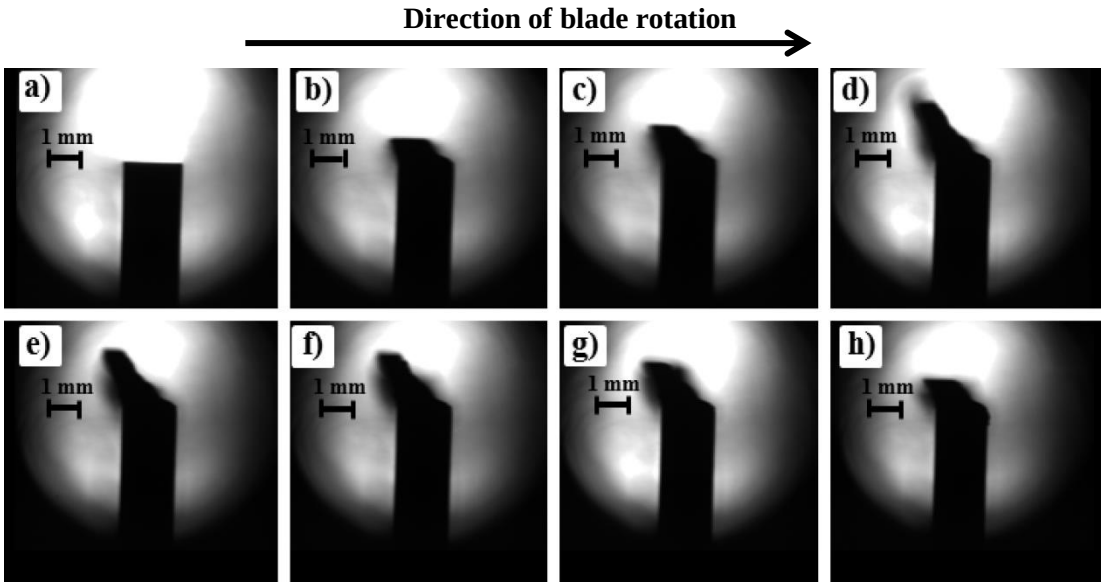

Figure 6.2. Stroboscopic imaging of the blade tip recorded on the test performed with blade speed of 100m s^{-1}, incursion rate of 0.02µm $pass^{-1}$, with abradable coating hardness R15Y 72.3, at time of: a) 0s; b) 66.4s; c) 112.988s; d) 294.554s; e) 303.037s; f) 349.778s; g) 417.884s; h) 582.248s.

As shown in the figure, the stroboscopic imaging technique captured the blade profile during the test at every 13 strikes of the blade. The image highlighted an evolution of the material transfer on the blade tip profile, as investigated in the previous chapter, and represented a material transfer from the coating. Figure 6.2a shows the blade profile before the blade started to make contact with the abradable material, and therefore represents the initial blade length of the test. Observation of the rest of the images recorded (Figure 6.2 b, c, d) highlighted a progressive increase of the material transfer, and determined that the blade length grew continuously until a maximum length was reached (Figure 6.2d), after which a progressive blade tip length reduction was observed (Figure 6.2 e, f, g) until the end of the test. At the end of the test, the blade tip profile showed adhesive transfer (Figure 6.2h), as observed from the image analysis post-test in Figure 5.2, but the final blade length did not represent the amount of adhesion recorded during the test, and did not represent the maximum length of the blade. Additionally, as shown in Figure 6.2 b, c, d, e, f, g, the material transfer adhered on the blade tip with a non-uniform shape and developed on the left of the blade tip with respect to the image acquired (Figure 6.2b).

The analysis of adhered material at the end of a test was the standard practice performed by previous researches on abradable material [3, 7, 11, 15, 30]; however,

the progression of the adhesive transfer as shown in Figure 6.2 highlights that the final condition does not represent the maximum adhesion during the test and does not adequately characterise the overall mechanics of adhesive transfer. Also, as shown in Chapter 5, an increase of the incursion rate determined a progressive change of wear mechanism from adhesive transfer to cutting wear, where the blade cut the surface well, and therefore images of the blade captured at an intermediate incursion rate were acquired in order to observe the progression of the mechanism during the test (Figure 6.3).

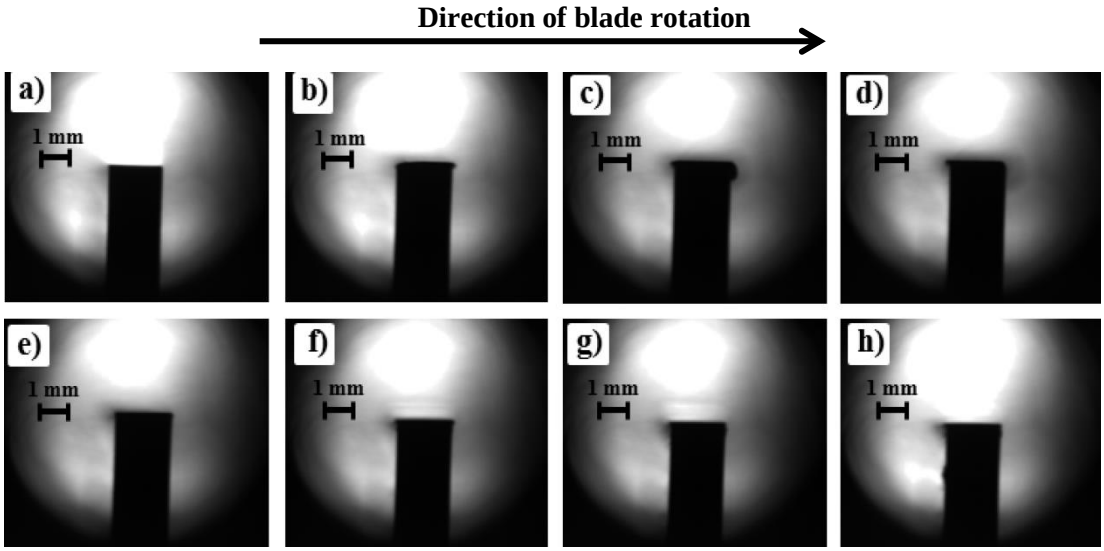

Figure 6.3. Stroboscopic imaging of the blade tip recorded on the test performed with blade speed of 100m s^{-1}, incursion rate of 0.2μm $pass^{-1}$, with abradable coating hardness R15Y 72.3, at time of: a) 0s; b) 6.86s; c) 16.5s; d) 17.1s; e) 24.5s; f) 34.4s; g) 48.3s; h) 58.1s.

As shown in the figure, an initial material transfer was observed (Figure 6.3 b, c, d, e) followed by blade wear observed from the blade length reduction, while the analysis of the sample post-test highlighted only a slight blade reduction. It is interesting to note that a part of the material adhesion, observed in Figure 6.3c, broke away and therefore was not present in the successive pictures, as shown in Figure 6.3d. Material adhesion breaking away could cause further damage to the jet engine, being carried in the flow and blocking the holes of the combustion chamber. As described in the previous chapter, at a high incursion rate, a well cut surface with no damage on the blade was observed, which suggested a cutting wear mechanism. Therefore, in order to monitor the wear mechanism a series of blade tip images were

recorded for the test performed at high incursion rate (2µm pass^{-1}), at a blade speed of 100m s^{-1} with the coating hardness R15Y 72.3 (Figure 6.4).

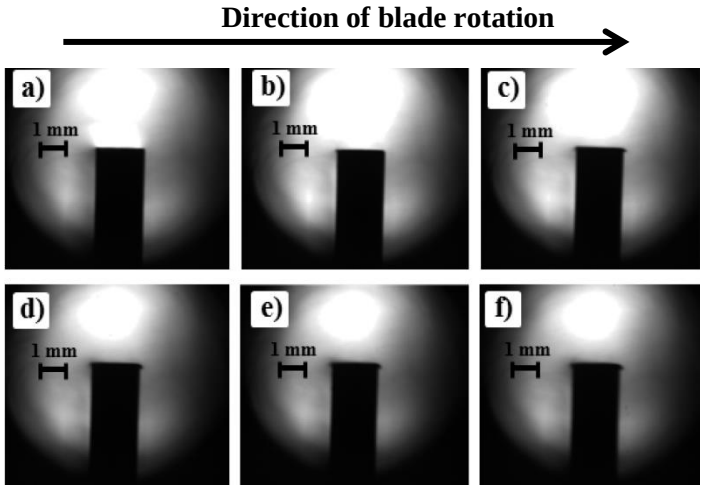

Figure 6.4. Stroboscopic imaging of the blade tip recorded on the test performed with blade speed of 100m s^{-1}, incursion rate of 2µm pass^{-1}, with abradable coating hardness R15Y 72.3, at time of: a) 0s; b) 1.77s; c) 3.24s; d) 4.24s; e) 4.93s; f) 5.86s.

As shown in the figure, there was an initial adhesive transfer (Figure 6.4 b, c,) followed by no variation of the blade profile, as shown in Figure 6.3 d, e, f. The observation of the sample highlighted a well-cut surface, therefore suggesting that a cutting mechanism was occurring, where the blade acted like a cutting tool.

Overall the stroboscopic imaging technique monitored the wear mechanics on the blade tip, as highlighted in Figures 6.2, 6.3, 6.4. Additionally, through the image progression, as discussed in Section 4.2.3, a maximum blade length change was obtained after a number of strikes and will be presented in the next section.

6.2. Blade length change

This section describes the analysis of the maximum change in blade length and how it was investigated by plotting against the theoretical rub length. As shown in Section 4.2.3, the post-processing of the images acquired allowed the determination of the blade length change after a constant number of strikes. The blade length change could be plotted against time, incursion depth or rub length, as shown in Figure 6.5.

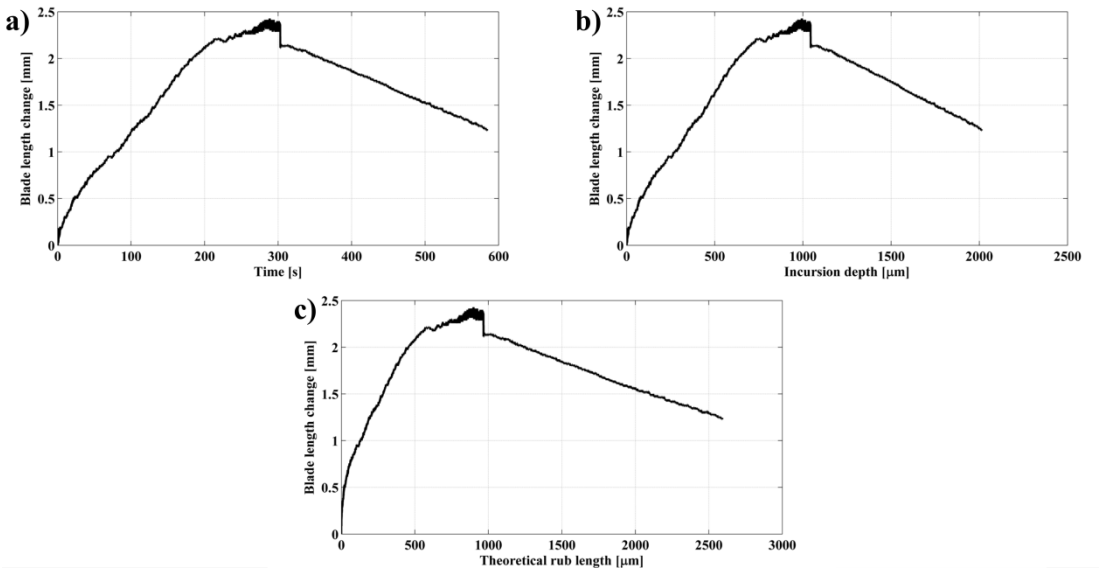

Figure 6.5. Blade length change for the test at incursion rate 0.02µm pass^{-1}, 100m s^{-1}, R15Y 72.3 plotted against: a) Time; b) Incursion depth; c) Theoretical rub length.

The time and the incursion depth are parameters connected with the blade speed and the incursion depth per pass, as mentioned in Chapter 4 and represent an input parameter of the test. However, the theoretical rub length was a combination of input parameters such as incursion speed, time, radius of the blade and incursion depth, and is limited by the available coating thickness. Additionally, previous research [34, 36] highlighted that progressive abradability of the material, or rather the ability to remove material, is related to the length of the groove generated, and in Archard's [34] equation the wear also depended on the sliding distance during the contact. Therefore, the theoretical rub length represented the progression of the rub during the test, or rather the length of groove generated, which was also a combination of the input parameters of the test and noted in previous research as important for evaluation of the abradability of the coating. Therefore, the blade length changes were plotted against the theoretical rub length.

Furthermore, the observation of the coating sample post-test highlighted an increase in the rub length corresponding to the point of adhesive transfer observed on the blade tip, and there was a reduction of the theoretical value when the blade wore. Using the measured blade length change, an assessment was made of the actual rub length change compared with the calculated theoretical value. This was achieved by updating the blade length on a pass-by-pass basis, when a calculation of the rub length was made using equation (4.2). As the camera is side-on and maximum blade lengths are recorded, the calculated rub length is in turn the maximum value experienced along the blade face. Table 6.1 summarises the result calculated with coating hardness R15Y 72.3, where adhesive transfer was observed.

Incursion rate per pass [µm]	**Calculated rub length [m]**	**Theoretical rub length [m]**
0.02	4328.7	2567.5
0.04	1824.5	1283.8
0.06	999.0	855.8
0.1	519.7	513.5
0.14	358.0	366.8
0.2	261.6	256.7
1	52.4	51.4
2	26.6	25.7

Table 6.1. Theoretical vs. measured rub length with respect to test conditions for hardness R15Y 72.3, at blade speed of 100m s^{-1}.

In the tests where material adhered to the blade tip, rub length was significantly increased. This was evidenced by the increased arc of contact on the abradable sample for the low incursion rate test. However, it should be noted that the maximum length may occur at different points along the blade face during the rub, because the adhesive transfer was not uniform on the blade tip, particularly in cases where breakaway of adhered material occurred. Therefore, this actual rub length could only serve as an estimate of the maximum value. Conversely, for all but the most adhesive

conditions, and in particular where good cutting was reported, theoretical and actual rub lengths were similar.

In general, for most of the tests, the calculated rub length coincided with the theoretical value. This also represented the evolution of the rub during the test, which, as mentioned before, is a combination of the key input parameters, and previous research has shown that the abradability is related to the groove generated, and so for this reason it was chosen to plot the evolution of the blade length change during each test against the theoretical rub length, notwithstanding the issues discussed at the most adhesive conditions.

In the next section the test performed on the coating R15Y 72.3 will be analysed, with blade speed 100m s^{-1}, while the influence of the speed will be dealt with in Section 6.2.2.

6.2.1. Blade length change for R15Y 72.3

Figure 6.6 shows the blade length change against the theoretical rub length for the coating R15Y 72.3 for different incursion rates and a constant speed of 100m s^{-1}.

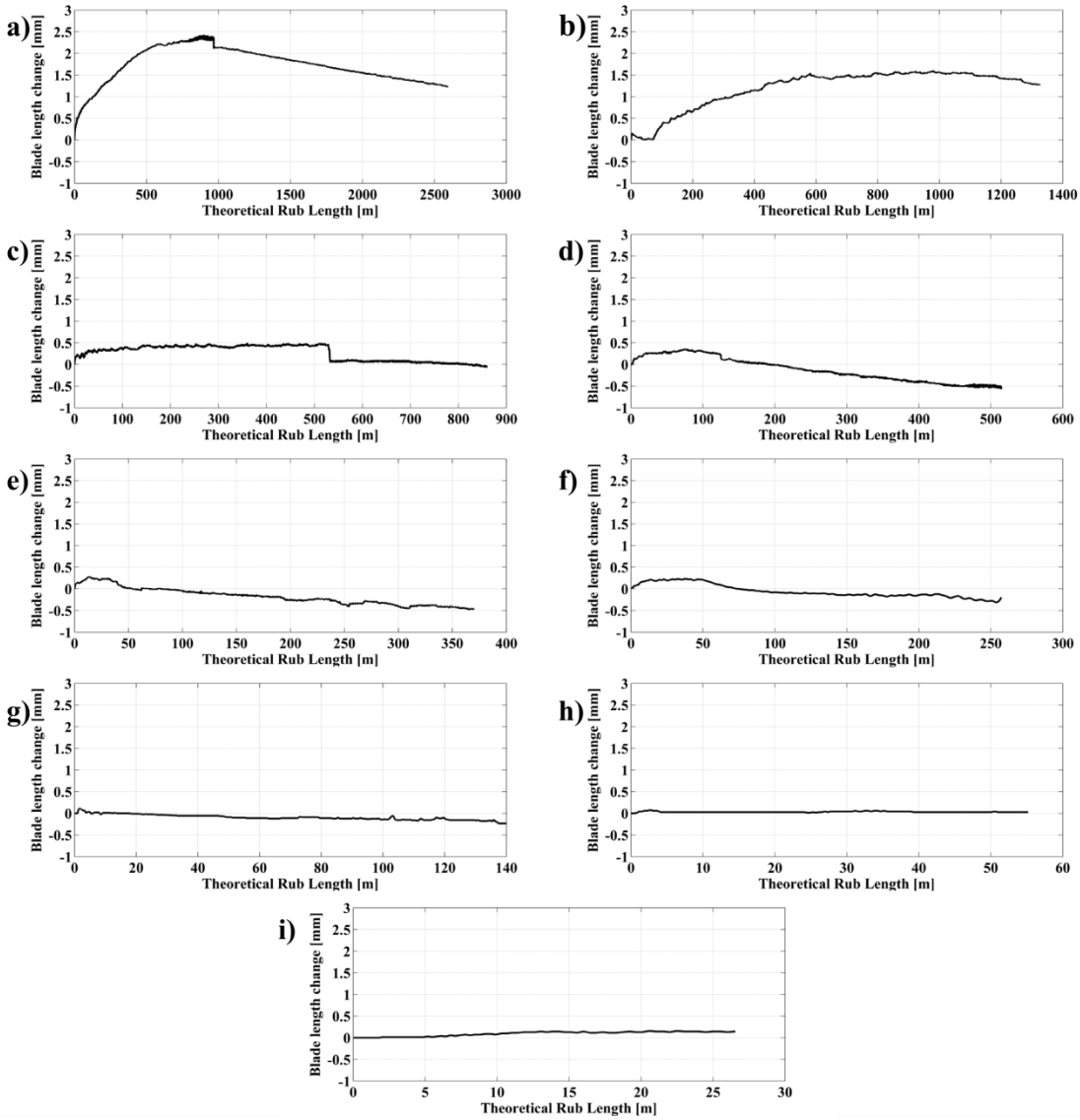

Figure 6.6. Blade length change expressed in terms of theoretical rub length, speed 100m s^{-1} and abradable R15Y 72.3 hardness, at incursion rate of: a) 0.02µm·$pass^{-1}$; b) 0.04µm·$pass^{-1}$; c) 0.06µm·$pass^{-1}$; d) 0.1µm·$pass^{-1}$; e) 0.14µm·$pass^{-1}$; f) 0.2µm·$pass^{-1}$; g) 0.4µm·$pass^{-1}$; h) 1µm·$pass^{-1}$; i) 2µm·$pass^{-1}$.

As highlighted in the figure, the final condition does not represent the amount of adhesive transfer and did not represent the maximum blade length. At low incursion rate (0.02µm $pass^{-1}$, Figure 6.6a), significant adhesive transfer from the coating to the blade tip occurred, with a continuous increase of the blade length until a maximum was reached, and then partially adhered material broke away, and a progressive blade length reduction was observed. Progressively, as the incursion rate increases, the level of adhesive transfer reduced; this was evident when comparing the test

performed at incursion rates of 0.02, 0.04 and 0.06µm pass^{-1} at a blade speed of 100m s^{-1} and coating hardness R15Y 72.3 (Figure 6.6 a, b, c).

As shown in Figure 6.6c, at an incursion rate of 0.06µm pass^{-1} adhesion occurred initially, then broke away and failed to re-initiate, resulting in a cut-like appearance on the abradable surface. Figure 6.6 d, e, f, show that, at incursion rates respectively of 0.1, 0.14 and 0.2µm pass^{-1}, an initial adhesion was observed, followed by blade wear with a cut appearance on the abradable surface.

High incursion rates, 1 and 2µm pass^{-1} (Figure 6.6 g, h) highlighted an initial negligible adhesive transfer followed by a cutting mechanism, where there was no relevant variation of the blade tip length. It should also be noted that, as previously stated (Section 4.1.1 and Section 6.2), the theoretical rub length varies for a given test due to the limitation of the abradable sample depth.

Overall, the blade length change highlighted an initial increase in length, followed by a more steady state period. For example, on the test at an incursion rate of 0.02µm pass^{-1}, a positive gradient represented the adhesive transfer, while with a higher incursion rate the gradient decreased to become nearly constant. Further analysis will be made during this chapter.

The stroboscopic imaging technique monitored different wear mechanisms in relation to incursion rate, with adhesive transfer and blade wear at low incursion rate, and a progressive decrease of the adhesive transfer was observed with an increase of the incursion rate, with a slight initial variation of the blade length followed by a cutting mechanism observed on the sample, and highlighted from there being no variation of the blade tip length. This technique revealed that the final condition may not represent the maximum level of adhesion. The next section describes how the blade length change was analysed at different speeds in order to observe the influence of speed on the wear mechanism.

6.2.2. Blade length change for R15Y 72.3 at different blade speeds

Observation of the samples in the previous chapter highlighted similar wear mechanisms with an increase of the speed; however, the influence of the speed was subsequently analysed again through the blade length change plotted against the theoretical rub length. The speed influence was analysed at low and high incursion rates, where adhesion and cutting mechanisms were observed. Then an intermediate incursion was analysed in order to cover the full range of incursion conditions.

Figure 6.7 shows the blade length change plotted against the theoretical rub length at incursion rates of 0.02, 0.2, 2µm pass^{-1} for the test with the coating hardness R15Y 72.3 and blade speeds of 100, 150, 200m s^{-1}.

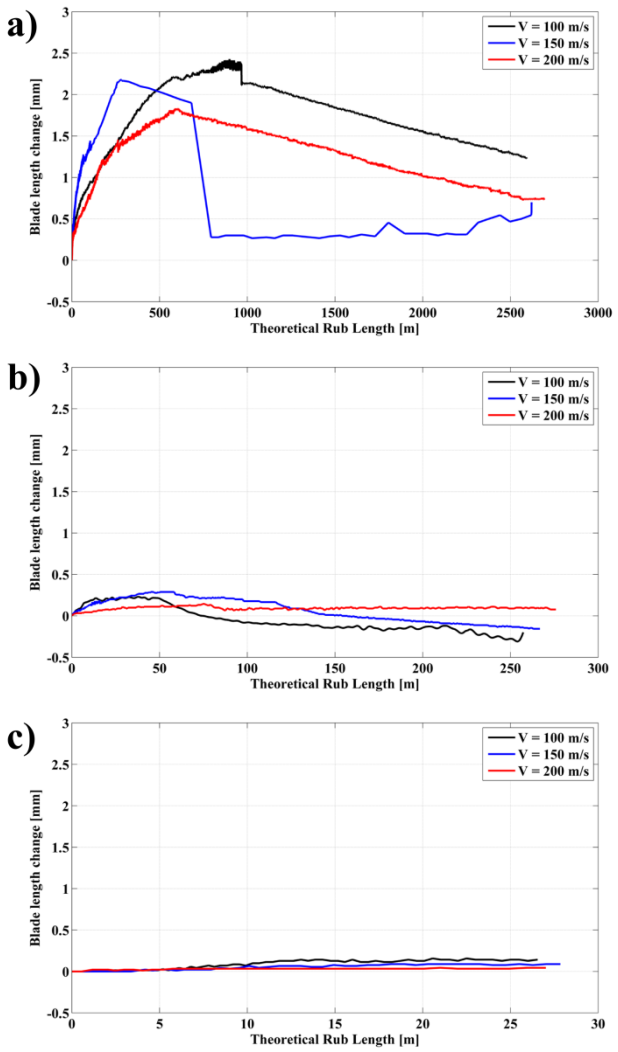

Figure 6.7. Blade length change vs the theoretical rub length for different speeds, coating hardness R15Y 72.3 and incursion rates: a) 0.02µm pass^{-1}; b) 0.2µm pass^{-1}; c) 2µm pass^{-1}.

As shown in the figure, at a low incursion rate (Figure 6.7a), similar trends of blade length change were recorded, especially at 100 and 200m s^{-1}, with a progressive increase of blade length followed by a progressive reduction of the blade length. At 150m s^{-1}, after the maximum length was reached a progressive reduction was observed at a similar rate with respect to the other speeds, and then fracture was recorded, highlighted on the graph by the immediate reduction of the blade length. The adhesive transfer lead to an increase of the blade length, and a maximum of 2.5mm of adhesive transfer was measured. This value was greater than the overall programmed rub depth of the incursion, which was 2mm. This occurs as the blade strikes an arc on the abradable, and interacts over a sliding distance of sufficient duration throughout the test (upwards of 2000m) to facilitate adhesive transfer to a length beyond the maximum programmed incursion depth. Additionally, the maximum adhesive transfer decreased with speed, with this particularly evident at high speed.

At an intermediate incursion rate (Figure 6.7b), at low speed an initial adhesion followed by blade wear was recorded, but an increase of the speed highlighted a decrease of the initial adhesion and also a decrease of the blade wear until at high speed no blade wear was measured, and no significant variation of the blade length was recorded during the test (Figure 6.7b).

At a high incursion rate, a similar trend was observed with different speeds, with an initial increase of the blade length followed by no variation, suggesting a cutting mechanism where the blade clearly removed material, as highlighted in the previous chapter; while an increase of the speed reduced the initial negligible adhesion measured.

Overall, with an increase of the speed, similar trends in blade length change were observed, with a decrease of the maximum adhesive transfer. The stroboscopic technique also clearly highlights the influence of incursion rate, and provides a basis for quantitative analysis. This analysis will involve considering the blade length change in relation to the theoretical rub length in order to characterise and compare the results with the ones already analysed. However before discussing these, first a series of images from the stroboscopic technique will be presented in the next section, for tests where different morphologies of adhesion and wear were observed with respect to hardness.

6.3. Images captured for the rest of the sample hardnesses

The previous sections analysed the progression of the adhesive transfer for the test performed with the hard coating, and showed that the final condition might not be representative of the level of adhesion. But, as highlighted in the previous chapter, the wear mechanisms were hardness dependent, especially at low incursion rate, and different wear mechanisms were observed compared with the sample with hardness R15Y 72.3. The images obtained from the stroboscopic technique were observed in order to analyse the morphology of the different mechanisms observed in the rest of the tests performed, especially at low incursion rate, like blade wear with coating R15Y 54.6, but also the mix of adhesion and wear with the coatings R15Y 63 and R15Y 59.6.

In this section a series of blade tip images are presented, which were recorded for the intermediate and low hardness coating at a blade speed of 100m s^{-1}. The rest of the test conditions will be presented in the blade length change analysis in Section 6.3.1, and the influence of the blade speed will be analysed in Section 6.3.2.

Figure 6.8 shows a series of blade tip images recorded from the test with an incursion rate of 0.02µm $pass^{-1}$ and blade speed of 100m s^{-1}, with abradable sample hardness R15Y 63, where a mix of adhesive transfer and wear were observed.

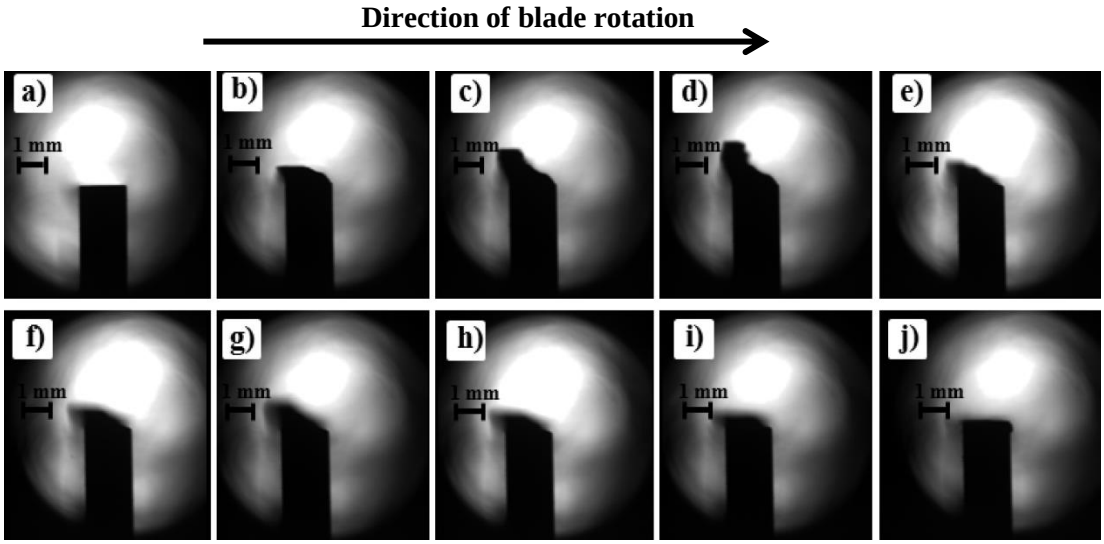

Figure 6.8. Blade tip images recorded with blade speed of 100m s^{-1}, incursion rate of 0.02µm $pass^{-1}$, with abradable coating with hardness R15Y 63, at time: a) 0s; b) 26.14s; c) 57.61s; d) 92.99s; e) 83.91s; f) 124.95s; g) 156.19s; h) 251.98s; i) 317.69s; j) 582.4s.

As shown in the figure, a continuous increase of the material transfer was observed (Figure 6.8 b, c), until the maximum was reached (Figure 6.8d). Then the material transfer broke away and the blade tip reduced in length (Figure 6.6e). Then blade wear took place (Figure 6.8f), followed by a re-start of adhesive transfer highlighted by the once again increasing blade length (Figure 6.8g), this was again followed by blade wear (Figure 6.8h, i, j). The blade tip images showed a difference with the hard coating, especially with respect to adhered material breaking away, but also in the re-start of adhesion, and in the sequence of these events. Additionally, as the camera was focused on the nearest side of the blade with the far side just beyond the depth of field of the lens (Section 4.2.3), the re-adhering material was slightly blurred (Figure 6.8g). This highlighted that material was re-adhering at a new point on the blade tip and that fracture might lead to a gap between the blade and coating in the vicinity of the fracture, as it reflected a reduction in blade length. It is also reasonable that adhesion would re-initiate at points along the blade edge, where the blade was still in contact and abrading the coating.

Similarly in the test performed at an incursion rate of 0.02μm pass^{-1} and a blade speed of 100m s^{-1} with coating R15Y 59.6, an adhesive transfer from the coating to the blade, along with transfer of blade material on the rub surface was observed. The series of blade tip images is shown in Figure 6.9.

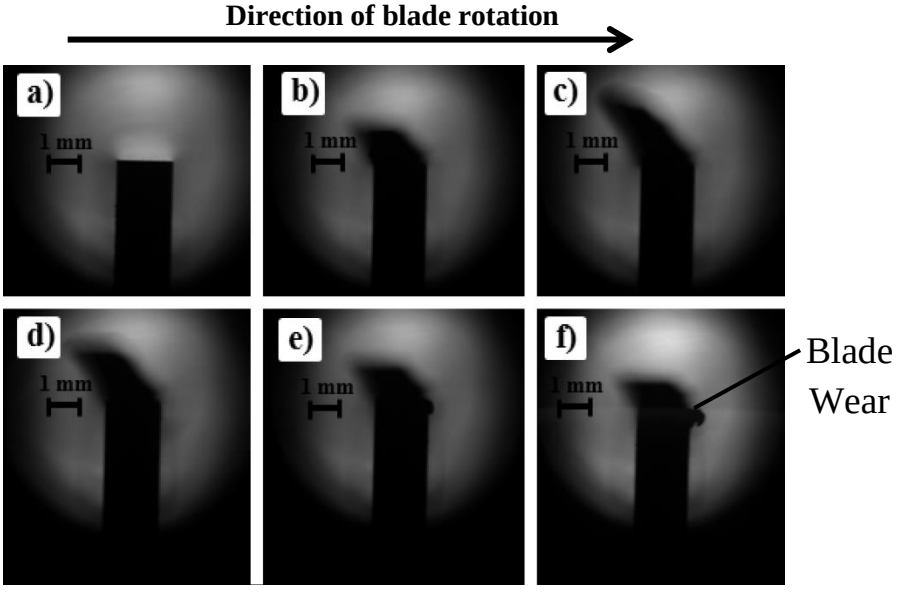

Figure 6.9. Blade tip images recorded with blade speed of 100m s^{-1}, incursion rate of 0.02μm pass^{-1}, with abradable coating with hardness R15Y 59.6, at time: a) 0s; b) 57.23s; c) 120.71s; d) 314.38s; e) 496.41s; f) 591.35s.

The images highlighted a sequence of adhesive transfer (Figure 6.9 b, c) and blade wear (Figure 6.9 d, e, f). Also, the adhesive material in the pictures was blurred (Figure 6.9 b, c, d). This highlighted that the location of the adhesive material was not necessarily on the near side of the blade tip edge, with Figure 6.9f in particular showing wear of the material transfer and also wear on the blade tip. Therefore, uniform mechanisms along the blade tip were not observed.

The mix of mechanisms observed in the tests performed with the coating R15Y 59.6 and R15Y 63 seem different, even with the close values of hardness, where on the sample R15Y 59.6 higher levels of adhesion and wear were observed along the blade, as illustrated in Figure 6.9f, compared with the test with coating R15Y 63 (Figure 6.8). Additionally, observation of the sample suggests that it represented a transition value of hardness for the wear mechanism at low incursion rate. Further comparison will be made after calculating the blade length change.

As mentioned during the previous chapter, on the soft coating significant blade wear was observed; and is shown in the images in Figure 6.10.

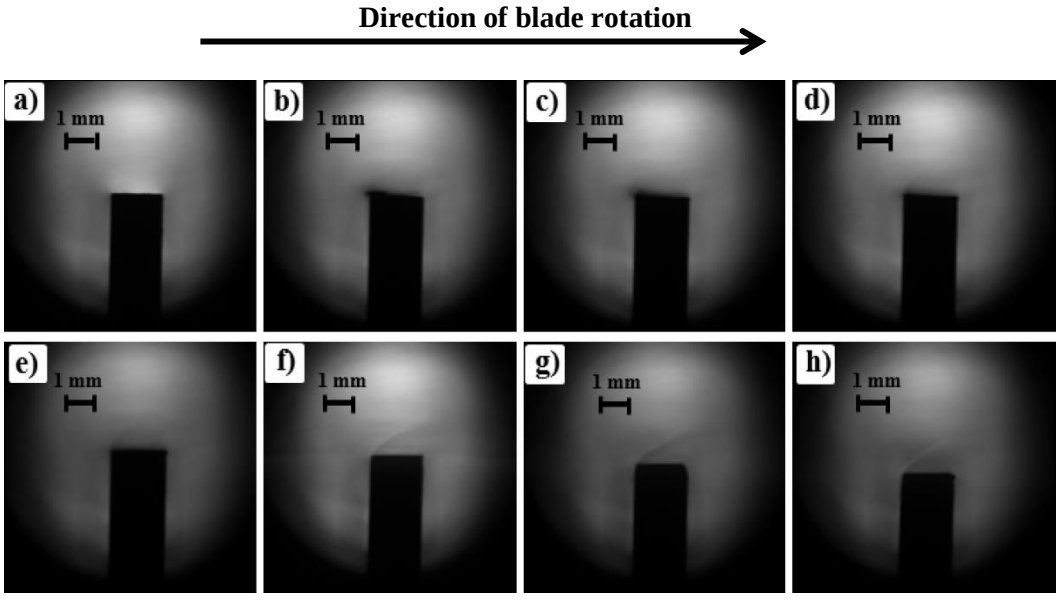

Figure 6.10. Blade wear recorded with blade speed of 100m s^{-1}, incursion rate of 0.02µm $pass^{-1}$, with abradable coating with hardness R15Y 54.6, at time: a) 0s; b) 42.34s; c) 60.78s; d) 84.53s; e) 105.97s; f) 339.29s; g) 446.58s; h) 591.36s.

The series of images revealed a progressive reduction of the blade length during the test (Figure 6.10 c-h), but also highlighted a negligible initial adhesive transfer (Figure 6.8b) compared with the overall level of wear.

Overall, at low incursion rate the stroboscopic imaging technique highlighted the progression of the mechanism with a mix of adhesion and blade wear with intermediate hardness coating, and a dominant blade wear in the test performed with the soft coating, and showed that the final condition was not always representative of the wear mechanism.

Furthermore, whilst observation of the samples highlighted similar behaviour at high incursion rate with different hardnesses, a series of blade images were observed for the soft coating in order to analyse if there were differences compared with the hard coating. Figure 6.11 shows a series of blade tip images for the test performed at incursion rate of 2µm pass^{-1}, blade speed 100m s^{-1} and coating hardness R15Y 54.6.

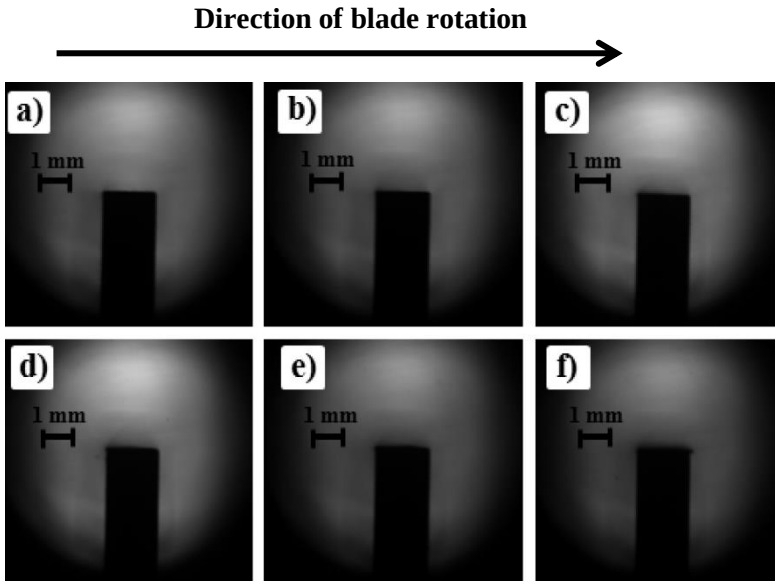

Figure 6.11. Blade tip images recorded with blade speed of 100m s^{-1}, incursion rate of 2µm pass^{-1}, with abradable coating with hardness R15Y 54.6, at time: a) 0s; b) 1.61s; c) 3.62s; d) 4.39s; e) 4.78s; f) 5.93s.

As shown in the figure, there was no significant variation of the blade length, through the progression of the contact; hence the main wear mechanism was cutting wear.

This section has described the morphology of adhesion and wear for the rest of the tests performed. In order to compare the wear mechanism with respect to the one observed on the hard coating, the blade length change was calculated and plotted against the theoretical rub length, and this is presented in the next section.

6.3.1. Blade length change for the rest of the tests

This section describes how the series of blade profiles, as shown previously, were used to plot the blade length change against the theoretical rub length for the rest of the tests performed at different incursion rates and at low blade speed; the influence of the blade speed will be analysed in the next section. Figure 6.12 shows the blade length change against the theoretical rub length calculated for different incursion rates at 100m s^{-1} for abradable coating hardness R15Y 63.

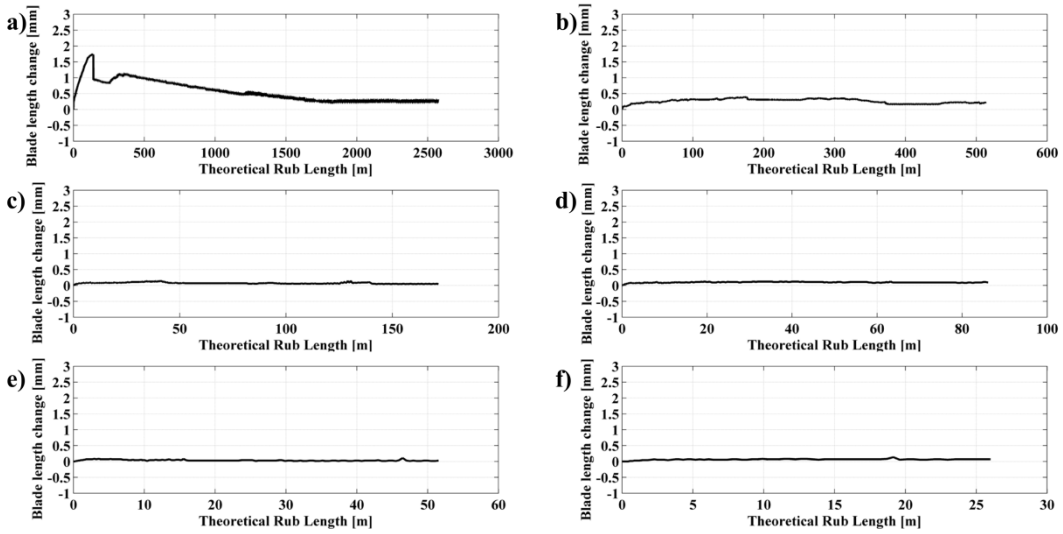

Figure 6.12. Blade length change expressed in terms of theoretical rub length, speed 100m s^{-1} and abradable R15Y 63 hardness, at incursion rates of: a) 0.02µm·$pass^{-1}$; b) 0.1µm·$pass^{-1}$; c) 0.3µm·$pass^{-1}$; d) 0.6µm·$pass^{-1}$; e) 1µm·$pass^{-1}$; f) 2µm·$pass^{-1}$.

As shown in the figure, at low incursion rate (Figure 6.12a) an increasing blade length was recorded, until the maximum was reached, and then the transfer material fractured. Following this the blade length started to reduce up to a certain point, and then a re-initiation of adhesion was observed after 244m of rub length, followed again by blade wear for the rest of the test. A reduction of adhesive transfer was recorded in comparison with the test performed on the harder coating (Figure 6.6a and Figure 6.12a). The blade length change highlighted an evolution of mixed wear mechanisms. With an increase of the incursion rate, the blade length change reduced, with an initial adhesive transfer followed by no variation of blade length, and with a well-cut surface being dominant (Figure 6.12 b, c, d, e, f).

Subsequently, the blade length change against the theoretical rub length was calculated for different incursion rates and a blade speed of 100m s^{-1} for abradable coating hardness R15Y 59.6, as shown in Figure 6.13.

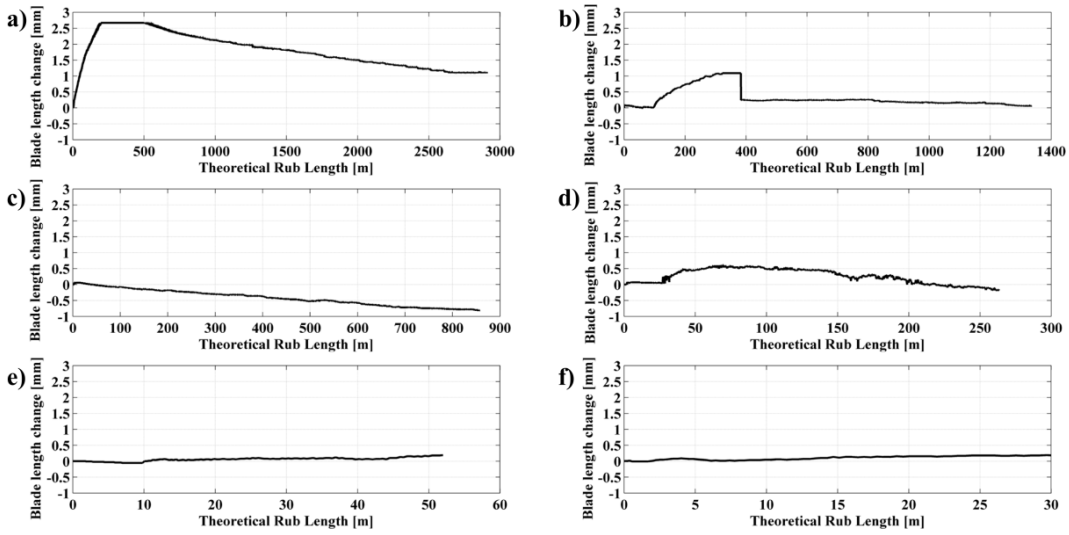

Figure 6.13. Blade length change expressed in terms of theoretical rub length, speed 100m s^{-1} and abradable R15Y 59.6 hardness, at incursion rate of: a) 0.02µm·$pass^{-1}$; b) 0.04µm·$pass^{-1}$; c) 0.06µm·$pass^{-1}$; d) 0.2µm·$pass^{-1}$; e) 1µm·$pass^{-1}$; f) 2µm·$pass^{-1}$.

As shown in the figure, at low incursion rate an initial adhesive transfer was recorded followed by blade wear (Figure 6.13a).The level of adhesion was comparable to the hard coating, but the adhesive phase was a shorter and for around 200m of rub length. For the rest of the test blade wear occurred. In the test performed at 0.04µm $pass^{-1}$, an initial adhesion followed by material fracture and mild blade wear (Figure 6.13b), was observed, while on the hard coating only adhesion was observed (Figure 6.6b). At an incursion rate of 0.06µm $pass^{-1}$ only blade wear was observed (Figure 6.13c), and at 0.2µm $pass^{-1}$ an initial adhesion followed by blade wear (Figure 6.13d) was observed, with a level of wear higher compared with that for the hard coating.

Finally, at high incursion rates, at 1 and 2µm $pass^{-1}$ (Figure 6.13 e, f) a negligible blade variation represented a cutting wear mechanism, as observed in the previous test.

The sample at intermediate hardness at low incursion rate highlighted an adhesive transfer for a short period of rub length, but also blade wear, and a re-start of adhesion especially on the coating R15Y 63. This confirmed that these two coatings had a mix of wear mechanisms. However, more variability of wear mechanisms with

the incursion rate was observed on the coating R15Y 59.6, with higher levels of adhesion and wear also evident.

Finally, the blade length change against the theoretical rub length was calculated for different incursion rates at a blade speed of 100m s^{-1}, with abradable hardness R15Y 54.6, as shown in Figure 6.14.

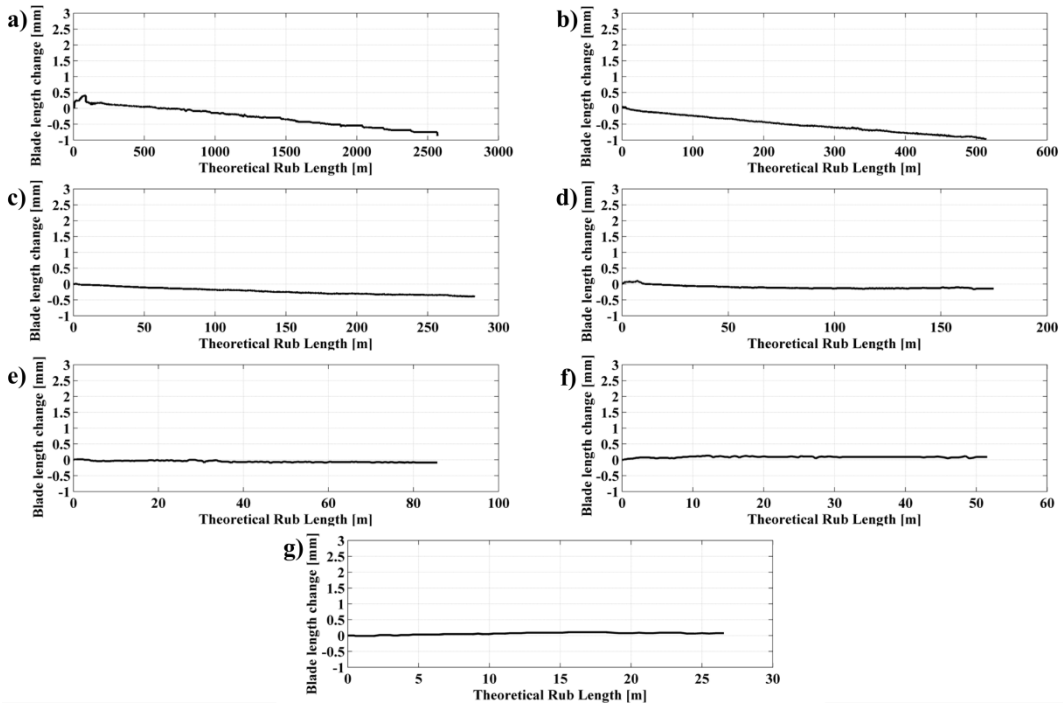

Figure 6.14. Blade length change expressed in terms of theoretical rub length, speed 100m s^{-1} and abradable R15Y 54.6 hardness, at incursion rates of: a) 0.02µm·$pass^{-1}$; b) 0.1µm·$pass^{-1}$; c) 0.2µm·$pass^{-1}$; d) 0.3µm·$pass^{-1}$; e) 0.6µm·$pass^{-1}$; f) 1µm·$pass^{-1}$; g) 2µm·$pass^{-1}$.

At a low incursion rate (Figure 6.14a), a progressive reduction of the blade length was observed that highlighted a significantly different wear mechanism compared with the rest of the tests, and the blade wear was around 1mm. Similar levels of blade wear were observed at an incursion rate of 0.1µm $pass^{-1}$ (Figure 6.14b). An increase of the incursion rate generated a reduction of the blade wear from 0.2 to 0.3µm $pass^{-1}$ (Figure 6.14 c, d), with negligible blade wear recorded at 0.6µm $pass^{-1}$ (Figure 6.14e). Then at high incursion rates (Figure 6.14 f, g) there was a minimal change of the blade length corresponding to good cutting. Overall, the soft coating highlighted a dominant blade wear mechanism at a low incursion rate, while at a high incursion rate a blade length change similar to the rest of the tests was measured.

The analysis of the sample post-test, as well the analysis performed with the stroboscopic imaging technique, highlighted different wear mechanisms in relation to the incursion rate and hardness. At low incursion rate, a progressive blade length reduction was observed on the soft coating, while with an increase of the hardness there was a gradual change in wear mechanism with an increase of the blade length, and a decrease that highlighted a mix of adhesion and blade wear, and finally on the hard coating an increase of the blade length with adhesive transfer. With an increase of the incursion rate, a gradual change of the wear mechanism to cutting occurred at all hardness, with no evident blade length variation.

In the test performed at intermediate hardness, a mix of mechanisms was observed in both samples, R15Y 63 and R15Y 59.6. However, the sample with hardness R15Y 59.6 showed more variability in wear mechanism at low incursion rate, but also along with the other incursion rates, with a high level of adhesion for a short rub period and as well as a high level of blade wear; this suggests that the value of the hardness represented a transition between the adhesive transfer observed, especially in the R15Y 72.3 test, and blade wear observed mainly in the R15Y 54.6 test.

Overall, the analysis of the blade length with a stroboscopic technique highlighted the progression of the contact during the test. Also, it can be seen from the graphs that when adhesive transfer was observed, an initial growth phase of the length was observed, followed by a steadier period with a positive gradient, while when the incursion rate increased the gradient was near constant, and finally when blade wear was observed, the gradient was negative and fracture of the transfer material was also observed. This suggests that different phases of the contact could be identified and quantified; therefore further analysis will made in Section 6.4.

Even though on the hard coating the influence of the speed did not generate a change in the wear mechanism, but only a reduction of adhesive transfer, the influence of the speed will be analysed for the rest of the tests in terms of blade length change against the theoretical rub length, and will also be presented in the next section.

6.3.2. Blade length change with R15Y 63, R15Y 59.6 and R15Y 54.6 at different blade speeds

In this section the influence of the blade speed is presented through the analysis of the blade length change for the tests performed on coating hardnesses R15Y 63, 59.6 and 54.6 for low, intermediate and high incursion rates. The intermediate incursion rate presented is 0.3µm pass^{-1} instead of 0.2µm pass^{-1} in relation to the tests performed during this research on coating R15Y 63. Figure 6.15 shows the blade length change for the test performed on coating R15Y 63 with blade speeds 100, 150 and 200m s^{-1}.

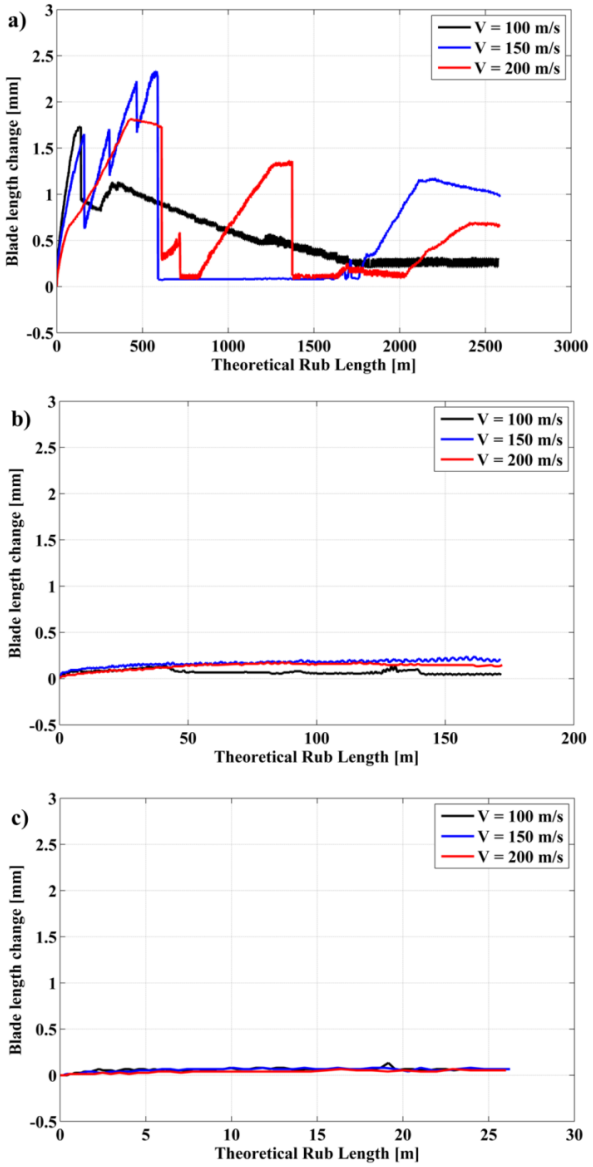

Figure 6.15. Blade length change against the theoretical rub length for different speeds with coating R15Y 63 and incursion rates: a) 0.02µm pass^{-1}; b) 0.3µm pass^{-1}; c) 2µm pass^{-1}.

At a low incursion rate, adhesive transfer, fractured material and re-initiation of adhesion were observed at all blade speeds. A decrease in the rate of adhesion was observed with an increase of speed. It is also interesting to note that, in cases where fracture occurred, once adhesion re-initiated it continued at a similar rate, especially at intermediate and high speeds (Figure 6.15a, blue curve 150m s^{-1} and red curve 200m s^{-1} respectively). When fracture occurred, the adhesion patterns changed with speed, because the fracture of adhered material represented to a degree a probabilistic event, with the subsequent re-adhesion of material influenced by the fracture surface. However, overall a similar wear mechanism was observed with an increase of the speed, even with a different progression of blade length. At high incursion rate, similar blade length change was observed, with a decrease of blade variation with speed (Figure 6.15 b, c).

The influence of speed was also analysed for the coating with hardness R15Y 59.6, as shown in Figure 6.16.

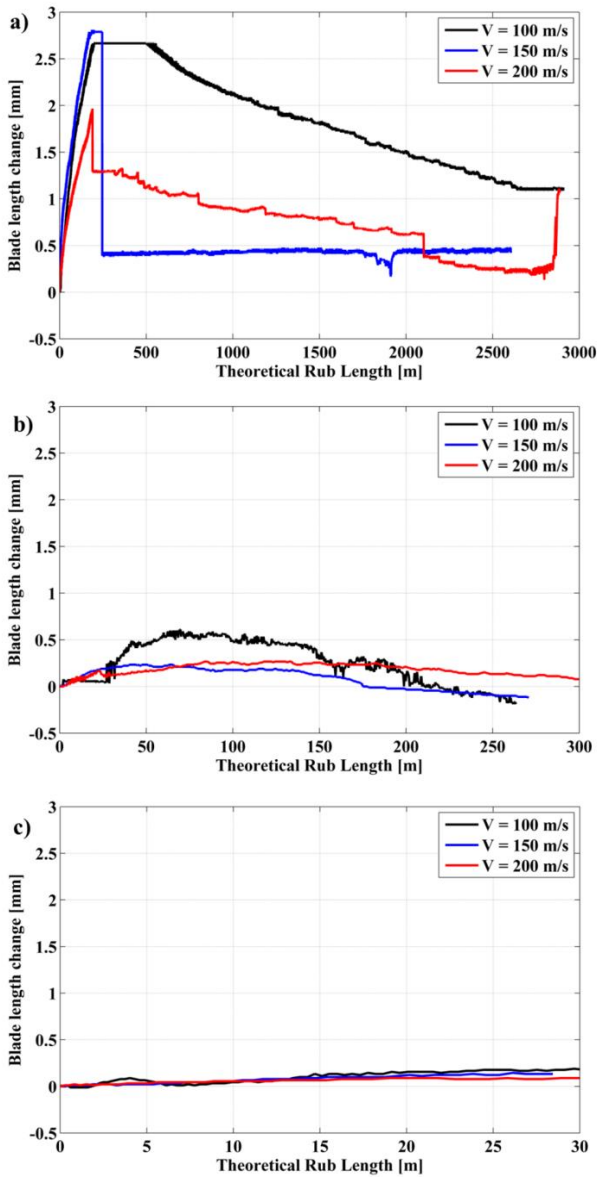

Figure 6.16. Blade length change against the theoretical rub length for different speeds with coating hardness R15Y 59.6 and incursion rates: a) 0.02µm pass^{-1}; b) 0.2µm pass^{-1}; c) 2µm pass^{-1}.

As shown in the figure, similar levels of adhesion at low incursion rates were observed, along with progressive blade wear, especially at low and high speeds (Figure 6.16a black and red curves respectively), with a decrease of the level of adhesion especially at high speed.

At an intermediate incursion rate (Figure 6.16b) there was a similar trend at different blade speeds, especially at low (black curve) and intermediate (blue curve) speeds with an initial adhesion (increase of the blade length) followed by blade wear. At a high incursion rate, a similar trend was also observed, with no relevant variation of

the blade length. Overall, as stated before, this hardness sample was characterised by a mix of wear mechanisms, with a similar result occurring at higher speeds.

Finally, the speed influence was analysed for the coating with hardness R15Y 54.6, as shown in Figure 6.17.

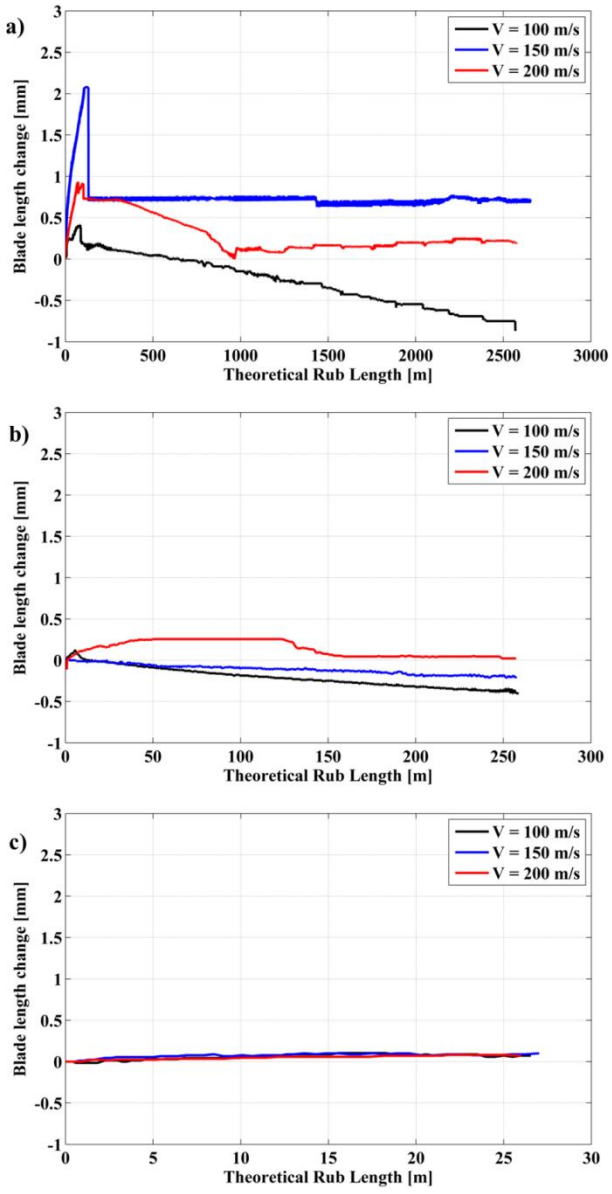

Figure 6.17. Blade length change against the theoretical rub length for different speeds with coating hardness R15Y 54.6 and incursion rates: a) 0.02µm pass^{-1}; b) 0.2µm pass^{-1}; c) 2µm pass^{-1}.

As shown in the figure, at low incursion rate (Figure 6.17a), after an initial adhesive transfer a continuous reduction in the blade length was observed at 100m s^{-1}. A similar trend was also observed on the test at high speed, with a re-initiation of

adhesion after a continuous blade length reduction (Figure 5.32). A difference was observed at the middle speed, where an initial adhesion was followed by further break away and a slight reduction of the blade length.

At an intermediate incursion rate, similar trends were observed with blade wear (Figure 6.17b), and also with an increase of the speed a decrease of the blade wear was observed; this was also observed at high speed after an initial adhesion was observed, as at low speed, and no evident variations in blade length were observed (Figure 6.17b). Finally, at a high incursion rate, no different trends and no significant blade length variations were observed with different speeds.

Overall, a change in the blade speed produced no change in the wear mechanism. However, some differences highlighted during the analysis could be related to a higher speed producing higher energy and therefore higher heat, and this could promote higher adhesion or blade wear. But, on the other hand, an increase of the impact speed would lead to more fracture of the transfer material, and therefore further investigation was required during this research.

The stroboscopic imagining technique allowed this research to determine the blade length change during all tests and allowed it to be quantified. In addition it enabled understanding of the evolution of the mechanism during the test and not only before and after the test. The blade length change against theoretical rub length highlighted the increase and decrease of the blade length that represented adhesive transfer and blade wear, but also a negligible blade length variation highlighted a cutting wear mechanism.

Also, the analysis of the graph highlighted an initial growth of adhesion, usually followed by a positive gradient of adhesion where it was observed that the blade length increased, or in the case of the soft coating a negative gradient where the blade length decreased. Therefore, the next section describes a quantitative analysis that was introduced based on the rate of adhesion and wear in order to quantify the wear mechanism observed.

6.4. Adhesion and wear analysis

This section describes analysis of the results for blade length change with respect to theoretical rub length. The analysis of the blade length change highlighted adhesive transfer, blade wear and fracture. In all cases an initiation period with a rapid change in blade length, followed by more steady state behaviour was observed. This was followed by fracture in the case of adhesive wear. Figure 6.18 shows an example of the phases when adhesive transfer occurred.

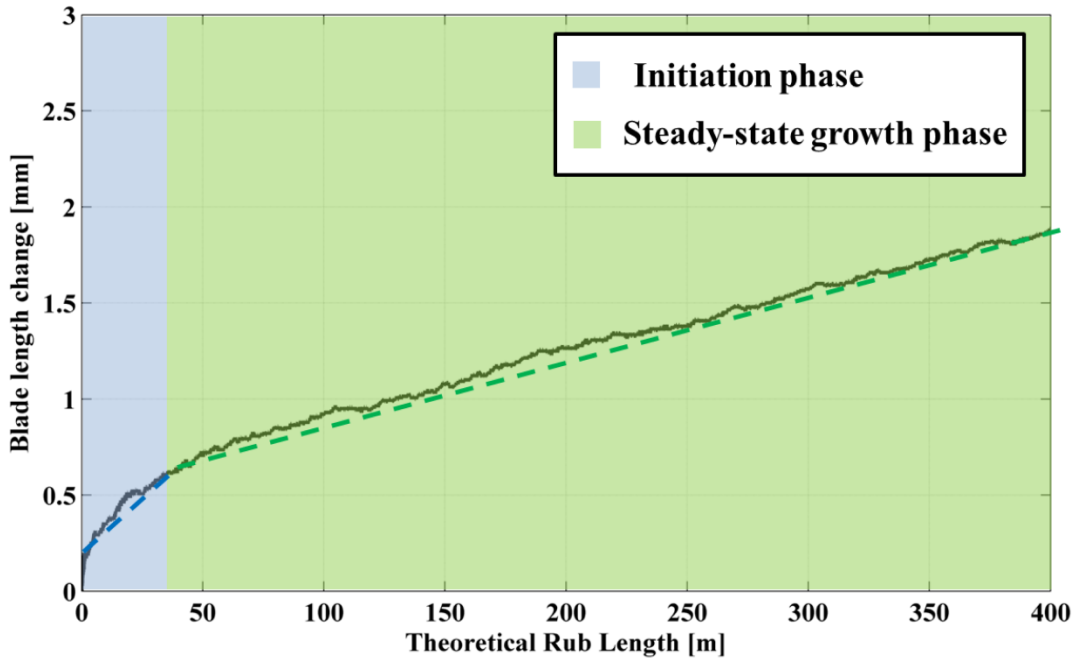

Figure 6.18. Phase of adhesion highlighted on test at incursion rate 0.02µm pass^{-1}, speed of 100m s^{-1} and coating hardness R15Y 72.3.

As shown in the figure, the length change can be characterised by an initial period of rapid growth, followed by a more steady-state period. In the case of a low incursion rate test, this steady-state area is marked by a positive gradient when adhesion was observed, at higher incursion rates this gradient decreases, and at very high incursion rates it is near constant, when no variation of blade length was measured.

Also a similar consideration could be made when a reduction of the blade was recorded. The blade wear was characterised by a steady-state period, as shown in Figure 6.19.

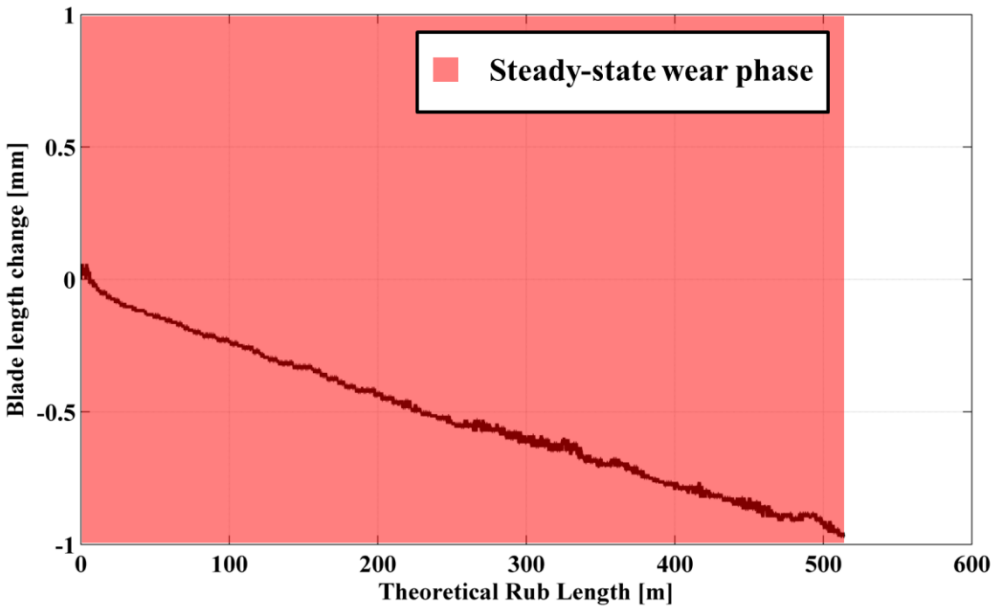

Figure 6.19. Phase of blade wear highlighted on test at an incursion rate of 0.1µm pass^{-1}, speed of 100m s^{-1} and coating hardness R15Y 54.6.

As shown in the figure, at low incursion rate a steady period is marked by a negative gradient when blade wear was observed, and at higher incursion rates this gradient increases, and at very high incursion rate was near constant.

These regions will now be investigated numerically and explored in relation to the test parameters.

6.4.1. Initiation phase and rate of adhesion / wear calculation

In this section the experimental results of the blade length change with respect to the theoretical rub length will be analysed in order to identify the value of rub length at which the gradient becomes approximately constant, i.e. the initiation phase of adhesion, and as well the rate of adhesion and wear during the steady-state period. This process was performed with a program developed in MATLAB during this research. The analysis was divided into three main steps: calculation of the gradient of the curve, identification of the initiation phase, and identification of the steady state gradient in relation to the boundary condition.

In the first part, the gradient of the curve was calculated using the coefficient of linear interpolation of the curve. The interpolation was made over the duration of the test in order to identify the steady state period numerically. Therefore, the graph was

divided into variable areas, with a variable value of the start ('*S*') and end ('*E*'). These values represented the value of rub length at the steady state start and end, respectively, as shown in Figure 6.20. The values of '*S*' and '*E*' were chosen to be variable because the start of the steady-state phase, i.e. initiation value, and the end of the steady-state phase were calculated in a numerical way in order to have a uniform analysis to apply for all graphs analysed.

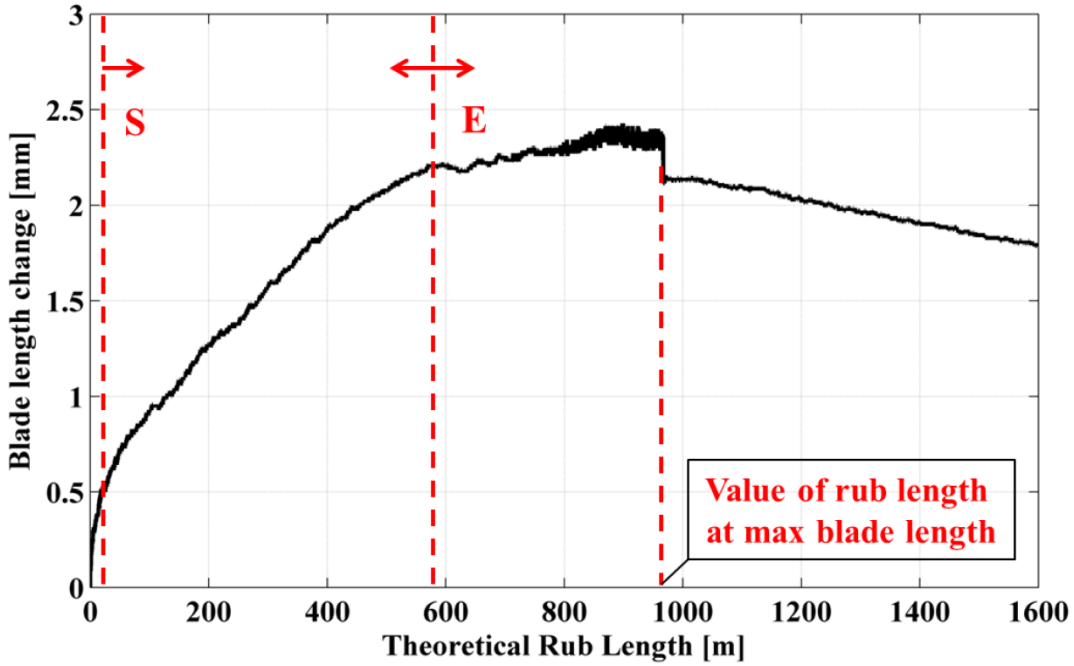

Figure 6.20. Area of analysis of the rate of adhesion, test at incursion rate of 0.02µm pass^{-1}, blade speed of 100m s^{-1}, coating hardness R15Y 72.3.

As shown in the figure, the program varied the value of *'S'* from zero to the value of the rub length that corresponded to the maximum length change, while when blade wear was observed the value of *'S'* was changed to the value of the rub length that corresponded to the end of the test. The variable *'E'* was a function of the value of *'S'*, a simple increment of rub length with respect to the current value of *'S'*, and in this way all rub lengths of the test were analysed and the gradients were calculated.

In the series of areas identified by *'S'* and *'E'*, the section of the graph defined was interpolated with a polynomial of the first order, as shown in Figure 6.21.

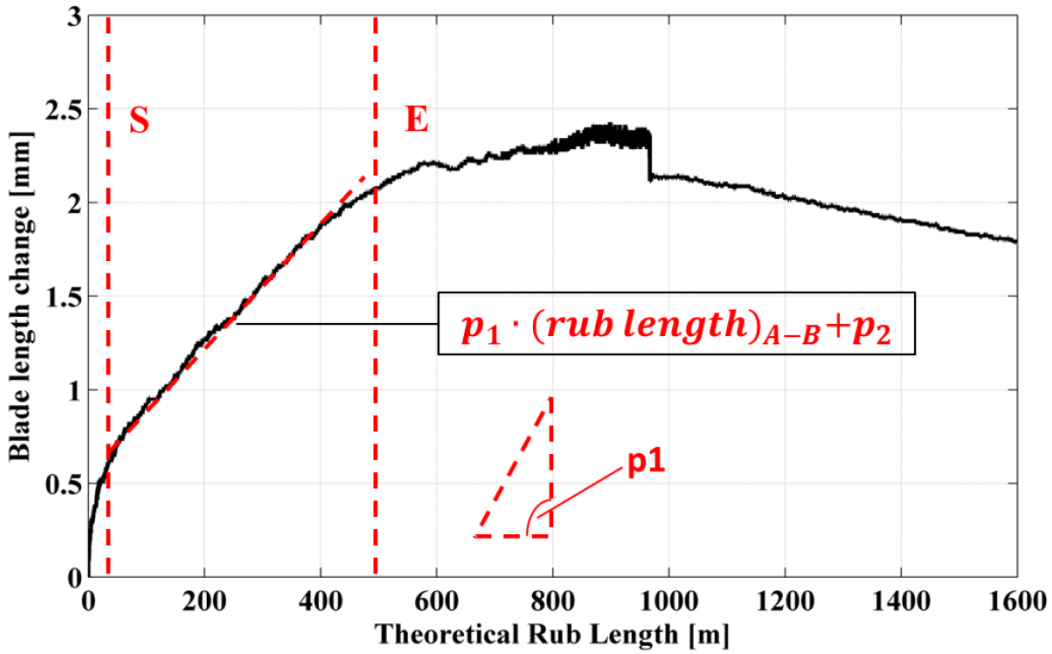

Figure 6.21. Interpolation on distance '*S-E*,' test at incursion rate of 0.02µm pass^{-1}, blade speed of 100m s^{-1}, coating hardness R15Y 72.3.

As shown in the figure, the coefficient of linear fitting represented the gradient of the curve, namely the rate of adhesion or rate of wear, obtained from the Equation (6.1).

$$\boldsymbol{Blade\ length\ change = p_1 \cdot rub\ length_{S-E} + p_2} \qquad (6.1)$$

where 'p_1' and 'p_2' are the coefficients of linear fit calculated on the curve over the distance '*S-E*'.

As highlighted before, the values of *'S'* and *'E'* changed during the analysis; therefore different distances *'S-E'* were identified in relation to the distance, and different coefficients of fit were calculated. The coefficient 'p_1' represented the rate of adhesion or wear depending on whether the gradient was positive or negative in the area analysed.

However, in order to determine the gradient of the curve, a series of boundary conditions were used. The first boundary condition was the coefficient of determination 'R^2' [99] that represented a number that indicates how well the data fits to a statistical model. In order to calculate the coefficient of determination, the average of the blade length in the area '*S-E*' was calculated, as shown in Equation (6.2).

$$\overline{\boldsymbol{blade\ length}} = \frac{\mathbf{1}}{\boldsymbol{n}}\sum_{\boldsymbol{i=1}}^{\boldsymbol{n}} \boldsymbol{blade\ length_i} \tag{6.2}$$

where '*n*' represented the number of data analysed.

Then the variability of the measured set was calculated in relation to the average value (total sum of squares) and then in relation to the interpolation data (f_i) (total sum of squares of residual), as shown in Equations (6.3) and (6.4).

$$\boldsymbol{SS_{tot}} = \sum_{\boldsymbol{i}} \left(\boldsymbol{blade\ length_i} - \overline{\boldsymbol{blade\ length}}\right)^{\mathbf{2}} \tag{6.3}$$

$$\boldsymbol{SS_{res}} = \sum_{\boldsymbol{i}} (\boldsymbol{blade\ length_i} - \boldsymbol{f_i})^{\mathbf{2}} \tag{6.4}$$

Then the coefficient of determination was defined as unity minus the ratio between the total sum of squares of residuals and the total sum of squares as shown in Equation (6.5).

$$\boldsymbol{R^2} = \mathbf{1} - \frac{\boldsymbol{SS_{res}}}{\boldsymbol{SS_{tot}}} \tag{6.5}$$

The coefficient of determination was used in order to find the best interpolation with the curve evaluated in the area of rub length, a higher value representing better fitting of the curve. The first step identified the value of *'S'*, the initiation phase, which was determined in relation to the gradient variation between an initial phase where the adhesion grew rapidly, and the steady state period.

The rate of adhesion was determined in order to have a better interpolation with the curve evaluated in the maximum distance '*S-E'*. Therefore, the program identified the gradient, namely rate of adhesion / wear, that maximised the coefficient of determination that was chosen to be between 0.8 and 0.99. Again, a higher value meant better fitting of the curve. The lower limit was chosen in order to also apply the analysis to the test at high incursion rate, where negligible adhesion or variation of blade length was observed, and the lower limit permitted the software to calculate the gradient for that condition.

Then finally the rate was calculated for the distance *'S-E'* that was at least 60% of the rub length corresponding to the maximum blade length. This area was maximised in order to be sure to analyse a steady-state area that represented the rate of adhesion or wear of the test analysed.

Table 6.2 summarises the value of theoretical rub length of the initiation period and the rate of adhesion obtained for the test performed with coating hardness R15Y 72.37, blade speed 100m s^{-1}, at low, intermediate and high incursion rates.

Test condition	**Initiation phase**	**Steady-state phase**		
Incursion per pass [µm]	**Rub length of the initiation phase [m]**	**Rate of adhesion [10^{-3} mm m^{-1}]**	**R^2**	**Distance '*S-E*' [m]**
0.02	45.92 ± 8.09	3.34	0.99	325.1
0.04	92.88 ± 11.03	3.11	0.98	200.5
0.06	25.6 ± 13.60	2.36	0.87	150.4
0.1	10.85 ± 4.62	2.26	0.87	75.4
0.2	8.33 ± 1.33	1.81	0.81	45.2
2	10.16 ± 2.53	1.43	0.81	12.6

Table 6.2. Initiation phase and rate of adhesion for the test performed with coating hardness R15Y 72.3 and blade speed 100m s^{-1}.

As shown in the table, the initiation period, i.e. the theoretical rub length required for steady state adhesion, seemed to decrease with an increase of the incursion rate, with a lower value measured at high incursion rate, where adhesive transfer was not

present or was negligible, and, as highlighted previously, it seems reasonable that the initiation period is similarly reduced and tends to a low value. However, the scatter observed in the acquired value was high, and also the trend was a non-uniform decrease. For example, the value at an incursion rate of 0.04μm pass^{-1} was almost double that of the value observed at 0.02μm pass^{-1}, and consequently the focus was moved on to the rate of adhesion and wear.

The value measured from the steady state phase highlighted a decrease of the rate of adhesion with an increase of the incursion rate. Hence a negligible blade growth was measured at high incursion rate, and also the high value of the coefficient of determination showing a good fit was used in order to calculate the gradient. Based on the success of this analysis, the rate of adhesion and wear was calculated for all tests performed in order to quantify the wear mechanics, and the rate was plotted against the incursion rate for different hardness coatings, and for different speeds.

6.4.2. Rate of adhesion / wear results

The rate of adhesion and the rate of wear were calculated as the rate of change of the blade length with respect to theoretical rub length, as shown in Section 6.4.1. This analysis was performed for all investigated incursion rates, hardnesses and blade speeds. The rate of adhesion / wear was plotted against the incursion rate, and therefore the main differences in wear mechanics were observed with an increase of incursion rate with the same coating hardness.

Figure 6.22 shows the rate of adhesion calculated for the coating with hardness R15Y 72.3 for the tests performed.

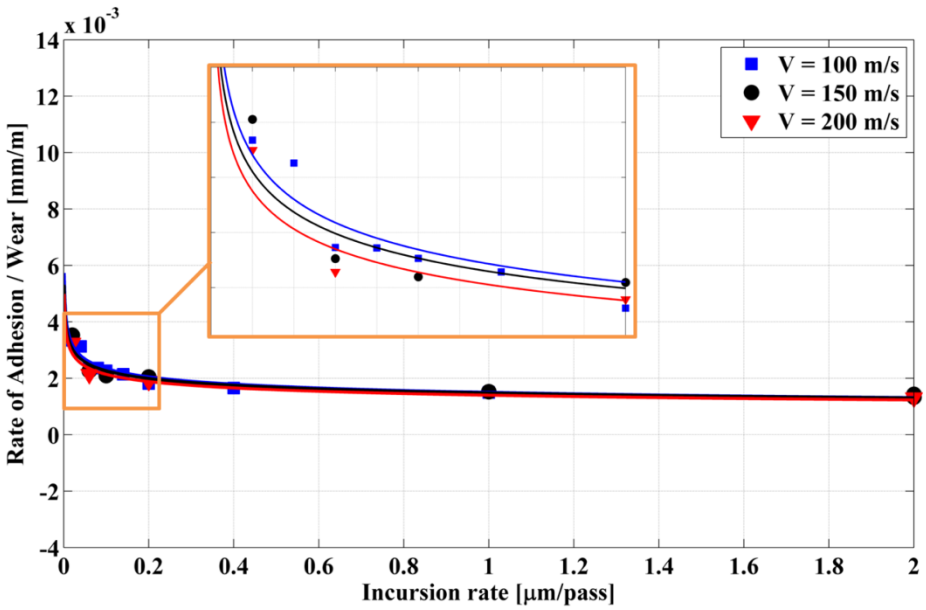

Figure 6.22. Rate of adhesion in terms of incursion rate, with abradable sample hardness R15Y 72.3, R^2 fitting curve: 100m s^{-1} 0.93, 150m s^{-1} 0.918, 200m s^{-1} 0.94.

As shown in the figure, an increase of the incursion rate decreased the rate of adhesion, and another important aspect was that with an increase of the blade speed, the rate of adhesion decreased. The rate of adhesion was initially high before reducing rapidly as the incursion rate increased, where in the test performed at high incursion rate, a negligible initial blade growth determined a rate of adhesion that was different from zero in the mathematical calculation analysis.

The same analysis was made for the test performed with coating hardnesses R15Y 63 and 59.6, as shown in Figure 6.23.

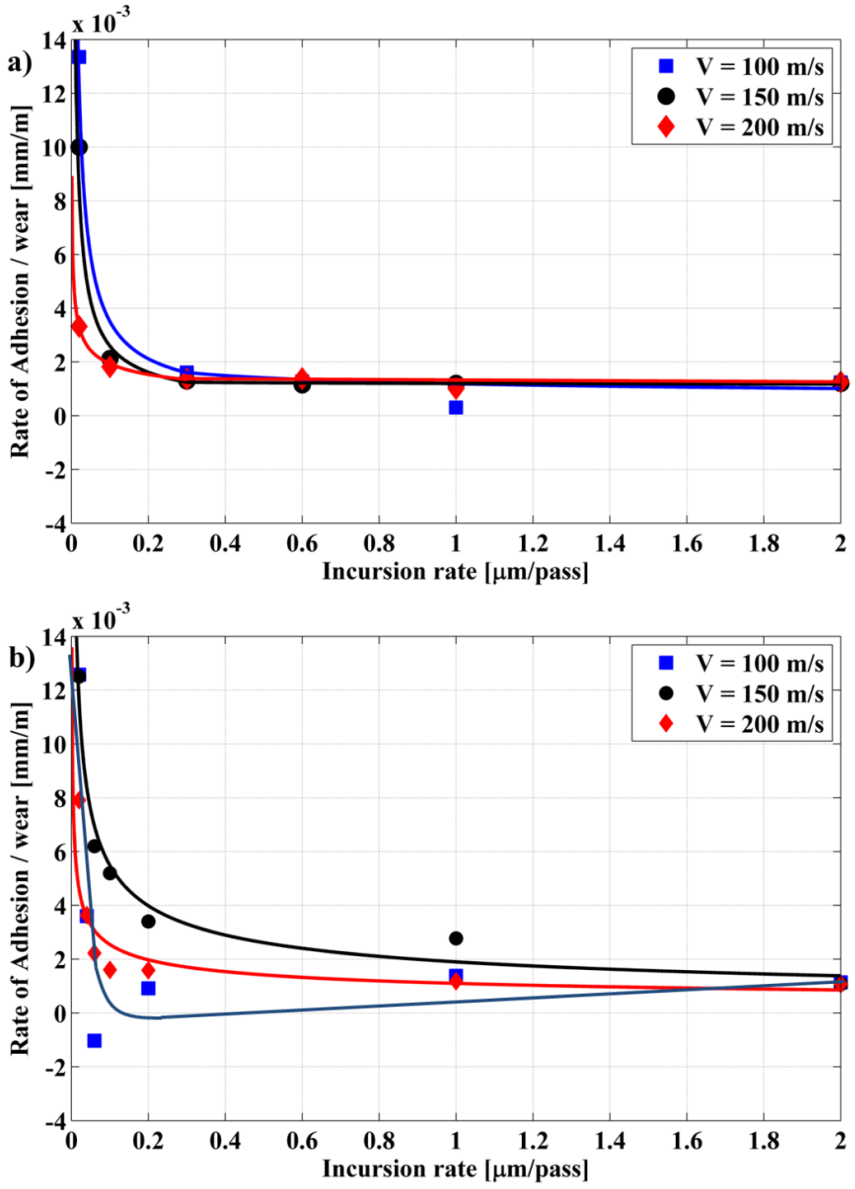

Figure 6.23. Rate of adhesion in terms of incursion rate, with abradable sample hardness: a) R15Y 63, R^2 fitting curve: 100m s^{-1} 0.91, 150m s^{-1} 0.97, 200m s^{-1} 0.98; b) R15Y 59.6, R^2 fitting curve: 100m s^{-1} 0.5, 150m s^{-1} 0.93, 200m s^{-1} 0.76.

As shown in the figure, in both tests performed with coating hardnesses R15Y 63 and R15Y 59.6, a decrease of adhesion rate was observed with an increase of the incursion rate. In the test performed with the coating with hardness R15Y 63, as observed also on the harder coating test, an increase of the speed produced a decrease of the rate of adhesion (Figure 6.23a). In the tests performed with hardnesses R15Y 63 and R15Y 59.6, the rate of adhesion calculated was higher than for the test with hardness R15Y 72.3, because the adhesion period happened in a shorter rub length

period compared with the test performed with hard coating, and then after the adhesion phase a material fracture or blade wear was observed, as highlighted in Figures 6.12 - 6.13.

The observation of the rate of adhesion / wear calculated for the test performed with coating hardness R15Y 59.6 was characterised by a large amount of scatter along the incursion rate axis, with less unclear trends. Therefore the coefficient of determination of the fitted curve was low, especially at low speed (Figure 6.23b), where adhesion and also wear were measured from the graph of the evolution of blade length. Figure 6.23b highlights that, at low incursion and low speed, the rate adhesion / wear was positive where adhesion occurred, then at an incursion rate of 0.06μm $pass^{-1}$ there was a negative rate, where blade wear occurred, and it was positive again corresponding to cutting wear mechanism at high incursion rate. Also, an increase of the speed determined an increase of the rate of adhesion, and therefore at middle speed a higher rate of adhesion was measured at low incursion rate. The scatter of the trend observed at middle hardness R15Y 59.6 and the variability between adhesion and wear, and also the observation of the sample post-test where a mix of wear mechanisms was observed, and the observation of the change in blade length, suggest that the hardness could represent a transition value for the wear mechanism of the coating, especially at low incursion rate.

Figure 6.24 shows the rate of adhesion / wear calculated for the test performed with coating hardness R15Y 54.6.

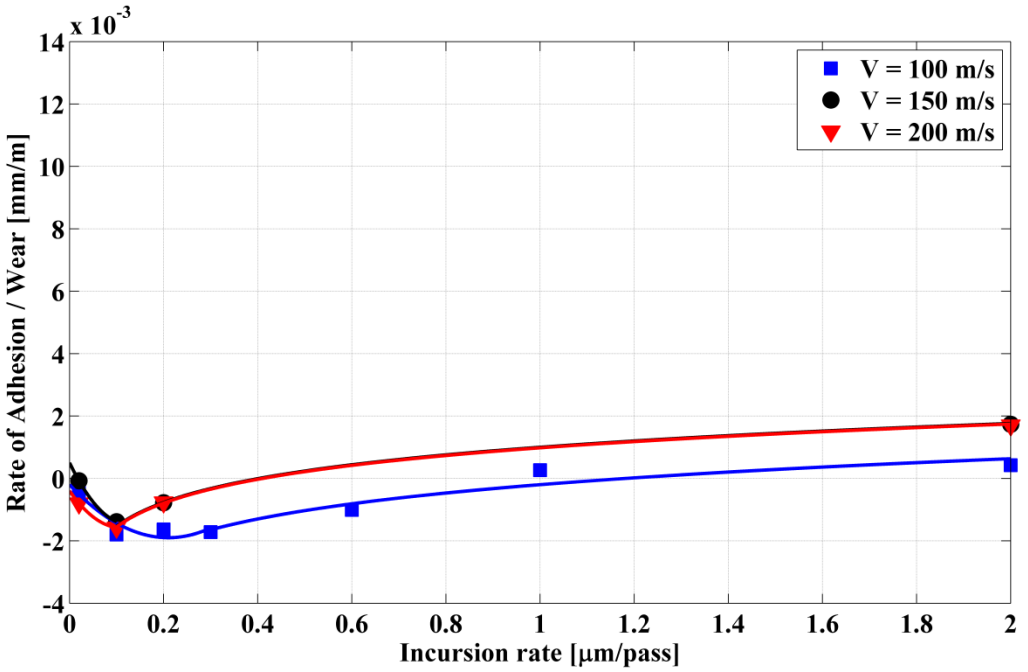

Figure 6.24. Rate of wear in terms of incursion rate, with abradable sample hardness R15Y 54.6, R^2 fitting curve: 100m s^{-1} 0.87, 150m s^{-1} 0.82, 200m s^{-1} 0.82.

As shown in the figure, at low incursion rate a negative gradient was resulted, and therefore there was blade wear, with a progressive decrease corresponding to an increase of the incursion rate, where the mechanism went from blade wear to good cutting with negligible variation of the blade length. It is interesting to note, from the outlined trend, that at 0.02µm $pass^{-1}$, even with a higher level of wear the rate of wear was lower, possibly due to an initial adhesion, as observed in Figure 6.14a, and also this trend was observed at all speeds. An increase of the speed highlighted a decrease of the blade wear, where similar values of the rate of adhesion / wear were measured at intermediate and high speeds.

The rates of adhesion / wear were compared for different coating hardnesses at different speeds as shown in Figure 6.25.

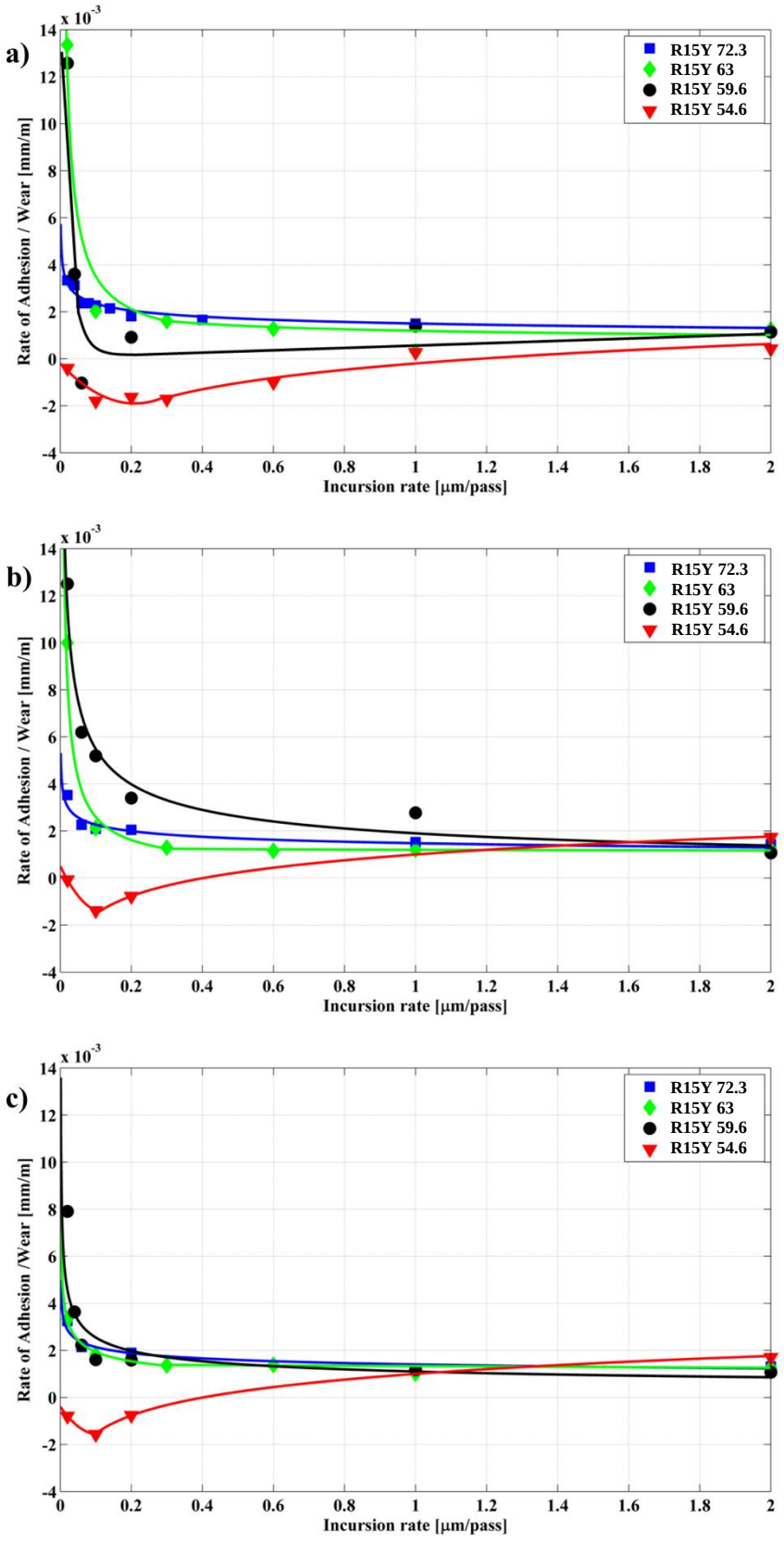

Figure 6.25. Rate of adhesion / wear in terms of incursion rate, for different abradable sample hardness and blade speed: a) 100 m s^{-1}; b) 150 m s^{-1}; c) 200 m s^{-1}.

As shown in the figure, at low speed (Figure 6.25a) there is a progressive decrease of the rate of adhesion / wear from high to soft hardness, with a uniform and similar trend when the incursion rate increases. However, especially at low incursion rate, the tests performed with coatings R15Y 63 and R15Y 59.6 were characterised by higher rates of adhesion, because the adhesion phase happened for a short period of the theoretical rub length, followed by blade wear. Similar trends were observed at intermediate and high speeds (Figure 6.25 b, c), where at high speed similar values were measured, especially at high and intermediate hardness.

Overall the graphs illustrate a decrease of the rate of adhesion / wear with the incursion rate, and therefore the wear mechanism changed from adhesion to blade wear, and especially on the harder and softer coatings a decrease of adhesion and wear was observed with increasing speed. Furthermore, the trend observed on the intermediate hardness was characterised by more scatter, especially in the test with R15Y 59.6.

6.5. Discussion

This chapter has considered how the introduction of the stroboscopic imaging technique highlighted the progression of the wear mechanism during the tests, and a higher level of adhesion was measured during tests, indicating that the final condition does not necessarily represent the overall level of adhesion. The stroboscopic technique further highlighted the evolution of the mix of wear mechanisms and the sequence of mechanisms, something that it was not possible to obtain from simple observation of the sample. However, blade profile analysis was required in order to have an insight into the wear mechanism, while the observation of the sample still represented a quick way to identify the wear mechanism.

Otherwise the analysis of the blade length change highlighted different periods during the contact: an initiation phase of adhesion, a more steady-state period where adhesion or wear were observed, and material transfer fracture. Although the identification of the initiation period highlighted a high scatter and difficulty to observe a general trend, otherwise the analysis of the steady state period with the calculation of the rate of adhesion / wear did suggest general trends. A decrease in the rate of adhesion was observed when the mechanism changed progressively from adhesive transfer to cutting at higher incursion rates on the hard coating, but also a

decrease in the blade wear was observed with an increase of the incursion rate on the softer coating. A similar well-cut surfaces were observed at high incursion rates for all test conditions, while, as highlighted previously, at low incursion rates different wear mechanisms were observed and quantified with the rate of adhesion / wear. However, further analysis is still needed to be made in order to understand the nature of the wear mechanism observed. Blade speed highlighted a reduction in the rate of adhesion with increasing speed on the hard coating, and a reduction in the rate of wear on the soft coating, while for the intermediate hardness coating a non-uniform reduction with the speed was observed, suggesting that high speed corresponds to high contact energy which could be converted into heat during the contact and could be due to adhesion or wear. However on the other hand, high impact energy could increase the probability of fracture, and therefore more fractures were observed at high speed.

The change in adhesion and wear to cutting with incursion conditions is suggested to be linked to a different material response in relation to the test conditions, and the relative ability of the constituent phase to dislocate [4, 6, 13, 15]. As a result, fracture and pitting were observed at high incursion rates, thus suggesting that the analysis of contact force could give more information on the nature of the wear mechanism from a material point of view, and also the thermal analysis of the coating could give information as to the nature of the adhesive transfer and blade wear. Therefore, the next chapter describes the measurement of the contact forces and Chapter 8 will present the measurement of the material and its thermal properties.

6.6. Chapter summary

- The stroboscopic imaging technique revealed the progression of the wear mechanism during the test: when the adhesive transfer was observed the final length did not represent the overall adhesive transfer.
- The introduction of the theoretical rub length highlighted the blade length change during the test, with progression of adhesion and blade wear, but also fracture of transferred material f and a mix of mechanisms.
- The analysis of the rate of adhesion / wear highlighted a trend in relation to the incursion rate, where a reduction of adhesion and wear were observed with increasing incursion rate, highlighting different gradients in relation to different wear mechanisms.
- Especially on hard and soft coatings, a decrease of the rate of adhesion / wear was observed with increase of the speed.
- Different wear mechanisms were quantified in relation to incursion rate, coating hardness and blade speed.

7. Normal and Tangential Force Measurement

The previous chapter described how the stroboscopic imaging technique captured the evolution of the wear mechanism during the contact, and highlighted that the incursion rate and the hardness of the coating were the dominant parameters in the wear mechanism. Therefore, in order to further investigate the material behaviour and understand the influence of the input parameters, contact force was measured during the tests, and the results will be described in this chapter. As presented in Section 3.4.2, a dynamometer was introduced below the abradable coating, and the post-processing of the acquired signal provided the force measurements during the

contact, as shown in Section 4.2.4. The measured force will be plotted against the theoretical rub length, as the previous chapter has established that the theoretical rub length represented the evolution of the rub during the test.

In the first part of the chapter the force measured for the test performed on the coating hardness R15Y 72.3 is presented in relation to the incursion rate, then the influence of the blade speed is introduced, and later the contact force for the rest of the tests performed with different hardnesses and speeds will be presented.

In the second part of the chapter, in order to highlight the force results for different incursion rates, coating hardness and speeds, an average contact force is calculated. This suggests a different behaviour in relation to the incursion rate; therefore further investigations will be made by analysing machining parameters, such as the efficiency of cut and the force ratio, in order to understand the energy necessary for cutting the material and to understand the material's behaviour.

7.1. Force measurements

The normal and tangential forces are the normal component to the coating and the longitudinal component along the direction of the rotating blade, respectively, as shown in Figure 7.1.

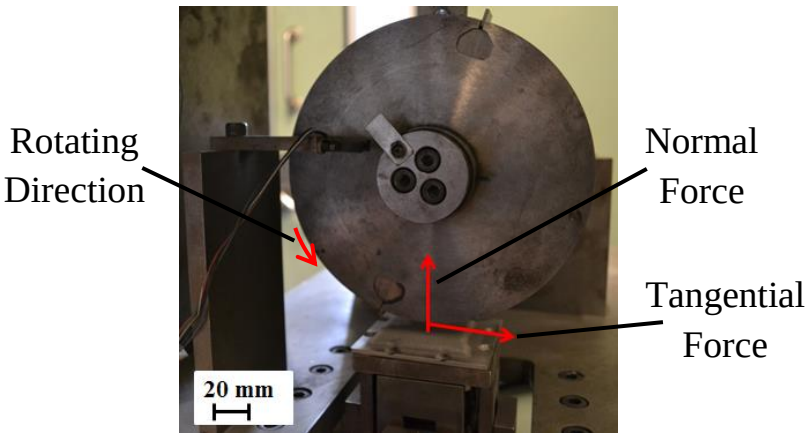

Figure 7.1. Direction of the contact force.

The normal and tangential forces were plotted against the theoretical rub length for different incursion rates, at a blade speed of 100m s^{-1} and abradable hardness R15Y 72.3, as shown in Figures 7.2 and 7.3.

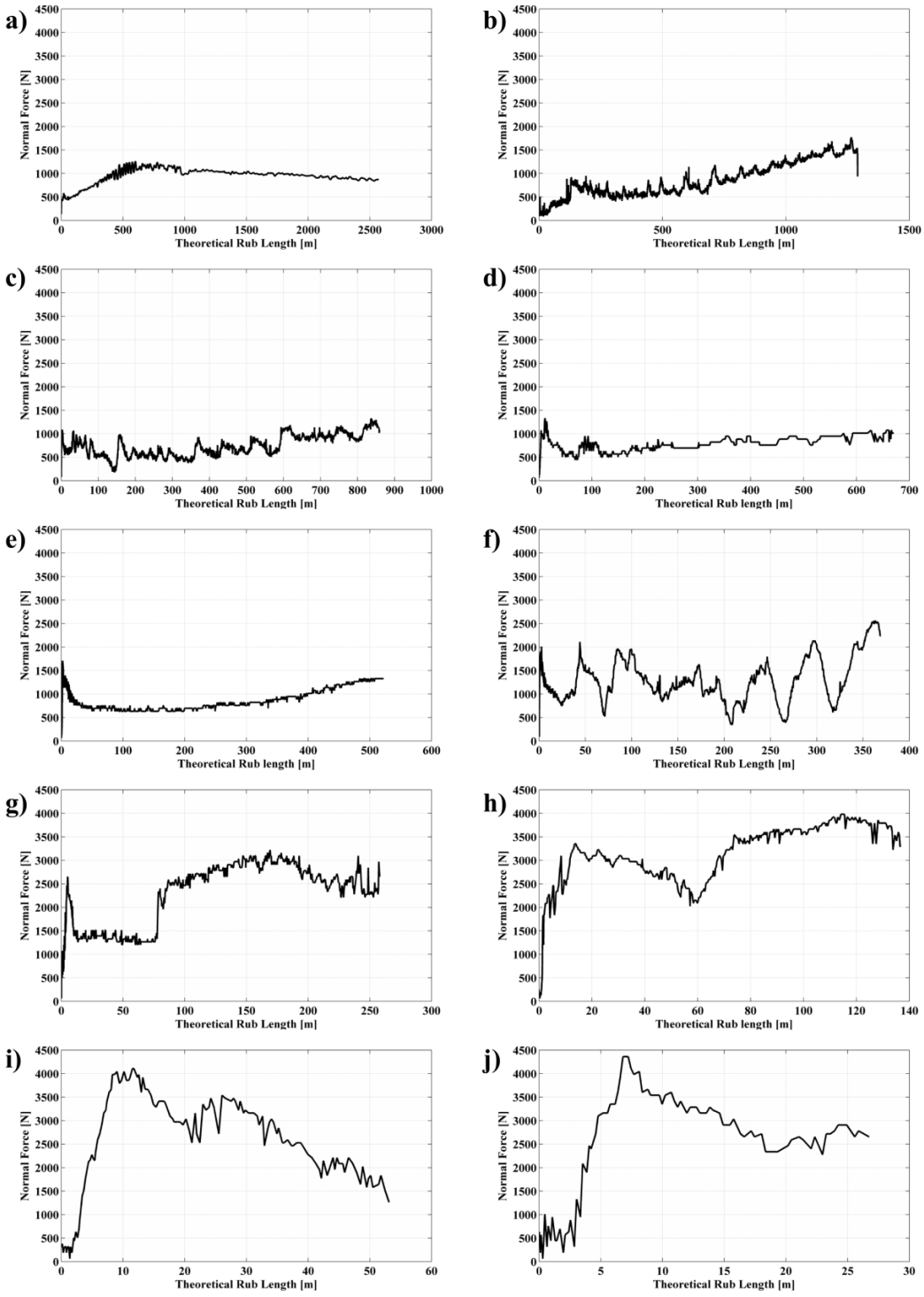

Figure 7.2. Normal force measurement at blade speed of 100m s^{-1} and abradable coating hardness R15Y 72.3, at incursion rates of: a) 0.02µm·$pass^{-1}$; b) 0.04µm·$pass^{-1}$; c) 0.06µm·$pass^{-1}$; d) 0.08µm·$pass^{-1}$; e) 0.1µm·$pass^{-1}$; f) 0.14µm·$pass^{-1}$; g) 0.2µm·$pass^{-1}$; h) 0.4µm·$pass^{-1}$; i) 1µm·$pass^{-1}$; j) 2µm·$pass^{-1}$.

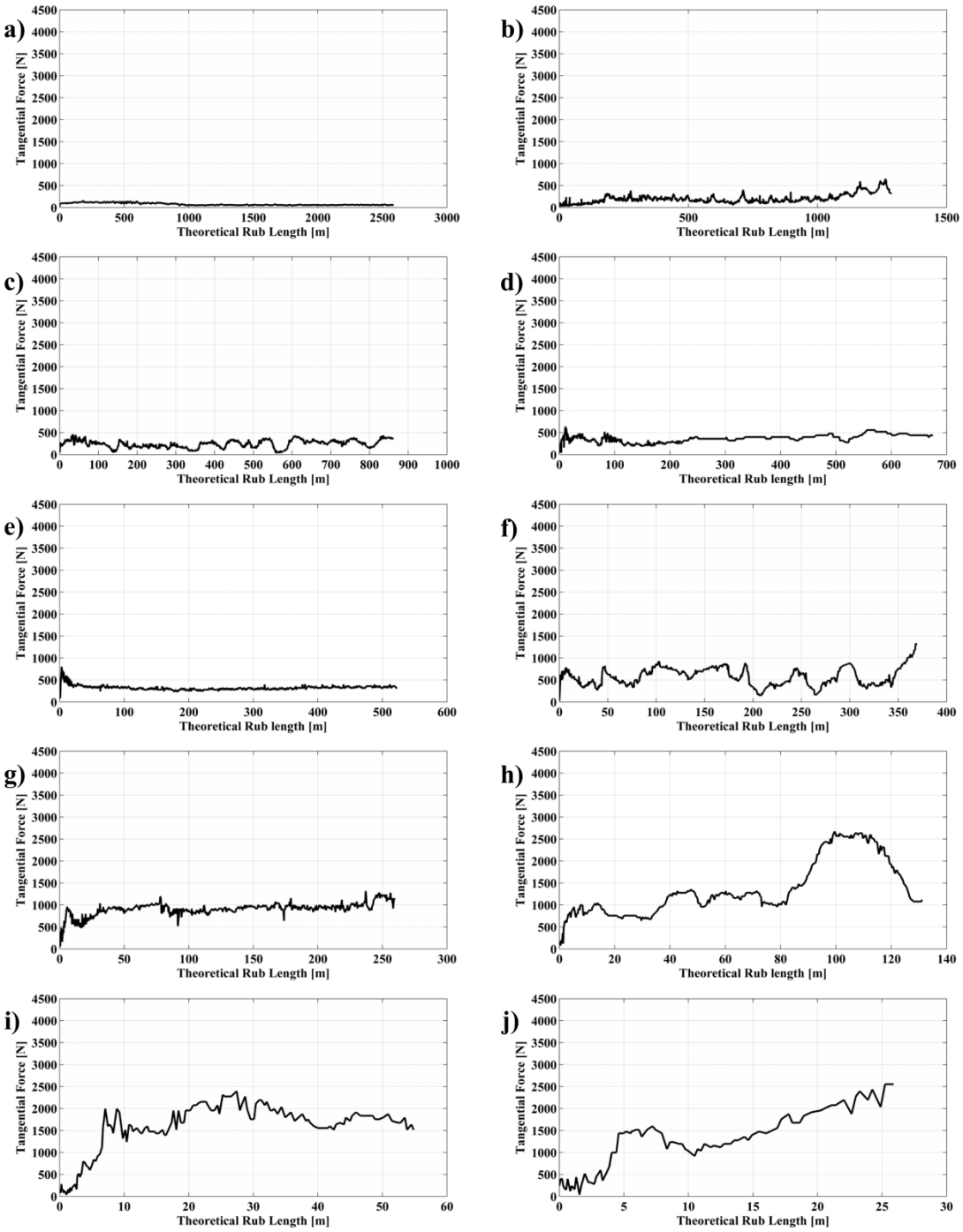

Figure 7.3. Tangential force measurement at blade speed of 100m s^{-1} and abradable coating hardness R15Y 72.3, at incursion rates of: a) 0.02µm·$pass^{-1}$; b) 0.04µm·$pass^{-1}$; c) 0.06µm·$pass^{-1}$; d) 0.08µm·$pass^{-1}$; e) 0.1µm·$pass^{-1}$; f) 0.14µm·$pass^{-1}$; g) 0.2µm·$pass^{-1}$; h) 0.4µm·$pass^{-1}$; i) 1µm·$pass^{-1}$; j) 2µm·$pass^{-1}$.

As shown in the figures, especially at a low incursion rate (e.g. Figure 7.2a), the normal force rises to a maximum, and then remains at a more steady state value for the remainder of the test. A similar trend was observed with respect to the tangential force (Figure 7.3a), but in this case the trend was less pronounced. An increase in the

incursion rate produced an overall increase of the cutting forces as shown in the figures. Intermediate incursion rates (Figures 7.2, 7.3 c, d, f) were characterised by a continuous variation of the force along the theoretical rub length. At a high incursion rate (Figures 7.2j and 7.3j), an overall higher force was measured, increasing to a maximum value followed by a slight variation of the force, especially for the normal force (Figure 7.2j). As shown in Figures 7.2 and 7.3, the normal and tangential forces were subject to significant variation throughout a given test and over the range of test conditions analysed. However, the force results can also be compared to the evolution of blade length change results, as shown in Figure 7.4 at low, intermediate and high incursion rates.

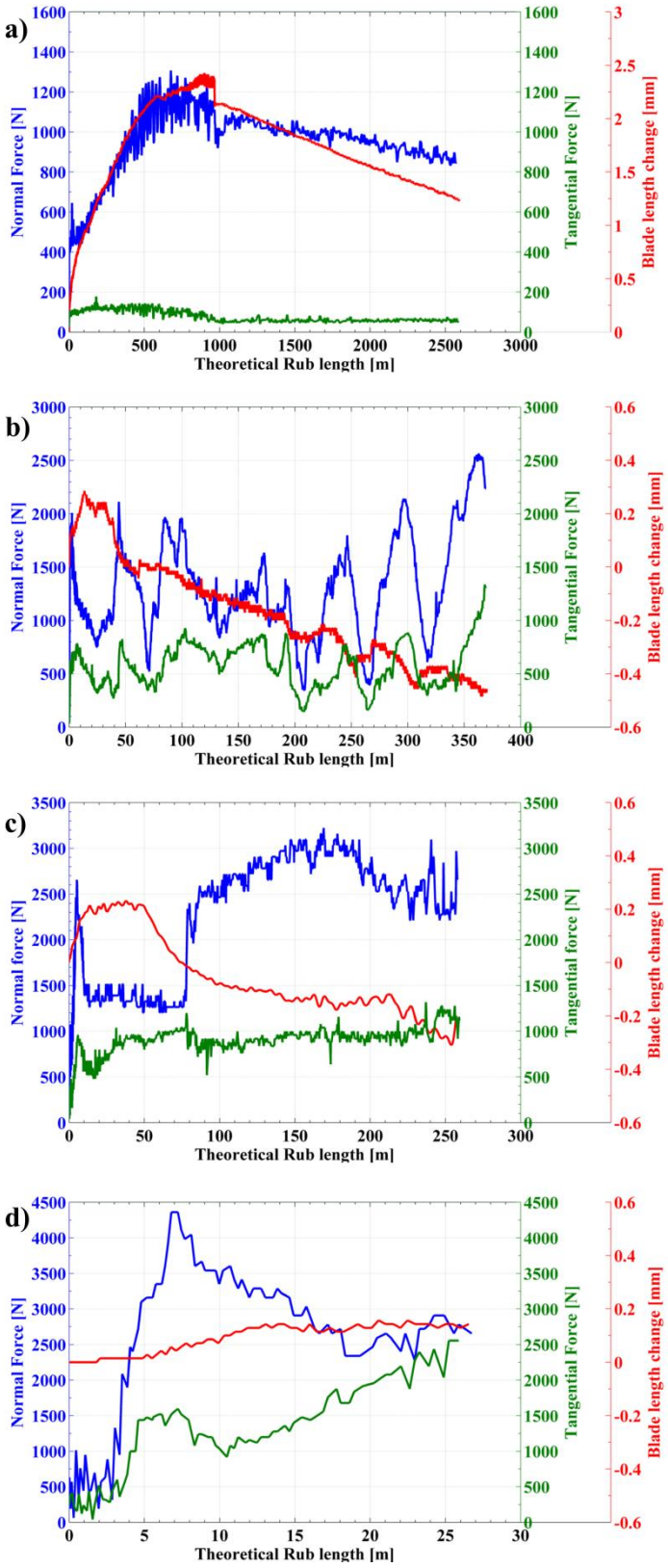

Figure 7.4. Blade length change and normal and tangential forces measurement at blade speed 100m s^{-1} hardness coating of R15Y 72.3 and incursion rate of: a) 0.02µm $pass^{-1}$; b) 0.14µm $pass^{-1}$; c) 0.2µm $pass^{-1}$; d) 2µm $pass^{-1}$.

As shown in the figure, the blade length and force scales were set differently in order to observe better the force trend compared with the blade length change at different incursion rates. Figure 7.4 shows the correlation between the blade length change, which articulates the evolution of the wear mechanism, and the contact force that represents the energy required to break the material. At a low incursion rate (Figure 7.4a) where adhesive transfer was observed, an increase in the force corresponded to an increase of blade length. Then, corresponding to the adhesive material fracturing, a decrease of the force was observed, where in the steady-state phase of the force a slight decrease of the normal force was measured, with a corresponding blade length reduction, suggesting a decrease of the blade contact. The test performed at an incursion rate of 0.14μm $pass^{-1}$ (Figure 7.4b) highlighted a correlation between the spikes observed on the force and the blade length results. The similar variation of the blade length compared with the spike observed in the force signal, suggested a non-continuous contact between the blade tip and the coating during the rub phase.

However, some differences between the force and evolution of blade length were observed for the data measured at an incursion rate of 0.2μm $pass^{-1}$ (Figure 7.4c). After an initial increase of the normal and tangential forces, evident differences of normal force were measured, with a decrease in the force followed by a uniform value that corresponded to zero variation of the blade length. This was followed by an increase in the normal force corresponding to blade wear. The non-variation of the blade length suggested that there was no variation in the contact, while when the blade started to wear a change of the force was recorded. Finally, at a high incursion rate (Figure 7.4d), a slight variation of the blade length was measured, corresponding to a higher force, where a well-cut surface was observed.

Overall, the trend of the force showed a correlation with the wear mechanism articulated by the blade length change. When adhesive transfer was observed, an increase of the force followed by a steady state phase was recorded, while when a blade wear was observed, with in addition a continuous variation of the blade length, a corresponding spike of the force was measured, suggesting a non-uniform contact. However, the correlation between blade length and force was not always observed very clearly; for example, for the data measured at an incursion rate of 0.2μm $pass^{-1}$. This could be associated with the stroboscopic technique which acquired a side view of the blade tip and acquired the current maximum blade length, and had limitations

for acquiring adhesive transfer and wear along the blade depth, but overall the technique articulated the contact mechanism.

Additionally, significantly different forces were measured in relation to the incursion rate, where from low to high incursion rates the wear mechanism changed from adhesion to cutting. As highlighted in the previous chapter, an increase in the speed did not determine different wear mechanisms. However, the next section presents the analysis that was made of the influence of the speed on the force measurement.

7.2. R15Y 72.3 force measurements at different blade speeds

The influence of the speed was observed in relation to force measurements for the test performed with coating R15Y 72.3; the rest of the hardnesses investigated will be presented in the next sections. The force measurements for different speeds were plotted for three different incursion rates: low, 0.02µm pass^{-1}, where adhesive transfer was recorded; intermediate, 0.2µm pass^{-1}, where initial adhesion and cutting were recorded; and finally high incursion rate, 2µm pass^{-1}, where cutting wear was recorded. The intermediate value was chosen on a scale proportional to the low and high incursion conditions. The results are shown in Figure 7.5.

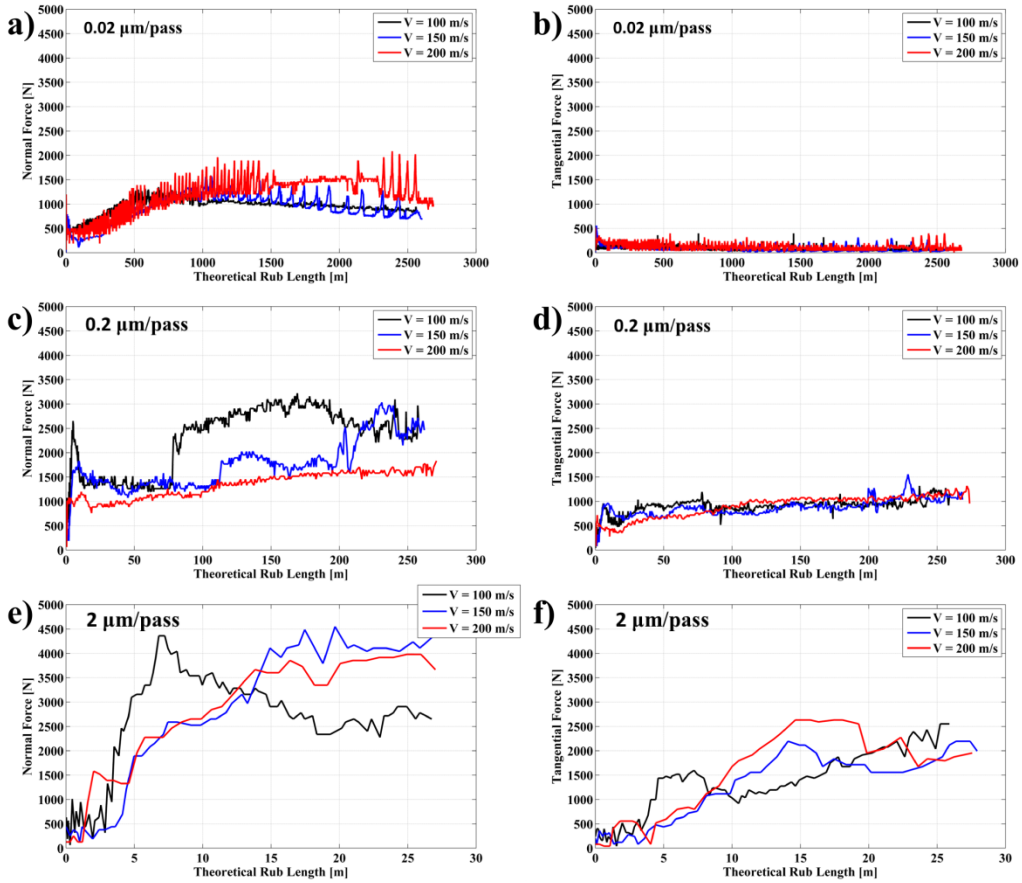

Figure 7.5. Force measurement at blade speed of 100m s^{-1} (black curve), 150m s^{-1} (blue curve) and 200m s^{-1} (red curve), with abradable coating hardness R15Y 72.3, at incursion rates of: a) 0.02µm·pass^{-1} normal force; b) 0.02µm·pass^{-1} tangential force; c) 0.2µm·pass^{-1} normal force; d) 0.2µm·pass^{-1} tangential force; e) 2µm·pass^{-1} normal force; f) 2µm·pass^{-1} tangential force.

As shown in the figure, similar trends were observed at different speeds. The only different trend observed with speed was at an incursion rate of 0.2µm pass^{-1} for

normal force (Figure 7.5c). Therefore, the force trends were compared with the blade length changes in order to understand the change, as shown in Figure 7.6.

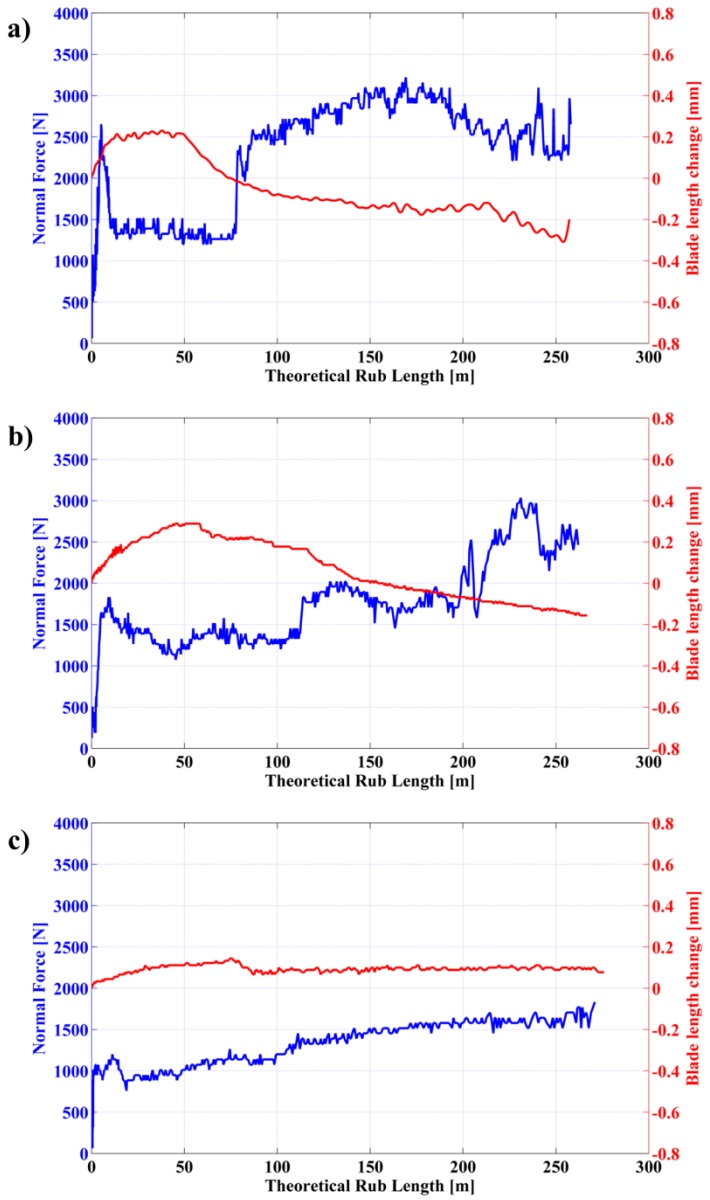

Figure 7.6. Normal force measurement and blade length change at an incursion rate of 0.2µm pass^{-1}, hardness coating of R15Y 72.3 and blade speed of: a) 100m s^{-1}; b) 150m s^{-1}; c) 200m s^{-1}.

As shown in the figure, similar trends at all speeds were observed when initial adhesion was measured, and then more variability in the contact force was observed, especially at low and intermediate speeds (Figure 7.6 a, b), when the blade wore. At high speed (Figure 7.6c), however, after a slight blade wear no variation of the blade length was measured and no significant changes in the force were observed.

The increase and variability of the force when the blade wore suggests a non-uniform contact of the blade during the rub phase, and therefore different levels of wear and adhesion were observed along the blade. Furthermore, the change observed only in the normal force could be associated with variability of the wear mechanism during the contact where different levels of adhesion and wear were observed, but also with the variability of the thermal spray coating process [13, 14, 45, 46] and the associated variability of the achieved coating [5, 13].

However, overall similar trends were observed with an increase of the speed, and a similar wear mechanism was observed, highlighting that the speed did not generate a significant change in force measurements for the hard coating. As previously mentioned, different wear mechanisms were observed with different hardnessess; therefore in the next section the force measurements for the rest of the tests performed were compared with the measurement with the hard coating.

7.3. Force measurements at different coating hardness

The force measurements for the rest of the tests are presented in this section. The observation of the post-test wear mechanisms (Figure 5.18) and the blade length change indicated different wear mechanisms with changing hardness, especially at low incursion rate, and therefore the force measurements performed with coatings R15Y 59.6 and 54.6 were compared with those with coating R15Y 72.3 in order to understand if different wear mechanisms resulted in different contact forces. The force measurements on the test performed with coating hardness R15Y 63 were not recorded, because the samples were tested at a stage of the research where only the stroboscopic technique was introduced, therefore in relation to the samples provided from Rolls Royce, samples with a hardness R15Y 59.6 were tested, and the analysis of the wear mechanism output and blade length change highlighted comparable results.

Figure 7.7 shows the measurements of normal and tangential forces at a blade speed of 100m s^{-1} for all coating hardnesses at incursion rates of 0.02, 0.2, 2μm $pass^{-1}$ respectively, where the intermediate value was chosen on a scale proportional to the low and high incursion conditions, while the force measurements recorded for the rest of the incursion rates are shown in Appendix 4.

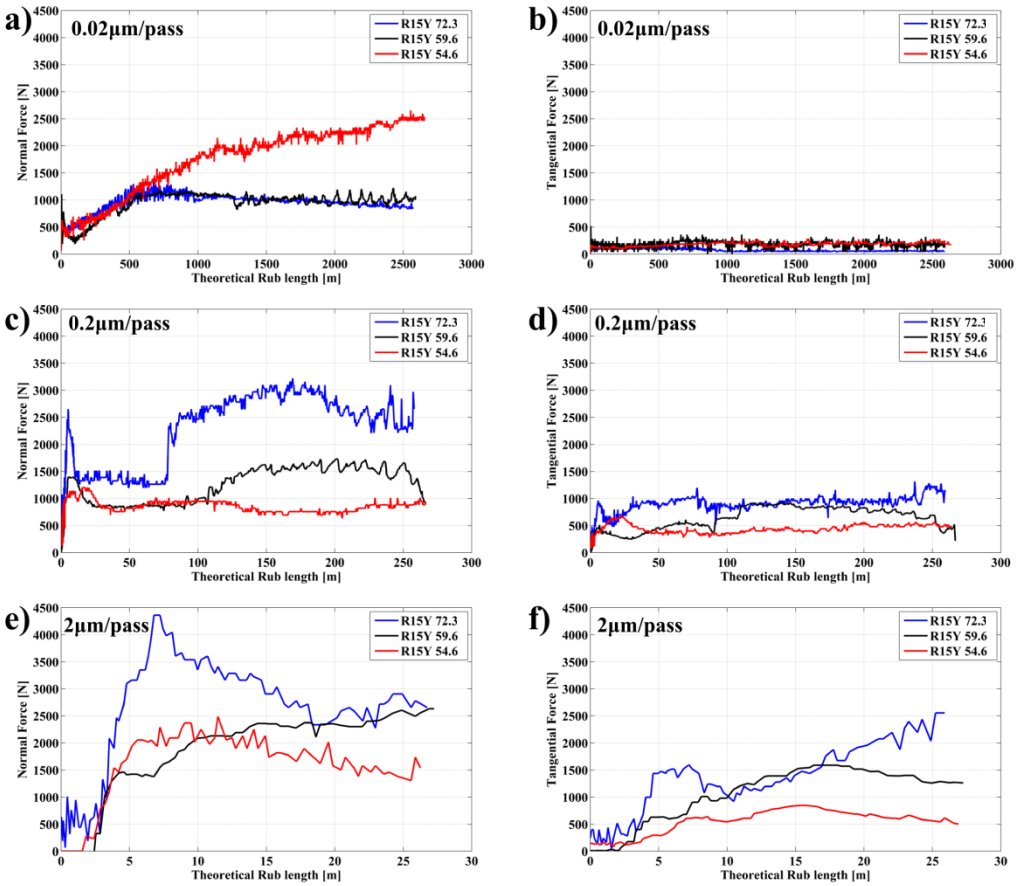

Figure 7.7. Normal and tangential forces measurement at blade speed of 100m s^{-1} with coating hardness R15Y 72.3, R15Y 59.6 and R15Y 54.6, at an incursion rate of: a) 0.02µm $pass^{-1}$ normal force; b) 0.02µm $pass^{-1}$ tangential force; c) 0.2µm $pass^{-1}$ normal force; d) 0.2µm $pass^{-1}$ tangential force; e) 2µm $pass^{-1}$ normal force; f) 2µm $pass^{-1}$ tangential force.

As shown in the figure, corresponding to different wear mechanisms observed, a different trend of the contact force was measured especially at low incursion rate, where adhesive transfer on the hard coating and blade wear on the soft coating were observed.

For the test performed against the hard coating (R15Y 72.3), the normal force increased until the maximum value was reached, followed by a steady state force, with low tangential force, and adhesive transfer followed by blade wear was observed. The force increased when the adhesive transfer increased, and then, corresponding to the maximum adhesive transfer, the force reached a maximum, and in the steady-state phase a slight blade reduction was measured. In the test performed against the coating with hardness of R15Y 59.6 (Figure 7.7 a, b), a similar force trend to that with the hard coating was measured, but was characterised by spikes in

the steady-state phase, corresponding to the blade wear phase, suggesting non-continuous contact of the blade. Therefore, a mix of adhesion and blade wear was observed for this coating. On the coating with hardness R15Y 54.6, a continuous increase of the normal force was recorded (Figure 7.7 a, b, red curve), with a constant low value of the tangential force corresponding to a continuous blade wear, with a melt layer evident on the rub surface (Figure 5.7). Hence a different wear mechanism was observed and the force suggests different material behaviour.

At the intermediate incursion rate (Figure 7.7 c, d), a decrease of the force was measured with a decrease of the coating hardness. The trends in the force data were similar for the tests performed with hard and intermediate coatings, where adhesion and blade wear were observed, and an overall lower force was seen on the soft coating characterized by blade wear. The spikes observed at the intermediate incursion rate, once again implied a non-continuous contact between the blade and abradable (Figure 7.4b).

At a high incursion rate, similar trends were observed at different hardnesses, with an increase of the force up to the maximum value, followed by a steady phase, with a decrease of the force as coating hardness reduced. This suggested that less force was necessary to remove the softer material during the contact.

Overall, different wear mechanisms, especially at low incursion rate, highlighted different force trends between the hard coating and the soft coating, characterised respectively by an increase of the force followed by a steady phase, and a continuous increase of the force for the soft coating, suggesting a different material behaviour that led to a different wear mechanism.

In order to have an overall view of the parameters influencing the contact force, the influence of the blade speed for the rest of the tests was analysed, and will be presented in the next section.

7.4. Influence of blade speed for intermediate and low coating hardness

Different wear mechanisms and force trends were found with different coating hardnesses, especially at low incursion rate. The influence of the blade speed on the force measurement was also analysed for the rest of the tests, even though no significant changes were observed on the hard coating. Figure 7.8 shows the normal and tangential forces at incursion rates of 0.02, 0.2 and 2µm pass^{-1}, with blade speeds of 100, 150, 200m s^{-1} for coating hardness R15Y 59.6.

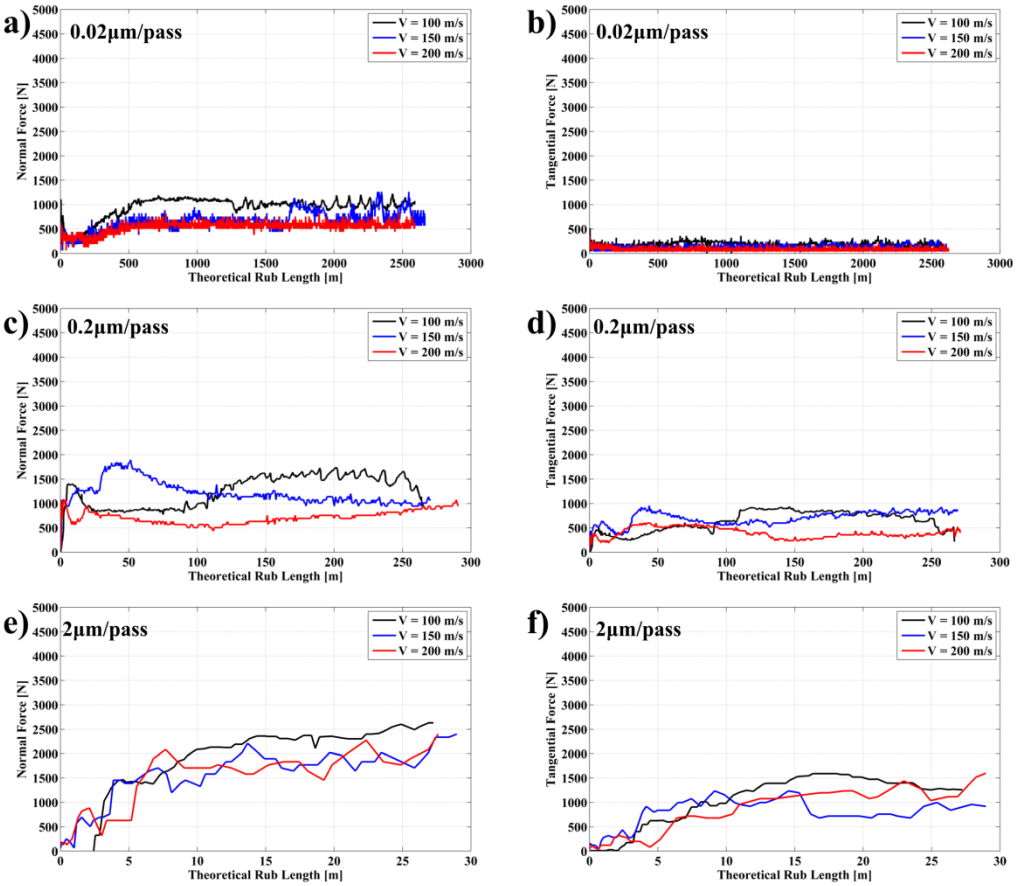

Figure 7.8. Normal and tangential force measurement at blade speed of 100m s^{-1} (black curve), 150m s^{-1} (blue curve) and 200m s^{-1} (red curve), with abradable coating hardness R15Y 59.6, at incursion rates of: a) 0.02µm·pass^{-1} normal force; b) 0.02µm·pass^{-1} tangential force; c) 0.2µm·pass^{-1} normal force; d) 0.2µm·pass^{-1} tangential force; e) 2µm·pass^{-1} normal force; f) 2µm·pass^{-1} tangential force.

As shown in the figure, an increase of the speed did not highlight a different trend, especially at intermediate and high incursion rates (Figure 7.8 c, d, e, f), when cutting occurs, and similar values of forces were measured at the different speeds. Whilst analysis of machining processes [61] suggests an increase in the speed may lead to material softening and improve shearing [62], leading to a decrease of the force necessary to remove material at higher speeds, this was not evident here. Whilst it could be argued that the higher forces observed at the low incursion rate at the slowest speed support this view, this result results is isolated and further investigation is required.

Overall, no clear consistent trends were observed with the speed and similar wear mechanisms were observed. Furthermore, it was difficult to discern an influence of the speed due to the variability of the wear evolution and material, which suggested that the speed range might also not be wide enough to observe change.

Finally, the influence of the speed was observed for the test performed with the coating with hardness R15Y 54.6, because previous analysis had highlighted differences in the wear mechanism, especially at low incursion rate (Figure 7.9).

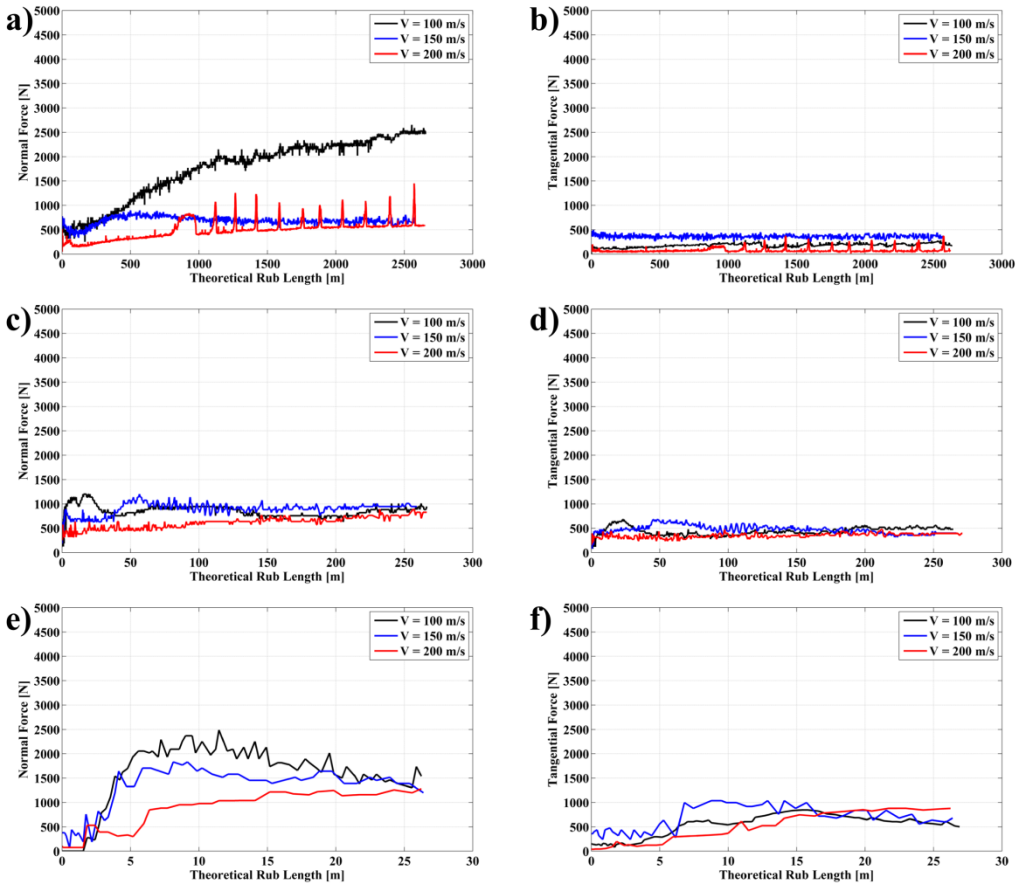

Figure 7.9. Normal and tangential force measurement at blade speed of 100m s^{-1} (black curve), 150m s^{-1} (blue curve) and 200m s^{-1} (red curve), with abradable coating hardness R15Y 54.6, at incursion rates of: a) 0.02µm·$pass^{-1}$ normal force; b) 0.02µm·$pass^{-1}$ tangential force; c) 0.2µm·$pass^{-1}$ normal force; d) 0.2µm·$pass^{-1}$ tangential force; e) 2µm·$pass^{-1}$ normal force; f) 2µm·$pass^{-1}$ tangential force.

As shown in the figure, at intermediate and high incursion rates, similar trends were observed. The forces at intermediate and high incursion rates (Figure 7.9 c, d, e, f) were also largely ordered with respect to speed. This implied that less force was required to cut at higher speed, but the difference in the result was still marginal, as observed in the test performed on the coating R15Y 59.6.

However, at low incursion rate (Figure 7.9 a, b) a clear difference with speed was observed when compared to the coating with hardness R15Y 59.6, with a higher force measured at low speed and a progressive decrease of the force with speed. At low incursion rate and low speed a continuous increase of the normal force was recorded, and coincided with continuous blade wear, while intermediate and high speeds were characterised by similar force trends but with a lower force required.

The different trends observed with speed, especially at a low incursion rate between low and high speed, were further investigated bringing together the force data, the blade length change and the images of the specimens post-test, as shown in Figure 7.10.

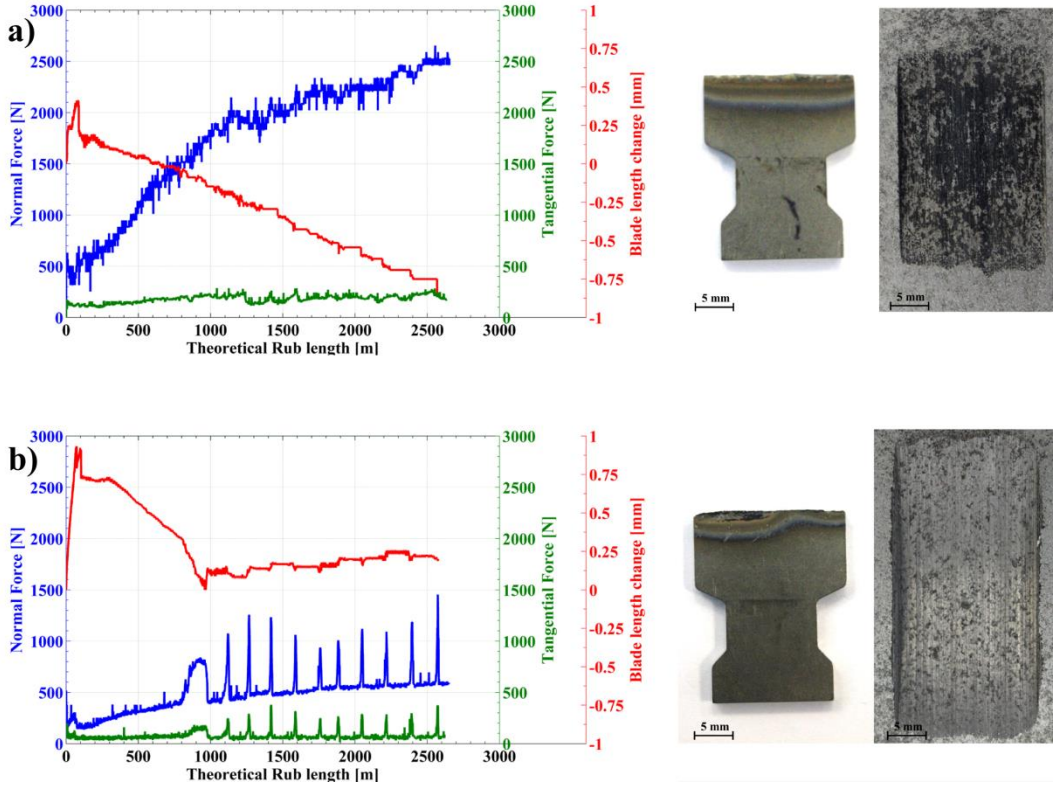

Figure 7.10. Blade length change (Red curve), Normal (Blue curve) and Tangential force (Green curve) measurement and blade sample post-test for the test performed with hardness coating of R15Y 54.6, and incursion rate of 0.02µm pass^{-1} and blade speed of: a) 100m s^{-1}; b) 200m s^{-1}.

As shown in the figure, a link between the blade length change and the force measurement was observed. At low speed (Figure 7.10a), a higher force was observed, with a continuous increase of the normal force and a steady low value of the tangential force, while the blade length change showed continuous blade wear, thermal damage on the blade tip, and also melt wear in the rub surface. At high speed (Figure 7.10b), a lower force was observed, with initial adhesion followed by blade wear and cyclic behaviour with less thermal effect and a well-cut appearance on the surface.

Observing the specimens, the speed caused a transition from melt wear to cutting, which was suggested from the reduction of melt wear and thermal damage, and also from the well-cut rub surface at high speed. In the case where melting material was observed (Figure 7.10a), the material was not cut well, and the blade pressed into the coating, resulting in a high normal force and a steady low value for the tangential force, resulting ultimately in blade wear. Conversely, at high speed (Figure 7.10b), some adhesion occurred followed by a small amount of blade loss. However, a steady state phase was reached where good cutting and lower forces compared with the low speed test, and periodic spikes in force were observed.

This observation suggests a transition to a cutting mechanism with an increase of the speed, and implies an associated lower temperature. Whilst higher speed suggests higher energy in the contact, and therefore higher heat which could promote higher adhesion or blade wear, it may also lead to an increase in impact speed and more fracture of the material. Therefore, further investigation was carried out by sectioning the samples and analysis the contact temperature (Chapter 8).

7.5. Average force measurements

In order to highlight the contact force results for different incursion rates and hardness coatings, an average of the normal and tangential forces over the duration of a given test was made. As shown before, the overall theoretical rub length was different at each incursion condition due to the limitation of the incursion depth and thickness of the coating. However, as demonstrated by Wang [64], steady-state thermal conditions were reached quickly for the range of rub lengths investigated in this study. Therefore the average was taken over the duration of the test. The average components of normal and tangential forces were plotted against the incursion rate at blade speeds of 100, 150 and 200m s^{-1}, for hardnesses R15Y 72.3, R15Y 59.6 and R15Y 54.6. Indicative trend lines were then plotted in order to highlight the change in the average force, as shown in Figures 7.11 and 7.12.

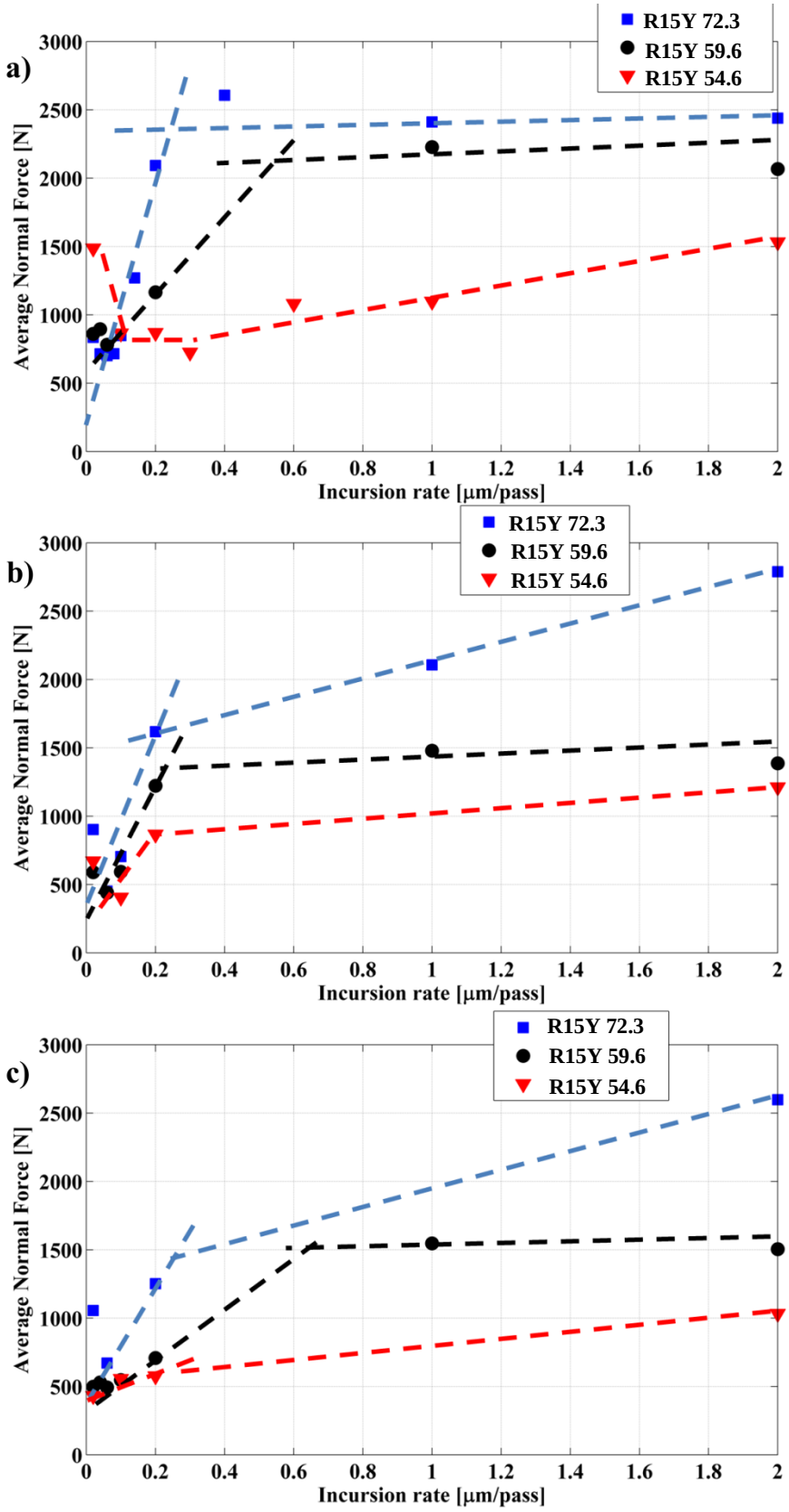

Figure 7.11. Average normal force measurement for different hardness tested (blue curve R15Y 72.3, black curve R15Y 59.6 and red curve R15Y 54.6) and blade speed of: a) 100m s^{-1}; b) 150m s^{-1}; c) 200m s^{-1}.

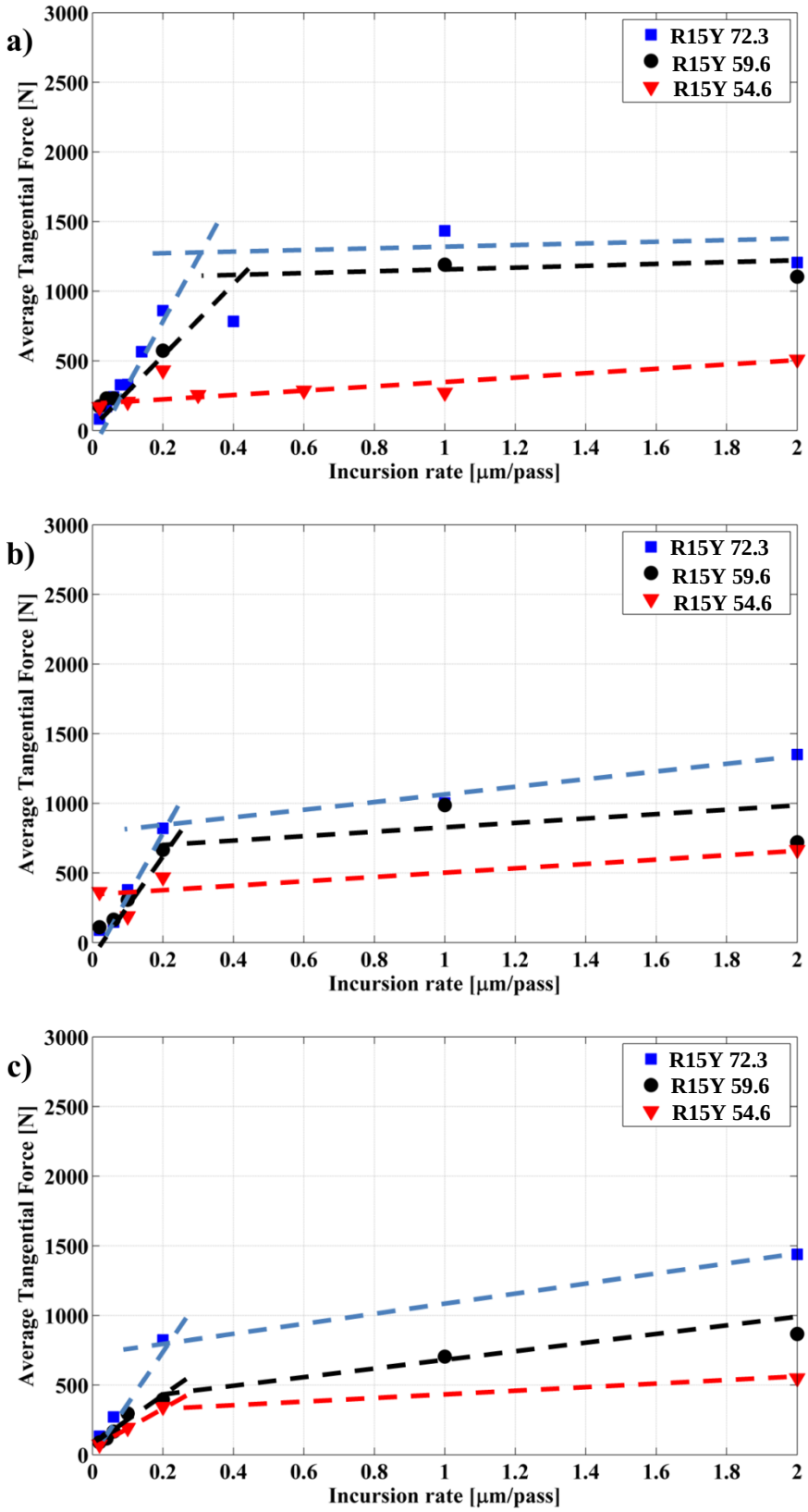

Figure 7.12. Average tangential force measurement for different hardness tested (blue curve R15Y 72.3, black curve R15Y 59.6 and red curve R15Y 54.6) and blade speed of: a) 100m s^{-1}; b) 150m s^{-1}; c) 200m s^{-1}.

As shown in the figures, the average normal and tangential forces had similar trends, with a rapid increase with the incursion rate before plateauing off showing a slow rate of increase at higher values of incursion rate, especially observed with the tests performed with the coatings with hardness R15Y 72.3 and R15Y 59.6. On the test performed with coating R15Y 54.6, a different trend was observed, especially at low speed (Figure 7.11a), and a different wear mechanism was observed compared with that for the hard coating. In this case a high force was evident at low incursion rate, then a decrease was followed by no variation and then a progressive increase of the force until high incursion rates were reached, while Figure 7.12a shows a gradual increase of the force for the tangential component. Additionally different average forces were measured in relation to coating hardness, with a decrease of the cutting force with a decrease of the hardness, suggesting that less energy was required to remove material when the coating hardness decreases. Furthermore, similar forces were observed with an increase of the speed, especially on hard and intermediate coating tests, while some change was observed with the soft coating, as highlighted in Figure 7.10 at the low incursion rate.

The force data analysis highlighted an increase of the average force with an increase of the incursion rate; however, on the soft coating a difference was observed as described above. A higher normal average force was measured at low incursion rate where the material was observed not to be cut well, while with an increase of the incursion rate a lower average force was measured. The lower force required to remove material and the well-cut surface suggest a transition from melt wear to cutting at low speed. Also an increase of the speed highlighted a decrease of the average normal force at low incursion rate and also the well-cut rub surface, suggesting a transition from melt wear to cutting happening at lower incursion rates compared to the test performed at low speed. This will be further analysed in Section 8.1 by sectioning and observing the material response.

In addition, the variation of the average force for the hard coating was inverse in form when compared to the graph of rate of adhesion, while the average force trend for the soft coating was similar to the trend of the rate of wear, as shown in Figure 7.13.

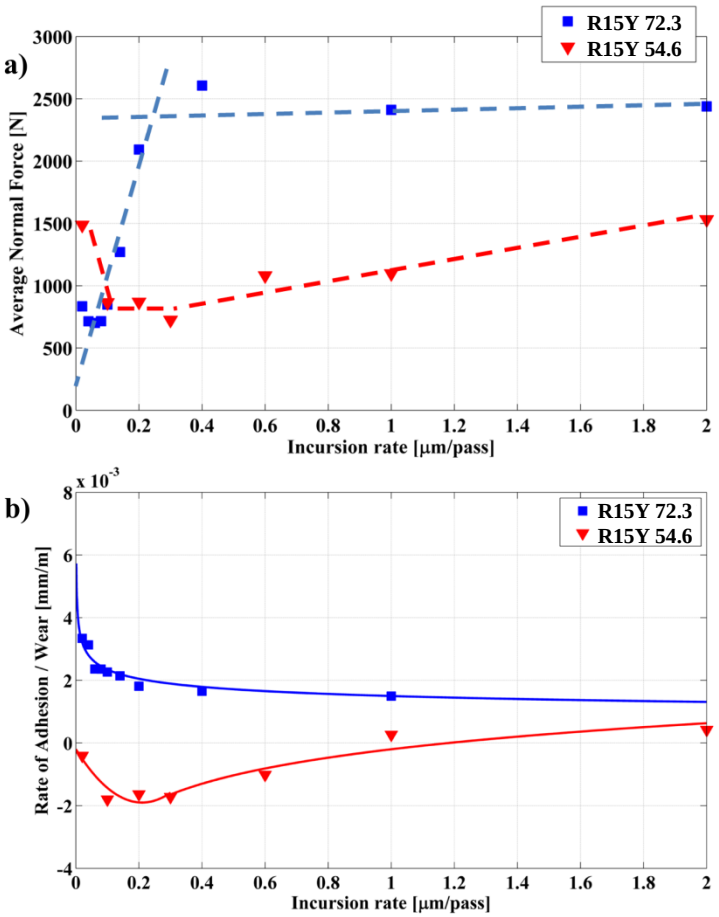

Figure 7.13. Average normal force and rate of adhesion / wear for the sample with hardness R15Y 72.3 and R15Y 54.6 at blade speed 100m s^{-1}: a) Normal force; b) Rate of adhesion / wear.

As shown in the figure, a rapid increase of the force corresponded to a high adhesion rate (blue curve), and was followed by a decrease of the rate of force and of the rate of adhesion as well. On the soft coating, a similar trend was observed between the average normal force and the rate of wear (red curve), where a high average force corresponded to a high rate of wear, with a gradual decrease in the rate of wear as the force increases with high incursion rate. This highlighted the relationship between average force and the rate of adhesion / wear that characterised the wear mechanism, and this holds with Archard's [34, 35] model of wear, where the wear increased with a decrease of the hardness, and increases with an increase of load.

Overall a different trend was observed between the hard and soft coating, from adhesion to cutting for the hard coating, and melt wear to a cutting mechanism for the soft coating. This analysis also highlighted that a different force was required to

remove material in relation to the incursion rate. Overall it suggests that factors such as hardness and incursion rate lead to significantly different material removal mechanisms, with different efficiencies and associated energies. Therefore, in the next section further investigation was made regarding the analysis of the energy required to remove material and the efficiency of this process.

7.6. Discussion

The previous analysis highlighted a link between the wear mechanisms characterised by the stroboscopic technique and the different forces measured, as well as a relationship between the average force and the rate of adhesion / wear. As discussed, these results suggested that a different energy was necessary to remove material and therefore the efficiency of cut, or rather the energy input, was calculated, and will be discussed in the next section.

7.6.1. Efficiency of cut

The efficiency of cut represents the energy to remove material; in a machining process it is determined from analysis of the energy required to remove a unit of volume of material [18-22]. In this case, the analysis was performed at each incursion rate. The force at a defined incursion rate (F_i) was determined from the square root of the sum of the squares of the average components ($F_{normal}, F_{tangential}$), as shown in Equation (7.1).

$$\boldsymbol{F_i = \sqrt{F_{normal}^2 + F_{tangential}^2}} \tag{7.1}$$

Then the resultant force was divided by the incursion per pass (I_{pass}), as shown in Equation (7.2).

$$\boldsymbol{\frac{F_i}{I_{pass}} = \frac{\sqrt{F_{normal}^2 + F_{tangential}^2}}{I_{pass}}} \tag{7.2}$$

The force per unit of incursion rate per pass was plotted against the incursion rate. This parameter could be correlated to the efficiency of cut, and therefore a high value represented that a high force per unit of incursion was required to remove material, and therefore it was difficult to cut the material. Otherwise a lower value expressed that a low force per unit of incursion was necessary in order to cut the material.

Figure 7.14 shows the average force per unit of incursion rate per pass plotted against the incursion rate.

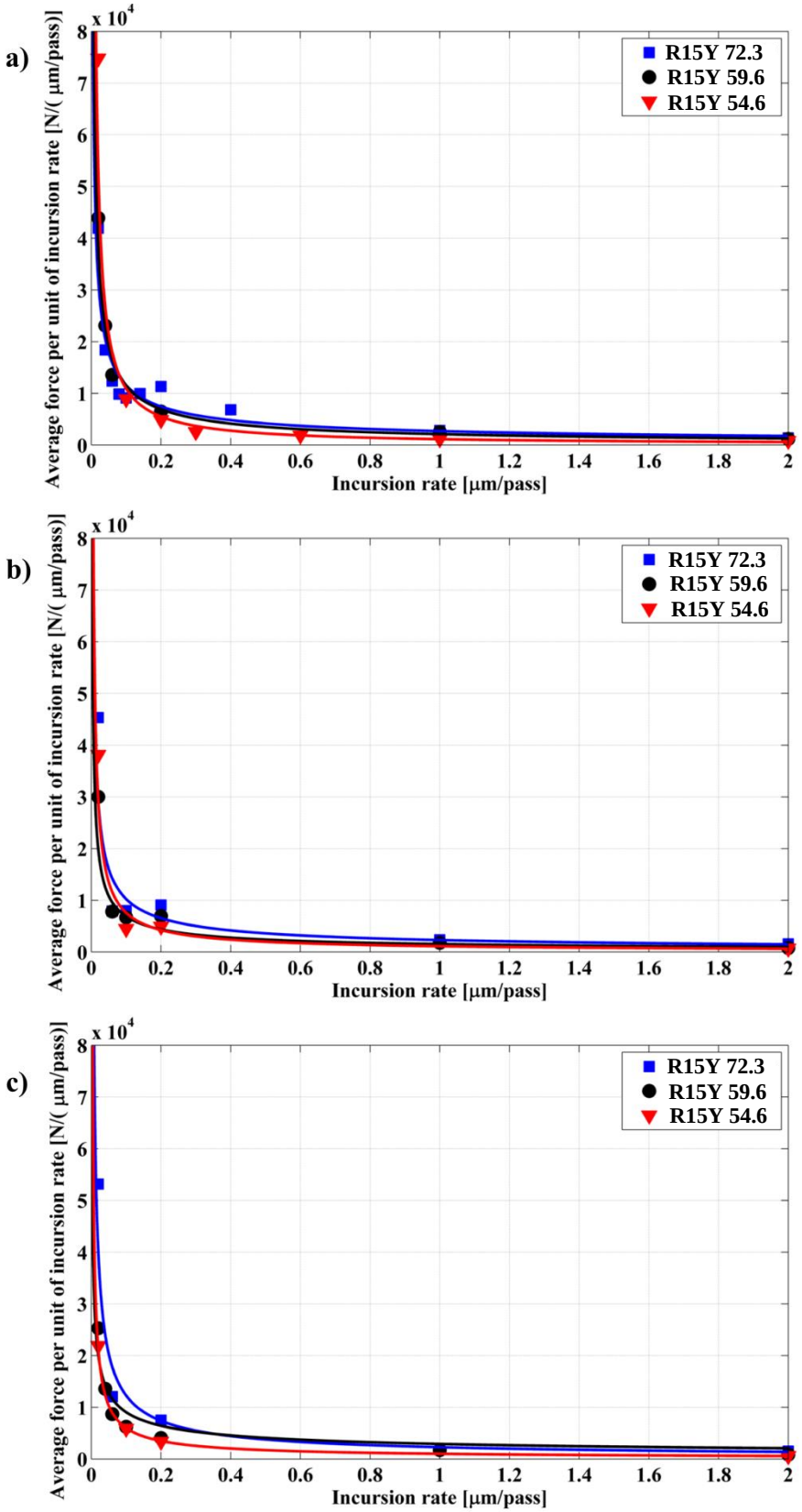

Figure 7.14. The average force per unit of incursion per pass against the incursion rate for the test performed at blade speed: a) 100m s^{-1}; b) 150m s^{-1}; c) 200m s^{-1}.

As shown in Figure 7.14, an increase of the incursion rate determined a progressive decrease of the force per unit of incursion rate. This meant that an increase of the incursion rate resulted in an increase of efficiency of cut because less force was required to cut a unit of material.

At a low incursion rate, a high value of the force per unit of incursion rate represented a lower efficiency of cut and a difficulty in removing material. This was based on the observed wear mechanism and the fact that adhesive transfer and blade wear are thermally driven processes, and the high energy required to remove material leads to heat generation. At a low incursion rate and low speed (Figure 7.14a) on the soft coating (R15Y 54.6) the force per unit of incursion rate was almost double that for the hard coating, suggesting a lower efficiency of cut on the soft coating and a difficulty in removing material, and therefore a high energy was likely produced in the contact, leading to the observed blade wear and thermal damage.

At a high incursion rate, all coatings (Figure 7.14 a, b, c) had a lower force per unit of incursion. This means a high efficiency of cut, indeed the material post-test was well-cut with no blade damage. Also, a slightly lower value of force per unit of incursion for the soft coating was observed at a high incursion rate, suggesting a better efficiency of cut, and less energy was required for cutting a soft material. As shown in Section 3.1.4, the percentage of the constituent phases varied with hardness, with an increase of dislocator phase correlating to a decrease of the hardness, and being likely responsible for this observation.

An increase in the speed decreased the energy required to remove material, increasing the efficiency of cut, especially on the soft coating (7.14c) where a significant reduction suggests an increase in the ability to remove material. Therefore, a well-cut surface was observed at high speed (Figure 7.10b), suggesting transition of the wear mechanism. Additionally, an increase of the speed for the hard and intermediate coatings produced a similar value for efficiency of cut, and therefore a similar wear mechanism was observed at different speeds.

The introduction of the efficiency of cut highlighted the different energies required between low and high incursion rates, and a difference between hard and soft coatings, especially at low incursion rate. The high energy required at low incursion rate suggests difficulty in cutting the material. This suggests that the material

behaviour changed between low and high incursion rates, and also between hard and soft coatings, where a higher energy was required at low speed and low incursion rate, where blade wear and a high level of thermal damage were observed. In order to understand the reason for more energy being required at a low incursion rate and to understand the material behaviour, the force ratio between the tangential and normal forces was calculated, which represented the material behaviour in a machining process [98].

7.6.2. Force ratio

The material behaviour was analysed in terms of force ratio, namely the ratio between the average tangential and normal contact forces. The force ratio represents the material behaviour in relation to chip formation in material cutting [18 – 25]. In the machining process, a low tangential motion, and therefore a low force ratio, implies a deformation of the material, with the blade rubbing on the surface with consequent difficulty in cutting the material [20]. This occurs when the incursion is smaller than the minimum un-deformed chip [100], as shown in Figure 7.15a. With an increase of the incursion, the blade starts to remove material with part of the chip starting to shear over elastic deformation, as shown in Figure 7.15b, until the incursions are higher than the un-deformed chip, with high force ratio, and the entire depth of cut is fractured and removed as a chip [101], as shown in Figure 7.15c. This analysis gives an insight to the mechanics of the process.

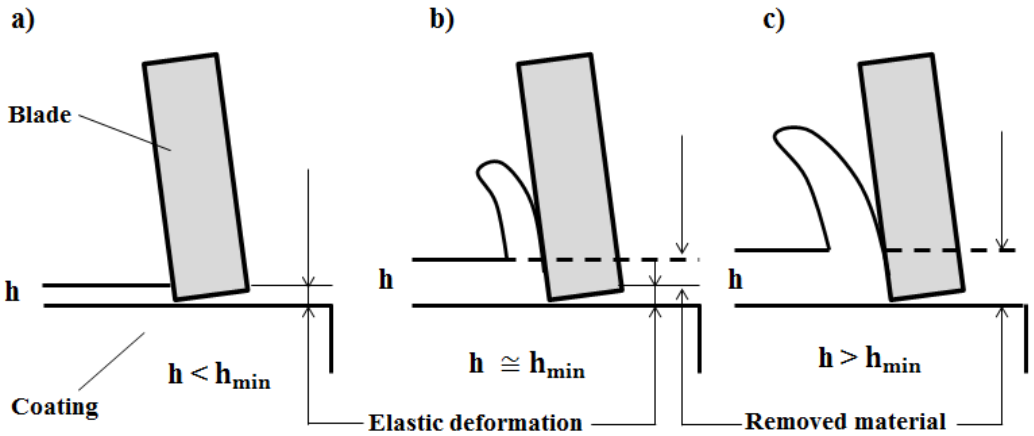

Figure 7.15. Schematic of chip formation: a) Elastic deformation; b) Elastic deformation and material removed; c) Material removed.

As shown in the figure, force ratio gives a representation of the material behaviour in machining in relation to the chip formation during a cutting process [100]. Figure 7.16 shows the force ratio as a function of the incursion rate, with indicative trend lines, at different blade speeds and in relation to the coating hardness.

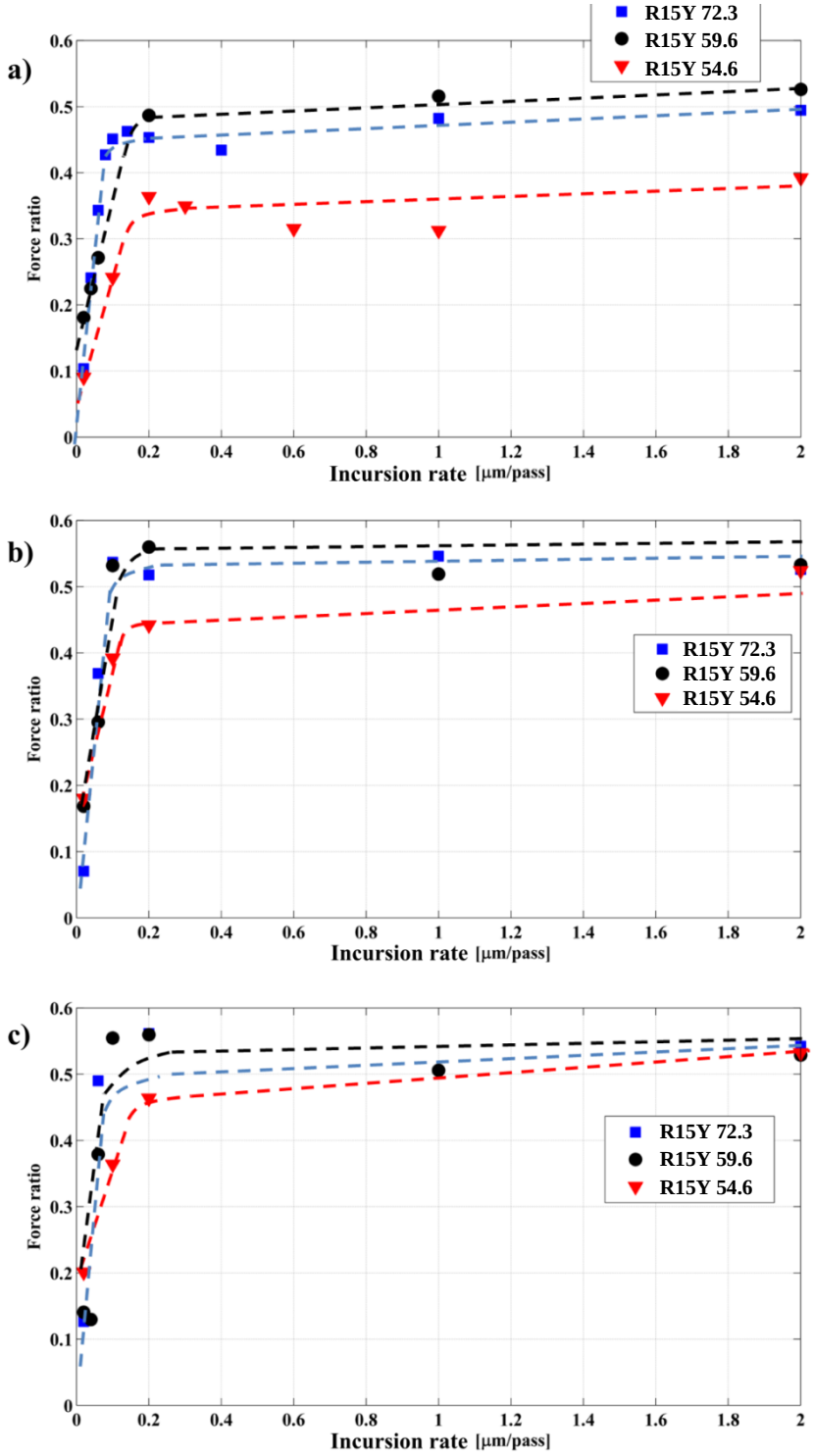

Figure 7.16. Force ratio vs incursion rate for abradable hardness R15Y 72.3, R15Y 59.6, R15Y 54.6, at blade speed of: a) 100m s^{-1}; b) 150m s^{-1}; c) 200m s^{-1}.

As shown in the figure, a similar trend was observed for different hardnesses and speeds, with a rapid increase with incursion rate before levelling off and only showing a slow rate of increase at higher values of incursion rate.

At low incursion rate it was observed that more energy was required to remove material, and this coincides with the force ratio being low. This implies a low resistance to tangential motion, with a high normal force, suggesting that the blade rubbing on the coating surface. From a machining point of view this suggests that the blade is deforming and rubbing the material [100]. Thermal damage, adhesive transfer and blade wear were observed on the blade and grooving on the coating surface. This suggests that the material was difficult to dislocate, even with high energy input. Also, the value of the force ratio was similar to that for a lubricated contact [102], and it is interesting to note that a melt layer was observed especially on the test performed against the soft coating and on the head of the groove on the hard coating.

Conversely, an increase of incursion rate led to an increase of force ratio. This suggests an increase in shearing over elastic deformation of the chip, increasing the ability to remove the material until a transition from adhesion / wear to cutting was observed. A similar force ratio to that found in orthogonal cutting of brittle materials [103, 104, 105] was then observed, where the entire depth of cut was removed without generating a continuous chip or large particles. This corresponds to the well-cut surface that was observed for all hardnesses and speeds at a high incursion rate.

As shown in Figure 7.16, at the lower speeds, a lower force ratio was measured on the soft coating compared to the test performed with the harder coatings. As discussed this is linked to the aforementioned rubbing and melt wear detailed at low incursion rate, but also highlights an increased ability to dislocate at high incursion rate. This is likely as a consequence of the previously highlighted increase in dislocator phase at this hardness [13].

With regard to the test performed with the intermediate coating hardness, a non-uniform wear mechanism was highlighted during this research. A slightly higher value of force ratio was observed and the material response will be analysed in the next chapter. The variability of the mechanism and the mix between adhesion and wear at low incursion, and also the scatter in the force, suggested a threshold

hardness for the change in wear mechanism, with more variable behaviour and output between the hard and the soft coatings.

In addition, the observation of the force ratio at different speeds highlighted similar trends as for low speed, confirming that a similar wear mechanism was observed. However, a higher force ratio with an increase of speed highlighted a greater ability to dislocate the material. For the soft coating, at a low incursion rate and a high speed, the force ratio was almost double compared to that at low speed, confirming a transition from predominantly melt layer to an increased amount of cutting that was highlighted from the force analysis. Therefore, the material response will be analysed in the next chapter.

Furthermore, the curve of the force ratio for the coating with hardness R15Y 72.3 was inverse in form when compared to the plot of the adhesion / wear curve. Additionally, the force ratio and rate of wear for the coating R15Y 54.6 were plotted, characterised by a different wear mechanism when compared with the hard coating, as shown in Figure 7.17.

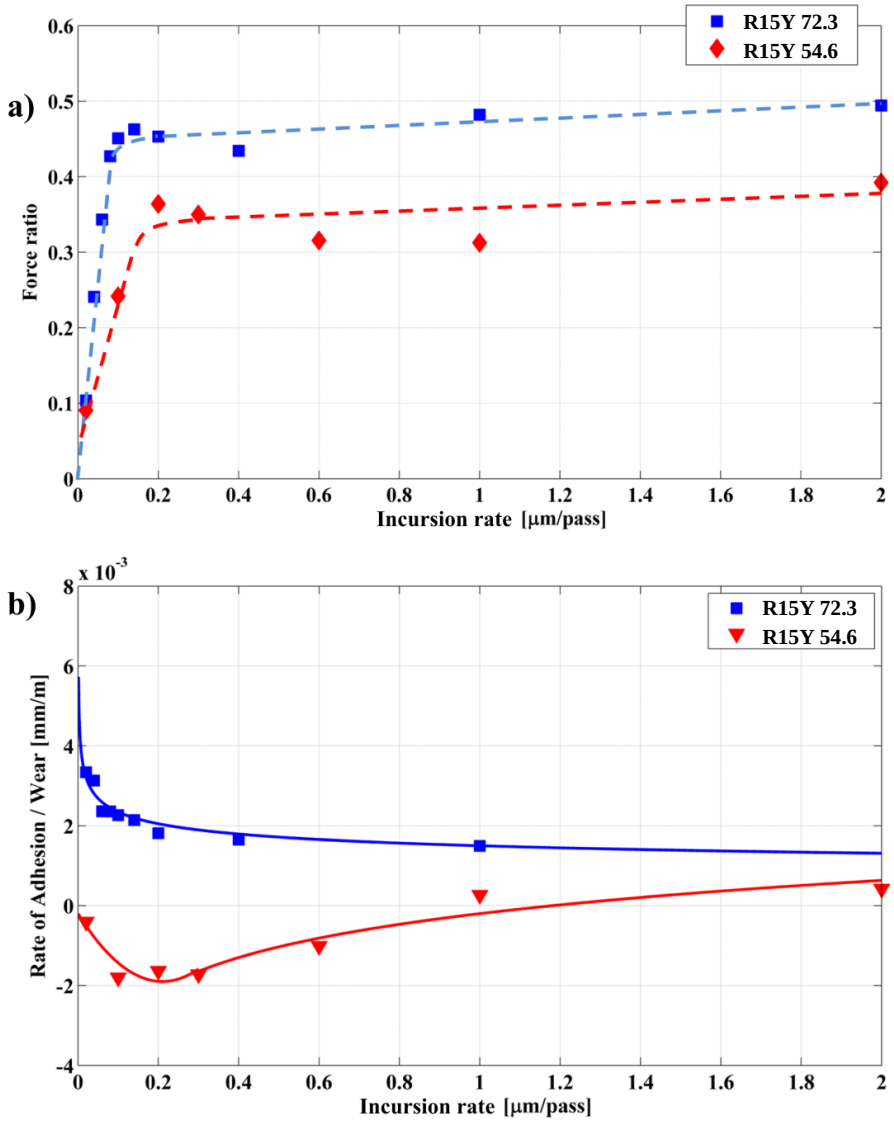

Figure 7.17. Force ratio and rate of adhesion/wear for the test performed with hardness coating R15Y 72.3 and R15Y 54.6 at blade speed of 100m s^{-1}: a) Force ratio; b) Rate of adhesion / wear.

As shown in the figure, by characterising the wear mechanism using the rate of adhesion / wear, along with the ability of the material to form a chip as represented by the force ratio, provided further information concerning the transition in wear mechanism. On the hard coating, the observation of the material post-test suggested a transition from adhesion to cutting at an incursion rate of 0.06µm $pass^{-1}$. This coincided with a drop in the rate of adhesion (Figure 7.17b), also a force ratio comparable to a value for orthogonal cutting. This confirms that it represented a value of incursion rate where the blade started to cut the coating. For the soft coating, the value of transition of the incursion rate was at 0.2µm $pass^{-1}$, where the force ratio

suggested cutting and the rate of wear decreased. It is also interesting to note, as highlighted in the previous chapter, that a lower wear rate was observed at low incursion rate, and an initial adhesion might reduce the rate. However, the low force ratio still indicated a melt layer and a difficulty in dislocating. For the test performed with hardness R15Y 59.6, the force ratio suggested a transition at around 0.2μm $pass^{-1}$, but the test highlighted a mix of adhesion and wear and therefore the transition value was less clear. Further investigation into the material response was therefore made with material sectioning (Section 8.1). Also, almost all of the tests performed with an increase of the speed produced similar wear mechanisms, and a comparable transition was observed, except on the soft coating, where an increase of the speed highlighted at a low incursion rate a transition from melt wear to an increasing amount of cutting. In this case almost double the force ratio was observed compared with that at the low speed.

As the force ratio suggested different material behaviour, material sections were made, and will be described in the next chapter. These were performed in order to understand if material rubbing or cutting was occurring in relation to the force ratio. Also, the difficulty to dislocate at low incursion rate and the high energy input required suggested the generation of heat in the contact, based on the observation of high level of thermal damage. Therefore, thermal analysis of the material was also performed using a pyrometer in order to measure the temperature during the contact, and also the thermal properties of the coating was also investigated.

7.7. Progress of analysis

As assessed in chapter 5, the observation of images post-test, clearly revealed different wear mechanisms and highlights the bulk changes in relation to incursion rates, hardness and speed. However, quantitative analyses based on blade length and weight change post-test failed to identify clear numerical relationships with respect to input parameters. Using the stroboscopic technique developed in this work the adhesion and wear could be quantitatively assessed and these relationships explored. However, this still gave limited insight into the reasons behind the different behaviour observed.

In this chapter the force data presented has gone a long way to explaining how the material behaves, and why the different wear mechanisms are likely to occur. For example, whilst force increased with incursion rate, the energy input per unit volume and efficiency of cut were shown to be unsatisfactory at low incursion rate. These metrics both highlighted that different energies were required between low and high incursion rates, and between hard and soft coatings. This suggests a change in material behaviour and revealed difficulties in cutting the material at certain conditions. Accordingly, measurement of the force ratio went further in highlighting the difficulty in dislocating the material, especially at low incursion rates where a low value was measured. While at high incursion rate a similar value to orthogonal cutting, suggest ability to dislocate the material.

Whilst this discussion is able to clearly link the wear mechanics (based on the stroboscopic technique) and the energy input (through the measurement of force), further investigation is still required with respect to the thermo-mechanical response of the material. For example, the high force and high energy required to remove material at low incursion rates and thermal damage observed suggest heat build-up in the contact, however, the outcome of this in terms of the blade was different as a function of hardness. Therefore the material response by material sectioning will be examined and coating temperature measured, in order to try to understand the nature of the wear mechanism further.

7.8. Chapter summary

- The contact force highlighted that the wear mechanism was incursion rate dependent, from adhesion / wear to cutting, but also hardness dependent, especially at low incursion rate. There was no evident change with an increase of the speed, except on the soft coating where an increase of the speed generated a transition to cutting.

- The contact force was linked to the evolution of the blade length that characterised the wear mechanism.

- A different force was required to remove material depending on the incursion rate between low and high incursion rates, and also there was a difference between hard and soft coatings at low incursion rate.

- A different energy input in relation to the incursion rate highlighted that a high energy was required at low incursion rate with relative difficulty in removing material, and a thermal mechanism was observed.

- Low energy was required to remove the material at high incursion rate, and a well-cut surface was observed.

- The force ratio gives a representation of the material behaviour, and suggests blade rubbing and deforming of the coating at low incursion rate, while fracturing of the material and removal of the entire depth of cut occurred at high incursion rate.

8. Thermo-Mechanical Material Response

As described in the previous chapters, the wear mechanism was incursion rate dependent, as well as hardness dependent. This was especially the case at low incursion rate where adhesion transfer and blade wear were observed with hard and soft coatings, respectively. The previous chapter highlighted that a different energy was required to remove material depending on the incursion rate, and the coating hardness. The different value of force ratio in these cases also suggested different material behaviour. At high incursion rate, a high efficiency of cut was measured, suggesting an ability to dislocate the material and to remove the entire depth of cut,

and a well-cut surface was observed with no thermal damage. However, at low incursion rate, a high energy required suggested difficulty in cutting the material. Indeed the force ratio suggested that the blade deformed the coating dislocation not occurring. This resulted in a thermal wear mechanism where adhesion, thermal damage and blade wear with titanium transfer were observed. Therefore, this chapter describes how the material response was analysed with material sectioning in order to understand if the material was rubbing or cutting, as suggested from the force ratio observed. Also, when cutting efficiency was low, and high energy was required, a thermal damage and thermal wear mechanism were observed; accordingly, a measurement of the coating temperature and thermal properties were performed in order to understand if the energy input led to a high temperature and to justify the different nature of the wear mechanisms in relation to the incursion rate and coating hardness.

8.1. Material response

The analysis of the efficiency of cut, and the force ratio, suggested a different material response when a different wear mechanism was observed. Therefore, as discussed in Section 4.2.6, the material post-test was sectioned in the longitudinal and transverse directions with respect to the blade strike. Once prepared, the samples were inspected using an optical microscope. The sectioning was performed for the sample at hardnesses R15Y 72.3, R15Y 59.6 and R15Y 54.6, where differences in the wear mechanism were observed. As previously discussed, a different wear mechanism was observed between low and high incursion rate, and in relation to the hardness.

Table 8.1 summarises the material sectioned, showing the test condition, the rate of adhesion / wear that characterised the wear mechanism and the force ratio that characterised the material response in terms of chip formation.

Coating hardness [R15Y]	Incursion per pass [µm]	Blade speed [m s^{-1}]	Rate of adhesion / wear [10^{-3} mm m^{-1}]	Force ratio	Wear mechanism
72.3	0.02	100	3.34	0.10	Adhesion
72.3	0.06	100	2.36	0.34	Adhesion / Cutting
72.3	0.2	100	1.81	0.45	Cutting
72.3	2	100	1.43	0.49	Cutting
54.6	0.02	100	-0.41	0.09	Melt wear
54.6	0.2	100	-1.63	0.36	Wear / Cutting
54.6	2	100	0.42	0.39	Cutting
54.6	0.02	150	-0.08	0.18	Wear / Cutting
54.6	0.02	200	-0.79	0.20	Melt wear / Cutting
59.6	0.02	100	12.57	0.18	Adhesion / Melt wear
59.6	0.2	100	0.91	0.49	Adhesion / Cutting
59.6	2	100	1.11	0.53	Cutting

Table 8.1. Material sectioned with summaries of the test conditions and rate of adhesion / wear and force ratio.

As shown in the table, the coatings characterised by predominant adhesion and blade wear, R15Y 72.3 and 54.6, respectively, were sectioned at low incursion rate, characterised by a low force ratio suggesting difficulty in dislocating. Therefore, the abradable was compressed due to the low superficial hardness of the coating, meaning fractured did not take place and rubbing as opposed to cutting occurred. A low force ratio means a low efficiency of cutting process observed for the soft and the hard coating, where in both cases the blade rubs instead of cutting and deforms the material. This is because the value of the incursion is smaller than the minimum un-deformed chip [100]. Also the material response at high incursion rate was analysed, where a low rate of adhesion / wear and high force ratio suggested the blade was fracturing the material. With regard to the sample tested at intermediate

incursion rate, the sample that corresponded to the incursion rate value of the transition in wear mechanics was sectioned in order to observe the change of mechanism. The sectioning was performed mainly on the tests performed at low speed (100m s^{-1}), as no evident change in wear mechanism was observed with speed, expect for the soft coating (R15Y 54.6), where at low incursion rate the speed produced some differences in the wear mechanism. A transition from predominantly melt wear to increasing amounts of cutting with increasing speed was observed. This was suggested from observing the sample and the measured increase of force ratio. Finally, the sample performed with intermediate coating hardness where a mix of mechanisms was observed was analysed. In the next section the material response of the coating with hardness R15Y 72.37 will be presented.

8.1.1. Material response of coating R15Y 72.3

Figure 8.1 shows the longitudinal section with respect to the direction of the blade strike (Figure 8.1a) of the coating at an incursion rate of 2µm $pass^{-1}$, and coating hardness R15Y 72.3, where the sample post-test highlighted a well-cut surface.

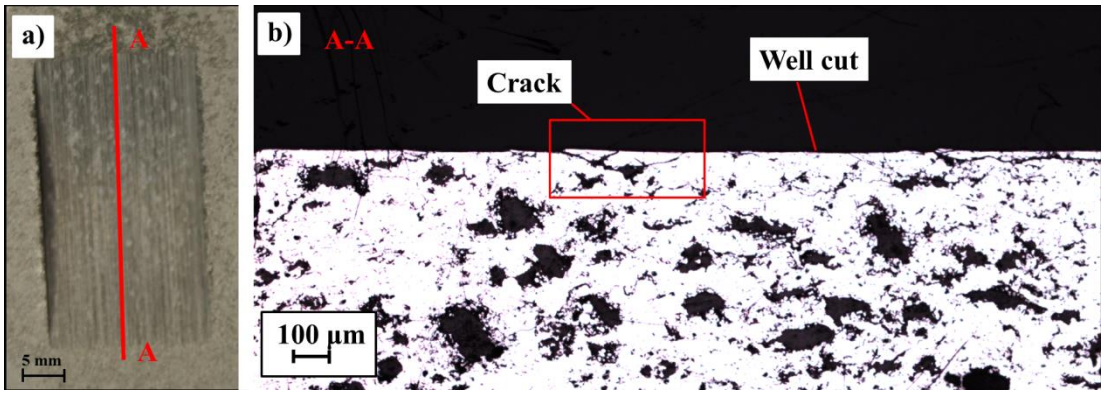

Figure 8.1. Image of section area of the coating and the microstructure of the sub-surface of the coating with hardness R15Y 72.3, at an incursion rate of 2µm $pass^{-1}$, blade speed 100m s^{-1}: a) Coating with the section A-A; b) Microstructure of the longitudinal section A-A.

As shown in the figure, the microstructure highlighted the metal phase, (AlSi) in white and hexagonal boron nitride (hBN) in black, of the abradable coating, and reflected the good cutting observed from the previous analysis. The smooth profile highlighted in the microstructure image showed what the force ratio suggested previously, and that the blade fractured the material and removed the entire depth of

cut without significant deformation. Also, a series of cracks and fractured particles of hBN spotted on the surface further confirmed fracture, and the presence of the brittle solid dislocator (hBN) [105] breaking readily, initiating cracks, increased the ability to dislocate under the force of the blade.

The previous analysis highlighted a change of wear mechanics with a decrease of the incursion rate, with a progressive change from cutting to adhesive transfer and grooving of the rub surface. The decrease in the efficiency of cut and also the force ratio suggested a change in material response with deformation of the material, with the blade rubbing instead of cutting. Indeed, a section of the coating was made at low incursion rate to observe the microstructure when a high energy was required to remove material, and also when a grooved rub surface was observed. Figure 8.2 shows the area of the section of the coating and the respective microstructure of the coating with hardness R15Y 72.3, at an incursion rate of 0.02µm pass^{-1}, and blade speed of 100 m s^{-1}.

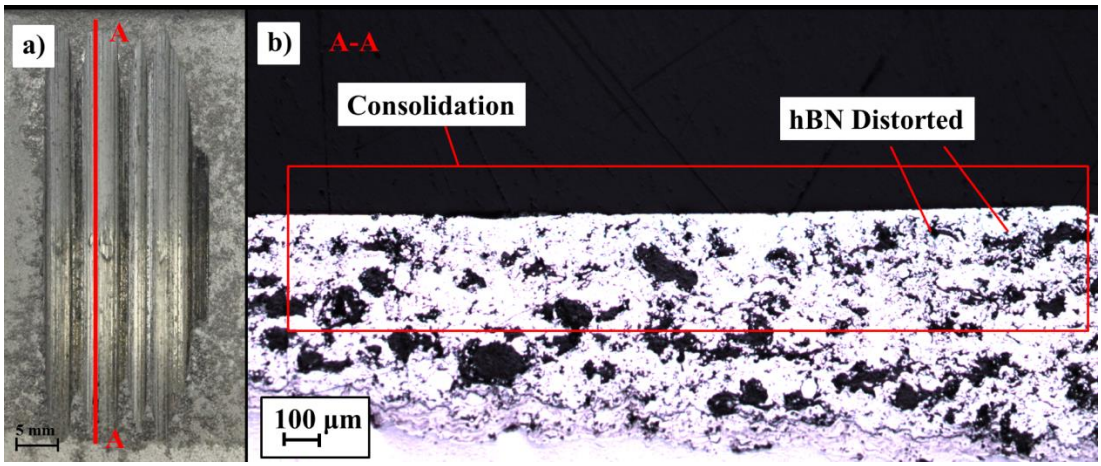

Figure 8.2. Image of section area of the coating and the microstructure of sub-surface of the coating with hardness R15Y 72.3, at an incursion rate of 0.02µm pass^{-1}, blade speed 100m s^{-1}: a) Coating with the section A-A; b) Microstructure of the longitudinal section A-A.

As shown on the microstructure of the longitudinal section, a consolidation of the coating occurred. This was highlighted by the fragmented, distorted hexagonal boron nitride phase (hBN black part, Figure 8.2b) in the proximity of the surface, along with a more continuous aluminium silicon phase (AlSi white part) at the surface itself, and confirmed a deformation of the material, as indicated by the low value of the force ratio.

The abradable surface was characterised by grooving as described in Chapter 5 and remarked on Figure 8.2a, with a different level of adhesion and blade wear along the blade. Therefore, a transverse section with respect to the direction of the blade cut was made in order to observe the microstructure of the groove. Figure 8.3a shows the location of the section performed along the rub, and Figures 8.3b and 8.3c respectively show the microstructure of the grooving at low locations, which correspond respectively to blade wear and adhesion transfer on the blade tip.

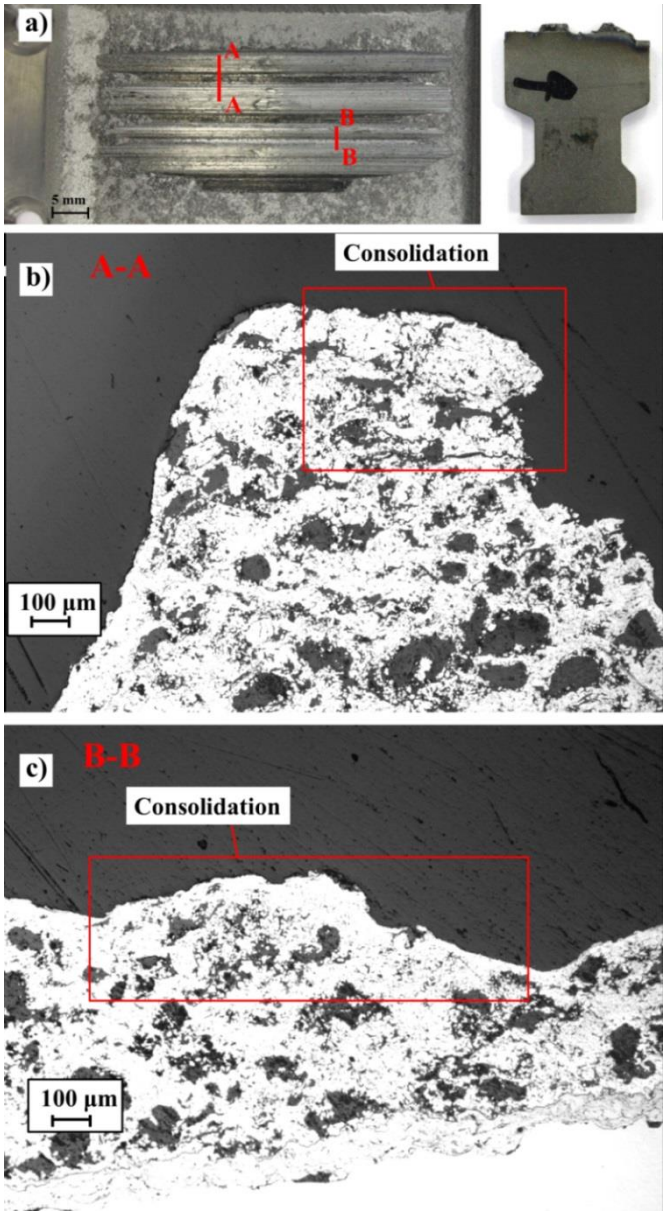

Figure 8.3. Image of the section area and the relative sections showing the microstructure of the sub-surface of the coating with hardness R15Y 72.3, at an incursion rate of 0.02µm·pass^{-1}, blade speed of 100m s^{-1}: a) Coating with section A-A and B-B; b) Transverse section A-A; b) Transverse section B-B.

As shown in the figure, consolidation was observed on the microstructure of the sample, suggesting rubbing rather than cutting of the material, evidenced by the distorted nature of boron nitride (hBN black constituent) on the top of the grooving where, corresponding to the blade, thermal damage was observed. Conversely, Figure 8.3c shows the transverse section taken from the trough of the groove, with less consolidation compared with the peak of the groove. At this location adhesive transfer on the blade was observed, therefore suggesting a different material response along the surface, and a different wear mechanism was observed. In order to investigate further, a magnification of the microstructure on the top of the groove was made, as shown in Figure 8.4. This was done in order to observe better the material response where melt layer was observed on the top of the groove (Figure 8.4a), corresponding to blade wear and thermal damage on the blade.

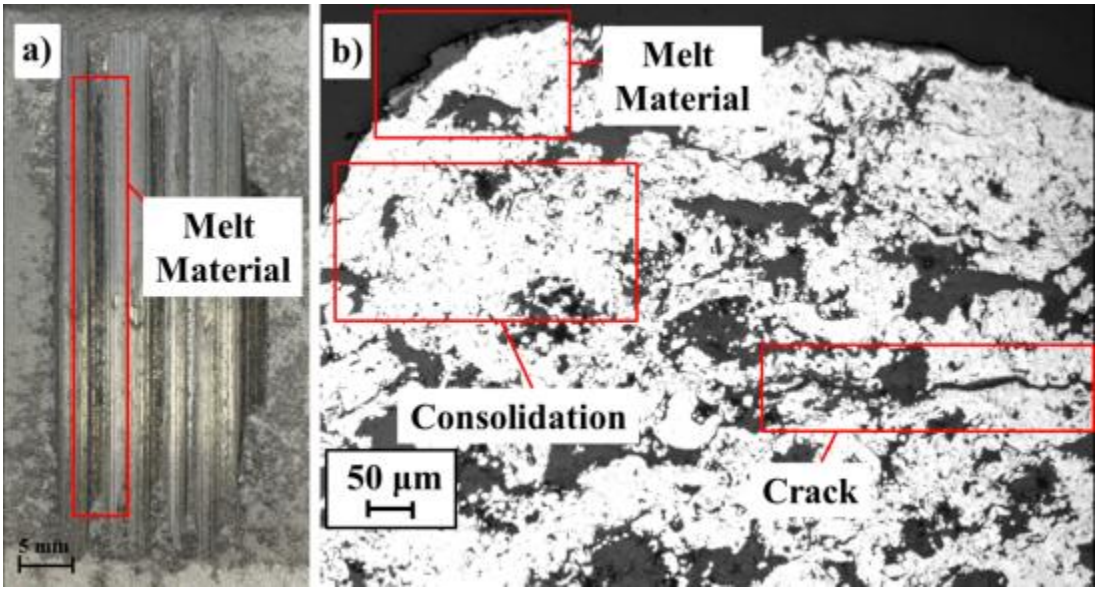

Figure 8.4. Section showing the microstructure of the sub-surface of the coating with hardness R15Y 72.3, at an incursion rate of 0.02µm·pass^{-1}, blade speed of 100m s^{-1}: a) coating after the test with melt material on the groove; b) higher magnification image of groove region.

The figure highlights the titanium transfer from the blade. A local concentration of hBN is also present in this area along with consolidation. Further investigation was made in relation to the concentration of hBN and will be discussed in Section 8.3. Also, a crack was evident on the groove (Figure 8.4b), perpendicular to the incursion and blade strike direction. The microstructure highlighted a different level of

consolidation along the rub area, reflecting a different wear mechanism and a level of thermal damage, suggesting a high temperature.

Previous analysis suggested a progressive change in wear mechanism from adhesive to cutting at a value of incursion rate of 0.06µm pass^{-1}, so a longitudinal section of microstructure was made, as shown in Figure 8.5.

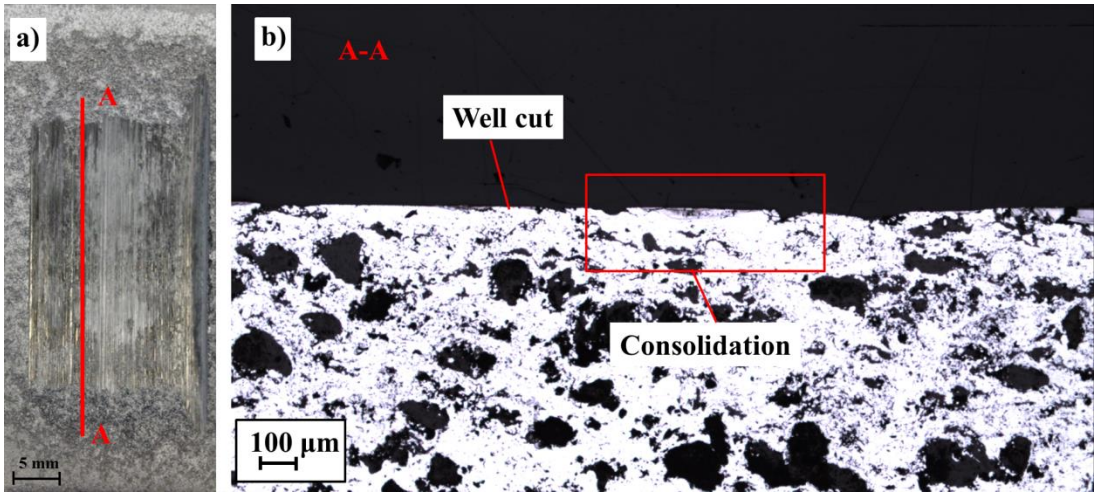

Figure 8.5. Image of the section area and the microstructure of the sub-surface of the coating with hardness R15Y 72.3, at an incursion rate of 0.06µm·pass^{-1}, blade speed of 100m s^{-1}: a) Coating with section A-A; b) Longitudinal section A-A.

As shown in the figure, the coating began to be well-cut, with minimal consolidation, and hBN fractured at the surface. This confirmed the suggestion that the efficiency of cut had increased, further evidenced by the increasing force ratio, with similar behaviour at an incursion rate of 0.2µm pass^{-1} (Figure 8.6).

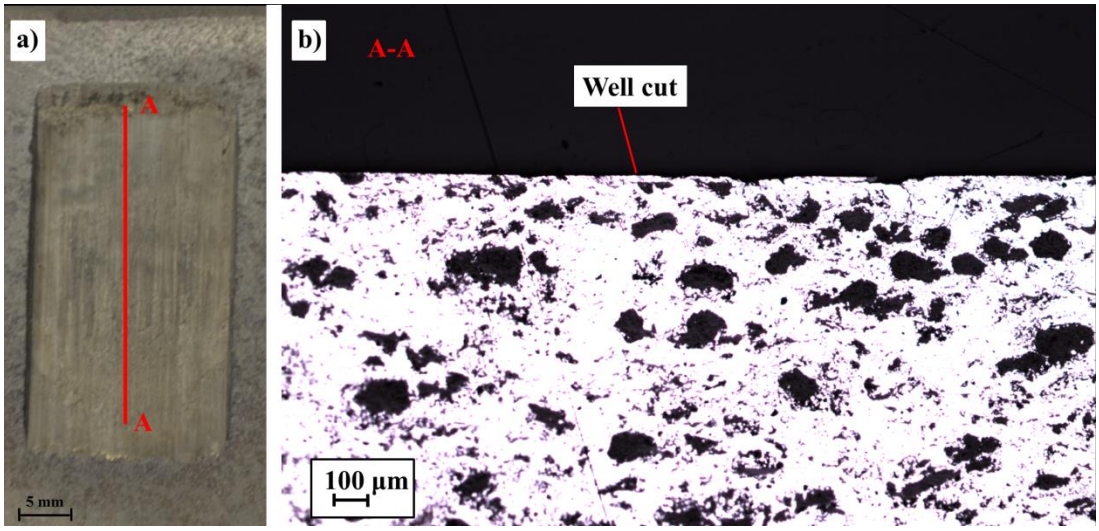

Figure 8.6. Image of the section area and the microstructure of the sub-surface of the coating with hardness R15Y 72.3, at an incursion rate of 0.2µm·pass^{-1}, blade speed of 100m s^{-1}: a) Coating with section A-A; b) Longitudinal section A-A.

As discussed previously, the microstructure showed negligible consolidation with fractured hBN, and compared favourably to the well-cut surface observed before at high incursion rate, confirming the increasing ability to cut.

Overall, the observation of the sample confirmed the different behaviour between low and high incursion rates, and highlighted the material response when adhesive transfer was observed, as well as when titanium transfer was present. The next section presents the analysis of the material response of the sample with hardness R15Y 54.6, which was conducted in order to observe the behaviour when blade wear was dominant.

8.1.2. Material response of coating R15Y 54.6

At a high incursion rate, the same cutting wear mechanism was observed, but with a higher efficiency of cut and lower force compared with the value measured on the harder coating. Therefore, the material post-test was sectioned in order to observe the material response. Figure 8.7 shows the longitudinal section of the coating with hardness R15Y 54.6, at an incursion rate of 2µm pass^{-1} and blade speed of 100m s^{-1}.

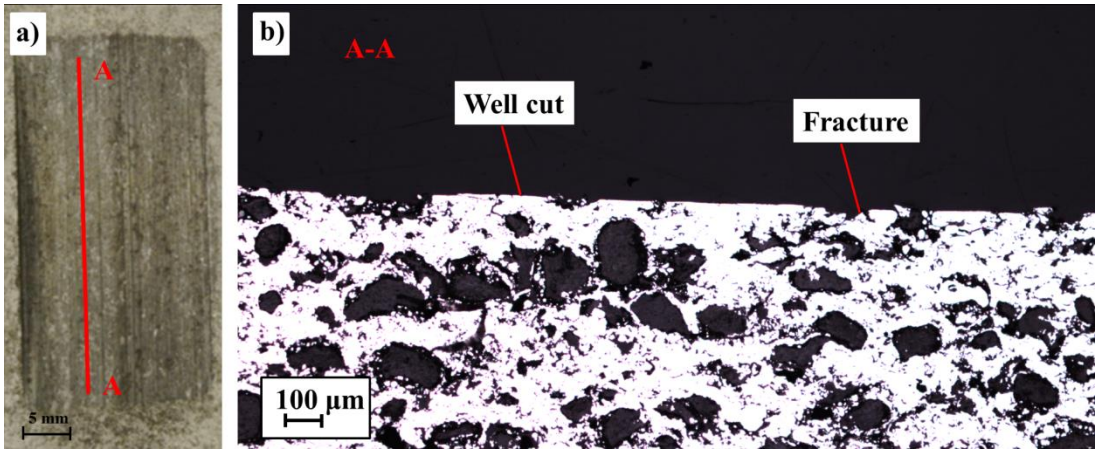

Figure 8.7. Image of the section area and the microstructure of the sub-surface of the coating with hardness R15Y 54.6, at an incursion rate of 2µm·pass^{-1}, blade speed of 100m s^{-1}: a) Coating with section A-A; b) Longitudinal section A-A.

As shown in the figure, a well-cut surface with fractured hBN confirmed the cutting mechanism suggested by the high efficiency of cut and the high force ratio. The microstructure when compared with the hard coating, as highlighted in Section 3.1.4, indicated a higher concentration of hBN (black phase). As shown, the brittle hBN phase appeared to break readily in the material, increasing its ability to dislocate [105]. Indeed the higher concentration increased the ability to remove the material compared with the harder coating, and consequently a lower contact force and energy required to remove the material were measured. A decrease of the incursion rate highlighted a progressively reducing ability to cut, with a low efficiency of cut and low force ratio suggesting deformation of the material. Therefore at low incursion rate the material response was observed.

Figure 8.8 shows the material section of the abradable material with hardness R15Y 54.6, at incursion rate of 0.02µm pass^{-1} and blade speed of 100m s^{-1}.

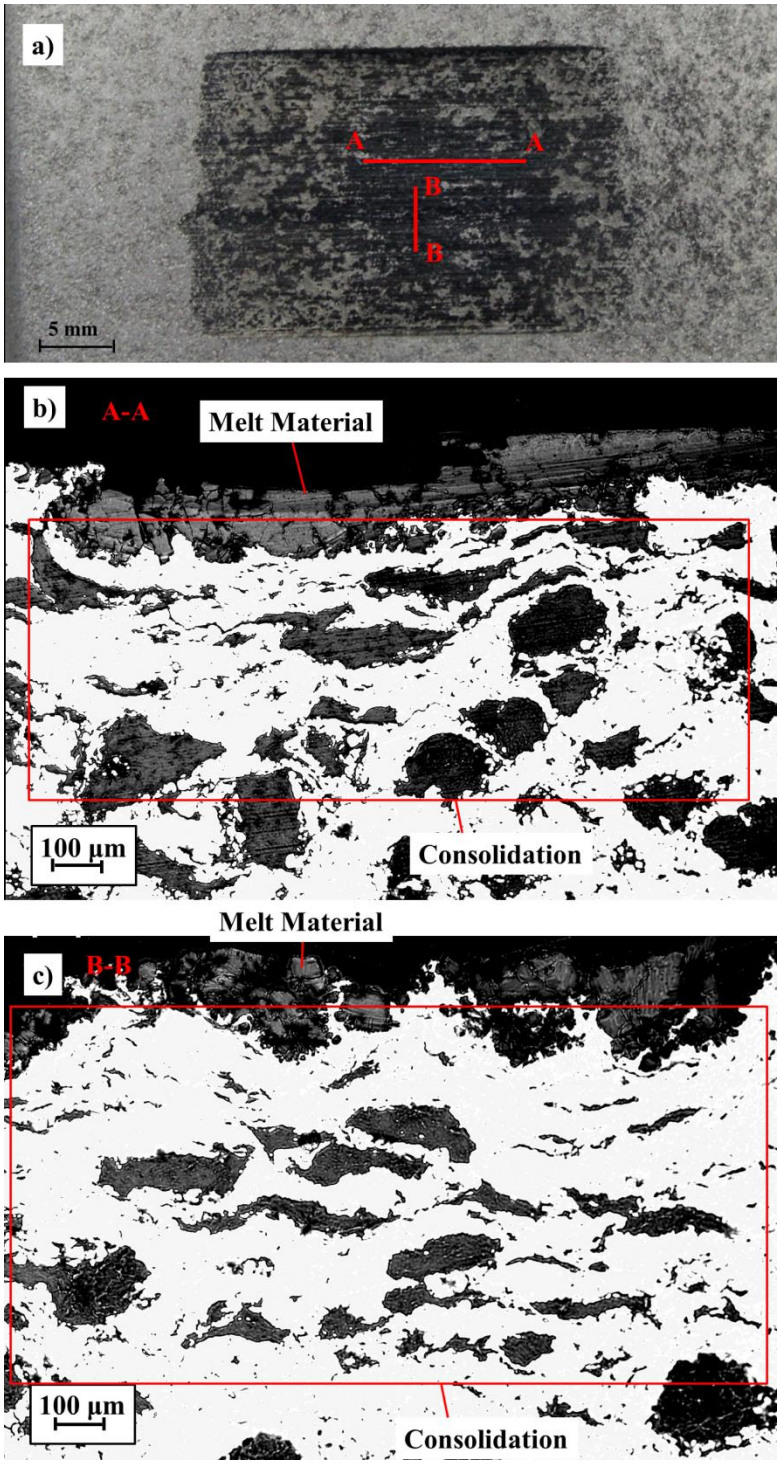

Figure 8.8. Image of the section area and the section showing the microstructure of the sub-surface of the coating with hardness R15Y 54.6, at an incursion rate of 0.02µm·pass^{-1}, blade speed of 100m s^{-1}: a) Image of section area A-A and B-B, b) Longitudinal section A-A; b) Transverse section B-B.

As shown in the figure, the abradable sample had significant consolidation on both sections, longitudinal (Figure 8.8b) and transverse (Figure 8.8c), with evident distortion of the hexagonal boron nitride particles compared with the harder coating

(Figure 8.2b). A high energy was required to remove material, and continuous increasing of the normal force with constant tangential force suggested compressive behaviour. Also, a dark layer of titanium from the blade is evident on the coating surface. This coincides with the increased consolidation and for higher force input when compared to the harder coating, and is presumably thermally driven. Therefore, the measurement of the coating temperature will be described in the second part of the chapter.

As highlighted in the previous analysis, the transition from blade wear / transfer to a cutting mechanism was observed at around 0.2µm pass^{-1}; therefore a material section was made as shown in Figure 8.9.

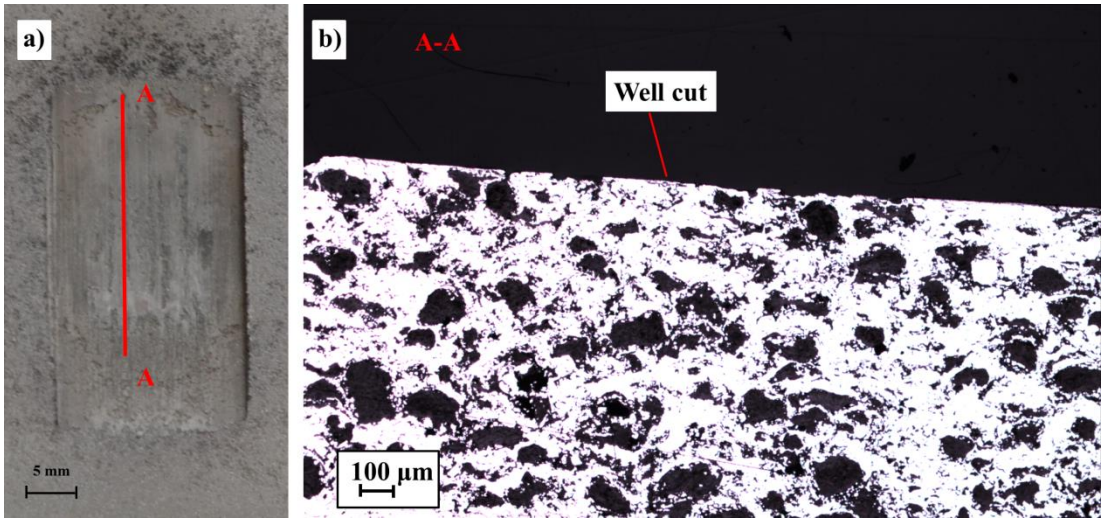

Figure 8.9. Image of the section area and the section showing the microstructure of the sub-surface of the coating with hardness R15Y 54.6, at an incursion rate of 0.2µm·pass^{-1}, blade speed of 100m s^{-1}: a) Image of section area A-A, b) Longitudinal section A-A.

As shown in the figure, the section of the rub surface revealed a well-cut surface, with fracture and no evident distortion of hBN. This confirmed that the incursion rate represented an initiation of wear cutting on the soft coating.

As highlighted in the previous chapter, with an increase of speed, at low incursion rate, a decrease of the contact force and a well-cut rub surface were observed, suggesting a transition from wear to an increasing amount of cutting, also an increase of speed highlighted an increase of the force ratio, suggesting an increase in the ability to remove material, and therefore the material section was analysed.

Figure 8.10 shows the material section performed for the coating R15Y 54.6 at an incursion rate of 0.02µm pass^{-1} with blade speeds respectively of 150m s^{-1} (Figure 8.10 a, b) and 200m s^{-1} (Figure 8.10 c, d).

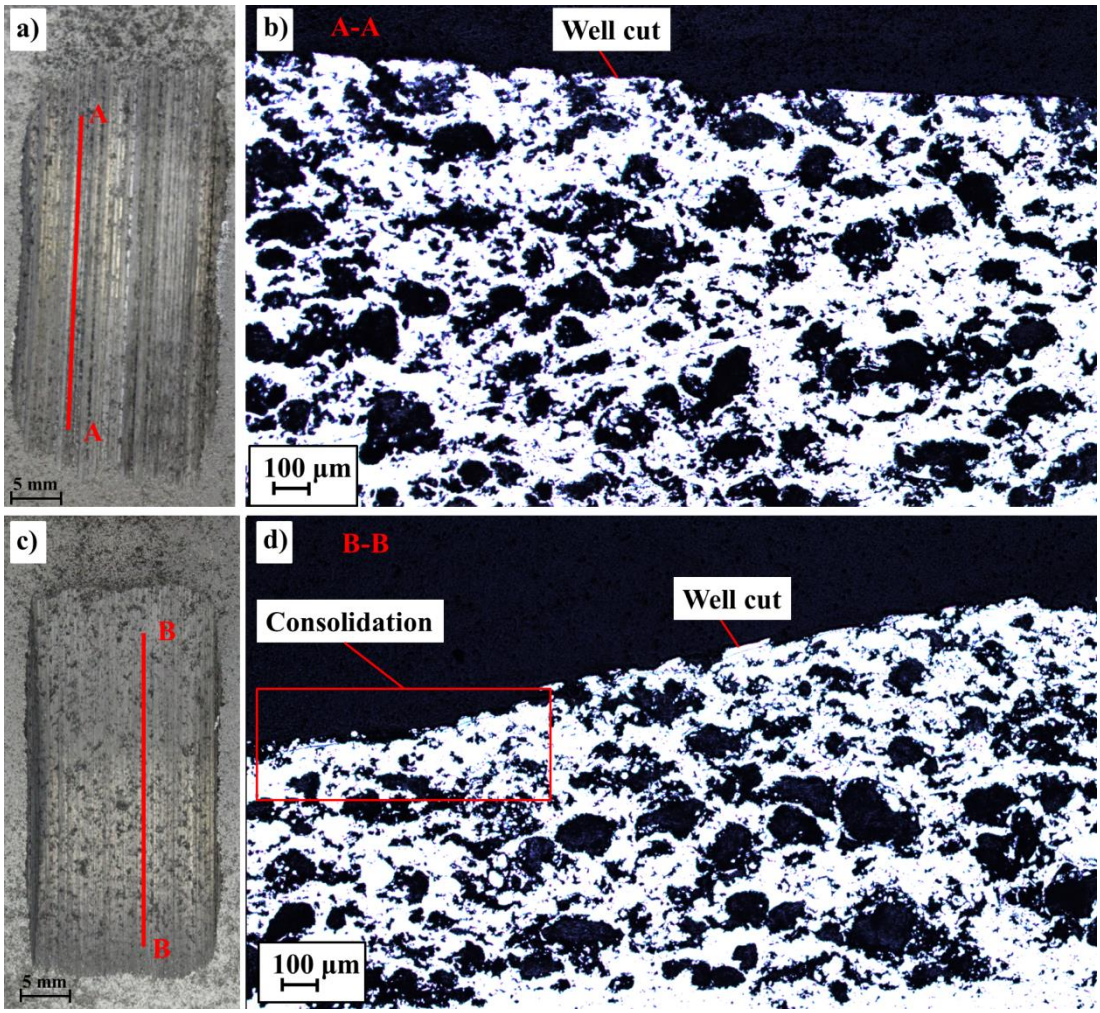

Figure 8.10. Image of the section area and the section showing the microstructure of the sub-surface of the coating with hardness R15Y 54.6, at an incursion rate of 0.02µm·pass^{-1}, blade speed of: a – b) 150m s^{-1}; c - d) 200 m s^{-1}, where a) Image of section area A-A; b) Longitudinal section A-A; c) Image of section area B-B; b) Longitudinal section B-B.

As shown in the figure, the surface is broadly well-cut with fractured hBN on the surface, and less consolidation. This is in contrast to the soft coating at low speed (Figure 8.8), and confirms, as suggested before, that an increase of the speed increased the amount of cutting.

Finally, in the test performed on the coating with intermediate hardness, a mix of melt layer and adhesion was observed. Therefore, the material response was analysed using material sectioning.

8.1.3. Material response of coating R15Y 59.6

The abradable sample tested with middle hardness was sectioned in order to observe the microstructure. At high incursion rate on the sample with hardness R15Y 59.6, a similar cutting mechanism was observed as for the rest of the coating hardnesses, with a similar high force and efficiency of cut compared with the values measured on the harder and softer coatings. Therefore, the material response was observed through the material section. Figure 8.11 shows the longitudinal section of the coating with hardness R15Y 59.6, at an incursion rate of 2µm pass^{-1} and blade speed 100m s^{-1}.

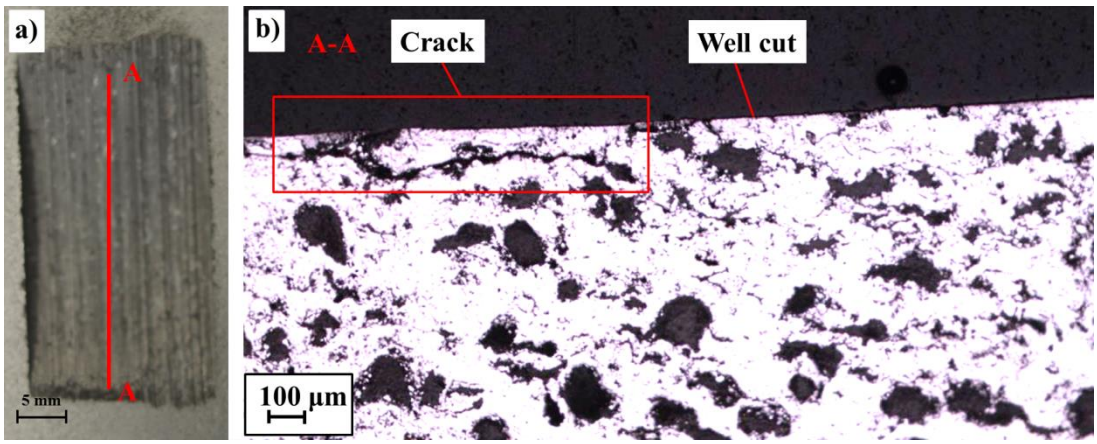

Figure 8.11. Image of the section area and the section showing the microstructure of the sub-surface of the coating with hardness R15Y 59.6, at an incursion rate of 2µm·pass^{-1}, blade speed of 100m s^{-1}: a) Image of section area A-A, b) Longitudinal section A-A.

As shown in the figure, the material response highlighted a well-cut surface with fractured hexagonal boron nitride, and also a crack on the subsurface, suggesting the blade fractures the coating, removing the material during the contact. Also, at intermediate incursion rate, a well-cut surface was observed. Figure 8.12 shows the longitudinal section of the coating with hardness R15Y 59.6, at an incursion rate of 0.2µm pass^{-1} and blade speed 100m s^{-1}.

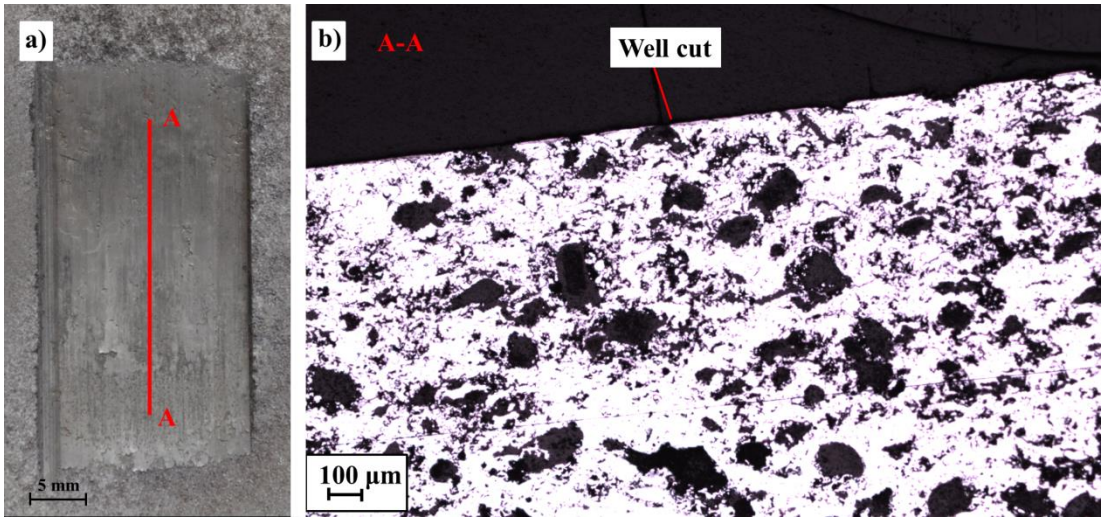

Figure 8.12. Image of the section area and the section showing the microstructure of the sub-surface of the coating with hardness R15Y 59.6, at an incursion rate of 0.2µm·pass^{-1}, blade speed of 100m s^{-1}: a) Image of section area A-A, b) Longitudinal section A-A.

The figure shows a well-cut abradable surface with a small amount consolidation, highlighted by a mixture of distorted well-fractured hBN. As highlighted for the rest of the hardnesses, a decrease in the incursion rate showed a progressive decrease in the ability to cut, with an increase of the energy required to a unit volume of remove material, and low force ratio. Observation of the coating highlighted a mix of the wear mechanisms for the hard and the soft coatings at low incursion rate, with a high level of adhesive transfer and titanium transfer along the rub surface. Figure 8.13 shows the material section at low incursion rate.

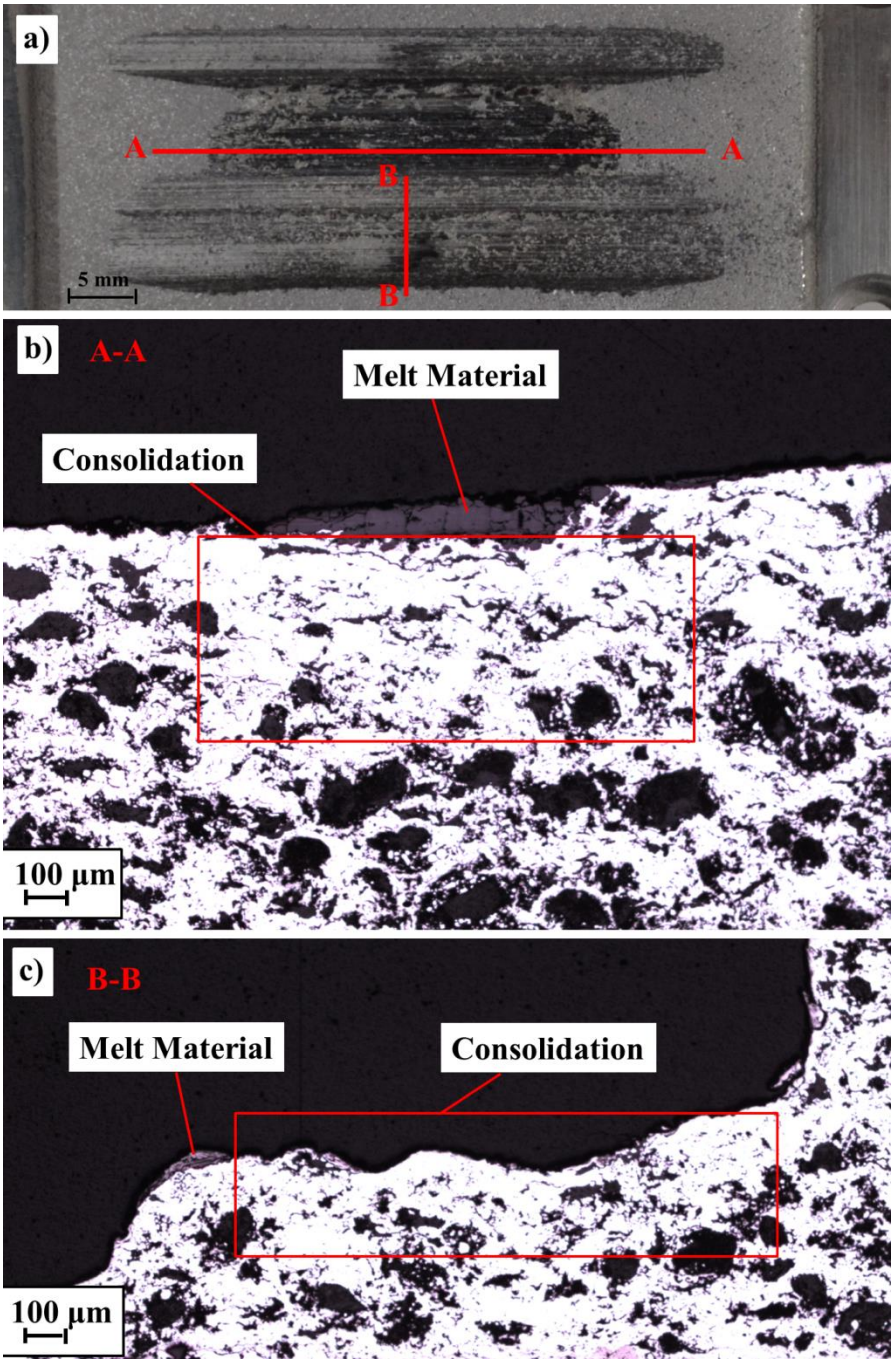

Figure 8.13. Image of the section area and the section showing the microstructure of the sub-surface of the coating with hardness R15Y 59.6, at an incursion rate of 0.02µm·pass^{-1}, blade speed of 100m s^{-1}: a) Image of section area A-A and B-B, b) Longitudinal section A-A; b) Transverse section B-B.

As shown in the figure, a high level of consolidation was observed in the proximity to transfer layer. This is similar to as observed on the soft coating (Figure 8.8b), but less pronounced. While on the area where adhesive transfer was observed, there was a grooved surface with a more continuous aluminium silicon phase (AlSi white part).

Thus, the material microstructure on the coating appears variable and corresponds to the different wear mechanics, with a mix of adhesion and titanium transfer observed. This coating indicated a transition hardness value between adhesion and titanium transfer, at low incursion rate. The variability of the wear mechanism may be correlated to the variability of the thermal spray coating [5, 12, 13], with its non-continuous properties reflected in the different microstructure responses and different wear mechanisms observed. Further investigation will be performed in Section 8.3, and this trend discussed.

Overall, the material response confirmed the ability to remove material at high incursion rate, with a well-cut surface and fractured hBN. It also confirmed the difficulty in removing material at low incursion rate, with the blade rubbing instead of cutting. A high energy to remove material was measured at low incursion rate, and corresponded to a high level of consolidation, a thermal effect was observed, therefore suggesting heat build-up in the contact, and a high temperature. Therefore the thermal behaviour of the coating was investigated in the next section.

8.2. Temperature measurement

As highlighted previously and in particular at low incursion rate, a low efficiency of cut corresponded with the coating failing to dislocate. The wear mechanism observed showed an adhesive transfer or blade wear during the contact, which suggest heat build-up, and therefore the coating temperature was measured. Using a non-contact infrared sensor as described in Section 3.2.3 [78], the temperature was measured in relation to the radiation emitted from the surface of the abradable material where the blade struck [106, 107]. In this way the sensor measured the temperature of the rub surface during the evolution of the test, as shown in Figure 8.14.

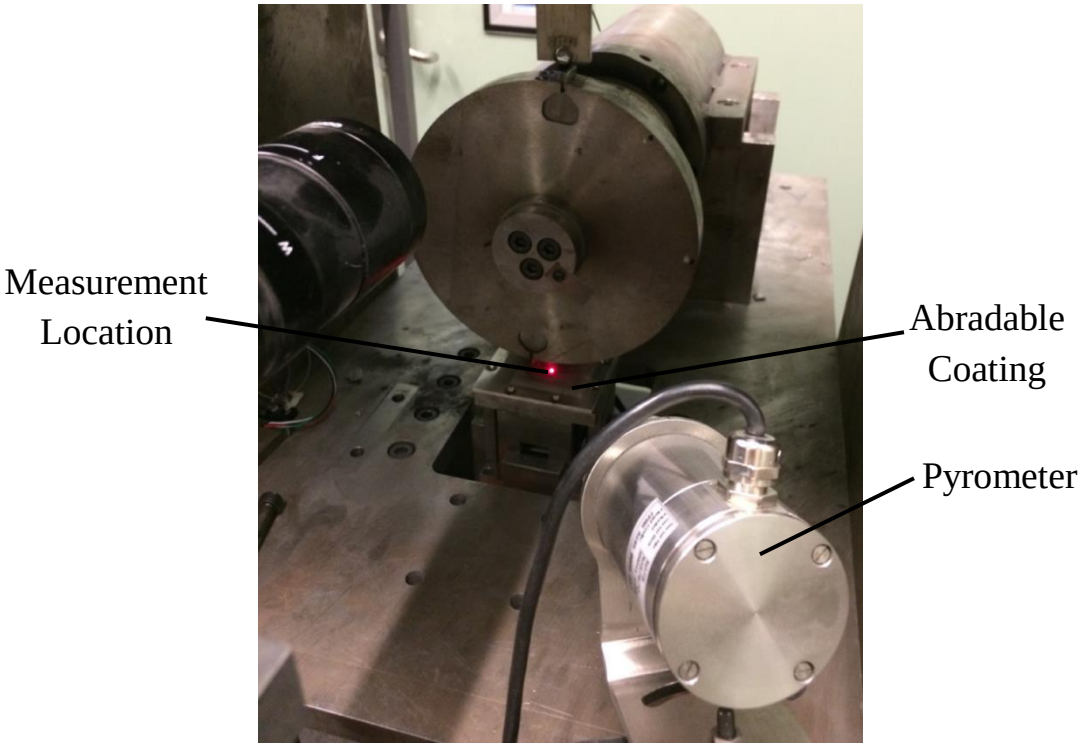

Figure 8.14. Position of the temperature sensor.

At high incursion rate it was observed that the abradable material worked well, with fracture of hBN and no evident material deformation. This result was independent of the coating hardness, where no thermal damage and variation of blade length was observed. The temperature measured was plotted against the theoretical rub length in order to observe the evolution of the temperature during the rub. Figure 8.15 shows the temperature measured and blade length change for the coatings with hardnesses R15Y 72.3 and R15Y 54.6, at high incursion rate.

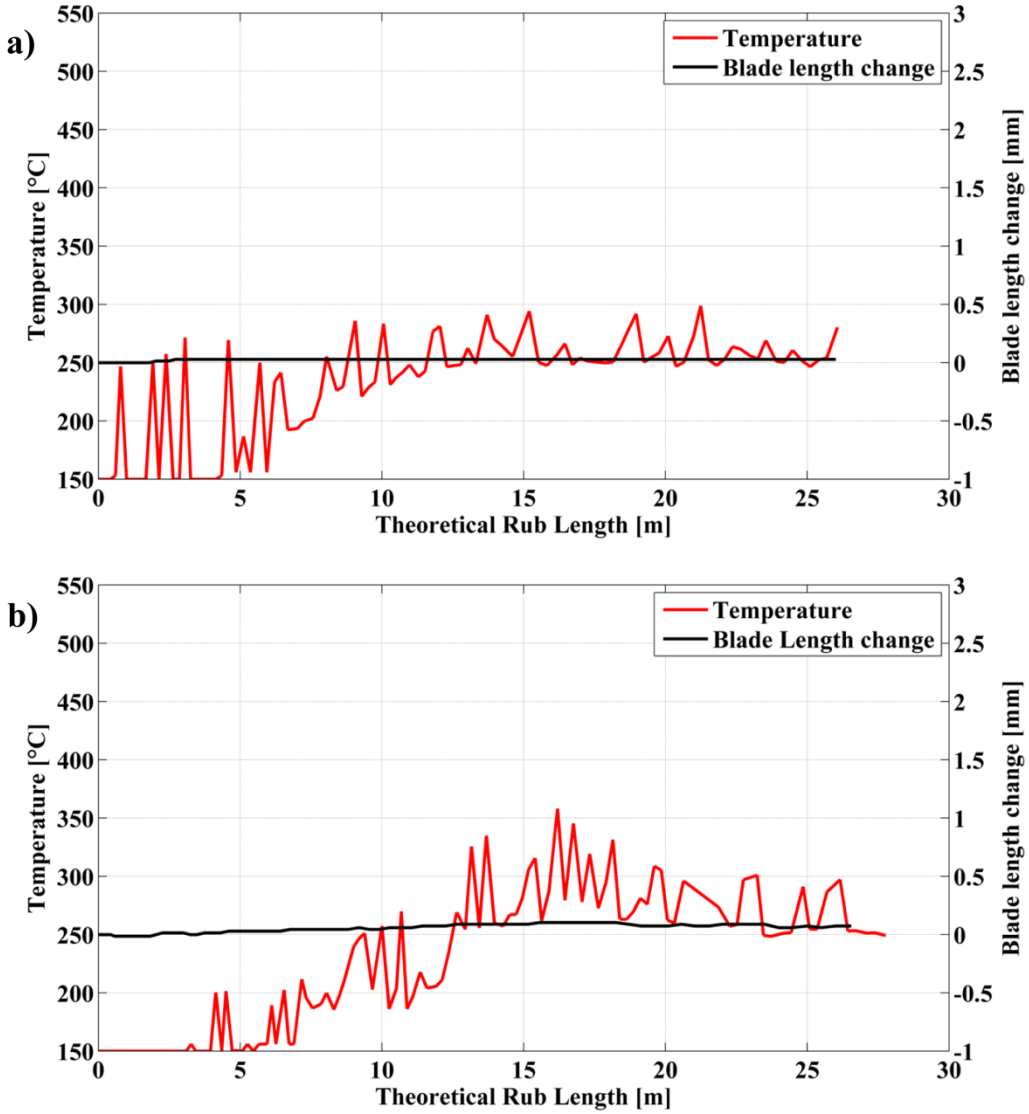

Figure 8.15. Temperature and blade length change against the theoretical rub length at incursion rate of 2µm pass^{-1}, blade speed of 100m s^{-1} and abradable coating hardnessess: a) R15Y 72.3; b) R15Y 54.6.

As shown in the figure, a slight increase of the temperature was measured, which corresponded to a negligible blade length change. The measured temperature highlighted a similar maximum temperature and similar trend, and no thermal damage was observed. Further, even with a short rub length, as demonstrated by Wang [64], steady-state thermal conditions were quickly reached.

At low incursion rate, as highlighted before, a failure to dislocate and a high energy required to remove material were observed, and suggested a higher temperature. Figure 8.16 shows the coating temperature and the blade length change plotted

against the theoretical rub length for the coatings with hardnesses R15Y 72.3 and R15Y 54.6 at an incursion rate of 0.02µm pass^{-1} and blade speed 100m s^{-1}, where evident differences in wear mechanism were observed.

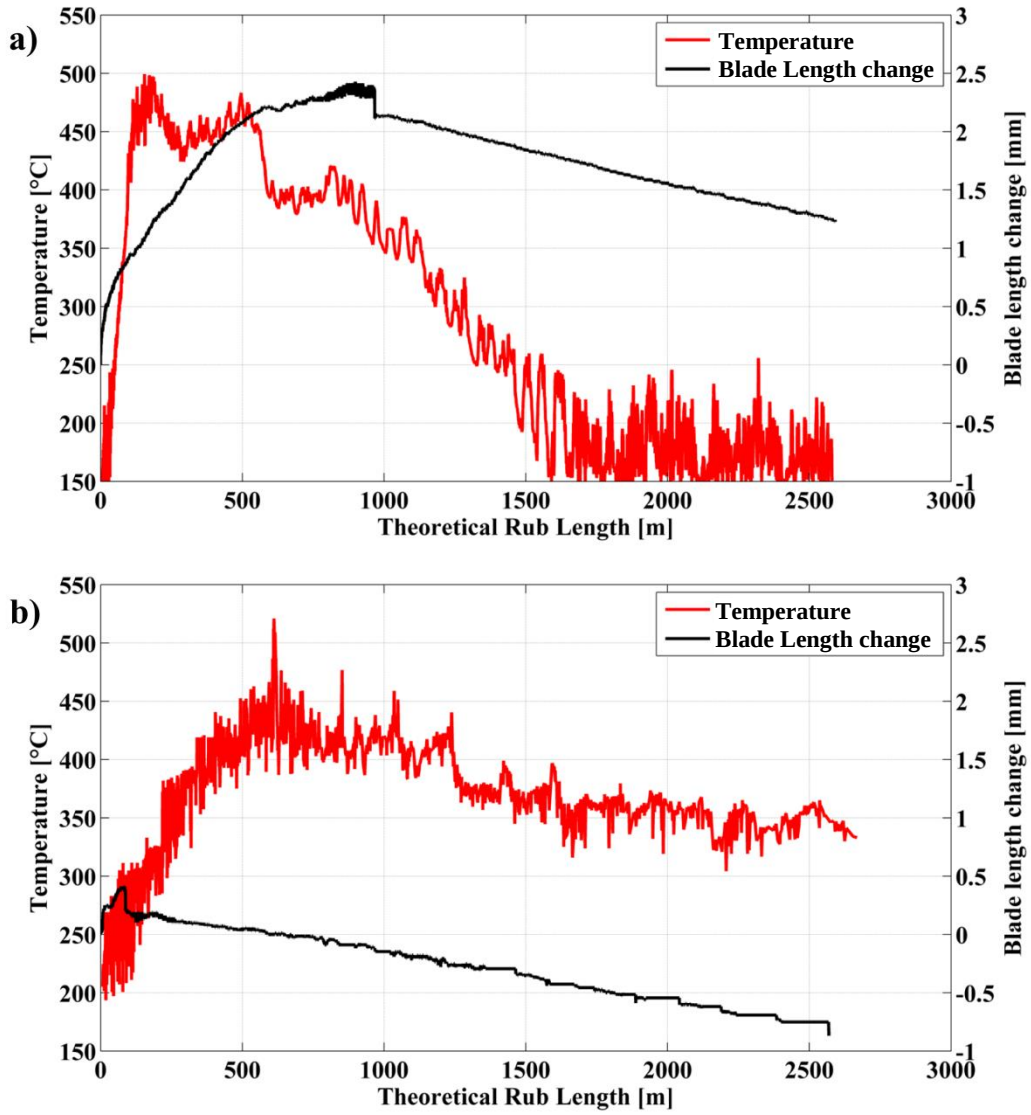

Figure 8.16. Temperature and blade length change against the theoretical rub length at incursion rate of 0.02µm pass^{-1}, blade speed of 100m s^{-1} and abradable coating hardness: a) R15Y 72.3; b) R15Y 54.6.

As shown in the figure, at low incursion rate the coating during the contact was hotter compared with the test performed at high incursion rate. On the hard coating the highest temperature measured was 497.2 °C, recorded in the phase when an increase of the blade length was measured, and then a decrease of the temperature was measured when the adhesion phase had ended. On the soft coating a slightly

higher temperature was recorded (520.9 °C), with a surface temperature trend characterised by higher temperatures over the length of the test. Previous analysis highlighted that a high energy was required to cut the material at low incursion rate, suggesting heat build-up in the contact, and indeed the higher temperature measured confirmed the heat generated in the contact, and then a thermal effect was observed.

It is interesting to note, as shown in Figure 8.16a, that after the adhesion occurred and the temperature peaked, that with fracture of adhered material cooling occurred. Therefore, in order to generalise, the maximum temperature was measured for all test conditions, as shown in Figure 8.17.

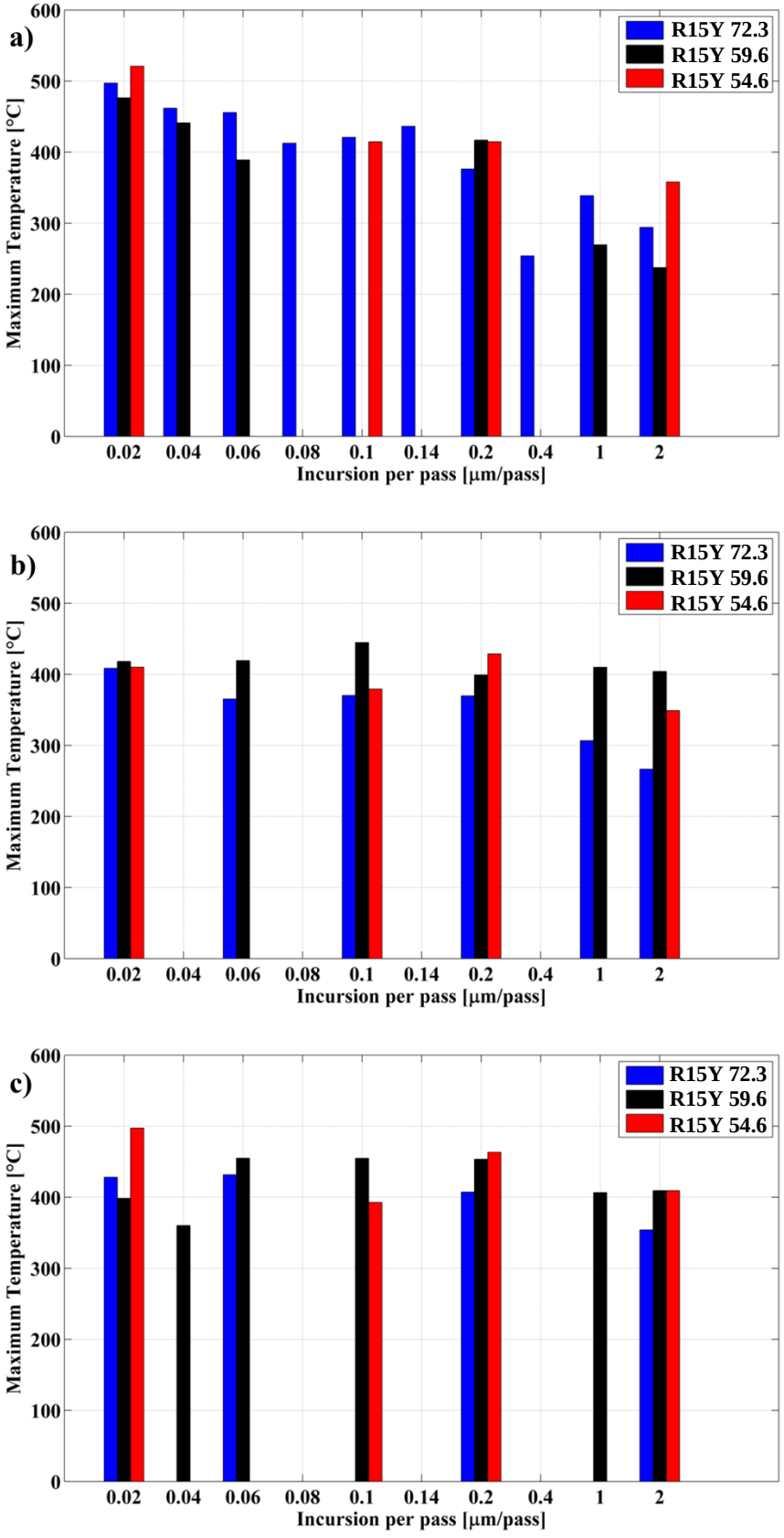

Figure 8.17. Maximum temperature against the incursion rate with different hardness coating and blade speed: a) 100m s^{-1}; 150m s^{-1}; 200m s^{-1}.

As shown in the figure, a decrease of the maximum temperature was measured with an increase of the incursion rate for different hardnesses. However this was less pronounced at high speed, and may correlate to an increasing amount of heat being removed in the incursion (e.g. as in the case of machining where more heat is carried away in the chip at higher machining speeds leading to a cooler work-piece [104]). It is also interesting to note, less thermal damage was observed with an increase of speed. Overall, a maximum temperature was observed at low incursion rate, which confirmed that a high level of heat was present in the contact. Furthermore the temperature variation measured for the coating R15Y 59.6 was less uniform with incursion rate, confirming the higher variability of the wear mechanism of this sample compared with the hard and the soft coatings.

As highlighted in the figure, the analysis of temperature showed that whilst lower incursion rate tests were slightly hotter, there were no significant differences. However, observing the blade tip of the test performed at low incursion rate for different coating hardnesses revealed significantly different levels of thermal damage on the blade, as shown in Figure 8.18. This latter point very much contrasts the temperature results.

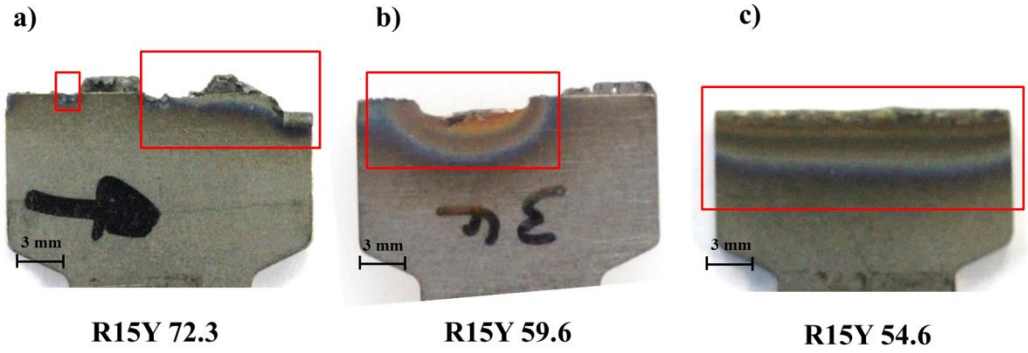

Figure 8.18. Blade tip tested at incursion rate of 0.02µm pass^{-1}, blade speed 100m s^{-1}, against coating hardness: a) R15Y 72.3; b) R15Y 59.6; c) R15Y 54.6.

As shown in the figure, even if a similar temperature was measured, the different levels of thermal damage, shown by the level of the discoloration, increased with a decrease of the coating hardness, suggesting different heat partition between the coating and the blade in relation to the coating hardness. Therefore the thermal properties of the abradable coating were measured and will be described in the next section.

8.3. Thermal properties

The difference in wear mechanism observed at low incursion rate, and the level of heat on the blade highlighted by discoloration, suggested a different penetration of heat into the coating with different hardnesses. Different constituent fractions of aluminium-silicon (AlSi), hexagonal boron nitride (hBN) and porosity were observed in relation to the hardness, as shown in Section 3.1.4, with an increase of the hexagonal boron nitride phase resulting in a decrease in hardness. The effect of the percentage of constituent phase on heat transfer was investigated through experimental investigation of the thermal properties of the coating [52], namely: thermal conductivity, specific heat capacity and thermal diffusivity. In order to perform the thermal analysis, a freestanding sample of abradable material (10mm x 10mm x 2mm) was prepared for each hardness. The thermal properties of the sample were measured using a laser flash based approach [53], performed by a LINSEIS apparatus LFA 1000 (LINSEIS Messgeräte GmbH, Vielitzerstraße 43, D-95100 Selb, Germany). The experimental apparatus measured specific heat capacity, density, thermal conductivity and thermal diffusivity of the sample over the temperature range 30°C to 500°C, at 50-100°C intervals.

Figure 8.19 shows the experimental results of the thermal conductivity measurement of the abradable sample with hardnesses R15Y 72.3, R15Y 59.6 and R15Y 54.6 respectively, and Table 8.2 summarises the average thermal properties measured in the temperature range 30°C to 500°C.

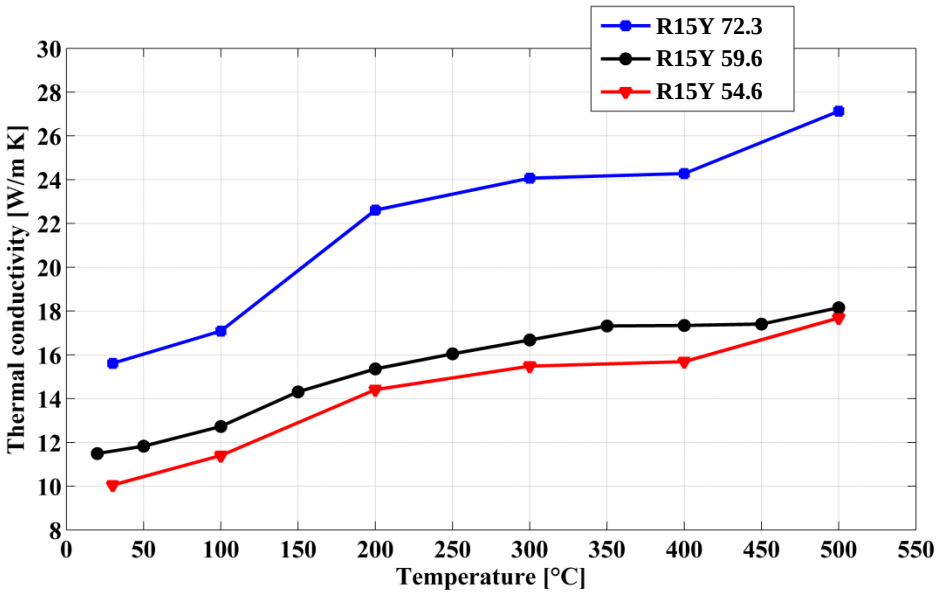

Figure 8.19. Thermal conductivity in relation to the coating temperature for the sample with hardnesses R15Y 72.3, R15Y 59.6 and R15Y 54.6.

Coatings Hardness [R15Y]	**Thermal Diffusivity [$cm^2\ s^{-1}$]**	**Heat capacity [J $(g\ K)^{-1}$]**	**Density [$g\ cm^{-3}$]**	**Thermal Conductivity [W $(m\ K)^{-1}$]**
72.3	0.104 ± 0.012	1.174 ± 0.126	1.77	21.79 ± 4.49
59.6	0.085 ± 0.006	1.074 ± 0.101	1.67	15.33 ± 2.39
54.6	0.069 ± 0.007	1.198 ± 0.138	1.67	14.12 ± 2.86

Table 8.2. Average thermal properties of the abradable coating for the temperature range 30°C to 500°C.

As shown in the figure, the thermal conductivity changed in relation to the temperature, with similar trends for all hardnesses. However, a different value of thermal conductivity was measured in relation to the coating hardness, with a decrease when the coating hardness decreased, as highlighted in the figure and in the table. The thermal conductivity of the soft coating was significantly lower compared with the hard coating, meaning that it was less efficient in the conduction of heat; therefore the coating was more thermally insulating and more heat passed to the blade, and a high level of thermal damage was observed on the blade. The sample

with intermediate hardness was characterised by a slightly higher thermal conductivity compared with the soft coating, and a mix of adhesion and blade wear was observed at low incursion rate, while the highest thermal conductivity of the hard coating indicated a higher ability of the heat to penetrate the coating, leading mainly to adhesive transfer. However, local blade wear with melt layer was observed, suggesting different local penetration due to the heterogeneous concentration of different phases because of the variability of the thermally sprayed coating [5, 13].

Overall, the thermal property analysis highlighted a different thermal conductivity in relation to the hardness, and therefore a different ability for the heat generated in the contact to penetrate the coating. This led different wear mechanisms for the different hardnesses, especially at low incursion rate.

8.4. Discussion

The previous chapter demonstrated that different levels of energy were required to remove material depending on hardness and incursion rate, highlighting that high energy was required at low incursion rate. In this chapter this aspect was further explored by analysis of the material response through sectioning. At a high incursion rate it was observed that the incursion was high enough to fracture the particles of hBN, and the blade was able to dislocate the material. Conversely, at low incursion rate the blade rubbed and consolidated the material. It also is interesting to note that whilst both incursion conditions are well below the scale of the material (constituent particles are typically 63 microns in diameter), that at the upper condition the material is able to fracture. In relation to the coating hardness, different levels of consolidation were evident observed through the distortion of the hBN phase, especially at low incursion rate. A decrease of the coating hardness also implied an increase in the level of consolidated sub-layer.

Furthermore, the thermal damage and thermally driven wear mechanism observed at low incursion rate, suggests heat build-up in the contact. Measurement of the temperature during the test showed that the rub surface was slightly hotter in this case, but no significant difference was observed in relation to coating hardness. However, this result was not reflective of the differing level of thermal damage

present on the blades tested, suggesting different heat penetration between the blade and coating depending on the coating hardness.

Measurement of the thermal properties revealed different thermal conductivity of the samples. A different thermal conductivity implied a differing ability to propagate the heat in the contact, and also implied a different heat partition between the coating and the blade. This lead to different wear mechanisms at low incursion rate, with blade wear on the soft coating and adhesive transfer on the hard coating. This result leads to a challenge with respect to abradable material design where aspects such as erosion resistance must be considered. Additionally, the material sections along with the thermal diffusivity results highlighted how local concentration of hBN in a nominally high hardness sample can lead to a mixture of wear mechanisms, as opposed to just adhesive wear. As discussed abradable materials are locally variable in structure due to the thermally spraying process [12, 13, 14, 45, 46], and this represents a particular challenge with respect to the use of intermediate hardness abradables.

Overall, the hardness and incursion rate had more impact on the cutting performance of the coating compared with the blade speed, with clear relationships established. In the next chapter the differing nature of the wear mechanics will be characterised in terms of incursion rates, speed and hardness, and a wear map produced.

8.5. Chapter summary

- At low incursion rate, the material response confirmed that the blade was rubbing and consolidation was observed, with a higher level of consolidation on the soft coating.

- At intermediate and high incursion rates, a clean well cut with hBN fracture confirmed the ability to dislocate, as suggested by a force ratio comparable with orthogonal cutting.

- The high temperature measured at low incursion rate confirmed that the high energy input required to remove the material generated heat in the contact.

- Different thermal conductivities of the sample were measured in relation to the hardness; a decrease in the hardness implied a decrease in the ability to propagate the heat, which implied a different heat distribution between coating and blade, and different wear mechanisms were observed.

9. Discussion

As described in the previous chapters, different wear mechanisms were observed at different incursion rates and in relation to the coating hardness, especially at low incursion rate, while less change was observed with an increase of speed. In the course of this research, the wear mechanism was analysed in terms of sample output post-test, evolution of blade length with a stroboscopic imaging technique, contact forces, material response and thermal properties of the coating. This chapter will characterise the different aspect of wear mechanics that were identified in terms of incursion rate, speed and hardness, and will create a wear map. The analysis

performed during this research will then be discussed step-by-step in order to understand the nature of the different wear mechanisms observed in the wear map. The repeatability of the test will be considered, as well a comparison with a full scale test rig.

9.1. Overview of the wear mechanisms identified

As described in the previous chapters, the incursion rate represented an input parameter that produced different wear mechanisms, with different abilities to dislocate the material in relation to the amount of material removed per pass. At a low incursion rate the blade rubbed instead of cutting the material, with high energy required to remove material and a high level of consolidated material indicating a difficulty in dislocating, while at high incursion rate the blade fractured the brittle solid dislocator, leading to good cutting.

However, adhesive transfer and titanium transfer were observed respectively in the tests performed at low incursion rate against the hard and soft coatings, with different levels of consolidation of the sub-layer with a higher level on the soft coating. Also, a high level of consolidation implied a high energy required to remove material that was converted in heat in the contact, as highlighted by the high coating temperature measured. However, different levels of thermal damage on the blade tip were observed in relation to the different coating hardnesses, with an increase of the thermal damage highlighted by material discoloration with a decrease of the coating hardness, implying a different heat partition between the coating and the blade.

A decrease of the coating hardness implied an increase of the dislocator phase and lead to a decrease of the thermal conductivity of the coating. The different thermal conductivity in relation to the coating hardness implied different abilities to propagate the heat in the coating between hard and soft coatings.

With the soft coating, the reduced ability to propagate the heat and the increased consolidation increased the heat in the contact until the heat led to blade thermal wear. With the hard coating, the higher thermal conductivity increased the ability to propagate the heat in the coating, thus compromising the integrity of the coating and leading to adhesive transfer.

However, as observed in the previous chapter, when adhesive transfer was observed, it was not uniform along the blade tip, with localised blade wear and titanium transfer on the coating. Additionally a mixed wear mechanism was observed in the test performed with intermediate hardness. Abradable samples, as consequence of the thermal spray process [12, 13, 14, 45, 46], have an anisotropic structure which was observed by the microstructure analysis, and implied a heterogeneous local concentration of the different constituent phases, which could thus generate different local properties of the coating. Figure 9.1 shows the microstructure of the hard coating where titanium transfer was observed, which corresponded to localised blade wear.

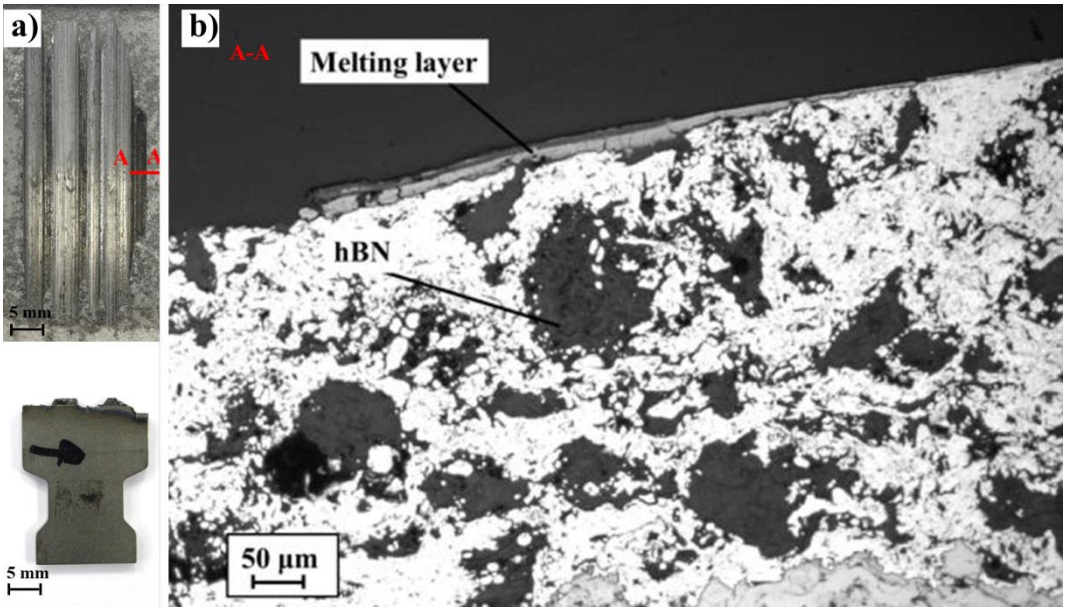

Figure 9.1. Melting layer observed on the hard coating R15Y 72.3 at incursion rate of 0.02µm pass^{-1} and a blade speed 100m s^{-1}: a) Coating and blade; b) Microstructure where melting layer was observed.

As shown in the figure, a high concentration of hBN and a reduced metal phase were observed in the sub-surface of this layer, confirming a possible lower local thermal conductivity, which generated an increased heat concentration in the region that led to local blade wear with melt titanium transfer, with a locally hotter blade highlighted by localised thermal discoloration of the blade.

Otherwise, at high incursion rate, independent of the coating hardness, the blade fractured the dislocator phase and removed the entire depth of cut, and the heat was carried away in the chip. Indeed a lower coating temperature was measured, and also

the observation of the microstructure highlighted fractured hBN and cracks on the surface and a well-cut surface with no damage on the blade tip.

The changes in incursion rate produced different wear mechanisms, with different material responses in relation to the different ability to remove material, from rubbing at low incursion rate to cutting at high incursion rate, and therefore this represented a key parameter in order to classify the different wear mechanisms. Also, the thermal analysis highlighted different heat partitions between the blade and coating at low incursion rate, but also different heat concentrations in the contact between low and high incursion rates, with a high coating temperature at low incursion rate and a progressive decrease of the temperature with an increase of the incursion rate. Furthermore this analysis highlighted the importance of the thermal properties of the coating and the blade that influenced the wear mechanism. Therefore, the wear mechanism needed to be characterised in relation to the incursion rate, the coating hardness, which reflects the different ability of the coating to conduct heat, and finally in relation to the speed, even though this was observed to have less impact on the cutting performance.

Therefore, in order to characterise the concentration of the heat in the contact, the Peclet number [19, 24, 34] was introduced. The Peclet number is a dimensionless number that represents the concentration of the heat in a sliding contact. This number is a combination of mechanical and thermal parameters like the speed (V), which in this case is the blade impact speed, a characteristic length in machining the uncut chip thickness, in this case the incursion rate (I_{rate} (m pass^{-1})) and the thermal diffusivity of the coating (α (m^2 s^{-1})), as shown on Equation (9.1).

$$\boldsymbol{Pe} = \frac{\boldsymbol{V_{blade} \cdot I_{rate}}}{\boldsymbol{\alpha}} \tag{9.1}$$

Where, for Pe > 10, the source, i.e. the rotating blade, moves faster than heat can expand, therefore the heat is carried in the chip, while a lower Peclet number means heat can expand in the coating. The Peclet number for the case at a low incursion rate was lower than ten, for all coating hardnesses, while at a high incursion rate the Peclet number was higher than ten. At high incursion rate, a Peclet number higher than ten [24, 25] represented that the heat built-up in the contact did not have time to penetrate the coating, and the heat was carried out in the chip. At low incursion rate,

a low Peclet number represented that the heat remained on the sliding contact, and the different thermal conductivity of the coating implied a different ability of the heat to conduct in the coating and generated a different wear mechanism. The Peclet number represented the mechanical input parameter, such as the incursion rate and the blade speed, but also the hardness of the coating was represented as it is linked to different thermal diffusivity, and therefore the Peclet number was used for the X-axis of the graph in order to characterise the wear mechanism in a wear map.

However, a different wear mechanism was observed at low incursion rate, with different coating hardness, and the different thermal conductivity of the sample highlighted a different heat partition between the blade and the coating. Therefore, in the machining process the fraction of the heat generated between the tool and work-piece proved useful for estimating the thermal damage and the temperature occurring on the tool and in the work-piece [104]. A heat partition coefficient was introduced by Kato and Fuji [108] in order to estimate the energy partition between the work-piece and the tool in surface grinding. A triple product of the specific heat (C_p), the density (ρ) and the thermal conductivity (λ), also called 'heat transmission ratio', was introduced, assuming a uniform heat source moving between two stationary surfaces, and was found to be independent of the cutting condition, as shown in Equation (9.2).

$$\frac{(\boldsymbol{C_p \cdot \rho \cdot \lambda})_{\boldsymbol{blade}}}{(\boldsymbol{C_p \cdot \rho \cdot \lambda})_{\boldsymbol{coating}}} \tag{9.2}$$

This partition coefficient was independent of the cutting condition. Therefore, different heat partitions were observed at the same cutting condition in relation to the coating hardness, and nevertheless the incursion parameter was introduced in the Peclet number. Additionally, the thermal properties increased with temperature. However, the same trend was observed between the different coating an overall hardness, and therefore an average value was used in the range of test temperatures.

The Peclet number highlighted the concentration of heat in the contact in relation to the incursion parameter and the thermal diffusivity of the coating, reflecting the coating hardness, and gave a representation of the different wear mechanisms

observed between low incursion rate, where the blade rubbed and generated high heat in the contact, and high incursion rate, where the blade fractured the material and the heat generated was carried away in the chip.

At low incursion rate, however a different heat partition between blade and coating was observed in relation to the coating hardness, and adhesive transfer and melt wear were observed. Therefore, the heat partition characterised the different wear mechanism at low incursion rate, and with the Peclet number was used in order to create a wear map.

The Peclet number introduced in the X-axis represented the heat concentration in relation to the consolidation and fracture of the coating, while the Y-axis represented the heat partition between the blade and the coating. Then the different wear mechanisms were characterised in relation to the rate of adhesion / wear, with different intensity of colour for the different experimental points in relation to the test performed highlighting the level of adhesion, wear or cutting. The red colour represented adhesion, the green colour represented the cutting mechanism and the blue colour represented blade wear, in order to identify different areas where different wear mechanisms were observed in relation to the input parameters.

Figure 9.2 shows the wear map of the tests performed with hardness R15Y 54.6, R15Y 59.6, R15Y 63, R15Y 72.3 and blade impact speed 100m s^{-1} plotted with a circle point, 150m s^{-1} plotted with a square point and 200m s^{-1} plotted with a triangle point. The X-axis was plotted with logarithmic scale in order to expand the distance between experimental data.

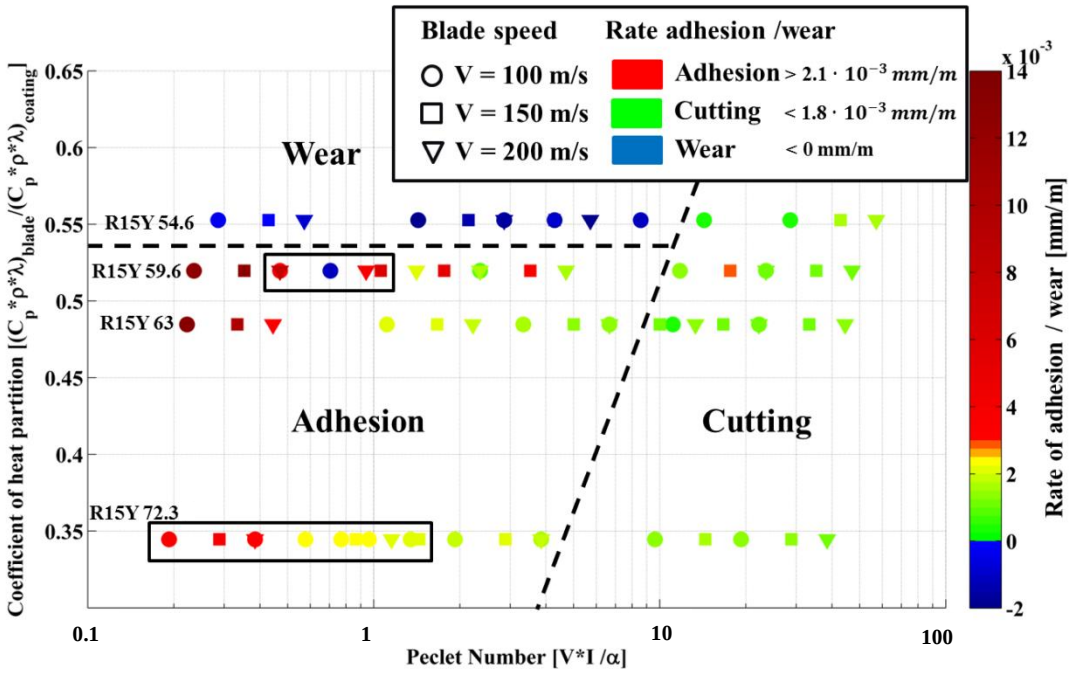

Figure 9.2. Wear map with coefficient of heat partition and Peclet number.

It is interesting to note that, as shown in the figure, a cutting mechanism was observed with a Peclet number higher than ten, where the heat was carried out on the chip. However, as highlighted with black boxes, the data sets overlap and the speed and adhesion rate are not well ordered. Also, previous cutting research [63] indicated that the Peclet number represented the heat partition when the cutting tool never passes in the same point of the work-piece; but, as shown during this research, a continuous contact between the blade and the coating builds up heat and effects a change in the structure, and also different wear mechanics were observed. Therefore, Astakhov [24] suggested a modified Peclet number where the velocity of in feed is considered the most important parameter, so that the heat from a previous pass penetrated below the depth of the cut line.

The velocity of the in feed is the cut per revolution multiplied by revolution per second, as shown in Equation (9.3).

$$\boldsymbol{V_{in\,feed} = (Cut\ per\ revolution) \cdot (Revolutions\ per\ second)} \qquad (9.3)$$

In this research the *'cut per revolution'* was the incursion per pass (I_{rate}) and the *'revolutions per second'* were the strikes per second, as shown in Equation (9.4).

$$V_{in\,feed} = I_{rate} \cdot Strikes\ per\ second = I_{rate} \cdot \frac{V_{blade}}{\pi \cdot D} \quad (9.4)$$

where *'D'* was the diameter of the rotating disc. Then, in the Peclet number (Equation 9.1), instead of blade velocity the velocity of in feed was inserted from Equation (9.4), as shown in Equation (9.5) which shows the modified Peclet number.

$$Pe_{modified} = \frac{V_{in\,feed} \cdot I_{rate}}{\alpha} = \frac{V_{blade} \cdot I_{rate}^2}{\alpha \cdot \pi \cdot D} \quad (9.5)$$

The modified Peclet number represents how the heat has propagated into the material before the next cut, and therefore defines how much heat is built up on the contact, highlighting the input energy that was applied during the contact in relation to the mechanical condition, incursion rate and blade speed. A low Peclet number represented that the heat built-up remained on the contact area and successive strikes increased the heat, while a high Peclet number represented that the heat did not propagate in the coating and successive strikes removed the entire damaged subsurface and the heat was carried away in the chip. The modified Peclet number, gives increased emphasis to incursion rate introducing a squared value, but retains blade speed, and also the hardness of the coating is represented by a different thermal diffusivity. This new number was therefore used instead of the previous Peclet number for the X-axis of the graph of the wear map, as shown in Figure 9.3.

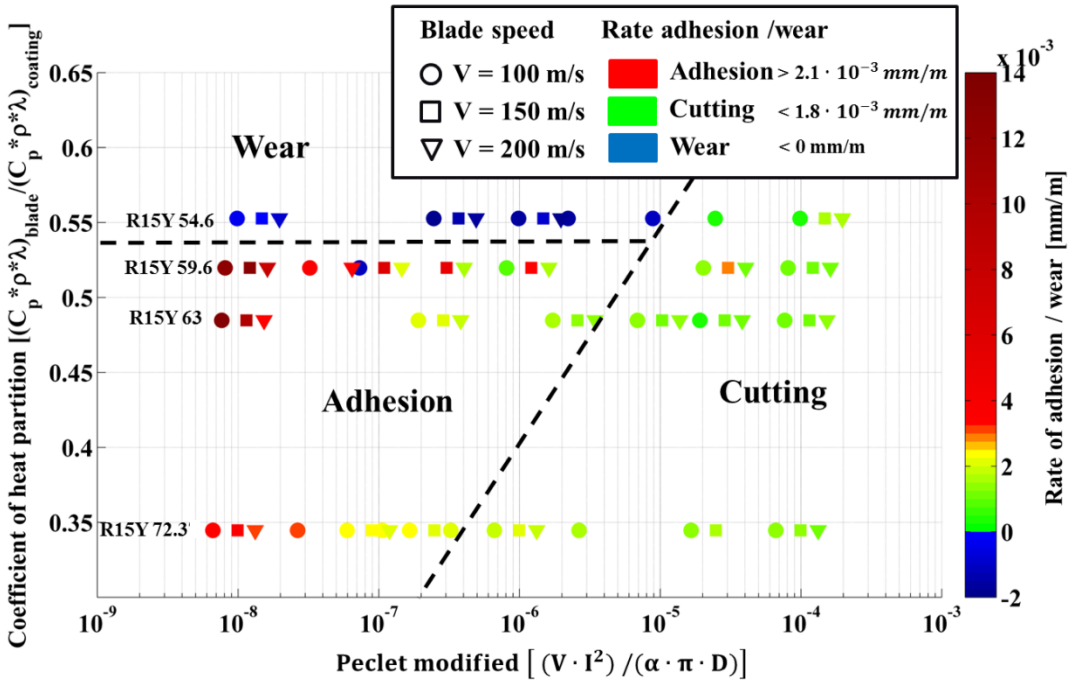

Figure 9.3. Wear map with the coefficient of heat partition and Peclet number modified.

As shown in Figure 9.3, and in the previous wear map (Figure 9.2), three general regions of wear mechanism were found: adhesive transfer, wear, and cutting region. In this wear map (Figure 9.3), the incursion rate was introduced in a squared value, highlighting more influence of the incursion rate compared with the speed. Therefore the points with the same incursion rate but different blade speeds are grouped progressively with an increase of X-axis and blade speed, which was not observed in the wear map with the normal Peclet number, and allows better observation of the progressive change of wear mechanism.

The Peclet number and the rate of adhesion / wear revealed a progressive wear mechanism change from low to high incursion rate, from adhesion or wear to a cutting mechanism in relation to the coating hardness. A decrease of the hardness implied a decrease of metal phase percentage and a decrease of thermal conductivity was measured. Therefore, in the wear region, at low incursion rate a high heat partition value meant low thermal conductivity of the coating and the heat generated in the contact had difficulty in passing through the coating, then successive strikes increased the heat in the contact until significant heat was propagated to the blade and softened it to a point to allow transfer. A low coefficient of partition between the blade and the coating, which corresponds to the adhesion region on the wear map,

meant higher thermal conductivity of the coating, and at low incursion rate the heat penetrated the coating, compromised the integrity of the coating and led to adhesive transfer.

Otherwise, in the cutting region that corresponded to a high incursion rate, for all hardnesses the blade fractured the hBN and removed the entire depth of cut, with no thermal damage evident, with the heat generated being carried out with the chip. It is also interesting to note that the transition is a diagonal line. This is likely to be linked to hardness (represented by thermal diffusivity) as highlighted by the material sections, less consolidation occurs at higher hardness with fracture easier at lower incursion rate and therefore lower Peclet number.

Observation of the wear map for the coating hardness R15Y 59.6 also highlighted a mixture of mechanisms where adhesion and wear were observed, which confirmed that it represented a value of hardness that determined the transition of the wear mechanism at low incursion rate. In fact the test of R15Y 59.6 was characterised by a higher adhesive rate because the adhesion phase was reached in a short period of rub length and then blade wear was the dominant wear mechanism, and therefore on the wear map a high rate of adhesion was observed, but also a high rate of wear. The abradable material being locally variable in structure due to the thermal spray process [12, 13, 14, 45, 46] was highlighted by an anisotropic structure of the coating observed in the microstructure in Chapter 8, but also spotted in Figure 9.1, which determined the variability of the wear mechanism observed, and was more evident on the coating with hardness R15Y 59.6.

The wear map also highlighted a progressive reduction of adhesion transfer to cutting wear mechanism, and as well a decrease of blade wear with an increase of the incursion rate, highlighting a progressive transition of the wear mechanics with the incursion rate. Overall a similar wear mechanism was observed with an increase of the speed, and a decrease of adhesion and wear with an increase of the speed. Some differences were observed, especially in the test performed on the soft coating, where an increase of the speed generated a decrease of blade wear and an increase of the amount of cutting.

Therefore, an increase of the speed determined an increase of the input energy, which generated a higher heat that promoted higher adhesion like that observed especially

in the coating R15Y 59.6 at middle speed and low incursion rate, but also observed in the soft coating at middle speed. But also a high speed implied more impact speed, leading to more fracture of the material transfer observed with the evolution of the blade length, and increased as well the ability to fracture the dislocator phase due to the high contact speed. Therefore, the material response at middle and high speeds on the soft coating at low incursion rate highlighted a well-fractured surface and fractured hBN on the surface, due to the increase of the speed generating an early transition from dominant melt wear to cutting mechanism, which was due also to the increased hBN concentration on the soft coating, increasing the ability to cut.

In the next section, the different wear mechanism observed in each region of the wear map will be analysed in order to explain the nature of the different mechanical behaviours through the series of analyses performed during this research.

9.2. Analysis of the nature of the wear mechanics

The wear map in the previous section was produced in order to characterise the wear mechanics of the abradable material in relation to the input parameters. In this section, the series of analyses performed during this research will be brought together in order to explain the different mechanistic behaviour in each area that can be observed in the wear map.

Previous research was based the analysis of the abradable material and on the observation and the analysis of the wear mechanics in relation to the post-test sample. However, during this research a series of analyses between the input and the output were performed, in order to explain the nature of the different material behaviour observed. These were analyses of: the material response through material sectioning; the cutting force; the temperature and thermal property measurement; and the rate of adhesion and wear. Figure 9.4 shows a block diagram that summarises the research from the start point of the input parameter to the final output of the wear mechanics observed, and also the series of analyses performed that were used to obtain the final wear map (Figure 9.3).

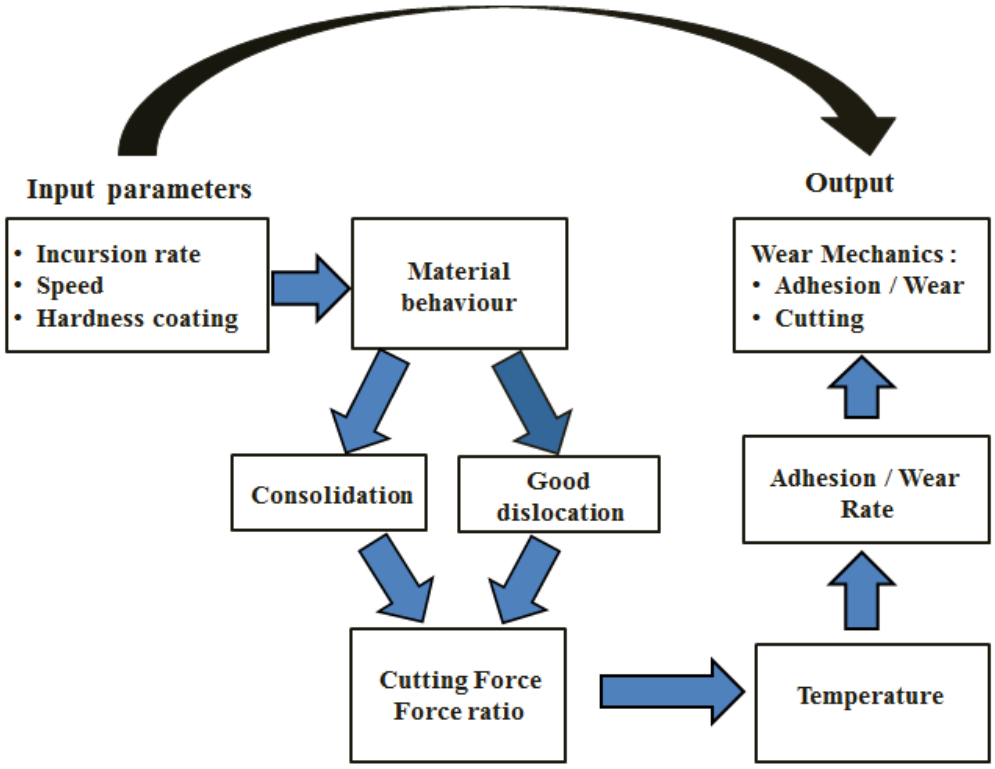

Figure 9.4. Overview of the research.

As highlighted previously, three main regions are shown in the wear map, namely adhesive transfer, blade wear and a cutting mechanism, which correspond to the different wear mechanism outputs of the test observed from the analysis of the sample post-test as shown in Figure 9.5, and especially for the soft and the hard coatings, where at low incursion rate two different wear mechanisms were observed.

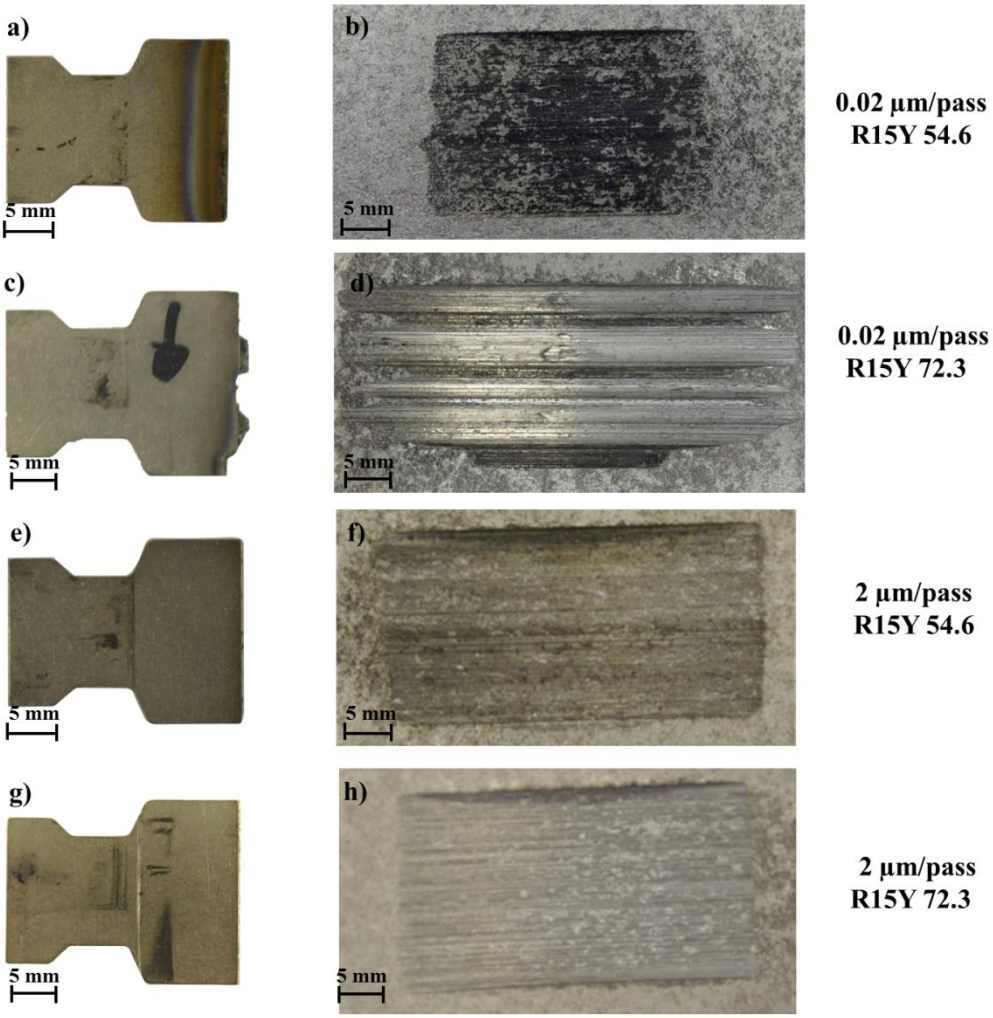

Figure 9.5. Blade and coating after the test at blade speed at 100m s^{-1}, at incursion rate of 0.02µm $pass^{-1}$: a) Blade, b) Coating R15Y 54.6; c) Blade, d) Coating R15Y 72.3; incursion rate of 2µm $pass^{-1}$: e) Blade, f) Coating R15Y 54.6; g) Blade, h) Coating R15Y 72.3.

As shown in the figure, clearly different wear mechanisms were observed between low and high incursion rates, with a well-cut rub surface at high incursion rate independent of the coating hardness (Figure 9.5 e, f, g, h), while there were different thermal wear mechanics at low incursion rate with blade wear and titanium transfer on the soft coating (Figure 9.5 a, b) and adhesive transfer and a grooved surface on the hard coating (Figure 9.5 c, d).

Therefore the different wear mechanics reflected different material behaviour responses, highlighted by the observation of the material response through the sections of the rub surface as shown in Figure 9.6.

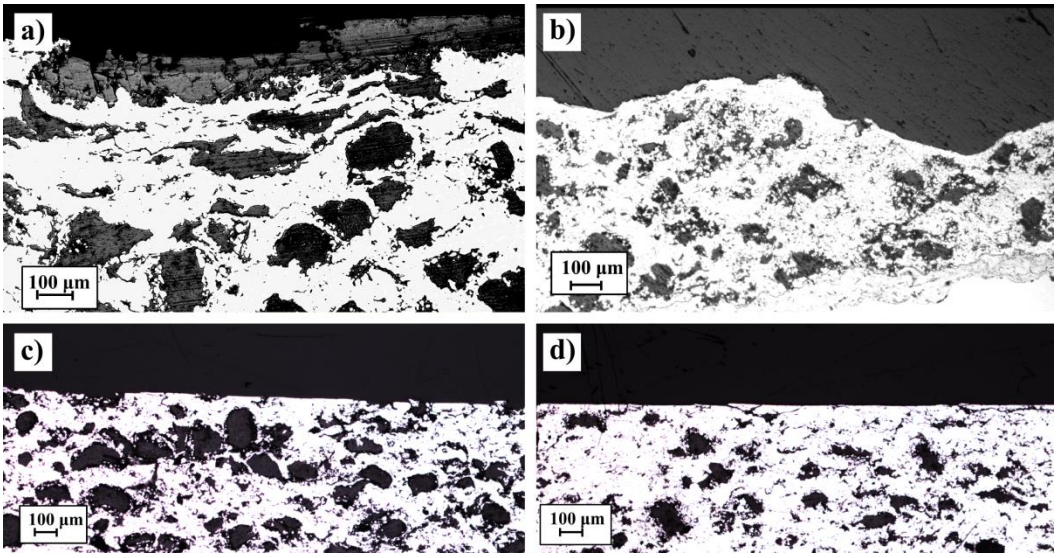

Figure 9.6. Section of the coating at incursion rate 0.02µm pass^{-1}: a) R15Y 54.6; b) R15Y 72.3; and at incursion rate of 2µm pass^{-1}: c) R15Y 54.6; d) R15Y 72.3.

As shown in the figure, significant changes to the material response in relation to the incursion rate and coating hardness were observed. Some cracks and fractured hBN indicated that the blade cut the material at high incursion rate, independently of the coating hardness. hBN is a brittle material that breaks readily, initiating cracks and increasing the ability to dislocate under the force of the blade. Also the fractured hBN and the well-cut surface confirmed that the incursion rate of 2µm pass^{-1} was high enough to fracture the particles of hBN with average dimension of 63µm [6, 12] and the blade was able to dislocate the material. While at low incursion rate a consolidation layer was observed with distorted hBN confirming the difficulty in dislocating the material during the contact, and it is also interesting to note that there was a different wear mechanism between soft and hard coatings at low incursion rate corresponding to different levels of consolidation, with a higher level of consolidation on the soft coating (Figure 9.7a). An increase of the speed did not generate a different wear mechanism, but it increased the amount of cutting due to an increased impact energy input. However, a significantly different material behaviour was observed, as highlighted in the wear map, in relation to the incursion rate and the hardness.

The different ability to dislocate the material was confirmed from the different energy input required to remove the material, measured as average contact force per unit of incursion per pass, as shown in Figure 9.7.

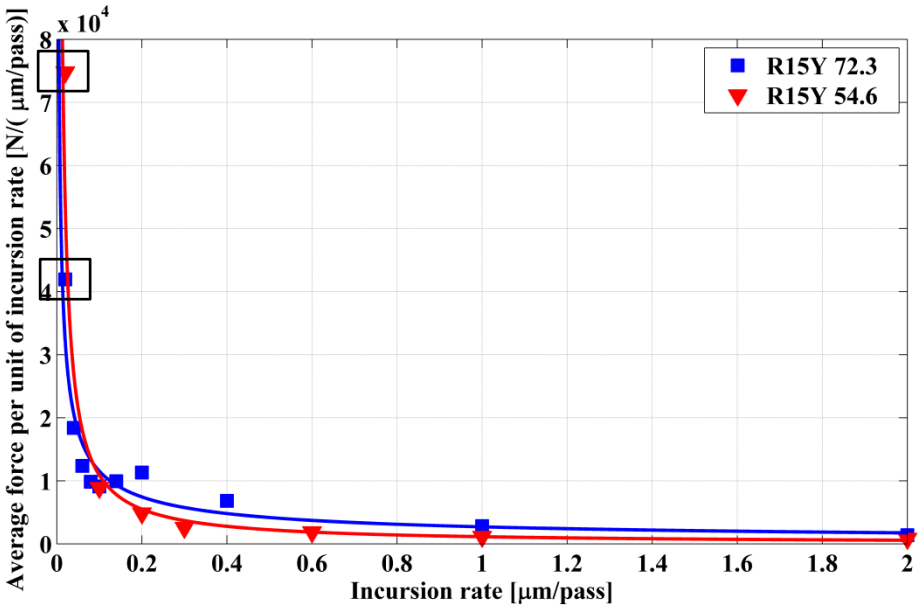

Figure 9.7. Average force per unit of incursion per pass against the incursion rate, for the test performed with coatings with hardnesses R15Y 72.3 and R15Y 54.6 at blade speed of 100m s^{-1}.

As shown in the figure, a high level of energy is required to remove material at low incursion rate, and it is therefore difficult to dislocate the material. The contact force confirmed what was observed for the material response with a consolidation of the sub-layer and with a higher level of consolidation in the soft coating, and therefore double the energy was required to remove the material at low incursion rate. Otherwise, an increase of the incursion rate reduced the force per unit of incursion rate, namely the energy input required to remove the material, and therefore the material response highlighted a well-cut surface with fractured hBN.

Additionally, the analysis of the cutting force in terms of force ratio, in relation to the incursion rate for the hard and soft coatings, provided further evidence on the different material behaviour as shown in Figure 9.8.

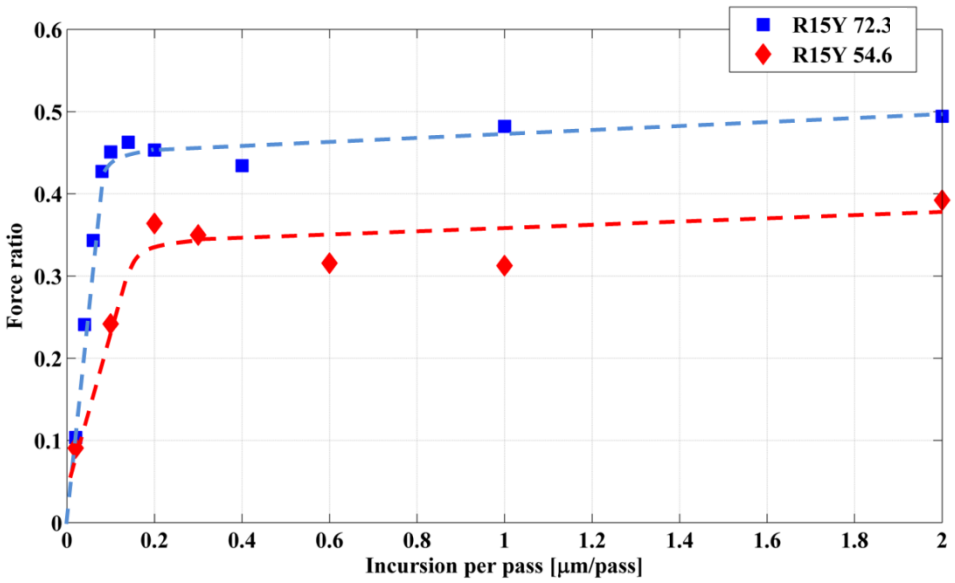

Figure 9.8. Force ratio.

As shown in the figure, a different force ratio was measured between low and high incursion rates, confirming a different material behaviour. Therefore, at low incursion rate, a low force ratio means a low efficiency of the cutting process, where the blade rubs instead of cutting and deforming the material because the value of the incursion is smaller than for the minimum un-deformed chip [100]. Also, a lower force ratio is comparable to the value of lubricant contact condition [102], indeed a transfer layer of titanium was observed on the soft coating and on the tip of the groove of the hard coating. At high incursion rate, a low energy input was required with a value of the force ratio comparable with orthogonal cutting [103, 104], confirming that the blade removed the entire depth of cut, and therefore no deformation and fractured hBN was observed. On the soft coating, a lower normal and tangential force along with the force ratio at high incursion rate suggests an increase of the ability to dislocate the material due the higher content of hBN compared with the hard coating [13]. Therefore, the hBN content of abradable material AlSi-hBN is designed to increase the ability to shear, indeed a decrease of the coating hardness implied an increase of hBN content, as highlighted in Section 3.1.4, and therefore the bond strength of the material decreases with the hardness [13].

Additionally, the high energy input required to remove material at low incursion rate generated heat in the contact and therefore a higher coating temperature was

measured, as evident from the thermal damage and thermal driven wear mechanism observed, and a progressive decrease of the temperature with an increase of the incursion rate was measured, as shown in Figure 9.9.

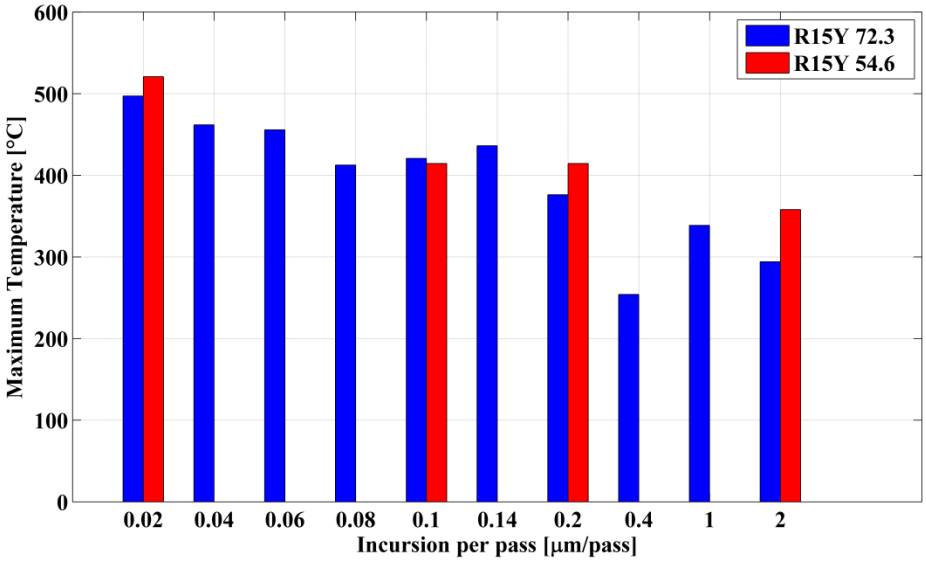

Figure 9.9. Maximum temperature for the coating R15Y 72.3 and R15Y 54.6 vs the incursion rate.

However, even with similar maximum temperatures at low incursion rate on the soft and the hard coatings, a different level of heat was observed in the blade tip, evidenced by the discoloration of the titanium, as shown in Figure 9.10.

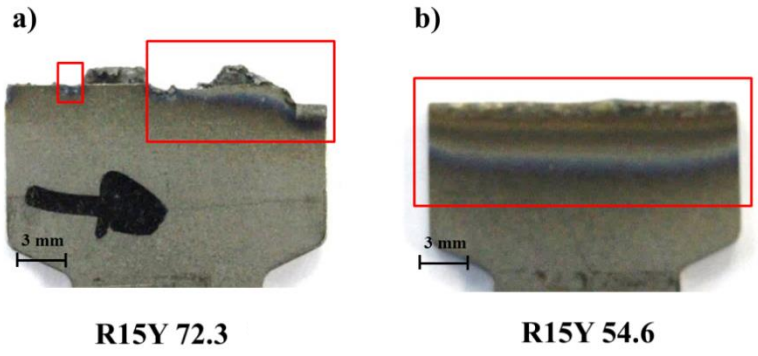

Figure 9.10. Blade tip tested at incursion rate of 0.02µm pass^{-1}, blade speed 100m s^{-1}, against: a) Hard coating; b) Soft coating.

A higher level of thermal damage was observed on the blade that had performed against the soft coating, therefore the different thermal conductivity of the coating in

relation to the coating hardness generated a different ability of the heat to propagate between the blade and the coating and led to different thermal wear mechanics, as shown in the wear map, with different heat partition between the blade and heat.

In the regions of wear in the wear map, on the soft coating at low incursion rate that corresponded to a low value of Peclet number, the blade rubbed and deformed the material, highlighted by the force ratio and the material response. The difficulty in removing material implied generation of heat in the contact, which had difficulty to penetrate into the coating because the coating had low thermal conductivity. Thus the insulated heat remained in the coating surface, and successive blade strikes interacted with the consolidate layer, a harder layer, and the force and the heat increased, and therefore the normal force was recorded as continuously increasing, until a significant heat started to penetrate into the blade and it started to melt. The thermal damage of the blade was suggested from various observations, namely the titanium transfer layer measured on the coating rub surface, the blade wear and the high level of thermal damage on the blade tip, the high level of consolidation observed with the material response, and finally from an image of the test rig captured during the test where an incandescent rotating blade was observed, as shown in Figure 9.11.

Figure 9.11. Image of the test rig during the test performed with coating hardness R15Y 54.6, incursion rate of 0.02μm pass^{-1} at blade speed of 100m s^{-1}.

In the areas where adhesion was observed, on the hard coating at low incursion rate the blade rubbed and consolidated the material, with less consolidation compared

with the soft coating due to it being a harder material to deform. A high energy required to remove material and a high contact force confirmed the difficulty in dislocating and the high temperature measured confirmed a heat build-up in the contact. However, having a higher thermal conductivity compared with the soft coating allowed the heat built up in the contact to pass through into the coating. This increased the temperature of the sub-surface of the coating, and heated the binding organic phase of the coating. The binder is used to agglomerate the metallic phase (AlSi) with the dislocator phase (hBN) when the melting point of the binder phase is reached, compromising the integrity of the abradable material and leading to the adhesive transfer from the coating to the blade tip. Therefore the mechanism of adhesion was correlated with the penetration of the heat through the coating that led the organic phase to burn off, and also led to sufficient interaction with the binder phase, this confirmed the initial analysis presented by Borel where the influence of binder phase temperature was studied in AlSi-plastic [6].

Otherwise, in the cutting mechanism region that corresponded to a higher Peclet number, the heat was carried away in the chip. Therefore at high incursion rate the blade fractured the hBN and removed the un-deformed chip at each pass, and the damaged substrate was removed by each successive strike. Indeed, the coating temperature was lower compared to low incursion rate, and the material response showed fractured hBN and well-cut surface, like the coating rub surface and with no thermal damage on the blade tip.

As observed in the wear map, the heat generated in the contact led to adhesive transfer or blade wear, especially at low incursion rate, as shown in Figure 9.12 with the evolution of the blade length change obtained with the stroboscopic imaging technique.

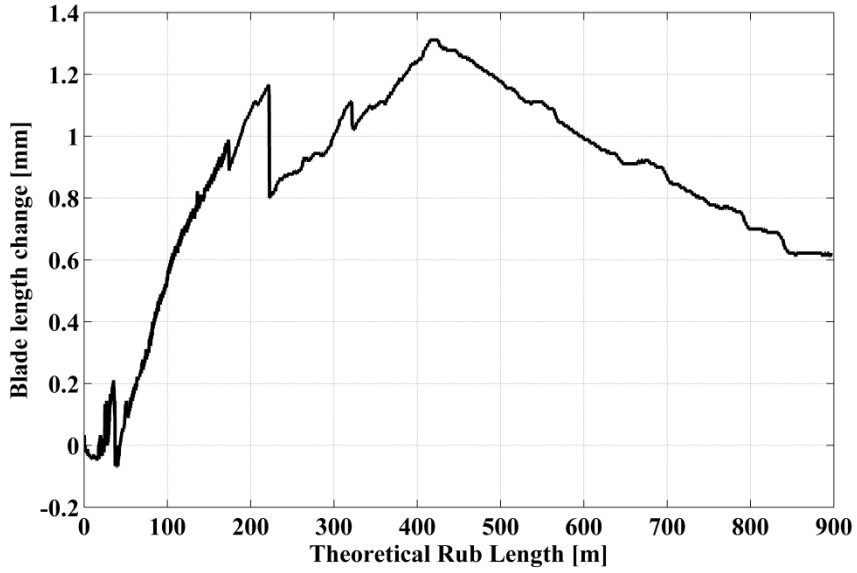

Figure 9.12. Blade length change against the theoretical rub length, test at incursion rate of 0.06µm pass^{-1} and blade speed of 150m s^{-1} and coating hardness R15Y 59.6.

This technique highlighted the evolution of the adhesive transfer and blade wear and, as shown in the figure, the final blade condition was not necessarily representative of the overall adhesive transfer during the test. Otherwise, the analysis of the graph highlighted a steady period of adhesion or wear, and the measure of this period with the rate of adhesion / wear confirmed it to be linked with the incursion rate and quantified the different wear mechanisms, as shown in Figure 9.13.

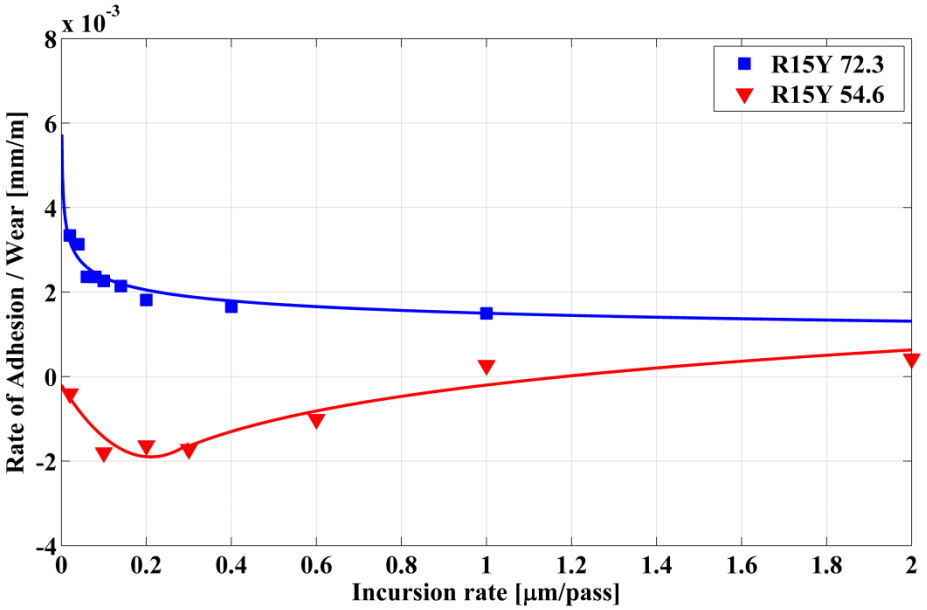

Figure 9.13. Rate of adhesion / wear for coating with hardness R15Y 72.3 and R15Y 54.6 at blade speed of 100m s^{-1}.

The figure illustrates the sample observation, where on the hard coating at low incursion rate a high rate of adhesion was measured, with a progressive reduction with an increase of the incursion rate, when the wear mechanism changed progressively from adhesive transfer to a dominant cutting wear mechanism. Meanwhile, on the soft coating, a negative wear rate represented the blade wear, and a progressive transition to cutting mechanism with increased incursion rate was observed. At low incursion rate, even with a higher level of thermal damage and blade wear, a lower rate of wear was measured, maybe reduced by an initial adhesion.

As highlighted in previous studies and this research, an increase of the speed did not generate a different wear mechanism, except on the soft coating, where an increase of the speed increased the amount of cutting. In this case, the increase of the dislocator phase increased the ability to dislocate. Additionally an increase of the impact speed increased the efficiency of cut [105], and a transition from wear to an increase of cutting was observed.

In conclusion, the research characterised the wear mechanism in relation to the incursion rate, blade speed, and coating hardness, which implied different thermal coating properties and was reflected in different wear mechanisms especially at low incursion rate. The wear map highlighted the different wear mechanisms in relation to the input parameters. Additionally, this research highlighted that it is better to have a higher thermal conductivity of the coating, and therefore the use of a hard AlSi-hBN is a better option, because less thermal damage was observed. The blade wear implied an overall reduction of the clearance between blade and linings, hence an overall decrease of the performance, and therefore it is preferable to have wear on the coating instead of on the blade. However, the abradable sample was characterised by an anisotropic structure, so it would be ideal to use a high thermal conductivity coating but a homogeneous structure. Furthermore, the wear map with the different areas corresponding to the different output wear mechanisms in relation to the input parameters could be used in a design phase in order to obtain a desired cutting mechanism. Therefore, the design phase could be used to decide a material with a high thermal diffusivity and conductivity, but also to decide on a material for the blade that permits a desirable cutting mechanism to be achieved.

9.3. Repeatability of the test and comparison with full test rig

In this section, the repeatability of the result is discussed, after which the results obtained during this research will be compared with those from a full test rig used previously by Rolls Royce to evaluate the wear mechanism.

Figure 9.14 shows the repeated material post-test at an incursion rate of 0.02μm pass^{-1}, blade speed of 100m s^{-1} and coating hardness R15Y 72.3.

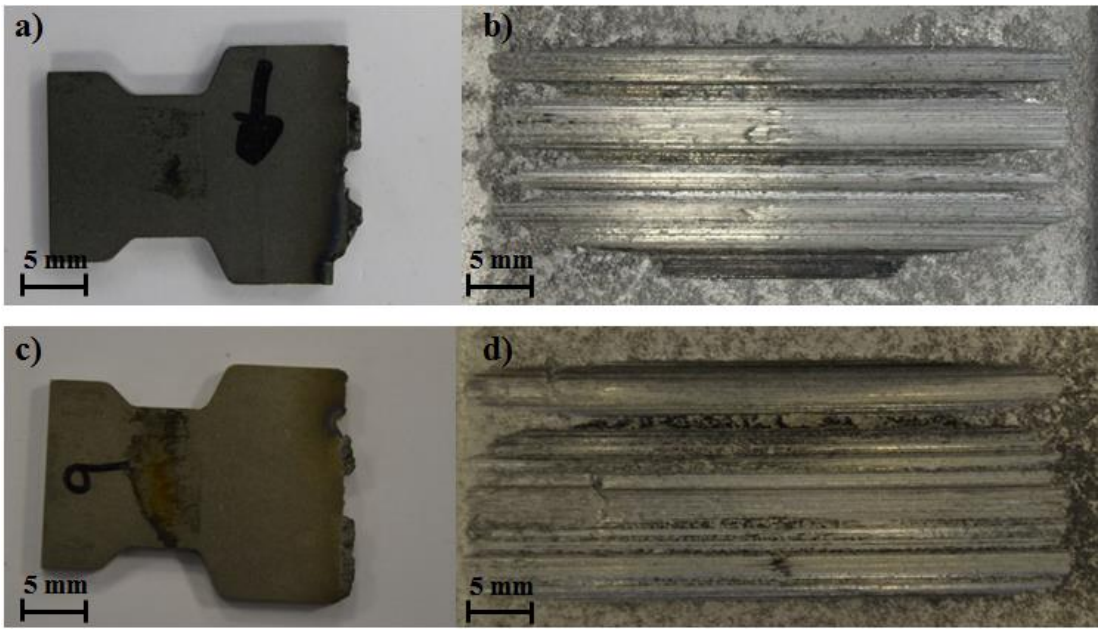

Figure 9.14. Image of the blade and coating post-test at 100m s^{-1} with abradable sample hardness R15Y 72.3 and incursion rate of 0.02μm pass^{-1}, a-b) Blade and coating test; c-d) Blade and coating repeated test.

As shown in the figure, in the repeated test (Figure 9.14c, d) a similar level of adhesion transfer was observed, with non-uniform adhesive transfer but different degrees of adhesion across the blade profile, with a grooved surface with a transfer layer of titanium on the top of the groove. The analysis performed during this research, such as the evolution of the blade length, the contact force and the temperature, was compared between the two tests as shown in Figure 9.15.

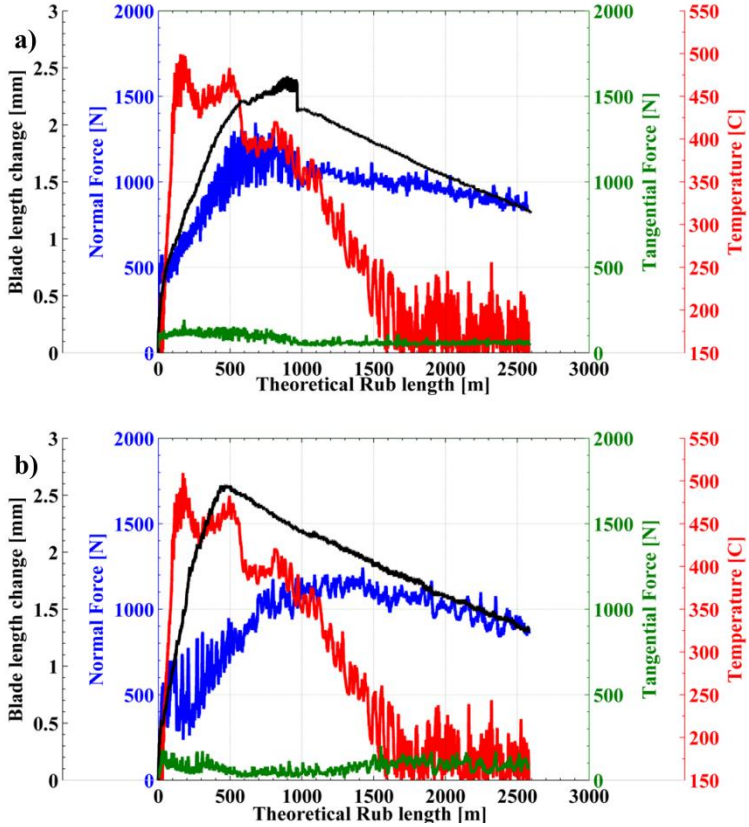

Figure 9.15. Blade length change, normal and tangential forces and temperature measurement for the test performed at incursion rate 0.02μm pass^{-1}, blade speed 100m s^{-1} and coating hardness R15Y 72.3, a) Test performed; b) Test repeated.

The abradable material is a heterogeneous and variable material due to the thermal spray process [12, 13, 14, 45, 46]. However, as shown in the figure, a similar evolution of the blade length change and a similar contact force and temperature of the coating were measured between the two tests. The similar results observed confirmed the repeatability of the test performed during this research with this test rig, and highlight was the abradable may vary on a local level, the global response is broadly consistent.

During this research a scaled test platform was used and developed in order to characterise the wear mechanism and compare it with a full dimension compressor aero-engine test rig at Sulzer [7, 8], previously used by the Rolls Royce Surface Engineering Group. The Sulzer test rig has a flame generator to heat the coating and reproduce the temperature operation of the coating. During this research the measurement of the coating temperature showed an average coating temperature around the maximum operation range of 450 °C for the abradable material AlSi-

hBN. In addition, a higher contact temperature was measured, confirming that a similar heat was reproduced in the contact. Additionally, the same test conditions reproduced similar wear mechanism outputs, with adhesion transfer at low incursion and a well-cut surface at high incursion rate, as shown in Figure 9.16.

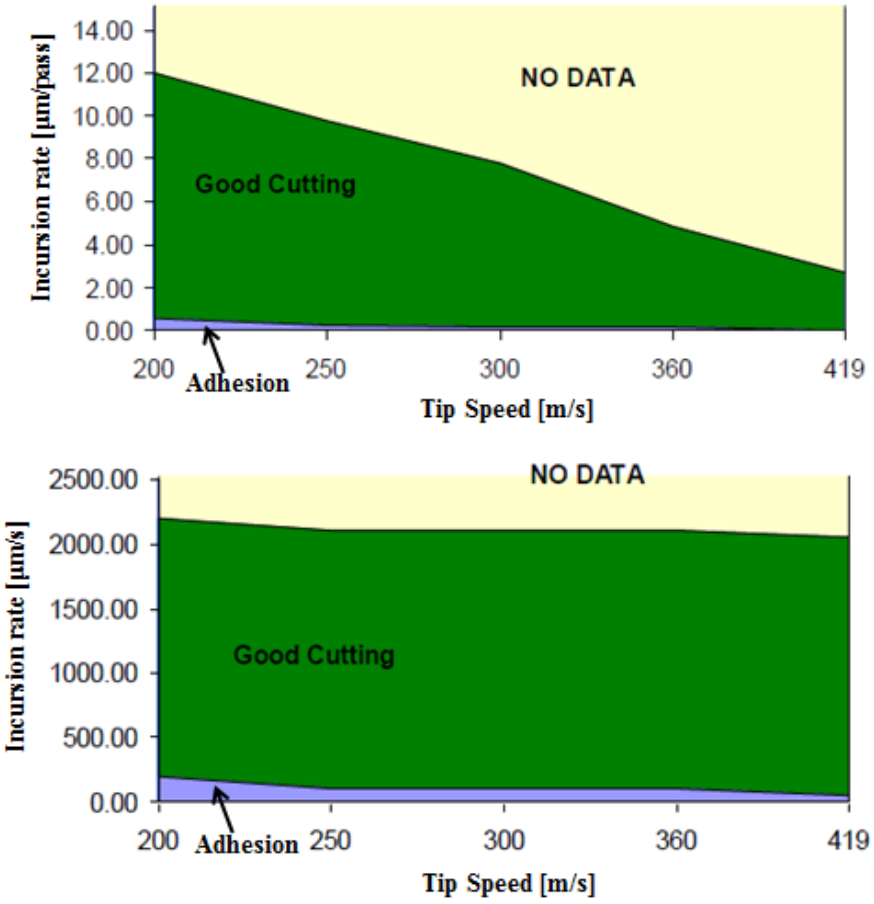

Figure 9.16. Wear mechanism observed with full test rig with abradable material AlSi-hBN and titanium blade (Ti-6Al-4V) (Data provided by Rolls Royce Surface Engineering Group).

As shown in the figure, the main mechanisms observed with a hard coating, most commonly in use in aero-engines, were adhesion transfer at low incursion rate of 0.02µm pass^{-1} that represented the interaction in the flight phase [8, 17], and a cutting mechanism for higher incursion rates like 2µm pass^{-1} observed during this research, which represented the handling phase [9, 10].

The slowest speed of the Sulzer test rig was the maximum speed analysed during this research. The slower speed led to a slight increase in adhesive transfer; however, at the highest speed of the Sulzer test rig adhesion was still observed. Even when a lower speed range was analysed, a similar wear mechanism was observed and the

characterisation performed provided a fundamental understanding of the nature of the wear mechanism, instead of the analysis only based on the variation post-test provided by the Sulzer test rig, and also the speed was found to be of reduced significance in the wear mechanism.

Additionally, the test rig used and developed during this research was a small-scale version of the full dimension test rig in order to be able to monitor the contact between the rotating blade and the coating and characterise the wear mechanism. The scaled dimensions did not represent a real issue, as the important aspect was to reproduce the same contact conditions, and these were obtained during this research. As highlighted in Figure 9.17, the rub surface obtained with the full dimension test rig had a grooving surface and well-cut surface at low (Figure 9.17a) and high (Figure 9.17b) incursion rates respectively, at high speed, showing a similar wear mechanism to that observed during this research.

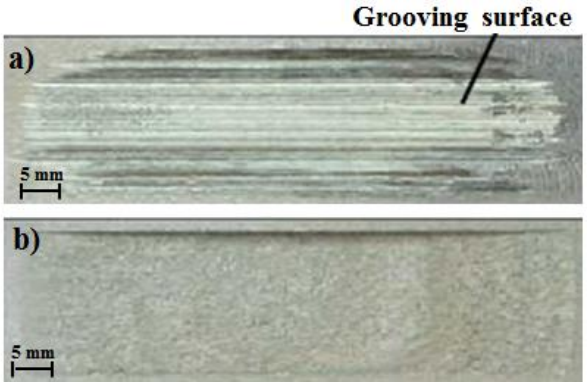

Figure 9.17. Wear mechanism observed with full test rig with abradable material AlSi-hBN and titanium blade (Ti-6Al-4V), a) Low incursion rate; b) High incursion rate (Data provided by Rolls Royce Surface Engineering Group).

Furthermore, during this research a flat titanium blade was used with the same design as for the full test rig, and additionally a flat substrate was used in order to simplify the contact. However, similar wear mechanisms were observed and characterised with a wider range of incursion rates and coating hardnesses.

10. Conclusions, Recommendations and Future Work

10.1 Conclusions and Recommendations

- The wear mechanism between a rotating blade of Ti-6Al-4V and an abradable sample AlSi-hBN were characterised, using an experimental platform that reproduced the contact, and a series of instruments were introduced in order to monitor the contact.

- This study highlighted different wear mechanisms in relation to the incursion rate and hardness, especially at low incursion rate, with blade speed showing a more limited influence.
- At low incursion rate, an adhesive transfer and grooved rub surface was observed on the test performed with the hard coating, while a decrease of the hardness highlighted a progressive change from adhesive transfer to blade wear with titanium transfer from the blade to the soft coating.
- At high incursion rate, independently of the coating hardness, a cutting mechanism was observed with a well-cut coating surface.
- A stroboscopic imaging technique developed during this study revealed material adhered to the blade on continuous basis. In some cases the material fractured off or wore, and the final condition was not representative of the level of adhesive transfer, highlighted for example in the analysis based on change in length and weight after test. This approach also highlighted progression of the wear mechanism.
- Analysis of the rate of adhesion / wear highlighted a decrease of the rate with increasing incursion rate, with a progressive change from adhesion or wear to cutting.
- The force measurement identified different force trends in relation to the incursion rate and coating hardness. The characterisation of the wear mechanism, in relation to the efficiency of cut and force ratio, showed that at low incursion rate, low efficiency of cut was measured, and increased with an increase of the incursion rate.
- The force ratio measured highlighted the material behaviour in term of chip formation, where a low force ratio at low incursion rate suggested that the blade rubbed and deformed the material instead of removing the entire depth of cut. At high incursion rate, a higher force ratio suggests chip formation and that the entire depth of cut was removed.
- Sectioning of the wear track from the blade confirmed that the blade rubbed the abradable material at low incursion rates, and consolidation of the coating

was observed, while at high incursion rate a well-cut surface with fractured hBN confirmed the cutting mechanism.

- The temperature measurement confirmed heat build-up in the contact, especially at low incursion rate, and different heat propagation was observed in relation to the coating hardness.
- Different coating hardness implied different constituent composition, and a different thermal conductivity. The thermal conductivity increased with an increase of the hardness, explaining the different wear mechanisms observed.
- At low incursion rate, the soft coating had poor thermal conductivity. The heat build-up in the contact had difficulty flowing through the coating, and thus the heat remained in the contact, until passing through the blade and melting it. On the hard coating, higher thermal conductivity helped the path of the heat to the coating, and heated the organic binding phase and led to adhesive transfer.
- At high incursion rate, independent of the coating hardness, the blade removed the un-deformed chip at each pass, and the heat was carried away in the chip.
- The wear map generated allowed identification and understanding of the wear mechanism in relation to the set conditions. This could be applied to different materials in relation to the input parameters and thermal properties, but in particular could be used in the design phase of a new abradable material in order to obtain a desired cutting mechanism.
- This research has highlighted that it is better have a coating with higher thermal diffusivity and conductivity; therefore, use of a AlSi-hBN hard coating will be a better option, because less thermal damage was observed with such a coating.
- The design phase could decide on a material with high thermal diffusivity and conductivity, but also to design a material for the blade that can achieve a desirable cutting mechanism. Also, the abradable sample is characterised by anisotropic structure, so it would be ideal having a coating with a high thermal conductivity but with homogeneous structure.

10.2 Current developments from this research

The future of research on abradable materials for aero-engines is currently focused on foam materials, as they can be engineered for the desired material properties, and the results of this research in terms of desired material properties are now feeding into the study of foams. This material has good mechanical and thermal properties and high stiffness in conjunction with very low specific weight and high thermal conductivity. The foam can be made with different pore sizes [109-111] in relation to the application. Also, it could have a plurality of sub-layers of varying pore size. For example [112], a top layer with small pore size can provide good cutting and sealing properties, and underneath a sub-layer with large pores would have an enhanced compliance which would reduce strain energy, and would permit the foam to collapse to an extent during rubbing, and would reduce the energy for cutting the abradable material. Also, the foam could be filled with abradable material, or polymer, or ceramic in relation to the application and the aero-engine stage where it would be located, in order to increase the cutting performance and sealing characteristics.

Different types of foam, metal material, different fillers and dimensions of porosity have been tested. In general, the foam material was characterised by a good cutting surface, without thermal damage on the blade, low contact force and low temperature. The tests of foam materials are in an early stage; however, Figure 10.1 shows an example of a well-cut surface performed with a titanium alloy blade and foam material after low and high incursion rates at a blade speed of 200m s^{-1}.

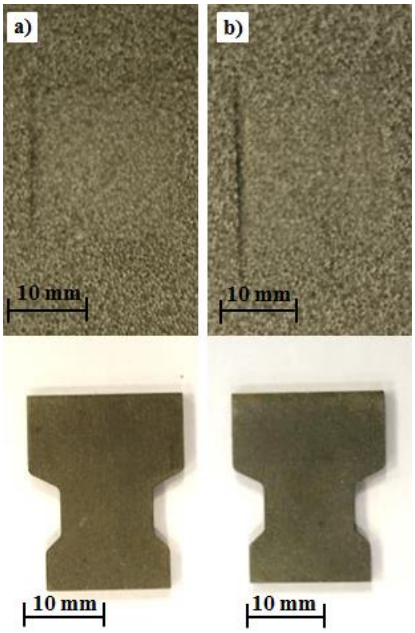

Figure 10.1. Foam material and titanium blade after the test at 200m s^{-1}: a) 0.02μm $pass^{-1}$; b) 2μm $pass^{-1}$.

As shown in the figure, the dominant wear mechanism was blade cutting, with no thermal damage on the blade, low force and low temperature. This research is in a development phase, and therefore more test information regarding the analysis cannot be released at present. In general, the preliminary results have highlighted a good behaviour of the foam material, which could represent a future valid material to insert in the aero-engine sealing with opportune size of porosity and filler material.

10.3 Future work

A novel high-speed test platform able to rotate with maximum blade tip speed of 400m s^{-1} is under construction in order to analyse the wear mechanism with the same speed as the aero-engine. The techniques developed in the current platform will be introduced in the new one. Also, an improvement will be made in the stroboscopic technique. The actual technique used here presented the blade length change captured from a side view of the blade; this limited the observation of the blade profile during the test and the understanding of which part of the blade tip was affected by the adhesive transfer or blade wear. Therefore, the technique needs to be improved so that blade variation can be analysed over the front profile of the blade instead of the side view. The current technique highlighted the nature of the adhesive transfer, and allowed this research to characterise the wear mechanics. The proposed

improvement will be a rotation of the camera by 90° with respect to the actual position in order to monitor the blade length change of the blade profile. This requires a bigger LED, so needing a higher energy pulse to drive the LED, and therefore a more powerful LED controller needs to be used. The analysis of the blade variation obtained from the blade profile will be combined with material modelling. Material sectioning will be used in order to capture the material microstructure and will be modelled in order to calculate how the heat has flowed through the material in relation to the heterogeneous microstructure and the coating hardness, and will be compared to the front image of the blade variation when adhesion and melt wear occurs along the blade profile. Also, another pyrometer will be introduced in order to measure the coating temperature at different points of the contact area, with the aim of obtaining more information during the contact.

10.4. Publications and conferences from this work

-N. Fois, J. Stringer, M.B. Marshall, Adhesive transfer in aero-engine abradable linings contact, Wear 304 (2013) 202-210.

-N. Fois, J. Stringer, M. B. Marshall, Adhesive transfer and cutting wear in aero-engine abradable lining contact, 5th World Tribology Congress, September 8-13, 2013, 730, Torino.

-N. Fois, J. Stringer, M. B. Marshall, Charactering the Wear Mechanics of Abradable Compressor Seals, Institute of Material, Minerals and Mining (IOM3) Young Member Committee (YMC) Research and Innovation Event, December 9, 2013, Burleigh Court – Loughborough University.

-N. Fois, M. Watson, J. Stringer, M. B. Marshall, An investigation of the relationship between wear and contact force for abradable materials, Proceedings of Institution of Mechanical Engineers, Part J: Journal of Engineering Tribology 229 (2015), 136-150.

-M. Watson, N. Fois, M. B. Marshall, Effects of blade surface treatments in tip – shroud abradable contact, Wear 338-339 (2015) 268-281.

-N. Fois, M. Watson, M. B. Marshall, The influence of the superficial hardness on the wear of abradable materials, Proceedings of Institution of Mechanical Engineers, Part J: Journal of Engineering Tribology, Submitted on 9 June 2015.

11. References

[1] J. Stringer, M.B. Marshall, High speed wear testing of an abradable coating, Wear 294-295 (2012) 257-263.

[2 Rolls Royce, The Jet Engine, 1971 Ed. by Rolls Royce.

[3] D. Sporer, S. Wilson, I. Giovanetti, A. Refke, M Giannozzi, On the potential of metal and ceramic based abradables in turbine seal application, Proceedings of the Thirty-Sixth Turbomachinery Symposium 2007, Texas A&M University, pp.79-86.

[4] H.I. Faraoun, T. Grosdidier, J.L. Seichepine, D. Goran, H. Aourag, C. Coddet, J. Zwick, N. Hopkins, Improvement of thermally sprayed abradable coating by microstructure control, Surface and Coating Technology 201 (2006) 2303-2312.

[5] R.E. Johnston, Mechanical characterisation of AlSi-hBN, NiCrAl-Bentonite, and NiCrAl-Bentonite-hBN freestanding abradable coatings, Surface & Coatings Technology 205 (2011) 3268-3273.

[6] M.O. Borel, A.R. Nicoll, H.W. Schlapfer, R.K. Schmid, The wear mechanisms occurring in abradable seals of gas turbines, Surface & Coatings Technology 39/40 (1989) 117-126.

[7] Scott Wilson, Thermally sprayed abradable coating technology for sealing in gas turbines. Future of gas turbine technology 6th International Conference October 17-18 2012, Brussels, Belgium Paper ID number 51.

[8] D.B. Allen, Abradable coating system. No.: US 7686570 B2, March 30 2010.

[9] M.J. Edmonson, R.J. Gritter, Turbine engine fan housing abradable material removal tool and method of abradable material removal. United States, Patent Application Publication, Pub. No.: US 2014/0017980 A1, January 16 2014.

[10] A.D. Munroe, P.E. Voyer, Abradable rub strip. No.: US 4349313, September 14 1982.

[11] D. Sporer, S. Wilson, Current and Next-Generation Titanium Blade Compatible Compressor Abradable coatings, Proceedings from the International Thermal Spray Conference and Exposition, May 21-24 2012, Houston, Texas, USA.

[12] Sulzer Metco, Oerlikon Metco, Material Product Data Sheet, Aluminum Silicon Hexagonal Boron Nitride, Thermal Spray Powder Products: Metco 320NS, http://www.oerlikon.com/metco/en/products-services/coating-materials/thermal-spray/abradables-polymer-fillers/ (Last accessed 14 September 2014).

[13] Sulzer Metco, Solutions Flash, Cause and Effect of Metco 320NS Spray Parameters for Optimisation of Coating Hardness and Service Life, http://www.oerlikon.com/metco/en/products-services/coating-materials/thermal-spray/abradables-polymer-fillers/ (Last accessed 14 July 2014).

[14] L. Pawlowski, The science and engineering of Thermal Spray Coatings, second ed., John Wiley & Sons Ltd. 2008. ISBN 978-0-471-490494.

[15] M.Bounazef, S. Guessasma, B. Ait Saadi, The wear, deterioration and transformation phenomena of abradable coating BN-SiAl-bounding organic element, caused by the friction between the blades and the turbine casing, Materials Letters 58 (2004) 3375-3380.

[16] Australia Government, Australia Transport Safety Bureau, Engine failure-Melbourne Airport, Victoria, August-25 2004, Boeing Company 777-312 9V-SYB, ATSB Transport safety investigation report, Aviation safety incident report – 200403110.

[17] N.P. Hopkins, Abradables, ODA Course Notes, Surface Engineering group, Rolls Royce Plc, February 2005.

[18] W. Grzesik, Advanced Machining Processes of Metallic Materials, Theory, Modelling and Applications. Ed. Elsevier, 2008, Orthogonal and Oblique cutting mechanics pp.69-84.

[19] N.N. Zorev. Metal cutting mechanics, Pegarmon Press, 1966.

[20] M.C. Shaw, Metal Cutting Principles. ISBN-13: 978-8123901367.

[21] H. El-Hofy, Fundamentals of Machining Processes, conventional and nonconventional process. Ed. CRC Press, 2006.

[22] P. Iskra, C. Tanaka, T. Ohtani, Energy balance of the orthogonal cutting process. Holz als Roh- und Werkstoff. 2005; 63: 358-364, DOI 10.1007/s0017-005-0021-8.

[23] S. Sun, M. Brandt, M.S. Dargusch, Characteristics of cutting forces and chip formation in machining of titanium alloys, International Journal of Machine Tools & Manufacture 49 (2009) 561-568.

[24] V.P. Astakhov, A treatise on material characterization in the metal cutting process. Part 1: A novel approach and experimental verification, Journal of Material Processing Technology 96 (1999) 22-33.

[25] W. Grzesik, Advanced Machining Processes of Metallic Materials, Theory, Modelling and Applications. Ed. Elsevier, Chip Formation and control, (2008), pp.85-113.

[26] C. Padova, M.G. Dunn, J. Barton, Casing treatment and blade tip configuration effects on controlled gas turbine blade tip/shroud rubs at engine conditions, Proceedings of ASME Turbo Expo 2008: Power for Land, Sea and Air, GT2008, June 9-13 2008, Berlin, Germany.

[27] C. Padova, J. Barton, M. G. Dunn, S. Manwaring, G. Young, M.L. Adams, M. Adams, Development of Capability to Produce Controlled Blade Tip/Shroud Rubs at Engine Speed, Journal of Turbomachinery, 127 (2005) 726-735.

[28] C. Padova, J. Barton, M.G. Dunn, S. Manwaring. Experimental Results from Controlled Blade Tip/Shroud Rubs at Engine Speed, Journal of Turbomachinery 129 (2007) 713–723.

[29] S. Baiz, J. Fabis, X. Boidin, Y. Desplanques, Experimental investigation of the blade/seal interaction, Proc. IMechE Part J: J. Engineering Tribology 227 (2013) 980-995.

[30] R. Mandard, J.F. Witz, X. Boidin, J. Fabis, Y. Desplanques, J. Meriaux, Interacting force estimation during blade/seal rubs, Tribology International, In press, February 6 2014.

[31] J. Ahrens, H. Ulbrich, G. Ahaus, Measurement of contact forces during blade rubbing, Vibration in Rotating Machinery, 7th International Conference, Nottingham, September 12-14 2000, IMechE, London, pp. 259-263.

[32] G. Sutter, S. Philippon, F. Garcin, Dynamic analysis of the interaction between an abradable material and a titanium alloy, Wear 261 (2006) 686-692.

[33] W.F. Laverty, Rub energetic of compressor blade tip seals, Wear 75 (1982) 1-20.

[34] J. Williams, Engineering Tribology, Cambridge University Press, 2005.

[35] I.M. Hutchings, Tribology Friction and Wear of Engineering Materials, Butterworth-Heinemann, 2001.

[36] M. Yi, J. He, B. Huang, H. Zhou, Friction and wear behaviour and abradability of abradable seal coating, Wear 231 (1999) 47-53.

[37] X. Ma, A. Matthews, Investigation of abradable seal coating performance using scratch testing, Surface & Coatings Technology 202 (2007) 1214-1220.

[38] D. Sporer, M. Dorfman, L. Xie, A. Refke, I. Giovannetti, M. Giannozzi, Processing and Properties of Advanced Ceramic Abradable Coatings, Proceedings of the 2007 International Thermal Spray Conference, May 14–16 2007, Beijing, People's Republic of China.

[39] R. Rajendran, Gas Turbine – An overview, Engineering Failure Analysis 26 (2012) 355-369.

[40] P. Fiala, K. Hajmrle, A.P. Chilkowich, L. Shiembo, New High Temperature Titanium Compatible Abradable seal, Proceedings of the 22nd Heat treating Society Conference and the 2nd International Surface Engineering Congress, September 15-17 2003, Indianapolis, USA.

[41] M. Yi, B. Huang, J. He, Erosion wear behaviour and model of abradable seal coating, Wear 252 (2002) 9-15.

[42] T.N. Rhys-Jones, The use of thermally sprayed coatings for compressor and turbine applications in aero engines, Surface and Coating Technology 42 (1990) 1-11.

[43] T.N. Rhys-Jones, Thermally sprayed coating systems for surface protection and clearance control applications in aero engines, Surface and Coating Technology 43/44 (1990) 402-415.

[44] M. Vardelle, P. Fauchais, Plasma spray process: diagnostics and control?, Pure Appl. Chem. 71, No.10 (1999) 1909-1918.

[45] M.R. Dorfman, P. Fiala, K. Hajmrle, S. Wilson, Future abradable requirements needed by aerospace OEM`s and their material and equipment suppliers, Proceedings of GT2007, ASME Turbo Expo 2007: Power for Land, Sea and Air, May 14-17 2007, Montreal, Canada.

[46] E. Lugscheider, J. Zwick, M. Hertter, D. Sporer, Control of Coating Properties of Abradable Seals by On-line Process Diagnostics, ITSC 2005, Conference & Exposition, Thermal Spray Potential, Basel, Switzerland, May 2-4 2005.

[47] Rolls-Royce specification CME 5033 Section 2, Standard No. E1 Appendix 1 (Manufacture of new parts) and TSD 594J OP 704 Subtask 70-00-00-300-704-A07 (Repair and overhaul).

[48] R.E. Johnston, W.J. Evans, Freestanding abradable coating manufacture and tensile test development. Surface & Coatings Technology 202 (2007) 725-729.

[49] Standard Test Method for Adhesion or Cohesion Strength of Thermal Spray Coatings, ASTM C633-13.

[50] G. Blann, G.F. Vander Voort, Tech- notes, Volume 1, Issue 2, Buehler Ltd, 1997.

[51] G.F. Vander Voort, Metallography Principles and Practice, McGraw-Hill, 1984, Chapter 2, Specimen Preparation for light microscopy. pp.267-318.

[52] G.A. Blann, Metallographic specimen preparation of thermally sprayed coating for microstructural analysis, Microstructural Science, IMS and ASM International, Metals Park, OH, 17 (1989) 139-151.

[53] G.A. Blann, The effects of Manual vs Semi-Automatic Metallographic Specimen preparation of Thermally Sprayed Coatings, Thermally Spray: A United

Forum for Scientific and Technological Advances, ASM International, Material Park, Ohio, USA, (1997) 965- 971, ISBN 0871706180.

[54] Buehler`s Technical Information Guide, Cutting recommendations, Buehler Ltd.

[55] S.D. Glancy, Universal Metallographic Procedure for Thermal Spray Coatings. Structure, Struers Journal of Materialography 29 (1996) 12-16.

[56] H.I. Faraoun, J.L. Seichepine, C. Coddet, H. Aourag, J. Zwick, N. Hopkins, D. Sporer, M. Hetter, Modelling route for abradable coatings, Surface & Coatings Technology 200 (2006) 6578-6582.

[57] J. Matejicek, B. Kolman, J. Dubsky, K. Neufuss, N. Hopkins, J. Zwick, Alternative methods for determination of composition and porosity in abradable materials, Materials Characterization 57 (2006) 17-29.

[58] Sulzer Metco, Identification of Hexagonal Boron Nitride in Amdry 958 Coatings Using Polarized Light Microscopy (PLM), Sulzer Metco Canada, May 2010.

[59] S. Deshpande, A. Kulkarni, S. Sampath, H. Herman, Application of image analysis for characterisation of porosity in thermal spray coatings and correlation with small angle neutron scattering, Surface and Coatings Technology 187 (2004) 6-16.

[60] J.P. Holman. Heat Transfer, eighth ed., Ed. Mcgraw-Hill Inc, 1997.

[61] W.J. Parker, R.J. Jenkins, C.P. Butler, G.L. Abbott, Flash Method of determining thermal diffusivity, heat capacity and thermal conductivity, Journal of Applied Physics 32 number 9 September 1961.

[62] R. Bolot, J.L. Seichepine, J.H. Qiao, C. Coddet, Predicting the Thermal Conductivity of AlSi/Polyester Abradable Coatings: Effects of the Numerical Method, Journal of Thermal Spray Technology 20 (2011) 39-47.

[63] Y. Tan, J.P. Longtin, S. Sampath, Modelling Thermal Conductivity of Thermal Spray Coatings: Comparing Predictions to Experiments, Journal of Thermal Spray Technology 15 (2006) 545-552.

[64] H. Wang, Criteria for analysis of abradable coatings, Surface and Coatings Technology 79 (1996) 71-75.

[65] H. Wang, An Analysis of Turbine Blade/Abradable Seal Rubbing, in H. Henein and T. Oki (eds), Proc. 1st Int. Conf. on Processing Materials for Properties, Honolulu, HI, 1993, Minerals, Metals and Materials Society, pp.1085-1088.

[66] M. Legrand, C. Pierre, Numerical investigation of abradable coating wear through plastic constitutive law: application of aircraft engines, ASME International Design Engineering Technical Conferences & Computers and Information in Engineering, San Diego: United States, 2009.

[67] F. Peyraut, J.L. Seichepine, H.I. Faraoun, M. Hertter, D. Sporer, N. Hopkins, C. Coddet, Simulation multi-physique et multi-echelle du comportement des revetements abradables – application a l'industrie aeronautique, 10 eme Colloque National AIP-PRIMECA, La Plagna, 17-20 Avril 2007.

[68] F. Peyraut, J.L. Seichepine, C. Coddet, M. Hertter, Finite element modelling of abradable materials –Identification of plastic parameters and issues on minimum hardness against coating's thickness, International Journal for Simulation and Multidisciplinary Design Optimization 2 (2008) 209-215.

[69] Sulzer Metco, Oerlikon Metco, Product Data Sheet, F4MB-XL Series, http://www.oerlikon.com/metco/en/products-services/coating-equipment/thermal-spray/spray-guns/plasma/f4mb-xl/ (Last accessed 14 September 2014)

[70] Sulzer Metco, Oerlikon Metco, Product Data Sheet, Single / Twin 120 and 140 Series Powder Feeders. http://www.oerlikon.com/metco/en/products-services/coating-equipment/thermal-spray/feeders/plasma/twinsingle-120a/ (Last accessed 14 September 2014).

[71] Sulzer Metco, Oerlikon Metco, Product Data Sheet, 9MC and 9MCD, http://www.oerlikon.com/metco/en/products-services/coating-equipment/thermal-spray/systems/plasma/9mc/. (Last accessed 14 September 2014).

[72] G.A. Sileo, Method for producing an abradable seal. United States Patent, Patent Number: 5780116, Date of Patent: July 14 1998.

[73] Standard Test Method for Rockwell Hardness of Metallic Materials, ASTM E18-14.

[74] W. Rasband, National Institute of Health, USA. http://rsbweb.nih.gov/ij/. (Last accessed 14 September 2014).

[75] A.C. Fisher – Cripps, The IBIS Handbook of Nanoindentaion, Fischer-Cripps Laboratories Pty Ltd, ISBN 0 9585525 4 1.

[76] http://www.ni.com/labview/ (Last accessed 22 August 2014).

[77] M.J. Langford, Basic Photography, third ed, Garden City, NY: Amphoto, 1973, ISBN 0-8174-0640-9.

[78] http://www.micro-epsilon.co.uk/download/products/cat--thermoMETER Infrared--en.pdf (Last accessed 22 August 2014).

[79] L. Michalski, K. Eckersdorf, J. Kucharski, J. McGhee, Temperature Measurement, second edi., John Wiley & Sons Ltd, 2001, ISBN 0 471 86779 9.

[80] http://www.micro-epsilon.com/download/products/dat--infrared-basics--en.pdf (Last accessed 01 February 2015).

[81] The principles of Noncontact Temperature Measurement http://support.fluke.com/raytek-sales/Download/Asset/9250315_ENG_D_W.PDF. (Last accessed 01 February 2015).

[82] G. M. Levin, V.I. Vol'mir, Method for testing thermal inertia in thermocouples and resistance thermometers, Measurement techniques, 3 (1960) Issue 4 309-313.

[83] S.E Sayed Oraby, Mathematical modelling and in-process monitoring techniques for cutting tools. Thesis submitted to University of Sheffield for the Degree of Doctor of Philosophy in the Faculty of Engineering. October 1989.

[84] S. Yaldiz, F. Unsacar, H. Saglam, H. Isik. Design, development and testing of a four-component milling dynamometer for the measurement of cutting force and torque, Mechanical Systems and Signal Proceedings 21 (2007) 1499-1511.

[85] R. Barthorpe, K. Worden, Signal processing and instrumentation, MEC 409, University of Sheffield, 2012.

[86] L. Ricardo Castro, P. Vieville, P. Lipinski, Correction of dynamic effects on the force measurements made with piezoelectric dynamometers. International Journal of Machine Tools & Manufacture 46 (2006) 1707-1715.

[87] N. Tounsi, A. Otho, Dynamic cutting force measuring, International Journal of Machine Tools & Manufacture 40 (2000) 1157-1170.

[88] W.J. Palm III, Modeling, Analysis, and Control of Dynamic Systems, second edi., John Wiley & Sons, Inc, Chapter 6, Frequency Response and Vibration, pp.421-478.

[89] http://www.mathworks.co.uk/help/signal/ref/tfestimate.html. MATLAB help website all function. (Last accessed 14 September 2014).

[90] H. Moore. MATLAB for Engineers. fourth ed., E source. ISBN-13: 978-0133485974.

[91] Kistler, Force, 3-Component Force Link, Type 9347C. http://www.kistler.com/uk/en/product/force/9317C. (Last accessed 10 November 2014).

[92] Kistler, measure, analyse, innovate, Manufacture, sensor and signal analysis in high performance cutting, international conference cutting (HPC), Aachen, Germany, 2004.

[93] C. Ferraresi, T. Raparelli, Meccanica Applicata, Ed. C.L.U.T; ISBN 978-88-7992-254-8.

[94] W. T. Thomson, Theory of Vibration with applications, fourth ed., Chapman & Hall.

[95] G. Rodriguez, Algoritmi numerici. Ed. Pitagora. ISBN 88-371-1714-0.

[96] R. Boyer, Material properties handbook titanium alloys, Material Park, OH: ASM International, 1994.

[97] J. Cai, F. Li, T. Liu, B. Chen, Investigation of mechanical behaviour of quenched Ti-6Al-4V alloy by microindentation, Material Characterization 62 (2011) 287-293.

[98] W.C. Oliver, G.M. Pharr, Measurement of hardness and elastic modulus by instrumented indentation: Advances in understanding and refinements to methodology. Journal of Materials Research 19 (2004) 3–20.

[99] R. Vallascas, Fondamenti di misure meccaniche e termiche, grandezze statiche e sistemi. Ed. Hoepli. ISBN: 078-88-203-4071.

[100] J. Chae, S.S. Park, T. Freiheit, Investigation of micro-cutting operations. International Journal of Machine Tools & Manufacture 46 (2006) 313-332.

[101] V.P. Astakhov, A treatise on material characterization in the metal cutting process. Part 2: cutting as the fracture of workpiece material, Journal of Material Processing Technology 96 (1999) 34-41.

[102] M.M. Khonsari, E.R. Booser, Applied Tribology, Bearing design and lubrication, Ed. John Wiley & Son, Inc., 2001.

[103] M. San-Juan, O. Martin, F. Santos, Experimental study of friction from cutting forces in orthogonal milling, International Journal of Machine Tools & Manufacture 50 (2010) 591-600.

[104] W. Grzesik, Advanced Machining Processes of Metallic Materials, Theory, Modelling and Applications. Elsevier, (2008), pp.149-160.

[105] F. Ghasripoor, R.K. Schmid, M.R. Dorfman, L. Russo, A review of clearance control wear mechanisms for low temperature aluminium silicon alloys, Proceedings of the 15th International Thermal Spray Conference 25-29 (1998) 139-144. Nice France.

[106] D.P. Dewitt, G.D. Nutter, Theory and Practice of Radiation Thermometry, Chapter 1: Physics of Thermal Radiation, (1988), pp.25-87. ISBN-13 978-0471610182.

[107] R. Siegel, Thermal Radiation Heat Transfer, McGraw-Hill, (1972), ISBN 0070573182.

[108] T. Kato, H. Fujii, Energy Partition in Conventional Surface Grinding, Journal of Manufacturing Science and Engineering 121 (1999) 393-398.

[109] N.P. Hopkins, Rolls-Royce Plc, London, Seal between relatively moveable members, United States Patent, Patent No.: US 7955049 B2, June 7 2011.

[109] C. Sellars, G. Pattinson, J.T. Gent, Rolls-Royce Plc, London, Seal and a method on manufacturing a seal. United States, Patent Application Publication, Pub. No.: US 2010, 0143103 A1, June 10 2010.

[110] W.E. Azzi, A systematic study on the mechanical and thermal properties of open cell metal foams for aerospace applications, A thesis submitted to graduate faculty of North Carolina State University in partial fulfilment of the requirements for the Degree of Master of Science, 2004.

[111] G. Pattinson, A. Hewitt, Rolls-Royce Plc, London, Abradable Liner, United States, Patent Application Publication, Pub. No.: US 2012/0248708 A1, October 4, 2012.

Appendix 1

1.1. LabVIEW program for data acquisition and synchronisation

A LabVIEW program was developed in order to control the experimental test platform and to acquire all the data from all devices used. The software was developed in order to synchronise the data acquisition and save all data at known times during the test. In this appendix the software will be analysed step by step. The main software was divided into four parts: Z-microscope stage control program, acquisition camera program, acquisition force program, and acquisition temperature program.

1.2. Z-microscope stage control program

The software needed to communicate with the Z-microscope stage, so it was necessary to use a LabVIEW 'palette' that recognised the device and was able to communicate with it. The company SIGMA-KOKI (Tokyo, Japan) provide control software and also the basic 'palette' that allowed LabVIEW to communicate with and control the Z-microscope. The aim was to use this 'palette' to control the stage motion and the speed in order to keep the input parameter under control during the contact between the blade and the coating located on the Z-microscope stage. First, the software moved the Z-microscope stage up by 5mm, therefore decreasing the distance between the blade tip and abradable coating before the first contact. The distance of 5mm was chosen because it was a reasonable distance to avoid any contact between the rotating blade and the coating before the test started and the blade reached the optimal speed. Then the Z-microscope stage with the coating incurred the blade tip at the previously set required constant speed, until a previously set incursion depth was reached. The microscope stage was then withdrawn and brought back to the position where the distance between the blade tip and the coating was again 5mm. So the first aspect was the initialisation of the device, then a 'speed palette' enabled to setting up the low and high speed and also the acceleration of the motion of the Z-microscope. The motion control was made using a 'move palette', where the condition 'True' or 'False' allowed the user to set the direction of movement and also set the pulse value of 5mm that would represent the distance of

movement. The control of the microscope stage was inserted inside a sequence structure in order to make every step in the same sequence. Also, the single control of the program was inserted inside a case structure in order to work only when there was communication between the software and the device, and if a problem occurred the program would stop automatically. Figure 1 shows the LabVIEW block diagram of the initialisation, control speed and motion of the stage for 0.5mm.

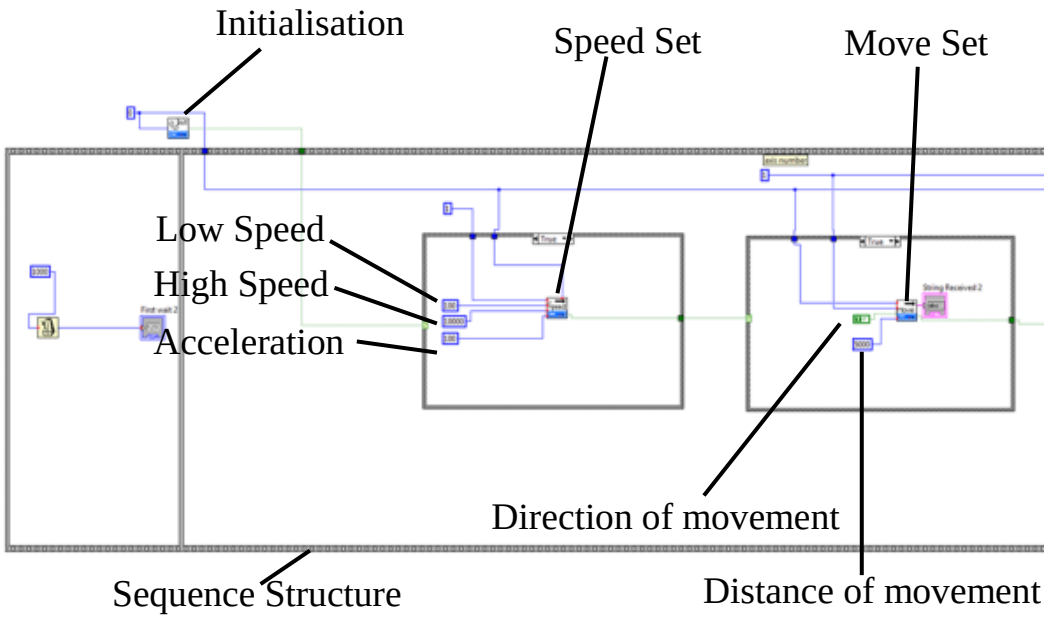

Figure 1. First step of block diagram program of Z-microscope stage control.

The second step was to set the incursion speed (μm s^{-1}), the acceleration of the microscope stage, and in the second case structure the movement of the stage was set until the distance of the total depth of the rub (2mm) was reached. In this case the LabVIEW 'palettes' were the same as those in the previous step, but the movement parameter of the Z-microscope stage could change for each test in order to change the test condition of incurring between the blade and the coating. Figure 2 shows the block diagram of the incurring phase.

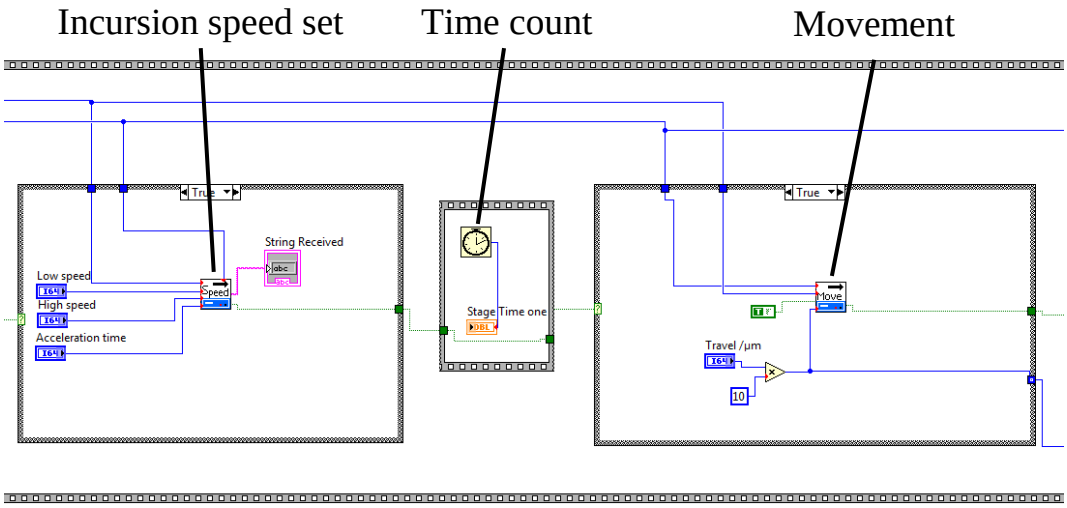

Figure 2. Block diagram program of Z-microscope stage control, setting incursion speed.

When the movement of 2mm was reached, the program proceeded to the next step and moved the microscope stage forward (down) from the blade tip; then the movement of the microscope stage was stopped. So this software allowed the user to set the incursion speed of the microscope stage, the acceleration and total distance travelled. Figure 3 shows the block diagram of the withdrawal phase.

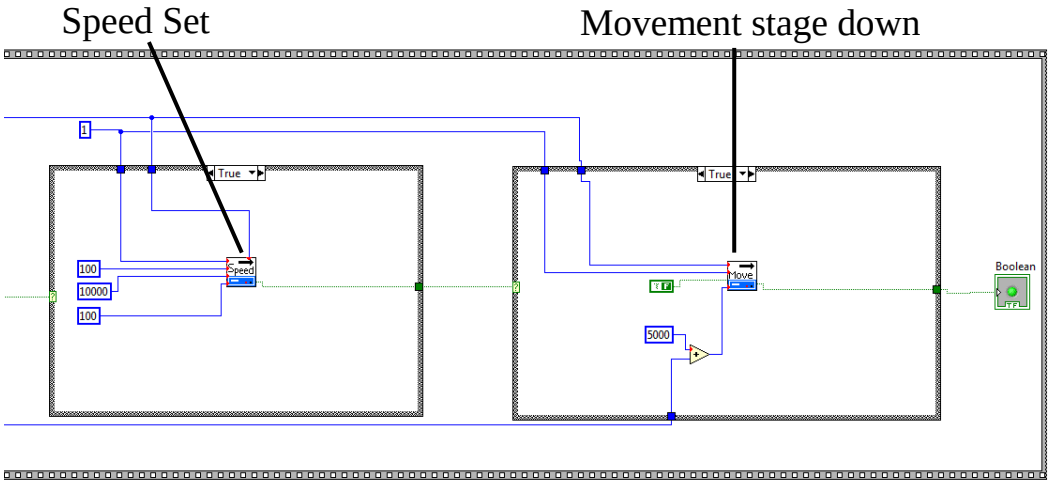

Figure 3. Block diagram program of Z-microscope stage control, withdrawal phase.

1.3. Stroboscopic imaging technique control program

The LabVIEW program allows continuous image acquisition from the camera and saves the image at known times in order to synchronise the data acquisition of the test. The communication with the camera was made using a 'Vision and Motion' (NI-IMAQdx), driver software for LabVIEW to allow the acquisition and recording of the image from the camera. The acquisition of the image was divided into five main phases: initiation, setting, real time acquisition, saving and closing acquisition. Figure 4 shows the block diagram of the initialisation and the setting of the camera acquisition.

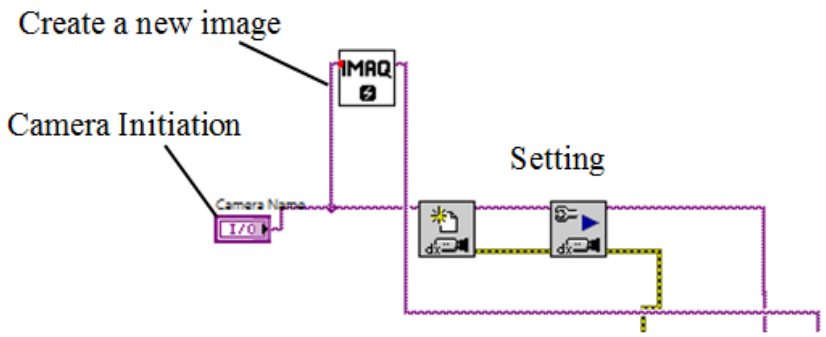

Figure 4. Block diagram program of camera acquisition, initiation camera and setting.

The initialisation of the camera and the setting was inside a while structure but outside the while structure, of the real time acquisition in order to avoid re-initialisation of the camera from every single image acquired. The palette 'IMAQ', which allows creation of a new image, was connected with the real time acquisition. The 'setting palettes' allow the communication to start and set the continuous image acquisition. Figure 5 shows the block diagram of the real time acquisition, saving and closing acquisition.

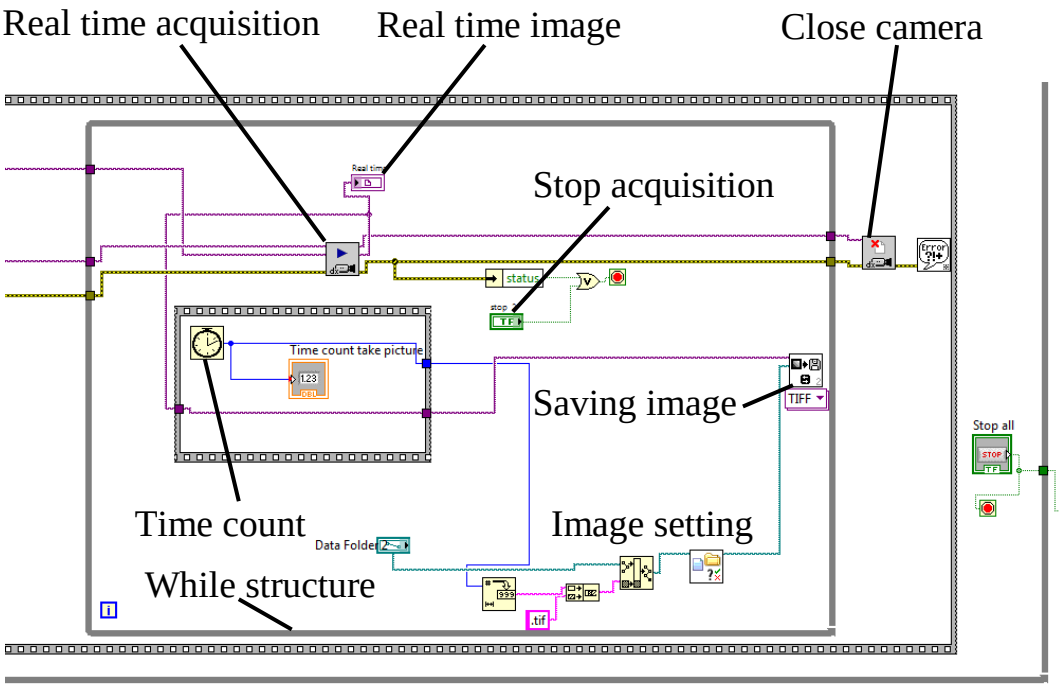

Figure 5. Block diagram of the real time acquisition, saving and closing acquisition.

The 'palette grab' allows the image acquisition and visualisation of the image on the front panel in real time. The acquisition phase continues until the user stops the acquisition with a stop button, which closes the camera acquisition. The images are continuously saved in '.tif' format in an opportune path's folder and with name convention based on the time that a given image was taken, measured with the time count. The software was capable of recording approximately 13 pictures every second. Using this approach with image analysis it was possible to understand how the blade length changes during a test.

1.4. Force measurement acquisition program

The force signal was acquired with a digital oscilloscope (Pico-scope) through a program developed in LabVIEW in order to synchronise all of the acquired data during the experiment. The program was divided into six main phases: initiation of the Pico-scope, setting, acquisition, converting dates, saving, and closing. Figure 6 shows the block diagram of the initiation phase of the Pico-scope.

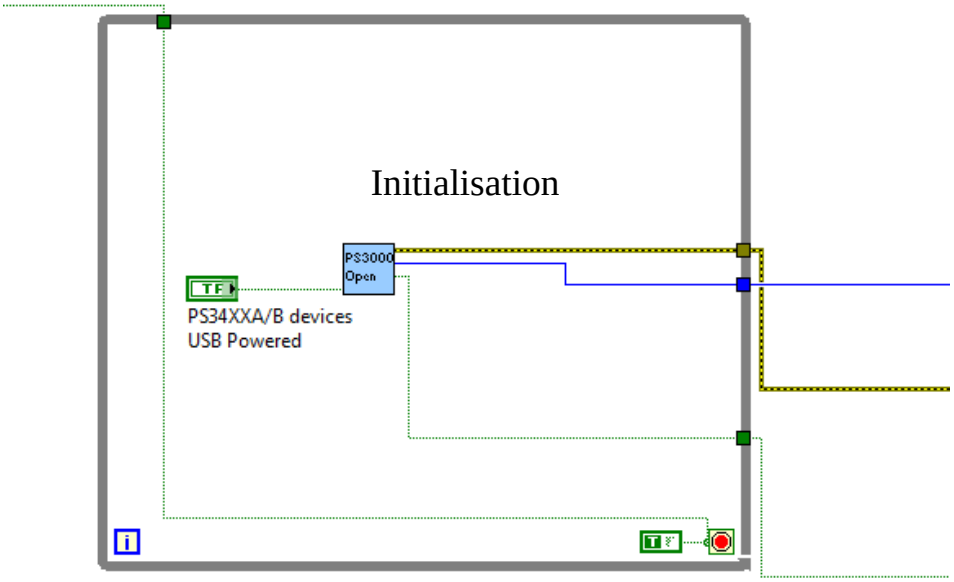

Figure 6. Block diagram of the initiation phase.

The Pico-scope initialisation takes a couple of seconds before beginning the real acquisition of the data, therefore firstly LabVIEW program initialise the Pico-scope. The acquisition would only start, when the operator pushed the start button.The second phase was the setting of the acquisition signal from the channels, as shown in Figure 7.

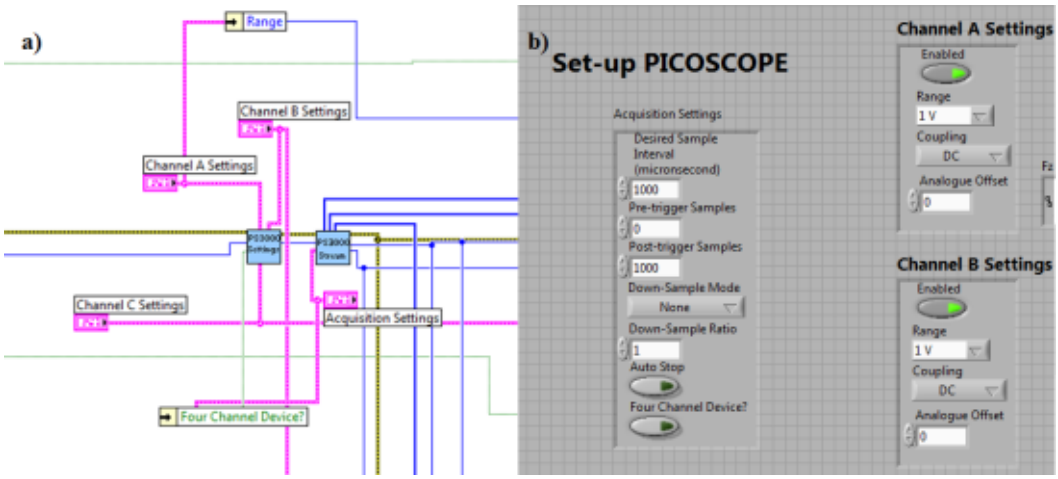

Figure 7. Setting phase of the LabVIEW program: a) Block diagram; b) Front panel.

In the setting phase the acquisition setting of the signal for the Pico-scope was chosen for each channel. The most important parameter was the ‘desired sample interval’ of acquisition, expressed in µs. This parameter represented the resolution of

the signal acquired. During the test, the frequency of strike was 172Hz or 344Hz for blade speeds of 100m s^{-1} or 200m s^{-1}, respectively. So with a sample interval of 10µs, around 580 points of the signal between contact strikes at low blade speed could be obtained. This represented a good value in order to analyse the force contact strike. Additionally, the voltage range for each channel was set at 10V; in fact the correlation between voltage and force was previously set on the charge amplifier at 800N/V, so the program could acquire easily forces up to 8000N. For higher force, the calibration correlation between force and voltage could be changed on the charge amplifier. Figure 8 shows the block diagram of the acquisition and the convert data.

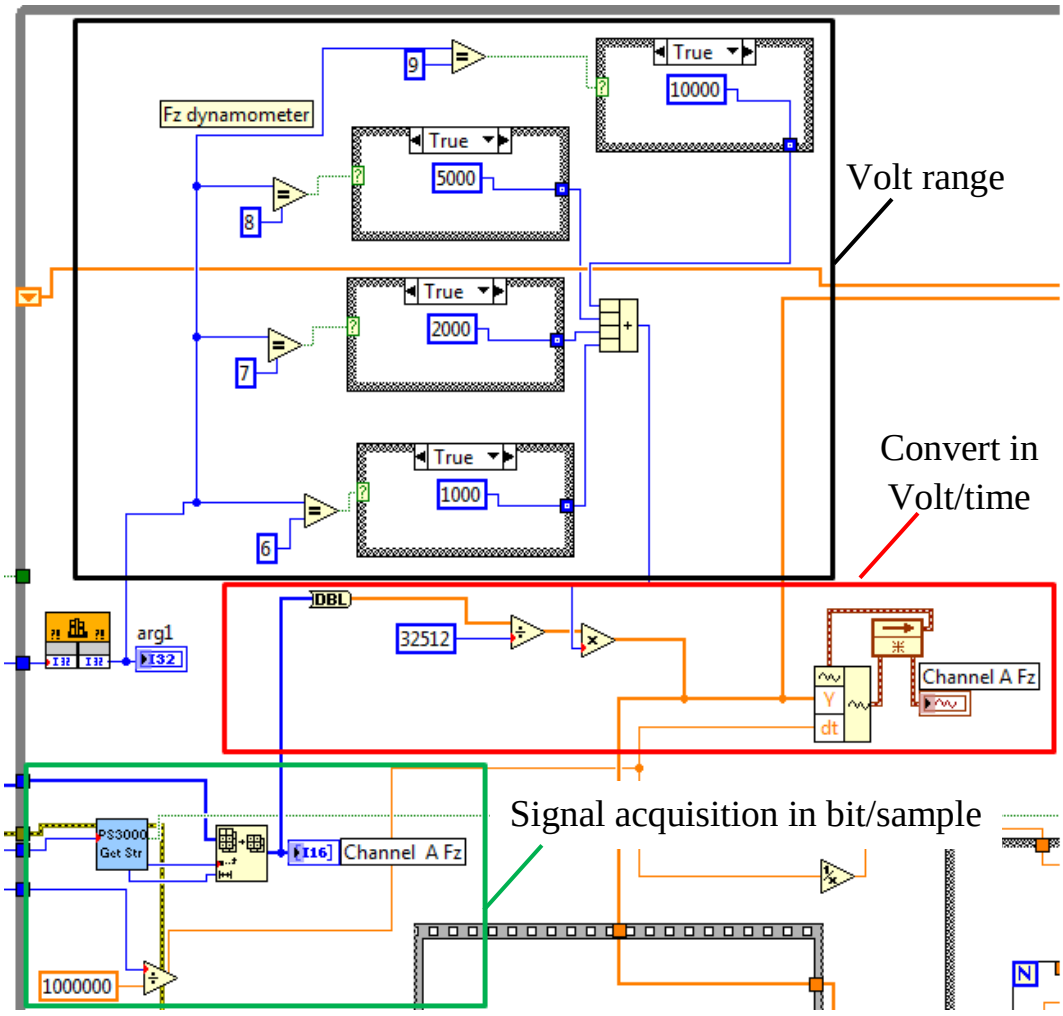

Figure 8. Block diagram of the acquisition: black box reads the volt range; green box acquisition signal in bit per sample; red box converts the signal in volt per time.

As shown in the figure, the green box highlighted the acquisition of the signal expressed in bit per sample, while the black box highlighted the possible choices of

the voltage range; 1V, 2V, 5V and 10V. Finally, the signal was converted into Volt per time, as highlighted in the red box. Figure 9 shows the saving phase and the stop acquisition.

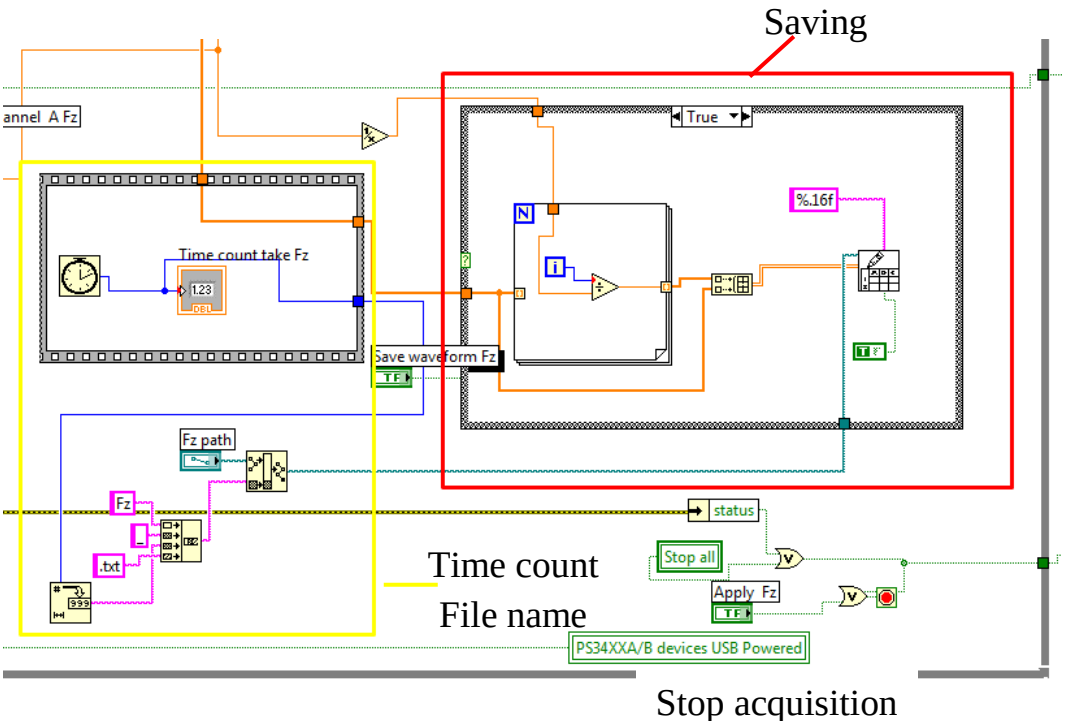

Figure 9. Block diagram of the acquisition: yellow box time counting and file naming, red box saving.

As shown in the figure, inside the yellow box a counter gives the time of the acquisition of the signal and the name of the text file that it will save is shown inside the red box. The stop of the acquisition was related to the stop of the camera. All blocks in the diagram, except the setting phase, need to be inserted for each channel of the Pico-scope, in this case three channels: normal force and two plane forces. Figure 10 shows the front panel of the force acquisition, with the graph of the signal for normal force and tangential plane force, expressed in bit per sample and Volt per second.

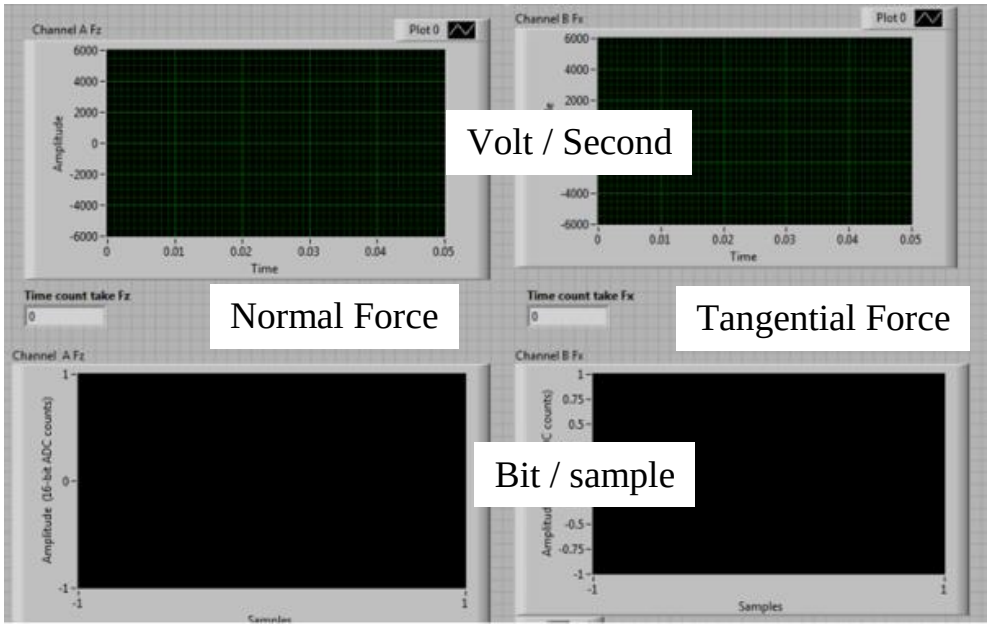

Figure 10. Front panel of the force acquisition.

The LabVIEW program allows the acquisition of the force signal at a known time of the acquisition.

1.5. Temperature measurement acquisition program

The pyrometer was controlled with a LabVIEW program that allows it to save, at known times, the acquisition of the temperature. Communication with the instrument was made using the VISA palette (Virtual Instrument Software Architecture) of LabVIEW. Figure 11 shows the phase of initiation of the device, definition of the serial port, write information, and read the output bit.

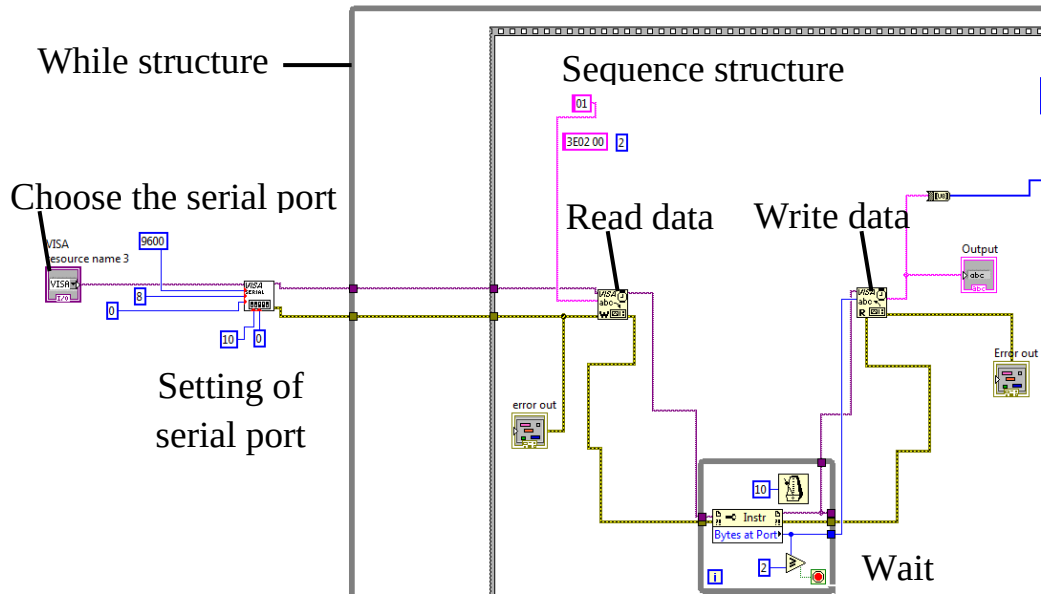

Figure 11. Block diagram of the initiation, setting, read, write for the temperature device.

The first step was to choose the serial port, then set the 8 bit port, 9600 pulse per second, then after this initialisation, inside a while and sequence structure, the sequence of bits was read, then a wait was introduced in order to avoid errors in the write bit sequence, and finally the bits were recorded. The next step was to convert the sequence of bits in temperature measurement (inside the red box) and save it (black box save) at known time (yellow box, time count, and naming the data), as shown in Figure 12.

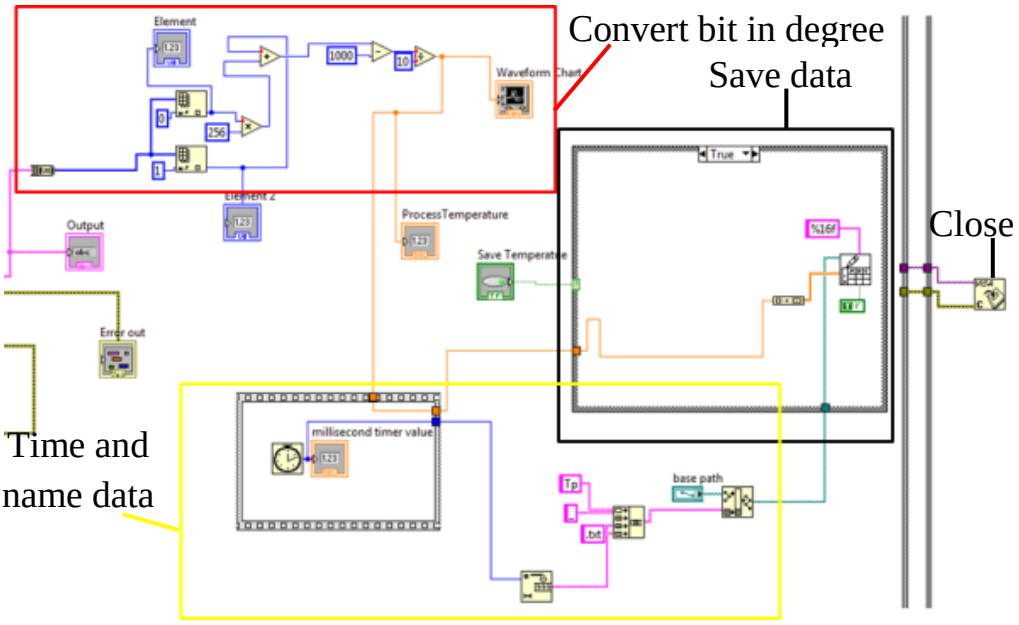

Figure 12. Block diagram of the data conversion and data save.

1.6. LabVIEW program integration

Each single program was analysed in the section before being inserted into the same LabVIEW block diagram, and then inserted inside a case structure in order to start at the same time after the 'Start' button was clicked. In order to have more accuracy in the time synchronisation, all data were saved with a name convention based on the time when acquired. Figures 13, 14 show a front panel of the LabVIEW program.

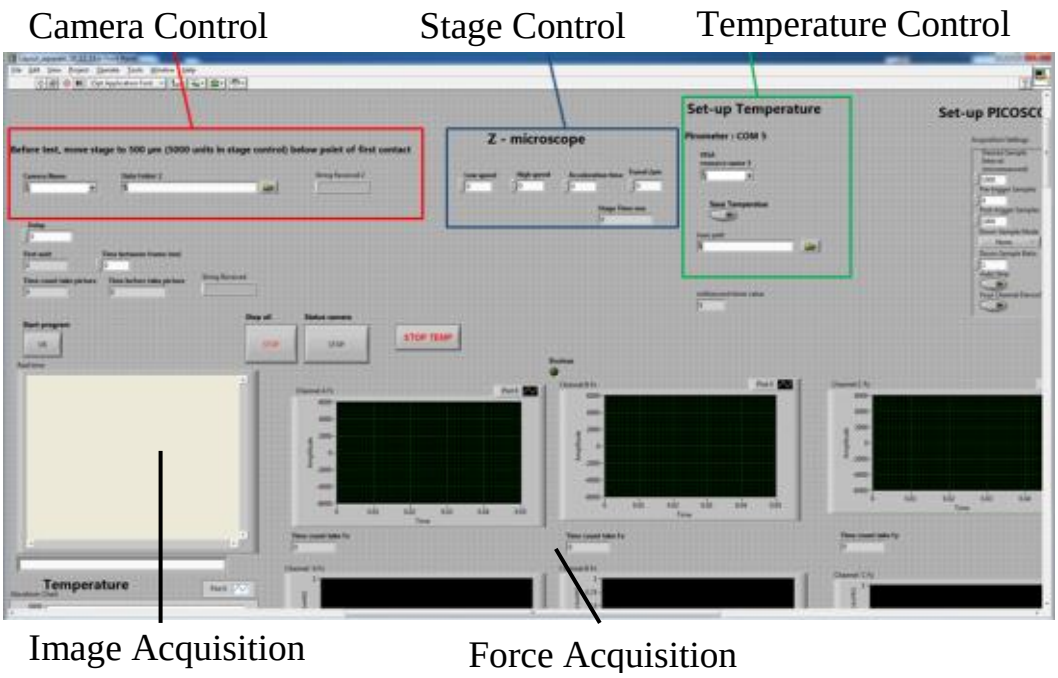

Figure 13. Front panel of LabVIEW program.

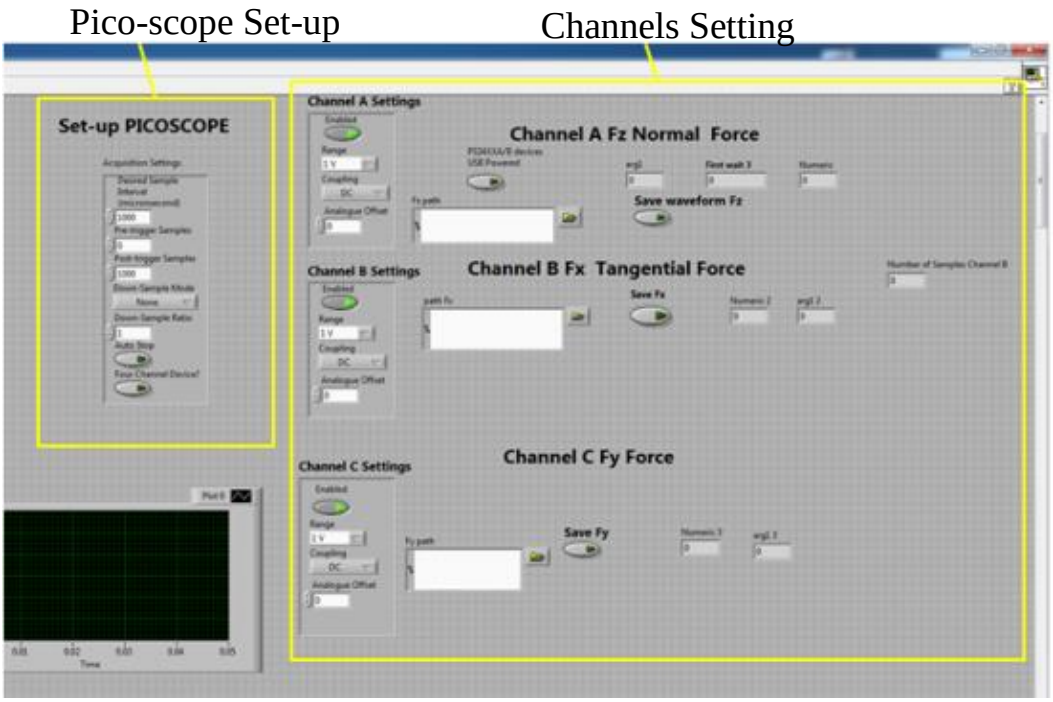

Figure 14. Front panel of LabVIEW program.

Under the 'Camera Control' red box, the port device needed for initialisation is selected and then the path where the image will be saved is set. In the 'Stage Control' blue box, the incursion speed and incursion depth will be set in relation to the test condition. In the 'Temperature Control' green box, the port device and the saving path need to be set. On 'Pico-scope set-up' yellow box, the sample acquisition time of 10µs, the range of each channel, 10V, and the saving path need to be set.

Appendix 2

2.1. Stroboscopic imaging analysis

The images acquired with the stroboscopic imaging technique were processed using IMAGE J and MATLAB in order to determine the length change of the blade on a pass by-pass basis. The first step determined the profile of the blade edge in a Cartesian co-ordinate system using IMAGE J. In this step the image was segmented from the rest of the picture, then de-speckled, converted to binary, the edge of the blade was determined, and finally the x, y co-ordinates of the blade edge were saved. Figure 1 shows the step-by-step of the image analysis.

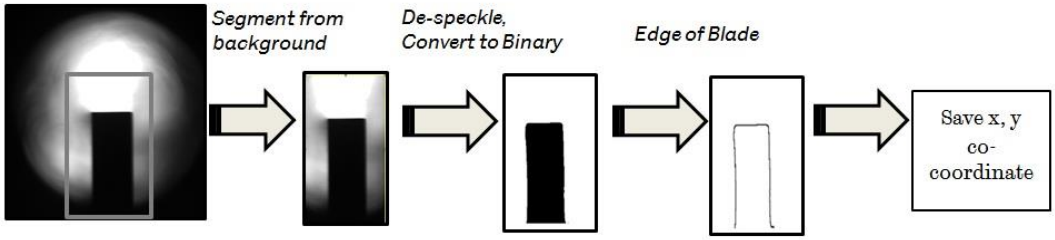

Figure 1. Analysis of the image with IMAGE J.

As highlighted in Chapter 4, the number of images recorded in a test could vary from 100 to 9000, in related to the incursion parameters, and therefore a macro program was developed in order to automatically process all of the images. The program shown below (Figure 2) processed all the images, and wrote the co-ordinates of the blade edge in a text file.

```
dir1 = getDirectory("Choose Source Directory ");
dir2 = getDirectory("Choose Destination Directory ");
list = getFileList(dir1);
z=0;
f=File.open(dir2+"log.txt");
setBatchMode(true);
for (i=0; i<list.length; i++) {
        showProgress(i+1, list.length);
        open(dir1+list[i]);
makeOval(674, 316, 370, 530);
run("Clear Outside");
run("Despeckle");
run("Make Binary");
run("Outline");
dir=getDirectory("image");
name=File.nameWithoutExtension;
path=dir2+name;
z=z+1;
test="file_"+d2s(z,0);
txtPath=dir2+"file_"+d2s(z,0)+".txt";
print(txtPath);
print(f, d2s(z,0) + ", " + name);
run("Save XY Coordinates...", "  save=["+txtPath+"]");

};
```

Figure 2. Program elaborates the images and obtains the co-ordinates of the blades.

Then, with a MATLAB program (Figure 3) the co-ordinates of the blade edge were analysed and the maximum length of the blade was extracted. A blade length was calculated with respect to the initial measurement recorded pre-test, and a vector called ‘dl’ gave the blade length change at each time the image was acquired during the test.

```
firstFile = 1;
lastFile = 1100;
nSamples = 10;
columns = 2;
b=zeros(lastFile,1);
for n = firstFile : 1 : lastFile

    number = num2str( n );

    file = strcat('file_',number,'.txt');
    a=load(file);

    x1=(a(:,1)/70);
    y1=(a(:,2)/70);

    b(n)=max(a(:,2)/70);

    lengMAX=b;

    dl=lengMAX-b(1);



end
```

Figure 3. MATLAB program gives the maximum length of the blade and the blade length change at each time the image was acquired.

Appendix 3

3. Image of sample post-test

3.1. Test sample at hardness R15Y 72.3

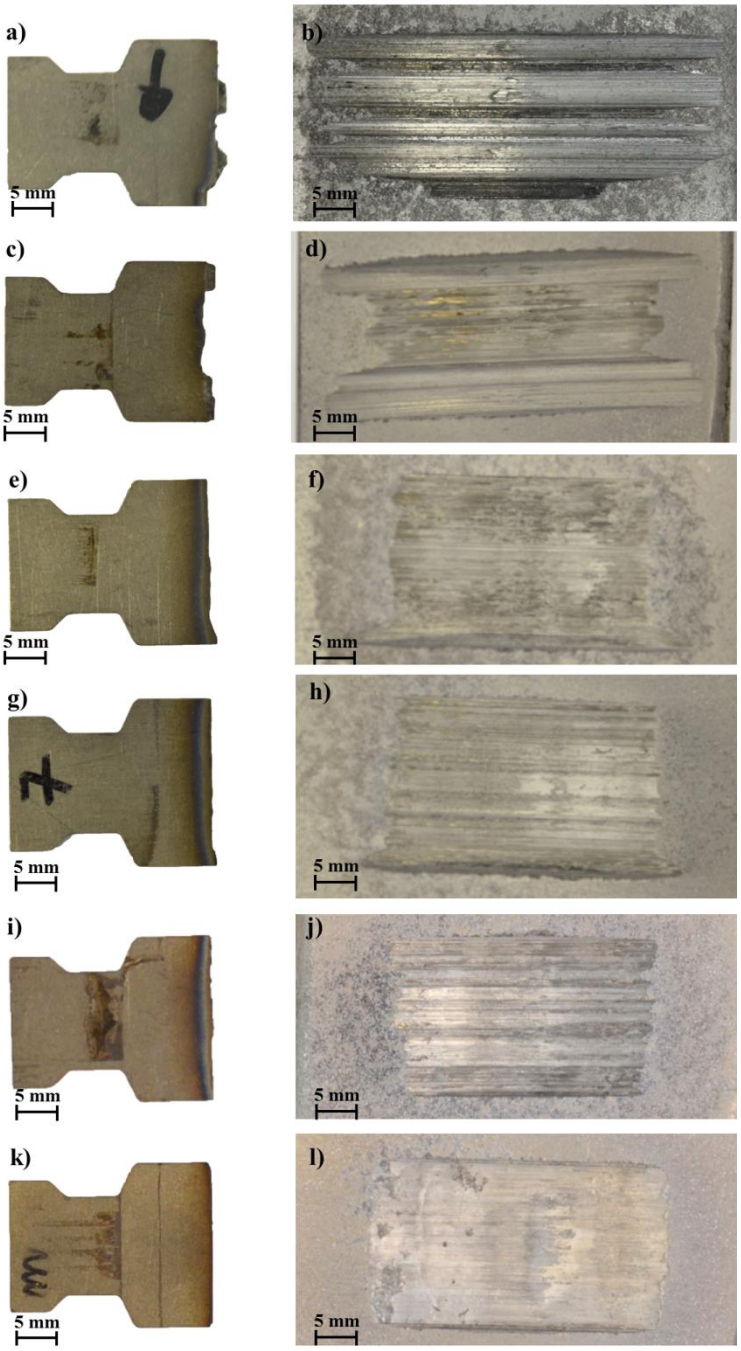

Figure 1. Image of the blade and coating post-test at 100m s^{-1} blade speed with abradable sample hardness R15Y 72.3 and incursion rate: 0.02µm $pass^{-1}$: a) blade, b) coating; 0.04µm $pass^{-1}$: c) blade, d) coating; 0.06µm $pass^{-1}$: e) blade, f) coating; 0.08µm $pass^{-1}$: g) blade, h) coating; 0.1µm $pass^{-1}$: i) blade, j) coating; 0.14µm $pass^{-1}$: k) blade, l) coating.

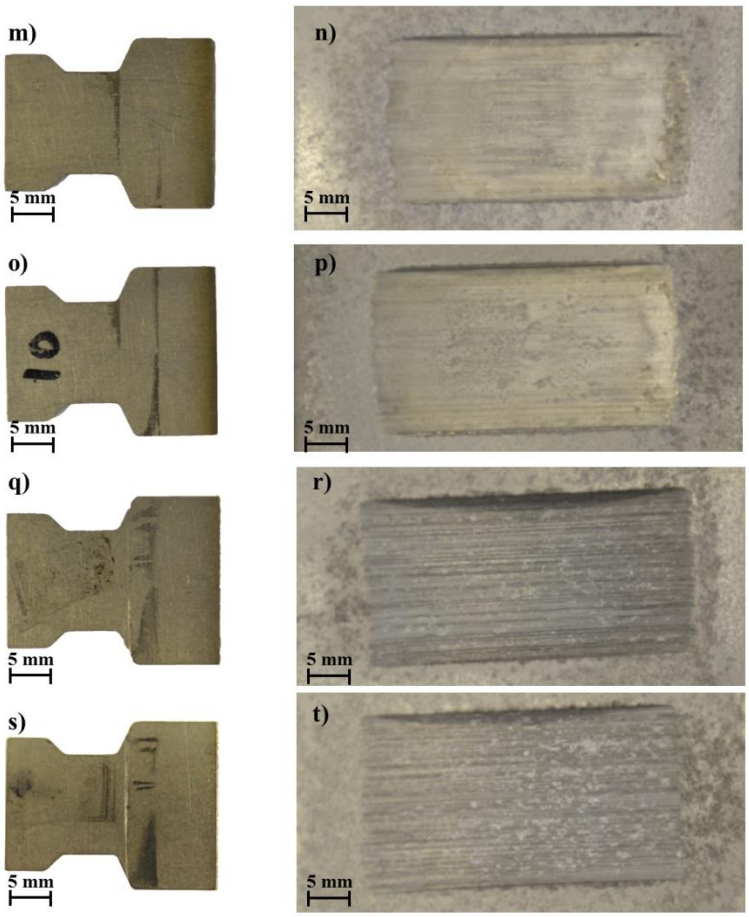

Figure 2. Image of the blade and coating post-test at 100m s^{-1} blade speed with abradable sample hardness R15Y 72.3 and incursion rate: 0.2µm $pass^{-1}$: m) blade, n) coating; 0.4µm $pass^{-1}$: o) blade, p) coating; 1µm $pass^{-1}$: q) blade, r) coating; 2µm $pass^{-1}$: s) blade, t) coating.

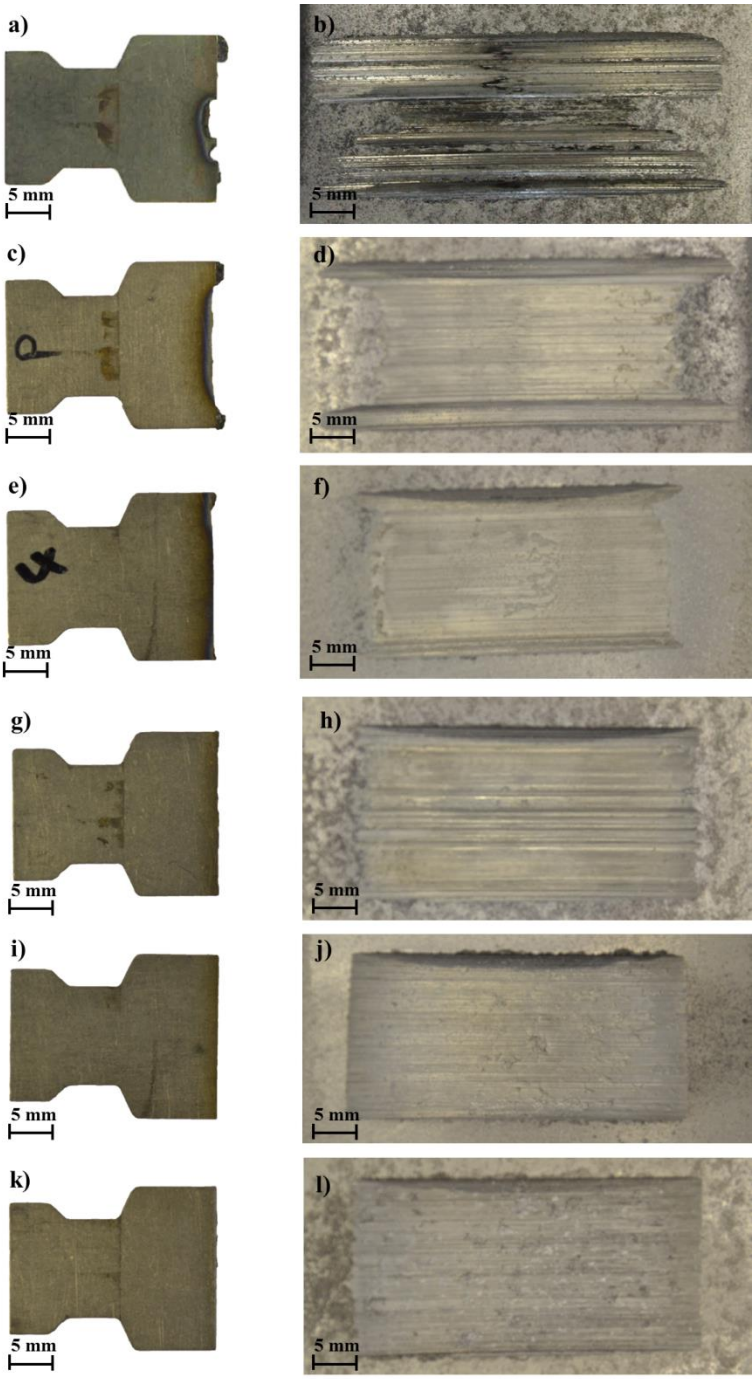

Figure 3. Image of the blade and coating post-test at 150m s^{-1} blade speed with abradable sample hardness R15Y 72.3 and incursion rate: 0.02µm $pass^{-1}$: a) blade, b) coating; 0.06µm $pass^{-1}$: c) blade, d) coating; 0.1µm $pass^{-1}$: e) blade, f) coating; 0.2µm $pass^{-1}$: g) blade, h) coating; 1µm $pass^{-1}$: i) blade, j) coating; 2µm $pass^{-1}$: k) blade, l) coating.

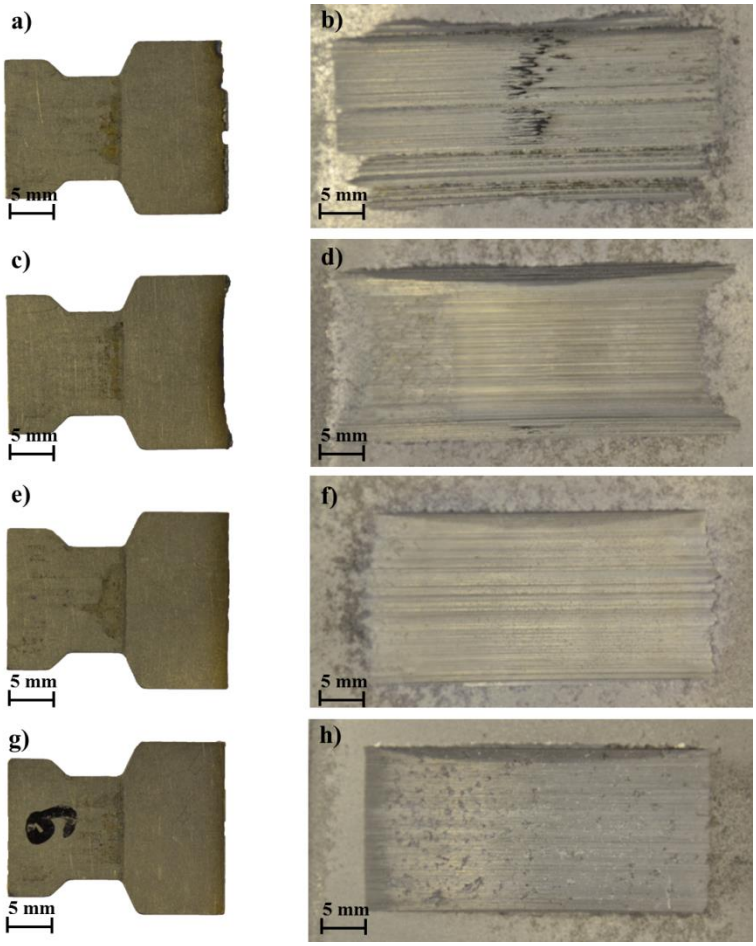

Figure 4. Image of the blade and coating post-test at 200m s^{-1} blade speed with abradable sample hardness R15Y 72.3 and incursion rate: 0.02µm $pass^{-1}$: a) blade, b) coating; 0.06µm $pass^{-1}$: c) blade, d) coating; 0.2µm $pass^{-1}$: e) blade, f) coating; 2µm $pass^{-1}$:g) blade, h) coating.

3.2. Test sample at hardness R15Y 63

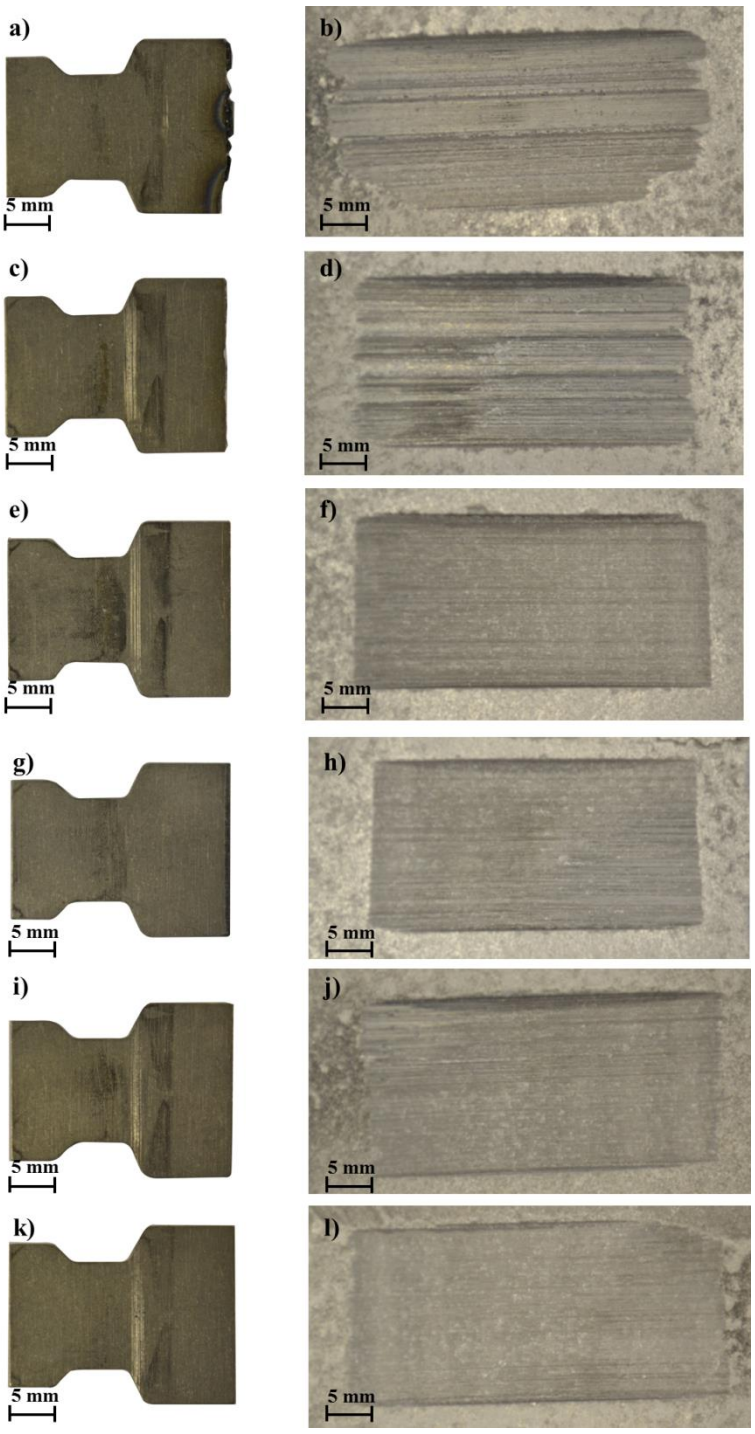

Figure 5. Image of the blade and coating post-test at 100m s^{-1} blade speed with abradable sample hardness R15Y 63 and incursion rate: 0.02µm $pass^{-1}$: a) blade, b) coating; 0.1µm $pass^{-1}$: c) blade, d) coating; 0.3µm $pass^{-1}$: e) blade, f) coating; 0.6µm $pass^{-1}$: g) blade, h) coating; 1µm $pass^{-1}$: i) blade, j) coating; 2µm $pass^{-1}$: k) blade, l) coating.

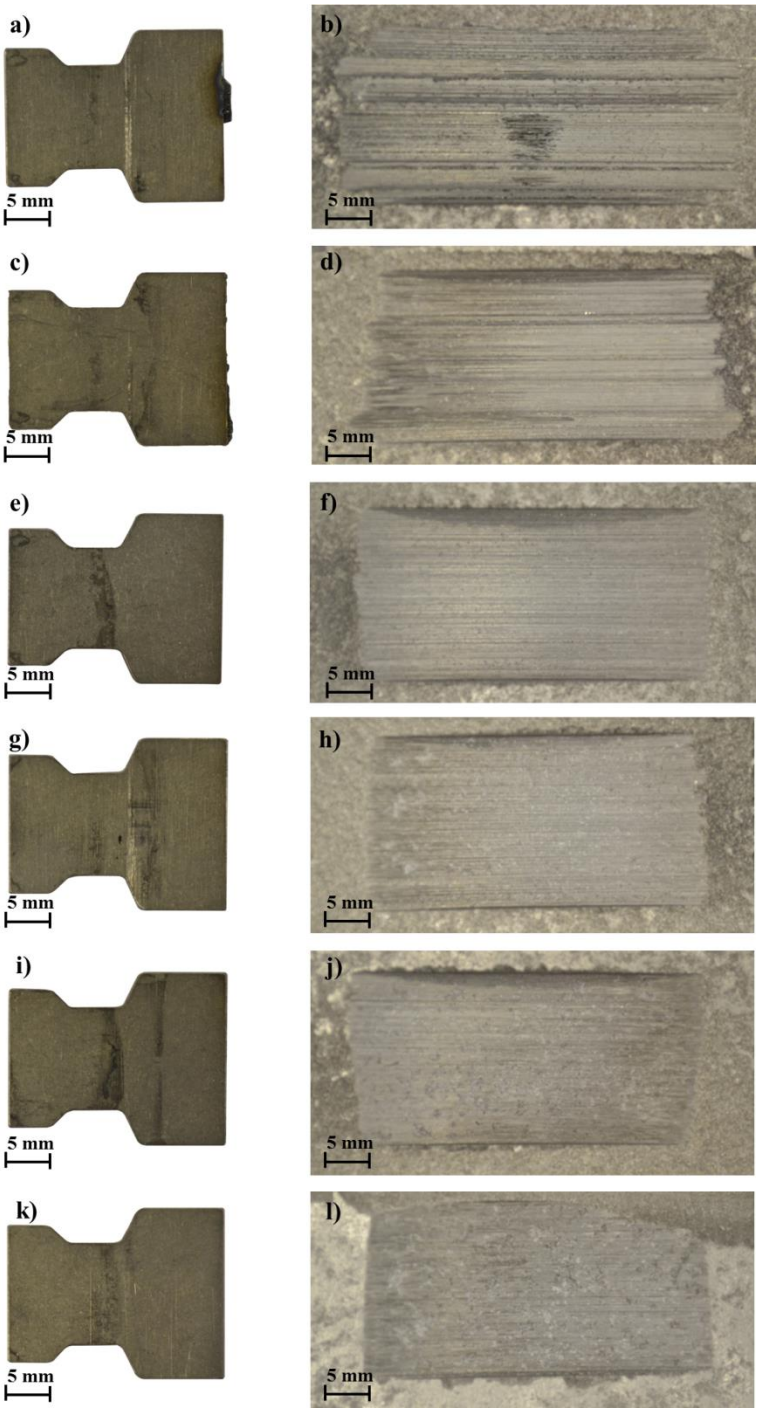

Figure 6. Image of the blade and coating post-test at 150m s^{-1} blade speed with abradable sample hardness R15Y 63 and incursion rate: 0.02µm $pass^{-1}$: a) blade, b) coating; 0.1µm $pass^{-1}$: c) blade, d) coating; 0.3µm $pass^{-1}$: e) blade, f) coating; 0.6µm $pass^{-1}$: g) blade, h) coating; 1µm $pass^{-1}$: i) blade, j) coating; 2µm $pass^{-1}$: k) blade, l) coating.

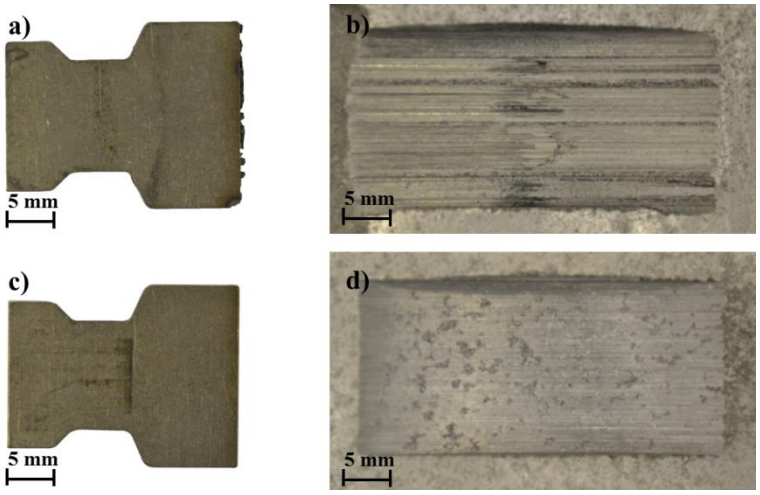

Figure 7. Image of the blade and coating post-test at 200m s^{-1} blade speed with abradable sample hardness R15Y 63 and incursion rate: 0.02µm $pass^{-1}$: a) blade, b) coating; 2µm $pass^{-1}$: c) blade, d) coating.

The rest of the coatings performed at intermediate incursion rate were given back to Rolls Royce Surface Engineering group in order to use the steel plate for thermal spraying of new samples, and only the image of the blade for intermediate incursion rate was acquired, as shown in Figure 8.

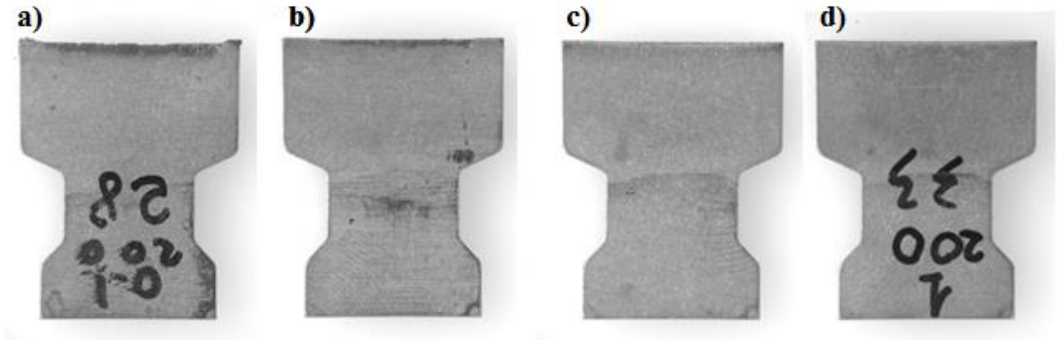

Figure 8. Image of the blade for the test performed at blade speed of 200m s^{-1} against the coating hardness R15Y 63, at incursion rate of: a) 0.1µm $pass^{-1}$; b) 0.3µm $pass^{-1}$; c) 0.6µm $pass^{-1}$; d) 1µm $pass^{-1}$.

3.3 Test sample at hardness R15Y 59.6

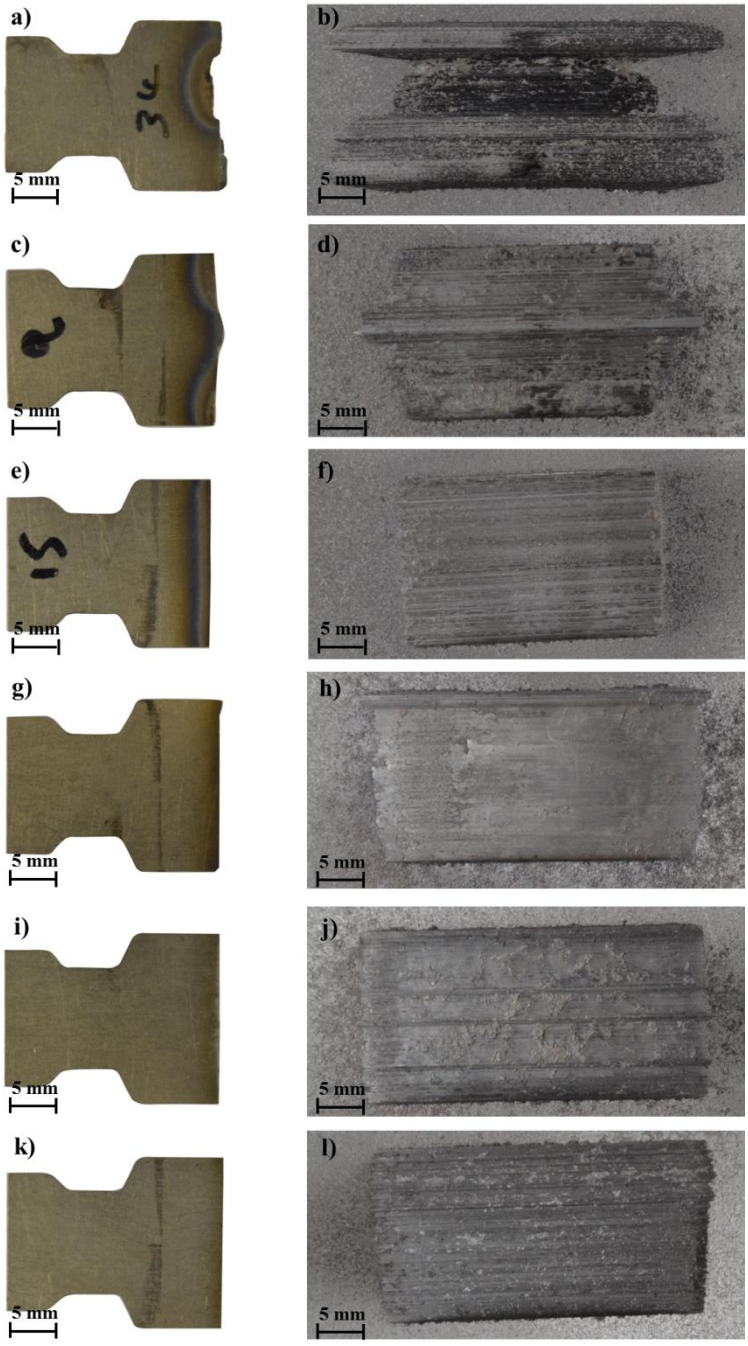

Figure 9. Image of the blade and coating post-test at 100m s^{-1} blade speed with abradable sample hardness R15Y 59.6 and incursion rate: 0.02µm $pass^{-1}$: a) blade, b) coating; 0.04µm $pass^{-1}$: c) blade, d) coating; 0.06µm $pass^{-1}$: e) blade, f) coating; 0.2µm $pass^{-1}$: g) blade, h) coating; 1µm $pass^{-1}$: i) blade, j) coating; 2µm $pass^{-1}$: k) blade, l) coating.

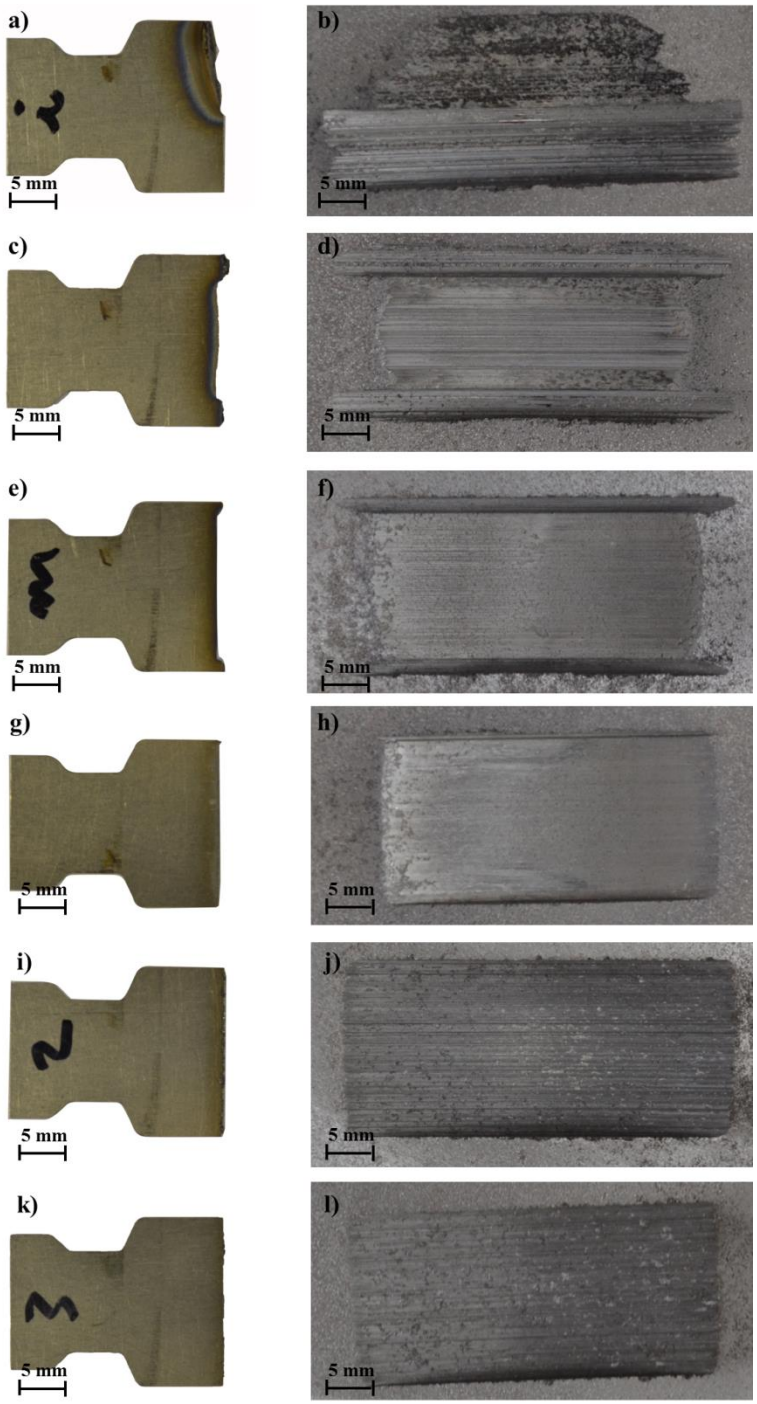

Figure 10. Image of the blade and coating post-test at 150m s^{-1} blade speed with abradable sample hardness R15Y 59.6 and incursion rate: 0.02µm $pass^{-1}$: a) blade, b) coating; 0.06µm $pass^{-1}$: c) blade, d) coating; 0.1µm $pass^{-1}$: e) blade, f) coating; 0.2µm $pass^{-1}$: g) blade, h) coating; 1µm $pass^{-1}$: i) blade, j) coating; 2µm $pass^{-1}$: k) blade, l) coating.

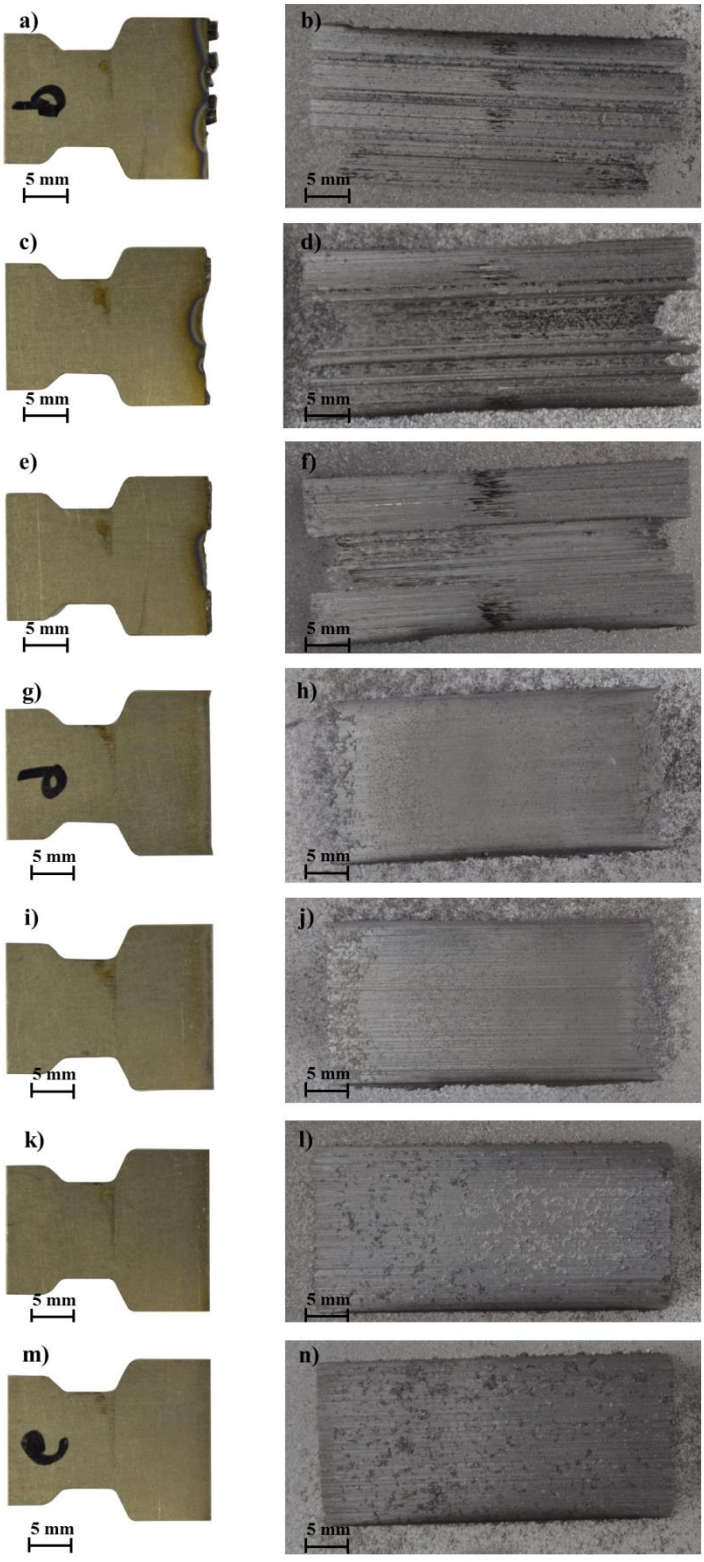

Figure 11. Image of the blade and coating post-test at 200m s^{-1} blade speed with abradable sample hardness R15Y 59.6 and incursion rate: 0.02µm $pass^{-1}$: a) blade, b) coating; 0.04µm $pass^{-1}$: c) blade, d) coating; 0.06µm $pass^{-1}$: e) blade, f) coating; 0.1µm $pass^{-1}$: g) blade, h) coating; 0.2µm $pass^{-1}$: i) blade, j) coating; 1µm $pass^{-1}$: k) blade, l) coating; 2µm $pass^{-1}$: m) blade, n) coating.

3.4 Test sample at hardness R15Y 54.6

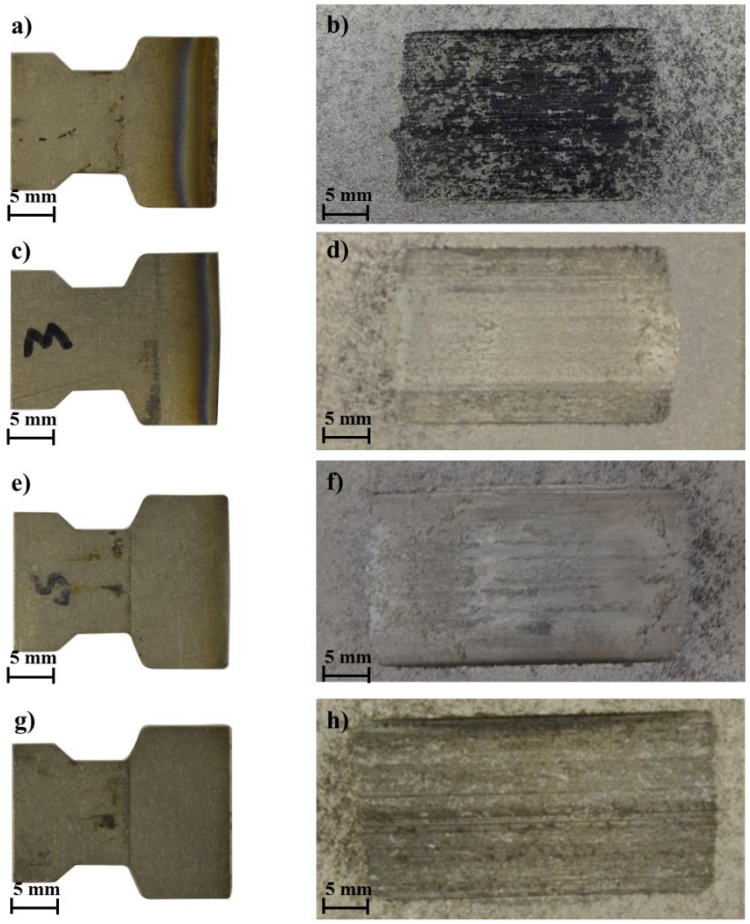

Figure 12. Image of the blade and coating post-test at 100m s^{-1} blade speed with abradable sample hardness R15Y 54.6 and incursion rate: 0.02µm $pass^{-1}$: a) blade, b) coating; 0.1µm $pass^{-1}$: c) blade, d) coating; 0.2µm $pass^{-1}$: e) blade, f) coating; 2µm $pass^{-1}$: g) blade, h) coating.

The rest of the coating tested at intermediate incursion rate were given back to Rolls Royce Engineering group in order to use the steel plate for thermal spray of new samples, and images of the post-test were not acquired.

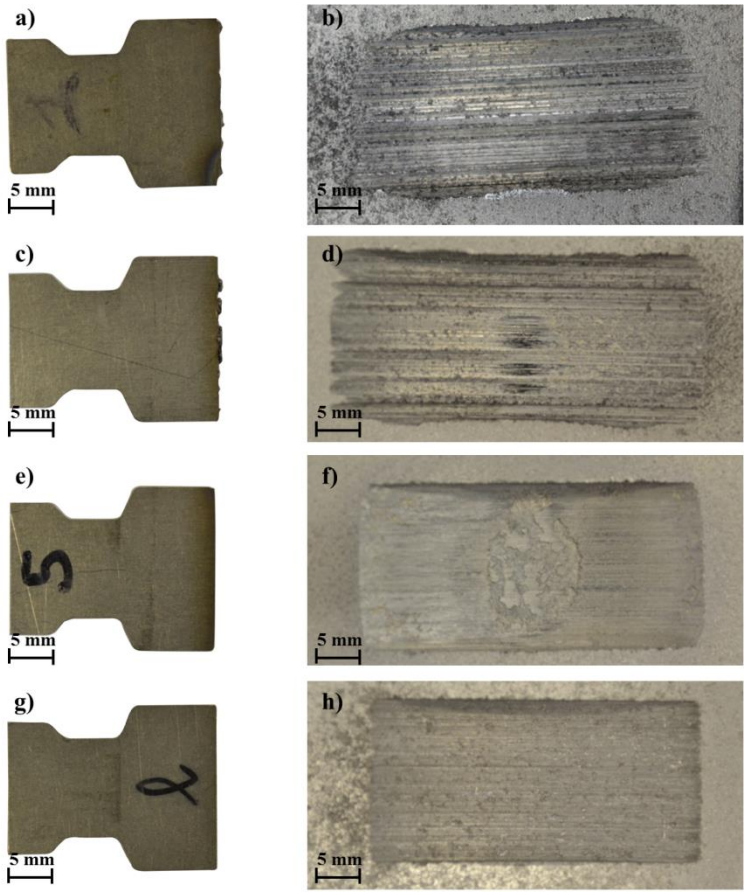

Figure 13. Image of the blade and coating post-test at 150m s^{-1} blade speed with abradable sample hardness R15Y 54.6 and incursion rate: 0.02µm $pass^{-1}$: a) blade, b) coating; 0.1µm $pass^{-1}$: c) blade, d) coating; 0.2µm $pass^{-1}$: e) blade, f) coating; 2µm $pass^{-1}$: g) blade, h) coating.

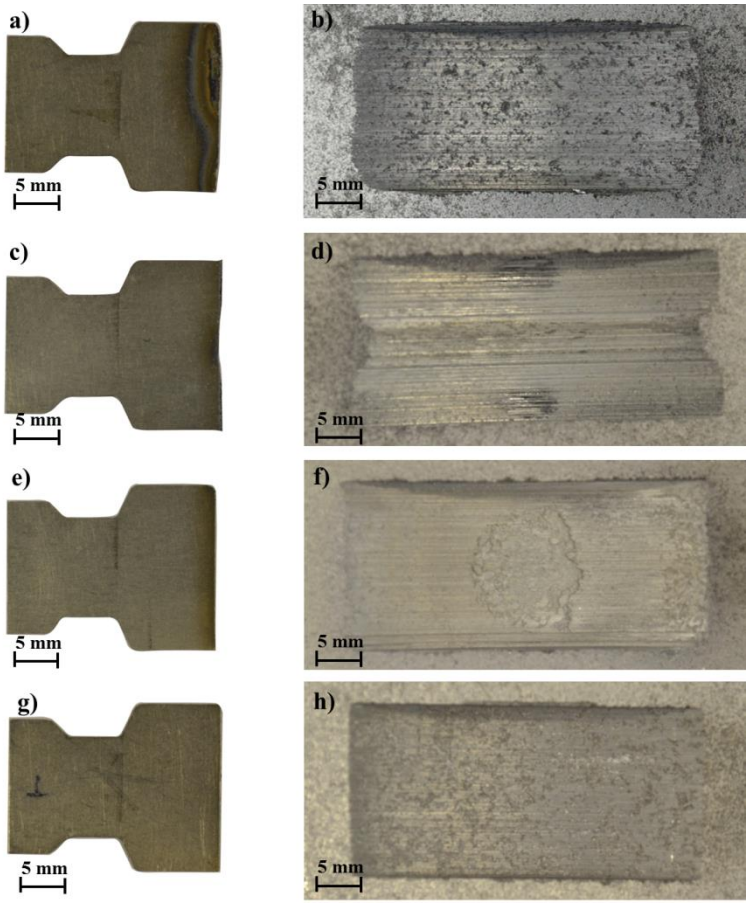

Figure 14. Image of the blade and coating post-test at 200m s^{-1} blade speed with abradable sample hardness R15Y 54.6 and incursion rate: 0.02µm $pass^{-1}$: a) blade, b) coating; 0.1µm $pass^{-1}$: c) blade, d) coating; 0.2µm $pass^{-1}$: e) blade, f) coating; 2µm $pass^{-1}$: g) blade, h) coating.

Appendix 4

4. Force measurements at different coating hardnesses

4.1. Test sample R15Y 72.3 at 150m s^{-1}

Figure 1 and 2 shows the normal and tangential forces measured with blade speed of 150m s^{-1} with coating hardness R15Y 72.3.

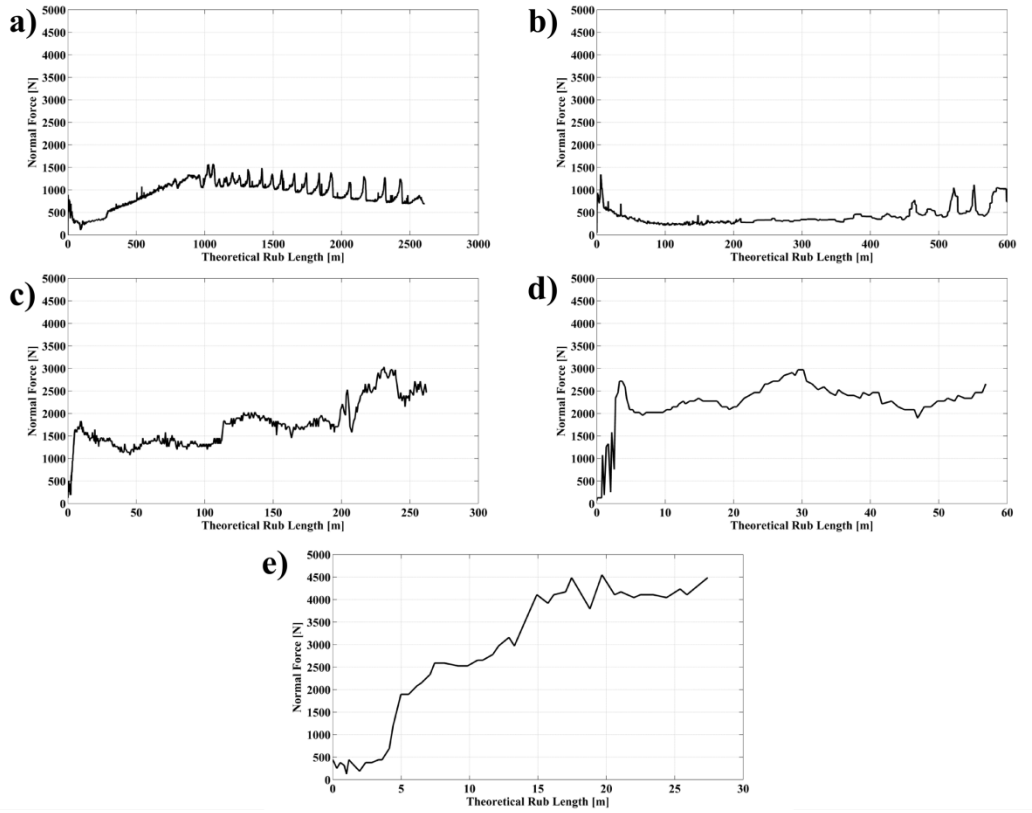

Figure 1. Normal force measurement at blade speed of 150m s^{-1} and abradable coating hardness R15Y 72.3, at incursion rates of: a) 0.02µm·$pass^{-1}$; b) 0.06µm·$pass^{-1}$; c) 0.2µm·$pass^{-1}$; d) 1µm·$pass^{-1}$; e) 2µm·$pass^{-1}$.

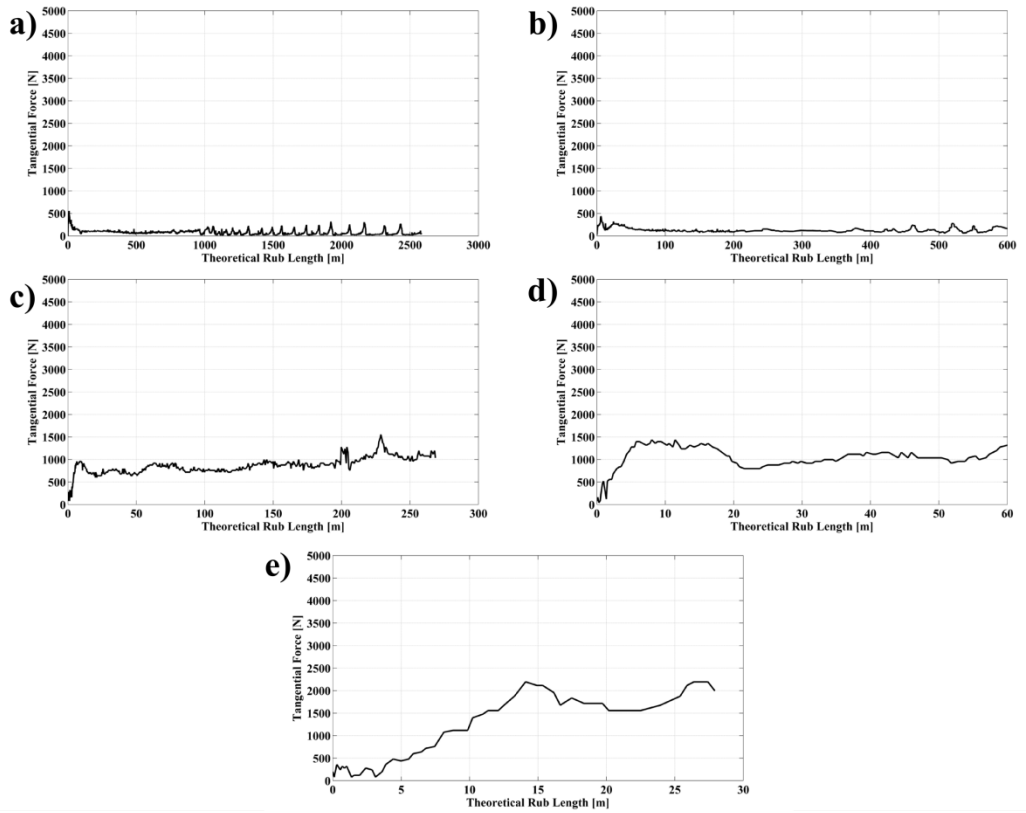

Figure 2. Tangential force measurement at blade speed of 150m s^{-1} and abradable coating hardness R15Y 72.3, at incursion rates of: a) 0.02µm·$pass^{-1}$; b) 0.06µm·$pass^{-1}$; c) 0.2µm·$pass^{-1}$; d) 1µm·$pass^{-1}$; e) 2µm·$pass^{-1}$.

4.2. Test sample R15Y 72.3 at 200m s^{-1}

Figure 3 and 4 shows the normal and tangential forces measured with blade speed of 200m s^{-1} with coating hardness R15Y 72.3.

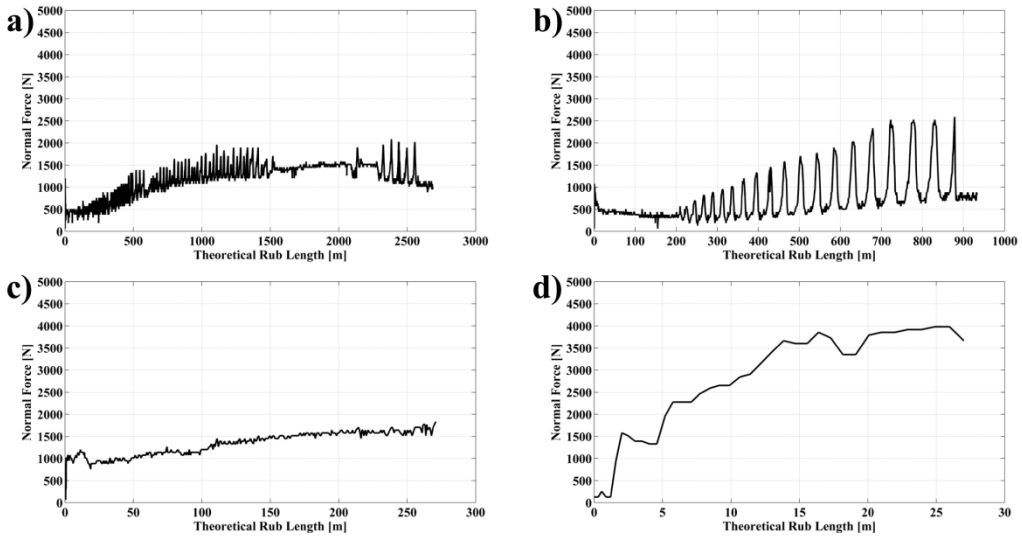

Figure 3. Normal force measurement at blade speed of 200m s^{-1} and abradable coating hardness R15Y 72.3, at incursion rates of: a) 0.02µm·$pass^{-1}$; b) 0.06µm·$pass^{-1}$; c) 0.2µm·$pass^{-1}$; d) 2µm·$pass^{-1}$.

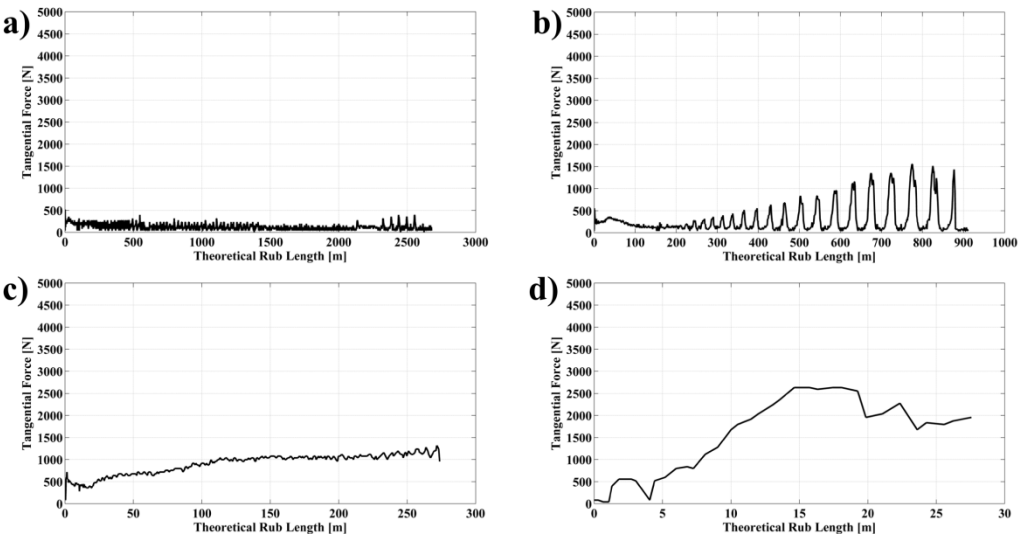

Figure 4. Tangential force measurement at blade speed of 200m s^{-1} and abradable coating hardness R15Y 72.3, at incursion rates of: a) 0.02µm·$pass^{-1}$; b) 0.06µm·$pass^{-1}$; c) 0.2µm·$pass^{-1}$; d) 2µm·$pass^{-1}$.

4.3 Test sample R15Y 59.6 at 100m s^{-1}

Figure 5 and 6 shows the normal and tangential forces measured with blade speed of 100m s^{-1} with coating hardness R15Y 59.6.

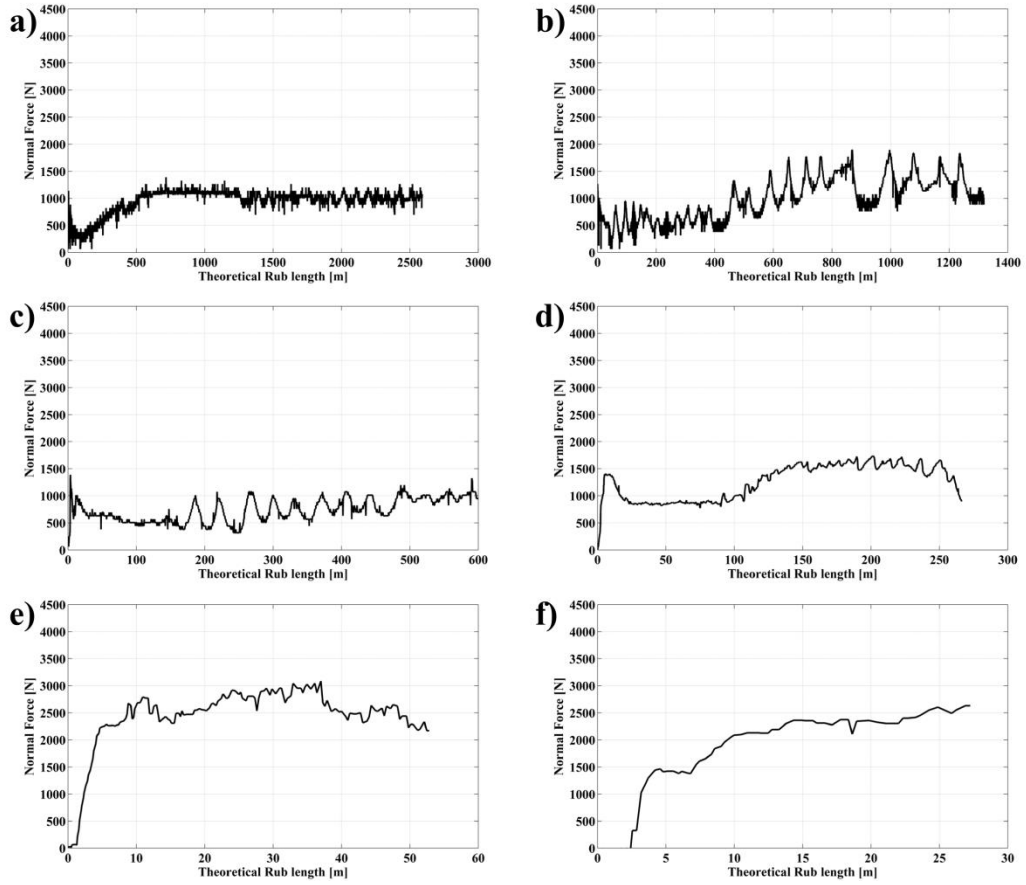

Figure 5. Normal force measurement at blade speed of 100m s^{-1} and abradable coating hardness R15Y 59.6, at incursion rates of: a) 0.02µm·$pass^{-1}$; b) 0.04µm·$pass^{-1}$; c) 0.06µm·$pass^{-1}$; d) 0.2µm·$pass^{-1}$; e) 1µm·$pass^{-1}$; f) 2µm·$pass^{-1}$.

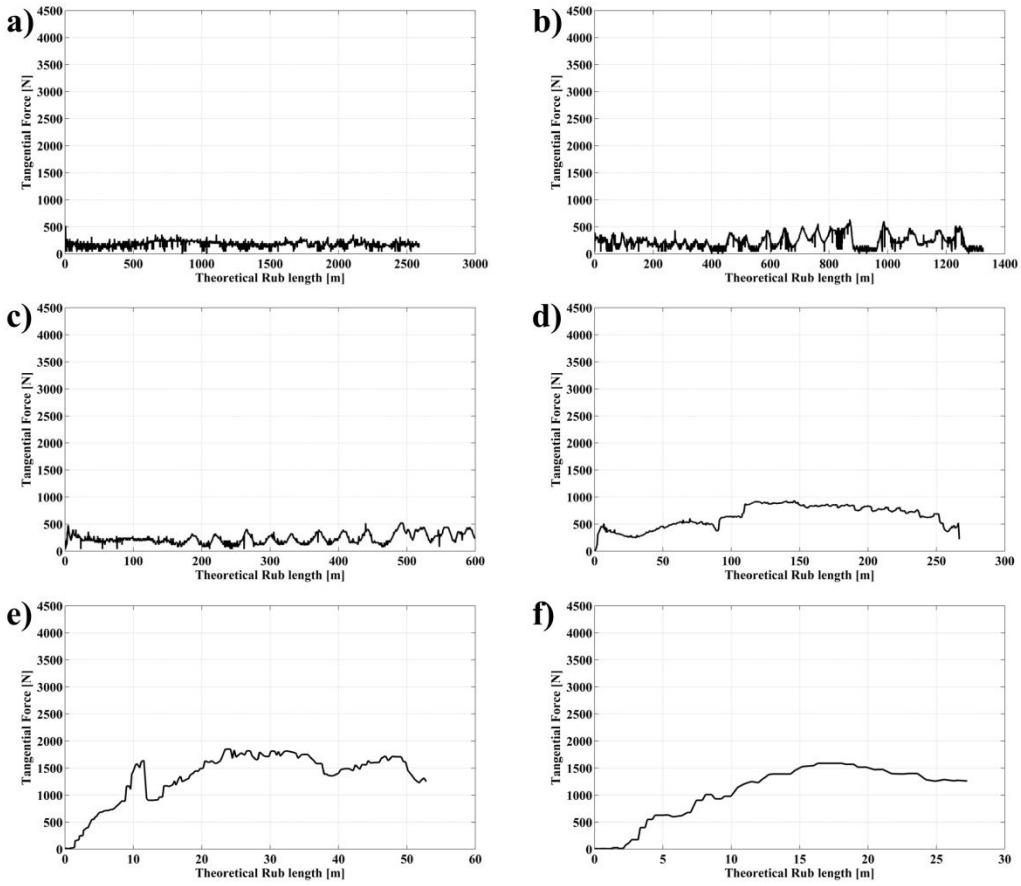

Figure 6. Tangential force measurement at blade speed of 100m s^{-1} and abradable coating hardness R15Y 59.6, at incursion rates of: a) 0.02µm·$pass^{-1}$; b) 0.04µm·$pass^{-1}$; c) 0.06µm·$pass^{-1}$; d) 0.2µm·$pass^{-1}$; e) 1µm·$pass^{-1}$; f) 2µm·$pass^{-1}$.

4.4. Test sample R15Y 59.6 at 150m s^{-1}

Figure 7 and 8 shows the normal and tangential forces measured with blade speed of 150m s^{-1} with coating hardness R15Y 59.6.

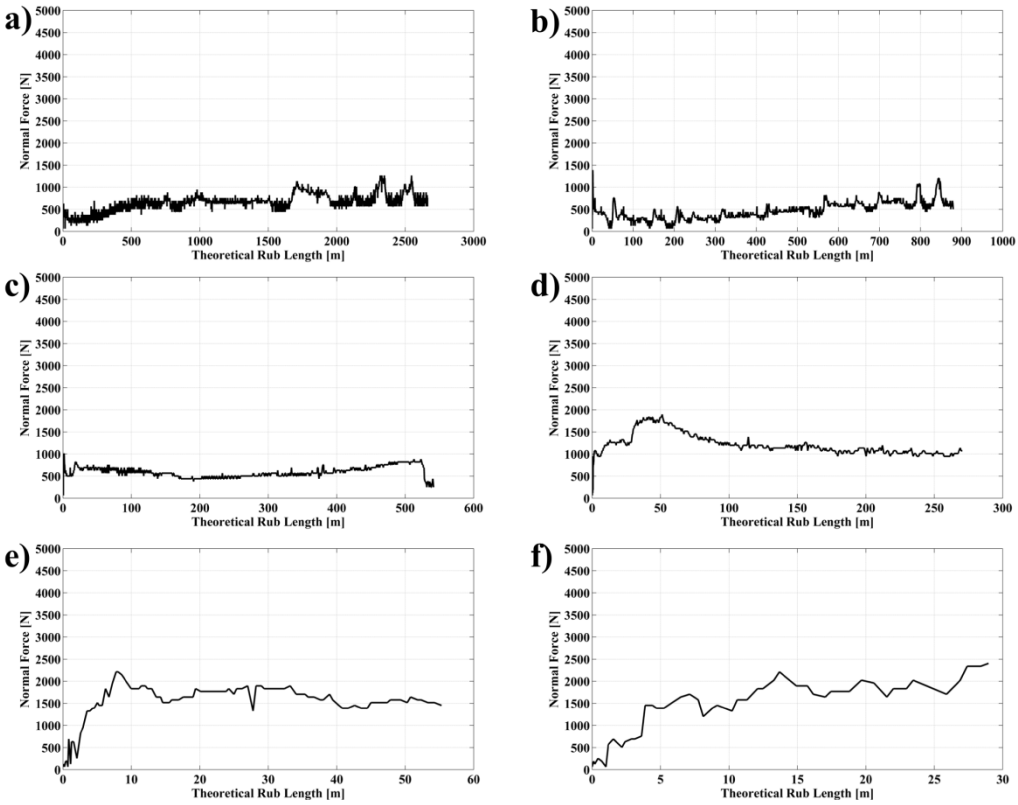

Figure 7. Normal force measurement at blade speed of 150m s^{-1} and abradable coating hardness R15Y 59.6, at incursion rates of: a) 0.02µm·$pass^{-1}$; b) 0.06µm·$pass^{-1}$; c) 0.1µm·$pass^{-1}$; d) 0.2µm·$pass^{-1}$; e) 1µm·$pass^{-1}$; f) 2µm·$pass^{-1}$.

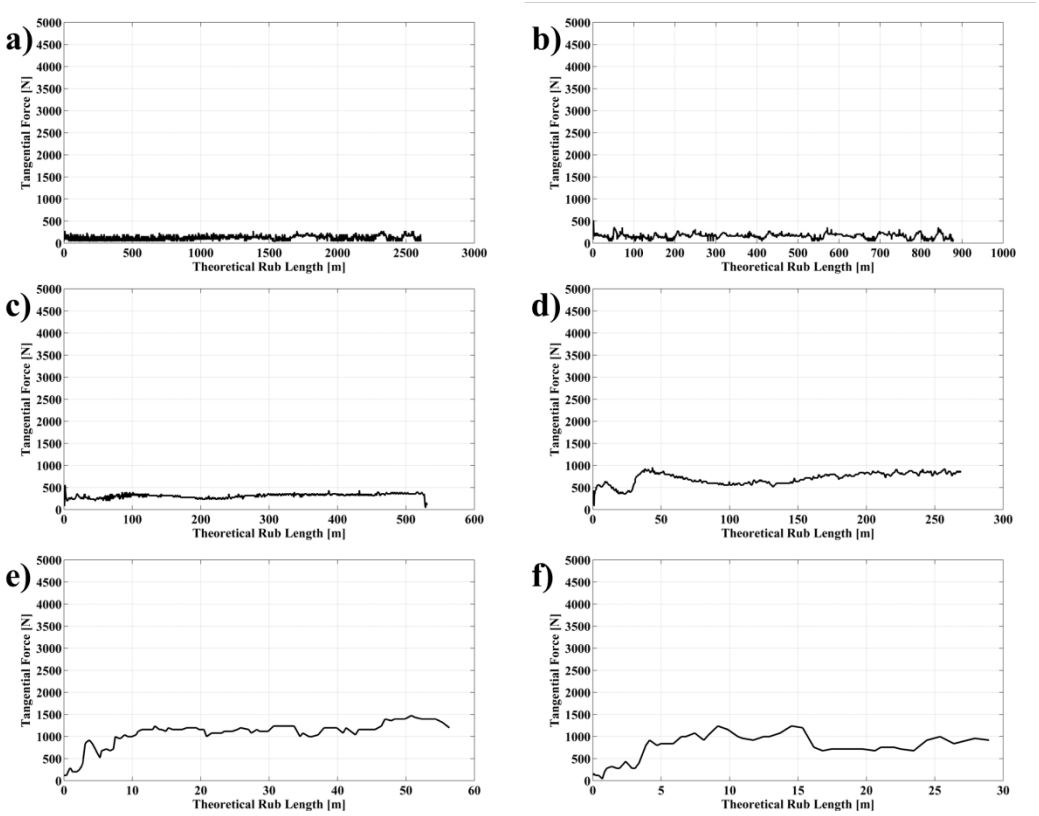

Figure 8. Tangential force measurement at blade speed of 150m s^{-1} and abradable coating hardness R15Y 59.6, at incursion rates of: a) 0.02µm·$pass^{-1}$; b) 0.06µm·$pass^{-1}$; c) 0.1µm·$pass^{-1}$; d) 0.2µm·$pass^{-1}$; e) 1µm·$pass^{-1}$; f) 2µm·$pass^{-1}$.

4.5. Test sample R15Y 59.6 at 200m s^{-1}

Figure 9 and 10 shows the normal and tangential forces measured with blade speed of 200m s^{-1} with coating hardness R15Y 59.6.

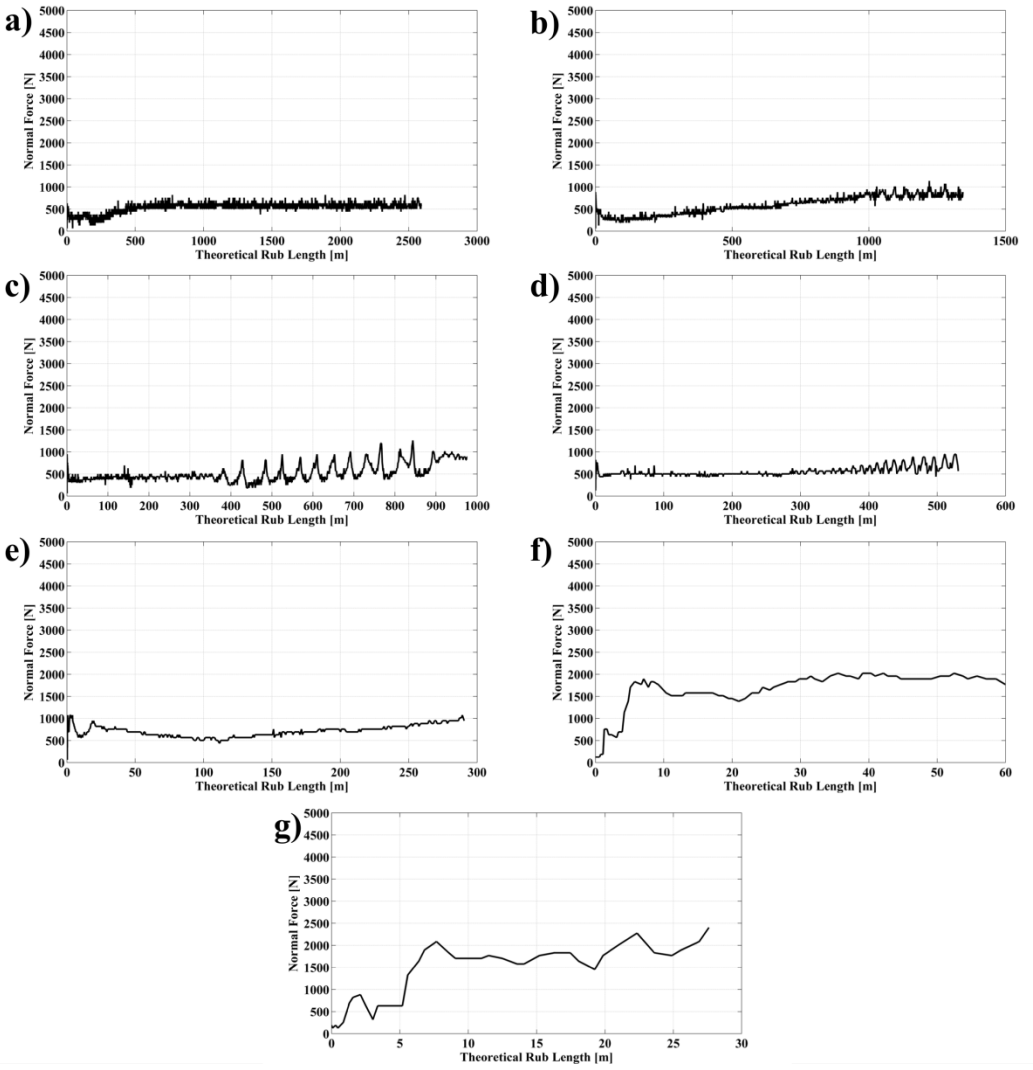

Figure 9. Normal force measurement at blade speed of 200m s^{-1} and abradable coating hardness R15Y 59.6, at incursion rates of: a) 0.02µm·$pass^{-1}$; b) 0.04µm·$pass^{-1}$; c) 0.06µm·$pass^{-1}$; d) 0.1µm·$pass^{-1}$; e) 0.2µm·$pass^{-1}$; f) 1µm·$pass^{-1}$; g) 2µm·$pass^{-1}$.

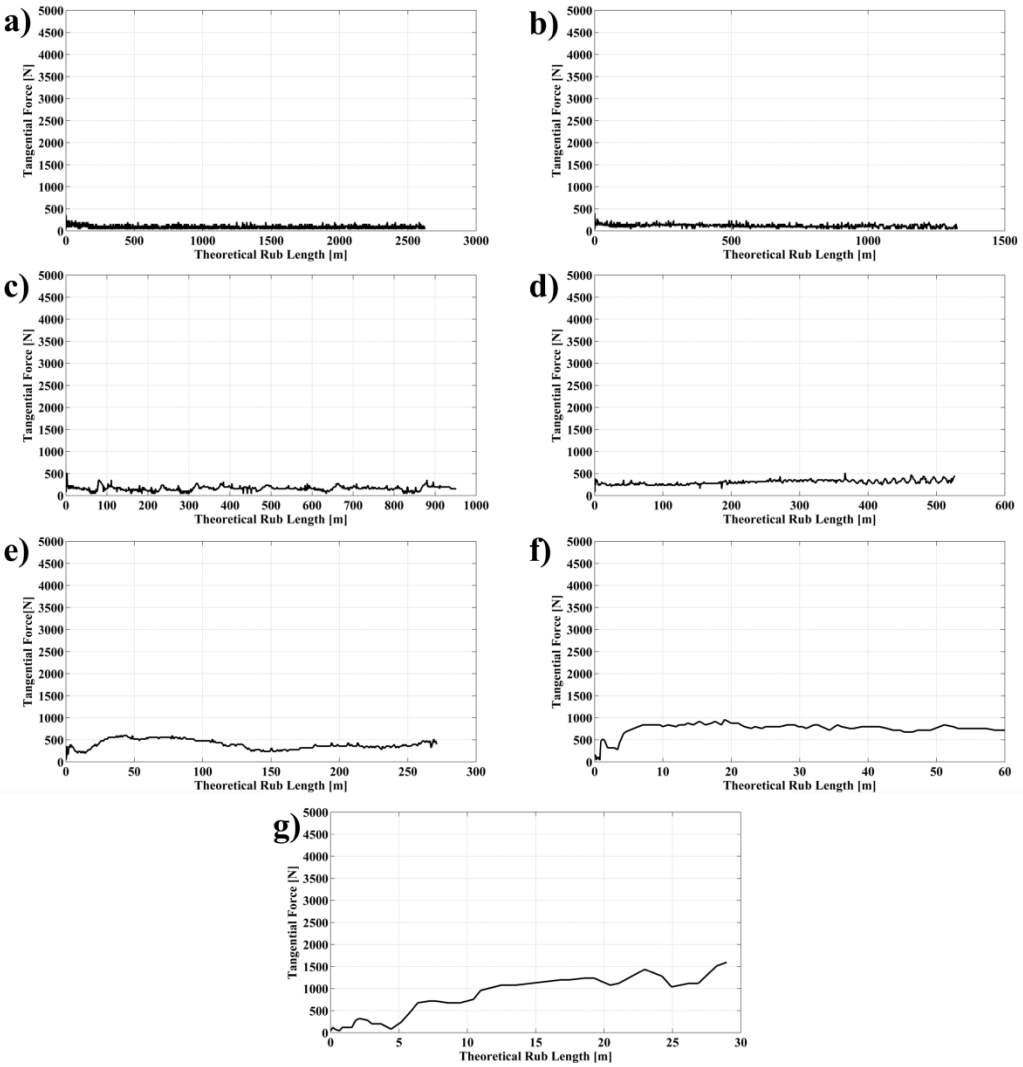

Figure 10. Tangential force measurement at blade speed of 200m s^{-1} and abradable coating hardness R15Y 59.6, at incursion rates of: a) 0.02µm·$pass^{-1}$; b) 0.04µm·$pass^{-1}$; c) 0.06µm·$pass^{-1}$; d) 0.1µm·$pass^{-1}$; e) 0.2µm·$pass^{-1}$; f) 1µm·$pass^{-1}$; g) 2µm·$pass^{-1}$.

4.6 Test sample R15Y 54.6 at 100m s^{-1}

Figure 11 and 12 shows the normal and tangential forces measured with blade speed of 100m s^{-1} with coating hardness R15Y 54.6.

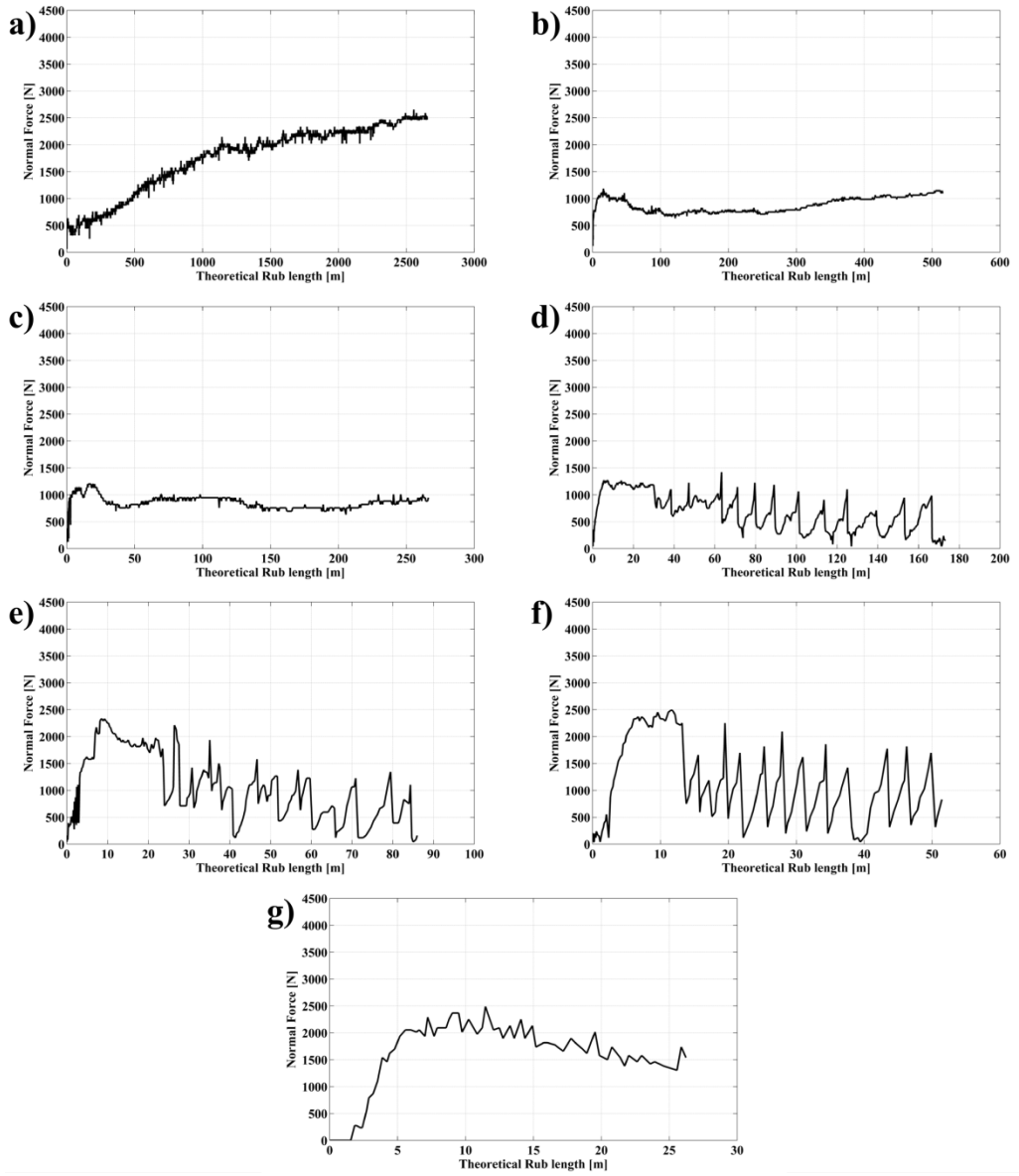

Figure 11. Normal force measurement at blade speed of 100m s^{-1} and abradable coating hardness R15Y 54.6, at incursion rates of: a) 0.02µm·$pass^{-1}$; b) 0.1µm·$pass^{-1}$; c) 0.2µm·$pass^{-1}$; d) 0.3µm·$pass^{-1}$; e) 0.6µm·$pass^{-1}$; f) 1µm·$pass^{-1}$; g) 2µm·$pass^{-1}$.

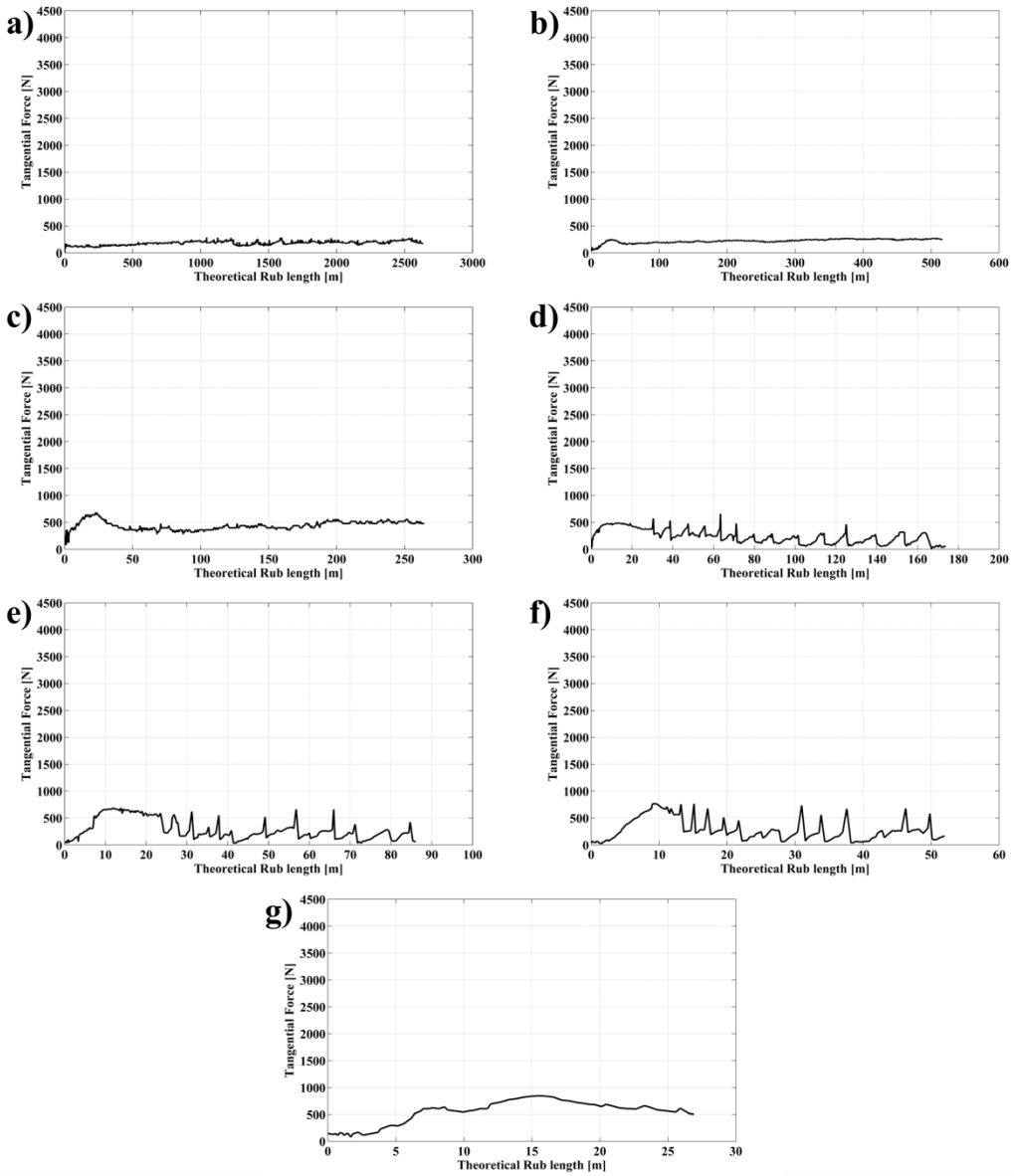

Figure 12. Tangential force measurement at blade speed of 100m s^{-1} and abradable coating hardness R15Y 54.6, at incursion rates of: a) 0.02µm·$pass^{-1}$; b) 0.1µm·$pass^{-1}$; c) 0.2µm·$pass^{-1}$; d) 0.3µm·$pass^{-1}$; e) 0.6µm·$pass^{-1}$; f) 1µm·$pass^{-1}$; g) 2µm·$pass^{-1}$.

4.7. Test sample R15Y 54.6 at 150m s^{-1}

Figure 13 and 14 shows the normal and tangential forces measured with blade speed of 150m s^{-1} with coating hardness R15Y 54.6.

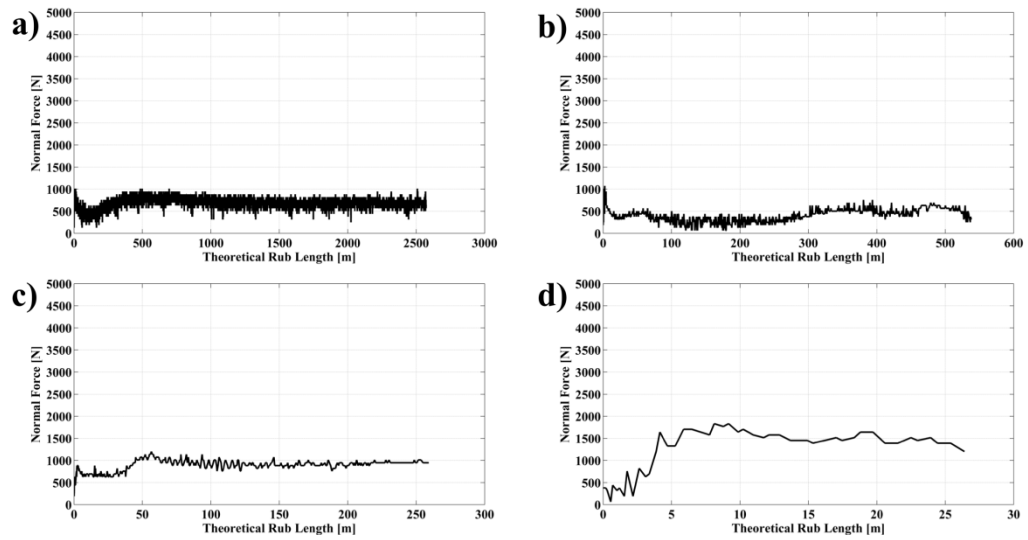

Figure 13. Normal force measurement at blade speed of 150m s^{-1} and abradable coating hardness R15Y 54.6, at incursion rates of: a) 0.02µm·$pass^{-1}$; b) 0.1µm·$pass^{-1}$; c) 0.2µm·$pass^{-1}$; d) 2µm·$pass^{-1}$.

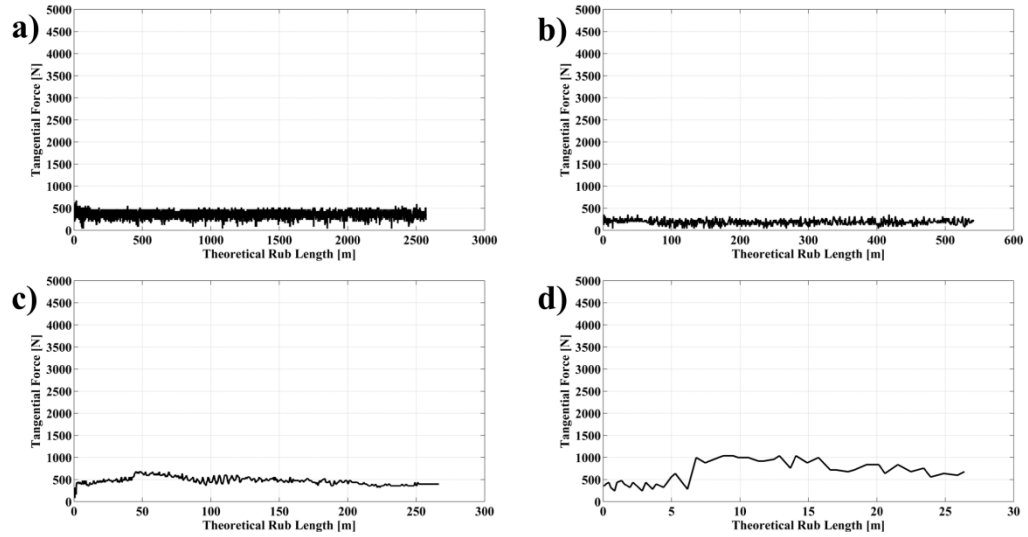

Figure 14. Tangential force measurement at blade speed of 150m s^{-1} and abradable coating hardness R15Y 54.6, at incursion rates of: a) 0.02µm·$pass^{-1}$; b) 0.1µm·$pass^{-1}$; c) 0.2µm·$pass^{-1}$; d) 2µm·$pass^{-1}$.

4.8. Test sample R15Y 54.6 at 200m s^{-1}

Figure 15 and 16 shows the normal and tangential forces measured with blade speed of 200m s^{-1} with coating hardness R15Y 54.6.

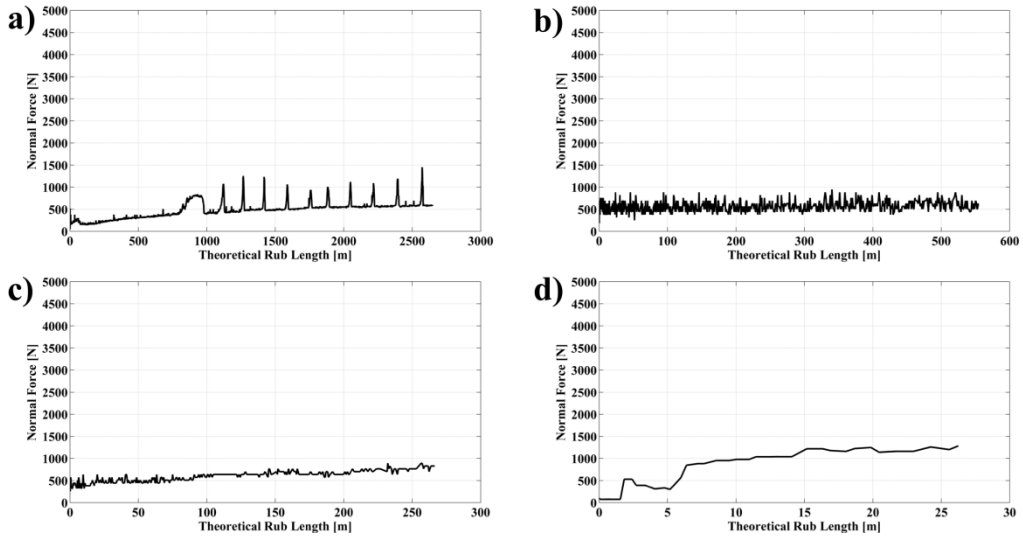

Figure 15. Normal force measurement at blade speed of 200m s^{-1} and abradable coating hardness R15Y 54.6, at incursion rates of: a) 0.02µm·$pass^{-1}$; b) 0.1µm·$pass^{-1}$; c) 0.2µm·$pass^{-1}$; d) 2µm·$pass^{-1}$.

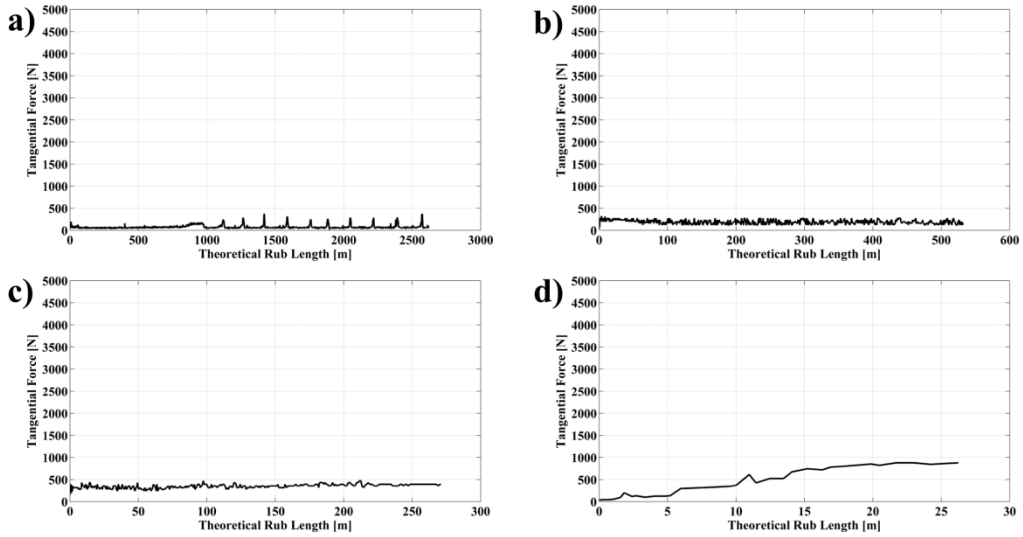

Figure 16. Tangential force measurement at blade speed of 200m s^{-1} and abradable coating hardness R15Y 54.6, at incursion rates of: a) 0.02µm·$pass^{-1}$; b) 0.1µm·$pass^{-1}$; c) 0.2µm·$pass^{-1}$; d) 2µm·$pass^{-1}$.